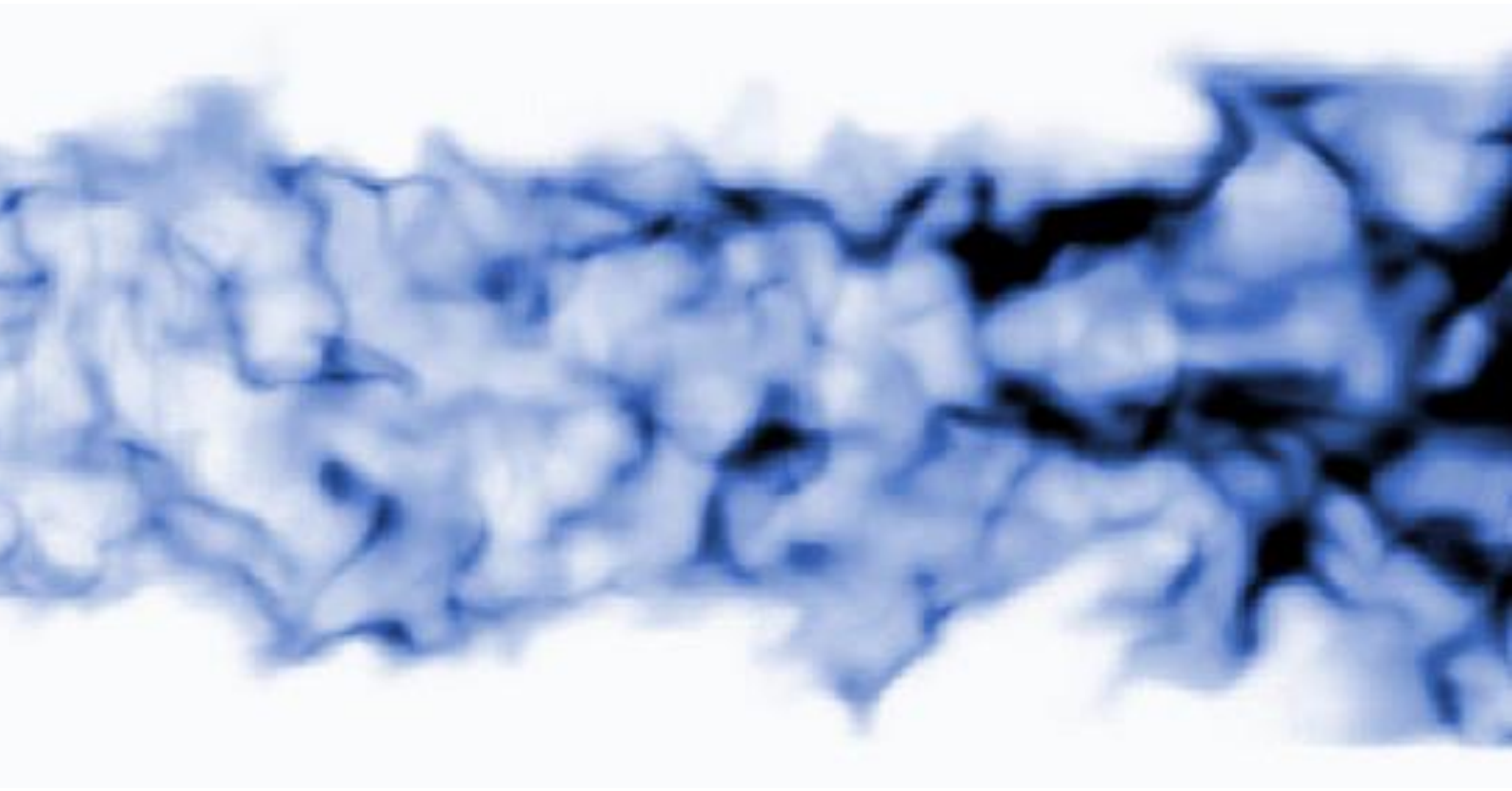

MEFTE 2014

Editors

Paulo Avilez-Valente
Elsa Carvalho
Alexandre Silva Lopes

APMTAC ASSOCIAÇÃO PORTUGUESA DE MECÂNICA TEÓRICA APLICADA E COMPUTACIONAL

FEUP FACULDADE DE ENGENHARIA UNIVERSIDADE DO PORTO

MEFTE 2014

MEFTE 2014

V Conferência Nacional de Mecânica dos Fluidos, Termodinâmica e Energia

11–12 Setembro 2014, Porto, Portugal

Editors

Paulo Avilez-Valente
Elsa Carvalho
Alexandre Silva Lopes

APMTAC ASSOCIAÇÃO PORTUGUESA DE MECÂNICA TEÓRICA APLICADA E COMPUTACIONAL

FEUP FACULDADE DE ENGENHARIA UNIVERSIDADE DO PORTO

APMTAC — Associação Portuguesa de Mecânica Teórica, Aplicada e Computacional
Laboratório Nacional de Engenharia Civil
Av. do Brasil 101
1700-066 Lisboa
apmtac@lnec.pt
www-ext.lnec.pt/APMATC

FEUP — Faculdade de Engenharia da Universidade do Porto
Rua Dr. Roberto Frias s/n
4200-465 Porto
feup@fe.up.pt
www.fe.up.pt

MEFTE 2014
Paulo Avilez-Valente, Elsa Carvalho, Alexandre Silva Lopes (Eds.)

First Edition: December 2014

Foreword

This book is a compilation of the papers presented at the 5th MEFTE conference—V Conferência Nacional de Mecânica dos Fluidos, Termodinâmica e Energia, MEFTE 2014—which took place at the Faculdade de Engenharia da Universidade do Porto (FEUP), Portugal, from 11 to 12 September 2014.

MEFTE 2014 was jointly promoted and organized by the Faculdade de Engenharia da Universidade do Porto (FEUP), the Centro Interdisciplinar de Investigação Marinha e Ambiental (CIIMAR-UP), the Instituto Superior Técnico da Universidade de Lisboa (IST-UL), the Faculdade de Ciências e Tecnologia da Universidade de Coimbra (FCTUC), the Escola de Engenharia da Universidade do Minho (EEUM) and the Laboratório Nacional de Engenharia Civil (LNEC), under the auspices of the Associação Portuguesa de Mecânica Teórica, Aplicada e Computacional (APMTAC).

The APMTAC biennially promotes this national scientific event, which aims to provide a discussion forum for researchers working in the fields of fluid dynamics, thermodynamics and energy. The previous four venues were held in Caparica in 2006, Aveiro in 2008, Bragança in 2009, and Lisbon in 2012. The Conference has, since its first edition, promoted the participation of young researchers and students, contributing to the dissemination of their work and fostering their links with other researchers and research groups.

MEFTE 2014 had three keynote lectures, and six sessions where 40 papers were orally presented, from a total of 63 abstracts submitted for evaluation. From these, a total of 41 papers or extended abstracts have been compiled into this book. The Organizing Committee expresses its appreciation and thanks all those who contributed to this event, in particular, the members of the Scientific Committee, as well as all authors and participants for their effort and dedication.

Finally, we thank the invited speakers for the keynote lectures for their contribution, making this conference a place to share knowledge and the state-of-the-art in fluid mechanics, thermodynamics and energy.

Porto, December 2014

The Conference Chairman

Paulo Avilez-Valente | U.Porto

Committees

Organizing Committee

Alexandre Silva Lopes	U.Porto | FEUP
António Manuel Gameiro Lopes	U.Coimbra | FCTUC
Carlos Bettencourt da Silva	U.Lisboa | Técnico
Conceição Juana Fortes	LNEC
Elsa Carvalho	U.Porto | FEUP
José S. Antunes do Carmo	U.Coimbra | FCTUC
Manuel Alves	U.Porto | FEUP
Manuela Lemos Lima	U.Minho | EEUM
Paulo Avilez-Valente	U.Porto | FEUP : Chairman
Rui Aleixo	U.Mississipi | NCCHE
Rui Caldeira	U.Porto | CIIMAR
Rui Ferreira	U.Lisboa | Técnico

Scientific Committee

Alejandro Crespo	U.Vigo | EPHYSLAB
António F. Miguel	U.Évora
A. Heitor Reis	U.Évora
Abel Rouboa	UTAD
Almerindo Domingues Ferreira	U.Coimbra | FCTUC
André Fortunato	LNEC
António Carlos Mendes	UBI
António Moreira	U.Lisboa | Técnico
António Sarmento	U.Lisboa | Técnico
Carlos Pinho	U.Porto | FEUP
Celestino R. Ruivo	U.Algarve | ISE
Domingos Xavier Viegas	U.Coimbra | FCTUC
Eric Didier	UNL | FCT
Fernando Tavares de Pinho	U.Porto | FEUP
Helena Ramos	U.Lisboa | Técnico
Jerónimo Puertas Agudo	U.Coruña
João Alfredo Santos	I.P.Lisboa | ISEL
João Campos	U.Porto | FEUP
João Melo de Sousa	U.Lisboa | Técnico
João Peças Lopes	U.Porto | FEUP
José Conde	UNL | FCT

Scientific Committee (cont.)

José Leonel M. Fernandes	U.Lisboa | Técnico
José Laginha Palma	U.Porto | FEUP
Luís Adriano Oliveira	U.Coimbra | FCTUC
Luís Eça	U.Lisboa | Técnico
Maria Graça Neves	LNEC
Mário Costa	U.Lisboa | Técnico
Miguel Teixeira	U.Reading
Paulo Oliveira	UBI
Paulo Piloto	I.P.Bragança
Pedro Coelho	U.Lisboa | Técnico
Roger Moreira	U.Federal Fluminense
Sílvio Gama	U.Porto | FCUP
Toste Azevedo	U.Lisboa | Técnico
Vicente Pérez-Muñuziri	U.Santiago de Compostela
Viriato Semião	U.Lisboa | Técnico
Vítor Costa	U.Aveiro

Secretariat

Manuel Carvalho	FEUP | DEC

Table of Contents

Keynote Lecture 1

Vicente Pérez-Muñuzuri | U.Santiago de Compostela

Lagrangian Coherent Structures in Nature

This page was intentionally left blank

Lagrangian analysis of atmospheric rivers

D Garaboa[1], J Eiras[1], F Huhn[2], V Pérez-Muñuzuri[1]

[1]Group of Nonlinear Physics, University of Santiago de Compostela. 15706 Santiago de Compostela. Spain
[2]ETH Zurich, Institute for Mechanical Systems, Center of Mechanics. Tannenstrasse 3, 8092 Zurich, Switzerland
email: angeldaniel.garaboa@usc.es, jorge.eiras@usc.es, florian.huhn@imes.mavt.ethz.ch,
vicente.perez.munuzuri@usc.es

ABSTRACT: Based on data retrieved from ERA-Interim, atmospheric rivers (AR) events over the North Atlantic Ocean that affect Iberian Peninsula were analyzed in terms of the Lagrangian transport. A two-dimensional approach was derived from water vapor flux to study the ARs spatiotemporal patterns occurring in the region. Using the Finite-Time Lyapunov Exponents (FTLE), Lagrangian Coherent Structures (LCS) were derived from the FTLE field. The LCS allow to identify separatrices of fluid regions with different advective properties. Our findings suggest that for strong filamentous AR, the transport of water vapor is advected from low latitudes, due to the presence of LCS heading the transport eastward.

KEY-WORDS: Atmospheric rivers; Lagrangian coherent structures; Lyapunov exponents.

1 INTRODUCTION

The transport of moisture from the tropics to mid-latitudes is not mild and uniform. More than 90% of poleward water vapor transport is accomplished by narrow and elongated (longer than 2000 km and narrower than 1000 km) structures within the mostly pre-cold frontal Warm Conveyor Belt (WCB), and the Low Level Jet (LLJ) of extratropical cyclones [1] commonly associated to the polar front. These structures, labeled as Tropospheric or Atmospheric Rivers (ARs), are defined as areas of Integrated Water Vapor (IWV) column over 2cm and winds stronger than 12.5 m/s, transporting water vapor in the lower troposphere, close to the 850 hPa level [2,3,4]. AR advection is the key to explain extreme precipitation and flood events, especially when they are forced to rise over the mountains. This connection has been analyzed over Western US Coast [3,5] and Europe [6,7], and a very high percentage of coincidence was found. For some AR events, a filament pattern develops in many parts of the world that lives enough time and strongly affects the overall mixing properties of a region where the AR takes place to be considered as a coherent structure.

The goal of this paper is to study the role that advection plays on the water vapor transport in the troposphere using Lagrangian measures such as the Finite Time Lyapunov Exponents (FTLE). The FTLE measures the maximum stretching rate over a fixed interval time of trajectories derived from neighboring fluid particles. Ridges of maximum separation rates in the FTLE are used to estimate the Lagrangian Coherent Structures (LCS) [8,9]. Lagrangian Coherent Structures (LCS) allow to identify regions with different transport properties and it is a tool to identify the invariant barriers in dynamical systems which head passive transport. The detection of coherent structures through Lagrangian measures was used to study complex dynamic of atmospheric, to characterize large scales phenomena, such as the Polar Vortex [10,11], the Subtropical Jet Stream [12], the transport in the troposphere by transient baroclinic eddies [13], or the transport of plankton bloom by the South Indian Ocean Countercurrent [14], among many others [15].

Specifically, our analysis is based on the study of spatiotemporal patterns formed during an AR event. Advection by unsteady wind fields in this kind of events shapes the water vapor transport structures, showing a widely variety of distributions. In particular for our region of interest, our data shows that AR events are dominated by eastward propagation, being some of them a strong jet from low latitudes. We show that for AR events with a filamentous shape, wind flow dominates the transport over other advection mechanisms and LCS along the AR event head the transport eastward [16].

2 DATA AND METHODS

We analyze the AR based on data retrieved from the European Center for Medium-Range Weather Forecast reanalysis, ERA-Interim, in terms of the Vertical integrals of Water Vapor and Eastward/Northward Water Vapor Flux at 0.7º×0.7º spatial resolution and six hours' time resolution.

$$Q = \frac{1}{g}\int_0^1 q\frac{\partial p}{\partial \eta}d\eta \tag{1}$$

$$\Phi_\lambda = \frac{1}{g}\int_0^1 uq\frac{\partial p}{\partial \eta}d\eta \qquad \Phi_\phi = \frac{1}{g}\int_0^1 vq\frac{\partial p}{\partial \eta}d\eta \tag{2}$$

with η a hybrid coordinate.

Variables given by Equations (1) and (2) were used to determine the Eastward and Northward Average Drift Velocities,

$$<\dot{\lambda}>=\frac{\Phi_\lambda}{Q} \qquad <\dot{\phi}>=\frac{\Phi_\phi}{Q} \tag{3}$$

with these new variables, the 2D flow velocity field is,

$$\mathbf{V_f} = (<\dot{\lambda}(\theta,\varphi,t)>,<\dot{\phi}(\theta,\varphi,t)>) \tag{4}$$

To obtain particle trajectories, we advect an uniform rectangular grid of tracers 1/5º from an initial position $\mathbf{r}_0(t_0)$ using the velocity fields given by Equation (4) to a final position $\mathbf{r}(t+\tau)$ with an integration time of $\tau = 120$ hours, typical time scale for the formation and propagation of the AR. Finally, after each finite time advection, τ, $\mathbf{r}(t_0+\tau) = \Omega_{t_0}^{t_0+\tau}(\mathbf{r_0}(t_0))$ we compute the Finite Time Lyapunov Exponents (FTLE) using:

$$\sigma(\mathbf{r}_0, t_0, \tau) = \frac{1}{|\tau|} log\sqrt{\mu_{max}(\mathbf{C}(\mathbf{x}_0))} \tag{5}$$

where $\mu_{\max}$ is the maximum eigenvalue of the right Cauchy-Green deformation tensor $\mathbf{C} = \mathbf{F}^{\mathrm{T}}\mathbf{F}$, where **F** is defined by $\mathbf{F}(\mathbf{r}_0) = \nabla\Omega_{t_0}^{t_0+\tau}(\mathbf{r_0}(t_0))$.

The FTLE at a given location measures the maximum stretching rate over the interval $\tau = t - t_0$ of trajectories starting near the point $\mathbf{r_0}$ at time t_0. Ridges of the FTLE field are used to estimate finite time invariant manifolds in the flow that separate dynamically different regions. Repelling (attracting) Lagrangian Coherent Structures for $\tau > 0$, ($\tau < 0$) are time-dependent generalizations of the stable (unstable) manifolds of the system. These structures govern the stretching and folding mechanism that control flow mixing.

3 RESULTS

Atmospheric Rivers have been observed as filamentous jet structures on the integrated water vapor column Q, Equation (1). Figure 1(a) shows an example of an AR jet transporting water vapor over the North Atlantic Ocean towards the Iberian Peninsula. As a result of this jet, intense precipitation rates were recorded at the North-West of the Iberian Peninsula. The ridge larger values of Q connecting the tropics with the North Atlantic Ocean shape a continuous AR structure. The backward FTLE field is shown in Figure 1(b). Note that the filament joining the Iberian Peninsula to the Gulf of Mexico shows a clear relationship to the Atmospheric River depicted previously. From a Lagrangian point of view, AR can be considered as an attracting LCS or unstable manifold of the flow dynamical system.

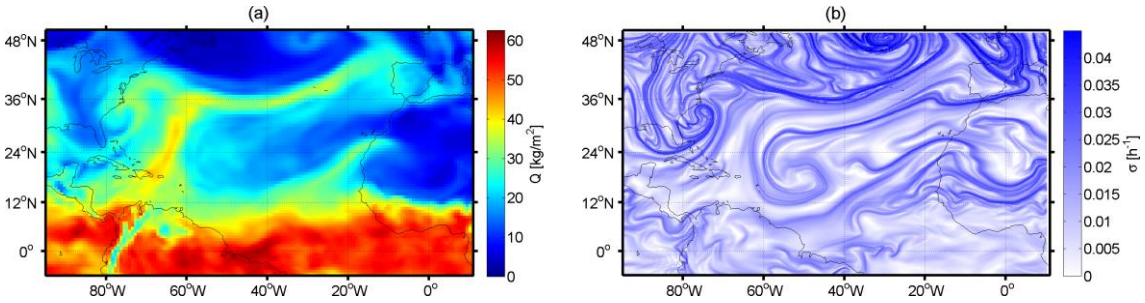

Figure 1: Atmospheric River event on May 19, 2000 in terms of the integrated water vapor column Q (a), and the corresponding backward FTLE field (b).

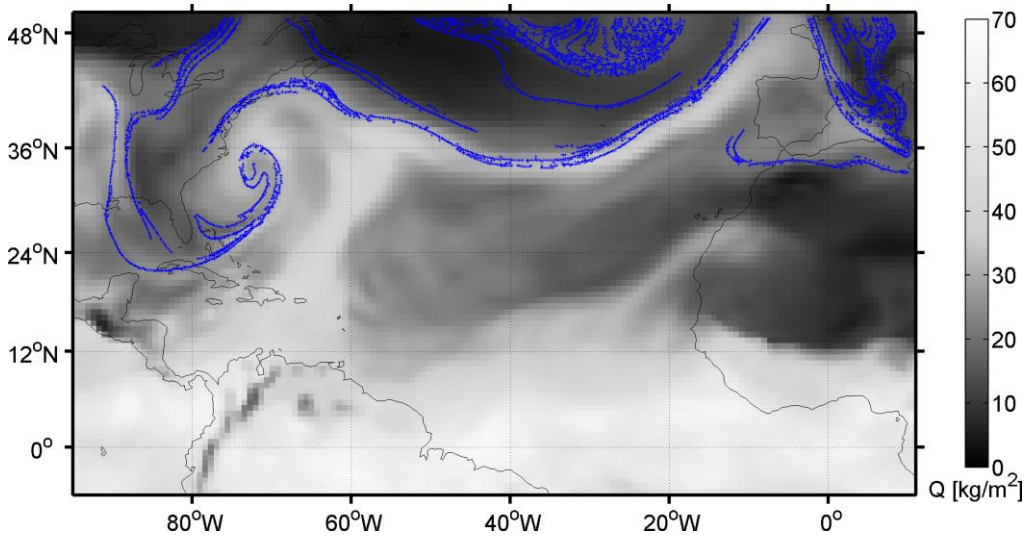

Figure 2: Lagrangian Coherent Structures (blue dots) and integrated water vapor column Q for the same Atmospheric River than in Figure 1.

Lagrangian Coherent Structures calculated from the backward FTLE fields are compared to the Q field, Equation (1), in Figure 2 for the AR shown previously. LCS and Q ridges show a filamentous structure, and have one or two narrow jets growing from low latitudes transporting water vapor to medium latitudes. This kind of ARs develop in winter season.

We hypothesized, that for AR with a narrow, well defined, shape, the main water vapor transport from the low latitudes is the passive advection due to wind advection, but for AR with a scattered shape (mainly during summer season), large areas with high concentrations of water vapor have been observed which have not a correspondence with advected passive tracers. In these regions, our approach is not valid, and the water vapor does not come only from low latitudes, but the source of water vapor maybe comes from a continuous evaporation mechanism, vertical transport between different pressure layers, or other physical transports that our approach cannot describe. In terms of the Lagrangian transport, LCS identified as attracting manifolds of the flow develop and follow the AR only if the wind is the main mechanism that advects water vapor from low latitudes into the northern ones.

4 CONCLUSIONS

The propagation of Atmospheric Rivers over the Iberian Peninsula has been studied in terms of Lagrangian tools. Based on an integrated water vapor flow obtained from the ERA-Interim database, AR events have been clearly identified with LCS. Two different events have been analyzed. On the one hand, for narrow filamentous ARs, with a fast and persistent eastward transport, an attracting LCS that acts as a boundary develops and heads the transport with the same shape than the river. This kind of AR is dominated by a strong wind advection which transports water vapor from low latitudes and typically develops in winter. On the other hand, for unstructured rivers, mostly occurring during the summer season, no jet-type LCS seems to develop. This kind of events is not only defined in terms of wind

transport, and the separation between passive advection and other transport mechanisms, is not solved by our approach.

Finally, we conclude that this connection between LCS and an AR in terms of Lagrangian transport, should be take into account for future studies and help to characterize this kind of events. An extensive analysis with more AR events could help to set up a definition of AR in terms of Lagrangian analysis. Our results presented here maybe of importance for other regions where AR activity exists.

REFERENCES

[1] PJ Neimann, FM Ralph, GA Wick, Y-H Kuo, T-K Wee, Z Ma, GH Taylor, MD Dettinger (2008). Diagnosis of an intense atmospheric river impacting the Pacific Northeast: Storm summary and offshore vertical structure with COSMIC satellite retrievals. *Monthly Weather Review* **136**:4398–4420.

[2] Y Zhu, RE Newell (1994). Atmospheric rivers and bombs. *Geophysical Research Letters* **21**:1999–2002.

[3] FM Ralph, PJ Neimann, GA Wick (2004). Satellite and CALJET aircraft observations of atmospheric rivers over the eastern North Pacific Ocean during the winter of 1997/1998. *Monthly Weather Review* **132**, 1721–1745.

[4] J Bao, S Michaelson, P Neiman, F Ralph, J Wilczak (2006). Interpretation of enhanced integrated water vapor bands associated with extratropical cyclones: Their formation and connection to tropical moisture. *Monthly Weather Review* **134**:1063–1080.

[5] LR Leung, Y Qian (2009). Atmospheric rivers induced heavy precipitation and flooding in the western US simulated by the WRF regional climate model. *Geophysical Research Letters* **36**(3):L03820.

[6] DA Lavers, G Villarini (2013). The nexus between atmospheric rivers and extreme precipitation across Europe. *Geophysical Research Letters* **40**(12):3259–3264.

[7] A Stohl (2001). A 1-year Lagrangian ”climatology” of airstreams in the northern hemisphere troposphere and lowermost stratosphere. *Journal of Geophysical Research* **106**:7263–7279.

[8] G Haller (2000). Finding finite-time invariant manifolds in two-dimensional velocity fields, *Chaos* **10**, 99–108.

[9] SC Shadden, F Lekien, JE Marsden (2005). Definition and properties of Lagrangian Coherent Structures from finite-time Lyapunov exponents in two-dimensional aperiodic flows. *Physica D* **212**:271–304.

[10] FJ Beron-Vera, MJ Olascoaga, MG Brown, H Koçak, II Rypina (2010). Invariant-tori-like Lagrangian coherent structures in geophysical flows. *Chaos* **20**:017514.

[11] T-Y Koh, B Legras (2002). Hyperbolic lines and the stratospheric polar vortex. *Chaos* **12**(2):382–394.

[12] W Tang, M Mathur, G Haller, DC Hahn, FH Ruggiero (2010). Lagrangian coherent structures near a subtropical jet stream. *Journal of the Atmospheric Sciences* **67**:2307–2319.

[13] J von Hardenberg, K Fraedrich, F Lunkeit, A Provenzale (2002). Transient chaotic mixing during a baroclinic life cycle. *Chaos* **10**(1):122–134.

[14] F Huhn, A von Kameke, V Pérez-Muñuzuri, MJ Olascoaga, FJ Beron-Vera (2012). The impact of advective transport by the South Indian Ocean Countercurrent on the Madagascar plankton bloom. *Geophysical Research Letters* **39**:L06602.

[15] F Huhn, A von Kameke, S Allen-Perkins, P Montero, A Venancio, and V Pérez-Muñuzuri (2012). Horizontal Lagrangian transport in a tidal-estuary—Transport barrier attached to prominent coastal boundaries. *Continental Shelf Research* **39–40**:1–13.

[16] A Garaboa, J Eiras, F Huhn, V Pérez-Muñuzuri (Submitted). Lagrangian Coherent Structures as a measure of Atmospheric Rivers strength coherence. *Geophysical Research Letters*.

Session 1

Chairman

Alexandre Silva Lopes | U.Porto

This page was intentionally left blank

Ground-effect simulations based on an efficient boundary element method

G Farinha[1], P Quental[1], L Eça[1], D Matos Chaves[2]

[1]Departmento de Engenharia Mecânica, Instituto Superior Técnico, Universidade de Lisboa, Av. Rovisco Pais 1, 1049-001 Lisboa, Portugal
[2]Technip UK Limited, UK
email: guilherme.a.farinha@tecnico.ulisboa.pt; pauloricardoquental@tecnico.ulisboa.pt; luis.eca@tecnico.ulisboa.pt, diogo_chaves@hotmail.com

ABSTRACT: This paper presents the application of a boundary element method (commonly known as a panel method), which is able to solve the steady, two-dimensional, potential flow around airfoils, with an arbitrary number of components, to the calculation of airfoils in the vicinity of a wall, i.e. including ground-effect. The method requires modest computer requirements and extremely small calculation times even for discretizations that lead to negligible numerical uncertainties. At small angles of attack, the results obtained from this simple approach are qualitatively similar to those obtained experimentally.

KEY-WORDS: Boundary element method; Airfoils; Ground-effect; Numerical uncertainty.

1 INTRODUCTION

The fast development of computer hardware has replaced mathematical models based on potential flow theory by viscous flow solvers based on the Reynolds-Averaged Navier-Stokes (RANS) equations in many practical applications including the calculation of the flow around airfoils, see for example [1]. However, there are specific problems, as for example optimization and/or uncertainty quantification, where the number of solutions required makes the use of RANS solvers extremely time consuming. Therefore, fast and robust potential flow solvers can still play a useful role in engineering applications.

In this paper, we address the calculation of the lift coefficient in single and two-component airfoils in the vicinity of a wall, i.e. including the presence of ground effect. To this end we apply a boundary element method (commonly known as a panel method) that is able to solve the steady, two-dimensional, potential flow around airfoils with an arbitrary number of components with modest computer requirements and an extremely small calculation time. The presence of the wall is modeled by the method of images, which means that we will double the number of components of each test case. The goal of the present work is twofold:

1. Assess the grid density required to obtain negligible numerical uncertainties in the predicted lift coefficient.
2. Check the ability of this simple approach to obtain reasonable predictions of the ground effect in the lift coefficient.

The first topic is addressed with grid refinement studies performed to a single element airfoil in an unbounded domain and for an airfoil with a high-lift device in the vicinity of a wall. This type of studies requires a careful definition of the airfoil geometry to allow the generation of geometrically similar grids with an arbitrary number of panels.

Naturally, we cannot expect to make quantitative predictions of the lift coefficient based on potential flow theory. Therefore, our aim is to compute the ratio between the lift coefficients obtained with and without ground effect for single and double element airfoils and compare it with values obtained from experiments.

The paper is organized in the following way: section 2 gives a brief description of the boundary element method (panel method); the interpolation of airfoil geometries and grid generation is described in section 3 and the results of the application to single and double element airfoils is presented and discussed in section 4; Finally, section 5 summarizes the main conclusions of this study.

2 BOUNDARY ELEMENT METHOD

2.1 Mathematical formulation

The flow of an ideal fluid around an arbitrary number of lifting bodies (airfoils) is assumed to be steady, two-dimensional, incompressible and irrotational. In such conditions, the velocity potential ϕ satisfies the Laplace equation $\vec{\nabla}\cdot\left(\vec{\nabla}\phi\right)=0$. The boundary conditions are obtained from the impermeability condition on the airfoils surface $\vec{\nabla}\phi\cdot\vec{n}=0$ and the velocity vector at infinity is equal to the undisturbed velocity $\vec{\nabla}\phi=\vec{U}_{\infty}$.

An efficient way to obtain ϕ is to explore the linearity of the problem, see for example [2], and to decompose the velocity potential into $\phi=\phi_{\infty}+\Phi$, where ϕ_{∞} is the known velocity potential of the undisturbed flow and Φ is the perturbation potential represented by line sources/sinks distributed on the surface of the foils. All these velocity potentials satisfy the Laplace equation and so the application of the boundary condition at each point P on the surface of the N_c components of the airfoil determines the strength σ of the sources/sinks.

$$\frac{\sigma(P)}{2}+\left[\sum_{i=1}^{N_c}\int_{S_i}\frac{\sigma(q)}{2\pi}\frac{\partial}{\partial n_P}\left[\ln\left(r(P,q)\right)\right]dS\right]+\vec{\nabla}\phi_{\infty}\cdot\vec{n}_P=0 \tag{1}$$

The velocity potential defined by $\phi=\phi_{\infty}+\Phi$ gives a flow with no circulation, which does not satisfy the Kutta condition, i.e. finite velocity at the trailing edge of all airfoil components. In the present method, vortices are distributed along the mean line of each airfoil component (with a velocity potencial defined by $\gamma_i\left(\phi_\Gamma\right)_i$ to guarantee the satisfaction of the Kutta condition. γ_i are $N_{airfoils}$ constants to be determined by the application of the Kutta condition to each airfoil component. This leads to

$$\frac{\sigma(P)}{2}+\left[\sum_{i=1}^{N_c}\int_{S_i}\frac{\sigma(q)}{2\pi}\frac{\partial}{\partial n_P}\left[\ln\left(r(P,q)\right)\right]dS\right]+\sum_{i=1}^{N_c}\gamma_i\left(\left(\vec{\nabla}\phi_\Gamma\right)_i\cdot\vec{n}_P\right)+\vec{\nabla}\phi_{\infty}\cdot\vec{n}_P=0 \tag{2}$$

2.2 Discretization

There are three different approximations required for the transformation of equation (2) into a system of algebraic equations: the geometric description of the airfoil components; the function that defines the strength of the source/sink distributions and the distribution of the vortices along the mean lines of the airfoil components.

Each airfoil component is discretized with NCP_i flat panels (half on each side of the airfoil component) which are defined by NBP_i boundary points, which is the simplest choice available for the geometric discretization. Nevertheless, it is a consistent approach, i.e. the discretization error tends to zero when the number of panels/elements goes to infinity. In each linear element/flat panel, the source/sink strength $\sigma(q)$ is assumed to be constant. This means that will have NCP_i unknown source/sinks strengths for each airfoil element.

The vortices that guarantee the satisfaction of the Kutta condition are located on mean line panels that are obtained from the average of the surface boundary points. The strength of the vortex distribution is piecewise constant and is proportional to $s_{m_i}^{0.4}$ [2], where s_{m_i} is the distance of the mid-point of the panel to the trailing edge.

The present discretization leads to $NT_{eq}=\sum_{i=1}^{N_{airfoils}}\left(NCP_i+1\right)$ unknowns that are determined by satisfying the boundary condition of zero normal velocity (equation (2)) at the midpoint (control points) of each surface panel ($\sum_{i=1}^{N_c}NCP_i$ equations) and satisfying the Kutta condition at the trailing edge of all the airfoil components (N_c equations). Following the results presented in [2], the Kutta condition is numerically satisfied by the equality of the tangential velocity components at the control points of the two panels that contain the trailing edge. Therefore, we obtain a system of NT_{eq} algebraic equations that has the following structure for a single component airfoil:

$$\begin{aligned}&\sum_{j=1}^{NCP}A_{ij}\sigma_j+\gamma A_{i(NCP+1)}=-\vec{\nabla}\phi_{\infty}\cdot\vec{n}_i \text{ for } i=1 \text{ to } NCP\\&\sum_{j=1}^{NCP}A_{(NCP+1)j}\sigma_j+\gamma A_{(NCP+1)(NCP+1)}=-\vec{\nabla}\phi_{\infty}\cdot\vec{t}_1-\vec{\nabla}\phi_{\infty}\cdot\vec{t}_{NCP}\end{aligned} \tag{3}$$

where

$$
\begin{aligned}
A_{i(NCP+1)} &= \left(\vec{\nabla}\phi_{\Gamma} \cdot \vec{n}_P\right) \\
A_{(NCP+1)j} &= B_{1j} + B_{NCPj} \\
A_{(NCP+1)(NCP+1)} &= \vec{\nabla}\phi_{\Gamma} \cdot \vec{t}_1 + \left(\vec{\nabla}\phi_{\Gamma} \cdot \vec{t}_{NCP}\right)
\end{aligned} \tag{4}
$$

In the previous equations, A_{ij} and B_{ij} are the matrices of influence coefficients [2] and $\vec{t}_i$ are the unit vectors tangent to the panels. The system of $(NCP+1)\times(NCP+1)$ linear equations can be designated by $Aq = b$. For $N_{airfoils}$, the system of NT_{eq} equations has a similar structure to that defined above $C_{ij}Q_j = B_i$, where each entry of matrix C_{ij} and vectors Q_j and B_i correspond to A, q and b defined above.

$$
\begin{bmatrix}
C_{11} & C_{12} & \cdots & C_{1N_c} \\
C_{21} & C_{22} & \cdots & C_{2N_c} \\
\vdots & \vdots & \ddots & \vdots \\
C_{N_c1} & C_{N_c2} & \cdots & C_{N_cN_c}
\end{bmatrix}
\begin{bmatrix} Q_1 \\ Q_2 \\ \vdots \\ Q_{N_c} \end{bmatrix} =
\begin{bmatrix} B_1 \\ B_2 \\ \vdots \\ B_{N_c} \end{bmatrix} \tag{5}
$$

For example, C_{12} contains the influence of the singularity distributions on the second component of the airfoil in the first component.

With the present method it is straightforward to study ground effect using the method of images. The ground is assumed to be a mirror and so we just have to include the mirrored airfoil components to guarantee that the ground is a streamline.

2.3 Solution procedure

The method has been implemented in MATLAB© [3] with a modular structure. There are four basic routines required: geometry definition that includes the determination of control points, panel length and normal and tangential vectors; calculation of the influence coefficients and post-processing for the determination of the pressure distribution on the surface of the airfoil components, which allows the determination of the force coefficients by integration.

3 GRID GENERATION

Although grid generation for the present method seems to be a trivial problem, the fact that many airfoil configurations are defined by tables of points leads to the need to use interpolation in the grid generation procedure. Furthermore, typical grid generation procedures use cosine distributions along the chord that must be done carefully to avoid geometric discretization errors that do not vanish with grid refinement.

The present grid generation procedure relies on an interpolation procedure that splits any airfoil component into three regions: leading edge, upper surface and lower surface. The generation of a grid for an airfoil defined by a table of points that has the x coordinate aligned with the chord and the y coordinate perpendicular to it includes the following steps:

1. Determine a 4th order polynomial of $x = f(y)$ based on the leading edge (replaced by the point with minimum *x* if the leading edge is not included) and the two surrounding points of the upper and lower surfaces (5 points in total).
2. Determine the minimum *x* coordinate defined by $x = f(y)$, designated by $x_{\min}$.
3. Determine two 3rd order splines for the upper and lower surfaces of the airfoil including all points available on the table except the leading edge and the nearest point to it. The first-derivatives on the left side (closest to the leading edge) are obtained from $x = f(y)$ and the second derivative at the trailing edge ($x_{\max}$) is assumed to be zero.
4. Make a cosine distribution along the line defined by $x_{\min}$ and $x_{\max}$ and determine the *y* coordinates from the 4th order polynomial or the 3rd order spline of the upper and lower surfaces.

An example of the interpolation procedure is given in Figure 1 that presents a 160 panels grid of the NACA 4412 airfoil with an enlarged view of the leading edge region.

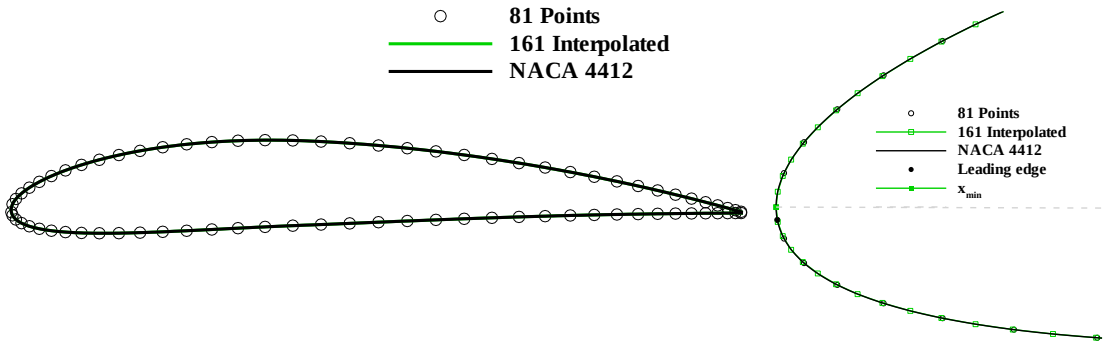

Figure 1: Interpolation of a 161 points grid from a table of 81 points of the NACA 4412 airfoil. Comparison with the analytical definition of the airfoil.

4 RESULTS

4.1 Test cases

We have studied ground effect for two different airfoil configurations: a single element airfoil [4] and a two component airfoil [5,6] in two different configurations. Figure 2 illustrates the geometries of the selected test cases. The plots include the images used to simulate the ground effect and the definition of the distance to the ground *h*.

4.2 Numerical uncertainty

The first step of our study is the estimation of the numerical uncertainty of the calculated lift coefficient C_l of the single and double element airfoils for different values of h/c where c is the chord for the single element or the distance between the leading edge of the main element and the average location of the trailing edge for the double element. c is also used as the reference length for the determination of C_l. To this end we have made 13 grids for each case that range from 160 to 1280 panels per airfoil element, which correspond to a grid refinement ratio of 8. The numerical uncertainty is determined with the procedure proposed in [7] based on the data of the 5 finest grids.

Figure 3 presents the convergence of the lift coefficient C_l with the grid refinement as a function of the typical grid size h_i/h_1 for the three geometries tested and different values of h/c. The results suggest the following remarks:

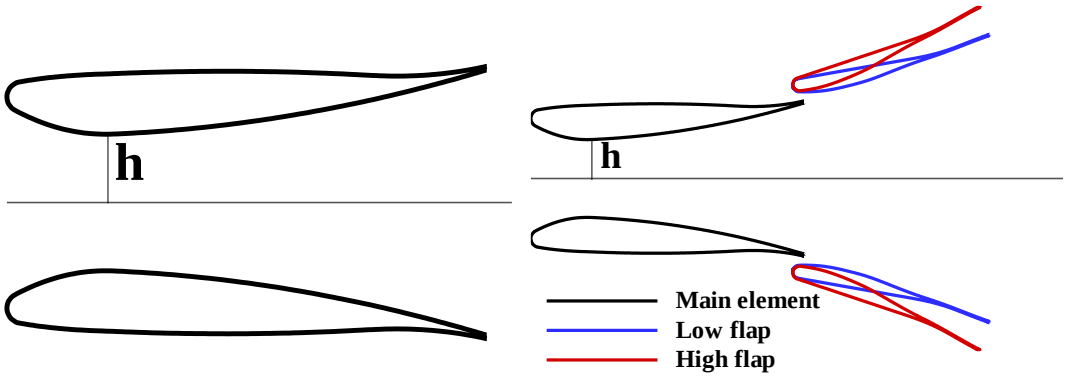

Figure 2: Illustration of the single component airfoil and of the two configuration of the double component airfoil.

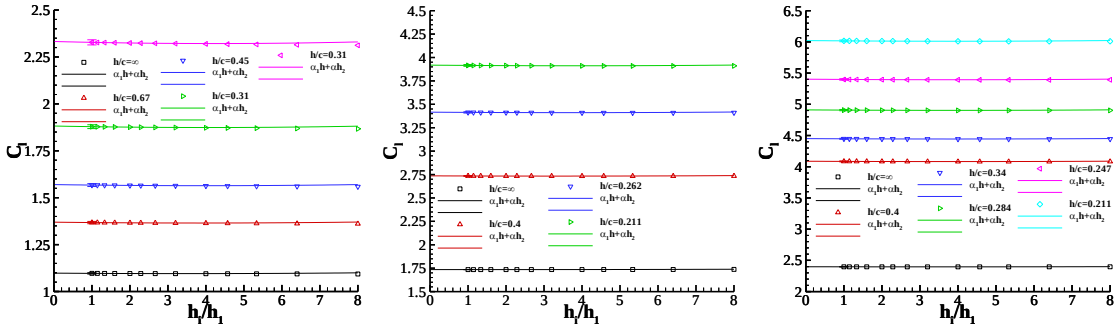

Single element Low flap High flap

Figure 3: Convergence of the lift coefficient C_l of the three configurations (single and double element airfoils) tested with the typical grid size h_i/h_1 .

- The convergence properties are similar for all the geometries tested. The best fit is obtained with a two terms power series expansion, but the results exhibit a nearly linear behaviour with h_i/h_1 that changes slope for the three finest grids (the scale of the plots does not allow a clear identification of this data behaviour).
- The numerical uncertainty of the lift coefficient determination is smaller than that obtained from the size of the symbols in the plots. For the present level of grid refinement, the largest estimated uncertainty of all the cases plotted in Figure 3 is smaller than 0.4%.

4.3 Ground effect

Naturally, we cannot expect to make realistic predictions of the lift coefficient of such configurations with a model based on potential (ideal) fluid theory. Our aim is to explore the ability to determine in a fast and efficient way the qualitative consequences of ground effect. Therefore, our quantity of interest is the ratio between the lift coefficients obtained with and without ground effect. Unfortunately, we do not have the experimental lift coefficient for the double element airfoils without ground effect and so for those cases we have assumed that $C_{l\infty}$ corresponds to the largest value of h/c .

Figure 4 presents the results obtained for the three geometries tested. The data suggest the following remarks:

- The qualitative effect of the ground effect is reasonably captured by the present potential flow model, which was the main goal of the present exercise.
- The numerical uncertainty of the calculations is much smaller than the difference between predictions and experiments confirming the quantitative limitations of potential flow models, especially for the smallest values of h/c tested.

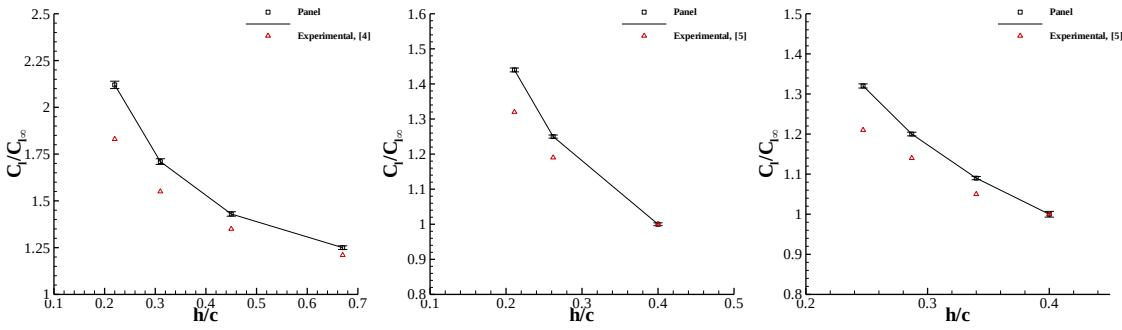

Single element Low flap High flap

Figure 4: Ratio of lift coefficient C_l without and with ground effect as a function of the non-dimensional distance to the ground h/c .

5 CONCLUSIONS

The present paper presents a simple potential flow model for the calculation of the flow around airfoils with multi-components, which allows a fast and efficient evaluation of the ground effect. Naturally, the method is limited to the evaluation of lift coefficients. Nevertheless, the qualitative trends of ground effect are reasonably captured for three practical test geometries with very modest computer requirements (at the level of a cell phone in nowadays!).

REFERENCES

[1] C Rumsey (2014). *2D NACA 0012 Airfoil Validation Case* [WWW]. Available from: http://turbmodels.larc.nasa.gov/naca0012_val.html/.

[2] LRC Eça, JAC Falcão de Campos (1993). Analysis of two-dimensional foils using a viscous-inviscid interaction method. *International Shipbuilding Progress* **40**(422):137–163.

[3] MATLAB (2010). MATLAB version 7.10.0. Natick, Massachusetts, The MathWorks Inc.

[4] J Zerihan, X Zhang (2000). Aerodynamics of a single element wing in ground effect. *Journal of Aircraft* **37**:1058–1064.

[5] X Zhang, J Zerihan (2003). Aerodynamics of a double-element wing in ground effect. *AAIA Journal* **41**:1007–1016.

[6] X Zhang, W Toet, J Zerihan (2006). Ground effect aerodynamics of race cars. *Applied Mechanics Reviews* **59**(1):33–49.

[7] L Eça, M Hoekstra (2014). A procedure for the estimation of the numerical uncertainty of CFD calculations based on grid refinement studies. *Journal of Computational Physics* **262**:104–130.

Application of blade element momentum theory to the analysis of a horizontal axis wind turbine

C Godreau[1], J Caldeira[2], JAC Falcão de Campos[2]

[1]MARETEC, Instituto Superior Técnico, Universidade de Lisboa, Av. Rovisco Pais 1, 1049-001, Lisboa Portugal
[2]Department of Mechanical Engineering, Instituto Superior Técnico, Universidade de Lisboa, Av. Rovisco Pais 1, 1049-001, Lisboa Portugal
email: cyrilgodreau@gmail.com, joaomcaldeira@tecnico.ulisboa.pt, falcao.campos@tecnico.ulisboa.pt

ABSTRACT: The prediction of the aerodynamic performance of horizontal axis wind turbines is of great importance in the design and analysis of such systems. Recent progress in computational power made Computational Fluid Dynamics (CFD) suitable for accurate simulations of such systems. However, reduced order models are still used in design studies because of their simple implementation and their light computational cost. The Blade Element Momentum theory (BEM) is commonly employed to model horizontal axis wind turbines. In this work two implementations of this model are considered, respectively, in an in-house code at IST and in the widely used FAST code developed by NREL. The codes are used to compute the performance of the 10-meter diameter NREL wind turbine, tested in the NASA Ames wind tunnel. The effects of including the tip and hub loss factors, and the drag in the momentum equations on the performance predictions are shown. The importance of using lift and drag data corrected for the effects of rotational augmentation and stall delay is discussed. The turbine blade radial load distributions and the rotor power and thrust are compared with experimental data in a range of tip speed ratios. Reasonable agreement is found between the results from the two codes and the experimental data.

KEY-WORDS: Horizontal axis wind turbines; Blade Element Momentum theory; Comparison with experiment.

1 INTRODUCTION

Between the 90's and early 2000s, the NREL in conjunction with the NASA has instrumented and tested a 20 kW horizontal wind turbine in order to produce extensive measurements for the wind turbine modeling community [1]. The turbine considered in the last phase (Phase VI) had a 10 m diameter rotor, with twisted and tapered blades. The airfoil profile used was the S809 and the turbine was stall regulated. This turbine has been investigated by many authors, and was the object of a code comparison exercise [2]. The objective of this work is to assess the predictions of NREL's aerodynamic model, in comparison with a simple implementation of the BEM theory in use at IST, in a simple axial inflow condition.

NREL's aerodynamic model, AeroDyn v14.02.00c [3] (distributed in FAST v8.03.02b [4]), is used to calculate aerodynamic forces. AeroDyn uses the quasi-steady blade-element momentum (BEM) theory including the effects of axial and tangential induction and Glauert correction for high induction factors. The BEM aerodynamic calculations include tip and hub losses models based on Prandtl's model, and a skewed wake correction. BEM-IST [5] is a direct implementation of the Blade Element Momentum theory by the IST, with Prandtl tip loss correction.

2 BLADE ELEMENT MOMENTUM THEORY AND IMPLEMENTATION

2.1 Basic BEM relations

The BEM theory relies on the application of the momentum theory on rotating blade elements, defining the turbine's rotor by annular regions. The elemental axial and tangential blade forces, F_x and F_θ respectively, are related to the lift and drag of blade sections by:

$$\begin{cases} \dfrac{dF_x}{dr} = L\sin(\beta_i) + D\cos(\beta_i) \\ \dfrac{dF_\theta}{dr} = L\cos(\beta_i) - D\sin(\beta_i) \end{cases} \quad (1)$$

The application of axial and tangential momentum equations ultimately leads to the iterative calculation of the axial and tangential induction factors $a = v_a/U$ and $a' = v_t/\Omega r$, defined as the non-dimensional axial and tangential induced velocities, respectively. The relations are:

$$\frac{a}{1-a} = \frac{ZcC_L \cos\beta_i (1+\varepsilon \tan\beta_i)}{8\pi r \sin^2 \beta_i}$$
$$\frac{a'}{1-a'} = \frac{ZcC_L (1-\varepsilon \cot\beta_i)}{8\pi r \cos\beta_i} \quad (2)$$

where Z is the number of blades, r is the section radius, β_i the aerodynamic pitch angle, c the section chord, $C_L = \frac{L}{\frac{1}{2}\rho V^2 c}$ the lift coefficient and $\varepsilon = \frac{C_D}{C_L}$ the drag to lift ratio.

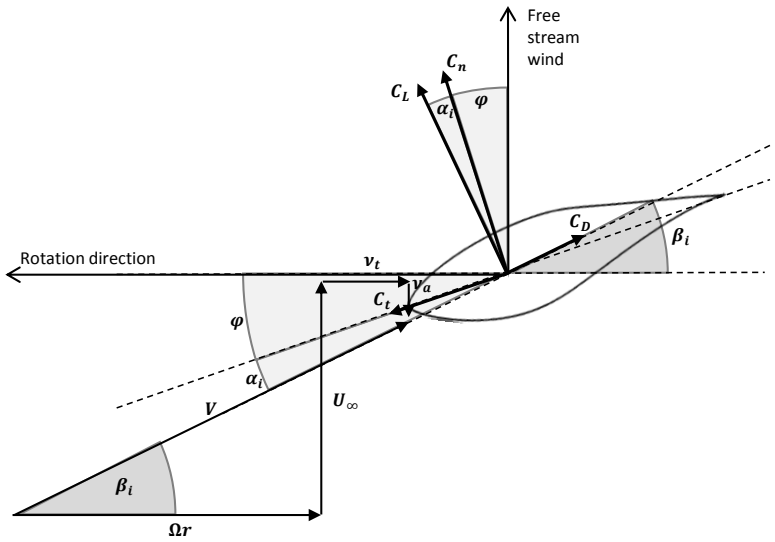

Figure 1: Velocity vectors and used coefficients.

2.2 Lift and drag data

In 2002, Schreck and Robinson studied the aerodynamics of the UAE rotor Phase VI [6]. They found out that rotating blades had different aerodynamic behavior than stationary blades. In rotational blades, stall occurs for higher angles of attack than for stationary blades, providing higher lift and thrust. This is called stall delay. It results in the augmentation of the blade normal forces along the blade. It is most pronounced at inboard locations, where normal force can be 2.5 times larger than for a stationary blade at stall levels. This phenomena is attenuated at blade locations farther outboard on the rotating blade.

In order to take this phenomenon into account and for comparison consistency, the same C_L and C_D tables are input for both BEM-IST and FAST. These tables are preprocessed by a spreadsheet called AirfoilPrep [7]. It uses Viterna's method to extrapolate lift and drag tables of a reduced range of angles of attack. It applies a rotational augmentation correction for stall delay using Du's method to augment lift and Eggers' method to modify the drag.

3 RESULTS

The calculations were performed for turbine operation conditions with and without flow separation, with a 3 degrees fixed pitch and a zero nacelle yaw angle. The flexibility of the blades and tower was not taken into account. In FAST, 31 elements were defined spanwise, with thinner elements at the tip and a cylinder approximated blade root. In BEM-IST, 30 elements were defined in the spanwise direction for the present work.

3.1 Effect of rotational augmentation

As mentioned above, the rotational effects, are of great importance when modelling the performance of such a wind turbine. Being stall regulated, the turbine is strongly affected by stall delay. Figures 2 and 3 show an example of the lift and drag coefficients used in the simulations. These data are derived from an

experiment conducted in Ohio State University (OSU) in the 90s [8]. Lift and drag coefficients were measured for a limited range of angles of attack, the tables were then extended and adjusted for stall delay due to rotational augmentation at different blade locations (8 in total). It can be seen that in near stall conditions the difference in lift and drag is large. These conditions are reached at low tip speed ratios $\left(\mathrm{TSR} = \Omega R / U_{\infty}\right)$ and this explains the difference between the power and thrust curves in Figures 4 and 5. Figures 4 and 5 also show that when using the same adjusted tables, both models display a fair agreement along the range of TSRs considered. BEM-IST seems to underestimate the thrust at low TSRs and underestimate the power at the highest TSR. FAST power and thrust curves seem to match tightly experimental results.

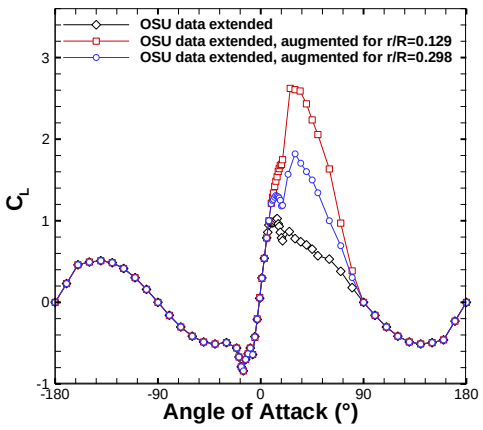

Figure 2: Rotational augmentation correction on lift coefficients.

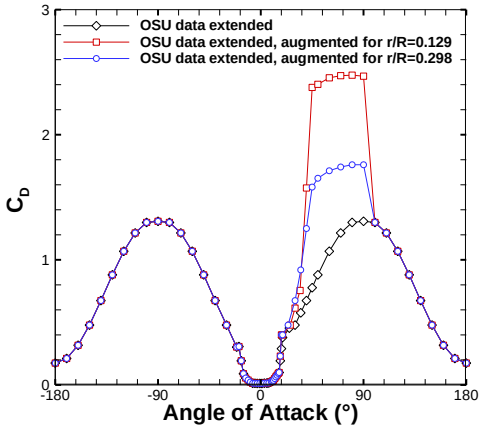

Figure 3: Rotational augmentation correction on drag coefficients.

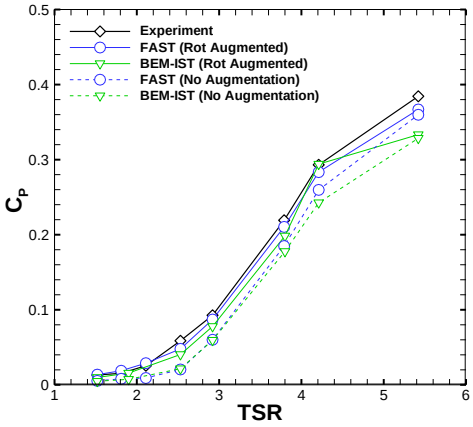

Figure 4: Effect of rotational augmentation correction on power coefficients.

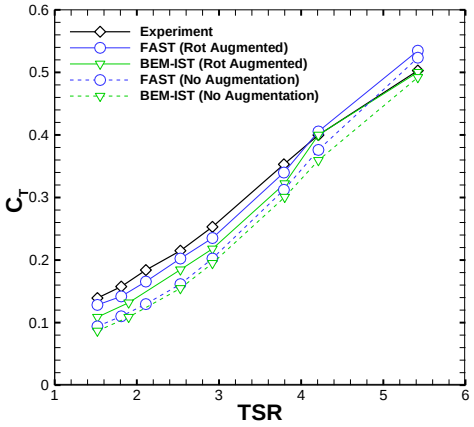

Figure 5: Effect of rotational augmentation correction on thrust coefficients.

3.2 Drag forces in the momentum equations

There is no consensus in the aerodynamic community considering the way drag forces should be taken into account in the momentum equations. In FAST, the default option excludes drag forces in these calculations. However, it can be included in the axial and/or tangential balances. Figure 6 and 7 show the effects of this inclusion on the induced velocities in FAST.

At high TSRs, the influence of drag inclusion is not of great importance. However at low TSR, one can observe that the inclusion of drag forces in the axial balance leads to a larger estimation of induced velocities at inboard elements. Notably, tangential velocities take negative values at the tip elements when

drag forces are included in the tangential balance. This occurs at all TSRs. It would suggest that each blade drags the flow at the tip.

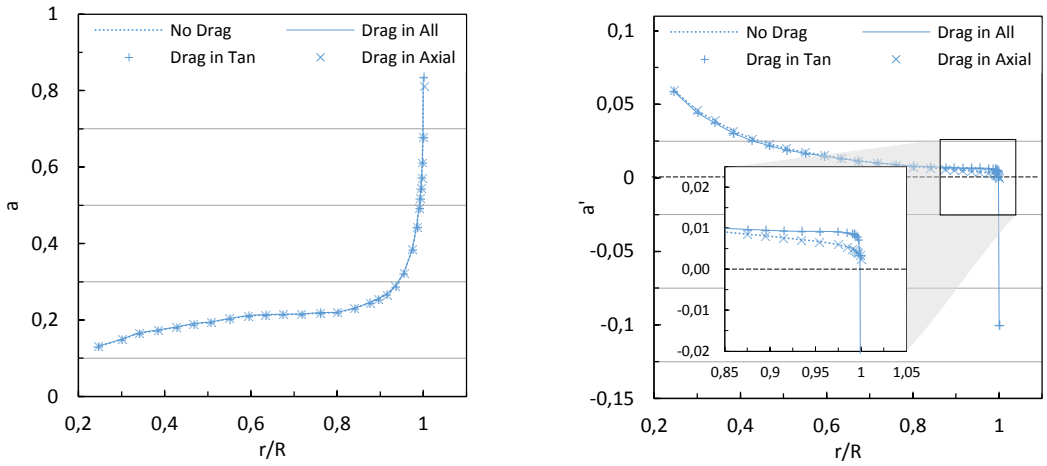

Figure 6: Radial distributions of induced velocities in FAST at TSR=5.42.

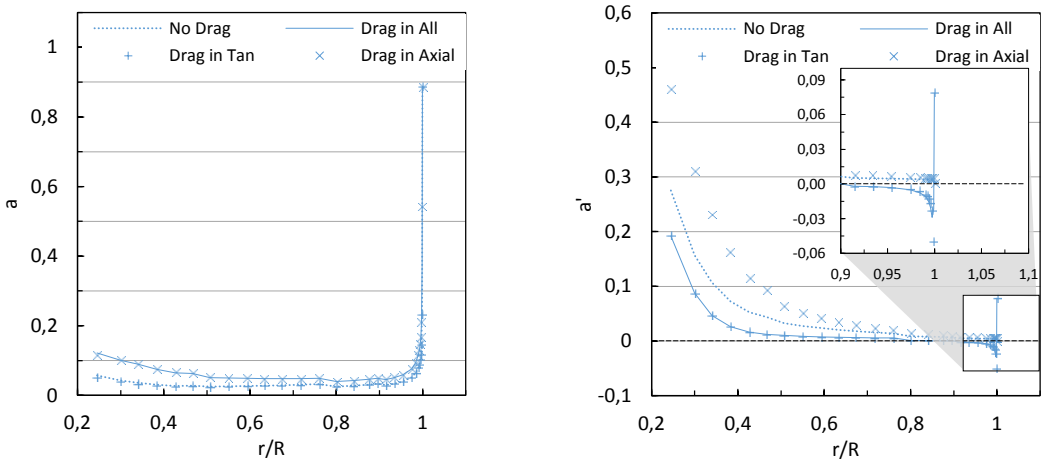

Figure 7: Radial distributions of induced velocities in FAST at TSR=1.52.

3.3 Comparison of results

In order to compare the two implementations of the BEM theory, the same lift and drag tables are input in BEM-IST and in FAST. For comparison consistency, they both include drag forces in all momentum equations.

The results shown in Figures 8 and 9 display a good general agreement. The normal and tangential force coefficients (C_n and C_t) generally fall in the same region than the average measured coefficients. FAST's distributions are more stepped due to the absence of interpolations between lift and drag tables. In both models lift and drag coefficients are determined according to the angle of attack at each element and to the location of the element along the blade. FAST determines these values from a single table, while BEM-IST interpolates between two tables. This allows BEM-IST to provide smoother distributions, especially at low TSRs where the rotational augmentation correction varies considerably along the blade.

The axial and tangential radial distributions are similar. Both models exhibit the same trends and negative values of tangential velocities at the tip, except for the last blade element in FAST. Remaining differences close to the hub might be due to the hub loss correction which is not implemented in BEM-IST. Note that the absolute differences in tangential induction factor at TSR=5.42 is of the same order of magnitude than the differences in the axial induction factor.

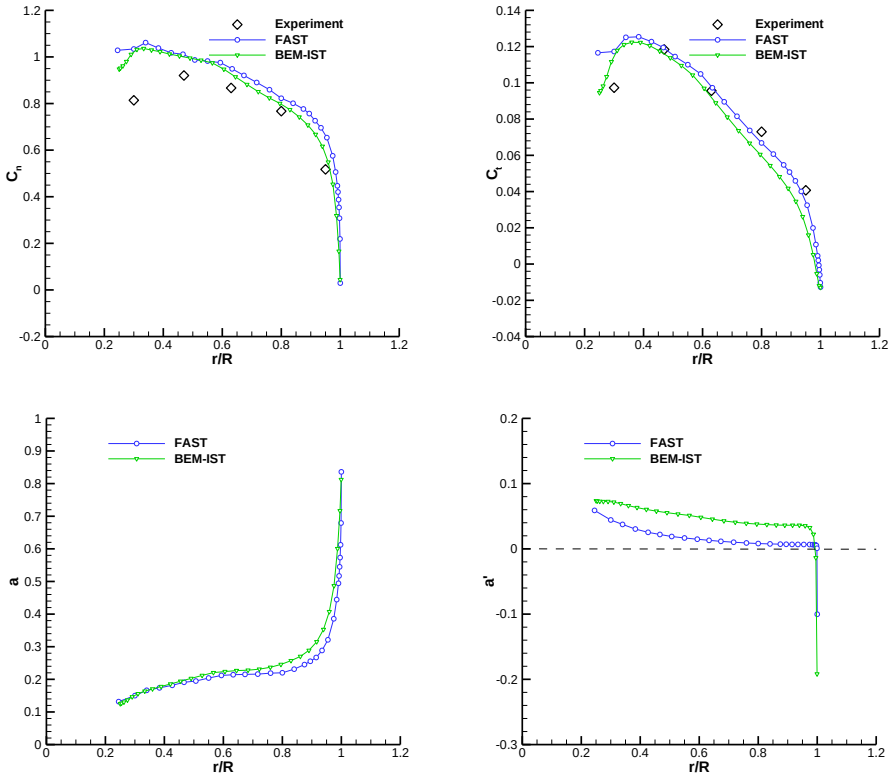

Figure 8: Model comparison at TSR=5.42.

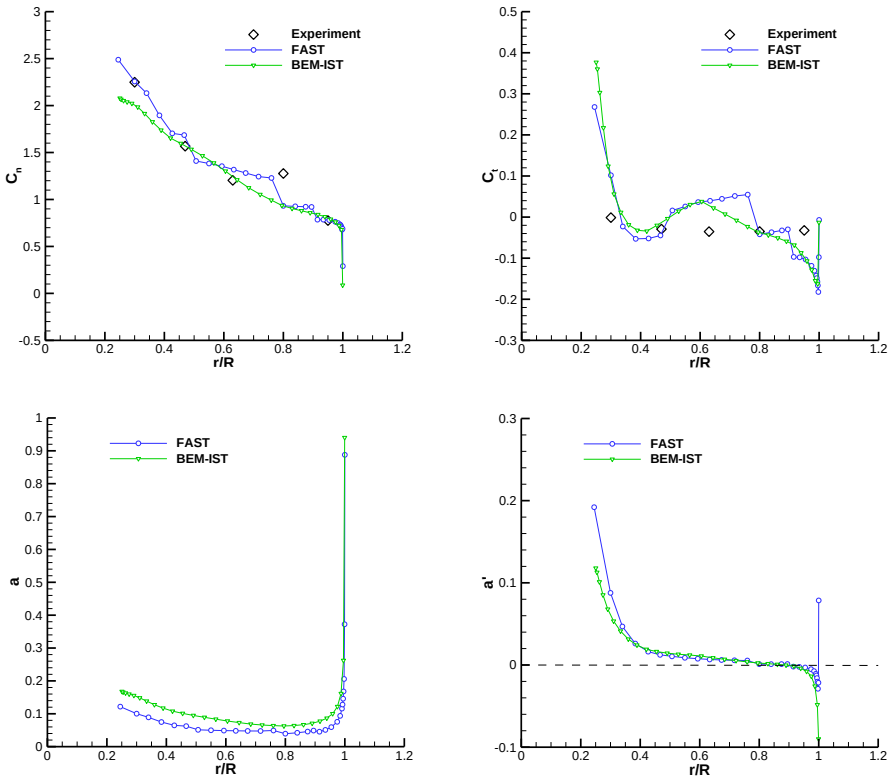

Figure 9: Model comparison at TSR=1.52.

4 CONCLUSION

This work addresses the influence of two important aerodynamic issues when simulating horizontal wind turbines with BEM theory. Stall delay issues due to rotational augmentation seems to be of great importance when specifying lift and drag data. Using stationary blade data would lead to a significant underestimation of the generated power, especially at low TSRs.

The effect of including or not the drag forces in the momentum equations seems limited. Mainly the radial distributions of the induced velocity were modified by the inclusion. Since the modification was larger at low TSRs (high inflow speed), a limited influence is felt on the calculation of the angles of attack, and thus limiting the influence on the calculation of power and thrust over the turbine rotor. However, drag inclusion leads to unusual induced velocity distributions at the blade tip, with negative values of tangential induced velocities.

Similar results for the effects studied in this work are obtained with the implementations of BEM in FAST and BEM-IST.

ACKNOWLEDGEMENTS

The work was performed in the scope of the project "Operability and extreme loads on offshore floating wind turbines", which is financed by Fundação para a Ciência e a Tecnologia (FCT) under contract PTDC/EME-MFE/120593/2010.

REFERENCES

[1] MM Hand, DA Simms, LJ Fingersh, DW Jager, JR Cotrell, S Schreck, SM Larwood (2001). *Unsteady Aerodynamics Experiment Phase VI: Wind Tunnel Test Configurations and Available Data Campaigns*, Technical Report NREL/TP-500-29955.

[2] D Simms, S Schreck, M Hand, LJ Fingersh (2001). *NREL Unsteady Aerodynamics Experiment in the NASA-Ames Wind Tunnel: A Comparison of Predictions to Measurements*, Technical Report NREL/TP-500-29494.

[3] PJ Moriarty, AC Hansen (2005). *AeroDyn Theory Manual*, Technical Report NREL/TP-500-36881.

[4] JM Jonkman, ML Buhl Jr (2005). *FAST User's Guide*, Technical Report NREL/EL-500-38230.

[5] MDP Dias (2012). *Análise Aerodinâmica da Turbina Eólica NREL: Uma Comparação entre Diferentes Modelos*, Tese de Mestrado, Instituto Superior Técnico, Universidade de Lisboa.

[6] S Schreck, M Robinson (2002). Rotational augmentation of horizontal axis wind turbine blade aerodynamic response. *Wind Energy* **5**:133–150.

[7] C Hansel (2014). AirfoilPrep. An Excel workbook for generating airfoil tables for AeroDyn and WT_Perf. *NWTC Computer-Aided Engineering Tools* [WWW]. Available from: http://wind.nrel.gov/designcodes/preprocessors/airfoilprep/.

[8] R Damiani (2011). *Algorithmic Outline of Unsteady Aerodynamics (AERODYN) Modules*, NREL REPORT WE-201103.

[9] RR Ramsay, RJ Hoffman, GM Gregorek (1995). *Effects of Grit Roughness and Pitch Oscillations on the S809 Airfoil*, NREL/TP-442-7817.

Numerical simulation of the airflow around airfoils for small wind turbines applications

AM Gameiro Lopes[1], JA Villar Ale[2]

[1]ADAI, Departamento de Engenharia Mecânica, Polo II da Universidade de Coimbra, Rua Luis Reis Santos, 303-788 Coimbra, Portugal
[2]CE-EÓLICA, Faculdade de Engenharia, PUCRS, Av. Ipiranga, 6681-Prédio 30, Sala 120, CEP: 90619-900, Porto Alegre, Brasil
email: antonio.gameiro@dem.uc.pt, villar@pucrs.br

ABSTRACT: The numerical prediction of aerodynamic coefficients is not an easy task, as it is highly dependent on the correct simulation of the flow in the very close proximity of walls. The aerodynamic flow around airfoils when operating in small wind turbines is subjected to a wide range of angles of attack, which, combined with the relatively low Reynolds number, makes its numerical simulation a demanding task. The present work addresses this problem, by simulating the flow around airfoils used in small-wind turbines using EasyCFD_G software. The influence of the advection scheme and turbulence models on the computed drag and lift coefficients is presented and an evaluation of the obtained results is made when comparing with published experimental data. It is concluded that predictions for lift and drag agree very well with experimental data at low angles of attack. Limitations of simulations are shown, especially for airfoils operating at high angles of attack, where unsteady periodic flow is verified. Influence of the turbulence model and advection scheme is mostly important for drag and not so much for lift. Predictions at high angles of attack considerably overestimate both aerodynamic coefficients.

KEY-WORDS: Wind turbines; CFD; Aerodynamic coefficients; turbulence models.

1 INTRODUCTION

Wind turbines rotor blades are designed to optimize the energy captured from the wind. Most computer codes used to determine the aerodynamic performance of wind turbines are based on the blade element theory (BEM), which requires data of airfoils lift (CL) and drag (CD) coefficients. When blades operate at low angles of attack, numerical simulation is able to correctly reproduce experimental CL and CD values. However, when the angle of attack reaches and exceeds the stall angle, there is a wide divergence of computational results when compared with experimental results. Moreover, the vast majority of experimental data pertains conditions of interest for aviation industry, namely high Reynolds number and low angles of attack. Efforts have been made by the wind industry to overcome these shortcomings, allowing available data specific to wind rotors airfoils. Yet there are other limitations when working with wind turbine airfoils. The rotor blades of large turbines can operate in the Reynolds range of 2×10^6 to 6×10^6. However, small wind turbines operate in the Reynolds range of 5×10^4 to 5×10^5. In both cases, the available information is still limited to experimental results mostly in post stall region. These challenges have motivated the use of CFD models using the RANS equations to predict the aerodynamic coefficients of airfoils for wind turbines. Despite several efforts, there is a wide divergence of results mainly in the post stall. This paper makes a contribution in this research, presenting CFD results for the flow around the NACA 0012, obtained with EasyCFD_G [1] software, and comparing with experimental data.

2 THEORETICAL BACKGROUND

2.1 Basic transport equations

The Navier-Stokes equations, describing momentum conservation, are taken in their transient, 2D form, taking as variables the space *x* and *z* and velocity *u* and *w* velocity components. Their formulation is:

$$\frac{\partial(\rho u)}{\partial t}+\frac{\partial}{\partial x}\left(\rho u^2\right)+\frac{\partial}{\partial z}(\rho uw)=\frac{\partial}{\partial x}\left[\Gamma\left(2\frac{\partial u}{\partial x}-\frac{2}{3}div\vec{V}\right)\right]+\frac{\partial}{\partial z}\left[\Gamma\left(\frac{\partial u}{\partial z}+\frac{\partial w}{\partial x}\right)\right]-\frac{\partial p}{\partial x} \quad (1)$$

$$\frac{\partial(\rho w)}{\partial t}+\frac{\partial}{\partial x}(\rho uw)+\frac{\partial}{\partial z}\left(\rho w^2\right)=\frac{\partial}{\partial z}\left[\Gamma\left(2\frac{\partial w}{\partial z}-\frac{2}{3}div\vec{V}\right)\right]+\frac{\partial}{\partial x}\left[\Gamma\left(\frac{\partial u}{\partial z}+\frac{\partial w}{\partial x}\right)\right]-\frac{\partial p}{\partial z} \quad (2)$$

where p is pressure and Γ is the total viscosity, which includes the contributions of the dynamic and turbulent components Γ, i.e. $\Gamma = \mu + \mu_t$. The three unknowns u, w, and p in these equations need the mass conservation equation to close the problem:

$$\frac{\partial \rho}{\partial t} + \frac{\partial}{\partial x}(\rho u) + \frac{\partial}{\partial z}(\rho w) = 0 \tag{3}$$

The turbulent viscosity is solved with the turbulence model. The k-ε and the SST models, described next, are available in the present code, EasyCFD_G.

2.2 The k-ε turbulence model

The standard formulation of the k- ε model is described in [2]. The turbulent viscosity is given by:

$$\mu_t = C_\mu \frac{\rho k^2}{\varepsilon} \tag{4}$$

The turbulence kinetic energy, k, and its dissipation rate, ε, are computed with the following transport equations:

$$\frac{\partial(\rho k)}{\partial t} + \frac{\partial}{\partial x}(\rho u k) + \frac{\partial}{\partial z}(\rho w k) = \frac{\partial}{\partial x}\left[\left(\mu + \frac{\mu_t}{\sigma_k}\right)\frac{\partial k}{\partial x}\right] + \frac{\partial}{\partial z}\left[\left(\mu + \frac{\mu_t}{\sigma_k}\right)\frac{\partial k}{\partial z}\right] + P_k - \rho\varepsilon \tag{5}$$

$$\frac{\partial(\rho \varepsilon)}{\partial t} + \frac{\partial}{\partial x}(\rho u \varepsilon) + \frac{\partial}{\partial z}(\rho w \varepsilon) = \frac{\partial}{\partial x}\left[\left(\mu + \frac{\mu_t}{\sigma_\varepsilon}\right)\frac{\partial \varepsilon}{\partial x}\right] + \frac{\partial}{\partial z}\left[\left(\mu + \frac{\mu_t}{\sigma_\varepsilon}\right)\frac{\partial \varepsilon}{\partial z}\right] + \frac{\varepsilon}{k}\left(C_1 P_k - C_2 \rho \varepsilon\right) \tag{6}$$

where P_k is the production rate of k as the results of the velocity gradients:

$$P_k = \mu_t \left[2\left(\frac{\partial u}{\partial x}\right)^2 + 2\left(\frac{\partial w}{\partial z}\right)^2 + \left(\frac{\partial u}{\partial z} + \frac{\partial w}{\partial x}\right)^2 \right] \tag{7}$$

The remaining model constants are:

$$C_\mu = 0.09 \qquad \sigma_k = 1.0 \qquad \sigma_\varepsilon = 1.3 \qquad C_1 = 1.44 \qquad C_2 = 1.92 \tag{8}$$

2.3 The k-ω SST turbulence model

The *SST* model [3] represents a combination of the *k-ε* and the *k-ω* models, taking benefit of the advantages of each of these models. The *k-ω* model is more accurate near the wall but presents a high sensitivity to the ω values in the free stream region, where the *k-ε* model shows a better behavior. The *SST* model blends the k-*ε* and the k-*ω* by using a weighting factor based on the nearest wall distance. The governing equations are:

$$\frac{\partial(\rho k)}{\partial t} + \frac{\partial(\rho u k)}{\partial x} + \frac{\partial(\rho w k)}{\partial z} = \overline{P_k} - \beta^* \rho \omega k + \frac{\partial}{\partial x}\left(\left(\mu + \sigma_k \mu_t\right)\frac{\partial k}{\partial x}\right) + \frac{\partial}{\partial z}\left(\left(\mu + \sigma_k \mu_t\right)\frac{\partial k}{\partial z}\right) \tag{9}$$

$$\frac{\partial(\rho \omega)}{\partial t} + \frac{\partial(\rho u \omega)}{\partial x} + \frac{\partial(\rho w \omega)}{\partial z} = \frac{\partial}{\partial x}\left(\left(\mu + \sigma_\omega \mu_t\right)\frac{\partial \omega}{\partial x}\right) + \frac{\partial}{\partial z}\left(\left(\mu + \sigma_\omega \mu_t\right)\frac{\partial \omega}{\partial z}\right) +$$

$$+ \frac{\alpha \overline{P_k}}{\nu_t} - \beta \rho \omega^2 + 2\left(1 - F_1\right)\rho \sigma_{\omega 2}\frac{1}{\omega}\left(\frac{\partial k}{\partial x}\frac{\partial \omega}{\partial x} + \frac{\partial k}{\partial z}\frac{\partial \omega}{\partial z}\right) \tag{10}$$

where ω is the frequency of dissipation of turbulent kinetic energy [s^{-1}]. The production of turbulent kinetic energy is limited to prevent the build-up of turbulence in stagnant regions:

$$\overline{P_k} = \min\left(P_k, 10\,\beta^* \rho\, k\, \omega\right) \tag{11}$$

The weighting function $F1$ is given by:

$$F_1 = \tanh\left\{\left\{\min\left[\max\left(\frac{\sqrt{k}}{\beta^* \omega y};\frac{500\nu}{y^2\,\omega}\right);\frac{4\,\rho\,\sigma_{\omega 2}\,k}{CD_{k\omega}\,y^2}\right]\right\}^4\right\} \tag{12}$$

$$CD_{k\omega} = \max\left(2\,\rho\,\sigma_{\omega 2}\frac{1}{\omega}\frac{\partial k}{\partial x_j}\frac{\partial \omega}{\partial x_j}, 10^{-10}\right) \tag{13}$$

where y represents the distance to the neighbour wall and ν is the laminar dynamic viscosity. F_1 is zero away from the wall (k-ε model) and changes to unit inside the boundary layer (k-ω model). The turbulent viscosity is given by:

$$\nu_t = \frac{a_1\,k}{\max\left(a_1\,\omega; S\,F_2\right)} \tag{14}$$

where S represents the invariant measure of the strain rate:

$$S = \sqrt{S_{ij}S_{ij}} \quad ; \quad S_{ij} = \frac{1}{2}\left(\frac{\partial u_i}{\partial x_j} + \frac{\partial u_j}{\partial x_i}\right) \tag{15}$$

$$F_2 = \tanh\left\{\left[\max\left(\frac{2\sqrt{k}}{\beta^* \omega y};\frac{500\nu}{y^2\,\omega}\right)\right]^2\right\} \tag{16}$$

The constants are computed as a blend of the k-ε and the k-ε models, through the following generic equation:

$$\alpha = F_1\,\alpha_1 + \left(1 - F_1\right)\alpha_2 \tag{17}$$

The constants are α_1 = 5/9; β_1 = 3/40; σ_{k1} = 0.85; $\sigma_{\omega 1}$ = 0.5; α_2 = 0.44; β_2 = 0.0828; σ_{k2} = 1; $\sigma_{\omega 2}$ = 0.856; β^* = 0.09.

2.4 The numerical method

Discretisation and integration of the transport equations described previously are performed using a non-orthogonal mesh. The independent Cartesian coordinates (x, z), describing the physical domain, are, thus, replaced by a boundary fitted coordinate system (ξ, ζ), defined by the mesh lines which may have, locally, any orientation and inclination. Transformation of the original equations is accomplished by replacing the independent variables, using the chain rule. The mesh arrangement is of the collocated type (as opposed to the staggered mesh), with the two velocity components and scalar quantities (pressure, turbulence kinetic energy and its dissipation rate) located at the control volume centre. The mesh is unstructured constituted of quadrilateral 2D elements.

For the coupling between momentum and continuity equations, the present code adopts the *SIMPLEC* algorithm (Semi-Implicit Method for Pressure-Linked Equations - Consistent), proposed by Van Doormaal and Raithby [4], which is based on the original formulation *SIMPLE* by Patankar [5]. Due to the non-staggered mesh arrangement (collocated mesh), the Rie-Chow interpolation procedure [6], with the modifications proposed by Majumdar [7], is implemented. The transport equations for momentum and turbulent quantities are solved with the point Gauss-Seidel algorithm. The pressure correction equations, due to its elliptic character, are much harder to solve. In this case, the multigrid algebraic correction strategy [8] is adopted with very good results.

3 SIMULATION OF THE FLOW AROUND THE NACA 0012 AIRFOIL

3.1 Domain and boundary conditions

In order to minimize boundary effects, a quite large domain around the airfoil was employed, with dimensions as shown in Figure 1. Simulations were carried out for Reynolds numbers of 6×10^6 and 7×10^5. Although the first Reynolds number is too high for small wind turbines operating conditions, this

case was taken as a test for drag computations, comparing with data available in the literature. For the inlet boundary, a 5% turbulence intensity was assigned. Lateral boundaries were assigned a free slip flow condition. After mesh independence tests, a total of approximately 130 000 control volumes were employed, as shown in Figure 2. In order to optimize mesh nodes distributions, three mesh refinement regions were adopted, as may be perceived in Figure 2(a). Near the airfoil surface, an inflation layer of nearly structured elements was used, with a height of 0.00015 m. This allows y^+ values ranging from, typically, 0.1 to 6, with an average value of 1.7 all around the airfoil.

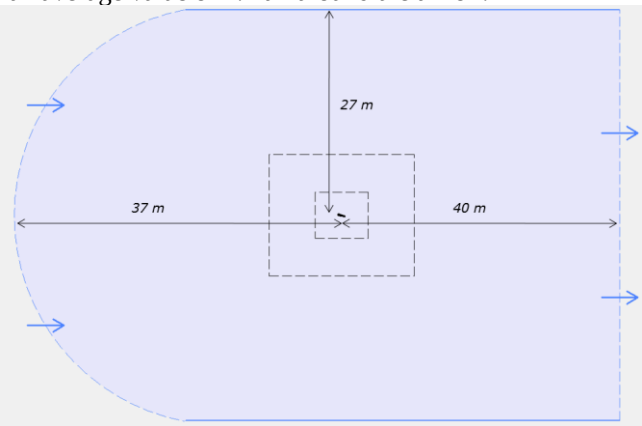

Figure 1: Domain dimensions. Airfoil cord is 1 m.

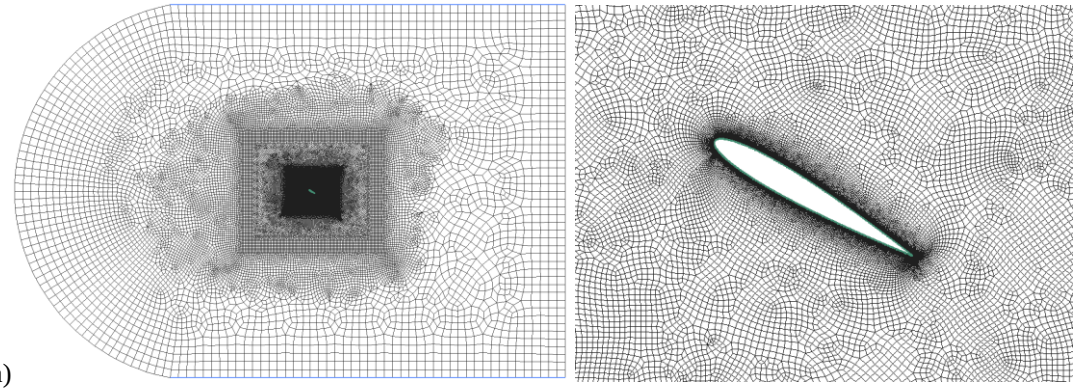

Figure 2: Non-structured quadrilateral mesh.

Figure 3 shows the dependence of the lift coefficient with the airfoil angle of attack α. Both the SST and the k-ε turbulence models were used in these simulations, as well as the hybrid and the Quick advection schemes. Experimental data is reported by Abbot and Doenhoff [9], and by Ladson [10] for the same Reynolds number. It apparent that CFD results produced by both turbulence models are quite similar and agree very well with experimental data up to separation, which presents its onset at $\alpha = 16^{\circ}$. The two advection models give similar results up to separation, after which the lift drop in the stall region is more pronounced with the hybrid model. Separation is completely established at $\alpha = 18^{\circ}$ and for $\alpha \geq 20^{\circ}$ the flow becomes unsteady, showing periodic oscillations on both aerodynamic coefficients. For the transient regime, presented data corresponds to average values over the oscillation period. It may be seen that data in the stall region is quite spread. It is recognized in the literature that it is difficult to obtain reliable experimental data in this region, due to the unsteady characteristics of the flow and tendency to present a 3D behaviour. The relation between the drag and the lift coefficients is shown in Figure 4. It is interesting to note that deviations from experimental data are substantially larger for the k-ε model (Figure 4(a)), certainly because the friction component plays an important role in drag and thus, correctly resolving the boundary layer is crucial for the drag computation. It is interesting to note that the advection scheme plays a very important role (Figure 4(b)), with the higher order scheme Quick showing much better results when compared with the experimental data.

Since from previous results it is evident that the SST turbulence model coupled with the high order Quick scheme represents the best modelling solution, these numerical options were used when computing

the aerodynamic coefficients for the same airfoil at a range of angles of attack between 0º and 90º, for a Reynolds number of 7×10^5. Experimental data are reported by Timmer [11]. Results presented in Figure 5 show that, in what concerns lift, the agreement is very good up to the minimum lift on the stall region, even for the unsteady regime that is verified for angles larger than 18º. Lift coefficient is considerably overestimated for large angles of attack, especially in the range $30^o < \alpha < 70^o$. Comparing with experimental results from Timmer (Figure 5(b)), nevertheless, one can conclude that drag is also overestimated, as the ratio of lift to drag agrees very well with experimental data. Figure 6 shows the time evolution of lift and drag for 45º angle of attack and Figure 7 depicts the flow visualization for the situations of maximum and minimum drag for the same angle of attack.

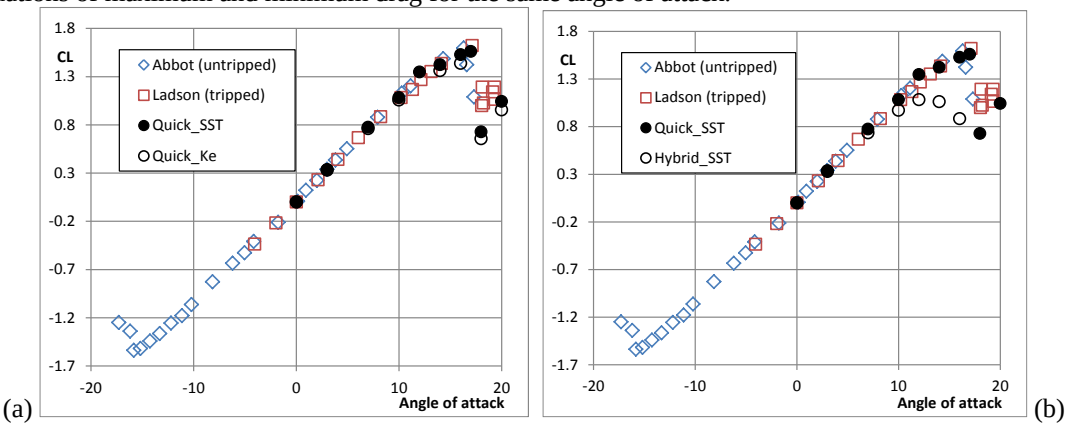

Figure 3: Lift coefficient *vs* angle of attack. Influence of: (a) turbulence model; (b) advection scheme.

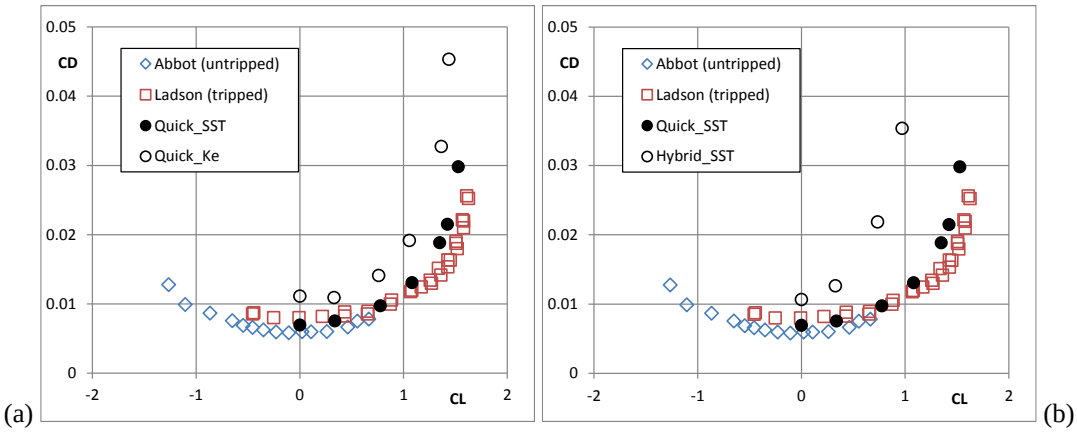

Figure 4: Drag coefficient *vs* lift coefficient. Influence of: (a) turbulence model; (b) advection scheme.

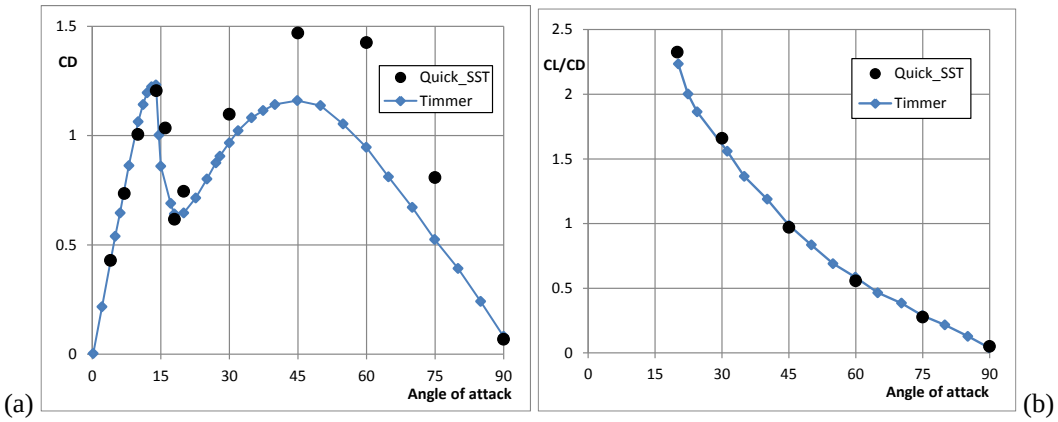

Figure 5: Aerodynamic coefficients for 90º angle of attack range. (a) drag coefficient; (b) lift /drag.

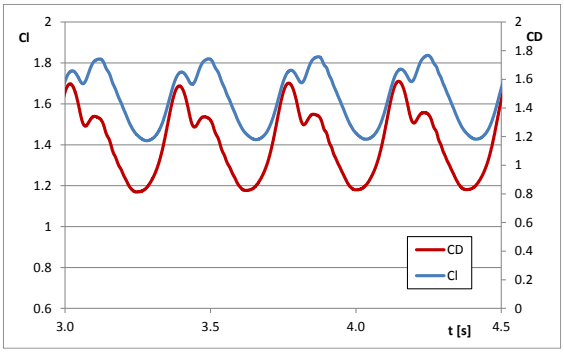

Figure 6: Time evolution of lift and drag coefficients for 45º angle of attack.

(a) 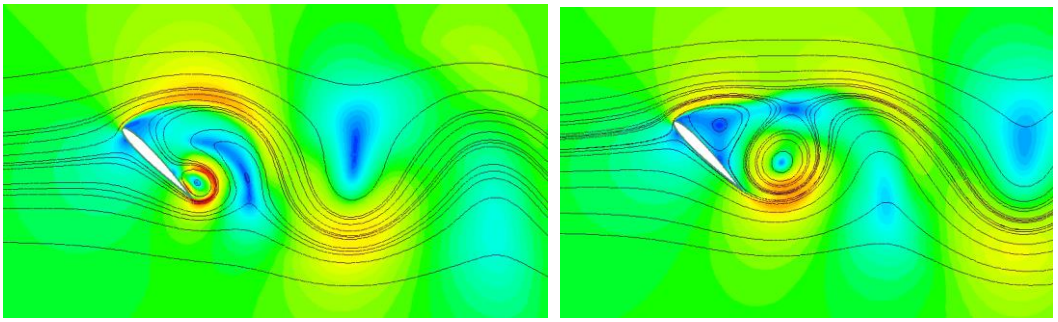 (b)

Figure 7: Flow visualization for 45º angle of attack: (a) maximum drag; (b) minimum drag.

4 CONCLUSIONS

The present work showed CFD simulations for the NACA 0012 airfoil at a range of angles of attack. It is concluded that predictions for lift and drag agree very well with experimental data at low angles of attack. Limitations of simulations are shown, especially for airfoils operating at high angles of attack, where unsteady periodic flow is verified. Influence of the turbulence model and advection scheme is mostly important for drag and not so much for lift. Predictions at high angles of attack considerably overestimate both aerodynamic coefficients.

REFERENCES

[1] AMG Lopes (2014). *EasyCFD_G User's Manual*. Available from: http://www.easycfd.net/.

[2] BE Launder, DB Spalding (1972). *Mathematical Models of Turbulence*, Academic Press London and New York, ISBN 0-12-438050-6.

[3] FR Menter (1993). Zonal two-equation k-ω turbulence model for aerodynamic flows. In *24th Fluid Dynamics Conference*, July 6–9, Orlando, Florida, AIAA Paper 93–2906.

[4] JP Van Doormaal, GD Raithby (1984). Enhancements of the simple method for predicting incompressible fluid flows. *Numerical Heat Transfer* **7**:147–163.

[5] SV Patankar (1980). *Numerical Heat Transfer and Fluid Flow*, Hemisphere Publishing Corporation, Washington, D.C., ISBN 0-89116-522-3.

[6] CM Rhie, WL Chow (1983). Numerical study of the turbulent flow past an airfoil with trailing edge separation. *AIAA Journal* **21**(11):1525–1532.

[7] S Majumdar (1988). Role of underrelaxation in momentum interpolation for calculation of flow with nonstaggered grids. *Numerical Heat Transfer* **13**(1):125–132.

[8] BR Hutchinson, GD Raithby (1986). A multigrid method based on the additive correction strategy. *Numerical Heat Transfer* **9**(5):511–537.

[9] IH Abbott, AE von Doenhoff (1959). *Theory of Wing Sections*, Dover Publications, New York.

[10] CL Ladson (1988). *Effects of Independent Variation of Mach and Reynolds Numbers on the Low-Speed Aerodynamic Characteristics of the NACA 0012 Airfoil Section*, NASA Technical Memorandum 4074, October 1988.

[11] WA Timmer (2010). Aerodynamic characteristics of wind turbine blade airfoils at high angles-of-attack. In *TORQUE 2010: The Science of Making Torque from Wind*, June 28–30, Crete, Greece.

Comparison between the results obtained with structured and unstructured grids for the cases of a laminar and a turbulent axisymmetric jet flow

ALA Leite, DMS Albuquerque, JCF Pereira

LASEF, Departamento de Engenharia Mecânica, IDMEC, LAETA, Instituto Superior Técnico, Universidade de Lisboa, Av. Rovisco Pais 1, 1049-001 Lisboa, Portugal
email: andre.leite@tecnico.ulisboa.pt, duartealbuquerque@tecnico.ulisboa.pt, jcfpereira@tecnico.ulisboa.pt

ABSTRACT: The classical axisymmetric jet problem was chosen to validate a second-order unstructured own finite volume code. A Reynolds number of 300 was considered to perform the simulations in the laminar regime. A comparison between the numerical and the analytical solutions is dis-cussed for verification of the code. Different boundary conditions are imposed to the lateral boundaries to understand the truncation of an unbounded domain of the real axisymmetric jet. The order of convergence of the code is also evaluated considering several grids up to 2 million cells. Furthermore, simulations using adaptive grid algorithms are effectuated to understand the behaviour of the error estimators available in the code. Large eddy simulation is performed to study the evolution of a turbulent jet at a Reynolds number of 25000. The results of the Smagorinsky model are compared with experimental data and reported spectral simulations. Structured and unstructured grids are compared in the light of the time-averaged decaying of the velocity in the centreline and the Reynolds stresses. Isosurfaces of the Q-criterion allow distinguish the evolution of the coherent structures typically found in turbulent circular jets.

KEY-WORDS: Finite volume method; Large eddy simulation; Axisymmetric jet; Adaptive grids; Validation and verification.

1 INTRODUCTION

Simulations of turbulent flows using LES with structured grids are limited to very simple geometrical configurations and usually require a great amount of computational resources, [1], [2]. In practical applications complex geometries are dominant and an unstructured grid is used in the majority of the situations, [3,4,5].

In order to improve the results using unstructured grids, commutative filters were developed by [6] and [7] in order to reduce the commutation error to negligible values. This approach involves explicit filtering and it is used, for example to calculate a turbulent channel flow, see [8] for details.

Only a few studies compared the results in unstructured grids using implicit and explicit filtering, the last being performed with commutative filters [9]. Their results seems to indicate an improvement in the results using explicit filtering. On the other hand [10] studied the flow over a cylinder using implicit filtering in un-structured mesh and affirmed that reasonable results could be achieved without any explicit filtering.

On the other hand, it is also known that in the presence of a regular grid, i.e. when adjacent cells vary smoothly, the commutation error will tend to zero [11].

However the quantification of the commutation error using implicit filters is not straightforward. In a numerical simulation the influence of the commutation error can be achieved by a direct comparison between the results obtained with a filter with and without a constant width, Δ. In the case studied a comparison between the results obtained with structured and unstructured grids is done as an attempt to evaluate quantitatively the importance of this error.

The present document was prepared with the following primary objectives:

- to implement the parallel computation with implicit time discretizations in order to be possible to have turbulent simulations converged in a reasonable amount of time;
- the verification of the SOL code, developed in [12,13], by comparing numerical and analytical solutions under laminar conditions in the case of an axisymmetric jet and to estimate qualitatively the influence of the computational domain and the boundary conditions;

- to understand the behaviour of the code in unstructured grids in laminar situations using adaptive refinement algorithms;
- to study the error estimator in the specific case of the laminar round jet under adaptive grid algorithms by comparing the refined meshes obtained with the error estimator used as refinement criterion against one criterion based on the analytical error;
- to compare LES results obtained with the Smagorinsky sub-grid scale model with implicit filtering for structured and unstructured grids under turbulent conditions with the results present in [14] and [15].

2 VERIFICATION OF A LAMINAR JET FLOW

2.1 Computational Set-up

The analytical solution describes a jet created from a singularity or a source point that spreads momentum along the longitudinal direction to the surrounding atmosphere, [16]. ξ is a non-dimensional coordinate.

$$u_x(\mathrm{x},\mathrm{r}) = \frac{3}{8\pi}\frac{K'}{\nu(x+x_0)}\frac{1}{\left(1+\frac{1}{4}\xi^2\right)^2} \tag{1}$$

$$u_r(\mathrm{x},\mathrm{r}) = \frac{1}{4}\sqrt{\frac{3}{\pi}}\frac{\sqrt{K'}}{(x+x_0)}\frac{\xi-\frac{1}{4}\xi^3}{\left(1+\frac{1}{4}\xi^2\right)^2} \tag{2}$$

2.2 Influence of the Boundary Conditions

Boundary conditions have to be carefully defined in order to represent accurately the physical phenomenon to simulate. Therefore, the definition of boundary conditions is one of the most challenging tasks when dealing with numerical calculations.

In round jets, the definition of boundary conditions add an increased difficulty since they confine a flow that is naturally free. In computational fluid dynamics this type of errors is known as modelling errors and in this section a quantitative comparison between the numerical errors introduced by using different types of boundaries is effectuated. The domain size was chosen to have the following dimensions: $L_x = 25D$, $L_y = 10D$, $L_z = 10D$ and the number of points was: 80 × 63 × 63 = 317 520. At the inlet was imposed the analytical velocity profile. To understand this influence four of the most used types of boundary conditions were prescribed to the lateral boundaries: *Pressure Outlet*, *Wall*, *Symmetry* and *Periodic*. The results from the simulations with different boundary conditions are reported in Figure 1.

In Figure 1 the presence of confinement effects are observed. These effects are more intense in the regions near the lateral boundaries and their influence is intensified along the downstream direction. The more accurate results are achieved by prescribing the lateral boundaries with a *Pressure Outlet* condition.

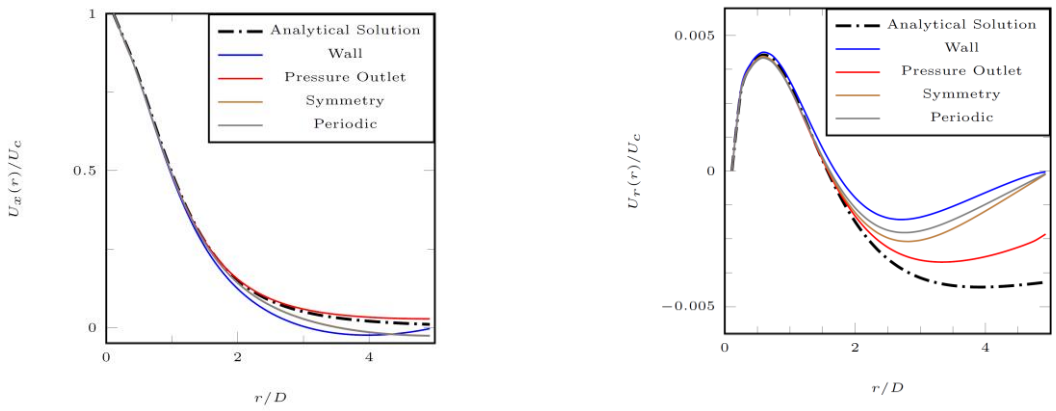

Figure 1: Comparison between the obtained results using different types of boundary conditions at the station $x/D = 25$. On the left it is represented the streamwise velocity and on the right the radial velocity.

The differences obtained using different types of lateral boundaries can be explained by analysing the mathematical treatment correspondent to each type of boundary and the radial component of the velocity. In the position $r = 5D$, the flow is still influenced by the development of the jet and one can conclude that a small portion of fluid is swallowed from the surrounding environment, Figure 1. The problem with the *Wall* and *Symmetry* boundaries lies on the imposition of a null velocity value in the normal direction of the boundary. In other words, these two boundaries are impermeable and so they do not allow the entrance of flow from the outside of the domain. This fact lead to a deficit of mass flow reported in Figure 1 where, for these two types of boundaries, the values of the streamwise velocity are below the analytical solution. The problem with the solution with *Periodic* BC is similar to the one described above because despite a null velocity value is not imposed to the boundary faces, the mass flow that enters in a specific face comes from its opposite face. This means that no mass flow is allowed to enter in the domain from the exterior environment. On the contrary, since *Pressure Outlet* imposes a null gradient to all of the velocity components, it is allowed the changing of mass flow between the exterior and the interior of the computational domain. This is reported in Figure 1 where, with Pressure Outlet the radial component of the velocity is not null at the faces of the boundary. In resume it was verified that the results achieved with *Pressure Outlet* were in the best agreement comparing with the analytical solution and therefore, using the facts enumerated above, hereinafter the lateral boundaries are always going to be treated as *Pressure Outlet.*

2.3 Order of convergence

In cases where analytical solutions are known, the order of the code can be found by comparing the numerical and the analytical solution. In this section only the spatial order of convergence will be analysed. To estimate the order of a generic code, several simulations are usually carried out varying the size of the mesh. The error between the numerical and the analytical simulations is then calculated for each simulation. Plotting the error *E*, against the hydraulic diameter *h*, the slope of the adjusted curve gives the order of the code. Mathematically the order p can be found through the following expression:

$$p = \frac{\ln(E_{i+1} / E_i)}{\ln(h_{i+1} / h_i)} \tag{3}$$

To estimate the order of the SOL code in the laminar round jet case, five meshes with different number of cells were used. The analytical solution was imposed to the inlet and the size of the do-main was $L_x = 25D$, $L_y = 20D$, $L_z = 20D$. The lateral and the outlet boundaries were treated as *Pressure Outlet*. Five grids were considered with the following number of cells: 130 331, 257 594, 528 750, 1 011 933 and 1 998 594. The *Norm*∞ error is plotted against the hydraulic diameter in Figure 2, for the streamwise component of velocity.

The slope of the curve present in Figure 2 indicates that the order of the convergence of the code is near 2 which was expected since all the discretizations used have second order accuracy.

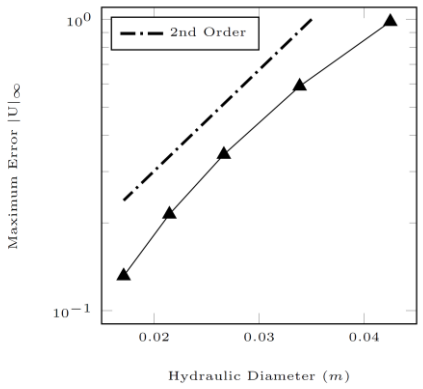

Figure 2: Evolution of the *Norm*$_\infty$ error with the decreasing of the hydraulic diameter.

2.4 Results with adaptive grids

The behaviour of the error estimator based on a Residual Least Squares RLS was evaluated by comparing the results using the error estimator and the analytical solution with the refinement criteria. The completed results are given in the Thesis, however here only a comparison between the grid and the analytical error of the streamwise velocity in the final refinement is given. The results are reported in Figure 3 and Figure 4.

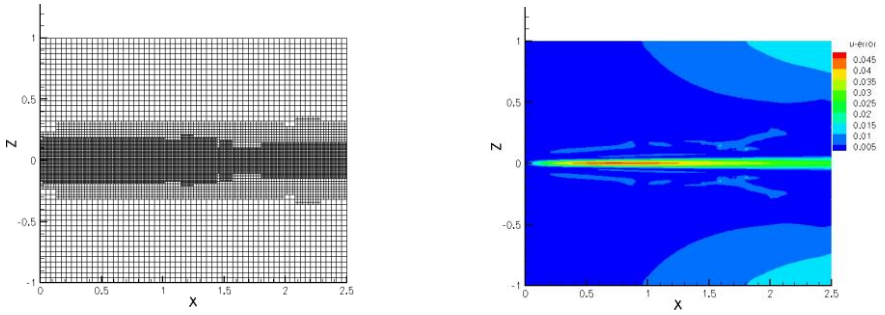

Figure 3: Grid obtained after 5 refinement levels with the error estimator – on the left. Analytical error of the streamwise velocity – on the right.

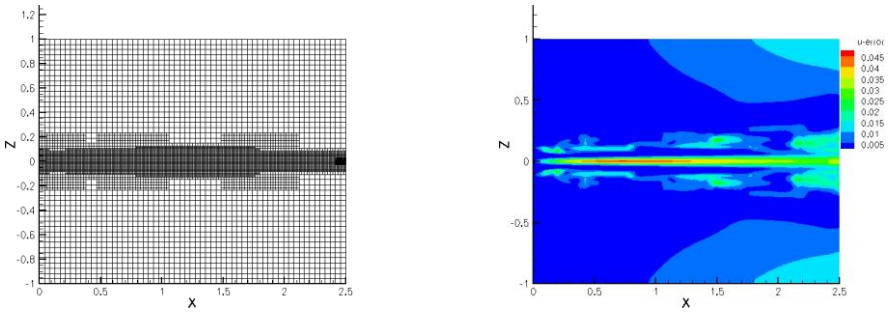

Figure 4: Grid obtained after 8 refinement levels with the analytical error – on the left. Analytical error of the streamwise velocity – on the right.

The Figure 3 indicate that the error estimator used along with the refinement criterion is producing good results. The cells with higher errors were selected for refinement and they all belong to the zone of centre of the jet.

The simulations where the analytical error of the streamwise velocity was used along the refinement criterion, indicate that comparing to the simulation using the error estimator, more refinements are needed to obtain cells with a higher level of refinement. Besides it is also observable that the global distribution of the error is lower in the simulation using the error estimator.

3 VALIDATION OF A TURBULENT JET FLOW

3.1 Computational domain and boundary conditions

The length of the computational domain was $L_x = 12.25D$ according to [14] and [15]. This domain length is long enough to have a transition of the jet to a fully developed turbulent state.

To treat the outlet it was considered an improvement of the Sommerfeld condition which takes into account the convective terms of the Navier-Stokes equations and also the diffusive ones to approximate the velocities at the boundary in the following time step, see [17].

3.2 Structured and unstructured grids

The considered grids used in the turbulent simulations are graphical represented in Figure 5.

The structured grid was constructed using the blockMesh tool from OpenFoam® while the un-structured grid was created by applying five transfinite interpolations using a Matlab® routine developed by the Author.

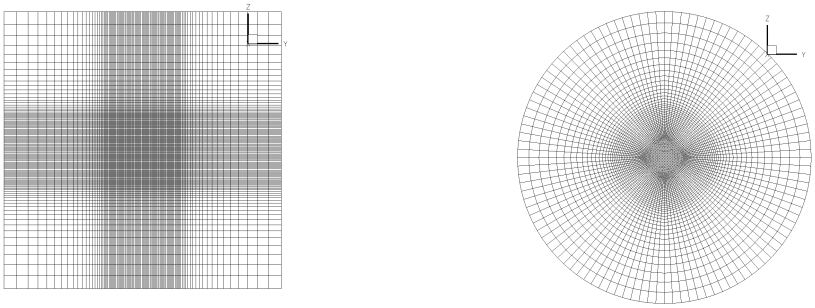

Figure 5: Grids used to conduct the turbulent simulations. On the left – structured. On the right – unstructured.

3.3 Results

The validation of the SOL code in turbulent conditions are achieved with a detailed comparison between experimental results [14], numerical results obtained with SOL code and more data obtained with high order spectral resolution available in [15]. In Figure 6, on the left, it is represented the evolution of the centreline's velocity along the longitudinal direction. The right hand side of Figure 6 shows the Q-contour evolution of the axisymmetric jet at a specific time step.

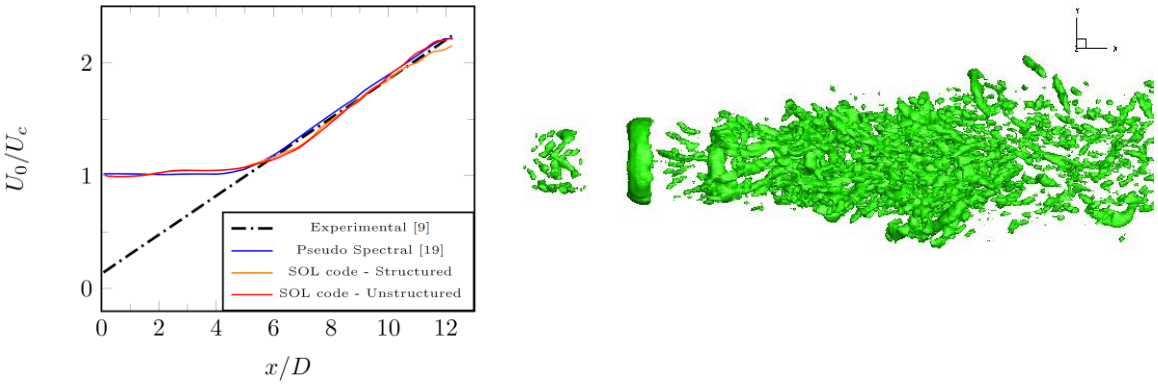

Figure 6: Evolution of the centreline velocity jet obtained with SOL code for structured and unstructured grids – on the left. Instantaneous contour of the *Q*-contour for the unstructured grid – on the right.

The results obtained with the SOL code incorporate both structured and unstructured grids. In the jet analysed here the Reynolds number considered was 25000. Observing the decaying of the centreline velocity of the jet shown in Figure 6, the results obtained with SOL code, for the considered grids are in good agreement with the other results present in Literature. The slope of the decaying velocity shown in the referred figure is particularly similar from $x/D = 7$ onwards. Until $x/D = 7$ the curves obtained with the SOL code show slight differences compared with [15]. These differences are probably caused by the excitation imposed to the inlet in the simulations conducted in this Thesis to allow a faster transition to a turbulent regime. The results with structured and unstructured are very similar.

The *Q*-contour represented in Figure 6 allows the clear visualisation of the coherent structures typical found in axisymmetric jets. Its appearance occurs around $x/D = 3$ and their time life with a perfectly circular shape happens until the end of the potential core which takes place around $x/D = 5$. At the end of the potential core they break-up leading to the appearance of higher frequency structures with lower wave numbers. These structures continues their process of breaking and near the outlet of the domain a fully turbulent range of scales is observed.

4 CONCLUSIONS

The classical axisymmetric jet for laminar and turbulent flow conditions was simulated using the SOL code. Under a laminar regime and for a Reynolds number equals to 300, different boundary conditions were analysed in order to understand their influence in the results: (*Wall*, *Pressure Outlet*, *Symmetric* and

Periodic). The numerical results closest to the analytical solution were obtained by treating the lateral boundaries with a *Pressure Outlet* condition.

The comparison of the results obtained with the grids varying the domain size allowed to conclude that the confinement effects increase with the streamwise distance of the domain. A convergence study was effectuated using several meshes varying the number of the points.

Simulations considering adaptive refinement algorithms were conducted to understand the behaviour of the code using an error estimator and the analytical solutions as refinement criteria. A direct comparison of the results obtained with an error estimator and the analytical solution to refine the grid allow to verify the efficiency and accuracy of the results produced using the error estimator.

Simulations with a Reynolds number equals to 25000 were conducted using the SOL code and the results were compared to high-order numerical data from spectral resolution and experimental data for validation and verification purposes. In order to understand the influence of the regularity and the anisotropy of the mesh, two grids were tested: one structured and another unstructured.

The predictions of the turbulent jet showed the time averaged velocity profile evolution of the centreline is in a very good agreement with the other results found in literature for structured and unstructured grids.

ACKNOWLEDGMENTS

The first Author would like to express his gratitude to the project EXTREME – PTDC/EME-MFE /114343/2009 from the Portuguese FCT (Foundation for Science and Technology).
The second Author would like to thank the support received through the Portuguese FCT (Foundation for Science and Technology) grant SFRH/BD/48150/2008.

REFERENCES

[1] CB da Silva, JCF Pereira (2004). The effect of subgrid-scale models on the vortices computed from large-eddy simulations. *Physics of Fluids* **16**(12):4506–4534.

[2] CB da Silva, RJN Reis, JCF Pereira (2011). The intense vorticity structures near the turbulent/non-turbulent interface in a jet. *Journal of Fluid Mechanics* **685**:165–190.

[3] K Mahesh, G Constantinescu, P Moin (2004). A numerical method for large-eddy simulation in complex geometries. *Journal of Computational Physics* **197**:215–240.

[4] L Selle, G Lartigue, T Poinsot, R Koch, K-U Schildmacher, W Krebs, B Prade, P Kaufmann, D Veynante (2004). Compressible large-eddy simulation of turbulent combustion in complex geometry on unstructured meshes. *Combustion and Flame* **137**:489–505.

[5] O Lehmkuhl, I Rodríguez, A Baez, A Oliva, CD Pérez-Segarra (2013). On the large-eddy simulations for the flow around aerodynamic profiles using unstructured grids. *Computers and Fluids* **84**:176–189.

[6] OV Vasilyev, TS Lund, P Moin (1998). A general class of commutative filters for LES in complex geometries. *Journal of Computational Physics* **146**:82–104.

[7] AL Marsden, OV Vasylyev, P Moin (2000). Construction of commutative filters for LES on unstructured meshes. In *Annual Research Briefs* 2000, Center for Turbulence Research, NASA, 179–192.

[8] J Gullbrand (2001). Explicit filtering and subgrid scale models in turbulent channel flow. In *Annual Research Briefs* 2001, Center for Turbulence Research, NASA, 31–42.

[9] ST Bose, P. Moin, D You (2008). Grid independent large-eddy simulation using explicit filtering. In *Annual Research Briefs* 2008, Center for Turbulence Research, NASA, 173–187.

[10] H Ouvrard, B Koobus, A Dervieux, MV Salvetti (2010). Classical and variational multiscale LES of the flow around a circular cylinder on unstructured grids. *Computers and Fluids* **39**:1083–1094.

[11] E de Villiers (2006). *The Potential of Large Eddy Simulation for the Modelling of Wall Bounded Flows*, PhD Thesis, Imperial College of Science, Technology and Medicine, London.

[12] JPP Magalhães, DMS Albuquerque, JMC Pereira, JCF Pereira (2013). Adaptive mesh finite-volume calculation of 2D lid-cavity corner vortices. *Journal of Computational Physics* **243**:365–381.

[13] DMS Albuquerque, JMC Pereira, JCF Pereira (Accepted). Residual least squares error estimate for unstructured h-adaptive meshes. *Numerical Heat Transfer, Part B: Fundamentals*.

[14] HJ Hussein, SP Capp, WK George (1994). Velocity measurements in a high-Reynolds-number, momentum-conserving, axisymmetric, turbulent jet. *Journal of Fluid Mechanics* **258**:31–75.

[15] CB da Silva (2001). *The Role of Coherent Structures in the Control and Interscale Interactions of Round, Plane and Coaxial Jets*, PhD Thesis, Institut National Polytechnique de Grenoble, and Instituto Superior Técnico.

[16] H Schlichting (1979). *Boundary-Layer Theory*, McGraw Hill.

[17] I Orlanski (1976). A simple boundary condition for unbounded hyperbolic flows, *Journal of Computational Physics* **21**, 251–269.

V Conferência Nacional de Mecânica dos Fluidos, Termodinâmica e Energia
MEFTE 2014, 11–12 Setembro 2014, Porto, Portugal
APMTAC, 2014

Impact of the distance between cylinders on vortex statistics

PM Sanches[1], AM Ricardo[1], S Di Carlo[2], MJ Franca[3], RML Ferreira[1]

[1]CEHIDRO, Instituto Superior Técnico, Universidade de Lisboa, Av. Rovisco Pais, 1049-001 Lisboa, Portugal
[2]Department of Civil and Mechanical Engineering, Università degli Studi di Cassino e del Lazio Meridionale, Italy
[3]Laboratory of Hydraulic Constructions, École Polytechnique Fédérale de Lausanne, Switzerland
email: pedro.miguel.sanches@tecnico.ulisboa.pt, ana.ricardo@tecnico.ulisboa.pt, smndicarlo@gmail.com, mario.franca@epfl.ch, ruimferreira@tecnico.ulisboa.pt

ABSTRACT: This paper focuses on the kinematic aspects of vortexes' development in a flow within an array of emergent and rigid cylinders. The relation between cylinder Strouhal numbers, vortex decay and vortex path statistics was investigated for the flow around four cylinders within an array of randomly placed cylinders and for the flow around an isolated cylinder. Experimental databases of instantaneous velocity acquired with a 2D Particle Image Velocimetry system were used. An original methodology to detect vortexes in two-dimensional flow fields is proposed, combining a point-based criterion, embedded in a global search to detect all the possible vortex core locations, with a curve-based criterion to decide whether the detected point corresponds to a vortex, depending on the geometry of streamlines. A statistical analysis reveals the impact of the presence of neighbouring cylinders on the amount of shed vortexes and on the vortex paths. The Strouhal number values, representing the normalized shedding frequency, show that the shedding mechanism is approximately the same for both the tests performed.

KEY-WORDS: Isolated cylinder; Array of cylinders; Vortex detection; Vortex interaction.

1 INTRODUCTION

Multiple-cylinder configurations present complex flow fields generated by interactions between shear layers, vortexes and wakes. For high stem-Reynolds numbers the flow exhibits well developed turbulence, produced essentially by the work of Reynolds shear stresses in the horizontal plane against the time-averaged shear rate characteristic of vertical-axis vortex shedding in the wake of cylinders. The interaction of vortexes shed by individual cylinders and the distance between cylinders determine the spatial pattern of turbulence.

Many research works have been carried out to study flows around isolated cylinders [1-3] and a review of studies about the effects of a second cylinder placed in close proximity arranged in tandem, side-by-side, or in staggered configurations was presented by Sumner [4]. However, less is known about the changes to the flow when a cylinder is placed in an array of randomly placed cylinders, which involve complex interaction between wakes, von Kármán vortex streets and shear layers. Therefore, this work is aimed at deepening the knowledge of vortex interaction in patches of randomly placed emergent and rigid cylinders by investigating the relation between cylinders' Strouhal numbers, vortex decay and vortex path statistics.

It is known that vortexes are among the most important and coherent structures that control the dynamics of flow fields [5]. The concept of vortex is commonly expressed as a helical pattern of flow in a localized region, yet there is not a universally accepted formal definition of a vortex. The essential characteristics of vortexes are hard to capture and none of the existing criteria to vortex detection is entirely satisfactory [5–7]. An operative definition, provided by Robinson [8], is that a vortex exists when instantaneous streamlines mapped onto a plane normal to the vortex core exhibit a roughly circular or spiral pattern, when viewed from a reference frame moving with the center of the vortex core. The drawback associated with this definition is that it requires the ability to recognize and track a vortex core. Since it is important to visualize the vortexes in order to understand the swirling features in flow fields, a methodology to detect the vortexes is proposed, combining a point-based criterion, embedded in a global search to detect all the possible vortex core locations, with a curve-based criterion to decide whether the detected point corresponds to a vortex, depending on the streamlines geometry.

This paper is organized in five main sections. After the introduction the experimental tests are described, followed by the explanation of the vortex detection methodology. Section 4 presents and discusses the results and the paper finishes with a summary of the main conclusions.

2 EXPERIMENTAL FACILITIES

The experimental work was carried out in a 12.5 m long and 0.408 m wide tilting recirculation flume of the Laboratory of Hydraulics of IST. The flume has glass side walls, enabling flow visualization and laser measurements. The flume bottom was covered with a horizontal layer of gravel and sand. The flow was controlled by a venetian-blind gate at the flume outlet.

Two experimental tests were considered in the present work:

- Test I – Array of cylinders: Cylinders with 1.1 cm of diameter were randomly placed with a uniform distribution of 980 cylinders/m^2 along a 3.5 m long reach. To enable the velocity measurements, a gap (narrow region without stems in the spanwise direction) was enforced, whose width is equal to the mean inter-stem distance (0.032 m). Figure 1a) shows a plan view of part of the reach covered by cylinders, identifying the four stems studied in the present work, in what concerns vortex shedding. Within the array the flow was uniform with a depth of 8.4 cm.
- Test II – Isolated cylinder: An isolated cylinder, also with diameter of 1.1 cm, was placed upstream of the reach populated with cylinders of test I (Figure 2a). The flow upstream the cylinders' array was gradually varied decelerating towards downstream.

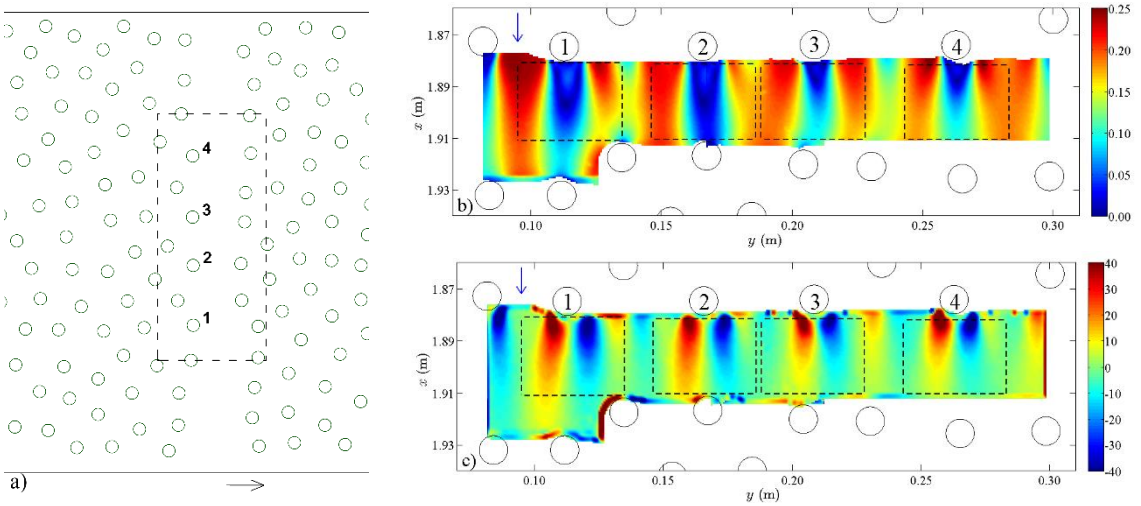

Figure 1: Test I: a) plan view of the region where the measurements were performed; b) time-averaged velocity map; c) time-averaged vorticity. The arrow indicates the flow direction. The dashed rectangles on the color maps identify the regions where the vortexes were searched for each stem.

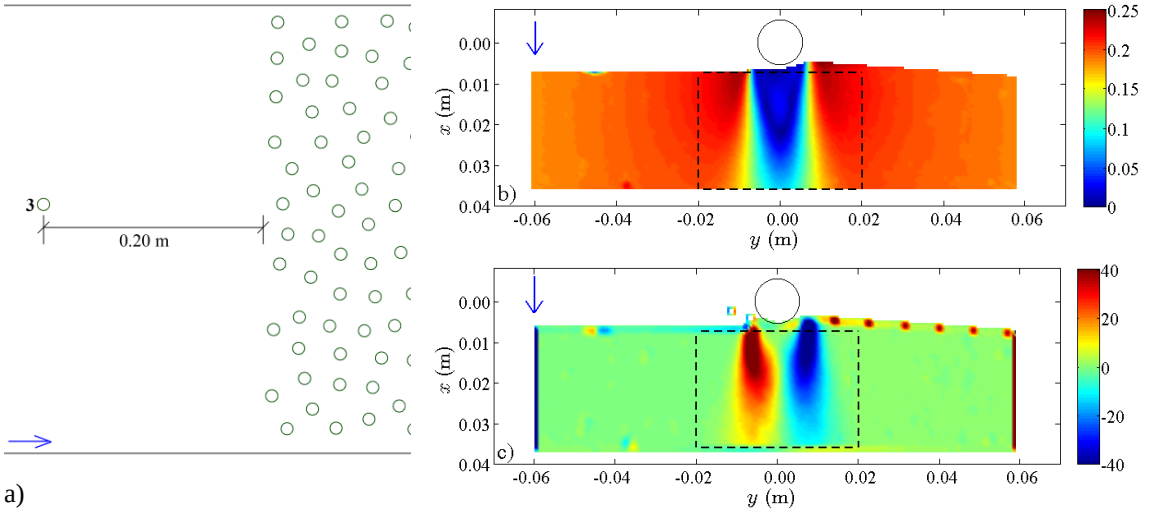

Figure 2: Test II: a) plan view of the region where the measurements were performed; b) time-averaged velocity map; c) time-averaged vorticity. The arrow indicates the flow direction. The dashed rectangle on the color maps identifies the regions where the vortexes were searched.

The measurements consisted in instantaneous velocity maps acquired with a 2D Particle Image Velocimetry system (PIV) of 30 mJ operated at a sampling rate of 15 Hz and with a time between pulses of 1500 µs. Polyamide seeding particles were employed for flow visualization and measuring. Its specific gravity is 1.03 and the diameters range from 30 to 70 µm, with 50 µm of mean. Using this seeding, the cut-off frequency of the turbulent signal, calculated with the theory of Hjemfelt and Mockros [9], is about 40 Hz. Given that the Nyquist frequency of the PIV measurements is 7.5 Hz, it is concluded that the seeding particles are adequate for the performed laboratory work. In the space domain, applying Taylor's frozen turbulence hypothesis [10, p. 253] and considering a mean velocity of 0.13 m/s, the frequency f_c = 40 Hz corresponds to a turbulent length scale λ_c = 3.3 mm. This means that the velocity of eddies smaller than 3.3 mm may be measured with less than 95% confidence.

The horizontal maps were acquired 3.8 cm above the bed in both tests. For each test, 4500 images couples were acquired, corresponding to 5 minutes of consecutive data. The CCD of the camera used has a size of 1600×1200 px^2 and the image correlation was performed with interrogation areas of 16×16 px^2 with 50% of overlap. An area of roughly 12 × 9 cm^2 was measured, yielding to interrogation volumes of 0.6 × 0.6 × 2 mm^3, since the laser light sheet has approximately 2 mm of thickness.

The tests were performed with a discharge of 4.5 ls^{-1}. Table 1 presents flow properties for each test, where h is the flow depth, U is the mean (time- and space-averaged) flow velocity, T is the water temperature during the experiments, and $\mathrm{Re}_p = Ud/\nu$ is the stem Reynolds number, d = 0.011 m being the diameter of the cylinder and ν the kinematic viscosity of the fluid.

Table 1: Flow properties.

	h (m)	U (m/s)	T (◦C)	Re_p (−)
Test I	0.084	0.131	24	1584
Test II	0.070	0.158	24	1910

Time-averaged velocity and vorticity maps for tests I and II are presented in Figure 1 and Figure 2, identifying the regions where the vortexes were searched for each stem.

3 METHODOLOGY

In the framework of 2D flow fields, the proposed methodology combines a point based criterion, embedded in a global search to detect all the possible vortex core locations, with a curve-based criterion to decide whether a detected point corresponds to a vortex, depending on the streamlines geometry.

First, for a given instantaneous velocity map, a global search is carried out in a rectangular area with dimensions $4d \times 3d$ (width × length) centered downstream of a cylinder. This search identifies possible vortex cores, finding the points where both longitudinal (u) and lateral (v) velocity components are zero. This criterion arises from the assumption that the center of the vortex is a point of maximum slope in the mean velocity plots. After the identification of all possible vortexes in a given region, a local approach is applied. The streamlines initiated in the near vicinity of each point are analysed to distinguish between vortex cores or stagnation points. For each point, four streamlines are drawn around starting at 0, $\pi/2$, π and $3\pi/2$ in the circle, with radius smaller than the size of interrogation areas, centred in that point. If at least two streamlines are closed (making a 2π revolution) and bounded and if there is a circulation pattern in the near vicinity of the point, then the candidate is considered a vortex.

A vortex database is built, each vortex is marked by the number of the vortex map to which it belongs and by a timestamp and is identified by the coordinates of the core and the value of the near-core circulation (including signal). This database is then processed to track vortexes into vortex paths. Vortex tracking methodology has been based on some assumptions: i) a vortex path is defined by at least two related vortex cores; ii) positive paths are formed by positive vortexes, while negative paths are formed by negative vortexes; iii) only one vortex can be added to an open path in each instantaneous velocity map.

The key steps are summarized below.

1. The first vector map with vortexes is used to initialize a record of open paths; the initial points of these paths are the coordinates of the vortexes in that map.
2. The next vector map with vortexes is processed. The open paths for which the difference between the timestamp of the current vector map and timestamp of their last entry is larger than a given flow-dependent threshold are closed (and killed if there was only one entry). The remaining open paths may be continued by the vortexes with the timestamp of the current vector map.

3. To determine if the vortexes with a given timestamp continue existing open paths or constitute initial points of new paths, four situations are considered: a) the current vector map has one vortex and there is only one open path; b) the current vector map has only one vortex but there are more than one open path; c) the current vector map has more than one vortex and there is only one open path; d) the current vector map has more than one vortex and there are more than one open path. The general criterion to map vortexes to paths employs a correlation analysis, with the key restriction that vortexes are not allowed to travel upstream.
4. Once step 3 is finished, the record of open paths is updated and the process returns to step 2. Databases of positive and negative vortex paths are thus built. Statistical treatment of these databases allows for the determination of mean vortex velocity, mean angle of vortex motion, path length distribution and vortex shedding frequency, among others.

4 RESULTS

The methodology described previously was applied to each instantaneous velocity map of both tests, distinguishing vortexes with positive and negative circulation. Then, the space distribution of vortexes is analyzed. Table 2 summarizes statistics of the detected vortexes. The row labelled as "C" identifies the sign of the vortex circulation, which was defined by the right-hand rule, therefore a vortex with counterclockwise circulation has a positive circulation, and it is mentioned, herein, as a positive vortex, for simplification. In Table 2, N stands for the number of vortexes detected, μ is the expected value of the longitudinal component of the path length, σ is the respective standard deviation and St is the Strouhal number. The last three rows indicate the percentage of vortexes detected between the shedding cylinder and 1d, 2d and 3d further downstream.

Globally the number of positive and negative vortexes is similar for each shedding stem. The number of detected vortexes is larger in test II than in each stem of test I, leading to the conclusion that the presence of neighboring stems contributes to the loss of coherence of the vortexes ejected by each stem. It should also be noted that the number of detected vortexes in Test I includes vortexes that were generated upstream and reached the studied area. Some of these vortexes can be visually identified in Figure 3a), but the applied algorithm did not distinguish if the vortex has been generated by a given stem or by upstream neighbors.

Table 2: Statistics of the detected vortexes and paths.

		Test I								Test II	
		Stem 1		Stem 2		Stem 3		Stem 4			
C		+	−	+	−	+	−	+	−	+	−
N		5525	5163	5517	5808	3014	2791	3022	3054	5948	6074
μ (cm)		1.10	1.08	1.19	1.30	0.70	0.65	0.93	0.86	0.99	0.94
σ (cm)		0.62	0.61	0.69	0.70	0.47	0.47	0.65	0.59	0.60	0.59
St (−)		0.27	0.27	0.26	0.26	0.23	0.22	0.23	0.23	0.26	0.27
% vortexes	1d	57.5	53.1	49.3	48.4	79.9	83.1	75.3	76.6	53.1	57.6
	2d	32.3	35.5	33.3	34.0	17.9	15.2	19.7	19.1	37.9	34.0
	3d	11.3	11.4	17.4	17.6	2.2	1.8	5.0	4.3	9.0	8.4

Being the flow within arrays of cylinders dominated by wake production of turbulence, the level of background turbulence is expected to be larger in tests where the analyzed stem has upstream neighbors than in the test where the cylinder is isolated. Thus, the mechanism of transferring turbulent energy to smaller scales is more likely to happen in test I. This higher level of background turbulence might be able to destroy the coherence of the vortexes ejected in a given cylinder, explaining the lower amount of vortexes detected in the stems of test I.

Figure 3 represents the location of the vortex cores detected during the entire acquisition time for all the four stems of test I (a) and for the single stem of test II (b). Longitudinal distributions of negative vortexes ejected by stem 4 of test I and by the single stem of test II are shown in Figure 4. Positive and negative vortexes of a given shedding stem present similar longitudinal distributions. Comparing the distributions of the stem with neighbors and the single stem, one observes that the decreasing rate of the number of detected vortexes is higher on the former case. The survival rate of vortexes is higher in test II

than in the stems 3 and 4 of test I. However, stems 1 and 2 of test I showed larger survival rates than stems 3 and 4 (Table 2 and Figure 3), what may indicate that the arrangement of the closest stems should impact the coherence of the vortexes shed by a given stem. Another explanation for that difference might be related with the lower velocity in the wake of stems 1 and 2 than in the wake of stems 3 and 4 (Figure 1b).

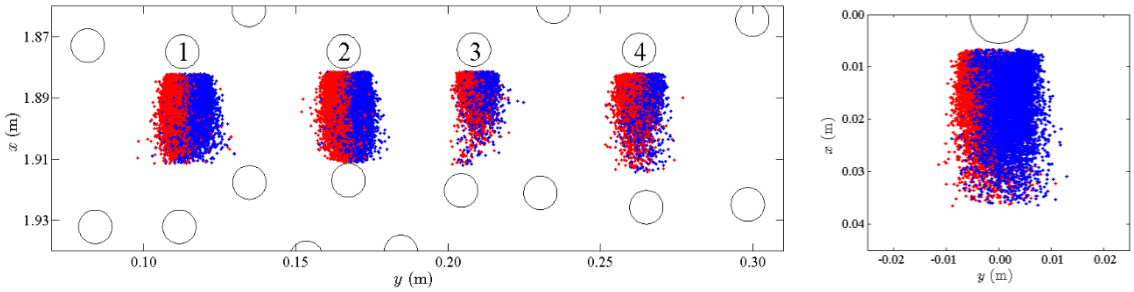

a) Test I b) Test II

Figure 3: Location of the detected vortex cores. Red points identify positive vortexes and blue points identify negative vortexes.

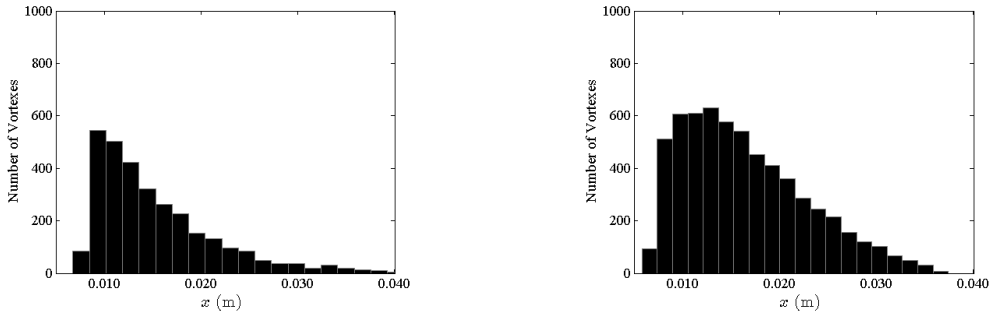

a) Test I (stem 4): negative vortexes b) Test II: negative vortexes

Figure 4: Distribution of vortexes along streamwise direction.

Figure 5 presents the mean vortex paths of the stems studied in both tests. In test I, the vortex paths show a curvature when arriving close to the nearest downstream cylinder, being effectively drawn to it. This curvature may be an effect of the pressure field gradient in front of that cylinder. Contrarily, the vortexes shed by an isolated cylinder (test II) travel downstream following an approximately linear paths that seem to converge until stabilizing into parallel paths.

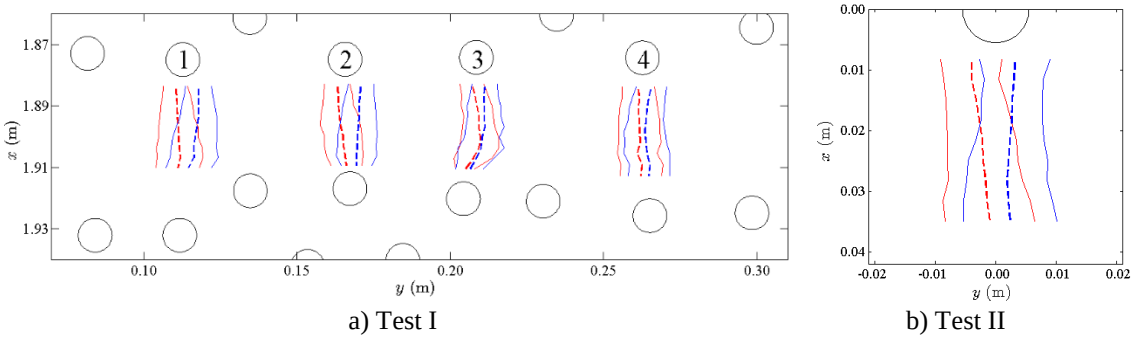

a) Test I b) Test II

Figure 5: Mean vortex paths. Red and blue lines concerned positive and negative vortexes, respectively. The dashed lines represent the mean vortex paths while the solid lines identify the standard deviation of the paths.

Figure 6 shows the distribution of vortex shedding periods for paths of positives vortexes for a stem of test I and for test II. One can observe that the expected value of the period is similar for both cases. Test I shows a more concentrated period distribution around the mode, expressed in a smaller value of the standard deviation. The normalized shedding frequency, Strouhal number, is similar for both tests (St ≈

0.26) which suggests that the mechanism of vortex shedding is the same. The obtained Strouhal numbers are in the range of values presented by Sumner [4].

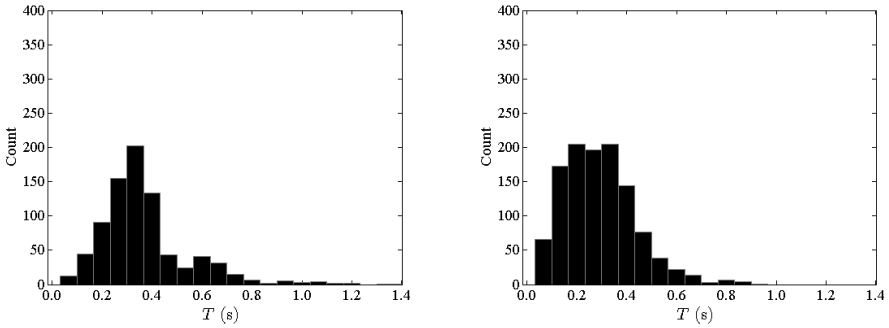

a) Test I (stem 4): positive vortexes b) Test II: positive vortexes

Figure 6: Distribution of vortex periods.

5 CONCLUSIONS

In this study a methodology to detect vortexes was introduced based in the detection of points of zero velocity and in streamlines analysis. The methodology was applied to identify vortexes shed by an isolated cylinder and by cylinders within arrays of cylinders.

The results allow the following conclusions:

- More vortexes are found in the case of an isolated cylinder and those vortexes can travel longer downstream before disappearing.
- The path of the vortexes is also affected by the presence of other stems. Vortexes are deviated from a straight path presumably due to the pressure field of the downstream stems.
- The mechanism of vortex shedding is not affected by the vicinity of others cylinders. This is evident by Strouhal numbers values, which are on average the same for both tests.
- Strouhal number is on average equal to 0.26, higher than the Strouhal number value (St=0.21) characteristic of the vortex shedding of an isolated cylinder at $Re_p \sim 10^3$, but still in the range of previous experimental outcomes.

ACKNOWLEDGMENTS

This research was partially funded by FEDER, program COMPETE, and by national funds through Portuguese Foundation for Science and Technology (FCT) projects RECI/ECM-HID/0371/2012 and PTDC/ECM/117660/2010.

REFERENCES

[1] CH Williamson (1996). Vortex dynamics in the cylinder wake. *Annual Review of Fluid Mechanics* **28**(1):477–539.
[2] MM Zdravkovich (1997). *Flow around Circular Cylinders: Fundamentals*, Volume 2, Oxford University Press.
[3] MM Zdravkovich (2003). *Flow around Circular Cylinders: Applications*, Volume 2, Oxford University Press.
[4] D Sumner (2010). Two circular cylinders in cross-flow: A review. *Journal of Fluids and Structures* **26**(6):849–899.
[5] DC Banks, BA Singer (1994). Vortex tubes in turbulent flows: identification, representation, reconstruction. In *Proceedings of the Conference on Visualization'94*, 132–139, IEEE Computer Society Press.
[6] I Sadarjoen, F Post, B Ma, D Banks, H-G Pagendarm (1998). Selective visualization of vortices in hydrodynamic flows. In *Visualization '98*, Proceedings, 419–422.
[7] M Jiang, R Machiraju, D Thompson (2005). Detection and visualization of vortices. In CD Hansen, CR Johnson, Eds., *The Visualization Handbook*, 295–309, Academic Press.
[8] SK Robinson (1991). Coherent motions in the turbulent boundary layer. *Annual Review of Fluid Mechanics* **23**(1):601–639.
[9] AT Hjemfelt, LF Mockros (1996). Motion of discrete particles in a turbulent fluid. *Applied Science Research* **16**:149–161.
[10] H Tennekes, J Lumley (1972). *A First Course in Turbulence*, The MIT Press.

Verification and validation of a moving immersed boundary method for applications to laminar flows

JAS Pereira, DMS Albuquerque, JCF Pereira

LASEF, Departamento de Engenharia Mecânica, IDMEC, LAETA, Instituto Superior Técnico, Universidade de Lisboa, Av. Rovisco Pais 1, 1049-001 Lisboa, Portugal
[1]email: jonas.pereira@ulisboa.tecnico.pt, duartealbuquerque@ulisboa.tecnico.pt, jcfpereira@ulisboa.tecnico.pt

ABSTRACT: The article reports the development and implementation of an Immersed Boundary Methods for a bi-dimensional structured grid. Three interpolations for the immersed boundary correction were verified against the cavity flow with analytical solution. Second order of accuracy was obtained with a polynomial regression using material points and neighbor fluid cells based on the Least Squares Method. Several applications of moving boundaries immersed in fluid flows are presented, accurately representing the behavior of the fluid and the interactions between the fluid and the body's structure. The comparison of the results with both empiric and computational data confirmed that the method is able to solve problems of immersed boundaries and that the computational cost decrease substantially in comparison with body-fitted meshes.

KEY-WORDS: Immersed boundary method; Moving boundary problems; Incompressible flow; Finite volume method; Least squares method.

1 INTRODUCTION

The fact that in the 21st century the aerospace industry is still relying in static analysis to study temporal variant phenomena leading to extrapolative and inductive reasoning enhanced the motivation to build a tool that could be able to provide the desired stability, efficiency and accuracy for these flows. The target objectives are not only for computational analysis of complex or arbitrary geometries but also to study the behavior of immersed bodies with an user prescribed motion and studies where the dynamic and mechanical behavior of an immersed body is ruled by the interaction between the fluid and the body's structure.

Since most of the nowadays fluid flow engineering software tools have quasi-second order of accuracy it's also important to provide a second order immersed boundary method and verify it against 2-D results from literature data and to study the history effects of the computational cells in the boundary's motion and the consequent integration of aerodynamic forces in the immersed boundary.

1.1 Applied Method

This method is based on the works from Sanjar et al. [1] and is established by the representation of the solid body as a set of material points (MP) whose motion is computed with the material point method (MPM), whilst the fluid flow is solved in a background polyhedral mesh. The position and the velocity components of the MP are known throughout the computation.

The fixed grid and the respective points and cells have a selection algorithm which is implemented in order to first classify all the vertex of the grid as either part of the fluid zone or as part of the solid zone.

Secondly the cells were catalogued in three different groups, a cell with all its vertex in the fluid zone was classified as a fluid cell, in the case of all vertices of a known cell were in solid zone the respective cell was classified as a solid cell. The third group isn't trivial as the first two and is defined as the cells that have both types of vertex, this type of cell have at least one vertex in the solid zone and the rest in the fluid zone, these cells will be from now on called "*IB cells*". Furthermore the faces from the IB cells that are connected to a fluid cell are marked as "*IB faces*".

Lastly this method performs an interpolation using the values of velocity from the neighboring cells and from the MP in order to obtain the velocity that will be used as a boundary condition. The interpolation could be performed either in a cell-centered or in a face-centered basis. In this specific case the chosen method was a finite-volume scheme so the collocation of the values in the faces of the IB cells would be more convenient. So in this method we use a set of velocity values from either material points in the

geometrical boundary and neighboring cell's centers in order to interpolate the value of the IB face's velocity components.

2 THE IMMERSED BOUNDARY METHOD

The feature that distinguishes the interpretation of the immersed boundary conditions is the fact that the computational boundary is not geometrically coincident with the physical boundary. So in order to maintain the accuracy of the results an interpolation of the velocity field must be made and this value will then be used as a Dirichlet BC on the computational boundary.

After the identification of the boundary cells and the discretization of the continuity and momentum equations with a finite volume scheme, the interpolation mentioned above is used to calculate the velocity face centered value, which do not exist as, in the finite volume schemes the velocity is stored in the cell center. In this work three types of interpolations, with different truncation error orders, were used.

In the interpolations algorithms some material points were used and so a routine that can retrieve the closest solid points to the boundary faces and their coordinates was implemented and executed.

2.1 First Order Interpolation – Interpolation 0

This interpolation scheme is the simplest and is based on the collocation of the closest solid point value in the face value of the immersed boundary. So for every immersed boundary face the above mentioned algorithm selects the closest solid point and uses its value on the boundary face, as in equation:

$$\phi_f = \phi_s \tag{1}$$

2.2 Linear Interpolation with Distance Weighting Factor – Interpolation 1

The linear interpolation with the distance weighting is made by the use of two points, one solid and one fluid and is of the form:

$$\phi_f = \phi_c(1-\eta) + \eta\phi_s \tag{2}$$

where ϕ_f represents the interpolated value for the face center variable, ϕ_c the cell center value for the variable in question for the cell containing the boundary face, ϕ_s represents the value of the variable in the solid material point closer to the immersed boundary face in question, in the end η represents the weighting factor of the interpolation and can be defined as:

$$\eta = d_1/(d_1 + d_2) \tag{3}$$

where d_1 the distance from the cell center to the face center and d_2 is defined as the distance between the computational boundary face center and the closest material point in solid region.

2.3 Second Order Interpolation with a Quadratic Polynomial obtained with the Least Squares Method – Interpolation 2

The two previous subsections described two different approaches to obtain the velocity face value at the boundary face, but they have at the most a first order of accuracy. The first is really outdated as it was the interpolation scheme used in the earlier computational fluid dynamics calculations and the second one even tough is better still has only a first order of accuracy. In order to obtain a breakthrough a second order interpolation was needed and based on the work of Sanjar et al. [1], this interpolation was implemented in the SOL software.

In order to obtain a second order of accuracy interpolation scheme a quadratic polynomial of the following form has been created:

$$\phi_f = \beta_0 + \beta_1 x + \beta_2 y + \beta_3 x^2 + \beta_4 y^2 + \beta_5 xy \tag{4}$$

where the β_n coefficients are determined by the least squares method. Which was chosen because it gives the user the possibility to obtain an approximated solution for a problem with more equations than unknowns.

The polynomial in equation 4 was formed using a stencil with some of the velocity values of the nearest neighbor cells, with shared vertex with the boundary face, and with the closest material points (points in geometrical boundary of the solid region). These points have a prescribed velocity vector, the velocity of the moving boundary and in case of a neighbor cell is an IB cell, the nearest material point to that IB face is taken in account to the construction of the stencil.

As there is variation in the number of IB faces near the interpolated face a selection algorithm was implemented in order to choose the number of solid or material points in the stencil. The dimension of the stencil varies for each IB face.

After choosing the points of the stencil the construction of the matrices and vectors for the least squares method is performed. For the polynomial construction the velocity of every point can be approximated in a matrix form of the equation 4 by $M\ \vec{\beta}$ where $\vec{\beta} = [\beta_0, \beta_1, \beta_2, \beta_3, \beta_4, \beta_5]^T$ and M:

$$M = \begin{bmatrix} 1 & x_1 & y_1 & x_1^2 & y_1^2 & x_1 y_1 \\ 1 & x_2 & y_2 & x_2^2 & y_2^2 & x_2 y_2 \\ \vdots & \vdots & \vdots & \vdots & \vdots & \vdots \\ 1 & x_n & y_n & x_n^2 & y_n^2 & x_n y_n \end{bmatrix} \tag{5}$$

where n is the number of points of the stencil, that must be at least 6. In the least square method the β_i values are calculated in order to minimize the square of the difference between the real variable ϕ and the interpolated value, so the objective is to get the minimization of $\left\|\phi - M\vec{\beta}\right\|$. The works of Kariya and Kurata [2] showed that this difference is minimized when the β coefficients are obtained as:

$$\beta = (M^T . M)^{-1} M^T \phi \tag{6}$$

A correction is necessary in order to maintain the continuity equation and to prevent the interpolation to inject mass in to the system. This correction is a multiplication of the negative fluxes by the ratio between the positive fluxes and negative ones. This correction is applied before the momentum equations are solved, in order to maintain mass conservation in the domain.

The implemented algorithm of the second order polynomial using the least squares method can be summarized as:

1. Identify the stencil's points, using the method explained above.
2. Obtain the coordinates of the selected cell's centroids as well as the material points coordinates in IB face centered referential.
3. Construct the M matrix obtaining the values of x and y of the velocity.
4. Computation of the β coefficients using equation 6 with the M matrix and the velocity values of the previous outer iteration.
5. Apply the mass flux correction in order to maintain the mass conservation.

As the referential used is an IB face centered one, the value of $\phi_f = \beta_0$ and no further calculations were needed.

3 RESULTS

3.1 Analytical Cavity

The interpolation schemes were tested for the boundary's correction using an analytical solution for a cavity flow in order to assert if it was possible to maintain the global discretization order of the Finite Volume. Using Figure 1 we can assert the premise that this interpolation is second order accurate, as the exponential value of the error decay with the hydraulic diameter from the grid is almost 2, as can be seen in Table 1.

Table 1: Order decay for the mean and maximum error of both velocities for the case of the analytical cavity with an immersed boundary.

Error	$\bar{\varepsilon}_u$	ε_{umax}	$\bar{\varepsilon}_v$	ε_{vmax}
P2	2.018	1.955	2.026	1.937

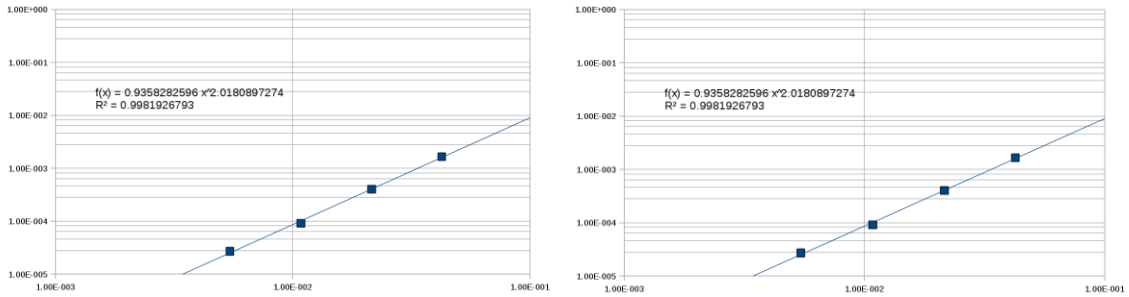

Figure 1: Decay of the mean error with the hydraulic diameter of the grid with Interpolation 2 on the left for the u component and on the right for the v component.

3.2 2-D Horizontally Oscillating Cylinder in a Static Flow

This section presents the results for a simulation of an oscillating moving boundary immersed in a static fluid, for $\mathrm{Re} = 100$ using the maximum velocity of the body and a Keulegen-Carpenter number $\mathrm{KC} = 5$.

The present results were compared with the data available in [3]. The computational experience performed in this section was carried out in order to reproduce one of the analyses performed in the mentioned literature.

In Figure 2 we can observe the comparison of the x component of the velocity for three different phases of the cycle. In each phase of the cycle the velocity was analyzed at two different lines. The velocities were analyzed at $x = -0.6D$ (a–c) and $x = 1.2D$ (d–f). There's a similar tendency of the experimental data with the results computed with the immersed boundary.

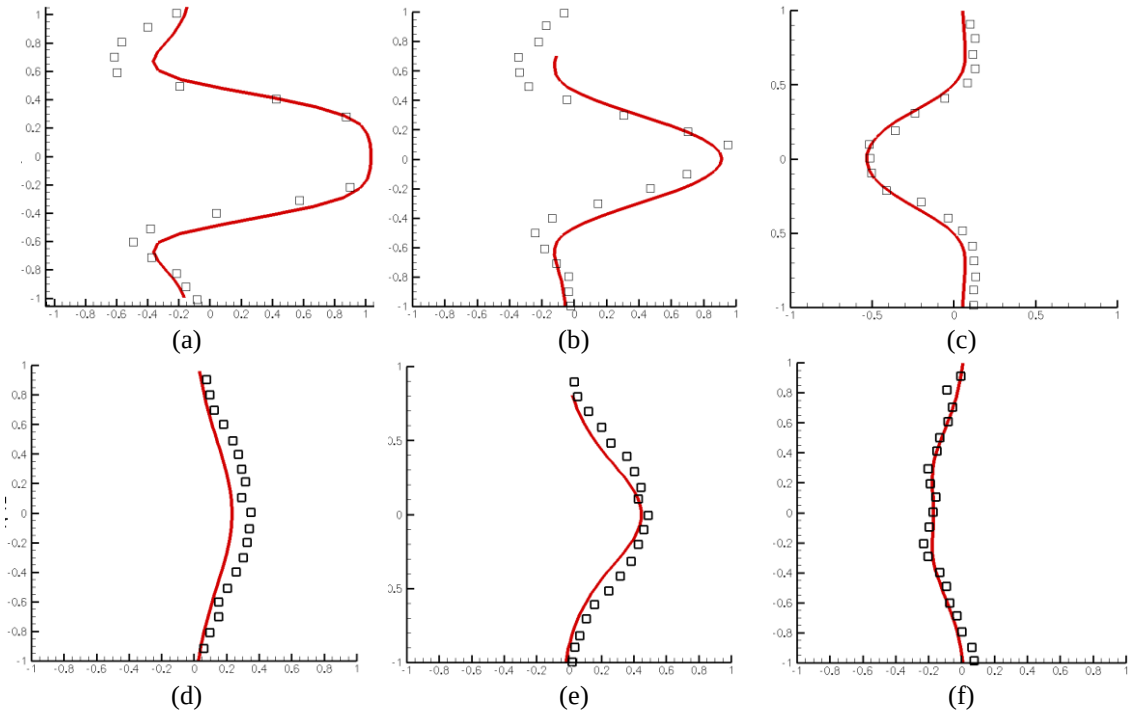

Figure 2: Numerical and experimental results for $x = -0.6D$ (a–c) and on the right $x = 1.2D$ (d–f). The red line represents the computational results obtain with the IBM and the black squares represent the empirical data from [3], pp 258, Figure 6.

3.3 Rotating Flattened Cylinder

This shape was defined by 3 semi-circles, one with radius equal to $r = 0.01$ and the other two with half of this radius. This geometry was chosen in order to have a simplified model of a section from a winding Eucalyptus peel tube, one of the most common reasons of the propagation for forest wild fires.

This part of work was mainly motivated as part of an ongoing investigation regarding forest fires. The premises of this investigation was that the winding Eucalyptus peel was usually animated with an angular frequency of 10 Hz which meant an angular velocity of $\omega=20\pi$ rad/s. We computed our solutions for a Re=40. Once again we expected a periodic solution for this flow. The asymmetry of the body and the rotation imposed on it made us expect that the perturbations induced on the fluid would have a sinusoidal behavior. In Figure 3 we can see the pressure distribution for 4 phases of half-period, namely $\theta = 0$, $\theta = \phi/8$, $\theta = \phi/4$ and $\theta = 3\phi/8$.

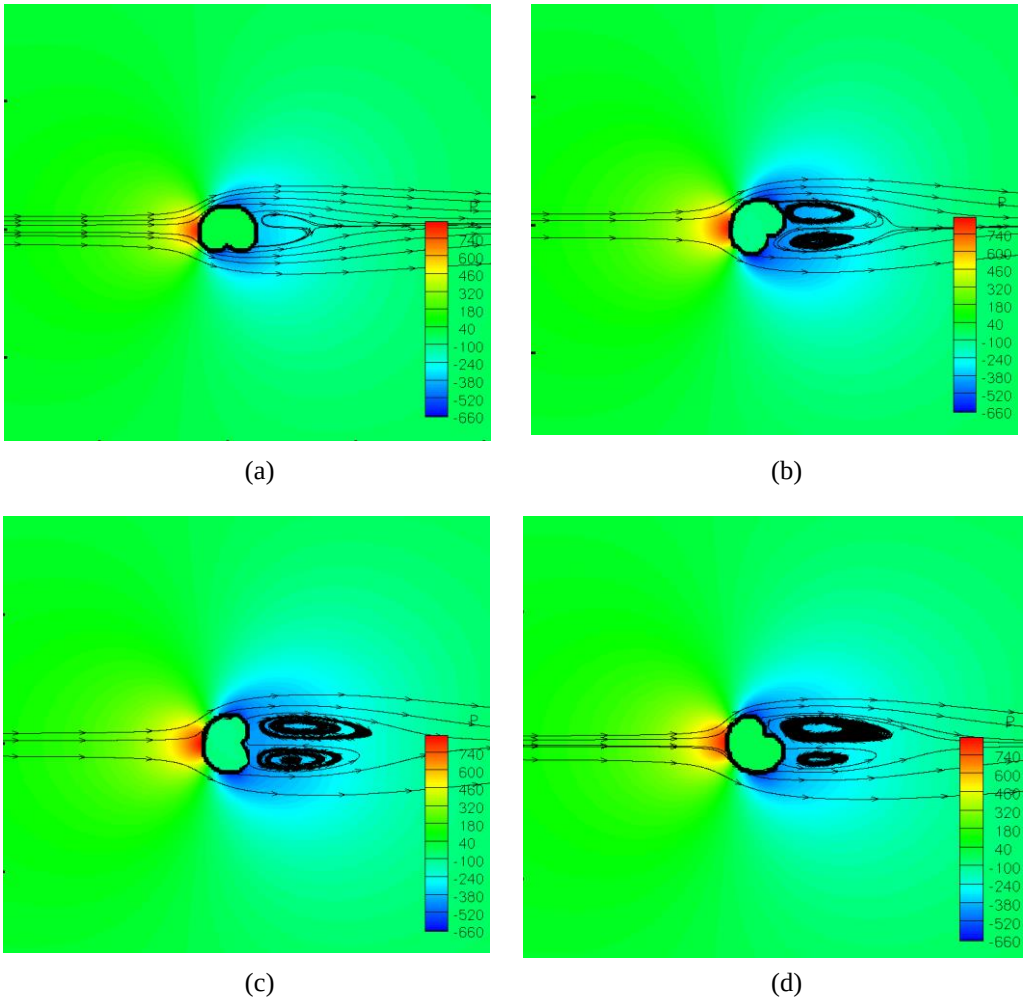

Figure 3: Four phases of the pressure distribution for one cycle of the flattened cylinder at Re $= 40$ and $f = 10$ Hz and streamlines representation.

In these 4 frames it is possible to observe that the pressure around the immersed boundary is changing with the position of the flattened half of the body. From those frames we can remark that in Figure 3(a) the peak of pressure in the stagnation point is lower than in the other phases of the motion. Just as the pressure in the leading edge varies with time the distribution of the pressure in the rest of the boundary is also changing accordingly which will produce a temporal variation in the aerodynamic forces

Another interesting fact present in Figure 3 is the variation of the streamlines with the rotation of the body. We can see in Figure 3(a) that the vortex is really small and in the following Figure 3(b) and 3(c) there a development of the vortexes until Figure 3(d) is reached, where the vorticity starts to decrease.

When we reach the second half of the motion we can see that once again there's formation of vorticity but in this case the length of recirculation is larger. The vortexes that were formed in the first half of the cycle are dissipated by the rotation of the body.

4 CONCLUSIONS

The IBM was implemented in an unstructured finite volume code and several verification and validation tests were undertaken.

Three different interpolation schemes for the boundary's correction using an analytical solution in order to assert if it was possible to maintain the global second order discretization of the Finite Volume method.

From this analysis we were able to conclude that if the polynomial used in the correction of the immersed boundary is of the same order (in this case second order) of the discretization method it is possible to obtain the FV global second order of accuracy. This polynomial was constructed using solid material points and the cell centroids from the fluid cells where the correction was supposed to be implemented. The polynomial is obtained using a regression based on the Least Squares Method.

The IBM was applied to a moving boundary for a periodic case experimentally investigated by H. Dustch *et al.* [3]. The pressure and vorticity contours as well as the velocity at different positions in different time instants were compared with the computational and the empirical data available. The comparison of these values was satisfactory thus asserting the validation of the method.

Finally the IBM was applied for the case of a rotating Eucalyptus peel tube with an incoming flow at $\mathrm{Re} = 40$ in order to study the aerodynamic behavior of this complex geometry.

The proposed method is reliable to solve problems that include the immersion of a body in a fluid flow and it improves the efficiency using parallel computation producing accurate results at a low computational cost, especially for low Reynolds number flows.

In summary this type of method is in an area of computational mechanics that has room for improvement and a promising investment thus providing the aerospace market with powerful tools to analyze the behavior of bodies immersed in fluids.

REFERENCES

[1] L Sanjar, R Marthur, J Murthy (2010). An unstructured finite-volume method for incompressible flows with complex immersed boundaries. *Numerical Heat Transfer, Part B: Fundamentals* **58**(4):217–241.

[2] T Kariya, K Kurata (2004). *Generalized Least Squares Methods*, John Willey & Sons.

[3] H Dütsch, F Durst, S Becker, H Lienhart (1998). Low-Reynolds-number flow around an oscillating circular cylinder at low Keulegan–Carpenter numbers. *Journal of Fluid Mechanics* **360**:249–271.

[4] JPP Magalhães, DMS Albuquerque, JMC Pereira, JCF Pereira (2013). Adaptive mesh finite-volume calculation of 2D lid-cavity corner vortices. *Journal of Computational Physics* **243**:365–381.

[5] DMS Albuquerque, JMC Pereira, JCF Pereira (Accepted). Residual least squares error estimate for unstructured h-adaptive meshes. *Numerical Heat Transfer, Part B: Fundamentals*.

Numerical simulation of transonic flow over a deep cavity

P Freitas[1], JCF Pereira[2]

[1]Instituto Superior Técnico, Universidade de Lisboa, Avenida Rovisco Pais 1, 1049-001 Lisboa, Portugal
[2]Departmento de Engenharia Mecânica, Instituto Superior Técnico, Universidade de Lisboa, Avenida Rovisco Pais 1, 1049-001 Lisboa, Portugal
email: pedrogfefreitas@tecnico.ulisboa.pt, jcfpereira@tecnico.ulisboa.pt

ABSTRACT: A transonic turbulent flow over a deep cavity is studied with the OpenFOAM code for LES (Smagorinsky model) and unsteady RANS (κ-ε and κ-ω models) and compared with available experimental and computational data. The main feature of deep cavities is the sound field that may induce fatigue and vibration on the structures. A numerical study was conducted to investigate the slanted aft wall on the shedding frequency to reduce the emitted noise of the cavity. So it is also done a simulation on a control device to reduce the emitted noise of the cavity. In general, LES simulations are in a better agreement with experimental and computational data. Finally, the noise reduction was achieved successfully by slanting the aft wall.

KEY-WORDS: Deep cavity; Transonic flow; LES; RANS; OpenFOAM.

1 INTRODUCTION

The flow for resonant open cavities is governed by a feedback mechanism between the shear layer instabilities and acoustic disturbances. This mechanism is illustrated in Figure 1 (c). The upstream boundary layer has instabilities that are increased after the separation point and they are convected downstream. Then they impinge on the downstream corner and a pressure wave is generated and travels upstream at the velocity of sound in the quiescent medium, this is the feedback in Figure 1 (c). Then this pressure wave interacts with the shear layer increasing the instabilities, and at the resonant frequency a vortex merging, see [1], occurs and a coherent structure is build see e.g. [3,4]. Then this coherent structure is convected downstream and collides with the aft wall generating stronger acoustic waves that made the discrete tones of high acoustic intensity.

This feedback mechanism in cavities was proposed by Rossiter in [8]. It was done a parametric experimental study to relate the frequencies of the tones and the geometrical relations of the cavity, and an empirical formula to predict the frequencies was deduced for cavities with $L/D \geq 1$. This formula is as follows:

$$St_n = \frac{f_n L}{U_\infty} = \frac{n-\gamma}{Ma_\infty + 1/\kappa} \quad (1)$$

St_n is the Strouhal number corresponding to the n-th mode frequency, κ and γ are empirical constants corresponding to the average convection speed of disturbances in the shear layer and the phase delay, respectively.

Subsonic and transonic cavities are geometrically classified as deep for $L/D < 1$, shallow for $L/D > 1$, two-dimension for $L/W < 1$ and three-dimensional for $L/W > 1$ ([11]).

It was seen that the flow over a cavity causes several concerns such as high SPL, forcing levels or pitching moments which influences the correct release of the stores or harm the avionics of the stores or weapons. Controlling the cavity high SPL and forcing levels is then a plus. Further cavity oscillation control serve as a model problem in the growing multidisciplinary field of flow control ([6]). In [8], the first known study to use a control device, a spoiler was used successfully. Despite the SPL was lowered, it had the same evolution and detachable frequencies.

To reduce the noise levels in an open cavity, it is needed to reduce the interactions between the shear layer and the aft wall. And three strategies are known to reduce this interaction, [12,2] by lifting the shear layer, [12,2] by slanting the aft wall and [2,13] by energizing the shear layer so that it contains smaller coherent structures.

A detailed review of control can be found in [6].

The main objectives of the present work are to validate the OpenFOAM code for transonic LES and RANS in a deep cavity, and also to see the effects on the flow of changing the geometry. The free-stream Mach number is 0.8 and the aspect ratio (L/D) is 0.42 the same as the L/W. Two geometries are studied, the clean cavity configuration which is a deep cavity or open cavity, and the cavity with the same free-stream conditions but with a slanted aft wall.

2 GOVERNING EQUATIONS

The governing equations are embodied in the Navier-Stokes model in the conservative form which expresses the conservation of momentum, the continuity equation or mass conservation and the energy equation. The approximations and hypothesis, following [10], are: the continuum hypothesis; compressible gas fluid flow; non-reactive mono-species gases; non-hypersonic flows (Ma < 6 for air); low temperature differences to neglect radiation; thermodynamic equilibrium so that the perfect gas equation can be used; Newtonian fluid with the dynamic viscosity varying only with the temperature; Froude number large enough to neglect gravity effects.

Two Reynolds-Averaged Navier-Stokes turbulence models were used, the κ-ε model and κ-ω SST model. The equations for the RANS κ-ε are from [7].

The κ-ω standard turbulence model is an improvement of the κ-ε turbulence model. The Shear Stress Transport model was derived in [14] and it is an improvement of the κ-ω standard model to have a better performance in the outer layer of the boundary layer. The improvement of the SST model over the original ([5]) is that the outer layer of the turbulent flow is modeled with the κ-ε model and the inner layer is solved with the original κ-ω, also the eddy viscosity is also modified to account for the transport of the principal turbulent shear stress.

The Smagorinsky model was used for LES and is as follows

$$\nu_{SGS} = C_s^2 \Delta^2 \left|\tilde{S}\right| \tag{2}$$

however this model has to be adjusted to work near the wall because the turbulent viscosity goes to zero near the wall (and in the standard Smagorinsky's model it does not), so the van Driest damping function is used.

3 RESULTS

3.1 Computational Domain

3.1.1 Geometry

The geometries for the present study are displayed in figures 1 a) and 1 b), we can named it cavity (for the standard case) and cut (for the cavity with a slanted wall, the angle of the cut is 45^o (it can be checked by trigonometry). It is the same cavity of the experimental work of [15] and the computational domain of [11,9]. The cavity and cut dimensions and relations are summarized in Table 1. The axis is also displayed, in green, in Figure 1 (a) and (b).

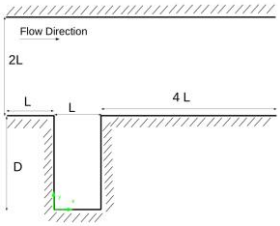

(a) Geometry of the cavity.

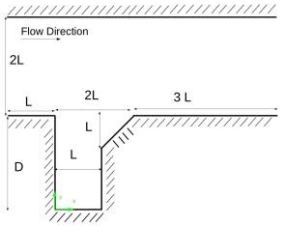

(b) Geometry of the deep cavity with the cut.

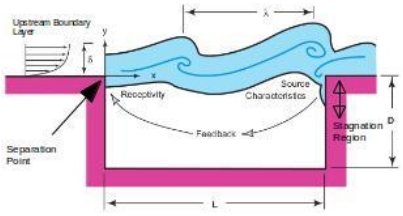

(c) Schematic illustrating of the flow in an open cavity, slightly modified from [6].

Figure 1: Geometries of the problem to be studied and the physics of the open cavities.

Table 1: Summary of the cavity dimensions and relations.

L [mm]	*D* [mm]	*W* [mm]	*L/D*	*L/W*	*D/L*	*W/L*	*D/W*
50	120	120	≈ 0.42	≈ 0.42	2.4	2.4	1

3.1.2 Boundary Conditions

The free-stream conditions of [9] are displayed in Table 2.

Table 2: Summary of the free-stream conditions.

U_∞ [m/s]	p [kPa]		T [K]		ρ [kg/m^3]		Ma
	Stagnation	Static	Stagnation	Static	Stagnation	Static	
258.5	98	64.3	293	259.8	1.17	0.86	0.8

3.2 Instantaneous Flow Field

In this section the instantaneous Mach number and isolines of the pseudo-schlieren are presented. Unfortunately due to memory issues only a few instantaneous fields have been recorder thus hindering to watch great part of the shedding cycle. The shedding frequency is around 2000 Hz or a period of 5×10^{-4} s and the results were recorded with a Δt of 2×10^{-4} s and 2.5×10^{-4} s, so at the best only two phases can be shown.

Figure 2(a) shows the instantaneous Mach number of the flow for the LES simulation set 1. As can be seen the Mach number is greater than one in some phase of the shedding cycle and this is going to cause a complex vortex-shock interaction, more details are given below.

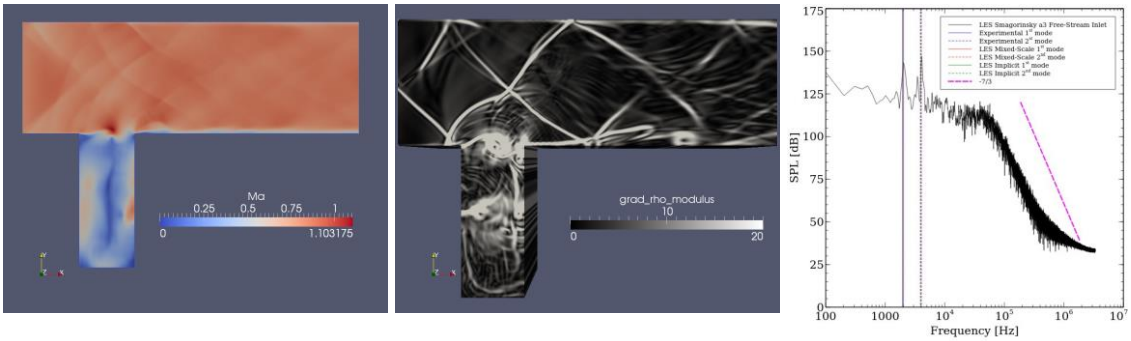

(a) Instantaneous Mach number for top-hat velocity inlet profile.

(b) Instantaneous pseudo-schlieren for power-law velocity inlet profile.

(c) SPL for LES top-hat velocity inlet profile.

Figure 2: Instantaneous results and SPL for the LES simulations.

Figure 2(b) displays the pseudo-schlieren for the LES simulation with a power-law inlet. It can be seen a reflected shock wave at the inlet which is the result of the interaction of the shear layer and the propagating upstream pressure waves. As said previously, the time steps saved is not as much as wished, but from [11,9,15] at some phase of the shedding cycle there is a strong shock-vortex interaction that deforms the acoustic wave travelling upstream and during this interaction (the sound wave and a coherent structure) acoustic waves are released during the passage of the wave by the structure.

It was also seen (but not shown) that RANS captured the wave patterns well however it does not capture the physics of the flow below the cavity like the coherent structures whereas LES provides a more realistic solution.

3.3 Pressure Spectral Density, Sound Pressure Level

The overall results are in agreement with the experiment [9], the greatest frequency difference is 4.3% and it is for the LES with a power-law inlet. It was noted that the frequencies did not have a great exchange from each mesh which means that the flow is governed by large scales instead of fine-grain turbulence ([11]). LES simulations do not have a great SPL because the length of the signal is not as large as wished. It was also seen that the cut is effective in reducing the frequency because both meshes diminished the SPL and the frequency for the first tone is the same.

Figure 2(c) shows the SPL for the LES top-hat velocity inlet profile and shows that the signal length is short because it does not capture more than two modes. It also shows a pressure spectrum decay rate at $-7/3$.

3.4 Mean Results

3.4.1 RANS Models Results

Figure 3 shows the computed mean longitudinal velocity and mean normal vertical Reynolds stress for RANS κ-ε and κ-ω mesh type b).

For the longitudinal mean velocity, Figure 3 (a), the power-law inlet is overall in satisfactory agreement with the literature and the velocity for the mesh 1 (32,000 cells), it also underestimates the velocity below the cavity ($y/L < 2.4$) and overestimates the results above the cavity ($y/L > 2.4$). The top-hat velocity profile overestimates too the mean velocity above the cavity.

The mean normal vertical Reynolds stress, Figure 3 (b), cannot be predicted by these models, and the results are worse if mesh type a) is used. RANS for the Reynolds stresses only predicted the peaks of the tensions at the shear layer influence zone.

The vertical velocities were in satisfactory agreement with the literature, as the mean longitudinal velocities.

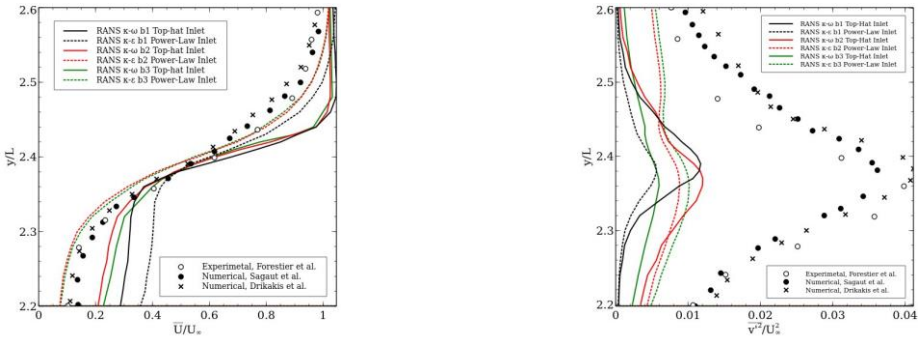

(a) Mean longitudinal velocity. (b) Mean normal vertical Reynolds stress.

Figure 3: Mean longitudinal velocity and mean normal vertical Reynolds stress for RANS κ-ε and κ-ω mesh type b) 1 (32 000 cells), 2 (64 000 cells) and 3 (130 000 cells) at $x/L = 0.4$.

3.4.2 LES Model Results

Figure 4 shows the computed mean longitudinal velocity for LES Smagorinsky. The LES results are in good agreement with the experiments [9] and fine LES calculations [11,15]. There are some influence between the top-hat velocity inlet and the power-law inlet and surprisingly the differences occur inside the deep cavity as a consequence of the small deviations in the shear layer.

Figure 5 shows the computed mean vertical velocity for LES Smagorinsky model. The overall results are in good agreement with the data. Comparing the top-velocity profile inlet and the power-law inlet the flow is both qualitatively and quantitatively correct. The power-law inlet produces the best accuracy, this is obviously due to the inlet; [15] said that the deviations from ILES and the selective mixed scale sub-grid model are due to the inlet conditions.

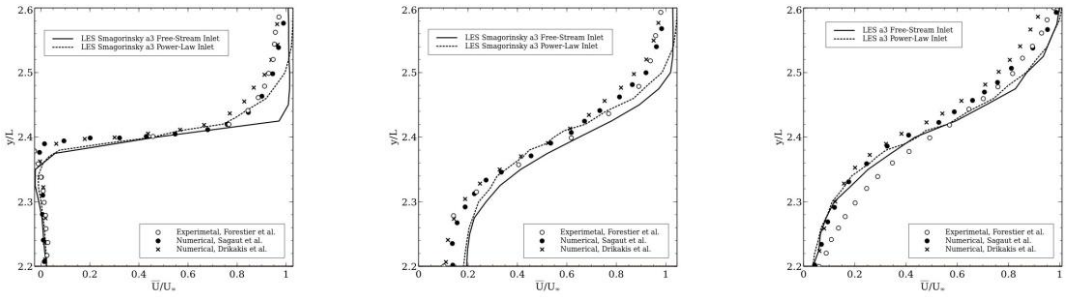

(a) $x/L = 0.05$. (b) $x/L = 0.4$. (c) $x/L = 0.95$.

Figure 4: Mean longitudinal velocity for LES Smagorinsky mesh type a) 3 (130 000×24 cells).

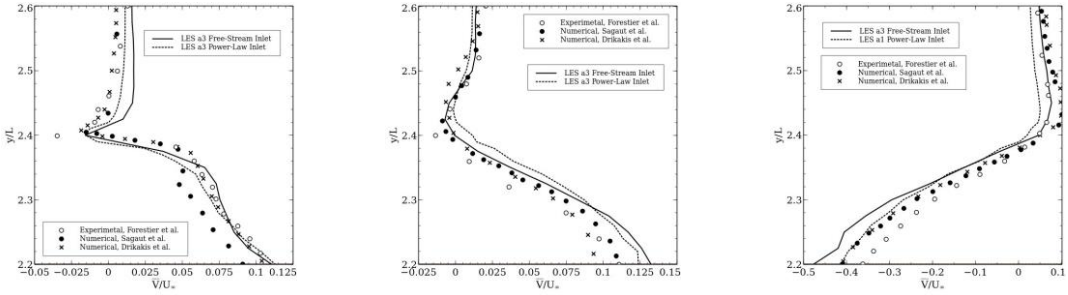

(a) $x/L = 0.05$. (b) $x/L = 0.4$. (c) $x/L = 0.95$.

Figure 5: Mean vertical velocity for LES Smagorinsky mesh type a) 3 (130 000×24 cells).

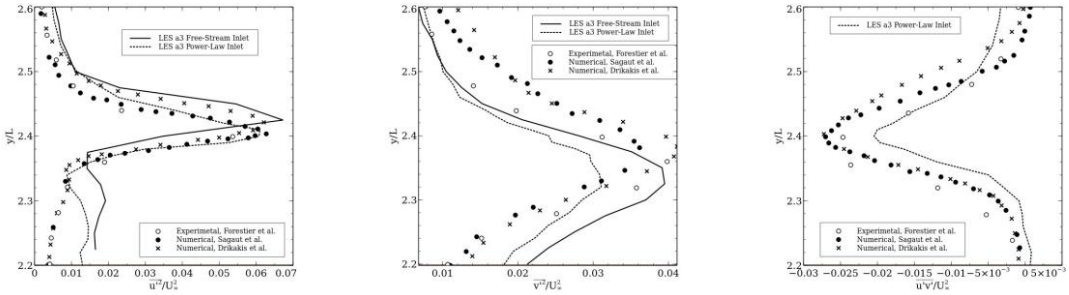

(a) $x/L = 0.2$, mean normal longitudinal. (b) $x/L = 0.4$, mean normal vertical. (c) $x/L = 0.3$, mean shear.

Figure 6: Mean Reynolds stresses for LES Smagorinsky mesh type a) 3 (130 000×24 cells).

4 CONCLUSIONS

Simulations of a deep cavity were obtained with the OpenFOAM code. The results were obtained with RANS (κ-ε and κ-ω turbulence models) and LES (Smagorinsky model). In addition the inlet velocity profile that generates the incoming boundary layer up to the cavity upstream edge was simulated by a free-stream velocity top-hat profile and a power-law velocity profile.

4.1 Grid

The influence of the mesh on the predicted dominant frequencies is low which means that the flow is governed by the large-scale coherent structures (see [11]).

The grid refining has influence on the mean velocity and the Reynolds stresses, and as could be expected the mesh which produces best results compared to the experimental and computational is the 130 000 cells mesh. The 3 million cells mesh provides better results for LES than 1.5 million cells mesh.

4.2 Upstream Boundary Layer

The major influence of the inlet profile is in the mean longitudinal velocity above the cavity, where the top-hat profile does not generate the momentum thickness measured.

4.3 Frequency and SPL

The frequencies obtained with LES and RANS are well predicted as well as the SPL, however RANS is unable to predict the random pressure fluctuations presented in the turbulent shear layer. The cut is effective in attenuating the SPL.

4.4 RANS and LES

The greatest differences between LES and RANS are in the turbulent flow quantities and the broadband noise. Overall LES predicts better results compared with the experiments as reported by fine mesh LES calculation.

For both techniques it was seen that the aft wall has a stabilizing effect because the mean velocities at $x/L = 0.95$ are quite well predicted when compared with the computations of [11,15]. Other common issue is that at $x/L = 0.8$ the mean vertical velocity is poorly predicted.

REFERENCES

[1] C-M Ho, NS Nosseir (1981). Dynamics of an impinging jet. Part 1. The feedback phenomenon. *Journal of Fluid Mechanics* **105**:119–142.

[2] S Arunajatesan, C Kannepalli, N Sinha, M Sheehan, G Shumway (2008). Suppression of cavity loads using leading edge blowing concepts. In *46th AIAA Aerospace Sciences Meeting and Exhibit*, 7–10 Jan 2008, Reno, Nevada, Paper AIAA 2008-44.

[3] JCF Pereira, JMM Sousa (1994). Influence of impingement edge geometry on cavity flow oscillations. *AIAA Journal* **32**(8):1737–1740.

[4] JCF Pereira, JMM Sousa (1995). Experimental and numerical investigation of flow oscillations in a rectangular cavity. *Journal of Fluids Engineering* **117**:68–74.

[5] DC Wilcox (1988). Multiscale model for turbulent flows. *AIAA Journal* **26**(11):1311–1320.

[6] LN Cattafesta III, Q Song, DR Williams, CW Rowley, FS Alvi (2008). Active control of flow-induced cavity oscillations. *Progress in Aerospace Sciences* **44**:479–502.

[7] JE Bardina, PG Huang, TJ Coakley (1997). *Turbulence Modeling Validation, Testing, and Development*, NASA Technical Memorandum 110446.

[8] JE Rossiter (1964). *Wind-Tunnel Experiments on the Flow over Rectangular cavities at Subsonic and Transonic Speeds*, Reports and Memoranda No. 3438, Aeronautical Research Council, Ministry of Aviation, London.

[9] N Forestier, L Jacquin, P Geffroy (2003). The mixing layer over a deep cavity at high-subsonic speed. *Journal of Fluid Mechanics* **475**:101–145.

[10] E Garnier, N Adams, P Sagaut (2009). *Large Eddy Simulation for Compressible Flows*, Springer.

[11] L Larchevêque, P Sagaut, I Mary, O Labbé, P Comte (2003). Large-eddy simulation of a compressible flow past a deep cavity. *Physics of Fluids*, **15**(1):193–210.

[12] SJ Lawson, GN Barakos (2009). Assessment of passive flow control for transonic cavity flow using detached-eddy simulation. *Journal of Aircraft* **46**(3):1009–1029.

[13] AM Lamp, N Chokani (1997). Multiple control surface utilization in active aeroelastic wing technology. *Journal of Aircraft* **34**(4):545–551.

[14] FR Menter (1994). Two-equation eddy-viscosity turbulence models for engineering applications. *AIAA Journal* **32**(8):1598–1605.

[15] B Thornber, D Drikakis (2008). Implicit large-eddy simulation of a deep cavity using high-resolution methods. *AIAA Journal* **46**(10):2634–2645.

Session 2

Chairman

Carlos Bettencourt da Silva | U.Lisboa

This page was intentionally left blank

V Conferência Nacional de Mecânica dos Fluidos, Termodinâmica e Energia
MEFTE 2014, 11–12 Setembro 2014, Porto, Portugal
APMTAC, 2014

Nonlinear wave-current interactions in deep water: vorticity effects

RM Moreira[1], JTA Chacaltana[2]

[1]UFF, Rua Passo da Pátria 156, bl.D, sl.563A, Niterói, RJ, 24210-240, Brazil
[2]UFES, Av. Fernando Ferrari 514, CT-4, sl.24, Vitória, ES, 29075-910, Brazil
email: roger@vm.uff.br, juliotac@gmail.com

ABSTRACT: The effects of uniform vorticity on a train of 'gentle' and 'steep' water waves interacting with underlying flows are investigated through a boundary integral method. It is shown that wave blocking and breaking are more prominent when positive values of vorticity are imposed on right-going progressive waves. Reflection continues to occur when sufficiently strong adverse currents are imposed on 'gentle' deep-water waves, though now affected by vorticity. For increasingly positive values of vorticity, the induced shear current reduces the wave speed and introduces significant changes to the free-surface profile, until waves are completely blocked by the underlying flow. A plunging breaker is formed at the blocking point when 'steep' deep-water waves undergo strong currents. Negative vorticities augment the speed of right-going progressive waves with wave breaking being detected for strong shear flows. The time of breaking is sensitive to the vorticity's sign and magnitude, with wave breaking occurring later for negative values of vorticity.

KEY-WORDS: Water waves; Free-surface flows; Wave blocking; Boundary integral method.

1 INTRODUCTION

Most of the theoretical works concerning surface waves on water make the initial assumption of irrotational flow. This approximation is often realistic since the velocity profile in the water – whether due to laminar viscosity or turbulent mixing – is usually established over time and length scales which are long compared with a wave period or wave length. However there are many circumstances in which vorticity plays an important role. For instance, in any region where the wind blows, a highly sheared current results with rotational waves being formed [1,2]; any 'rapidly' varying current generates vorticity, which affects directly the free-surface layer [3]. Furthermore, depending on their speed and surface curvature, waves also generate vorticity [4,5]; bores, spilling and plunging breakers usually create a strong vortical flow beneath the free surface [6,7,8]. Therefore many mechanisms of vorticity generation exist and may influence the form of the free surface. Depending on its sign and magnitude, vorticity can then become a dominant feature in the waves' dynamics.

Several authors have studied the propagation of weakly nonlinear waves on linear shear currents via perturbation expansion methods and found out that the vorticity distribution produces significant changes in the water-surface elevation [9,10,11,12]. Benjamin [13] found solitary wave solutions over a stream with an arbitrary vorticity distribution while Dalrymple [14] used a Fourier series expansion to study large-amplitude waves on linear shear currents. Simmen and Saffman [15] and Teles da Silva and Peregrine [16] computed fully nonlinear numerical solutions of periodic waves on constant-vorticity currents for deep and finite water depths. More recently, Constantin and Escher [17] discussed the symmetry of steady periodic surface water waves with vorticity and Ko and Strauss [18] computed two-dimensional finite-depth steady water waves with variable vorticity. Interesting wave profiles were predicted such as bulbous and extreme waves with stagnation points, confirming that vorticity has a profound effect upon the free surface as wave height increases.

At sea, waves are generated by the wind and can be shortened and steepened by opposing currents, foci by the shear at the currents' boundaries and refracted into caustics. These caustics arise as envelopes of the group velocity paths (or rays), which lead to a singularity of the amplitude where the linear approximation becomes invalid. At these regions the wave intensity is sufficient for nonlinear effects to begin to be important. If the opposing current is strong enough then waves can be blocked. A strong increase in wave steepness is observed followed by wave breaking, which can cause significant hazards to boats and ships navigating under these circumstances. For rapidly varying currents, Moreira and

Peregrine [19] showed that part of this wave energy can be released in the form of partial reflection before wave breaking occurs. Depending on its direction, Kharif et al. [2] observed that wind may sustain these steep waves which then evolve into breaking waves. The review papers of Peregrine [20], Jonsson [21] and Thomas and Klopman [22] give a full account on the varied physical aspects and the different mathematical approaches applied to wave-current interactions.

The effects of vorticity on wave-current interactions were discussed by Taylor [23], who investigated by linear theory the action of uniform and linearly varying surface currents to stop sea waves. Swan, Cummins and James [3] confirmed experimentally and via a multi-layered numerical model that the near-surface vorticity leads to an important change of the dispersion equation, showing that the Doppler-shifted solution is not sufficient to characterize the wave-current interaction. The effects of uniform vorticity to the linear dispersion relation were also investigated by Nwogu [24], who developed a fully nonlinear boundary-integral scheme to describe the three-dimensional interaction of steep gravity waves with ocean currents, and Choi [25], who studied via a pseudo-spectral method the interaction of nonlinear surface waves with a linear shear current. They both found that vorticity can influence significantly the envelope of modulated wave trains in deep water.

Despite the theoretical and experimental works on this field, very few consider the role of vorticity on fully nonlinear wave-current problems. The present work aims to study the nonlinear effects induced by wind-driven and non-uniform currents on deep-water waves. The influence of uniform vorticity on a train of free-surface gravity waves interacting with underlying flows is investigated through a boundary integral method. The waves are short compared with the length scale of the underlying flow and are affected by vorticity at the surface layer. In particular 'rapidly' varying surface currents with constant vorticity are imposed in order to verify the wave transformation that occurs at the blocking region. This study is motivated by recent experimental and numerical works towards the blocking region, where large-scale adverse currents vary over short-scale gravity waves, causing a strong increase in wave steepness, which may be prolonged by the imposed shear current until wave breaking occurs [3,26].

2 UNSTEADY NONLINEAR MODEL WITH VORTICITY

Consider a two-dimensional incompressible fluid flow in the (x, y) plane. Cartesian coordinates are defined by setting the x axis in the undisturbed water surface and the y axis vertically upwards so that the fluid occupies the half-plane $y \le 0$ when at rest. Attention is directed to cases in which a linear shear flow with constant vorticity τ is imposed [16,25] such that the total current $\vec{u} = \vec{u}_\tau + \vec{u}_\phi$, where the shear current $\vec{u}_\tau = (y\tau, 0)$ and the potential current $\vec{u}_\phi$ is given by the gradient of a velocity potential $\phi(x, y, t)$, which satisfies Laplace's equation.

The kinematic and dynamic boundary conditions are applied at the free surface

$$\frac{D\vec{r}}{Dt} = \vec{u}, \qquad \frac{D\phi}{Dt} = \frac{1}{2}|\nabla\phi|^2 - gy - \tau\psi - \frac{p}{\rho}, \tag{1}$$

where $\vec{r} = (x, y, t)$; $y = \eta(x, t)$ is the elevation of the free surface; g is the acceleration due to gravity; ψ is the stream function, which is related to the rotational flow; ρ is the fluid density; and p is the pressure on the exterior side of the free surface, which for simplicity is equal to zero. Capillarity is not taken into account.

It is assumed that the water is deep, satisfying the condition $|\nabla\phi| \to 0$ as $y \to -\infty$ and periodic in x, with $\nabla\phi(0, y, t) = \nabla\phi(2\pi, y, t)$ at the vertical boundaries, valid for $-\infty < y < \eta$ and $t > 0$. Here the length units are chosen to make the wave period equal to 2π, which is convenient for a periodic domain. To complete the model, an initial condition for the free surface is required such that $\eta(x, t) = \eta_0(x, 0)$ and $\phi(x, \eta, t) = \phi_0(x, \eta_0, 0)$. Cases of 'gentle' and 'steep' periodic surface waves with initially uniform wavenumber interacting with an underlying flow with constant vorticity are of interest. In a reference frame at rest, waves propagate in the positive x direction such that vorticity is positive when a following shear flow is imposed, and negative for an adverse shear current. Different magnitudes and directions of $\vec{u}_\tau$ were tested aiming to understand the role of vorticity on wave-current interactions.

The potential current $\vec{u}_\phi$ depends on the velocity potential ϕ, which is decomposed in our model as $\phi = \phi_S + \phi_W$, where ϕ_S is the contribution due to singularities and ϕ_W represents the velocity potential of the surface waves. This methodology was used by Moreira and Peregrine [19,27], who employed doublets, vortices, sinks and sources to model the desired underlying flow; the chosen singularity distribution satisfies Laplace's equation in the fluid domain. The underlying velocity $\nabla\phi_S$ is then

designed to be uniform over the depth of the free-surface layer but variable in the x direction. Two counter-rotating vortices at fixed positions in time are introduced to obtain a steady, 'rapidly' varying surface current. Here the strength and depth of vortices are conveniently chosen such that the maximum adverse current is equal to the stopping velocity of the free-surface waves under still water conditions. This situation is particularly relevant since, under blocking conditions, linear solutions become singular. For more details of the imposed free-surface current, see [19].

The method of solution consists of solving the principal value of an integral equation that arises from Cauchy's integral theorem of a complex variable function. To apply Cauchy's integral theorem, the velocity potential ϕ must be known on the surface for each time step; ϕ_S is then subtracted from the surface value of ϕ such that the remaining surface wave potential ϕ_W can be used to calculate the velocity $\nabla\phi_W$ on the free surface. The total current is then given by $\vec{u} = \vec{u}_\tau + \nabla\phi_S + \nabla\phi_W$; $\vec{r}$ and ϕ are then stepped in time using a Taylor time series truncated at the sixth power. Thus $\vec{u}$ and its Lagrangian derivatives are affected directly in our model by vorticity and the vortex dipole. For more details of the numerical method, see [28].

To avoid the formation of free-surface waves due to the impulsive motion of the underlying flow, a suitable initial condition is built using a similar methodology proposed by [19]. Firstly the influence of vorticity on a stationary free-surface flow induced by two counter-rotating vortices is analysed under the light of linear wave theory, with a second-order linear steady solution derived for the free-surface elevation. Then a uniform wave train with constant vorticity is generated and superimposed onto the linear steady solution. The resulting initial condition reduces significantly the disturbances generated by the impulsive initial motion, contributing to a better analysis of the effects of vorticity on wave-current interactions.

For a steady regime the kinematic and dynamic boundary conditions (1) simplify to

$$\frac{\partial\phi}{\partial x}\frac{\partial\eta}{\partial x} = \frac{\partial\phi}{\partial y}, \qquad \frac{1}{2}\left[\left(\frac{\partial\phi}{\partial x}\right)^2 + \left(\frac{\partial\phi}{\partial y}\right)^2\right] + g\eta - \tau\eta\frac{\partial\phi}{\partial x} = 0, \tag{2}$$

both valid on $y = \eta(x)$. At the vertical boundaries $\nabla\phi(0, y) = \nabla\phi(2\pi, y)$ for $-\infty < y < \eta$; in addition $|\nabla\phi| \to 0$ as $y \to -\infty$. Laplace's equation is satisfied for the whole fluid domain excluding the singularities.

For small surface waves the velocity potential $\phi(x,\eta)$ and the free-surface profile $\eta(x)$ can be approximated by algebraic expansions of the wave steepness ε, such that $\phi(x,\ \eta) = \varepsilon\phi_1 + \varepsilon^2\phi_2 + O(\varepsilon^3)$ and $\eta(x) = \varepsilon\eta_1 + \varepsilon^2\eta_2 + O(\varepsilon^3)$, where $\phi_i\ (i = 1, 2, \cdots)$ depends on x and η, and η_i is a function of x. Substituting these approximations into (2) and extracting the ε and ε^2 terms provides a linear steady solution with vorticity for the free surface

$$\eta(x) = -\frac{1}{2}\frac{\left(\frac{\partial\phi_S}{\partial x}\right)^2}{\left(g - \tau\frac{\partial\phi_S}{\partial x}\right)}, \tag{3}$$

where, to simplify the notation, ϕ_1 and η_2 were replaced by ϕ_S and η; ϕ_S denotes the velocity potential induced by the eddy couple. When $\tau = 0$, solution (3) reduces to expression (2.8) of [19].

All variables are non-dimensionalised such that $X = k\,x$, $T = t\sqrt{g\,k}$, $U = u\sqrt{k/g}$ and $\zeta = \tau/\sqrt{g\,k}$, where k is the wavenumber; X, T, U and ζ are the respective dimensionless parameters for space, time, velocity and vorticity. The Froude number is also defined as $Fr = \gamma/\sqrt{gd^3}$, where γ and d are the strength and the depth of submergence of the vortex couple, which are conveniently chosen to characterise 'weak' free-surface flows $(Fr \le 0.1)$. This is particularly important to guarantee that the singularities have little effect on the surface waves such that their existence can be considered unimportant.

To avoid the formation of disturbances at the free surface due to the impulsive initial motion of the vortex flow, several tests were carried out employing the linear steady solution with vorticity as the initial condition of the unsteady fully nonlinear model. All the computed cases have an initial distribution of 120 points per wavelength. To guarantee that the crest of steep waves – as well as reflected and overturning waves – are well resolved as time evolves, regridding with respect to the arclength is used. A

redistribution of points along the surface at every 10 regular intervals in time is done by using a tenth-order interpolation algorithm. This tenth-order polynomial is centred on the nearest point in the current space distribution and then used to interpolate each surface variable in order to find its value at the new position along the surface. Sawtooth numerical instabilities were not observed in the computations, therefore smoothing was not necessary. All the simulations were done on a Dell workstation with an Intel i7 processor. For more details of the accuracy of the numerical scheme, see [19,28].

3 VORTICITY EFFECTS ON WAVE-CURRENT INTERACTIONS IN DEEP WATER

Figures 1 and 2 compare the wave transformation caused by shear currents with different directions and magnitudes ($|\zeta| = 0; 0.063; 0.316$) onto a train of 'gentle' and 'steep' deep-water waves ($\varepsilon_0 = 0.02; 0.2$) propagating over an adverse current at the blocking condition according to linear theory ($|U_{min}|=|U_s|$). For clarity, only the surroundings of the U_{min} region are shown, with the stacked free-surface profiles being vertically exaggerated. Waves propagating over a stream flow without vorticity are represented by the solid lines.

For 'gentle' waves (see Figure 1), reflection accompanied by wave breaking was observed in the blocking region, with vorticity causing a shear at the free-surface layer. Negative vorticities augment wave speed, postponing wave breaking (compare the solid and dashed lines in Figure 1 and their corresponding breaking times). In this case, nonlinear results show that negative vorticities can attenuate the highest amplitude waves at the blocking point with breaking occurring within the reflected waves as they are swept downstream. Conversely, for $\zeta > 0$, waves reduce their speed and are blocked earlier (compare the solid and dashed-dotted lines in Figure 1 and their corresponding breaking times). Wave blocking and breaking are more prominent in these cases, with shorter breaking times being registered. Note that, for any ζ, the surface wave pattern clearly shows some reflected waves as soon as 'steeper' waves appear.

The effects of vorticity on waves with greater steepness propagating over an opposing current under the blocking condition predicted by linear theory ($|U_{min}|=|U_s|$) are shown in Figure 2. Results are vertically exaggerated 5 times in this case. Waves evolve from the stationary free-surface profiles to the unsteady nonlinear solutions depicted in Figure 2. At their final stages waves are noticeably affected by nonlinearity. For $\zeta = 0$, the breaking wave takes the form of an upward breaker jet, approaching Stokes' limiting shape of 120^o at the crest. As stronger shear flows are imposed (e.g. $\zeta = 0.316$), vorticity clearly affects the free-surface layer with a plunging breaker being formed (see the dashed-dotted line in Figure 2b). Oppositely, for $\zeta < 0$, wave breaking is postponed.

4 CONCLUSIONS

The presence of vorticity induces shear at the water surface which changes the properties of the free-surface waves when meeting an underlying current. It is shown that wave blocking and breaking are more prominent for positive values of vorticity. Reflection continues to occur when sufficiently strong adverse currents are imposed on 'gentle' deep-water waves, though now affected by vorticity. For increasingly positive values of ζ, the shear current reduces the speed of the surface waves until they are completely blocked by the underlying flow. A plunging breaker is formed at the blocking point when 'steep' deep-water waves undergo strong currents. Negative vorticities augment the speed of right-going progressive waves with wave breaking being detected for strong currents. The time of breaking is sensitive to the vorticity's sign and magnitude, with wave breaking occurring later for negative values of ζ.

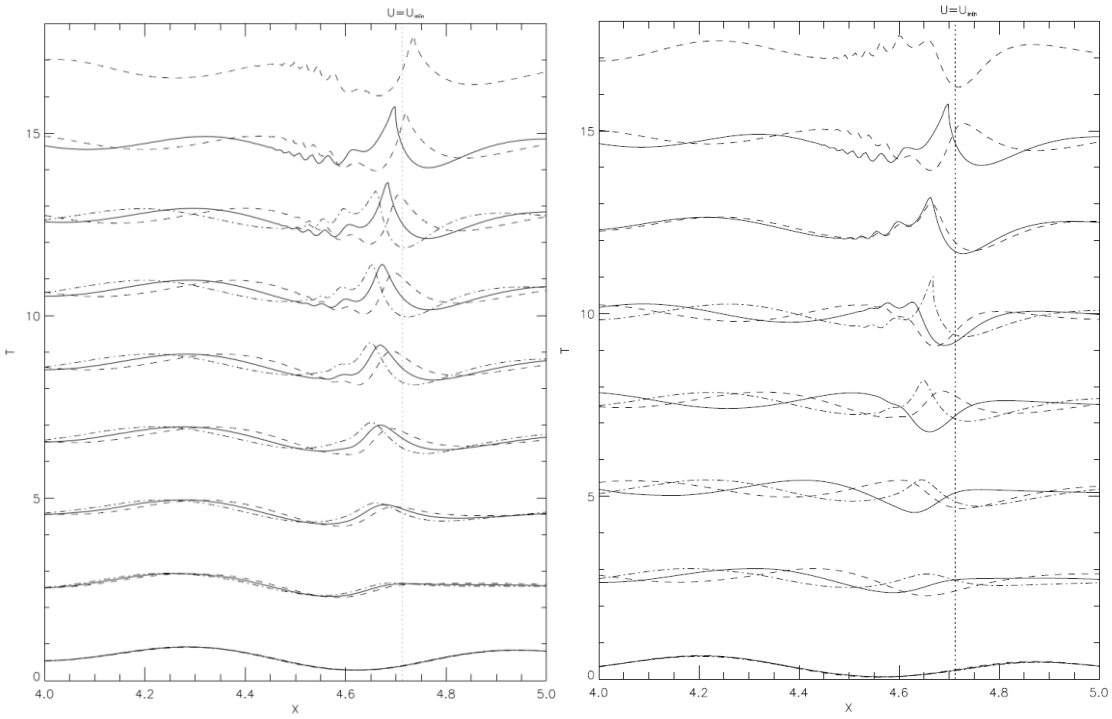

(a) (b)

Figure 1: Evolution of 'gentle' deep-water waves ($\varepsilon_0 = 0.02$) propagating over an adverse current at blocking condition ($|U_{min}|=|U_s|$) with: (a) $\zeta = 0.063$ (– · – · –); $\zeta = 0$ (———); $\zeta = -0.063$ (– – – –); $T_{breaking}$ = 13.1; 14.7; 17.5; (b) $\zeta = 0.316$ (– · – · –); $\zeta = 0$ (———); $\zeta = -0.316$ (– – – –); $T_{breaking}$ = 10.0; 14.7; 18.8. Vertical exaggeration 100 : 1.

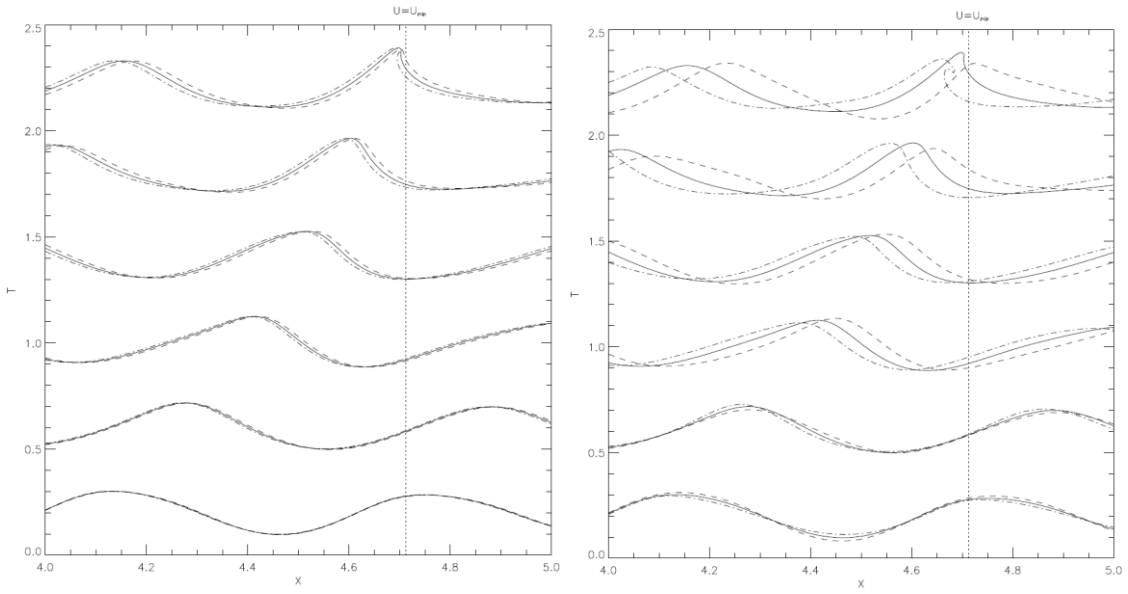

(a) (b)

Figure 2: Evolution of 'steep' deep-water waves ($\varepsilon_0 = 0.2$) propagating over an adverse current at blocking condition ($|U_{min}|=|U_s|$) with: (a) $\zeta = 0.063$ (– · – · –); $\zeta = 0$ (———); $\zeta = -0.063$ (– – – –); $T_{breaking}$ = 2.2; 2.3; 2.4; (b) $\zeta = 0.316$ (– · – · –); $\zeta = 0$ (———); $\zeta = -0.316$ (– – – –); $T_{breaking}$ = 2.2; 2.3; 4.1. Vertical exaggeration 5 : 1.

ACKNOWLEDGMENTS

RMM and JTAC acknowledge the research grant from CAPES, the national agency for postgraduate education (processes numbers 11787/13-9 and 2149/14-1).

REFERENCES

[1] WL Peirson, ML Banner (2003). Aqueous surface layer flows induced by microscale breaking wind waves. *Journal of Fluid Mechanics* **479**:1–38.

[2] C Kharif, J-P Giovanangeli, J Touboul, L Grare, E Pelinovsky (2008). Influence of wind on extreme wave events: experimental and numerical approaches. *Journal of Fluid Mechanics* **594**:209–247.

[3] C Swan, IP Cummins, RL James (2001). An experimental study of two-dimensional surface water waves propagating on depth-varying currents. Part 1. Regular waves. *Journal of Fluid Mechanics* **428**:273–304.

[4] MS Longuet-Higgins (1998). Vorticity and curvature at a free surface. *Journal of Fluid Mechanics* **356**:149–153.

[5] T Lundgren, P Koumoutsakos (1999). On the generation of vorticity at a free surface. *Journal of Fluid Mechanics* **382**:351–366.

[6] TCD Barnes, M Brocchini, DH Peregrine, PK Stansby (1996). Modelling postwave breaking turbulence and vorticity. In *Proceedings of the 25th International Conference on Coastal Engineering*, 186–199, ASCE.

[7] D Dabiri, M Gharib (1997). Experimental investigation of the vorticity generation within a spilling water wave. *Journal of Fluid Mechanics* **330**:113–139.

[8] DH Peregrine (1999). Large-scale vorticity generation by breakers in shallow and deep water. *European Journal of Mechanics - B/Fluids* **18**:403–408.

[9] S Tsao (1959). Behaviour of surface waves on a linearly varying flow. *Tr. Mosk. Fiz.-Tekh. Inst. Issled. Mekh. Prikl. Mat.* **3**:66–84.

[10] I Brevik (1979). Higher-order waves propagating on constant vorticity currents in deep water. *Coastal Engineering* **2**:237–259.

[11] N Kishida, RJ Sobey (1988). Stokes theory for waves on a linear shear current. *Journal of Engineering Mechanics* **114**:1317–1334.

[12] OS Pak, KW Chow (2009). Free surface waves on shear currents with non-uniform vorticity: third-order solutions. *Fluid Dynamics Research* **41**:1–13.

[13] TB Benjamin (1962). The solitary wave on a stream with an arbitrary distribution of vorticity. *Journal of Fluid Mechanics* **12**:97–116.

[14] RA Dalrymple (1974). A finite amplitude wave on a linear shear current. *Journal of Geophysical Research* **79**:4498–4504.

[15] JA Simmen, PG Saffman (1985). Steady deep-water waves on a linear shear current. *Studies in Applied Mathematics* **75**:35–57.

[16] AF Teles da Silva, DH Peregrine (1988). Steep, steady surface waves on water of finite depth with constant vorticity. *Journal of Fluid Mechanics* **195**:281–302.

[17] A Constantin, J Escher (2004). Symmetry of steady periodic surface water waves with vorticity. *Journal of Fluid Mechanics* **498**:171–181.

[18] J Ko, W Strauss (2008). Effect of vorticity on steady water waves. *Journal of Fluid Mechanics* **608**:197–215.

[19] RM Moreira, DH Peregrine (2012). Nonlinear interactions between deep-water waves and currents. *Journal of Fluid Mechanics* **691**:1–25.

[20] DH Peregrine (1976). Interaction of water waves and currents. *Advances in Applied Mechanics* **16**:9–117.

[21] IG Jonsson (1990). Wave-current interactions. In B LeMehaute, DM Hanes, Eds., *The Sea: Ocean Engineering Science* 9A, 65–120, Wiley Interscience.

[22] GP Thomas, G Klopman (1997). Wave-current interactions in the nearshore region. In JN Hunt, Ed., *Gravity Waves in Water of Finite Depth*, 215–319, Computational Mechanics Publications.

[23] GI Taylor (1955). The action of a surface current used as a breakwater. *Proceedings of the Royal Society of London A* **231**:466–478.

[24] OG Nwogu (2009). Interaction of finite-amplitude waves with vertically sheared current fields. *Journal of Fluid Mechanics* **627**:179–213.

[25] W Choi (2009). Nonlinear surface waves interacting with a linear shear current. *Mathematics and Computers in Simulation* **80**:29–36.

[26] RM Moreira, JTA Chacaltana (2012). Nonlinear interactions between water waves and currents with constant vorticity. In *Proceedings of the 33rd International Conference on Coastal Engineering*, abstract no.1172, ASCE.

[27] RM Moreira, DH Peregrine (2010). Nonlinear interactions between a free-surface flow with surface tension and a submerged cylinder. *Journal of Fluid Mechanics* **648**:485–507.

[28] JW Dold (1992). An efficient surface-integral algorithm applied to unsteady gravity waves. *Journal of Computational Physics* **103**:90–115.

V Conferência Nacional de Mecânica dos Fluidos, Termodinâmica e Energia
MEFTE 2014, 11–12 Setembro 2014, Porto, Portugal
APMTAC, 2014

Serre type model for wave propagation from arbitrary depths to shallow waters

JS Antunes do Carmo

Departamento de Engenharia Civil, Faculdade de Ciências e Tecnologia, Universidade de Coimbra, Pólo II da Universidade, Coimbra, Portugal
email: jsacarmo@dec.uc.pt

ABSTRACT: Numerical models are a useful instrument for studying complex superposition of wave-wave and wave-current interactions in coastal and estuarine regions, and to investigate the interaction of waves with complex bathymetries or structures built in nearshore areas. The ability of Boussinesq-type models and Serre equations (or Green and Naghdi) to reproduce these nonlinear processes is well known. However, these standard models are restricted to shallow water conditions, and the addition of other terms of dispersive origin has been considered since 90's. Some recent works have extended the Boussinesq equations to deep waters ($h_0/\lambda > 0.50$) by adding more or less terms of dispersive origin. Less common are extensions of the Serre equations. Starting from an approximation developed by [1] and [2], a new coefficient is introduced, function of the local water depth. It is shown that the new model is able to propagate waves from deep water conditions to very shallow waters. The model is validated by comparisons of waves propagating in deep water conditions through the analytical solution and with available experimental data. Following, the model performance is tested by the propagation of a linear wave over bottoms with large slopes, from intermediate waters ($h_0/\lambda < 0.50$) to and in very shallow water conditions ($h_0/\lambda < 0.05$). Finally, numerical results and a discussion of them are presented.

KEY-WORDS: Serre equations; Improved dispersive characteristics; Arbitrary depths; Applications.

1 INTRODUCTION

Knowledge of the flow characteristics associated with surface waves and currents, and their dependency on the bathymetry and coastal geometry, is of considerable importance when designing structures commonly found in the coastal environment, like groynes and breakwaters. Such knowledge also helps to predict the modifications thereby introduced into sea disturbance and into the transport and deposition of sediments.

To the end of the 70's linear models were used to simulate the refraction effect produced by the depth variation along the direction of the crest wave propagation and the diffraction effect produced by the gradient of the amplitude along the wave crest. In the 80's other models, that take into account not only de refraction but also the diffraction process, have been proposed and commonly used by [3], [4], [5], [6] and [7], among many others. However, as they are based on the linear theory, those models should not be utilized in shallow water conditions.

Even at that time, models based on the Saint-Venant equations were frequently used in practical applications. However, as has been widely demonstrated, in shallow water conditions and for some types of waves, models based on a non-dispersive theory, of which the Saint-Venant model is an example, are limited and are not usually able to compute satisfactory results over long periods of analysis [8]. Nowadays, it is generally accepted that for practical applications the combined gravity wave effects in shallow water conditions must be taken into account. In addition, the refraction and diffraction processes, the swelling, reflection and breaking waves, all have to be considered.

A number of factors have made it possible to employ increasingly complex mathematical models. Not only has our theoretical knowledge of the phenomena involved improved greatly, but also the numerical methods have been used more efficiently. The great advances made in computer technology, especially since the 1980s, improving information processing and enabling large amounts of data to be stored, have made possible the use of more mathematical models, of greater complexity and with fewer restrictions.

Therefore, only models of order σ^2 ($\sigma = h/\lambda$, where h and λ represent, respectively, depth and wavelength characteristics) or greater, of the Boussinesq or Serre types, are able to reproduce effects other than the dispersive effects, including the non-linearities resulting from wave-wave and wave-current

interactions, and the waves resulting from sudden time-bed-level changes that cause *tsunamis*, wherein submerged landslides in reservoirs, or landslides on reservoir banks, are examples of such changes. In the last few years, the possibility of using more powerful computational facilities, and the technological evolution and sophistication of control systems have required thorough theoretical and experimental research designed to improve the knowledge of coastal hydrodynamics. Numerical methods aimed to applications in engineering fields, more sophisticated and with a higher degree of complexity, have also been developed.

In Section 2 the general shallow water wave theory is used to develop different mathematical approximations, which are nowadays the basis of the more important models in the ambit of hydrodynamics and sedimentary dynamics. An extension of the equations for deepwater applications and results of the more general approach (order σ^2) are presented in Sections 3 and 4. The first example shows the model's ability to propagate a highly nonlinear solitary wave ($a/h_0 = 0.60$). The second application is a real world problem, with the objective of designing a submerged breakwater to protect a coastal area, for example. Finally, the third example shows the performance of the model for the propagation of a wave in a domain with $h_0/\lambda = 0.50$, which is the limit between intermediate waters and deep water conditions.

2 FORMULATION

We start from the fundamental equations of the Fluid Mechanics, written in Euler's variables, relating to a three-dimensional and *quasi*-irrotational flow of a perfect fluid [Euler equations, or Navier-Stokes equations with the assumptions of non-compressibility ($d\rho/dt = \mathrm{div}\,\vec{v} = 0$), irrotationality ($\mathrm{rot}\,\vec{v} = 0$, i.e. $u_z = w_x$; $v_z = w_y$; $v_x = u_y$) and perfect fluid (dynamic viscosity, $\mu = 0$)].

Proceeding by suitable dimensionless variables of these equations, considering appropriate boundary conditions, and defining the dimensionless quantities $\varepsilon = a/h_0$ and $\sigma = h_0/\lambda$, in which a is a characteristic wave amplitude, h_0 is the mean water depth and λ is a characteristic wavelength, the fundamental equations and the boundary conditions are written [9]:

A – Fundamental equations

$$\begin{aligned}
&u_x + v_y + w_z = 0 \\
&\varepsilon u_t + \varepsilon^2 u u_x + \varepsilon^2 v u_y + \varepsilon^2 w u_z = -p_x \\
&\varepsilon v_t + \varepsilon^2 u v_x + \varepsilon^2 v v_y + \varepsilon^2 w v_z = -p_y \\
&\varepsilon\sigma^2 w_t + \varepsilon^2\sigma^2 u w_x + \varepsilon^2\sigma^2 v w_y + \varepsilon^2\sigma^2 w w_z = -p_z - 1 \\
&u_z = \sigma^2 w_x \\
&v_z = \sigma^2 w_y \\
&v_x = u_y
\end{aligned} \tag{1}$$

B – Boundary conditions

$$\begin{aligned}
&w = \varsigma_t + \varepsilon u \varsigma_x + \varepsilon v \varsigma_y && , && p = 0 \\
&w = (1/\varepsilon)\xi_t + u\xi_x + v\xi_y && , && z = -1 + \xi \\
&p = 0 && , && z = \varepsilon\varsigma
\end{aligned} \tag{2}$$

where ς is free surface elevation, ξ represents bathymetry, u, v and w are velocity components, and p is pressure. Integrating the first of equations (A) between the bottom and the free surface yields the continuity equation:

$$\left[\varsigma - (1/\varepsilon)\xi\right]_t + \left[(1 + \varepsilon\varsigma - \xi)\bar{u}\right]_x + \left[(1 + \varepsilon\varsigma - \xi)\bar{v}\right]_y = 0 \tag{3}$$

where the bar over the variables represents the average value along the vertical. Following, accepting the fundamental hypothesis of the shallow water theory, $\sigma = h_0/l \ll 1$, and developing the dependent variables in power series of the small parameter σ^2, we obtain, after some algebraic manipulations, the following equations (4) in second approach [9]:

$$\begin{aligned}
&u^*_t + \varepsilon u^* u^*_x + \varepsilon v^* u^*_y + \varsigma_x\left(1 + \varepsilon\sigma^2\Gamma^*\right) = 0 \\
&v^*_t + \varepsilon u^* v^*_x + \varepsilon v^* v^*_y + \varsigma_y\left(1 + \varepsilon\sigma^2\Gamma^*\right) = 0
\end{aligned} \tag{4}$$

where

$$\begin{aligned}\Gamma^{*} = &\left[-\left(1+z-\xi\right)\left(\bar{A}_t + \varepsilon\bar{u}\bar{A}_x + \varepsilon\bar{v}\bar{A}_y - \varepsilon\bar{A}^2 \right) \right]_{\text{horiz}} \\ &+\left[w_{*t} + \varepsilon\bar{u}w_{*x} + \varepsilon\bar{v}w_{*y} \right]_{\text{bottom}} + O\left(\sigma^2\right)\end{aligned} \tag{5}$$

in which the terms within the first parenthesis (straight parenthesis) represent the vertical acceleration when the bottom is horizontal, and the terms within the second parenthesis (straight parenthesis) represent the vertical acceleration along the real bottom. By developing expressions (4) in second approach (order 2 in σ^2), the following equations of motion are obtained [9]:

$$\begin{aligned}&\bar{u}_t + \varepsilon\bar{u}\bar{u}_x + \varepsilon\bar{v}\bar{u}_y + \varsigma_x \\ &\quad + \sigma^2 \left\{ \left[(2/3)\left(\varepsilon\varsigma - \xi\right)_x + (1/2)\ \xi_x \right] P + (1/3)\left(1+\varepsilon\varsigma-\xi\right) P_x \right\} \\ &\quad + \sigma^2 \left[\varepsilon\varsigma_x Q + (1/2)\left(1+\varepsilon\varsigma-\xi\right)\ Q_x \right] + \sigma^4 = 0 \\ &\bar{v}_t + \varepsilon\bar{u}\bar{v}_x + \varepsilon\bar{v}\bar{v}_y + \varsigma_y \\ &\quad + \sigma^2 \left\{ \left[(2/3)\left(\varepsilon\varsigma - \xi\right)_y + (1/2)\ \xi_y \right] P + (1/3)\left(1+\varepsilon\varsigma-\xi\right) P_y \right\} \\ &\quad + \sigma^2 \left[\varepsilon\varsigma_y Q + (1/2)\left(1+\varepsilon\varsigma-\xi\right)\ Q_y \right] + \sigma^4 = 0 \\ &P = \left(1+\varepsilon\varsigma-\xi\right)\left(\varepsilon\bar{A}^2 - \varepsilon\bar{u}\bar{A}_x - \varepsilon\bar{v}\bar{A}_y - \bar{A}_t \right) \\ &Q = w_t + \varepsilon\,\bar{u}w_x + \varepsilon\,\bar{v}w_y \\ &w = (1/\varepsilon)\ \xi_t + \bar{u}\xi_x + \bar{v}\xi_y \\ &\bar{A} = \bar{u}_x + \bar{v}_y\end{aligned} \tag{6}$$

where, likewise, the bar over the variables represents the average value along the vertical. In dimensional variables and with a solid/fixed bottom ($\xi_t = 0$), the complete set of equations is written, in second approach:

$$\begin{aligned}&h_t + \left(h\bar{u}\right)_x + \left(h\bar{v}\right)_y = 0 \\ &\bar{u}_t + \bar{u}\bar{u}_x + \bar{v}\bar{u}_y + g\varsigma_x \\ &\quad + \left[(2/3)h_x + (1/2)\ \xi_x \right] P + (1/3)hP_x + h_x Q + (1/2)\ hQ_x = 0 \\ &\bar{v}_t + \bar{u}\bar{v}_x + \bar{v}\bar{v}_y + g\varsigma_y \\ &\quad + \left[(2/3)h_y + (1/2)\ \xi_y \right] P + (1/3)hP_y + h_y Q + (1/2)\ hQ_y = 0 \\ &P = h\left(\bar{A}^2 - \bar{u}\bar{A}_x - \bar{v}\bar{A}_y - \bar{A}_t \right) \\ &Q = w_t + \bar{u}w_x + \bar{v}w_y \\ &w = \bar{u}\xi_x + \bar{v}\xi_y \\ &\bar{A} = \bar{u}_x + \bar{v}_y\end{aligned} \tag{7}$$

The one-dimensional system of equations (1HD) is written, also with a fixed bottom:

$$\begin{aligned}&h_t + \left(\bar{u}h\right)_x = 0 \\ &h\bar{u}_t + h\bar{u}\bar{u}_x + gh\varsigma_x + \left[h^2\left(P/3 + Q/2\right) \right]_x + \xi_x h\left(P/2 + Q\right) = 0 \\ &P = -h\left(\bar{u}_{xt} + \bar{u}\bar{u}_{xx} - \bar{u}_x^2 \right) \\ &Q = \xi_x\left(\bar{u}_t + \bar{u}\bar{u}_x \right) + \xi_{xx}\bar{u}^2\end{aligned} \tag{8}$$

Assuming additionally a relative elevation of the surface due to the waves ($\varepsilon = a/h_0$) having a value close to the square of the relative depth ($\sigma = h_0/\lambda$), i.e. $O(\varepsilon) = O(\sigma^2)$, from the system (6), and at the same order of approximation, the following approach is obtained, in dimensional variables:

$$
\begin{aligned}
&h_t + \left(h\overline{u}\right)_x + \left(h\overline{v}\right)_y = 0 \\
&\overline{u}_t + \overline{u}\overline{u}_x + \overline{v}\overline{u}_y + g\varsigma_x \\
&\quad -\left[(1/6)\ \xi_x\right]P + (1/3)h_0 P_x + (1/2)\ h_0 Q_x = 0 \\
&\overline{v}_t + \overline{u}\overline{v}_x + \overline{v}\overline{v}_y + g\varsigma_y \\
&\quad -\left[(1/6)\xi_y\right]P + (1/3)h_0 P_y + (1/2)\ h_0 Q_y = 0
\end{aligned}
\tag{9}
$$

where P and Q are given by $P = -(1-\xi)\left(\overline{u}_x + \overline{v}_y\right)_t$ and $Q = \left(\overline{u}\xi_x + \overline{v}\xi_y\right)_t$. The momentum equations are written:

$$
\begin{aligned}
&\overline{u}_t + \overline{u}\overline{u}_x + \overline{v}\overline{u}_y + g\varsigma_x + (1/6)h_0\xi_x\left(\overline{u}_x + \overline{v}_y\right)_t \\
&\quad -(1/3)h_0^2\left(\overline{u}_x + \overline{v}_y\right)_{xt} + (1/3)h_0\xi_x\left(\overline{u}_x + \overline{v}_y\right)_t \\
&\quad +(1/2)h_0\left(\overline{u}\xi_x + \overline{v}\xi_y\right)_{xt} = 0
\end{aligned}
\tag{10}
$$

$$
\begin{aligned}
&\overline{v}_t + \overline{u}\overline{v}_x + \overline{v}\overline{v}_y + g\varsigma_y + (1/6)h_0\xi_y\left(\overline{u}_x + \overline{v}_y\right)_t \\
&\quad -(1/3)h_0^2\left(\overline{u}_x + \overline{v}_y\right)_{yt} + (1/3)h_0\xi_y\left(\overline{u}_x + \overline{v}_y\right)_t \\
&\quad +(1/2)h_0\left(\overline{u}\xi_x + \overline{v}\xi_y\right)_{yt} = 0
\end{aligned}
\tag{11}
$$

With $\xi_t = 0$, the complete system of equations (12) is obtained:

$$
\begin{aligned}
&h_t + \left(h\overline{u}\right)_x + \left(h\overline{v}\right)_y = 0 \\
&\overline{u}_t + \overline{u}\overline{u}_x + \overline{v}\overline{u}_y + g\varsigma_x - (1/3)\ h_0^2\left(\overline{u}_{xxt} + \overline{v}_{xyt}\right) + h_0\xi_x\overline{u}_{xt} \\
&\quad +(1/2)\ h_0\left(\xi_{xx}\overline{u}_t + \xi_y\overline{v}_{xt} + \xi_x\overline{v}_{yt} + \xi_{xy}\overline{v}_t\right) = 0 \\
&\overline{v}_t + \overline{u}\overline{v}_x + \overline{v}\overline{v}_y + g\varsigma_y - (1/3)h_0^2\left(\overline{u}_{xyt} + \overline{v}_{yyt}\right) + h_0\xi_y\overline{v}_{yt} \\
&\quad +(1/2)\ h_0\left(\xi_{yy}\overline{v}_t + \xi_y\overline{u}_{xt} + \xi_x\overline{u}_{yt} + \xi_{xy}\overline{u}_t\right) = 0
\end{aligned}
\tag{12}
$$

Further simplifying the equations of motion (6), retaining only terms up to order 1 in σ, i.e., neglecting all terms of dispersive origin, this system of equations is written in dimensional variables:

$$
\begin{aligned}
&h_t + \left(h\overline{u}\right)_x + \left(h\overline{v}\right)_y = 0 \\
&\overline{u}_t + \overline{u}\overline{u}_x + \overline{v}\overline{u}_y + g\varsigma_x = 0 \\
&\overline{v}_t + \overline{u}\overline{v}_x + \overline{v}\overline{v}_y + g\varsigma_y = 0
\end{aligned}
\tag{13}
$$

Approaches (7), (12) and (13) are known as Serre [10] equations, or Green & Naghdi [11], Boussinesq [12] and Saint-Venant [13], respectively, in two horizontal dimensions (2HD models).

3 EXTENSION TO DEEP WATER

Standard Boussinesq and Serre models are restricted to shallow water conditions, and the addition of other terms of dispersive origin has been considered since 90's. Some recent works have extended the Boussinesq equations to deep waters ($h_0/\lambda > 0.50$) by adding more or less terms of dispersive origin, as in [14], [15], [16], [17], [18] and [19], among others.

Starting from the standard Boussinesq equations and adopting the methodology introduced by [13], Beji and Nadaoka [20] presented a new approach that allows for applications until values of h_0/λ to the order of 0.25, and still with acceptable errors in amplitude and phase velocity up to values of h_0/λ near 0.50. A higher order of approximation, valid for values of h_0/λ to the order of 0.48, is presented in [21].

Less common are extensions of the Serre equations. Starting from equations (8), [1], [2] and [22] used an identical formulation to extend these equations for applications in intermediate-depth waters, to values of the frequency dispersion h_0/λ up to 0.50. The references [1], [2] and [22] consider that the coefficients introduced are constant. Here we consider a third coefficient, function of the local water depth, to improve the model properties up to deeper waters. Linearizing the equations system (7) and neglecting the higher order terms, the following system of equations is obtained:

$$\begin{aligned} h_t + \nabla \cdot \left(h\bar{u}\right) &= 0 \\ \bar{u}_t + g\nabla\varsigma &= 0 \end{aligned} \tag{14}$$

which is applicable to the propagation of monochromatic waves in deep waters (offshore); therefore, where the nonlinear terms and the terms of dispersive origin of system (7) are unimportant, but negatively affect the solution.

In order to become possible the use of the system of equations (7), under intermediate and deep waters, it is essential obtaining an equivalent approach, which solution, in terms of the group velocity, behaves according to the linear dispersion relation, given by $\omega^2 = gk\tanh\left(kh\right)$. Consequently, according to (14), variations in time of the velocity in equation (7) are combined with the system approach $\bar{u}_t = -g\nabla\varsigma$ through parameters, or scalar quantities, such that, under intermediate to deep waters, the dispersion relation of the linearized system tends to $\omega^2 = gk\tanh\left(kh\right)$. The parameters involved are then obtained so as to approximate, as closely as possible, the dispersion relation of the linearized system with the relation $\omega^2 = gk\tanh\left(kh\right)$. Neglecting higher order terms and the non-linear terms in equations (7) gives the dispersion relation (15), also obtained by [21] to the linearized form of system (12):

$$\frac{\omega^2}{gk} = \frac{kh\left[1+\left(\alpha/2-\gamma/6\right)k^2h^2\right]}{1+\left(1+\alpha\right)k^2h^2/2-\left(1+\gamma\right)k^2h^2/6} \tag{15}$$

where $\omega = 2\pi/T$ is the wave frequency, T is the period, and $k^2 = k_x^2 + k_y^2$, being k_x and k_y the wave number components in the directions x and y, respectively.

Equation (15) can be written in terms of the phase velocity and compared with the second order of Padé expansion of the exact linear solution for Airy waves, given by:

$$C_{Airy}^2 = \frac{\omega^2}{k^2} = \left(gh\right)\tanh\left(kh\right) = gh\left[\frac{1+\left(kh\right)^2/15}{1+2\left(kh\right)^2/5}\right] + O\left[\left(kh\right)^6\right] \tag{16}$$

In order to check that equality, the relationship $\beta = 1.5\,\alpha - 0.5\,\gamma = 0.20$ will have to be verified. For the parameters α e γ, Liu and Sun [21] obtained first approximations based on sensitivity analyses.

In addition to the parameters α and β, this work suggests a third coefficient μ, function of the local water depth to improve the model properties up to deeper waters. As is shown, this methodology allow us to obtain a general model, which tends to the Saint-Venant model under conditions of deep water (offshore) and to the Serre equations in shallow waters (onshore). The system of equations presented in [1], [2] and [22] is rewritten considering now the third parameter μ as follows:

$$\begin{aligned} & h_t + \left(uh\right)_x = 0 \\ & u_t + uu_x + g\left(h+\xi\right)_x \\ & \quad + \mu\left[\left(1+\alpha\right)\left(\Omega u_t - hh_x u_{xt}\right) - \left(1+\beta\right)\frac{h^2}{3}u_{xxt} + \alpha g\Omega\left(h+\xi\right)_x\right. \\ & \quad - \alpha g h h_x\left(h+\xi\right)_{xx} - \beta g\frac{h^2}{3}\left(h+\xi\right)_{xxx} - hh_x uu_{xx} + \frac{h^2}{3}\left(u_x u_{xx} - uu_{xxx}\right) \\ & \quad \left. + h\left(u_x\right)^2\left(h+\xi\right)_x + \xi_{xx}u^2\left(h+\xi\right)_x + \left(\Omega + h\xi_{xx}\right)uu_x + \frac{h}{2}\xi_{xxx}u^2\right] \\ & \quad - \left(1/\rho\right)\left(p_s\right)_x + \tau_b/\left(\rho h\right) = 0 \\ & \Omega = \xi_x h_x + \frac{1}{2}h\,\xi_{xx} + \left(\xi_x\right)^2 \end{aligned} \tag{17}$$

where p_s is a pressure on the free surface and τ_b represents friction stresses at bottom, $\alpha \approx 0.13$ and $\beta = 0.20$. Making $\mu = f\left(h\right)$ such that $\mu \to 1$ when $h \to 0$ and $\mu \to 0$ when $h \to \infty$ and, simultaneously, $\left(\alpha,\beta\right) \to 0$ when $h \to 0$, and $\alpha \approx 0.13$ and $\beta \to 0.20$ when $h \to \infty$ (although in this case the values of α and β are not at all relevant) we find the equation systems of Serre (8) and Saint-Venant (13) (1HD version). A function satisfying these conditions is given by (18):

$$f\left(h\right)=\frac{\left(kh\right)^2}{\sinh\left[\left(kh\right)^2\right]} \tag{18}$$

where $k=2\pi/\lambda$, being λ the wave length. In particular for the transitional zones, the following values are obtained: $f\left(h/\lambda=0.05\right)=0.998$ and $f\left(h/\lambda=0.50\right)=0.001$.

An implicit finite difference method is used to solve the system of equations (17), after grouping the terms containing derivatives in time of u in an additional equation. The equivalent system of three equations is solved numerically, as presented in [1], [2] and [22]:

$$\begin{aligned}
&h_t+\left(uh\right)_x=0\\
&q_t+\left(uq\right)_x-uu_x+g\,\varsigma_x\\
&\quad-\mu\left\{\frac{1}{2}\left[\left(1+2\alpha\right)h^2\left(u_x\right)^2+\left(1+2\alpha\right)\left(\xi_x\right)^2u^2-h\,\xi_x\left(u^2\right)_x\right]_x\right.\\
&\quad+\left[\alpha\,g\,\Omega+\alpha hu\,u_{xx}\right]\varsigma_x-\alpha ghh_x\varsigma_{xx}-\beta\,g\,\frac{h^2}{3}\varsigma_{xxx}+\beta\frac{h^2}{3}uu_{xxx}\\
&\quad\left.-\frac{\alpha}{2}\left[\left(h\,\xi_{xx}u^2\right)_x+h_x\,\xi_{xx}u^2-h\,\xi_{xx}u\,u_x\right]+\left(\alpha-\frac{\beta}{3}\right)h^2u_xu_{xx}\right\}\\
&\quad-\left(1/\rho\right)\left(p_s\right)_x+\tau_b/\left(\rho h\right)=0\\
&u+\mu\left[\left(1+\alpha\right)\,\Omega\,u-\left(1+\alpha\right)\,h\,h_xu_x-\left(1+\beta\right)\frac{h^2}{3}u_{xx}\right]=q\\
&\Omega=\xi_xh_x+\frac{1}{2}h\,\xi_{xx}+\left(\xi_x\right)^2
\end{aligned} \tag{19}$$

4 APPLICATIONS AND RESULTS

In order to test the robustness of the proposed model (19), several numerical tests were performed. Its good performance is proven through very demanding applications, namely: A1 - a solitary wave propagating in a channel 1.0 m depth and 250 m long, with $a/h_0=0.60$; A2 - a periodic wave propagating over a submerged bar in very shallow-depth ($h_0/\lambda\approx0.03$) and intermediate-depth waters ($h_0/\lambda\approx0.11$), and A3 - a periodic wave propagating in deep water condition ($h_0/\lambda=0.50$).

4.1 Solitary wave

To validate system (17), and to check the accuracy of the numerical method (19), with $\mu=1.0$, $\alpha=\beta=0$ and $\xi_t=\xi_x=\xi_{xx}=\xi_{xxx}=0$, a closed-form solitary wave solution of the Serre equations was used, which is expressed as:

$$h\,\left(x,t\right)=h_0+a\,\mathrm{sech}^2\left[K\left(x-Ct-x_0\right)\right] \tag{20}$$

$$u=C\,\left[1-h_0/h\right] \tag{21}$$

with

$$K=\sqrt{3a/\left[4h_0^2\left(h_0+a\right)\right]};\ C=C_0\sqrt{\left(1+a/h_0\right)},\ \text{and}\ C_0=\sqrt{gh_0}$$

where h_0 is the water depth at rest, x_0 is the initial position of the crest, a is the wave amplitude. A constant depth $h_0=1.0$ m and $x_0=25$ m were used.

The computational domain was uniformly discretized with a spatial step $\Delta x=0.05$ m. A time step $\Delta t=0.0025$ s has been used. A comparison of numerical results with the analytical solution (20)–(21) for a highly nonlinear propagating solitary wave ($a/h_0=0.60$) is plotted in Figure 1 at times t = 25 s and t = 50 s. It can be observed a perfect agreement, which confirms the accuracy of the numerical model implemented.

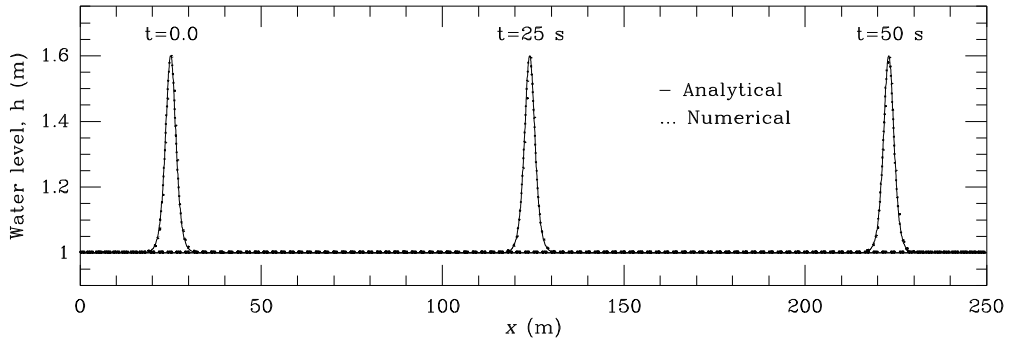

Figure 1: Solitary wave computation for a solitary wave with $a/h_0 = 0.60$. Comparison of the analytic solution (20) (——) with numerical results ($\cdots\cdots$) of model (19) with $\mu = 1$ and $\alpha = \beta = 0$.

4.2 Periodic wave propagating over a submerged bar

Experimental data are available in the literature and can be used for comparisons. Beji and Battjes [23] conducted experiments in a flume of 0.80 m width with a submerged trapezoidal bar with slopes 1:20 (upstream) and 1:10 (downstream).

As shown in Figure 2, the water depth in front and behind the bar was 0.40 m, with a reduction to 0.10 m above the bar.

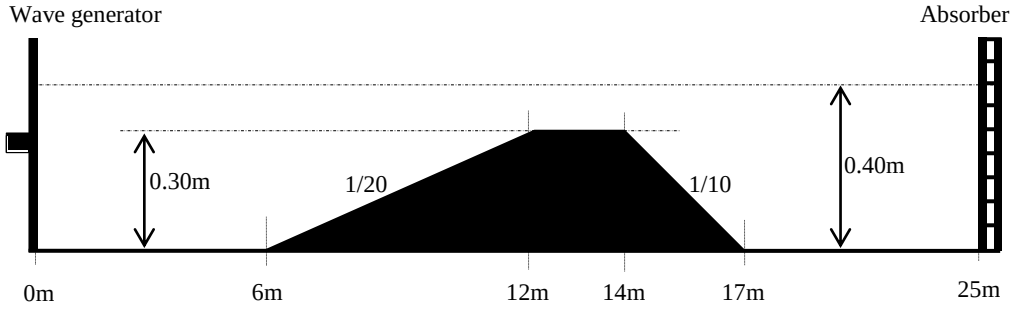

Figure 2: Bathymetry for a periodic wave propagating over a bar (not in scale).

A regular incident wave case with height 0.02 m, period T = 2.02 s and wavelength 3.73 m has been simulated. Three wave gauges were placed in points where the effects of wave nonlinearity and dispersivity are mostly manifested.

Numerical results obtained in a fourth gauge installed at x = 3.0 m were compared with Stokes 2nd order analytical solution.

At the inlet section and during the first 6 m (Figure 2) the relation $h/\lambda \approx 0.107$ is verified, thus satisfying the Stokes solution of 2nd order in this stretch, while the reflection effects have not been felt. According to the theory of second order Stokes, the elevation of the free surface is given by:

$$\varsigma = \frac{H}{2}\cos(kx-\omega t) + \frac{\pi H^2}{8L}\left\{\frac{\cosh(kh)\left[2+\cosh(2kh)\right]}{\sinh^3(kh)}\right\}\cos\left[2(kx-\omega t)\right] \tag{22}$$

and the (u , w) velocity components are:

$$u = \frac{\pi H}{T}\frac{\cosh\left[k(h_0+z)\right]}{\cosh(kh_0)}\cos(kx-\omega t) + \frac{3}{4}\frac{\pi H}{T}\frac{\pi H}{L}\frac{\cosh\left[2k(h_0+z)\right]}{\sinh^4(kh_0)}\cos\left[2(kx-\omega t)\right] \tag{23}$$

$$w = \frac{\pi H}{T}\frac{\sinh\left[k\left(h_0+z\right)\right]}{\cosh\left(kh_0\right)}\sin\left(kx-\omega t\right) + \frac{3}{4}\frac{\pi H}{T}\frac{\pi H}{L}\frac{\sinh\left[2k\left(h_0+z\right)\right]}{\sinh^4\left(kh_0\right)}\sin\left[2\left(kx-\omega t\right)\right] \tag{24}$$

where H is the wave height; $k = 2\pi/\lambda$ is the wave number, and $\omega = 2\pi/T$ is the wave frequency; with $z = 0$ the velocity at the surface is obtained.

The computational domain was discretized with a uniform grid interval $\Delta x = 0.025\,\text{m}$. A time step $\Delta t = 0.0010\,\text{s}$ was used. A comparison of the analytical solution (22) with our numerical results is shown in Figure 3.

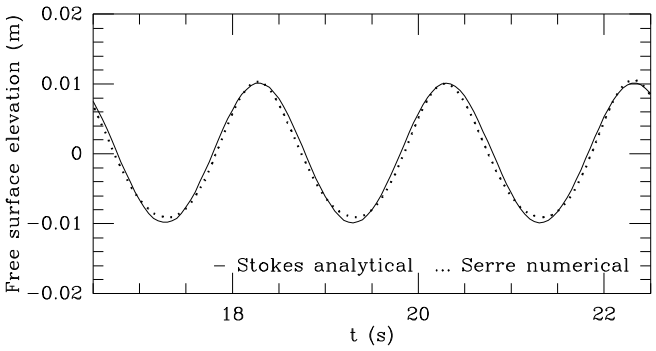

Figure 3: Periodic wave with 0.02 m height, 2.02 s period and 3.73 m wavelength propagating in a channel 0.40 m depth. Comparison of the analytical solution (22) with numerical results in a gauge installed at x = 3.0 m.

Additionally, numerical results are compared with measured data in three gauges installed at x = 10.5 m, x = 13.5 m and x = 17.3 m (Figure 2); these comparisons are shown in Figures 4 a), b) and c). Despite some discrepancies, numerical results of the improved Serre model agree quite well with the measured data. It should be noted that the standard Serre equations are not able to reproduce the input and propagation of a wave in conditions such that h_0/λ is greater than 0.09. In this case, with $h_0/\lambda \approx 0.11$ ($kh \approx 0.67$), the error could be significant.

4.3 Periodic wave propagating in deep water conditions ($h_0/\lambda = 0.50$)

A periodic wave of amplitude a = 0.025 m, period T = 0.85 s and wavelength $\lambda = 1.12\,\text{m}$, propagating into an initially undisturbed region of constant depth $h_0 = 0.56$ m, so already in deep water conditions, with $h_0/\lambda = 0.50$. At the input boundary, the relation (25) has been implemented:

$$u\left(0,t\right) = \frac{g}{\omega}\frac{\tanh\left(kh\right)}{h}\,\eta\left(0,t\right) \tag{25}$$

with $\eta\left(0,t\right) = a\cos\left(\omega t\right)$. The computational domain was discretized with a uniform grid interval $\Delta x = 0.05\,\text{m}$. A time step $\Delta t = 0.010\,\text{s}$ meets the stability condition. Figures 5 shows the free surface profile at t = 40 s. A steady periodic flow has been established, which confirms the good performance of the model in *quasi*-deep water conditions.

5 CONCLUSIONS

The standard Serre equations are restricted to shallow water conditions, and an extension for applications in intermediate-depth and to deep waters is essential; indeed, these are the conditions normally found in coastal zones. In this conformity, a new set of Serre equations, improved with additional terms of dispersive origin, is developed and solved numerically in this work. The ability of the numerical model to reproduce the general phenomena experienced by waves propagating from *quasi*-deep water conditions to very shallow waters is shown through very demanding applications.

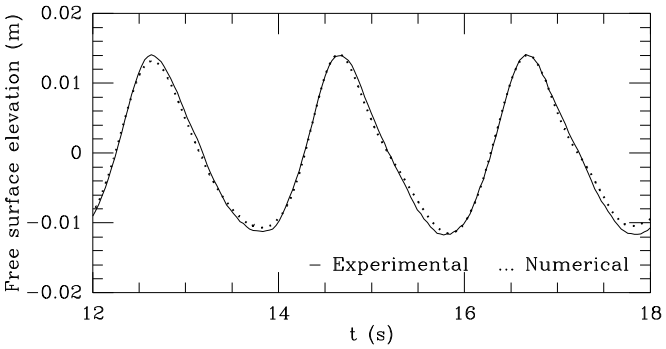

a) Gauge at 10.5 m.

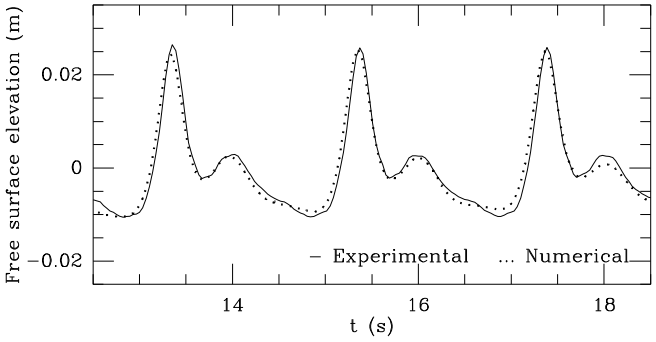

b) Gauge at 13.5 m.

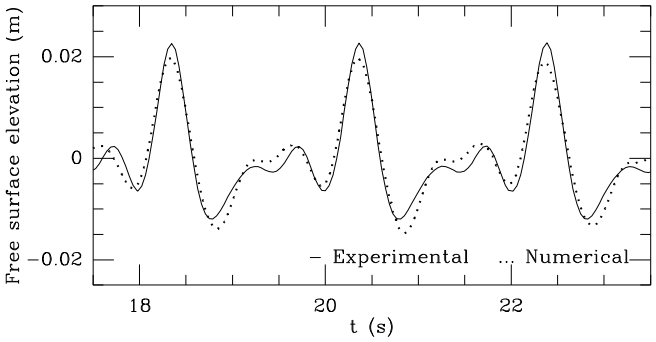

c) Gauge at 17.3 m.

Figure 4: Periodic wave propagating over a bar. Free surface evolution in three gauges installed at a) x = 10.5 m, b) x = 13.5 m and c) x = 17.3 m, as in [1] and [22].

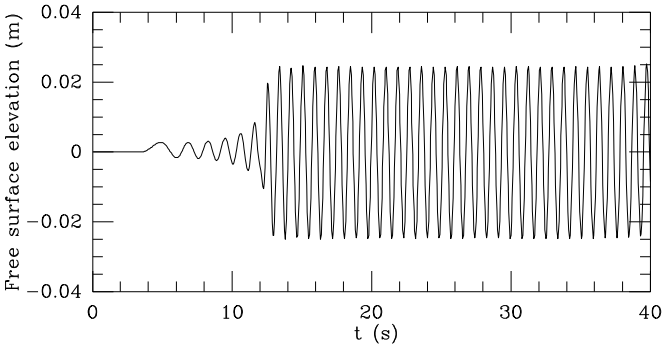

Figure 5: Sinusoidal wave with 0.05 m height, 0.85 s period, and 1.12 m wavelength, propagating in a channel 0.56 m depth. Numerical results obtained in a gauge installed at x = 10.0 m from the input boundary.

The numerical procedure is validated by comparison with the analytical solution of a highly nonlinear propagating solitary wave ($a/h_0 = 0.60$). The robustness of the model is tested through applications in intermediate-depth waters and bottoms with considerable slopes. It is shown that the extended Serre equations with additional terms of dispersive origin are able to propagate waves from deep water conditions to very shallow waters. The overall agreement of the model is very good both in shallow water conditions and in intermediate-depth waters.

The model extension for two dimensions in the horizontal plane is currently being developed, considering $\mu = f(h)$, using an implicit numerical method of finite elements based on the Galerkin technique.

REFERENCES

[1] JS Antunes do Carmo (2013a). Applications of Serre and Boussinesq type models with improved linear dispersion characteristics. In JM Blanco, I Arias, A Peña, J Miranda Guedes, N Silvestre, M Silva, Eds., *Congreso de Métodos Numéricos en Ingeniería – CMN 2013*, Bilbao, Spain, 2–28 June, 1552–1569, CIMNE, Barcelona.

[2] JS Antunes do Carmo (2013b). Boussinesq and Serre type models with improved linear dispersion characteristics: Applications. *Journal of Hydraulic Research* **51**(6):719–727.

[3] JCW Berkhoff, N Booij, AC Radder (1982). Verification of numerical wave propagation models foe simple harmonic linear water waves. *Coastal Engineering* **6**:255–279.

[4] JT Kirby, RA Dalrymple (1983). A parabolic equation for the combined refraction-diffraction of stokes waves by mildly varying topography. *Journal of Fluid Mechanics* **136**:435–466.

[5] N Booij (1983). A note on accuracy of the mild-slope equation. *Coastal Engineering* **7**:191–203.

[6] JT Kirby (1984). A note on linear surface wave-current interaction over slowly varying topography. *Journal of Geophysical Research* **89**(C1):745–747.

[7] RA Dalrymple (1988). Model for refraction of water waves. *Journal of Waterway, Port, Coastal, and Ocean Engineering* **114**(4):423–435.

[8] FJ Seabra Santos (1985). *Contribution à l'Ètude des Ondes de Gravité Bidimensionnelles en Eau Peu Profonde*, Thèse de Doctorat d'État, Université Scientifique et Médicale et L'Institut National Polytechnique de Grenoble.

[9] FJ Seabra Santos (1989). As aproximações de Wu e de Green & Naghdi no quadro geral da teoria da água pouco profunda. In *Simpósio Luso-Brasileiro de Hidráulica e Recursos Hídricos* (4º SILUSBA), Lisboa, Portugal, 14–16 June, 209–219.

[10] F Serre (1953). Contribution à l'étude des écoulements permanents et variables dans les canaux. *La Houille Blanche* **8**:374–388.

[11] AE Green, PM Naghdi (1976). A derivation of equations for wave propagation in water of variable depth. *Journal of Fluid Mechanics* **78**(2):237–246.

[12] J Boussinesq (1872). Théorie des ondes et des remous qui se propagent le long d'un canal rectangulaire horizontal. *Journal de Mathématiques Pures et Appliquées* **2**(17):55–108.

[13] B Saint-Venant (1871). Théorie du movement non permanent des eaux, avec application aux crues des rivières et à la introduction des marées dans leur lits. *Comptes Rendus des Séances de l'Académie des Sciences* **73**:147–154, 237–240.

[14] PA Madsen, R Murray, OR Sørensen (1991). A new form of the Boussinesq equations with improved linear dispersion characteristics. *Coastal Engineering* **15**:371–388.

[15] PA Madsen, OR Sørensen (1992). A new form of the Boussineq equations with improved linear dispersion characteristics: 2. A slowly varying bathymetry. *Coastal Engineering* **18**:183–204.

[16] O Nwogu (1993). Alternative form of Boussinesq equations for nearshore wave propagation. *Journal of Waterway, Port, Coastal, and Ocean Engineering* **119**:618–638.

[17] G Wei, JT Kirby, ST Grilli, R Subramanya (1995). A fully nonlinear Boussinesq model for surface waves. I. Highly nonlinear, unsteady waves. *Journal of Fluid Mechanics* **294**:71–92.

[18] MFG Gobbi, JT Kirby, G Wei (2000). A fully nonlinear Boussinesq model for surface waves. Part 2. Extension to $O(kh)^4$. *Journal of Fluid Mechanics* **405**:181–210.

[19] P Lynett, PL-F Liu (2002). *Modeling Wave Generation, Evolution, and Interaction with Depth Integrated, Dispersive Wave Equations COULWAVE Code Manual*, Cornell University Long and Intermediate Wave Modeling Package.

[20] S Beji, K Nadaoka (1996). Formal derivation and numerical modelling of the improved Boussinesq equations for varying depth. *Ocean Engineering* **23**:691–704.

[21] ZB Liu, ZC Sun (2005). Two sets of higher-order Boussinesq-type equations for water waves. *Ocean Engineering* **32**:1296–1310.

[22] JS Antunes do Carmo (2013c). Extended Serre equations for applications in intermediate water depths. *The Open Ocean Engineering Journal* **6**:16–25.

[23] S Beji, JA Battjes (1993). Experimental investigations of wave propagation over a bar. *Coastal Engineering* **19**:151–162.

On pressure disturbance waves

RM Moreira[1], JTA Chacaltana[2], JA Santos[3,4], SRA Rodrigues[3,5], CF Neves[6], MF Nascimento[7]

[1]UFF, Rua Passo da Pátria 156, bl.D, sl.563A, Niterói, RJ, 24210-240, Brazil
[2]UFES, Av. Fernando Ferrari 514, CT-4, sl.24, Vitória, ES, 29075-910, Brazil
[3]LNEC, Av. do Brasil 101, 1700-066 Lisboa, Portugal
[4]ISEL, Rua Conselheiro Emídio Navarro 1, 1959-007 Lisboa, Portugal
[5]IST, Av. Rovisco Pais 1, Lisbon, 1049-001, Portugal.
[6]UFRJ, CT, bl.C, sl.203, Cidade Universitária, Rio de Janeiro, RJ, 21945-970, Brazil
[7]UEZO, Rua Manuel Caldeira de Alvarenga 1203, Rio de Janeiro, RJ, 23070-200, Brazil
email: roger@vm.uff.br, juliotac@gmail.com, jasantos@dec.isel.pt, srodrigues@lnec.pt, neves@peno.coppe.ufrj.br, mfnascimento@yahoo.com

ABSTRACT: Pressure disturbance waves are computed via a fully nonlinear, unsteady, boundary integral formulation for various Froude numbers. Three moving pressure distributions are introduced in the numerical model to evaluate the produced wave patterns in a channel. For Froude numbers equal to one, classical runaway solitons are obtained on the fore of the moving pressure patch whereas "stern" waves are radiated away. "Step-like" pressure distributions give different responses to the free-surface flow, with upward breaker jets and steeper "stern" waves. For supercritical and subcritical flows, steady solitons and stationary trenches moving at the same speed of the pressure distribution are obtained, respectively. Nonlinear results show that the wave field is significantly affected by the chosen moving pressure distribution, with breaking "bow" waves and steeper "stern" waves when "step-like" pressure functions are used.

KEY-WORDS: Free-surface flows; Ship waves; Boundary integral method.

1 INTRODUCTION

The representation of a ship's motion by a moving pressure distribution was first proposed by Havelock in 1909 [1], followed by a series of papers published in the early 20th century [2, 3, 4]. Since then, researchers have used the pressure disturbance approach to model ship waves in shallow, intermediate and deep water, with open and bounded domains. Several one-dimensional (1D) pressure functions have been proposed aiming to model the far-field wave pattern. A sinusoidal pressure field distribution was introduced by Ertekin, Webster and Wehausen [5] and later followed by several authors [6, 7, 8, 9, 10, 11, 12],

$$p_0(x,t)=\begin{cases}\dfrac{1}{2}p_m\left\{1+\cos\left[\dfrac{2\pi}{l}(x+Ut)\right]\right\}, & \text{if } |x+Ut|<\dfrac{l}{2},\\ 0, & \text{if } |x+Ut|\geq\dfrac{l}{2}.\end{cases} \tag{1}$$

The x axis is in the direction of the motion i.e. the centerline of the ship; l is the length of the pressure distribution in the x direction; p_m is the pressure amplitude; U is the velocity of the left-going (positive) or right-going (negative) surface pressure. Grimshaw, Maleewong and Asavanant [13] used a hyperbolic function to study the stability of gravity-capillary waves,

$$p_0(x,t)=p_m\,\mathrm{sech}^2(x+Ut), \quad \text{for } |x+Ut|<\infty. \tag{2}$$

Some authors suggested a two-dimensional (2D) moving pressure distribution to represent the effect of the ship's hull at the free surface. The product of harmonic functions for the pressure distribution was proposed by Ertekin, Webster and Wehausen [14] and followed by Liu and Wu [10],

$$p_0(x,y,t)=p_m f(x,t)g(y), \tag{3}$$

where

$$f(x,t)=\begin{cases}1, & \text{if } 0\le |x+Ut|\le \dfrac{\alpha l}{2},\\ \cos^2\left[\dfrac{\pi}{l}\left(\dfrac{|x+Ut|-\alpha l/2}{1-\alpha}\right)\right], & \text{if } \dfrac{\alpha l}{2}<|x+Ut|<\dfrac{l}{2},\\ 0, & \text{if } |x+Ut|\ge\dfrac{l}{2},\end{cases}$$

$$g(y)=\begin{cases}1, & \text{if } 0\le |y|\le \dfrac{\beta b}{2},\\ \cos^2\left[\dfrac{\pi}{b}\left(\dfrac{|y|-\beta b/2}{1-\beta}\right)\right], & \text{if } \dfrac{\beta b}{2}<|y|<\dfrac{b}{2},\\ 0, & \text{if } |y|\ge\dfrac{b}{2}.\end{cases}$$

Here l and b are the length and the width of the pressure distribution in the x (centerline) and y (transverse) directions; α and β are dimensionless parameters, which are respectively equal to 0.7 and 0.4 according to Ertekin, Webster and Wehausen [14]. The pressure acts inside a rectangle of $l\times b$ dimensions, vanishing outside it. Li and Sclavounos [15] followed by other researchers [12, 16, 17, 18] also used equation (3) to model ship waves though with $\alpha=\beta=0$. For a 1D case, expression (3) is equivalent to equation (1).

Another 2D moving pressure distribution was suggested by Pedersen [19],

$$p_0(x,y,t)=\begin{cases}\dfrac{1}{2}p_m\left\{1+\cos\left[\pi\sqrt{\left(\dfrac{x+Ut}{l}\right)^2+\left(\dfrac{y}{b}\right)^2}\right]\right\}, & \text{for } \left(\dfrac{x+Ut}{l}\right)^2+\left(\dfrac{y}{b}\right)^2<1,\\ 0, & \text{for } \left(\dfrac{x+Ut}{l}\right)^2+\left(\dfrac{y}{b}\right)^2\ge 1.\end{cases} \tag{4}$$

In this case the pressure acts inside an ellipse with major and minor radii l and b. For a 1D case, expression (4) resembles equation (1) with the pressure distributed along a length $2l$ in the x direction. More recently 2D constant-pressure rectangular patches and non-uniform pressure distributions have been proposed to represent the effects of different hulls at a free surface. For instance, the following constant-pressure rectangular patch was proposed by Scullen and Tuck [20],

$$p_0(x,y,t)=\begin{cases}p_m, & \text{if } |x+Ut|<\dfrac{l}{2} \text{ and } |y|<\dfrac{b}{2},\\ 0, & \text{elsewhere.}\end{cases} \tag{5}$$

Figure 1 compares the pressure distribution functions proposed by [5, 14, 20] in 1D (see equations (1), (3) and (5)). Despite the step-function character along the sides of the patch, Scullen and Tuck [20] surprisingly found that no discontinuity was observed at the free surface, at least for subcritical flows. Far-field and local components at the leading and trailing edges cancel each other, such that the total free surface elevation is continuous everywhere. Accordingly Trinh, Chapman and Vanden-Broeck [21] show that the formation of waves near a ship is a necessary consequence of singularities in the ship's geometry. The use of "step-like" functions in the pressure distribution then seems to be a more realistic way to represent the resultant free-surface flow produced by certain hulls. According to Yih and Zhu [22], the geometric details of the hull modelled by a pressure disturbance are not relevant if the region under consideration is sufficiently far from the track of the ship; then the far-field wave pattern will be the same despite the pressure distribution used. However it seems quite reasonable to expect that at least the properties of the near-field waves would be directly influenced by the pressure distribution function used.

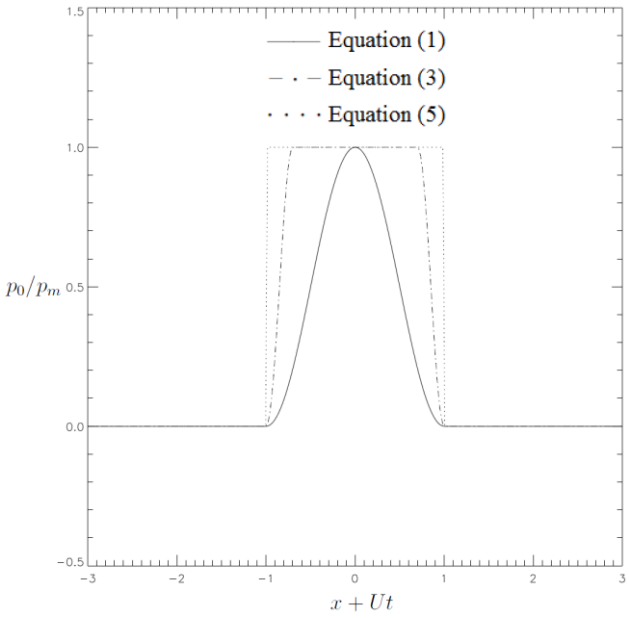

Figure 1: 1D pressure distribution functions (l = 2m).

Despite all the theoretical and experimental works on this field, none of them have studied in what extent the pressure disturbance model can be used to represent the geometric details of certain hulls and whether the ship waves would be equivalent. This paper aims to shed further light on the generation and propagation of free-surface waves due to pressure disturbance models in a channel. The fully nonlinear boundary-integral potential flow solver is adapted in order to include the 1D pressure distributions shown in Figure 1. "Bow" and "stern" waves are obtained and discussed. Our purpose is to determine numerically the wave field induced by pressure disturbance models and to present possible differences between their wave patterns.

2 UNSTEADY NONLINEAR MODEL

We consider a 2D incompressible, inviscid, fluid flow in the (x,z) plane. The x axis is located at the still-water surface, parallel to the ship's centerline, and the z axis points vertically upwards, such that the fluid occupies $-h<z<0$ when at rest, with a flat impermeable bottom at $z=-h$. Following Havelock's method, the ship's motion is represented by a 1D pressure disturbance function, which moves at a constant speed U in the x direction. The velocity field $\vec{u}(x,z,t)$ is given by the gradient of a velocity potential $\varphi(x,z,t)$, which satisfies Laplace's equation.

At the free surface, the kinematic and dynamic boundary conditions are applied

$$\frac{D\vec{r}}{Dt}=\nabla\varphi, \qquad \frac{D\varphi}{Dt}=\frac{1}{2}\left|\nabla\varphi\right|^2-gz-\frac{p}{\rho}, \tag{6}$$

where $\vec{r}=(x,z,t)$; $z=\eta(x,t)$ is the free-surface elevation; g and ρ are the gravitational acceleration and the fluid's density. The pressure exerted at the free surface is given by

$$p=p_0(x,t), \tag{7}$$

where $p_0(x,t)$ is the moving pressure distribution given by expressions (1), (3) or (5) (see Figure 1); surface tension is neglected.

As time evolves, pressure disturbance waves are formed and radiate away from the source. The desired "infinite" domain is then approximated by a finite extension in x, satisfying the condition $\nabla\varphi(\pm x_\infty,z,t)<\varepsilon$, valid for $-h\le z\le\eta(x,t)$ and $t>0$; ε is a specified small "precision" parameter; x_∞ is a finite distance, which is determined iteratively by the numerical scheme. To complete the model, a flat free surface is used as the initial condition of the fully nonlinear unsteady problem i.e. $\eta(x,0)=0$ and $\varphi(x,\eta,0)=0$.

The solution method is based on solving the principal value of an integral equation that arises from Cauchy's integral theorem of a complex variable function. The boundary-integral scheme described by Moreira and Peregrine [23] is modified in order to include the pressure disturbance models. For each time, φ is used to calculate the velocity $\nabla\varphi$ on the free surface. Then the surface profile and the velocity potential are stepped in time using a truncated Taylor series. Note that *p* and its corresponding Lagrangian time derivatives affect directly the calculation of the higher order time derivatives of φ, which are used in the time stepping process. Such stages are repeated until either the final time is reached, or the algorithm breaks down. This means that an insufficient number of points could be found if, for example, the wave approaches Stokes' limiting shape (120º at the crest of the calculated wave) or the crest overturns.

With the introduction of *p* and its Lagrangian derivatives, sawtooth numerical instabilities appear more frequently in the surface variables, which eventually cause the breakdown of computations. A low-order smoothing formula is employed. This proves to be efficient in the removal of unstable modes and also gives a slightly larger maximum steepness of surface waves rather than when employing a higher-order formula. A sufficient number of surface calculation points is then necessary in order to have any wave well resolved and thus not being smoothed away by the numerical scheme. All the computations presented in this paper have the same initial discretization and smoothing parameter. For more details of the numerical method see e.g. [24].

All variables are non-dimensionalized in such a way that $X = x/h$, $T = t\sqrt{g/h}$, $P = p/(\rho gh)$, and $Fr = U/\sqrt{gh}$; *X*, *T* and *P* are the dimensionless space, time and pressure; *Fr* is the Froude number, which is used to characterize the free-surface flow. Following the works [7,9,10], 2D unsteady nonlinear free-surface profiles are computed with the 1D pressure distributions illustrated in Figure 1 for various Froude numbers.

3 FULLY NONLINEAR RESULTS

Figures 2 and 3 show the pressure disturbance waves (with different vertical exaggerations) obtained with the pressure distributions illustrated in Figure 1 for $Fr = 0.1, 1.0, 1.5$ and $P_m = 0.10, 0.15$. Results are plotted in a reference frame moving with the left-going pressure distribution. The shaded area represents the region where the pressure models are applied. A good agreement is found between the present fully nonlinear unsteady computations and those obtained by [7]: runaway solitons are formed on the fore of the pressure distribution whereas "stern" waves are radiated away (see solid lines in Figure 2a); as the

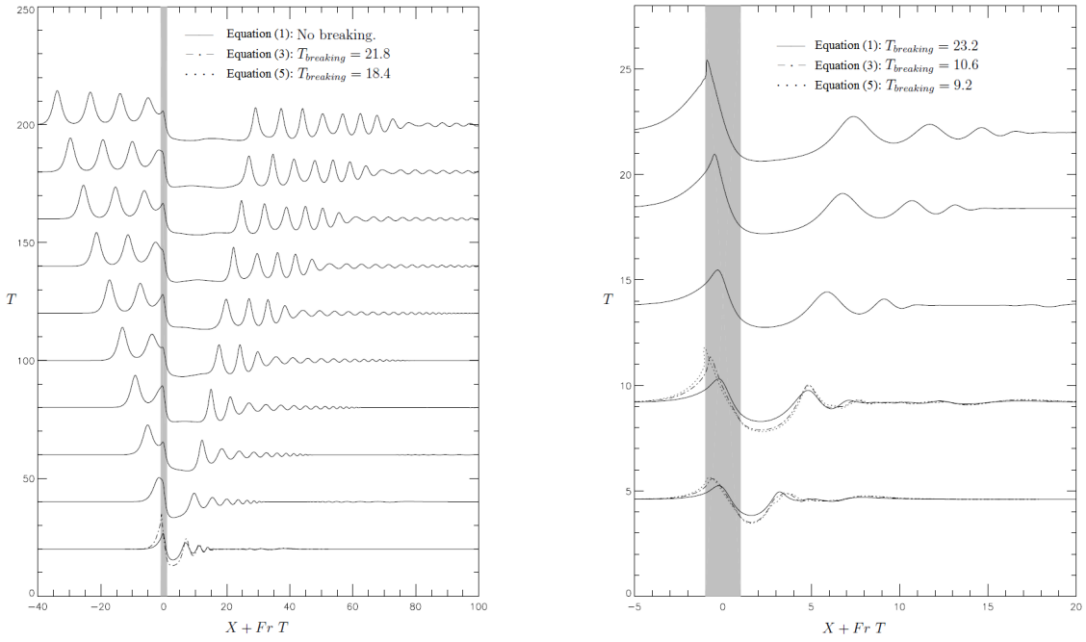

(a) (b)

Figure 2: Pressure disturbance waves for $Fr = 1.0$: (a) $P_m = 0.1$, vertical exaggeration 30:1; (b) $P_m = 0.15$, vertical exaggeration 5:1. Pressure distributions are applied in the shaded region.

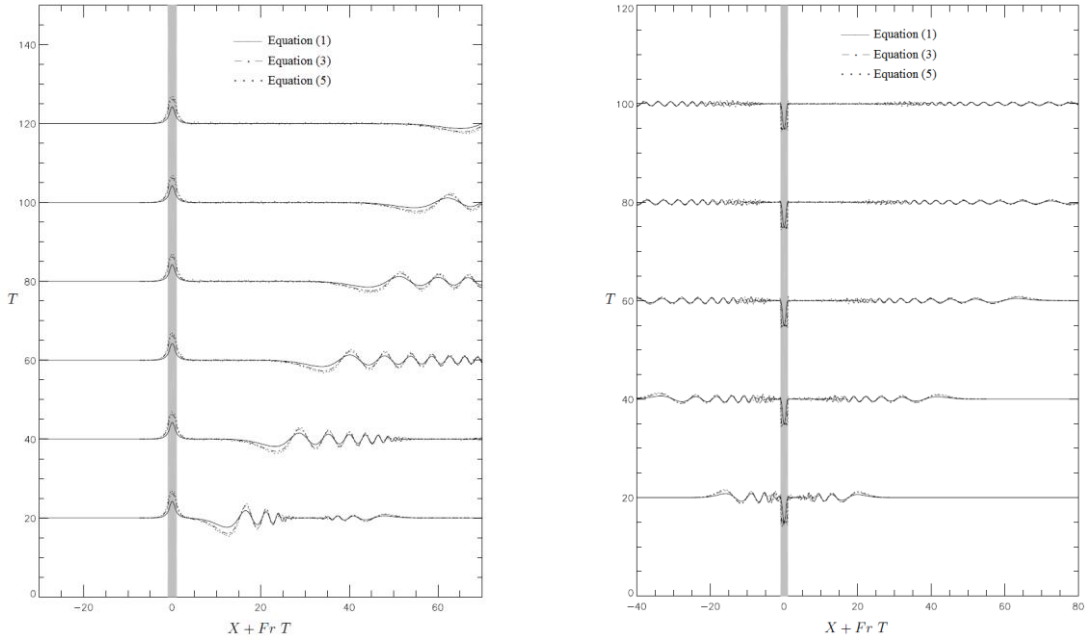

Figure 3: Pressure disturbance waves for $P_m = 0.10$: (a) $Fr = 1.5$, vertical exaggeration 100:1; (b) $Fr = 0.1$, vertical exaggeration 50:1.

pressure amplitude P_m increases, nonlinear effects take over causing wave breaking (see solid lines in Figure 2b). For weaker pressure disturbances e.g. $P_m = 0.02$ (not shown), runaway solitons were also observed after long computational run-times. Regardless the magnitude of P_m, the "step-like" pressure functions proposed by [14] and [20] (expressions 3 and 5) cause an earlier breaking of the "bow" wave in the form of an upward breaker jet (see the dashed-dotted and dotted lines in Figure 2).

For supercritical flows (see Figure 3a), a single steady solitary wave is formed, travelling at the same speed of the pressure distribution, with no breaking being observed at least for $P_m = 0.10$. Again a good agreement is found with [7]. "Step-like" pressure distributions give steeper solitons and "stern" waves when compared to the free-surface profiles obtained with expression (1) (compare the solid, dashed-dotted and dotted lines in Figure 3a). The appearance of wave instabilities when using the pressure distribution (5) was also observed, which prohibited longer computational runs. For subcritical flows (see Figure 3b), a single steady trench is formed in the region where the pressure distributions are applied, with "bow" and "stern" waves being radiated away. Accordingly pressure patches given by expressions (3) and (5) produce wider depressions when compared to expression (1).

4 CONCLUSIONS

Pressure disturbance waves are computed via a fully nonlinear, unsteady, boundary integral formulation for various Froude numbers. Classical runaway and single steady solitons are formed for critical and supercritical flows when applying the moving pressure distribution (1), while "stern" waves propagate away, agreeing with [7]. The introduction of "step-like" pressure functions, as suggested [14] and [20] (expressions 3 and 5), gives different responses to the free-surface flows, with upward breaker jets on the fore and steeper "stern" waves on the rear of the pressure patches. The use of "step-like" functions to supercritical flows proves to be more numerically unstable for the same discretization and smoothing parameter. For subcritical flows, "bow" and "stern" waves are radiated away while different trenches are formed in the region where the pressure distributions are applied. Nonlinear results show that wave patterns are significantly affected by moving pressure distributions. Further investigations are necessary to conclude whether the near and/or far-field ship waves would be equivalent to the pressure disturbance waves here presented. In this sense the introduction in our model of an impermeable 2D surface to represent the ship's hull is under development.

ACKNOWLEDGEMENTS

RMM and JTAC acknowledge the research grant from CAPES, the Brazilian agency for postgraduate education (processes no. 11787/13-9 & 2149/14-1).

REFERENCES

[1] TH Havelock (1909). The wave-making resistance of ships: a theoretical and practical analysis. *Proceedings of the Royal Society of London A* **82**:276–300.
[2] TH Havelock (1914). Ship resistance: the wave-making properties of certain travelling pressure disturbances. *Proceedings of the Royal Society of London A* **89**:489–499.
[3] TH Havelock (1917). The initial wave resistance of a moving surface pressure. *Proceedings of the Royal Society of London A* **93**:240–253.
[4] TH Havelock (1932). Ship waves: the calculation of wave profiles. *Proceedings of the Royal Society of London A* **135**:1–13.
[5] RC Ertekin, WC Webster, JV Wehausen (1984). Ship-generated solitons. In *Proceedings of the 15th Symposium on Naval Hydrodynamics*, Hamburg, Germany.
[6] TYT Wu (1987). Generation of upstream advancing solitons by moving disturbances. *Journal of Fluid Mechanics* **184**:75–99.
[7] Y Cao, RF Beck, WW Schultz (1993). Numerical computations of two-dimensional solitary waves generated by moving disturbances. *International Journal for Numerical Methods in Fluids* **17**:905–920.
[8] CM Casciola, M Landrini (1996). Nonlinear long waves generated by a moving pressure disturbance. *Journal of Fluid Mechanics* **325**:399–418.
[9] PLF Liu, TR Wu (2002). Waves generated by moving pressure disturbances in rectangular and trapezoidal channels. In *Proceedings of the 17th International Workshop on Water Waves and Floating Bodies*, Cambridge, UK.
[10] PLF Liu, TR Wu (2004). Waves generated by moving pressure disturbances in rectangular and trapezoidal channels. *Journal of Hydraulic Research* **42**(2):163–171.
[11] T Torsvik, K Dysthe, G Pedersen (2006). Influence of variable Froude number on waves generated by ships in shallow water. *Physics of Fluids* **18**:062102.
[12] CH Chang, KH Wang (2011). Generation of three-dimensional fully nonlinear water waves by a submerged moving object. *Journal of Engineering Mechanics* **137**:101–112.
[13] R Grimshaw, M Maleewong, J Asavanant (2009). Stability of gravity-capillary waves generated by a moving pressure disturbance in water of finite depth. *Physics of Fluids* **21**:082101.
[14] RC Ertekin, WC Webster, JV Wehausen (1986). Waves caused by a moving disturbance in a shallow channel of finite width. *Journal of Fluid Mechanics* **169**:275–292.
[15] Y Li, PD Sclavounos (2002). Three-dimensional nonlinear solitary waves in shallow water generated by an advancing disturbance. *Journal of Fluid Mechanics* **470**:383–410.
[16] MF Nascimento, CF Neves, GF Maciel (2008). Propagation of ship waves on a sloping bottom. In *Proceedings of the 31st International Conference on Coastal Engineering*, Hamburg, Germany.
[17] MF Nascimento, CF Neves, GF Maciel (2010). Waves generated by two or more ships in a channel. In *Proceedings of the 32nd International Conference on Coastal Engineering*, Shanghai, China.
[18] T Torsvik, G Pedersen, K Dysthe (2009). Waves generated by a pressure disturbance moving in a channel with a variable cross-sectional topography. *Journal of Waterway, Port, Coastal, and Ocean Engineering* **135**:120–123.
[19] G Pedersen (1988). Three-dimensional wave patterns generated by moving disturbances at transcritical speeds. *Journal of Fluid Mechanics* **196**:39–63.
[20] DC Scullen, EO Tuck (2011). Free-surface elevation due to moving pressure distributions in three dimensions. *Journal of Engineering Mathematics* **70**:29–42.
[21] PH Trinh, SJ Chapman, JM Vanden-Broeck (2011). Do waveless ships exist? Results for single-cornered hulls. *Journal of Fluid Mechanics* **685**:413–439.
[22] CS Yih, S Zhu (1989). Patterns of ship waves. *Quarterly of Applied Mathematics* **47**:17–33.
[23] RM Moreira, DH Peregrine (2010). Nonlinear interactions between a free-surface flow with surface tension and a submerged cylinder. *Journal of Fluid Mechanics* **648**:485–507.
[24] JW Dold (1992). An efficient surface-integral algorithm applied to unsteady gravity waves. *Journal of Computational Physics* **103**:90–115.

Geostrophic influence in the River Douro plume: a climatological study

I Iglesias[1,2], P Avilez-Valente[1,2,3], X Couvelard[4], RMA Caldeira[2]

[1]Centro Interdisciplinar de Investigação Marinha e Ambiental, Universidade do Porto, Rua dos Bragas 289, 4050-123 Porto, Portugal
[2]Instituto de Hidráulica e Recursos Hídricos, Universidade do Porto, Rua Dr. Roberto Frias, 4200-465 Porto, Portugal
[3]Faculdade de Engenharia, Universidade do Porto, Rua Dr. Roberto Frias, 4200-465 Porto, Portugal
[4]Centro de Ciências Matemáticas, Universidade da Madeira, 9020-105 Funchal, Portugal
email: iiglesias@fe.up.pt, pvalente@fe.up.pt, Xavier.Couvelard.@ifremer.fr, rcaldeira@ciimar.up.pt

ABSTRACT: The Douro is one of the most important rivers of the Iberian Peninsula. Its estuary is located in the northwest of Portugal and the flow is controlled by the Crestuma Dam, which induces a high variability of the river flow on the estuary. This variability produces a strong impact on the plumes formation and dispersion. On this work, the Regional Ocean Modelling System (ROMS) was selected to represent different plume scenarios. A multiyear climatological simulation was performed using climatological initial conditions. It was observed that the plume structure depends on the initial conditions imposed to the model. Bulge plus coastal current and southwest protruding jet-like plumes were observed depending on the season of the year. The wind conditions show an important influence on the plume dispersion, but this is also reactive to the offshore current. When the offshore current is at its highest strength it can force the plume to travel against the wind. On this work, a wide range of plume patterns were observed: jet-like features, bifurcations, jets protruding towards either north or south, patches, flapping filaments and mesoscale eddies. So we concluded that the Douro river plume response depends both on the wind and on the behaviour of the offshore geostrophic current system. Offshore eddies and filaments are also responsible for the cross-shore transport, through the horizontal advection of plume waters.

KEY WORDS: Buoyant plumes; Cross-shore transport; NW Iberian Peninsula; Advection; Alongshore currents; Coastal processes.

1 INTRODUCTION

River plumes are one of the most important mechanisms that transport terrestrial materials to the ocean. These might be pollutants, essential nutrients, which enhance the phytoplankton productivity, or sediments, which settle on the seabed producing modifications on the bathymetry and affecting the navigation channels. The mixing between the riverine and oceanic waters can induce instabilities, which might generate bulges, filaments, and buoyant currents over the continental shelf. Offshore, the buoyant riverine water can form a front with the oceanic waters often related with the occurrence of current-jets, eddies and strong mixing. The study and modelling of the river plumes is a key factor for the complete understanding of sediment transport mechanisms and patterns, and of coastal physical and dynamic processes.

There are three main processes that govern plume dynamics: (i) the mixing induced by the turbulence; (ii) the alongshore current produced by the balance between the Coriolis force and the cross-shore pressure gradient and (iii) the acceleration produced by the balance between buoyancy and gravity forces [1]. Plumes are superficial structures that can be trapped in the inner shelves with a baroclinic boundary coastal current structure [2] but they occupy a small portion of the total water column [3] and their behaviour varies with several variables like the wind characteristics, tides, bottom friction on shallow waters, and offshore currents.

2 GEOGRAPHICAL SETTINGS

The River Douro is located on the northwestern Iberian coast. The freshwater flow that reaches the estuary is controlled by the Crestuma Dam, located 21.6 km upstream. Its daily averaged freshwater discharge can range from 0 to 13 000 m^3/s, with a strong variability between dry and rainy months and years. This variability impacts the formation of the river plume and its dispersion along the continental shelf.

There are prominent capes, submarine canyons and promontories on the northwestern Iberian coast that produce persistent hydrodynamic features. The local tides have a semidiurnal regime, and their amplitudes range from 1 m to 1.7 m [4].

3 MODEL SET-UP

The study was carried out using the Regional Oceanic Modelling System (ROMS) [5,6]. The atmospheric forcing, the initial and boundary conditions and the model grid were built using the ROMSTOOL package [7]. To construct the bathymetry of the grid, the GEBCO 30 arc-second grid resolution database was selected [8]. 35 vertical levels, based on the stretched S-coordinates, were used to ensure an acceptable resolution of the upper ocean layer. The model domain extends from 39.5 ºN to 42.5 ºN and from 10.75 ºW to 8 ºW (cf. Figure 1), and a grid resolution of approximately 1 km x 1 km. The climatological salinity and temperature profiles used to force and initiate the simulations were extracted from the World Ocean Atlas climatology [9,10]. The tidal forcing was extracted from the OSU tidal data inversion [11], and the atmospheric fluxes from COADS [12].

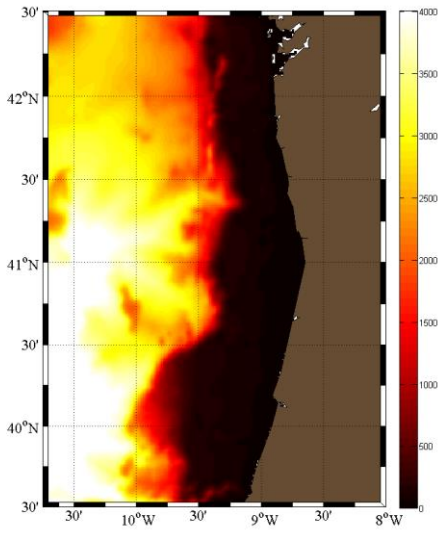

Figure 1: Bathymetry (m) and model domain.

A 3 year spin-up simulation was performed without river flux for the volume averaged kinetic energy to reach a steady-state, after which a 1 month-long simulation with tide-ramp was performed. The results of this simulation were used as initial conditions for the case study. The case study is a 3 year-long multi-year climatological simulation, with monthly prescribed river outflow and water temperature. The river flux was added as a point source positioned at the River Douro mouth location with null river water salinity and water temperature and flow rate changing according to the values shown in Table 1. The temperature values were extracted from previous works [13,14], while the river fluxes are climatic averages at the Crestuma dam extracted from historical records of Jan/1986 to Jan/2012 time period.

Table 1: River Douro mean temperature and monthly averaged discharge.

MONTH	Jan	Feb	Mar	Apr	May	Jun	Jul	Aug	Sep	Oct	Nov	Dec
T (ºC)	7	8	9	10	12	15	18	20	18	14	12	10
Q (m^3/s)	1083	855	762	522	402	272	165	101	160	273	473	862

The depth of the plume was calculated as the depth at which the maximum value of the vertical salinity gradient is reached. The water masses deeper than 100 m and with salinity above 35.7 were excluded from the gradient computation to avoid the deep water salinity gradient. The seasonal averaged values of the Equivalent Depth were calculated according to the Choi and Wilkin [15] definition, as

$$ED = \int_{-h}^{\eta} \frac{S_{SW} - S(z)}{S_{SW}} dz, \quad (1)$$

where η is the sea level elevation, h is the bottom depth, S_{SW} is a shelf water reference salinity, taken as 35.6 in this work, and $S(z)$ is the water column salinity.

4 RESULTS

In Figure 2, the monthly mean surface salinity was depicted for the most characteristic plume patterns in the simulation, showing the variation of the plume structure with the climatological conditions in the area. During the first months of the simulation, a southwest protruding jet-like plume can be seen, while during winter months, particularly for October, November and December, the bulge and the coastal current seem to evolve to the north, according with the climatic wind conditions. The climatic wind presents a northern component for most of the year except for October, November and December, when it veers westward and southward. The wind strength varied between 2 and 8 m/s and produced currents on the range of 0.2–0.5 m/s within the plume bulge and 0.1–0.2 m/s close to the coast.

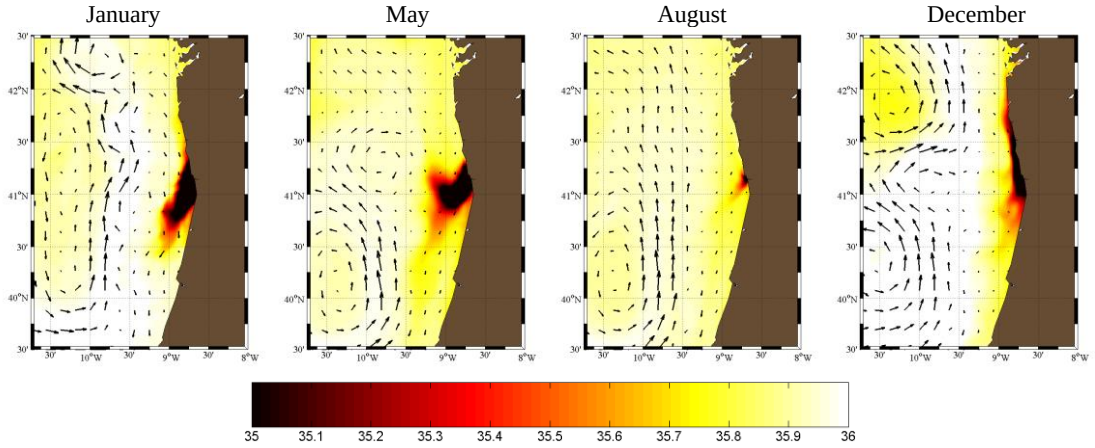

Figure 2: Monthly mean salinity and current vectors for four months of the multi-year climatological simulation.

The representation of the plume depth (see Figure 3) showed that the Douro plume suffers an important influence of the coastal current. Although the wind presents an important influence on the plume dispersion (cf. Figures 3a and 3b), there are times when the plume induced current propagates against the wind. This happens when the offshore current presents a high strength on the direction opposite to the wind (cf. Figure 3c). Sometimes, the surface offshore currents propagate in direction opposite to their coastal counterpart (cf. Figure 3d), but when a strong offshore current is present it is able to veer the inshore current to travel against the wind (cf. Figure 3c). These snapshots of the plume depth allow us to observe different plume scenarios: jetlike feature (cf. Figure 3b), flapping filaments that eventually break into patches (cf. Figure 3c), plume bifurcations or changes on the plume direction at the river mouth with jets protruding to the north and to the south simultaneously (cf. Figure 3a).

The analysis of the seasonal averaged values of ED (see Figure 4) allow for the identification of two distinct scenarios according to the season of the year: a bulge and an alongshore current for autumn and winter conditions, and a jet-like offshore protrusion of the river plume for spring and summer conditions.

In Figure 5, snapshots of the streamlines and surface salinity for a 9 day-long sequence show the formation of a mesoscale eddy on the southern part of the domain. This kind of structures interact with inshore waters and are able to advect the river plume fresh water across the shelf. They are a mechanism to transport plume waters to remote locations. The eddies interaction with the ocean bottom can result in their dissipation, causing the plume water contents, such as coastal materials, sediments, nutrients or even pollutants, to settle in offshore regions.

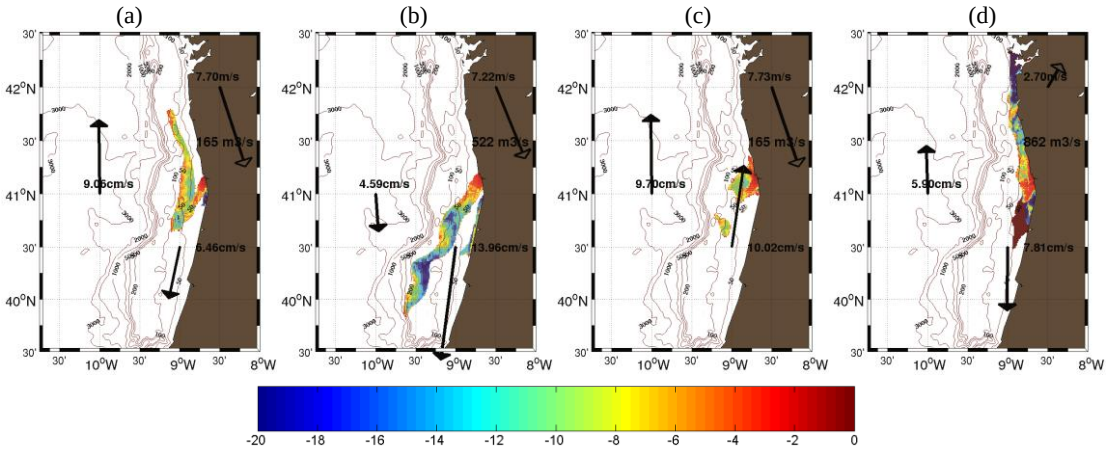

Figure 3: Plume depth (m) snapshots from the multi-year climatological simulation. Values over the land (from north to south) are the wind velocity (m/s) and direction, and the river flow rate (m^3/s).Values over the sea (from west to east) represent offshore and inshore current velocity (cm/s) and direction.

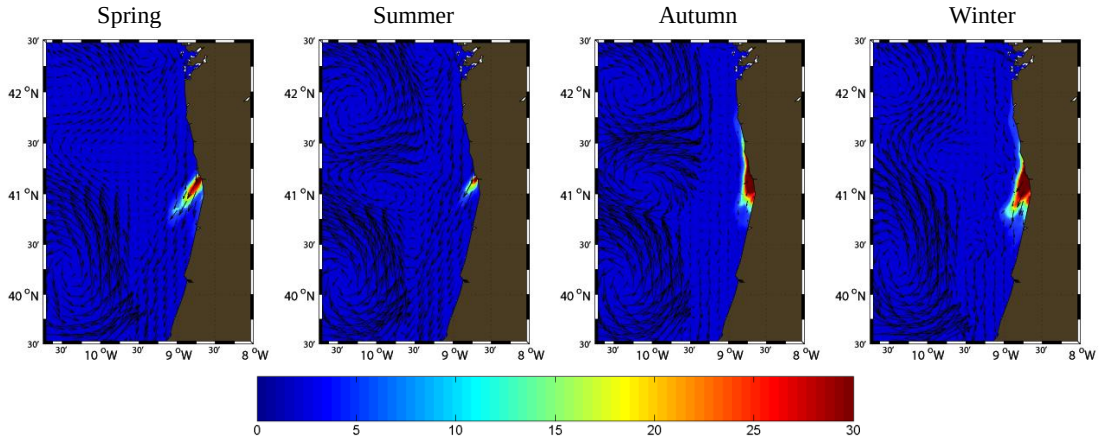

Figure 4: Seasonal *ED* (m) of the plume.

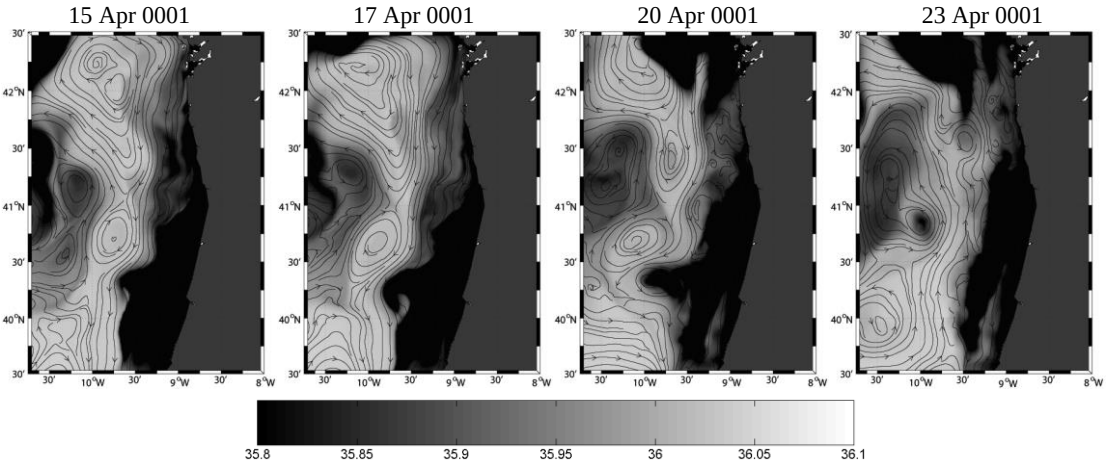

Figure 5: Surface salinity and streamlines for a 9 day-long sequence.

5 CONCLUSIONS

The River Douro plume structure varies with the climatology imposed to the model. Two distinct scenarios were identified: a bulge and an alongshore current for autumn and winter conditions and a jet-like offshore protrusion of the river plume for spring and summer conditions.

It was also found that the wind plays a dominant role on the control of the alongshore distribution of the plume over the continental shelf, but that it also depends on the behaviour of the offshore geostrophic current system.

The formation of offshore eddies, filaments and other structures was identified in the performed simulation. These structures transport the plume waters cross-shore by means of horizontal advection.

ACKNOWLEDGMENTS

RAIA (0313-RAIA-1-E) and RAIA.co (0520-RAIA-CO-1-E) projects provided postdoctoral funds for Isabel Iglesias. The RAIA Coastal Observatory has been funded by the Programa Operativo de Cooperación Transfronteriza España-Portugal (POCTEP 2007–2013). Numerical models were run at CIIMAR's HPC unit, acquired and maintained by FCT pluriannual funds (PesTC/Mar/LA0015/2013). Rui Caldeira was supported by funds from the ECORISK project (NORTE-07-0124-FEDER-000054).

REFERENCES

[1] TA McClimans (1986). Estuarine fronts and river plumes. In J Dronkers, W van Leussen, Eds., *Physical Processes in Estuaries*, Springer-Verlag, New York, 55–69.

[2] S Chao, WC Boicourt (1986). Onset of estuarine plumes. *Journal of Physical Oceanography* **16**:2137–2149.

[3] A Münchow, RW Garvine (1993). Dynamical properties of a buoyancy driven coastal current. *Journal of Geophysical Research: Oceans* **98**:20063–20077.

[4] M Benavent, J Arnoso, FG Montesinos (2009). Regional ocean tide loading modelling around the Iberian Peninsula. *Journal of Geodynamics* **48**:132–137.

[5] AF Shchepetkin, JC McWilliams (2003). A method for computing horizontal pressure-gradient force in an oceanic model with a nonaligned vertical coordinate. *Journal of Geophysical Research: Oceans* **108**:3090.

[6] AF Shchepetkin, JC McWilliams (2005). The regional oceanic modelling system (ROMS): A split-explicit, free-surface, topography-following-coordinate oceanic model., *Ocean Modelling* **9**:347–404.

[7] P Penven, P Marchesiello, L Debreu, J Lefèvre (2007). Software tools for pre- and post-processing of oceanic regional simulations. *Environmental Modelling & Software* **23**:660–662.

[8] GEBCO (2010). The GEBCO-08 Grid, version 20100927 [WWW]. Available from: http://www.gebco.net/.

[9] JL Antonov, RA Locarnini, TP Boyer, AV Mishonov, HE Garcia (2006). *World Ocean Atlas 2005. Volume 2: Salinity*, Volume 62 of NOAA Atlas NESDIS, U.S. Department of Commerce, NOAA, NESDIS, Washington, D.C.

[10] RA Locarnini, AV Mishonov, JI Antonov, TP Boyer, HE Garcia (2006). *World Ocean Atlas 2005. Volume 1: Temperature*, Volume 61 of NOAA Atlas NESDIS, U.S. Department of Commerce, NOAA, NESDIS, Washington, D.C.

[11] GD Egbert, SY Erofeeva (2002). Efficient inverse modeling of barotropic ocean tides. *Journal of Atmospheric and Ocean Technology* **19**:183–204.

[12] AM da Silva, CC Young-Molling, S Levitus (1994). *Atlas of Surface Marine Data 1994. Volume 1: Algorithms and Procedures*, Volume 6 of NOAA Atlas NESDIS, U.S. Department of Commerce, NOAA, NESDIS, Washington, D.C.

[13] IC Azevedo, PM Duarte, AA Bordalo (2006). Pelagic metabolism of the Douro estuary (Portugal) — Factors controlling primary production. *Estuarine, Coastal and Shelf Science* **69**:133–146.

[14] J Pinto (2007). *Influência do Regime de Escoamento Fluvial na Hidrologia e Dinâmica do Estuário do Douro*, Relatório Final de Estágio, Universidade de Évora, Portugal.

[15] B Choi, JL Wilkin (2007). The effect of wind on the dispersal of the Hudson River plume. *Journal of Physical Oceanography* **37**:1878–1897.

This page was intentionally left blank

Simulação numérica integrada do comportamento de um navio amarrado no Terminal XXI do Porto de Sines

LV Pinheiro[1], JA Santos[2], CJEM Fortes[1], JLM Fernandes[3]

[1]Núcleo de Portos e Estruturas Marítimas, Departamento de Hidráulica e Ambiente, LNEC, Av. do Brasil, 101, 1700-066 Lisboa, Portugal
[2]Instituto Superior de Engenharia de Lisboa. Rua Conselheiro Emídio Navarro 1, 1959-007 Lisboa, Portugal
[3]Instituto Superior Técnico, Av. Rovisco Pais 1, 1049-001 Lisboa, Portugal
email: lpinheiro@lnec.pt, jasantos@dec.isel.pt, jfortes@lnec.pt, leonel@dem.ist.utl.pt

RESUMO: Este trabalho apresenta a aplicação da ferramenta numérica SWAMS para caracterizar o comportamento de um navio amarrado na bacia do Terminal de Contentores do Porto de Sines. São analisados os movimentos do navio, as forças nas amarras e nas defensas. Analisa-se ainda a influência do vento e da introdução de pré tensionamento nas amarras assim como a resposta do sistema quando sujeito a ondas longas. Os resultados permitem avaliar qual destes fatores tem maior influência sobre os movimentos do navio e a sua segurança.

PALAVRAS-CHAVE: SWAMS; Navios amarrados; ondas longas; BOUSS-WMH; WAMIT; BAS.

1 INTRODUÇÃO

A agitação marítima pode perturbar as atividades de carga e descarga de navios bem como causar problemas significativos nas infraestruturas portuárias e nas embarcações presentes no interior de um porto. Uma previsão e caracterização corretas do campo de ondas dentro do porto, mais precisamente, ao longo das trajetórias dos navios e nos postos de acostagem permitem caracterizar a resposta dos navios aos estados de mar neles incidentes, quer estejam amarrados, parados ou em manobra.

A ferramenta SWAMS apresentada neste trabalho tem como característica inovadora o acoplamento de um modelo do tipo Boussinesq (o modelo BOUSS-WMH *BOUSSinesq Wave Model for Harbours,* [7]) para a propagação não linear das ondas com o modelo WAMIT [4] e BAS [5] para a interação navio-ondas.

Na secção 2 descreve-se a ferramenta SWAMS. Na secção 3 apresenta-se o caso de estudo, as condições de cálculo dos modelos e os resultados obtidos. A secção 4 é referente a conclusões.

2 FERRAMENTA SWAMS

2.1 Descrição

SWAMS – *Simulation of Wave Action on Moored Ships* – é uma ferramenta integrada para modelação numérica da propagação de ondas bem como do comportamento de navios amarrados no interior de bacias portuárias. Consiste num interface gráfico com o utilizador e num conjunto de módulos que tratam da execução dos modelos numéricos. O SWAMS divide-se em dois módulos: o módulo WAVEPROP – para a propagação das ondas e o módulo MOORNAV – para o comportamento do navio amarrado, Figura 1.

2.2 Módulo de propagação de ondas WAVEPROP

Este módulo inclui 3 modelos numéricos para a propagação de ondas e um gerador de malhas de elementos finitos:

- SWAN é um modelo não linear espectral, [1] baseado na equação de conservação da ação da onda e capaz de simular a propagação de ondas irregulares;
- DREAMS é um modelo linear de elementos finitos, [2], baseado na equação de declive suave para simular a propagação de ondas regulares;
- BOUSS-WMH é um modelo não linear de elementos finitos [8], baseado nas equações de Boussinesq estendidas deduzidas por [6] sendo capaz de simular a propagação de ondas regulares e irregulares;
- GMALHA é um gerador de malhas de elementos finitos triangulares [8], especialmente definidas para serem utilizadas pelos modelos DREAMS e BOUSS-WMH, sendo a densidade de nós das malhas variável de acordo com o comprimento de onda local.

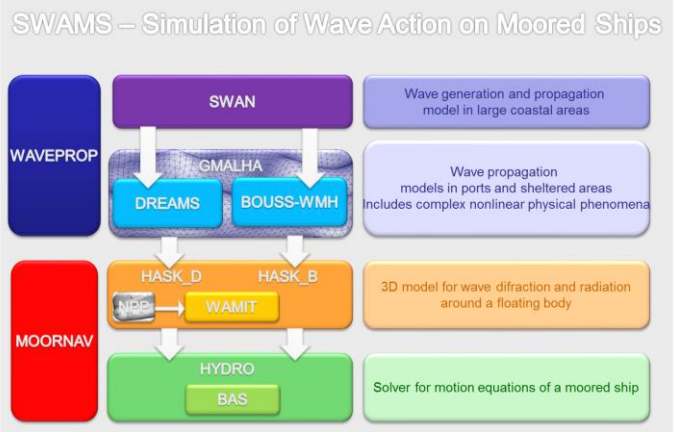

Figura 1: Ferramenta SWAMS.

2.3 Módulo de comportamento de navios amarrados MOORNAV

A determinação do movimento do navio amarrado num posto de acostagem sujeito à agitação incidente é realizada utilizando o pacote numérico MOORNAV [9]. Trata-se essencialmente de dois modelos numéricos e um conjunto de rotinas que faz a interligação entre eles:

- WAMIT [4] que resolve, no domínio da frequência, os problemas de radiação e de difração da interação de um corpo flutuante livre com as ondas nele incidentes;
- BAS [5] que monta e resolve, no domínio do tempo, as equações de movimento de um navio amarrado no posto de acostagem levando em conta as séries temporais das forças devidas às ondas incidentes no navio, as funções de resposta a impulso do navio e as relações constitutivas dos elementos do sistema de amarração (cabos de amarração e defensas)

2.3.1 Interação de corpos flutuantes com ondas monocromáticas

O WAMIT [4] é um modelo desenvolvido no Departamento de Engenharia Oceânica do *Massachusetts Institute of Technology* e que utiliza um método de painel para resolver no domínio da frequência os problemas de radiação e de difração de um corpo flutuante livre. Este modelo baseia-se na segunda igualdade de Green para determinar a intensidade das distribuições de fontes e dipolos nos painéis utilizados na discretização da superfície molhada do casco do navio com as quais é possível gerar os potenciais harmónicos dos escoamentos associados aos problemas de radiação e de difração de um navio livre colocado numa zona de profundidade constante mas não limitada horizontalmente. Nos pontos seguintes apresenta-se a formulação analítica dos problemas de radiação e de difração no domínio da frequência.

Potencial de velocidades

Seja ϕ o potencial de escoamento quando o navio se move sob a ação de ondas. Da linearidade do sistema navio / ondas é possível decompor o potencial na soma de vários potenciais devidos cada um deles a uma das seguintes causas: a) onda incidente, ϕ_0; b) onda difratada pelo navio parado, ϕ_7 ; c) ondas geradas pelo movimento do navio em águas de outro modo paradas, segundo cada uma das seis coordenadas generalizadas ϕ_1 a ϕ_6

$$\phi = \mathrm{Re}\left[\sum_{j=0}^{7} \phi_j\right] \tag{1}$$

Escrevendo cada um dos potenciais devidos ao movimento segundo a coordenada j em função da amplitude complexa da velocidade do mesmo movimento, a expressão (1) fica

$$\phi = \left[\phi_0 + \phi_7 + \sum_{j=1}^{6} -i\omega\phi_j\varepsilon_j\right] e^{-i\omega t} \tag{2}$$

onde ϕ_j é um potencial complexo estacionário e ε_j é a amplitude complexa do movimento do corpo segundo a coordenada j. Assim consegue separar-se o problema do escoamento do movimento do corpo,

sendo apenas necessário determinar os potenciais do escoamento para velocidades de amplitude unitária segundo cada uma das coordenadas generalizadas.

Conhecido o potencial de velocidade, a pressão sobre o corpo flutuante pode ser determinada a partir da equação de Bernoulli linearizada. Considerando apenas a parcela dinâmica da pressão, já que a parcela hidrostática está contabilizada no cálculo da matriz de restituição hidrostática, a força atuante segundo cada uma das coordenadas k vem dada por:

$$F_k = i\rho\omega\int_S (\phi_0 + \phi_7) n_k e^{-i\omega t} dS + \sum_{j=1}^{6} -\rho\omega^2 \varepsilon_j \int_S \phi_j n_k e^{-i\omega t} dS \tag{3}$$

A primeira parcela da soma anterior representa a força associada ao problema de difração (força exercida pela onda incidente no navio parado)

$$F_k^D = i\rho\omega\int_S (\phi_0 + \phi_7) n_k e^{-i\omega t} dS \tag{4}$$

enquanto a segunda força está associada ao problema de radiação (força que é necessário fazer para que o navio oscile segundo cada uma das coordenadas *j* em água de outra forma parada)

$$F_k^R = \mathrm{Re}\left[\sum_{j=1}^{6} T_{kj} \varepsilon_j e^{-i\omega t}\right] \tag{5}$$

Nas expressões anteriores, S representa a superfície molhada do corpo flutuante e n_k a normal segundo a coordenada generalizada k. Da parte real e da parte imaginária de cada elemento da matriz T_{kj} obtêm-se os coeficientes de massa adicionada, a_{kj}, e de amortecimento b_{kj}.

$$T_{kj}(\omega) = \omega^2 a_{kj}(\omega) + i\omega b_{kj}(\omega) \tag{6}$$

Relações de Haskind

Utilizando a segunda igualdade de Green é possível mostrar que não é necessário determinar o potencial da onda difratada pelo corpo, ϕ_7, para calcular as componentes da força associada ao problema de difração, equação (4). Com efeito, atendendo à equação da continuidade e às condições de fronteira satisfeitas pelos potenciais ϕ_1 a ϕ_7, a seleção de um volume adequado permite escrever a força associada ao problema de difração da forma apresentada em Haskind [3], habitualmente conhecida por relações de Haskind:

$$F_k^D = -i\rho\omega\int_S \left(\phi_0 \frac{\partial \phi_k}{\partial n} - \phi_k \frac{\partial \phi_0}{\partial n}\right) dS e^{-i\omega t} \tag{7}$$

Com base nestas relações, em vez de se determinar o potencial associado ao problema da difração ϕ_D para conhecer o valor da componente segundo k da força exercida pelas ondas no navio parado, basta conhecer o potencial da onda incidente nos pontos ocupados pela superfície molhada do corpo ϕ_0, bem como os potenciais associados ao problema de radiação para os mesmos pontos ϕ_k.

Ora, para o problema de radiação, obtém-se uma boa aproximação considerando apenas a fronteira do porto mais próxima do navio, o que torna mais simples a determinação destes potenciais.

Implementação numérica

A utilização do teorema de Green permite transformar em equações integrais as equações diferenciais que controlam os potenciais associados aos problemas de radiação e de difração. Em vez de se ter um conjunto de equações válidas em todo o domínio, obtém-se um conjunto de equações a satisfazer apenas nas fronteiras desse domínio, a região mais relevante para a determinação das forças induzidas pelo escoamento.

Aproximando a posição média da superfície molhada do corpo flutuante por um conjunto de painéis, triangulares ou quadrangulares, em cada um dos quais se assume um valor constante do potencial de velocidades, as equações integrais reduzem-se a um sistema de equações lineares para os valores do potencial de velocidade em cada um dos painéis. Para os potenciais de radiação vem

$$2\pi\phi_j(x_i) + \sum_{k=1}^{N} D_{ik}\phi_j(x_k) = \sum_{k=1}^{N} S_{ik}\frac{\partial\phi_j(x_k)}{\partial n} \tag{8}$$

em que $i = 1,...,N$, sendo N o número de painéis. Para o potencial de difração, o sistema de equações é dado por:

$$2\pi\phi_D(x_i) + \sum_{k=1}^{N} D_{ik}\phi_D(x_k) = 4\pi\phi_0(x_i) \tag{9}$$

As matrizes D_{ik} e S_{ik} são definidas por:

$$D_{ik} = \int_{S_k} \frac{\partial G(x_i,\xi)}{\partial n} d\xi \tag{10}$$

$$S_{ik} = \int_{S_k} G(x_i,\xi) d\xi \tag{11}$$

em que S_k representa a superfície do painel k , n a normal a essa superfície e ξ uma variável de posição na mesma superfície e $G(x_i,\xi)$ é a função Green, o potencial de velocidade num ponto ξ devido a uma fonte de intensidade -4π colocada em x_i e que satisfaz não só a condição de fronteira da superfície livre como a condição de radiação. Embora os pontos onde são escritas as equações integrais estejam localizados no centróide de cada um dos painéis, x_i e x_k , os integrais das equações (10) e (11) a realizar em cada um dos painéis k são obtidos utilizando uma fórmula de quadratura de Gauss com quatro pontos selecionados no painel k . A mesma fórmula de quadratura é utilizada pelo modelo WAMIT para calcular as forças de difração através das relações de Haskind [3], equação (7).

Na implementação das relações de Haskind [3] a onda monocromática incidente na posição do navio poderá já ter sido refratada ou difratada antes de chegar a esta posição. O campo correspondente a esta onda pode ser caracterizada a partir das amplitudes complexas da elevação da superfície livre, $\eta(x,y)$, e das componentes horizontais, $U_0(x,y)$ e $V_0(x,y)$ no nível de repouso, $z = 0$, da velocidade do escoamento por ela induzido.

3 CASO DE ESTUDO – TERMINAL XXI DO PORTO DE SINES

3.1 Introdução

A bacia do Terminal de Contentores do Porto de Sines, designado por Terminal XXI, situa-se na zona mais a Sul do porto e é protegida da agitação incidente pelo quebra-mar leste. É presentemente constituída por um quebra-mar de 1500 m e um cais acostável de 730 m. Junto à cabeça do quebra-mar, as profundidades variavam entre 18 e 20 m, aproximadamente, enquanto no interior da bacia variam entre 1 e 21 m, aproximadamente. Nesta bacia, são frequentes os relatos de agitação importante que induz movimentos excessivos nos navios amarrados ao cais, Figura 2.

Pretende-se avaliar, aplicando a ferramenta SWAMS, o comportamento de um navio amarrado no primeiro posto de acostagem, Figura 2.

A aplicação do SWAMS iniciou-se com a propagação de uma condição de agitação marítima ($H = 1\,\text{m}$, Direção de Sul e $T = 10\,\text{s}$) para o interior da bacia do Terminal XXI, com o modelo BOUSS-WMH.

Seguidamente com os modelos WAMIT e BAS determinaram-se as funções de resposta a impulso do navio livre, as massas adicionadas para frequência infinita e, a partir daqui, as séries temporais das forças exercidas pela agitação marítima incidente no navio. Finalmente, foram resolvidas, no domínio do tempo, as equações de movimento de um navio amarrado levando em conta as relações constitutivas dos elementos do sistema de amarração. Testaram-se situações com e sem vento (15 m/s), com e sem pré-tensionamento das amarras (10% da carga máxima).

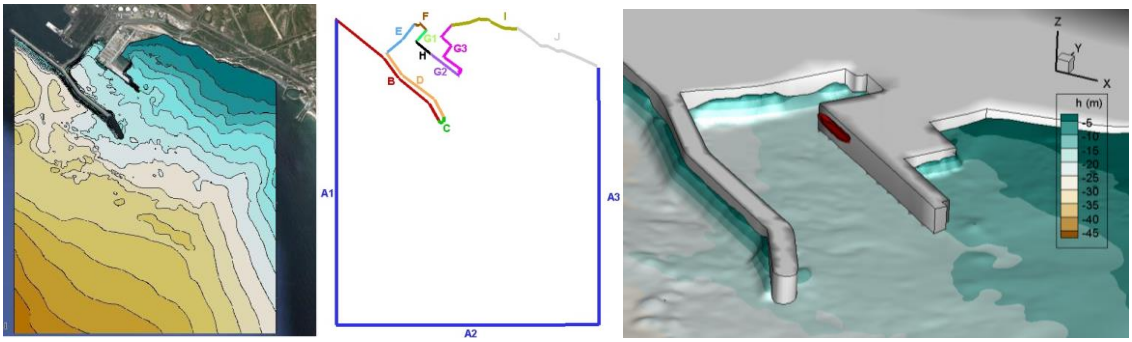

Figura 2: Porto de Sines. Batimetria. Fronteiras do domínio de cálculo. Pormenor da bacia.

3.2 Condições de aplicação dos modelos BOUSS-WMH, WAMIT e BAS

Para a aplicação do modelo BOUSS-WMH, é necessária a definição do domínio de cálculo e da batimetria da zona de estudo, a sua discretização por elementos finitos e o estabelecimento de condições de fronteira. O domínio e batimetria da zona em estudo são apresentados na Figura 2.

A malha de elementos finitos foi gerada com o GMALHA de modo ter um mínimo de oito pontos por comprimento de onda para um período de 10 s. Resultou então uma malha com 504 925 elementos e largura de banda de 978. Quanto às condições de fronteira, os troços A2, I e F são de saída (dissipativos). Nos restantes troços, foram estabelecidas condições de fronteira com reflexão parcial. Os valores dos coeficientes de reflexão foram determinados com base nas características de cada troço (tais como porosidade, declive do talude e profundidade no pé do talude) e ainda, as características da onda.

Para a aplicação dos modelos WAMIT e BAS, é necessário definir as características do navio e do sistema de amarração. O navio estudado tinha um volume deslocado de 108 416 m^3, um comprimento na flutuação de 243 m, uma boca de 42 m e um calado de 14.35 m. A forma do casco foi discretizada com 2694 painéis rectangulares e triangulares. Considerou-se que o navio estava colocado numa zona de fundo horizontal com a profundidade de 17 m.

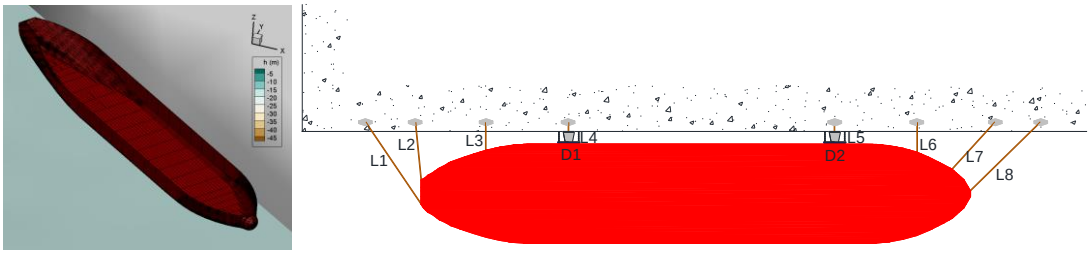

Figura 3: Painelização do casco do navio simulado. Esquema do sistema de amarração.

Na Figura 3 apresenta-se a configuração do sistema de amarração no qual o navio está amarrado ao cais por 8 amarras (2 lançantes à popa, L1 e L2, dois lançantes à proa, L7 e L8, e quatro traveses, L3, L6, L4 e L5). O contacto entre o navio e o cais é impedido por duas defensas pneumáticas (D1 e D2). Considerou-se a mesma relação constitutiva para todos os cabos do sistema de amarração: variação linear desde 0 kN até à carga máxima de 1862 kN a que corresponde uma extensão de 4%. A relação constitutiva das defensas é de 8900 kN para uma deflexão de 1 m.

3.3 Resultados

O modelo BOUSS-WMH para a condição de agitação marítima admitida ($T = 10$ s, $H = 1$ m, Direção Sul), permite obter a série temporal da elevação da superfície livre no centróide do navio.

Utilizou-se o modelo numérico WAMIT para resolver os problemas de radiação e de difração do navio livre para 87 frequências entre 0.0125 rad/s e 1.04 rad/s. Todas funções resposta a impulso foram calculadas com intervalo de tempo de 0.1 s e uma duração máxima de 50 s. Efetuaram-se cálculos considerando as situações, com e sem vento (15 m/s), com e sem pré-tensionamento das amarras (10% da carga máxima). Na Figura ?? apresentam-se as séries temporais do movimento de avanço e de afundamento do navio amarrado.

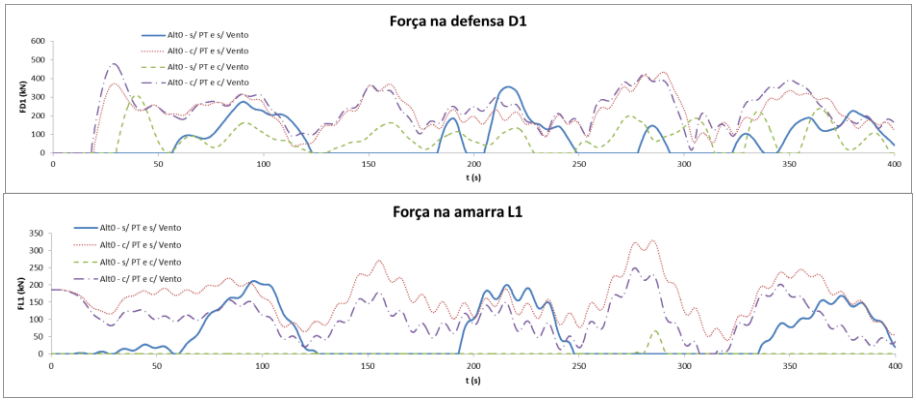

Figura 4: Série temporal dos esforços na defensa D1 e na amarra L1, com e sem vento (15 m/s), com e sem pré-tensionamento das amarras (10% da carga máxima).

A primeira ilustra bem o carácter não linear da resposta do conjunto navio–sistema de amarração. Com efeito, para ondas oscilações da superfície livre cujo período é cerca de 10 s, observam-se oscilações de período muito superior. O período destas oscilações é controlado pela existência das amarras e das defensas, como pode confirmar-se na Figura 4, com as séries temporais dos esforços na defensa D1 e na amarra L1. Uma vez que os elementos do sistema de amarração produzem forças atuantes no navio maioritariamente no plano horizontal, é para os movimentos neste plano que o comportamento não linear é mais evidente.

Verifica-se que, como o vento vem de Sul, empurra o navio em direção ao cais, e isto alivia as forças nas amarras. Pelo contrário o pré tensionamento aumenta as forças nas amarras. No caso das defensas tanto o vento como a pré-tensão aumentam os esforços de compressão.

Fizeram-se também simulações do comportamento do navio amarrado sujeito a um conjunto de ondas longas, desde 54 s até 390 s. Utilizou-se para tal uma altura de onda de 0.20m. Os resultados obtidos encontram-se sumarizados na Figura 5. Nesta figura apresenta-se a força máxima obtida em cada uma das 8 amarras para simulações com duração de 3000 s.

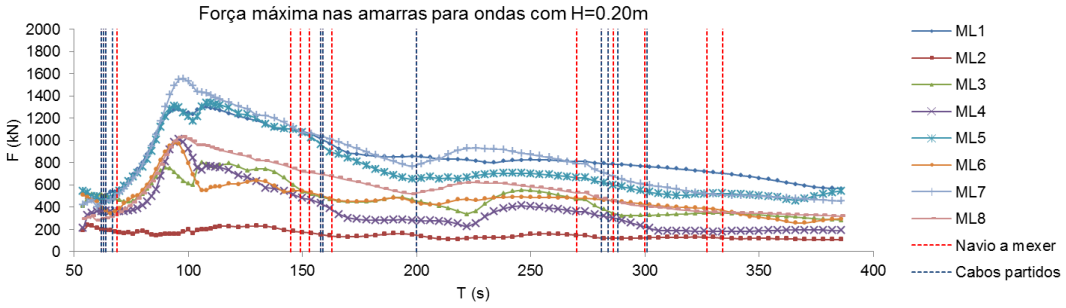

Figura 5: Força máxima nas amarras para ondas com $H = 0.20\,\mathrm{m}$.

Verifica-se que existe uma gama de períodos em que o sistema navio–ondas–amarração entra em ressonância, entre 80 s e 120 s. Se as ondas tiverem períodos nesta gama podem levar a forças muito próximas do limite de rotura (1860 kN) em certas amarras (L1, L5 e L7).

4 CONCLUSÕES

Descreveu-se uma ferramenta numérica integrada, SWAMS, capaz de caracterizar a resposta dum navio amarrado no interior dum porto sujeito à ação da agitação marítima. A ferramenta foi aplicada para avaliar a resposta de um navio estacionado no cais do terminal de contentores do porto de Sines, quando sujeito a ondas curtas e ondas longas. No caso de ondas curtas estudou-se também a influência do vento e do pré-tensionamento das amarras.

Os resultados obtidos com este exemplo para o caso das ondas curtas permitiu concluir que, o vento, neste caso de Sul, empurra o navio para trás e contra o cais. Isto traduz-se em maiores forças nas defensas e um alívio nas forças das amarras. A aplicação de pré-tensão nas amarras diminui o movimento de

avanço mas aumenta os esforços nas amarras. Os movimentos rotacionais, rolo, arfagem e guinada, não são influenciados pelo vento nem pelo pré tensionamento.

Existe uma gama de períodos em que o sistema navio–ondas–amarração entra em ressonância, levando as amarras a registar tensões muito próximas do seu limite de rotura. Assim, mais do que a altura das ondas, a existência de vento ou de pré-tensão, o fator que mais coloca em risco a segurança do navio amarrado é o período das ondas que incidem sobre este, se existir energia na gama de períodos críticos para o sistema navio-sistema de amarração, as forças exercidas sobre as amarras são amplificadas até valores próximos da rotura.

AGRADECIMENTOS

Agradece-se ao Porto de Sines, pela autorização concedida para a utilização dos dados de base. Agradece-se ainda à Fundação Para a Ciência e Tecnologia pelo financiamento concedido através da bolsa de doutoramento SFRH/BD/82637/2011 e através do projeto HIDRALERTA.

REFERÊNCIAS

[1] NR Booij, LH Holthuijsen, RC Ris (1996). The SWAN wave model for shallow water. In *Proceedings of the 25th Conference on Coastal Engineering*, 1996, Orlando, Florida, 668–676.

[2] CJEM Fortes (2002). *Transformações Não Lineares de Ondas em Portos: Análise pelo Método dos Elementos Finitos*, Tese de doutoramento, Instituto Superior Técnico, Lisboa.

[3] MD Haskind (1957). The exciting forces and wetting of ships in waves. Izvestia Akademii Nauk S.S.S.R, *Otdelenie Tekhnicheskikh Nauk* **7**:65–79, (David Taylor Model Basin Translation Nº307, March 1962).

[4] FT Korsemeyer, C-H Lee, JN Newman, PD Sclavounos (1988). The analysis of wave effects on tension-leg platforms. In *7th International Conference Offshore Mechanics and Arctic Engineering*, 1–14.

[5] AE Mynett, PJ Keunig, FC Vis (1985). The dynamic behaviour of moored vessels inside a harbour configuration. In JH Pounsford, Ed., *Papers Presented at the International Conference on Numerical and Hydraulic Modelling of Ports and Habours*, Birmingham, England, 23–25 Apr 1985.

[6] O Nwogu (1993). Alternative form of Boussinesq equations for near-shore wave propagation. *Journal of Waterway, Port, Coastal, and Ocean Engineering* **119**(6):618–638.

[7] L Pinheiro, CJEM Fortes, JA Santos, L Fernandes, M Walkley (2011). Boussinesq-type numerical model for wave propagation near shore and wave penetration in harbors. In *MARTECH 2011: 1st International Conference on Maritime Technology and Engineering*.

[8] L Pinheiro, CJ Fortes, JL Fernandes (2008). Gerador de malhas de elementos finitos para a simulação numérica de propagação de ondas marítimas. *Revista Internacional de Métodos Numéricos para Cálculo y Diseño en Ingeniería* **24**(4):369–391.

[9] JA Santos (1994). *MOORNAV – Numerical Model for the Behaviour of Moored Ships*, Report 3/94-B, Projecto NATO PO-Waves, Lisbon.

This page was intentionally left blank

Avaliação do desempenho de modelos numéricos na simulação de elevação de superfície livre e velocidade ao longo de um canal sujeito a uma onda regular com rebentação

CJEM Fortes[1], E Didier[1,2], DRCB Neves[1], RM Moreira[3], JMP Conde[2], R Carvalho[4], JTA Chacaltana[5]

[1]Laboratório Nacional de Engenharia Civil, Av. do Brasil 101, 1700-066 Lisboa, Portugal
[2]Faculdade de Ciências e Tecnologia, Universidade Nova de Lisboa, UNIDEMI, 2829-516 Monte de Caparica, Portugal
[3]Universidade Federal Fluminense, Laboratório de Fluidodinâmica Computacional, Rua Passos da Pátria 156, bl.D, sl.563A, Niterói, RJ 24210-240, Brasil
[4]IMAR-CMA, Departamento de Engenharia Civil, Universidade de Coimbra, Rua Luís Reis Santos, 3030-270 Coimbra, Portugal
[5]Universidade Federal do Espírito Santo, Laboratório de Escoamentos com Superfície Livre. Av. Fernando Ferrari 514, CT-4, sl.24, Vitória, ES 29075-910, Brasil
email: jfortes@lnec.pt, edidier@lnec.pt, roger@vm.uff.br, ritalmfc@dec.uc.pt, juliotac@gmail.com

RESUMO: Este trabalho analisa o desempenho dos modelos do tipo Boussinesq COULWAVE, e RANS (FLUENT®, versão 6.3.26, e IHFOAM®, versão 2.0) na simulação da elevação da superfície livre e da velocidade da onda ao longo da sua propagação num canal com um fundo de batimetria variável, sujeito a uma onda regular com rebentação. Os modelos numéricos foram aplicados para a condição de agitação incidente de $T = 2.0\,\mathrm{s}$ e $H = 0.12\,\mathrm{m}$, e os respetivos resultados são comparados com os resultados experimentais. Ambos os modelos simulam adequadamente a maioria das transformações das características das ondas ao longo da sua propagação, o que foi confirmado pelos valores de índice de concordância encontrados. As diferenças acentuam-se na zona à volta da rebentação, em que os valores numéricos são consistentemente inferiores aos resultados experimentais no caso do COULWAVE.

PALAVRAS-CHAVE: Rebentação; COULWAVE; FLUENT; IHFOAM.

1 INTRODUÇÃO

A determinação da zona de rebentação é essencial em estudos de hidrodinâmica costeira e de transporte de sedimentos. Mais concretamente, a localização e extensão da rebentação são dois dos factores principais para esses estudos uma vez que determinam a localização e estabilidade das estruturas marítimas e o transporte de sedimentos associado.

Os modelos baseados nas equações estendidas de Boussinesq permitem uma descrição adequada da evolução das ondas marítimas em zonas de profundidade variável tendo em conta os efeitos de fenómenos como a refracção, difracção, rebentação, geração de harmónicas e interacção não-lineares. Um exemplo deste tipo de modelo é o COULWAVE, Lynett e Liu [6] que é um modelo de diferenças finitas para a propagação de ondas fortemente não-lineares e dispersivas, em zonas de profundidade variável. Como é um modelo integrado em profundidade, não é possível descrever convenientemente o escoamento em zonas onde o efeito da profundidade tem importância (zonas de variação brusca da profundidade, de rebentação, de espraiamento, por exemplo). Por outro lado, os fenómenos de dissipação da energia são introduzidos através de termos adicionados à equação original. Em contrapartida, existem modelos mais complexos que permitem actualmente, graças à evolução dos meios de cálculo, simular com precisão a transformação das ondas em domínios compatíveis com as dimensões de pequenas regiões costeiras, como é o caso dos modelos de tipo RANS FLUENT®, versão 6.3.26, [2] e IHFOAM® 2.0 [3].

Os modelos FLUENT® e IHFOAM® se baseiam no método de volumes finitos, que resolvem as equações de Navier-Stokes e utilizam um método VOF (*Volume Of Fluid*) na determinação da posição da superfície livre. O modelo FLUENT® utiliza um algoritmo implícito e o IHFOAM® um algoritmo explícito.

Este trabalho é uma contribuição para a análise comparativa do desempenho dos modelos do tipo Boussinesq COULWAVE, completamente não-linear, e RANS (FLUENT®, versão 6.3.26, e IHFOAM® 2.0) na simulação da elevação da superfície livre e da velocidade da onda ao longo da sua propagação num canal com um fundo de batimetria variável, sujeito a uma onda regular com rebentação.

As simulações numéricas reproduzem os ensaios realizados num canal de ondas irregulares do LNEC, onde foram simuladas diferentes condições de agitação correspondendo a ondas regulares em situação com rebentação. Os modelos numéricos foram aplicados para a condição de agitação incidente de

$T = 2.0\,\text{s}$ e $H = 0.12\,\text{m}$, e os respetivos resultados são comparados com os resultados experimentais, no que se refere às séries temporais de elevação da superfície livre. Realizou-se uma análise no tempo e estatística com os três modelos. Avalia-se assim o desempenho de cada modelo, de forma a utilizá-los de forma sistemática em estudos deste tipo. Na realidade, tendo em conta as vantagens e limitações de cada modelo pode-se escolher o modelo mais adequado a cada caso de estudo e condição de agitação, inferir assim as incertezas dos resultados obtidos.

2 MODELOS NUMÉRICOS

2.1 Modelo COULWAVE

O modelo COULWAVE, [4], [5], [6], é um modelo de diferenças finitas para a propagação de ondas fortemente não-lineares (a razão entre a amplitude da onda e a profundidade pode ser da ordem até 1) e dispersivas, em zonas de profundidade variável. As equações do modelo, do tipo de Boussinesq, são deduzidas a partir da integração em profundidade das equações de continuidade e quantidade de movimento, utilizando o conceito de camadas múltiplas (multi-layer). Em cada camada admite-se um dado perfil de velocidades, através de funções quadráticas com valores iguais na interface que divide a coluna de água. Esta aproximação conduz a um sistema de equações sem as derivadas espaciais de ordem elevada resultantes do uso de funções polinomiais de ordem superior, que é normalmente utilizado na dedução das equações de Boussinesq. Lynett e Liu, [5], [6], [6] e [7], introduziram termos adicionais nas equações de modo a ter em conta o atrito de fundo, a rebentação de ondas e a geração de ondas no interior do domínio. Além disso, incluíram termos de profundidade dependentes do tempo para ter em conta as variações do perfil de fundo no tempo devido à ocorrência de um deslizamento ou de um sismo.

2.2 Modelo FLUENT

O código FLUENT (versão 6.3.26), [2], aplica uma técnica de volumes finitos para resolver a equação da continuidade e as equações de Navier-Stokes-Reynolds (RANS). As principais opções escolhidas são as seguintes: Formulação implícita; Integração no tempo por um esquema de 2ª ordem; Modelo de turbulência k-ε na sua versão standard; Termos difusivos discretizados pelo esquema de diferenças centrais de segunda ordem; Termos convectivos interpolados pelo esquema MUSCL de 3ª ordem; Pressão obtida através do esquema de interpolação PRESTO aconselhado para modelação de escoamentos com superfície livre; Acoplamento entre a velocidade e a pressão pelo algoritmo SIMPLE; Modelação da superfície livre usando o método VOF e utilizando o esquema CICSAM. Os coeficientes de sub-relaxação utilizados no método SIMPLEC são iguais a 1 para a velocidade, a pressão e a fracção de volume e 0.7 para a turbulência. Finalmente a geração da onda é feita através de um batedor numérico: Condição de fronteira nas componentes horizontal e vertical de velocidade e a correspondente amplitude da deformação da superfície livre. Em [1], [2] e [9] são dados mais detalhes.

2.3 Modelo IHFOAM

Este código, [3], foi desenvolvido com base no modelo OpenFoam® e aplica as equações VARANS (*Volume-Averaged Reynolds-Averaged Navier-Stokes*) incluindo as equações da continuidade e conservação da massa em regime transitório utilizando um esquema do tipo VOF para identificar a superfície livre, desenvolvido na Universidade de Cantábria, com base no modelo OpenFoam. É um modelo bifásico e utiliza uma discretização de Volumes Finitos para resolver as equações para as duas fases representativas de fluidos incompressíveis. Suporta vários modelos de turbulência κ−ε, κ−ω SST, LES. Possibilita a geração de ondas de acordo com as teorias de ondas (Stokes I, II, e V; Cnoidal, Onda solitária de Boussinesq, Onda irregular (incluindo direcção) de primeira e segunda ordem e a geração através de um batedor tipo pistão ou através de um perfil de velocidades. Possui absorção ativa das ondas para qualquer fronteira do domínio. O parâmetro de absorção é definido pelo utilizador. Acresce ainda a possibilidade de adoptar fronteiras dinâmicas que possuem a capacidade de gerar e absorver ondas. O modelo possui ainda uma formulação específica para adopção de meios porosos.

É adicionado um termo de compressão artificial cuja solução se encontra entre 0 e 1 que indica a posição da superfície livre. Esta solução é calculada através do método de cálculo MULES (*Multidimensional Universal Limiter for Explicit Solution*). As velocidades e a pressão são obtidas através do algoritmo PIMPLE que está baseado no algoritmo PISO (*Pressure Implicit with Splitting of Operators*) e o SIMPLE (*Semi-Implicit Method for Pressure-Linked Equations*). Desta forma, o modelo garante a convergência para todas as equações a cada passo de tempo.

3 APLICAÇÃO DOS MODELOS NUMÉRICOS

Os modelos foram aplicados na simulação da propagação de ondas em canal sobre um fundo de inclinação variável para uma condição de onda incidente de $T = 2.0\,\text{s}$ e $H = 0.12\,\text{m}$, Figura 1. Esta situação corresponde a um dos ensaios em modelo físico realizados no LNEC [8]. Neste caso de teste, à medida que a onda se propaga ao longo do canal, vai apresentando-se com características cada vez mais não lineares, verificando-se o aparecimento de harmónicas. Nesta propagação da onda, dá-se o empolamento de onda devido ao fundo. Entre $x = -300\,\text{cm}$ e $x = -200\,\text{cm}$, dá-se a rebentação da onda com a dissipação de energia da onda e redução da altura de onda até $x = 100\,\text{cm}$, a partir da qual se mantêm as características da onda.

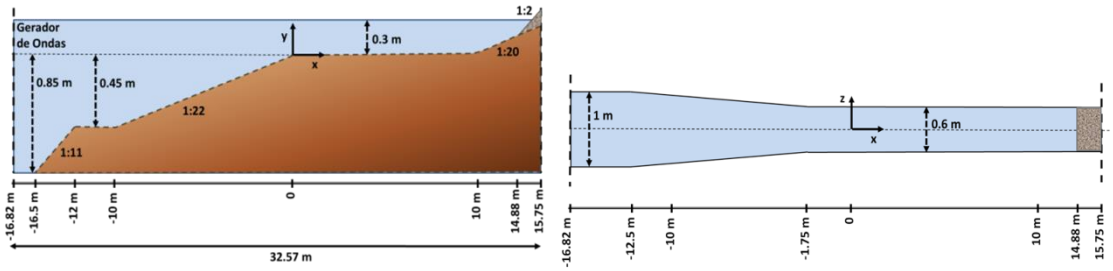

Figura 1: Ensaios em modelo físico. Características do canal de ondas.

No presente trabalho, avaliou-se o desempenho dos modelos numéricos comparando os respectivos resultados com os experimentais no que diz respeito às series temporais da elevação da superfície livre e valores de altura de onda significativa. Determinaram-se os parâmetros estatísticos (RMSE, bias e índice de concordância (ic)) relativos aos valores da altura de onda significativa.

Os cálculos com o modelo COULWAVE foram efectuados num PC Intel Core i5 de 2.80GHz, com 4GB de memória RAM. O modelo FLUENT foi executado num PC Intel Core (TM) i7 CPU 920 de 2.67GHz, com 8GB de memória RAM, utilizando as opções de paralelização para utilizar os 4 *cores*. O modelo IHFOAM foi executado num PC Intel Celeron N2830 de 2.41GHz com 4 GB de memória RAM. O tempo de cálculo é de 6 min (300 s de simulação do escoamento) com o COULWAVE, de 5h30min (35 s) por período de onda com o FLUENT e de 10 h (20 s) com o IHFOAM.

3.1 Condições de cálculo

No modelo COULWAVE, o domínio computacional reproduz exactamente a variação do fundo, mas a largura do canal é constante. O próprio modelo gera uma malha computacional de diferenças finitas com base num número mínimo de pontos fornecido pelo utilizador, que neste caso, foi de 40. O número de Courant admitido é igual a 0.2. A função fonte (geração de ondas) foi colocada na posição $x = -1600$ cm. Consideraram-se duas fronteiras de absorção de cada lado do domínio. Não foi incluído o atrito do fundo.

Para o modelo FLUENT, o domínio computacional é igual ao canal físico, Figura 1. A malha computacional é não uniforme e refinada na zona da superfície livre. O número de volumes de controlo é de cerca de 875000 (plano de simetria na direcção de propagação). O passo de tempo é 0.00234 s para a onda com $T = 2.0\,\text{s}$. O tempo total simulado foi de 35 s.

No modelo IHFOAM, foi elaborado um domínio 2D, a batimetria é igual à do canal físico nas zonas de geração e medição do canal. Não é assim considerada a variação da largura do canal. Como condições de fronteira, considerou-se: a) Fronteira esquerda – um perfil de velocidades; b) Fronteira direita - uma praia numérica com absorção idêntica à dos ensaios físicos. A malha computacional é uniforme na vertical e não uniforme na direcção de propagação das ondas, sendo mais refinada na zona de rebentação de onda. O esquema de turbulência utilizado foi o de fluxo laminar. Na zona final do canal (fronteira direita) foi adoptada um absorção parcial representativa da verificada nos ensaios físicos, [8]. O número total de volumes de controlo é de cerca de 200000 (plano de simetria longitudinal na direcção do eixo do canal). O passo de tempo foi de 0.001 s, um número de Courant inferior a 0.1, e o tempo de simulação de 20 s.

3.2 Série temporal da elevação da superfície livre

Na Figura 2 apresenta-se primeiramente para o caso de teste $T = 2.0\,\text{s}$ e $H = 12\,\text{cm}$, os resultados numéricos e experimentais da elevação da superfície livre ao longo do tempo para $x = -500$ cm e

$x = -100$ cm, que correspondem à situação antes e após a rebentação respectivamente. Como se pode observar, à medida que a onda se propaga para zonas de menor profundidade acontece a transformação na forma da onda. A deformada da superfície livre apresenta características cada vez mais não-lineares, com o aparecimento de harmónicas à medida que a onda se propaga para zonas de menor profundidade.

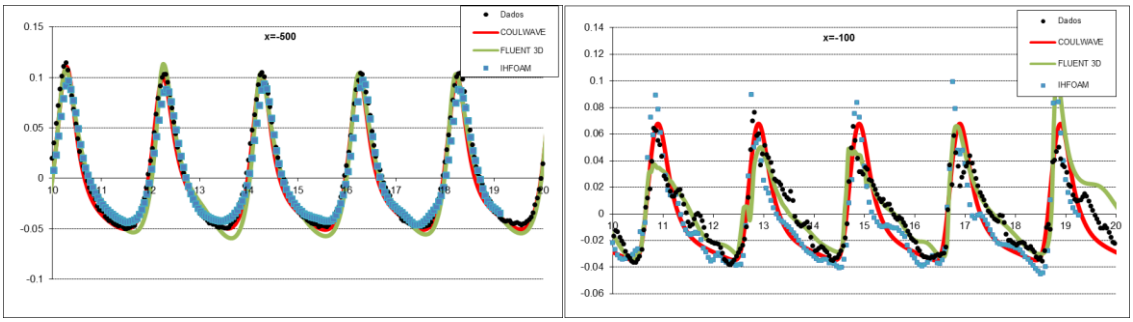

Figura 2: Elevação da superfície livre ao longo do tempo para $x = -500$ cm e $x = -100$ cm. Comparação entre resultados numéricos e experimentais.

De uma forma geral, constata-se uma boa concordância entre os resultados numéricos e experimentais em qualquer das posições das sondas, e claramente na localização antes da rebentação x=-500 cm, não havendo muitas diferenças quer entre os três modelos quer com as medições experimentais. Logo após a rebentação, em x=-100 cm, as diferenças acentuam-se, principalmente ao nível do aparecimento de harmónicas no caso dos dados medidos o que não acontece no caso dos modelos. Os resultados de IHFOAM e FLUENT em termos de amplitude são superiores aos medidos enquanto que os de COULWAVE são da mesma ordem de grandeza.

3.3 Altura significativa de onda

Na Figura 3 apresentam-se os valores da altura significativa que caracterizam as séries (numérica e experimental) de valores da elevação da superfície da água, para $T = 2.0$ s e $H = 12$ cm. Efetuou-se também uma análise estatística realizada com base nos valores de altura de onda de resultados numéricos e experimentais obtidos ao longo do domínio. Assim, foram calculados parâmetros estatísticos como o erro médio quadrático, RMSE, o desvio e o índice de concordância. Para os modelos, apenas se calcularam os valores correspondentes às sete localizações para as quais se obtiveram dados com FLUENT, i.e. $x = -1000$, -500, -150, -100, 0, 50, 100 cm, Tabela 1.

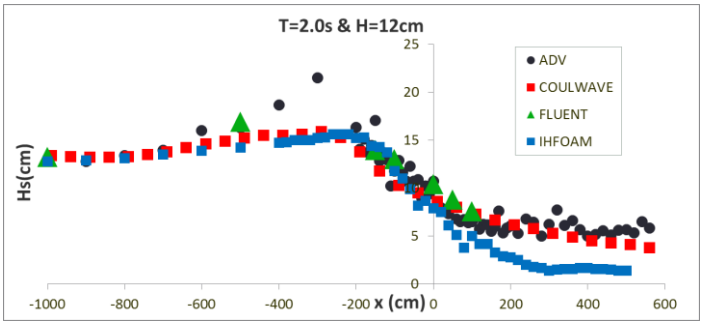

Figura 3: H_S − comparação entre resultados numéricos e experimentais. $T = 2.0$ s; $H = 12$ cm.

Tabela 1: Parâmetros estatísticos das alturas significativas de onda.

Modelo	*Desvio* (cm)	*RMSE* (cm)	*IC*
FLUENT	-0.156	1.389	0.999
COULWAVE	-0.933	1.995	0.999
IHFOAM	-2.041	2.246	0.998

De um modo geral, Figura 3, observa-se que o andamento dos resultados numéricos da altura de onda significativa é semelhante aos correspondentes dos resultados experimentais. Os modelos numéricos

simulam o aumento da altura de onda H_S à medida que a profundidade diminui, a ocorrência de rebentação, o decréscimo de H_S depois desta rebentação e a sua manutenção num valor constante mesmo após o fim da rebentação. Além disso, verifica-se que:

- O modelo COULWAVE não consegue reproduzir os elevados valores experimentais de altura de onda na zona da rebentação (entre $x = -400$ cm e $x = -200$ cm). Com efeito, o modelo COULWAVE não simula o empolamento significativo que se verifica nos dados medidos, e por isso não são atingidos os valores de H_S antes da rebentação. Após a rebentação, os valores numéricos e experimentais são bastante próximos, o que mostra que o modelo está a dissipar correctamente a energia e a produzir valores após a rebentação similares aos que se verificaram nas experiências.
- O modelo FLUENT reproduz de forma correcta a variação de altura de onda antes e após rebentação. Verifica-se que o estreitamento do canal produz um aumento da altura da onda (evidente na secção $x = -500$ cm). O resultado de H_S na secção $x = -500$ cm está bastante próximo do H_S experimental. No entanto, faltam resultados numéricos na zona de rebentação para analisar o desempenho do modelo nessa zona. Após a rebentação, os resultados são muito similares aos experimentais;
- O modelo IHFOAM reproduz com probidade a forma da onda e a zona de rebentação da onda. O modelo embora aplicado de forma bidimensional, consegue detectar a variação de altura de onda aquando da rebentação, reduzindo drasticamente após a dissipação energética gerada pela rebentação da onda. Contudo, o modelo requer (i) uma aplicação tridimensional para registar o efeito de estreitamento do canal; (ii) a aplicação de um modelo de turbulência do tipo $\kappa-\varepsilon$ de forma a reproduzir melhor a dissipação energética da onda e consequente propagação da onda pós-rebentação; (iii) refinamento da malha no eixo vertical refinando adequadamente a zona da superfície livre; e (iv) aumentando o tempo de simulação de forma a ter um número maior de ondas para uma análise mais cuidada dos resultados.

Os valores da Tabela 1 confirmam as conclusões anteriores. Com efeito, verifica-se que os valores obtidos pelo modelo COULWAVE são inferiores aos experimentais (desvio negativo) e apresentam um erro médio quadrático (RMSE) superior aos obtidos pelo FLUENT. Para estas 7 localizações, o valor do índice de concordância é bastante bom com ambos os modelos sendo o FLUENT o que fornece melhores resultados. No entanto, faltam resultados do FLUENT na zona de rebentação.

Quanto ao IHFOAM, estes mostram uma tendência semelhante ao COULWAVE e ao modelo FLUENT, apresentando tanto desvios positivos como negativos, o erro médio quadrático (RMSE) fica também entre os verificados pelos dois outros modelos, apresentando valores bastante próximos do experimental. O índice de concordância mostra que os valores calculados pelo IHFOAM seguem adequadamente os valores registados experimentalmente.

As diferenças observadas entre os modelos numéricos e os valores experimentais podem ser devidas a vários factores:

- O método de geração de onda é diferente quer nos modelos numéricos quer no modelo físico, ou seja, as condições de entrada dos modelos numéricos são diferentes da do batedor. No COULWAVE a elevação de superfície livre é imposta como condição limite na secção do batedor. Nos modelos FLUENT e IHFOAM a elevação de superfície livre e o perfil de velocidades (componente horizontal e vertical) são impostas na secção do batedor. Estas diferenças nas condições limite, e consequentemente de onda incidente (harmónicas e fases), explicam a existência de diferenças antes da rebentação e nas velocidades horizontais após a rebentação, assim como nas elevações da superfície livre, onde se obtêm valores inferiores aos medidos;
- O modelo COULWAVE é um modelo integrado em profundidade, o que na zona de rebentação tem as suas limitações. Além disso, o canal é caracterizado por um estreitamento progressivo da secção transversal que altera a altura da onda incidente antes da rebentação. O modelo COULWAVE para o qual o canal é considerado de secção constante, não pode, como é natural, reproduzir com total fidelidade os ensaios. A zona de rebentação é por consequência, diferente;
- No modelo FLUENT, a modelação da propagação das ondas necessita uma discretização da malha correspondente a 60 segmentos por comprimento de onda. Se este critério é respeitado para a frequência fundamental, não se verifica para as harmónicas (35 segmentos para a primeira harmónica). As harmónicas são assim dissipadas. No modelo FLUENT, o esquema de integração das equações no tempo é apenas de primeira ordem (existem problemas de convergência com o esquema

de segunda ordem). Neste caso, verificou-se que o período da onda é bem simulado mas a altura da onda é ligeiramente subestimada (5%), contribuindo para a alteração das características da onda incidente.

- O modelo IHFOAM possibilita vários tipos de geração de ondas, embora para o caso em estudo tenha sido aplicado uma forma de geração semelhante à do FLUENT, possibilita também a aplicação de fronteiras dinâmicas e da absorção de ondas em qualquer fronteira do domínio. No presente trabalho mostra-se que com um refinamento mais cuidadoso da malha computacional, com a inclusão de uma componente tridimensional do domínio e adoptando um modelo de turbulência apropriado se poderia chegar a resultados mais favoráveis. Contudo, o erro verificado através da análise estatística mostra que o modelo possui capacidades importantes para uma cuidada representação dos fenómenos físicos envolvidos.

4 CONCLUSÕES

Nesta comunicação, descreveu-se a aplicação dos modelos numéricos, COULWAVE, FLUENT e IHFOAM, à propagação de ondas num canal com um fundo de batimetria variável, para o qual existem resultados de ensaios experimentais. O caso de teste correspondeu a uma onda regular de $T = 2.0\,\mathrm{s}$ e $H = 12\,\mathrm{cm}$. Compararam-se resultados numéricos com experimentais, nomeadamente no que se refere: elevação da superfície livre e valores de altura de onda significativa, ao longo do canal. Calcularam-se os parâmetros estatísticos (RMSE, desvio e índice de concordância) relativos aos valores da altura de onda significativa

Os resultados mostraram que os modelos simulam adequadamente a maioria das transformações das características das ondas ao longo da sua propagação, o que foi confirmado pelos valores de índice de concordância encontrados.

Em relação à altura de onda, em geral, os modelos simulam bem o andamento dos valores experimentais ao longo do canal. Os valores numéricos antes da zona de rebentação e na zona final desta são bastante semelhantes aos experimentais, em especial no caso dos modelos IHFOAM e FLUENT. As diferenças acentuam-se na zona à volta da rebentação, em que os valores numéricos são consistentemente inferiores aos resultados experimentais no caso do COULWAVE. Com efeito, com este modelo não foi possível simular a altura de rebentação, embora depois na zona de dissipação de energia, os valores numéricos voltaram a aproximar-se bastante dos experimentais, o que indica que a dissipação da onda está a ser bem simulada no modelo. Como era espectável, a análise através dos parâmetros estatísticos indica que o COULWAVE é o modelo que apresenta menor concordância com os valores experimentais relativamente aos modelos FLUENT e IHFOAM.

As diferenças entre resultados numéricos e experimentais na zona de rebentação para além de estarem relacionadas com limitações da formulação de ambos os modelos, podem também estar relacionadas com o facto das condições de entrada dos modelos serem diferentes das do batedor em modelo físico, especialmente no que se refere ao perfil de velocidades imposto na fronteira de entrada.

AGRADECIMENTOS

Os autores agradecem à FCT pelo financiamento concedido pelos projetos HIDRALERTA - PTDC/AAC-AMB/120702/2010, DITOWEC - PTDC/ECM-HID/1719/2012 e EROS - PTDC/CTE-GIX/111230/2009, e "Amigos de Boussinesq – Modelagem de ondas aplicada a portos e navios", CAPES/FCT 352/2013.

REFERÊNCIAS

[1] E Didier, JMP Conde, PRF Teixeira (2011). Numerical simulation of an oscillating water column wave energy converter with and without damping. In *Com. Meth. Marine Eng. IV – MARINE 2011*, 90 (11 p. CDRom), Lisboa, Portugal.

[2] FLUENT (2006). *FLUENT 6.3 User's Guide*, ANSYS-FLUENT.

[3] P Higuera, JL Lara, IJ Losada (2013). Realistic wave generation and active wave absorption for Navier-Stokes models: Application to OpenFOAM. *Coastal Engineering* **71**:102–118.

[4] P Lynett, T Wu, PL-F Liu (2002). Modelling wave run-up with depth-integrated equations. *Coastal Engineering* **46**:89–107.

[5] P Lynett, PL-F Liu (2004). *Modelling Wave Generation, Evolution and Interaction with Depth-Integrated, Dispersive Wave Equations*, COULWAVE Code Manual, Cornell Univ. Long Inter. Wave Modelling Package.

[6] P Lynett, PL-F Liu (2004). A two-layer approach to water wave modelling. *Proceedings of the Royal Society of London A* **460**:2637–2669.

[7] P Lynett, PL-F Liu (2004). A numerical study of submarine landslide generated waves and run-up. *Proceedings of the Royal Society of London A* **460**:2637– 2669.
[8] DRCB Neves, CJEM Fortes, L Endres, T Okamoto (2011). Modelação física da propagação e rebentação de ondas num canal. In *7as Jornadas Portuguesas de Engenharia Costeira e Portuária*, Porto, Portugal.
[9] JM Paixão Conde, E Didier, MFP Lopes, LMC Gato (2009). Nonlinear wave diffraction by a submerged horizontal circular cylinder. *International Journal of Offshore and Polar Engineering* **19**(3):198–205.

This page was intentionally left blank

Session 3

Chairman

Mário Costa | U.Lisboa

This page was intentionally left blank

Bio-oil and bio-char characterization from microalgal biomass

AF Ferreira[1], AP Soares Dias[2], CM Silva[1], M Costa[1]

[1]IDMEC, Departmento de Engenharia Mecânica, Instituto Superior Técnico, Universidade de Lisboa, Lisboa, Portugal
[2]IDMEC, Departmento de Engenharia Química, Instituto Superior Técnico, Universidade de Lisboa, Lisboa, Portugal
email: filipa.ferreira@tecnico.ulisboa.pt, apsoares@tecnico.ulisboa.pt, carla.silva@tecnico.ulisboa.pt, mcosta@tecnico.ulisboa.pt

ASTRACT: The biomass conversion into fuels is pointed out as a way to mitigate environmental issues such as global warming in parallel with an improvement of the energy security by reducing fossil fuels dependence. Microalgae are emerging to be one of the most promising long-term sustainable sources of biomass. To evaluate the bio-oil production from microalgae (*Chlorella vulgaris* and *Scenedesmus obliquus*), pyrolysis in a fixed bed reactor was carried out with and without catalyst. The working temperature (375 ºC) was chosen from the thermal degradation profile obtained by thermogravimetry and commercial carbonates of alkaline and alkaline earths elements (Li, Na, K, Mg, Mn and Sr) were used as catalysts. The microalgae, rich in proteins and sugars (*Chlorella vulgaris* and *Scenedesmus obliquus*), showed significant differences on the pyrolysis behavior with bio-oils yields in the range 26-38 wt% and 28-50 wt%, respectively. Analogous bio-char yields were observed for both microalgae and only sodium carbonate was effective to decrease the bio-char yield. The infrared spectra (FTIR) of the char materials showed features associated to carbonyl and aromatic compounds. The *Scenedesmus obliquus* derived chars showed complex spectra presumably due to the low pyrolysis temperature. The bio-oil products were also characterized by FTIR. The spectra allowed underlining different compositions in carbonyl and aromatic compounds thus indicating an effective role of the catalysts on the pyrolysis process.

KEY-WORDS: Pyrolysis; Catalyst; Microalgae; Characterization.

1 INTRODUCTION

Biomass is one of future´s key renewable and alternative sources of energy, being the most important source for three quarters of the world's population living in developing countries [1]. Several studies identified microalgae as a promising biomass source for energy production [2-4] Microalgae contain high levels of oils, carbohydrates and proteins, which make them versatile raw materials for renewable fuels production in parallel with valuable chemicals and food. Microalgae can be used to produce energy even after extracting oils and carbohydrates.

Pyrolysis is a promising thermochemical conversion technique for energy recovery, waste management, and converting biomass into useful energy products, which has attracted considerable attention during the past decade [5]. In pyrolysis processes valuable products such as bio-char and bio-oil can be obtained. Bio-char is used as carbon source for producing different carbon based materials, and bio-oil as chemical feedstock for valuable chemical products [6]. Major research on characterization of pyrolysis products is focused on lignocellulosic biomass, such as woody and herbaceous plants because it is renewable and abundant. Corn cobs and stover [7,8], switchgrass [8,9], palm oil wastes [10] have been also used. However, microalgae are pointed out as a promising feedstock for pyrolysis processes. The thermogravimetric analysis is the usual technique to first characterize the microalgae behavior in pyrolysis atmosphere. Miao *et al.* [11,12] studied the fast pyrolysis of cultivated microalgae specie. They obtained 17.5 wt% and 23.7 wt% of oil from cultivated microalgae (*C. protothecoides* and *M. aeruginosa*), where the yield of bio-oil was 57.9% from heterotrophic *Chlorella protothecoides*. The physical properties of bio-oils from microalgae were more suitable for fuel use than bio-oils from lignocellulosic materials. Pan *et al.* [13] studied the influence of the temperature and catalyst on the slow pyrolysis of *Nannochloropsis* sp. Bio-oil yields of 31.1 wt% and 19.7 wt% were achieved at 400 ºC with and without HZSM-5, respectively. The results indicated that the bio-oil from catalytic pyrolysis had higher heating-value (32.7 MJ kg^{-1}) and higher aromatic hydrocarbon content than those obtained from thermal pyrolysis. Gong *et al.* [14] examined the yields and characteristics of bio-oil, bio-char, and noncondensable gas from the pyrolysis of *C. vulgaris* and *D. Salin*a at different temperatures (from 300

ºC to 700 ºC) and reported bio-oil yields of 49.2 wt% and 55.4 wt% at 500 °C, respectively. Yanick *et al.* [15] studied the fast pyrolysis of two lignocellulosic materials (safflower oil cake and grape seed) and three seaweed species (*Laminaria digitata*, *Fucus serratus* and mix macroalgae species) at 500 ºC. The bio-oil yields from seaweeds varied between 32 wt% and 37 wt%, whereas yields from lignocellulosic biomass were in the range of 36-60 wt%. Finally, the yields of char were in the range of 29-36 wt% for seaweeds and 23–26% for lignocellulosic biomass.

In this work the slow pyrolysis of two microalgae, *Chlorella vulgaris* and *Scenedesmus obliquus*, were performed to study the influence of the catalysts on the yields and characteristics of the produced bio-oil and bio-char.

2 METHODOLOGY

The *Chlorella vulgaris* (*C. vulgaris*) and *Scenedesmus obliquus* (*Sc. obliquus*) microalgae used in this study were grown and obtained by A4F-Algae for Future**,** Algae Technology Platform, AlgaFarm, Pataias (Portugal). A4F develops microalgae production units in high-emitting industries for CO_2 mitigation. These microalgae production units were composed by closed photobioreactors and gently spray dried and subsequently stored at room temperature. The proximate analyses were carried out according to the technical specifications UNEEN, UNE-EN 14775:2010, UNE-EN 15148:2010 and UNE-EN 1474-2 for ash, volatile matter and moisture determination, respectively. The ultimate analysis, ash analysis and heating values were also determined. Table 1 shows the chemical characteristics of the raw microalgae. The *C. vulgaris* and *S. obliquus* were grown in fresh water.

Table 1. Chemical characteristics of the raw microalgae.

Parameter		*C. vulgaris*	*Sc. obliquus*
Proximate analysis (wt%, as received)	Volatiles	72.7	76.8
	Fixed carbon	11.4	11.0
	Moisture	4.9	4.4
	Ash	11.0	7.8
Ultimate analysis (wt%, dry ash free)	Carbon	47.1	50.3
	Hydrogen	6.78	7.29
	Nitrogen	10.27	8.26
	Sulphur	0.72	0.62
	Oxygen	35.13	33.53
Heating value (MJ/kg)	Low	16.5	18.2
	High	17.9	19.7

2.1 Thermogravimetric analysis

The pyrolysis temperature was selected by a thermal analysis of several microalgae by Netzsch STA 409 PC thermogravimetry (TG-DTA) simulating pyrolysis conditions. The samples were heated from 30 ºC to 1100 ºC at a heating rate of 25 ºC/min in a nitrogen (99.996%) atmosphere.

Figure 1 shows an example of the behavior of the microalgal and pine bark under those conditions. The main mass change was verified between 250 ºC and 550 ºC. Pyrolysis was thus performed at 375 ºC.

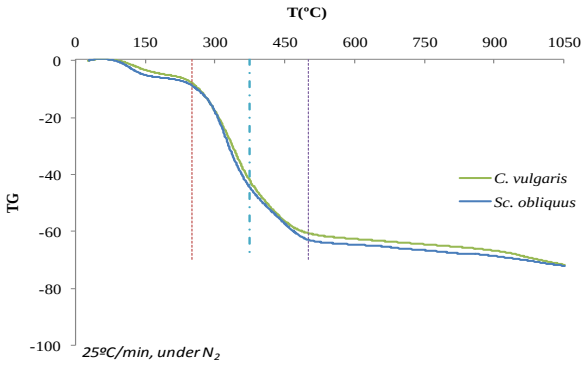

Figure 1: Example of microalgae thermal analysis.

2.2 Pyrolysis process

The pyrolysis experiments were performed in a quartz fixed bed reactor in a nitrogen atmosphere. The used reactor had an internal diameter of 16 mm and a length of 150 mm. The quartz reactor was filled with carborundum. The reactor was externally heated using a circular electric furnace equipped with a PID controlled to ensure the complete pyrolysis. Figure 2 shows the pyrolysis apparatus used.

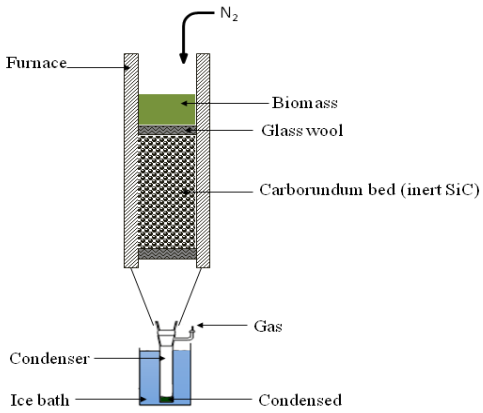

Figure 2: Pyrolysis apparatus.

Each pyrolysis test was started by placing a certain amount of raw microalgae (about 5 g) into the quartz reactor. The reactor was placed in the circular furnace pre-heated to 375 ºC. Nitrogen with purity of 99.99% was used as the carrier gas and its flow (83 mL/min) was monitored using a mass flow controller. A condenser coupled to the reactor was used immersed in an ice-water bath to obtain the liquid product. The uncondensed gas were not collected. Pyrolysis with and without catalysts was performed. Carbonates of alkaline and alkaline earth elements, (Li_2CO_3, Na_2CO_3, K_2CO_3, $MgCO_3$, $MnCO_3$ and $SrCO_3$) were used as catalysts. For each experiment, 5% ($w_{cat}/w_{biomass}$) of catalyst was used. The pyrolysis liquid amount was determined by the mass difference of the condensers before and after a pyrolysis test. The bio-oil was recovered by washing the reactor with acetone followed by rotating evaporation of acetone under a reduced pressure. The used acetone could be recycled for further tests. The weighted mass of char and bio-oil allowed calculating the yield of such products. The gas yield was computed from a mass balance.

2.3 Characterization of the bio-oil and bio-char

The bio-oil and bio-char materials obtained from the microalgae pyrolysis were characterized by infrared spectroscopy using a reflectance acquisition mode (HATR-FTIR). The reflectance bands were used to identify the main functional groups present in both products. Table 2 shows the FTIR bands and functional groups attribution.

Table 2: FTIR bands and functional groups attribution [16].

ν (cm)$^{-1}$	**Functional groups**
55	O—H stretching vibration
2935	C—H stretching vibration
2075	C≡C stretching vibration
1735–1705	Aromatic carbonyl/carboxyl C=O stretching
1605	C=C stretching vibration
1515	Aromatic C=C ring stretching
1445	Aliphatic CH_2 deformation
1370–1385	Aliphatic CH_3 deformation
1225–1270	Aromatic C—H stretching
1110	Ketone or ester bonding
1050	Aliphatic ether C—O and alcohol C—O stretching
840–885	Aromatic C—H out of plane deformation
760	Adjacent aromatic C—H deformation
615	Phenol O—H out of plane deformation

3 RESULTS AND DISCUSSION

The raw microalgae were characterized by HATR-FTIR. Figure 3 shows the HATR-FTIR spectra of raw microalgae. The spectra identifies, mainly, proteins (3400–3200, 1655 and 1545 cm^{-1}) and sugars (1200–900 cm^{-1}) for both biomass [17]. The *Sc. obliquus* is a protein rich microalgal.

As reported in the literature the catalysed pyrolysis of microalgae produces combustible gas (H_2, CH_4, CO, and CO_2) and bio-oil in parallel with bio-char [18]. Figure 4 shows a summary of the main data on the catalysed and unanalysed pyrolysis behaviours of biomass. Taking into account the bio-oil and bio-char yields the accomplished pyrolysis can be classified as intermediate pyrolysis [19]. The main differences observed for the two microalgae can be associated to their compositions: one with higher amount of sugar and the other of proteins.

For *C. vulgaris* all the catalysts improved the gas yield but only the sodium carbonate was effective on the bio-char yield reduction. Babich *et al*. [20] also reported the *C. vulgaris* pyrolysis using Na_2CO_3 as catalyst. They observed a more pronounced effectiveness of the catalyst on the gasification process eventually due to the fact that they used a liquid solution to disperse the carbonate salt on the biomass.

The *Sc. obliquus* presents a slight different pyrolysis behaviour with an improvement in gasification only reached using Mg and Sr salts.

The bio-oil yields obtained in the absence of catalyst for both microalgae are in accordance with previously published data. In fact, Demirbas [18] reported bio-oil yields of 25-40 wt% for pyrolysis temperatures in the range 350-400 ºC. Demirbas underlined a strong dependence of the bio-oil yield on the pyrolysis temperature.

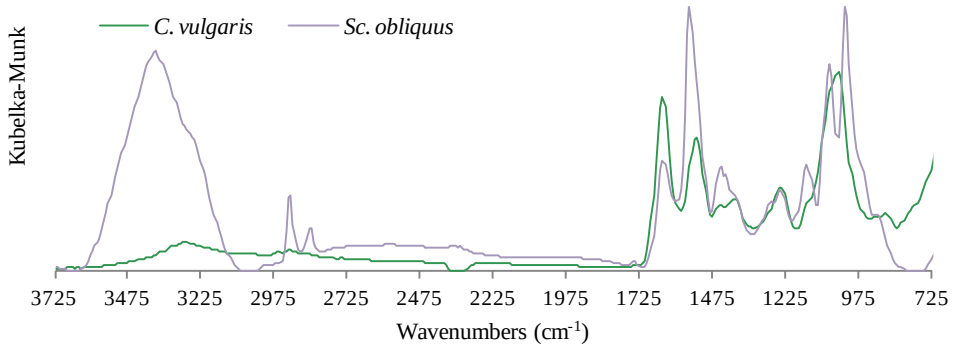

Figure 3: HATR-FTIR spectra of raw microalgae.

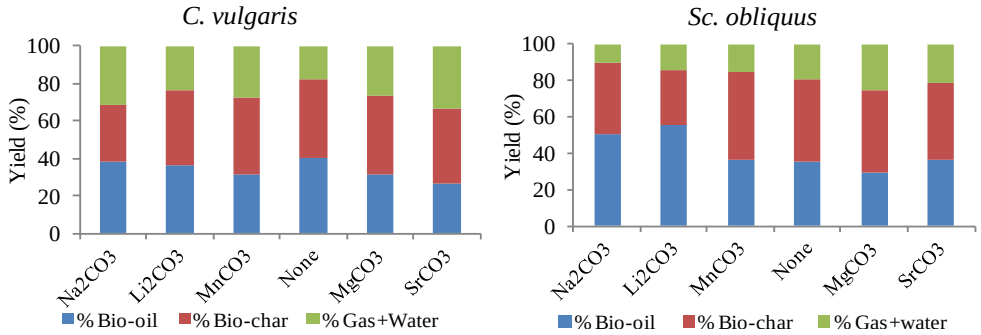

Figure 4: Pyrolysis products yields (%) versus catalysts (375 ºC; 30 min; N_2 83 mL/min).

In order to analyse the effect of the carbonate catalyst on the bio-oil characteristics, the dark and viscous liquids, dried in a rotavapor during 1 h at 120 ºC and a vacuum pressure of −630 mm Hg, were characterized by HATR-FTIR. Figure 5 shows the spectra of bio-oils. The FTIR data for bio-oils obtained from the two microalgae showed marked differences between them. The microalgal composition had a significant role on the bio-oil characteristics.

Reflectance bands are attributed (Table 2) to carboxyl and carbonyl groups (1735–1705 cm^{-1}) from acids and esters (CH_3- groups 2935 cm^{-1}) and features belonging to aromatics (1225–1270 cm^{-1}; 840–845 cm^{-1}) are common to all the analysed samples.

For the *C. vulgaris* the catalysts improved the alkyl groups of the obtained bio-oils eventually having a positive effect on the bio-oil acidity. Additionally, the Na and Li catalysts increased the amount of ketones (110 cm^{-1}) and, ethers and alcohols (1050 cm^{-1}). Adjacent aromatic groups also increased using catalysed pyrolysis.

The bio-oils obtained from *Sc. obliquus* should be more acidic since the features of alkyl groups in the spectra are weak and thus the bands in the range 1735–1705 cm^{-1} belong to carboxyl acids. The Mg and Sr catalysts prompted the aromatization of the *Sc. obliquus* bio-oils since there is an intensification of the band at 760 cm^{-1}

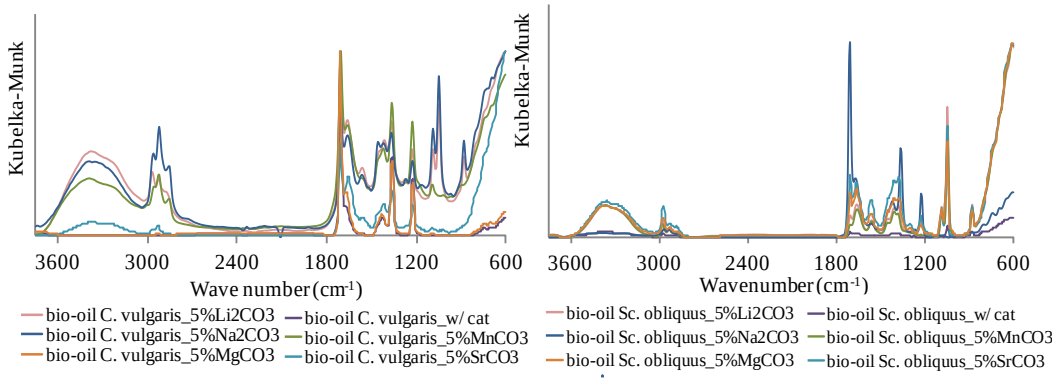

Figure 5: HATR-FTIR spectra of bio-oils.

The bio-char materials were also characterised by FTIR. Figure 6 shows the spectra of bio-char materials obtained for both microalgae.

The *C. vulgaris* derived bio-chars mainly presented reflectance bands associated to C=C aromatic (1590 cm^{-1}), C-O aromatic (1130–1100 cm^{-1}) and C-O (1040 cm^{-1}) from aliphatic ethers and alcohols. The bio-char from *Sc. obliquus* presented complex spectra with the main features associated to aromatic C-O. Such characteristics seem to result from insufficient pyrolysis temperature.

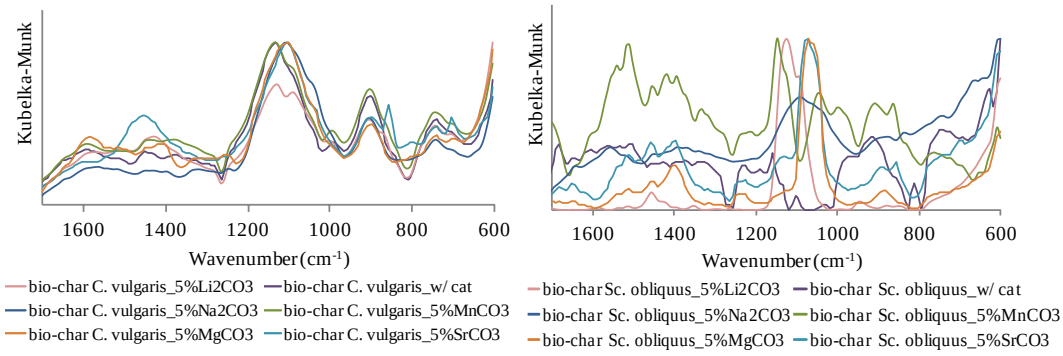

Figure 6: HATR-FTIR spectra of bio-chars.

4 CONCLUSIONS

In order to evaluate the bio-oil production from microalgae (*Chlorella vulgaris* and *Scenedesmus obliquus*), pyrolysis in a fixed bed reactor was performed with and without catalyst. The working temperature was chosen from the thermal degradation profile obtained by thermogravimetry and commercial carbonates of alkaline and alkaline earths elements (Li, Na, K, Mg, Mn and Sr) were used as catalysts.

The yield obtained of bio-oil and bio-char were respectively 26–38 wt% and 31–42 wt% for *C. vulgaris* and 28–50 wt% and 30–48 wt% for *Sc. obliquus*. The yield values indicate that the slow pyrolysis at low temperature of 375 ºC produced a higher amount of bio-char with and without use of catalysts. The use of the carbonate catalysts increased the gas and decreased the bio-oil productions for both microalgae used. Nevertheless, the alkaline salt catalysts improved the quality of the obtained bio-oil with a net gain on the alkyl groups.

FTIR measurements indicate that the microalgae studied in this work were composed mainly by carbohydrates and proteins than oil. In future research, other analytical techniques will be used to further characterize the products of pyrolysis, namely, gas chromatography with mass spectrometry (GC-MS) for the identification and quantification of compounds from bio-oil, and XRD technique, scanning electron microscope (SEM) and thermogravimetric analysis (TGA) for bio-char characterization.

ACKNOWLEDGMENTS

This work was supported by Fundação para a Ciência e a Tecnologia (FCT), through IDMEC, under LAETA Pest-OE/EME/LA0022. Ana F. Ferreira is pleased to acknowledge the FCT for the postdoc financial support SFRH/BPD/95098/2013.

REFERENCES

[1] Star−COLIBRI (2011). *Joint European Biorefinery Vision for 2030*.

[2] A Demirbas, M Fatih Demirbas (2011). Importance of algae oil as a source of biodiesel. *Energy Conversion and Management* **52**:163–170.

[3] AF Ferreira, J Ortigueira, L Alves, L Gouveia, P Moura, C Silva (2013). Biohydrogen production from microalgal biomass: Energy requirement, CO2 emissions and scale-up scenarios. *Bioresource Technology* **144**:156–164.

[4] HH Khoo, PN Sharratt, P Das, RK Balasubramanian, PK Naraharisetti, S Shaik (2011). Life cycle energy and CO2 analysis of microalgae-to-biodiesel: preliminary results and comparisons. *Bioresource Technology* **102**:5800–5807.

[5] A Demirbas (2001). Biomass resource facilities and biomass conversion processing for fuels and chemicals. *Energy Conversion and Management* **42**:1357–1378.

[6] D Özçimen (2013). *An Approach to the Characterization of Biochar and Bio-Oil*, Yildiz Technical University.

[7] CA Mullen, AA Boateng, NM Goldberg, IM Lima, DA Laird, KB Hicks (2010). Bio-oil and bio-char production from corn cobs and stover by fast pyrolysis. *Biomass & Bioenergy* **34**:67–74.

[8] CE Brewer, K Schmidt-Rohr, JA Satrio, RC Brown (2009). Characterization of biochar from fast pyrolysis and gasification systems. *Environmental Progress & Sustainable Energy* **28**:386–396.

[9] T Imam, S Capareda (2012). Characterization of bio-oil, syn-gas and bio-char from switchgrass pyrolysis at various temperatures. *Journal of Analytical and Applied Pyrolysis* **93**:170–177.

[10] F Abnisa, A Arami-Niya, WMA Daud, JN Sahu (2013). Characterization of bio-oil and bio-char from pyrolysis of palm oil wastes. *BioEnergy Research* **6**(2):830–840.

[11] X Miao, Q Wu, C Yang (2004). Fast pyrolysis of microalgae to produce renewable fuels. *Journal of Analytical and Applied Pyrolysis* **71**:855–863.

[12] X Miao, Q Wu (2006). Biodiesel production from heterotrophic microalgal oil. *Bioresource Technology* **97**:841–846.

[13] P Pan, C Hu, W Yang, Y Li, L Dong, L Zhu, D Tong, R Qing, Y Fan (2010). The direct pyrolysis and catalytic pyrolysis of Nannochloropsis sp. residue for renewable bio-oils. *Bioresource Technology* **101**(12):4593–4599.

[14] X Gong, B Zhang, Y Zhang, Y Huang, M Xu (2013). Investigation on pyrolysis of low lipid microalgae Chlorella vulgaris and Dunaliella salina. *Energy & Fuels* **28**:95–103.

[15] J Yanik, R Stahl, N Troeger, A Sinag (2013). Pyrolysis of algal biomass. *Journal of Analytical and Applied Pyrolysis* **103**:134–141.

[16] R Yin, R Liu, Y Mei, W Fei, X Sun. Characterization of bio-oil and bio-char obtained from sweet sorghum bagasse fast pyrolysis with fractional condensers. *Fuel* **112**:96–104.

[17] JJ Mayers, KJ Flynn, RJ Shields (2013). Rapid determination of bulk microalgal biochemical composition by Fourier-Transform Infrared spectroscopy. *Bioresource Technology* **148**:215–220.

[18] MF Demirbas (2011). Biofuels from algae for sustainable development. *Applied Energy* **88**:3473–3480.

[19] AV Bridgwater (2012). Review of fast pyrolysis of biomass and product upgrading. *Biomass & Bioenergy* **38**:68–94.

[20] IV Babich, M van der Hulst, L Lefferts, JA Moulijn, P O'Connor, K Seshan K (2011). Catalytic pyrolysis of microalgae to high-quality liquid bio-fuels. *Biomass & Bioenergy* **35**:3199–3207.

V Conferência Nacional de Mecânica dos Fluidos, Termodinâmica e Energia
MEFTE 2014, 11–12 Setembro 2014, Porto, Portugal
APMTAC, 2014

Effect of the H_2O concentration in the oxidizer on the performance of a combustor operating under flameless conditions

B Bernardes[1], M Costa[1], Y Levy[2]

[1]IDMEC, Mechanical Engineering Department, Instituto Superior Técnico, Universidade de Lisboa, Portugal
[2]Technion – Israel Institute of Technology, Haifa, Israel
email: bruno.bernardes@ist.utl.pt, mcosta@ist.utl.pt, levyy.technion@gmail.com

ABSTRACT: This study examines the effect of the H_2O concentration present in the oxidizer on the performance of a combustor operating under flameless conditions. The combustion chamber presents low NO_x emissions and it was developed for gas turbine applications. In the present study, the major gaseous pollutant emissions were measured using gas analysers for various operating conditions of the combustor. The results showed that for low values of the excess air, the greater the H_2O concentration in the oxidizer, the greater the CO emissions. For high values of excess air, however, the effect of H_2O concentration in the oxidizer on the CO emissions becomes negligible. For all conditions studied, NO_x emissions were always below 10 ppm @ 15% O_2 and combustion efficiencies greater than 99.8%. Overall, it was observed that the greater the concentrations of H_2O in the oxidizer the lower the NO_x emissions.

KEY-WORDS: Gas turbine; Flameless oxidation; Pollutant emissions.

1 INTRODUCTION

Flameless oxidation is a combustion regime first observed by Wunning and Wunning [1]. This mode of combustion was obtained by increasing the recirculation ratio between the inlet air and combustion products. The mixing provided by the recirculation creates a distributed reaction zone with reduced low oxygen concentration, a uniform temperature distribution, lower turbulence level and no flame luminescence. Since the reaction zone has a uniform temperature distribution, local temperature maxima are minimised resulting in sharp reduction of NO formation. This technology has received various names, such as high temperature air combustion (HiTAC) [2], flameless oxidation, moderate or intensive low oxygen dilution (MILD) combustion, and colourless distributed combustion (CDC).

Previous related studies include those reported in references [3-14]. These studies cover a wide range of aspects related to flameless combustion and helped to improve the understanding of the underlying physical and chemical processes associated to this combustion regime. An aspect that has received little attention from the combustion community is related to the impact of the presence of water vapour in the oxidizer on the establishment of the flameless regime. In this context, this study focus on the effect of the H_2O concentration in the oxidizer on the performance of a combustor operating under flameless combustion conditions

2 EXPERIMENTAL APPARATUS AND PROCEDURE

Figure 1 shows a perspective view of the 60º sector of the combustion chamber used in this study, its cross section as well as its major dimensions [12-14]. The fuel injection system is formed by 15 circular holes with 1 mm of diameter and a spacing of 2 mm. The fuel (natural gas) was injected through these holes into the combustion chamber at an angle of 45º with respect to the *r* axis, as schematically depicted in Figure 1. As shown in Figure 1, a mixture (oxidant) of O_2, N_2 and H_2O is admitted into the combustion chamber through two staggered series of 14 circular nozzles (84 in a complete 360º combustor) with 4 mm in diameter. These oxidant inlets were positioned at angles of 120º and 210º with respect to the *r* axis in the right and left sections, respectively. The secondary air is admitted into the combustion chamber through a series of 19 circular holes of 1 mm in diameter and at spacing of 2 mm. The secondary air inlets are oriented at an angle of 20º with respect to *z* axis. In this study, the air flow rates supplied through each of the staggered series of 14 holes were similar. Figure 2 shows the cross-sectional schematic and key dimensions of the combustion chamber.

In order to create the desired oxidant composition, a computer controlled system (CEM – Controlled Evaporation and Mixing) was used to introduce water vapour into the system. The water is evaporated

within a nitrogen stream with consequent air addition in order to create the required mixture composition (oxidant) with O_2, N_2 and H_2O. The CEM system includes two flow controllers and an evaporator capable to introduce up to 1200 g/h of water in the nitrogen flow.

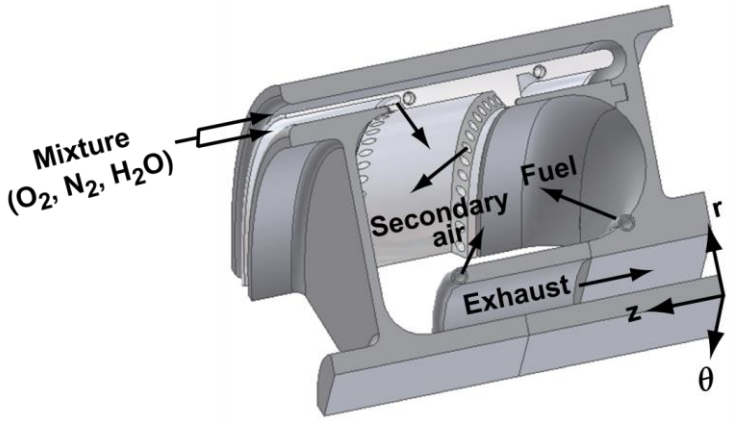

Figure 1: Perspective view of 60º sector of the combustion chamber.

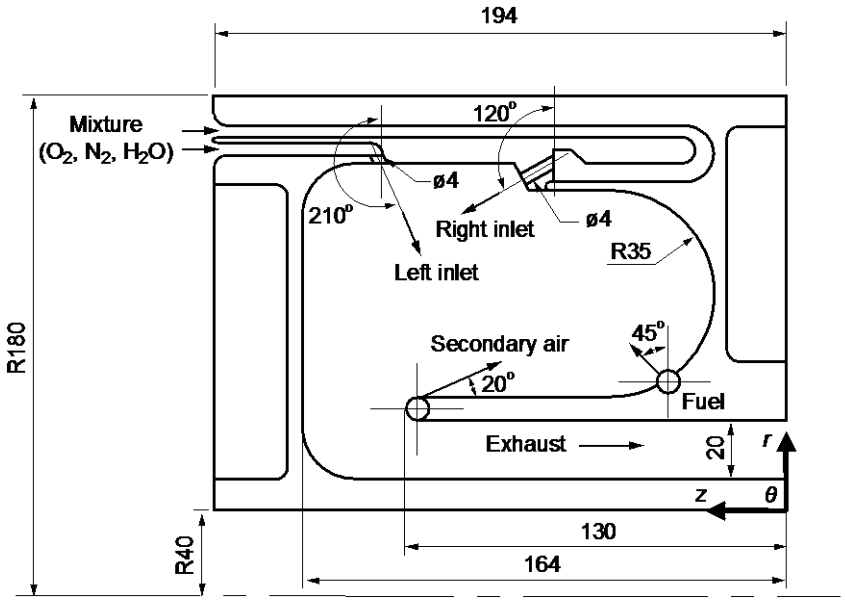

Figure 2: Cross-sectional schematic and key dimensions of the combustion chamber.

The experimental set-up included a gas analysis system used for the measurement of the (mean) gas species concentration at the exhaust of the combustor. The gaseous species measured in the flue-gas were O_2, CO, CO_2, unburnt hydrocarbons (UHC) and NO_x. The gas sample was collected using a water-cooled stainless steel probe installed in the exhaust of the combustor at approximately 1 m downstream from the combustion chamber exit, in a location where the gas composition was nearly uniform. The wet gas sample was drawn through the probe with the aid of an oil-free diaphragm pump. A condenser removed the main particulate burden and condensate. A filter and a drier removed any residual moisture and particles, so that a constant supply of clean dry combustion gases was delivered to each measurement instrument through a manifold, to obtain species concentrations on a dry basis. The analytical instrumentation included a magnetic pressure analyser for O_2 measurements, non-dispersive infrared gas analysers for CO_2 and CO measurements, a flame ionization detector for UHC measurements, and a chemiluminescent analysis for the NO_x measurements. The maximum drift in the calibration was within ±2% of the full scale. At the combustor exit, where the gas composition was nearly uniform, probe effects were negligible and errors arose mainly from quenching of chemical reactions and sample handling. Samples were quenched near the probe tip to about 150 ºC, which was found to be adequate.

3 WORKING PRINCIPLE OF THE PRESENT COMBUSTOR

The working principle of the present combustor is based on the establishment of a large recirculation zone within the combustion chamber, where part of the inlet air mixes with the combustion products. Figure 3a illustrates conceptually the development of the recirculation zone inside the combustor. Figure 3b represents schematically the recirculation zone. The oxidant enters at station 1 and is split into two streams with similar flow rates. One portion is entrained and its oxygen concentration is diluted by the recirculated combustion products and directed toward point 2. This mixed stream continuous to move in a toroidal pattern until it reaches point 3. At that point fuel is injected and mixed. The combustible mixture ignites at location downstream of station 3, after a certain ignition delay time. Combustion occurs between points 3 and 4, and thereafter the combustion products are split, partially recirculating with fresh air and partially exiting the combustor while diluting with fresh air (point 5). The two streams mix and exit the combustor at point 6, at the required combustor's exit temperature, typically determined by the performance of the turbine located immediately downstream [15].

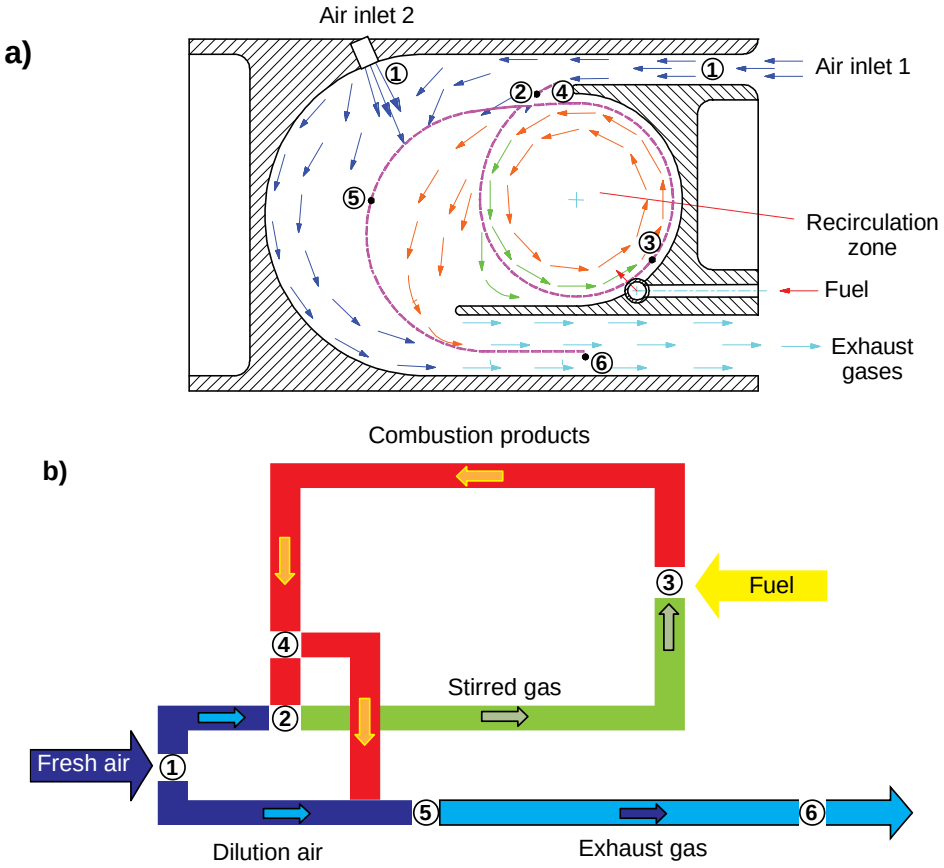

Figure 3: Schematic of the internal aerodynamics of the combustor: a) section of the annular combustor and b) main flow [15].

4 RESULTS AND DISCUSSION

The goal of the present experimental investigation was to evaluate the effects of the water vapour addition to the incoming air (and by that diluting the oxygen content of the reactants) while operating in the flameless oxidation regime. This work is associated with the FP7 AHEAD program (www.ahead-euproject.eu), where a new jet engine configuration is discussed and analysed, having a sequential combustion system with hydrogen combustion taking place in the primary (high pressure) combustion and hydrocarbon fuel combustion in the secondary combustor, located between the high pressure and low pressure turbines. Consequently, the secondary combustor is fed with vitiated air that exits from the hydrogen fuelled combustor; hence, the relevance for the water vapour addition in the oxidizer. The tests were made while varying the following parameters: excess air from 1.2 to 1.8, oxygen volumetric percentage from 21% to 14% and water vapour volumetric percentage from 0 to 8%. Nitrogen was used

to balance the composition. In all tests, the fuel thermal capacity and secondary air flow rate were kept constant at 4 kW and 40 L/min, respectively.

Figure 4 shows the UHC, CO and NO_x emissions as a function of the excess air coefficient (λ) for various water vapour concentrations in the oxidizer. Note that the UHC are marginal regardless of the combustor operating condition. It is seen that the evolution of the CO emissions with the excess air is similar for all conditions, with relatively high CO emissions when λ is close stoichiometry and relatively low and constant values when λ > 1.4. The experiments were performed in a flameless oxidation combustor, which was designed to operate with high excess air levels and large recirculation ratios; therefore, when it operates with relatively low values of λ, for example λ = 1.2, it is possible to establish in the recirculation zone conditions with significantly diluted oxygen content that may inhibit the CO oxidation. Similar results were obtained by other authors [5-9].

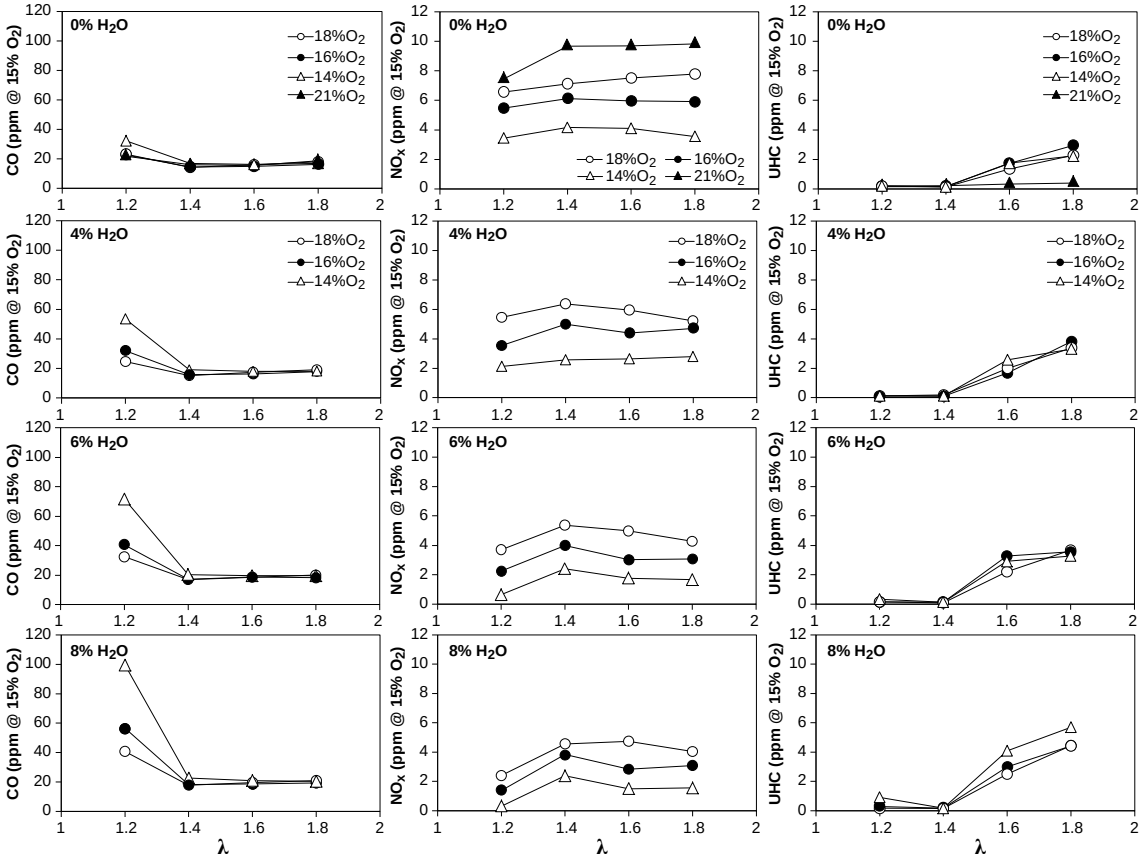

Figure 4: UHC, CO and NO_x emissions as a function of λ for various water vapour concentrations in the oxidizer.

Figure 4 also shows that, for a given water vapour concentration in the oxidizer and low values of λ, the lower the oxygen concentration in the oxidizer, the higher the CO emissions. This behaviour was expected for the same reason given above. For values of λ higher than 1.4 the oxygen concentration in the oxidizer has no impact on the CO emissions. This indicates that for these cases the environment inside the combustor has enough oxygen to oxidize almost all CO.

Figure 4 also reveals that, for low values of λ, the CO emissions increase as the water vapour concentration in the oxidizer increases. This effect could not be explained just by the variation of the temperature in the combustor. The adiabatic temperature is sensitive to the excess air but it is seen that the CO emissions remain almost independent of the water vapour concentration for values of λ greater than 1.4. This indicates that the temperature for these relatively high excess air levels does not play a decisive role in the establishment of the CO emissions. It can be observed that the CO emissions are particularly sensible in conditions of low O_2, mainly when the water vapour concentration increases. This suggests that the water vapour concentration must be chemically active to explain the observed behaviour.

Richard et al. [16] examined the chemical and physical effects of water vapor addition on diffusion flames. The authors considered the following reactions

$$H + O \rightarrow OH \quad (1)$$

$$H_2O \rightarrow H + OH \quad (2)$$

$$H_2O + O \rightarrow 2OH \quad (3)$$

$$CO + OH \rightarrow CO_2 + H \quad (4)$$

and concluded that the addition of water vapour to the oxidizer reduces the CO emissions due to the increase in the concentration of hydroxyl radicals (OH) in the reaction zone through reactions (2) and (3), which in turn favours the CO oxidation through reaction (4).

In the present study, the observed increase in the CO emissions with the water addition at low λ values may be interpreted as follows. When the present combustor operates under low excess air levels (λ = 1.2), the lack of oxygen in the reaction zone could inhibit the production of OH via reactions (1) and (3), with the CO oxidation (reaction 4) suffering accordingly.

In regard to the NO_x emissions, Figure 4 reveals that, for a given water vapour and oxygen concentration, the NO_x emissions increase in the range of $1.2 < \lambda < 1.4$ and then stabilize, which is in agreement with the results reported by other authors [5, 6, 8]. For a given water vapour concentration, Figure 4 also shows that the higher the oxygen concentration in the oxidizer, the higher the NO_x emissions, which is a rather expected result owing to the NO formation dependence on the oxygen concentration. For a given oxygen concentration, it is seen that an increase in the water vapour concentration in the oxidizer reduces the NO_x emissions. As discussed above, the temperature does not change considerably with the water vapour concentration in the oxidizer, so that the NO_x reduction is most probably due to the decrease in the molecular nitrogen concentration in the oxidizer as water vapour concentration increases.

Figure 5 shows the NO_x emissions as a function of the combustion efficiency for all conditions studied here. The graph includes data obtained previously from the same combustor operating under ultra-lean combustion conditions [14]. The combustion efficiency was calculated as

$$\eta = 1 - \frac{\mathrm{LHV_{CO}}}{\mathrm{LHV_{fuel}}} * \mathrm{EI_{CO}} - \frac{\mathrm{LHV_{CH_4}}}{\mathrm{LHV_{fuel}}} * \mathrm{EI_{UHC}} \quad (5)$$

where LHV is the low heating value and EI is the emission index. Overall, it is seen that the operation of the present combustor under flameless combustion conditions presents a very promising prospect as a future combustion method.

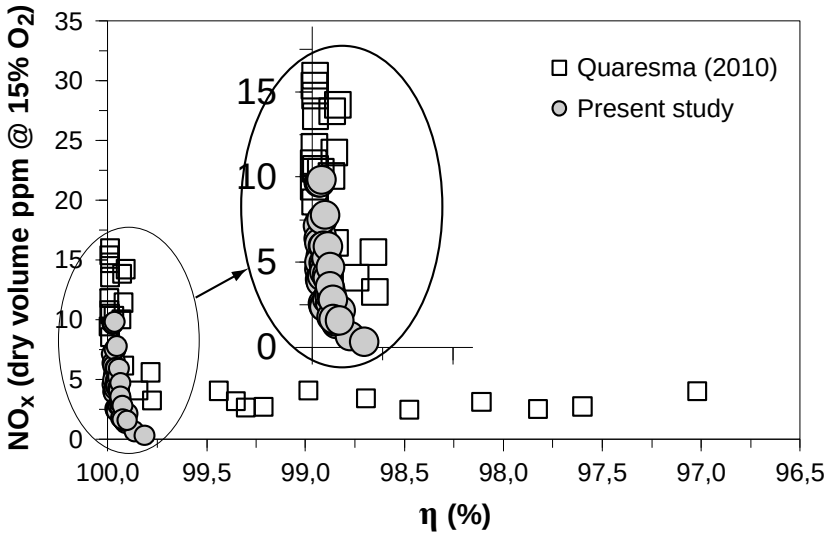

Figure 5: NO_x emissions as a function of the combustion efficiency.

5 CONCLUSIONS

This work concentrated on the effect of the H_2O concentration present in the oxidizer on the performance of a combustor operating under flameless conditions. The study showed that the combustor can operate under flameless oxidation conditions for a wide range of H_2O concentrations in the oxidizer. Despite the increase in the CO emissions with H_2O concentration in the oxidizer for lower values of excess air, the

combustor still yields very low CO emissions. The NO_x emissions were always below 10 ppm @ 15% O_2 and the combustion efficiency near 100% regardless of the combustor operating condition. This results show the positive prospects for the application of the flameless combustion regime to jet engines and gas turbines.

ACKNOWLEDGMENTS

Financial support for this work was provided by the European Commission through the project "Advanced Hybrid Engines for Aircraft Development – AHEAD" under the Seventh Framework Programme (Grant Agreement # 284636).

REFERENCES

[1] JA Wunning, JG Wunning (1997). Flameless oxidation to reduce thermal NO-formation. *Progress in Energy and Combustion Science* **23**:81–94.
[2] M Katsuki, T Hasegawa (1998). The science and technology of combustion in highly preheated air. *Proceedings of the Combustion. Institute* **27**:3135–3146.
[3] M Flamme (2004). New combustion system for gas turbine (NGT). *Applied Thermal Engineering* **24**:1551–1559.
[4] GG Szegö, BG Dally, GJ Nathan (2008). Scaling of NOx emissions from a laboratory-scale mild combustion furnace. *Combustion and Flame* **154**:281–295.
[5] GG Szegö, BG Dally, GJ Nathan (2009). Operational characteristics of a parallel jet MILD combustion burner system. *Combustion and Flame* **156**:429–438.
[6] VK Arghode, AK Gupta (2010). Effect of flow field for colorless distributed (CDC) for gas turbine combustion. *Applied Energy* **87**:1631–1640.
[7] VK Arghode, AK Gupta (2011). Development of high intensity CDC combustor for gas turbine engines. *Applied Energy* **88**:963–973.
[8] A Veríssimo, AMA Rocha, M Costa (2011). Operational, combustion, and emission characteristics of a small-scale combustor. *Energy and Fuels* **25**:2469–2480.
[9] VK Arghode, AK Gupta, KM Bryden (2012). High intensity colorless distributed combustion for ultra low emissions and enhanced performance. *Applied Energy* **92**:822–830.
[10] A Veríssimo, AMA Rocha, M Costa (2013). Experimental study on the influence of the thermal input on the reaction zone under flameless oxidation conditions. *Fuel Processing Technology* **106**:423–428.
[11] M Sánchez, F Cadavid, A Amell (2013). Experimental evaluation of a 20 kW oxygen enhanced self-regenerative burner operated in flameless combustion mode. *Applied Energy* **111**:240–246.
[12] M Melo, J Sousa, M Costa, Y Levy (2009). Experimental investigation of a novel combustor model for gas turbine. *Journal of Propulsion and Power* **25**:609–617.
[13] M Melo, J Sousa, M Costa, Y Levy (2011). Flow and combustion characteristics of a low NO_x combustor model for gas turbines. *Journal of Propulsion and Power* **27**:1212–1217.
[14] P Quaresma, M Costa, Y Levy (2010). Effect of the fuel composition on the performance of a low NO_x combustor model for gas turbines. In *Proceedings of the SPEIC10: Towards Sustainable Combustion*, Tenerife, Spain, 16–18 June.
[15] Y Levy, V Sherbaum, P Arfi (2004). Basic thermodynamics of FLOXCOM, the low-NOx gas turbine adiabatic combustor. *Applied Thermal Engineering* **24**:1593–1605.
[16] J Richard, J Garo, J Souil, J Vantelon, V Knorre (2003). Chemical and physical effects of water vapor addition on diffusion flames. *Fire Safety* **38**:569–587.

Redução da concentração de alcatrão no gás de síntese por combustão em meio poroso

T Carvalho[1], M Costa[1], C Casaca[1,2], RC Catapan[3], AAM Oliveira[4]

[1]IDMEC, Departamento de Engenharia Mecânica, Instituto Superior Técnico, Universidade de Lisboa, Lisboa, Portugal
[2]Instituto Superior de Engenharia de Lisboa, Instituto Politécnico de Lisboa, Lisboa, Portugal
[3]Centro da Engenharia da Mobilidade, Universidade Federal de Santa Catarina, Joinville, Brazil
[4]Departmento de Engenharia Mecânica, Universidade Federal de Santa Catarina, Florianópolis, Brazil
email: tiagobcarvalho@ist.utl.pt, mcosta@ist.utl.pt, ccasaca@dem.isel.ipl.pt, catapan@labcet.ufsc.br, amir.oliveira@gmail.com

RESUMO: O objectivo principal deste artigo é avaliar a destruição do alcatrão presente no gás de síntese a partir de gaseificação de biomassa por combustão em meios porosos. Uma mistura de gás foi utilizada para emular o gás de síntese, que inclui tolueno como um substituto de alcatrão. Inicialmente, o CHEMKIN foi utilizado para avaliar o potencial da solução proposta. As simulações revelaram a destruição completa do substituto de alcatrão para uma ampla gama de condições de funcionamento. Subsequentemente, os ensaios experimentais foram realizados num queimador poroso alimentado com metano puro e gás de síntese. Nestes ensaios, a concentração de gás de síntese em tolueno variou entre 50 e 200 g/Nm^3. De acordo com as previsões do CHEMKIN, os resultados revelaram que o tolueno foi quase completamente destruído para todas as condições testadas e que o processo não afectou o desempenho do queimador poroso relativamente às emissões de CO e NO_x.

PALAVRAS-CHAVE: Experimental; Modelação cinética; Queimador poroso; Destruição de alcatrão.

1 INTRODUÇÃO

Biomassa inclui plantas lenhosas, herbáceas/gramíneas, plantas aquáticas, e adubos [1,2], e é comummente convertida em combustíveis e/ou calor, através de processos termoquímicos ou de processos biológicos. Dentro dos processos de conversão de termoquímicos, a gaseificação da biomassa é uma tecnologia muito promissora. A gaseificação da biomassa dá origem a um combustível gasoso que pode ser utilizado directamente para a geração de energia e/ou de calor, para o fabrico de combustíveis para transporte e como matéria-prima química [3]. O combustível gasoso é conhecido como gás de síntese e é composto por H_2, CO, CO_2, CH_4, C_2H_4 e outros gases, e por impurezas, tais como compostos alcalinos e os alcatrões. A mistura de combustível tem geralmente um valor de aquecimento baixo, entre 4 e 6 MJ/Nm^3, quando o ar é usado como agente de gaseificação [4,5]. Basu [4] e outros investigadores [5–7] discutem em detalhe a configuração, a operação e a formação e composição de impurezas em gaseificadores. Os níveis de impurezas dependem da configuração do gaseificador e das condições de gaseificação. Woolcock e Brown [8] apresentam uma revisão bastante útil das principais técnicas disponíveis para a remoção de impurezas, que são sistemas muito dispendiosos e que podem gerar produtos residuais que necessitam de tratamento posterior.

Uma preocupação importante associada com os sistemas de limpeza de alcatrões é que estes podem condensar ou polimerizar antes de entrar no sistema de remoção ou de redução, e, portanto, podem bloquear ou danificar o equipamento a montante. Milne et al. [9] definiram alcatrões como sendo os orgânicos produzidos sob regimes térmicos ou de oxidação parcial (gaseificação) de qualquer material orgânico, que são geralmente aceites como sendo em grande parte aromáticos, enquanto Moersch et al. [10] consideram alcatrões todos os hidrocarbonetos aromáticos e poliaromáticos presentes no gás de síntese. Textos interessantes sobre tecnologias para a redução, remoção e destruição de alcatrões em gases de síntese através de processos catalíticos podem ser encontrados nas referências [11-16]. Estes métodos (craqueamento catalítico e térmico, e combustão parcial) para a destruição de alcatrão são muito apelativos, uma vez que aumentam a eficiência de gaseificação através da conversão do alcatrão em gases úteis, tais como hidrocarbonetos leves, sem a necessidade de separar o alcatrão do gás de síntese. Em particular, o craqueamento catalítico de alcatrão é um método muito vantajoso, uma vez que permite taxas de conversão elevadas a temperaturas moderadas, mas tem como principais desvantagens os altos custos associados e a necessidade de regeneração. A combustão parcial de gás de síntese também permite o craqueamento do alcatrão em hidrocarbonetos mais leves, mas uma quantidade relativamente elevada de compostos úteis pode ser encontrado no gás de combustão [16].

Neste contexto, a remoção de alcatrão através da combustão integral do gás de síntese pode ser uma alternativa interessante. A tecnologia adequada para alcançar este objectivo pode ser a combustão do gás de síntese em meios porosos. Revisões da literatura sobre os vários aspectos da combustão em meios porosos são fornecidas nas referências [17-19], e estudos específicos sobre queimadores porosos podem ser encontrados nas referências [20-29]. O presente estudo avalia a destruição do alcatrão presente no gás de síntese a partir da gaseificação de biomassa por combustão em meios porosos. Uma mistura de gás foi utilizada para emular o gás de síntese, que inclui tolueno como um substituto de alcatrão. Inicialmente, o CHEMKIN V4.1 com o modelo PREMIX [30] foi utilizado para avaliar o potencial da solução proposta. Subsequentemente, os ensaios experimentais foram realizados num queimador poroso alimentado com metano puro e gás de síntese. Nestes ensaios, a concentração de gás de síntese em tolueno variou de 50 a 200 g/Nm^3.

A Tabela 1 apresenta as composições de combustível e relações de equivalência utilizados neste estudo. A potência do queimador foi de 510 W para ϕ = 0.5 e de 420 W para ϕ = 0.4. A velocidade média do escoamento considerada para todas as composições e relações de equivalência foi de 8 cm/s.

Tabela 1: Composição do combustível e relações de equivalência utilizadas.

Combustível	Composição	ϕ
1	100% CH_4	0.5
2	20% CH_4; 8.9% H_2; 8.9% CO_2; 26.7% CO; 35.6% N_2	0.5 e 0.4

A literatura [9] revela que a maior concentração de alcatrão, que pode ser encontrada em aplicações reais é de cerca de 200 g/Nm^3. Neste trabalho, tolueno ($C_6H_5CH_3$) foi usada como um substituto de alcatrão com três concentrações diferentes de gás de síntese, 50, 100 e 200 g/Nm^3, para cada uma das condições apresentadas na Tabela 1. Note-se, no entanto, que o fluxo de massa de tolueno foi diferente para cada caso, variando de 41 mg/min para o combustível 1 com ϕ = 0.5 até 320 mg/min para o combustível 2 com ϕ = 0.5.

2 CONCLUSÕES

O queimador poroso provou ser uma maneira eficiente para a destruição de tolueno; os resultados indicaram percentagens de destruição superiores a 99.8%, independentemente do combustível utilizado para disparar o queimador.

A taxa de destruição de tolueno é sempre inferior com o queimador poroso que opera com um ϕ = 0.4 do que com um ϕ = 0.5, o que é atribuído às temperaturas mais baixas no interior do meio poroso para o primeiro caso.

As taxas de conversão de tolueno aumentam para as taxas mais elevadas de fluxo de massa de tolueno na mistura combustível, provavelmente devido à contribuição da oxidação de tolueno para o aumento da temperatura dentro do queimador poroso.

AGRADECIMENTOS

Este trabalho foi financiado pela Fundação para a Ciência e Tecnologia (FCT), através do IDMEC, no âmbito dos projectos Pest-OE/EME/LA0022 e PTDC/EME-MFE/116832/2010.

REFERÊNCIAS

[1] P McKendry (2002). Energy production from biomass (part 1): overview of biomass. *Bioresource Technology* **83**:37-46.

[2] A Demirbas (2009). Biorefineries: current activities and future developments. *Energy Conversion and Management* **50**:2782–2801.

[3] P McKendry (2002). Energy production from biomass (part 2): conversion technologies. *Bioresource Technology* **83**:47–54.

[4] P Basu (2010). *Biomass Gasification and Pyrolysis – Practical Design and Theory*, Elsevier, Oxford, UK

[5] T Damartzis, A Zabaniotou (2011). Thermochemical conversion of biomass to second generation biofuels through integrated process design – a review. *Renewable and Sustainable Energy Reviews* **15**:366–378.

[6] NL Panwar, R Kothari, VV Tyagi (2012). Thermochemical conversion of biomass – eco friendly energy routes. *Renewable and Sustainable Energy Reviews* **16**:1801–1816.

[7] P McKendry (2002). Energy production from biomass (part 3): gasification technologies. *Bioresource Technology* **83**:55–63.

[8] PJ Woolcock, RC Brown (2013). A review of cleaning technologies for biomass-derived syngas. *Biomass and Bioenergy* **52**:54–84.
[9] TA Milne, RJ Evans, N Abatzoglou (1998). *Biomass "tars": their nature, formation, and conversion*. NREL Report, Golden, CO, USA.
[10] O Moersch, H Spliethoff, KRG Hein (2000). Tar quantification with a new online analyzing method. Biomass and Bioenergy **18**, 79-86.
[11] S Anis, ZA Zainal (2011). Tar reduction in biomass producer gas via mechanical, catalytic and thermal methods: a review. *Renewable and Sustainable Energy Reviews* **15**, 2355-2377.
[12] C Li, K Suzuki (2009). Tar property, analysis, reforming and model for biomass gasification – an overview. *Renewable and Sustainable Energy Reviews* **13**, 594-604.
[13] DA Dayton (2002). *A review of the literature on catalytic biomass tar destruction*. NREL Report, Golden, CO, USA.
[14] J Han, H Kim (2008). The reduction and control technology of tar during biomass gasification/pyrolysis: an overview. *Renewable and Sustainable Energy Reviews* **12**, 397-416.
[15] L Devi, KJ Ptasinski, FJJG Janssen, SVB Paasen, PCA Bergman, JHA Kiel (2005). Catalytic decomposition of biomass tars: use of dolomite and untreated olivine. *Renewable Energy* **30**, 565-587.
[16] MP Houben, HC Lange, AA Steenhoven (2005). Tar reduction through partial combustion of fuel gas. *Fuel* **84**, 817-824.
[17] JR Howell, MJ Hall, JL Ellzey (1996). Combustion of hydrocarbon fuels within porous inert media. *Progress in Energy and Combustion Science* **22**, 121-145.
[18] MA Mujeebu, MZ Abdullah, MZA Bakar, AA Mohamad, RMN Muhad, MK Abdullah (2009). Combustion in porous media and its applications – a comprehensive survey. *Journal of Environmental Management* **90**, 2287-2312.
[19] S Wood, AT Harris (2008). Porous burners for lean-burn applications. *Progress in Energy and Combustion Science* **34**, 667-684.
[20] H Gao, Z Qu, X Feng, W Tao (2014). Combustion of methane/air mixtures in a two-layer porous burner: a comparison of alumina foams, beads, and honeycombs. *Experimental Thermal and Fluid Science* **52**, 215-220.
[21] GJ Rortveit, K. Zepter, O Skreiberg, M Fossum, J Hustad (2002). A comparison of low-NO_x burners for combustion of methane and hydrogen mixtures. *Proceedings of the Combustion Institute* **29**, 1123-1129.
[22] AJ Barra, JL Ellzey (2004). Heat recirculation and heat transfer in porous burners. *Combustion and Flame* **137**, 230-241.
[23] C Keramiotis, B Stelzner, D Trimis, M Founti (2012). Porous burners for low emission combustion: an experimental investigation. *Energy* **45**, 213-219.
[24] N Delalic, Dz. Mulahasanovic, EN Ganic (2004). Porous media compact heat exchanger unit – experiment and analysis. *Experimental Thermal and Fluid Science* **28**, 185-192.
[25] P Talukdar, SC Mishra, D Trimis, F Durst (2004). Heat transfer characteristics of a porous radiant burner under the influence of a 2-D radiation field. *Journal of Quantitative Spectroscopy & Radiative Transfer* 84, 527-537.
[26] RC Catapan, AAM Oliveira, M Costa (2011). Non-uniform velocity profile mechanism for flame stabilization in a porous radiant burner. *Experimental Thermal and Fluid Science* **35**, 172-179.
[27] RW Francisco, M Costa, RC Catapan, AAM Oliveira (2013). Combustion of hydrogen rich gaseous fuels with low calorific value in a porous burner placed in a confined heated environment. *Experimental Thermal and Fluid Science* **45**, 102-109.
[28] SK Alavandi, AK Agrawal (2008). Experimental study of combustion of hydrogen-syngas/methane fuel mixtures in a porous burner. *International Journal of Hydrogen Energy* **33**, 1407-1415.
[29] RW Francisco, F. Rua, M Costa, RC Catapan, AAM Oliveira (2010). On the combustion of hydrogen-rich gaseous fuels with low calorific value in a porous burner. *Energy & Fuels* **24**, 880-887.
[30] RJ Kee, JF Grcar, MD Smooke, JA Miller (1998). PREMIX: a Fortran program for modeling steady laminar one-dimensional premixed flames, Sandia National Laboratories, USA.

This page was intentionally left blank

V Conferência Nacional de Mecânica dos Fluidos, Termodinâmica e Energia
MEFTE 2014, 11–12 Setembro 2014, Porto, Portugal
APMTAC, 2014

Effect of exhaust gas recirculation and air staging on gaseous and particulate matter emissions in a domestic boiler

U Fernandes, M Henriques, M Costa

IDMEC, Departamento de Engenharia Mecânica, Instituto Superior Técnico, Universidade de Lisboa, Lisboa, Portugal
email: mcosta@ist.utl.pt

ABSTRACT: The present study evaluates the effect of the exhaust gas recirculation (EGR) and air staging on gaseous (CO and NO_x) and PM emissions in a domestic boiler. The two methods were examined for one boiler thermal input. In addition, to better understand the impact of the two methods on PM emissions, a number of selected PM samples were morphologically and chemically characterized. The results reveal that (i) EGR has no significant effect on total PM, PM2.5, CO and NO_x emissions; (ii) air staging has a positive impact on total PM, PM2.5 and CO emissions, but a negative impact on NO_x emissions; (iii) the impact of the level of air staging in the reduction of the PM2.5 emissions is larger than in the reduction of the total PM emissions; and (iv) the carbon (soot) present in the PM2.5 significantly decreases with the air staging level, unlike the amounts of inorganic elements that are solely marginally affected.

KEY-WORDS: Biomass; Domestic boiler; Gaseous and particulate matter emissions; Exhaust gas recirculation; Air staging.

1 INTRODCTION

Domestic biomass-fired boilers are an important source of gaseous and particulate matter (PM) emissions, which have negative implications on the environment and human health. The need to reduce emissions and the relatively high costs of advanced gas cleaning devices have recently driven research towards the application of strategies such as exhaust gas recirculation (EGR) and air staging to domestic boilers. These two methods can be applied to existing domestic boilers with low cost and few modifications to them.

Related recent studies include those of Lamberg et al. [1], Houshfar et al. [2], Liu et al. [3] and Nuutinen et al. [4], among others. Lamberg et al. [1] concluded that, under optimized operating conditions, air staging lowers the gaseous and PM emissions in a small-scale pellet boiler. The authors attributed the reduction in fine PM emissions under air staging conditions to both a decrease in alkali metal emissions and emissions of unburnt carbonaceous particles. Nuutinen et al. [4] also concluded that air staging considerably reduces the gaseous and PM emissions in masonry heaters, with the greatest reduction being observed in gaseous and particulate organic emissions. Liu et al. [3] observed that air staging can lead to significant reductions in NO_x emissions in domestic/small-scale biomass boilers, but pointed out that CO emissions may be problematical under these operating conditions, while Houshfar et al. [2] demonstrated the positive impact of combining EGR and air staging on NO_x emissions in a grate-fired laboratory-scale reactor.

Apart from demonstrating the potential to reduce gaseous and PM emissions in domestic/small-scale biomass boilers through combustion modifications, the above studies also revealed that there are possibilities to further improve the combustion process by optimization of these methods. The present study evaluates the effect of the exhaust gas recirculation (EGR) and air staging on gaseous (CO and NO_x) and PM emissions in a domestic boiler. The two methods were examined for one boiler thermal input. In addition, to better understand the impact of the two methods on PM emissions, a number of selected PM samples were morphologically and chemically characterized.

2 CONCLUSIONS

The main conclusions of this work are as follows.

- EGR has no significant effect on total PM, PM2.5, CO and NO_x emissions. This is presumably because the present boiler operates with high levels of excess air so that the changes in temperature

and oxygen concentration caused by the EGR are insufficient to introduce positive (or negative) impacts on pollutants formation and emission.

- Air staging has a positive impact on total PM, PM2.5 and CO emissions, but a negative impact on the NO_x emissions, which can be attributed to the increase in mixing, combustion intensity and temperature in the region above the grate caused by this strategy.
- The impact of the level of air staging in the reduction of the PM2.5 emissions is larger than in the reduction of the total PM emissions, which indicates that the higher soot oxidation rates are associated with the particles with sizes below 2.5 μm.
- The carbon (soot) present in the PM2.5 significantly decreases with the air staging level, unlike the amounts of inorganic elements that are solely marginally affected.

ACKNOWLEDGEMENTS

This work was supported by Fundação para a Ciência e a Tecnologia (FCT), through IDMEC, under LAETA Pest-OE/EME/LA0022, and COST Action CM0901. U Fernandes is pleased to acknowledge the Fundação para a Ciência e a Tecnologia (FCT) for the provision of the scholarship SFRH/BD/82438/2011.

REFERENCES

[1] H Lamberg, O Sippula, J Tissari, J Jokiniemi (2011). Effects of air staging and load on fine-particle and gaseous emissions from a small-scale pellet boiler. *Energy & Fuels* **25**:4952–4960.

[2] E Houshfar, RA Khalil, T Løvas, Ø Skreiberg (2012). Enhanced NO_x reduction by combined staged air and flue gas recirculation in biomass grate combustion. *Energy & Fuels* **26**:3003–3011.

[3] H Liu, J Chaney, J Li, C Sun (2013). Control of NO_x emissions of a domestic/small-scale biomass pellet boiler by air staging. *Fuel* **103**:792–798.

[4] K Nuutinen, J Jokiniemi, O Sippula, H Lamberg, J Sutinen, P Horttanainen, J Tissari (2014). Effect of air staging on fine particle, dust and gaseous emissions from masonry heaters. *Biomass and Bioenergy* **67**:167–178.

[5] U Fernandes, M Costa (2012). Particle emissions from a domestic pellets-fired boiler, *Fuel Processing Technology* **103**:51–56.

[6] U Fernandes, M Costa (2013). Formation of fine particulate matter in a domestic pellet-fired boiler. *Energy & Fuels* **27**:1081–1092.

V Conferência Nacional de Mecânica dos Fluidos, Termodinâmica e Energia
MEFTE 2014, 11–12 Setembro 2014, Porto, Portugal
APMTAC, 2014

Evaluation of particle fragmentation of raw and torrified biomass in a drop tube furnace

FF Costa, M Costa

IDMEC, Departamento de Engenharia Mecânica, Instituto Superior Técnico, Universidade de Lisboa, Lisboa, Portugal
email: francisco.costa@ist.utl.pt, mcosta@ist.utl.pt

ABSTRACT: Particle fragmentation is one of the most important concerns in biomass combustion as it strongly controls the ultra fine particulate matter emissions. Particle fragmentation corresponds to the particle collapse during combustion, resulting two or more particles of smaller size. Torrefaction consists on exposing biomass to an inert atmosphere between 260 ºC and 300 ºC. In such conditions, hemicellulose is partially decomposed allowing some low calorific volatiles to be released from the raw biomass, thus enhancing the remaining biomass energetic potential. One of the torrified biomass characteristics consists on its brittle nature, and therefore, more prone and easily breakable in milling processes. In this context, this study aims to understand whether torrefaction promotes particle fragmentation during biomass combustion. Pine shells, olive stones and wheat straw were torrified at 280 ºC. Subsequently, all fuels, both raw and torrified, were burnt in a drop tube furnace (DTF) at 1100 ºC. The results reported include burnout profiles and particle matter (PM) concentrations and size distributions measured along the DTF. Overall, the results reveal that (i) pine shells present the lowest PM concentrations due to its lower ash content and highest burnout values; (ii) particle fragmentation does not occur during the combustion of raw and torrified olive stones; and (iii) particle fragmentation occurs during the combustion of raw and torrified pine shells and wheat straw, but torrefaction promotes particle fragmentation only in the case of the straw.

KEY-WORDS: Particle fragmentation; Torrefaction; Biomass; Drop tube furnace.

1 INTRODUCTION

Biomass is one of the most favourable alternatives to coal in terms of energy production, but its combustion still poses a number of challenges. Particle fragmentation, which corresponds to the particle collapse during combustion, is one of the most important concerns in biomass combustion as it contributes to the ultra fine particulate matter emissions, which are especially harmful to the human health.

Particle fragmentation is a rather complex subject and the very few studies available in the literature have mainly concentrated on coal combustion. Xu et al. [1] examined the fragmentation of coal particles in a drop tube furnace (DTF) and reported that, in the final stages of the combustion process, particles tend to break and divide in more particles leading to a decrease in the particle mean diameter. Seames [2] used scanning electron microscope techniques to evaluate the fragmentation of coal particles and concluded that, as coal combustion occurs at constant diameter, the event of finding a collapsed particle may indicate particle fragmentation. It should be noted that, while coal burns at approximately constant diameter, biomass tends to retain its original desorbed shape during combustion, thus varying particle diameter during combustion [3]. This means that the evaluation of the particle fragmentation in biomass combustion using mean diameters or scanning electron microscope techniques may be inconclusive.

Torrefaction is a pre-treatment that consists on exposing biomass to an inert atmosphere. Under these conditions hemicellulose is partially decomposed and, thereby, some low calorific volatiles are released from the raw biomass, thus enhancing the remaining biomass energetic potential. In this way, it is possible to obtain new biomass fuels, whose properties range between biomass and coal [4-10]. One of the torrified biomass characteristics consists on its brittle nature, and therefore, more prone and easily breakable in milling processes [8]. Accordingly, it is important to understand whether torrefaction promotes particle fragmentation during biomass combustion.

In the present study biomass particle fragmentation is investigated based on the evolution of the burnout and particle matter (PM) concentrations and size distributions along a DTF for both raw and torrified biomass fuels (pine shells, olive stones and wheat straw). All biomass fuels were torrified in a

nitrogen inert atmosphere at 280 ºC. Then, both raw and torrified biomass fuels, were burnt in the DTF at a constant wall temperature of 1100 ºC.

2 MATERIALS AND METHODS

2.1 Drop tube furnace

The DTF used in this study is described in detail elsewhere [11,12]. The combustion chamber of the DTF is an electrically heated ceramic tube with an inner diameter of 38 mm and a length of 1.3 m. The furnace wall temperatures are continuously monitored by eight type-K thermocouples uniformly distributed along the combustion chamber. A water-cooled injector, placed at the top of the DTF, is used to feed the solid fuels and the air to the combustion chamber. A twin screw volumetric feeder transfers the pulverized solid fuels to an ejection system from which the particles are gas-transported to the water-cooled injector.

2.2 Experimental methods

2.2.1 Particle sampling

Particle sampling along the combustion chamber axis was performed with the aid of a 1.5 m long, water-cooled, nitrogen-quenched stainless steel probe [12]. The probe (see Figure 1) comprised a centrally located 3 mm inner diameter tube, through which quenched samples were evacuated with the aid of a pump. The quenching of the chemical reactions was achieved by direct injection of nitrogen jets through small holes very near to the probe tip. The tube for nitrogen delivery was surrounded by two concentric tubes for probe cooling. On leaving the probe, the solid samples were collected in a Tecora total filter holder equipped with a 47 mm diameter quartz microfiber filter. Subsequently, the collected solid samples were placed in an oven at approximately 105 °C to dehydrate. Complete dehydration was ascertained by repeated drying and weighing of the sample until the measured mass became constant. The ash content in the solid samples was finally evaluated following the procedures described in the standard CEN/TS 14775. Particle burnout data were obtained as follows:

$$\psi = \frac{1-\frac{\omega_f}{\omega_x}}{1-\omega_f} \tag{1}$$

where ψ is the particle burnout, ω_f is the ash weigh fraction in the input biomass fuel, and ω_x is the ash weigh fraction in the char sample.

Uncertainties in char burnout calculations based on the use of ash as a tracer are related to ash volatility at high heating rates and temperatures and ash solubility in water. Our best estimates indicated that the uncertainties in char burnout calculations using ash as a tracer in the present work were negligible [12].

Particulate matter (PM) concentrations and size distributions were made with the aid of a low pressure three-stage cascade impactor (LPI, TCR Tecora). PM was sampled isokinetically from the centreline of the combustion chamber in five axial positions of the DTF (300, 500, 700, 900 and 1100 mm from injection position), using the water-cooled, nitrogen-quenched stainless steel probe referred to above. The LPI used allowed collecting three particulate cut sizes during the same sampling: PM with diameters above 10 μm (PM10), PM with diameters between 2.5 μm and 10 μm, and PM with diameters below 2.5 μm (PM2.5). In order to avoid condensation along the line connecting the probe outlet to the impactor inlet and also inside the impactor, a heating jacket (model Winkler WOTX1187) was used during sampling. PM was collected on quartz microfiber filters, which were dried in an oven and weighted before each test. After each test, the filters were again dried, to eliminate moisture, and weighted to determine the quantity of PM captured.

2.2.2 Test conditions

The solid fuels studied in this work included raw and torrified pine shells, olive stones and wheat straw. All raw biomass fuels were sieved to 1 mm size and the particle size distribution was measured using the Malvern 2600 Particle Size Analyzer. The biomass fuels were then torrified in an insulated stainless steel container through which 3 L/min of nitrogen at 310 ºC passed during 1 hour. During the process the biomass temperature varied between 280 ºC and 300 ºC. Table 1 shows the characteristics of the raw and torrified biomass fuels, including the fuel ash composition. The table includes the properties of a United Kingdom bituminous coal for comparison purposes. Note that particle size distribution of the torrified biomass fuels were similar to those of the raw biomass fuels as indicated by the measurements performed with the aid of the Malvern Analyser.

In this study, measurements were carried out for all biomass fuels for DTF wall temperatures of 1100 ºC, and inlet air at room temperature. The solid fuels feed rate was around 23 g/h and the total air flow rate was 4 L/min. The initial particle velocity was estimated, from the inlet air flow at room temperature, to be ~0.3 m/s.

Table 1: Characteristics of the raw and torrified biomass. Coal is included for comparison purposes.

Parameter	Pine shells		Olive stones		Wheat straw		Coal
	Raw	Torrified	Raw	Torrified	Raw	Torrified	
Proximate analysis (wt%, as received)							
Volatiles	58.9	69.4	57.8	60.6	64.9	55.0	44.6
Fixed carbon	25.9	27.6	19.7	23.1	11,5	24.0	51.4
Moisture	13.9	1.0	9.4	0.3	8,9	0.9	1.7
Ash	1.3	2.0	13.1	16.0	14,7	20.1	2.3
Ultimate analysis (wt%, daf)							
Carbon	47.8	54.4	43.2	47.8	39.4	44.0	79.3
Hydrogen	5.6	5.5	5.6	5.1	5.2	4.3	5.9
Nitrogen	0.3	0.4	1.9	2.3	0.5	0.8	1.9
Sulphur	0.0	0.0	0.0	0.0	0.0	0.0	0.5
Oxygen	46.3	39.7	49.3	44.8	54.9	50.9	12.4
High heating value (MJ/kg)	18.82	23.52	17.54	20.67	19.0	19.4	35.04
Ash analysis (wt%, dry basis)							
SiO_2	9.6		30.4		34.3		39.4
Al_2O_3	11.9		10.6		7.7		23.2
Fe_2O_3	2.1		9.9		2.9		24.7
CaO	50.9		9.9		24.1		3.5
SO_3	2.0		0.7		2.6		1.5
MgO	12.1		7.2		3.7		1.0
TiO_2	0.0		0.9		0.4		1.7
P_2O_5	5.6		7.4		3.4		0.2
K_2O	4.1		18.7		15.1		1.2
Na_2O	0.8		2.9		0.8		2.6
Cl	0.0		0.7		3.5		0.0
Other oxides	0.9		0.7		1.5		1.0
Particle size (μm)							
Under 30	13.6		9.9		5.9		38.4
Under 70	28.5		17.5		12.4		61.4
Under 100	34.7		21.3		16.1		69.9
Under 300	53.1		37.1		37.6		94.2
Under 500	67.0		49.8		52.9		100
Under 1000	95.1		94.1		92.2		100
Under 2000	100		100		100		100
SMD	177.8		97.0		111.8		19.7

3 RESULTS AND DISCUSSION

3.1 Biomass characteristics

The biomass ash content and composition is very important for the evaluation of particle fragmentation. As seen in Table 1, the pine shells ash content is much lower than those of the olive stones and wheat straw. Moreover, the pine ashes are dominated by calcium (50.9 wt%), while the olives stones and wheat straw ashes are dominated by silica (30.4% and 34.3%, respectively). It is also important to underline the potassium content in the ashes, which are 4.1%, 18.7% and 15.1% for pine shells, olive stones and wheat straw, respectively. Note that the unburned carbon in the ashes has a significant dependence on the potassium content, as it enhances the ashes agglomeration [3].

Figure 1 shows the van Krevelen diagram for all biomass fuels studied, both raw and torrified, and for the coal used for comparison purposes. The data reported presents a high correlation coefficient and it is clear that torrified biomass fuels approach coal characteristics [13].

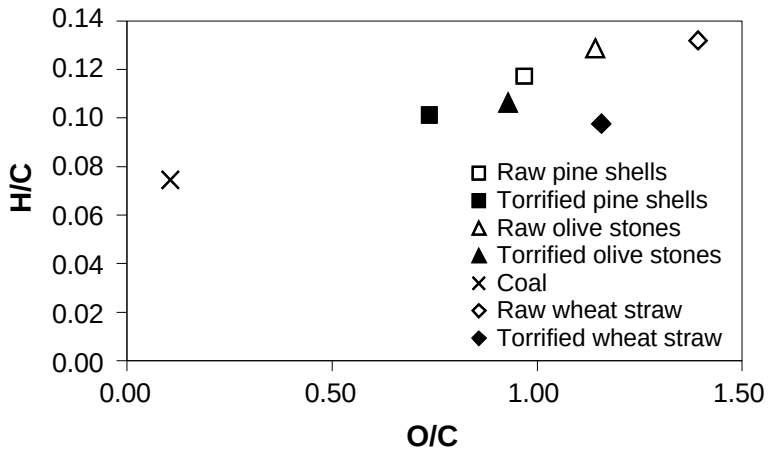

Figure 1: Van Krevelen diagram for all biomass fuels studied. Coal is included for comparison purposes.

3.2 Particle burnout

Figure 2 shows the particle burnout data obtained for all biomass fuels, both raw and torrified, at 1100 ºC. The data for pine shells and olive stones were taken from Costa et al. [13]. Figure 2 shows that the pine shells present the highest levels of burnout, as compared with olives stones and wheat straw. The figure also reveals that the wheat straw presents lower particle burnout values than the olive stones in the first half of the DTF, but the olive stones present higher values than the wheat straw near the exit of the DTF.

According to Figure 2c) for the raw wheat straw the char combustion stars at x = 900 mm, while for torrified wheat straw the char combustion starts at x = 700 mm. This is due to the volatiles release during torrefaction, which leads to an earlier onset of the char combustion process for the torrified biomass. Similar observations are valid for the olive stones, which are fully discussed in reference [13].

3.3 Particle matter concentrations

Figure 3 shows the PM concentrations for all biomass fuels studied, both raw and torrified. PM concentrations are divided in particles sizes above 10 μm (PM10), between 10 μm and 2.5 μm (PM2.5 – PM10), and below 2.5 μm (PM2.5). For pine shells the total PM concentrations are lower than those for the olive stones and wheat straw due to the lower pine shells ash content (cf. Table 1).

Figures 3a and 3b reveal that for the raw pine shells PM under 10 μm at x = 900 mm represent 10.9% of the total PM and at x = 1100 mm correspond to 24.6%, while for the torrified pine shells PM under 10 μm at x = 900 mm represent 17.9% and at x = 1100 mm account for 32.1%. However, the particle burnout data show little increase from x = 900 mm to x = 1100 mm; specifically from 98.4% to 98.9% for the raw pine shells and from 97.8% to 99.4% for the torrified pine shells at x = 900 mm and 1100 mm. This indicates that, near the exit of the DTF, particles strongly reduce size despite burnout almost remaining constant. In this case it is clear that particle fragmentation occurred, leading to a reduction in particle size and a higher concentration of smaller particles.

Figures 3c and 3d show that for the raw olive stones PM under 10 μm at x = 900 mm represent 6.5% of the total PM and at x = 1100 mm correspond to 6.9%, while for torrified olive stones PM under 10 μm at x = 900 mm represent 4.8% and at x = 1100 mm account for 5.6%. Particle burnout data show an increase between these two axial positions from 90.8% to 93.8% for the raw olive stones and from 82.1% to 86.1% for the torrified olive stones. In this case, near the exit of the DTF, the PM concentrations and distributions remain unchanged. It can therefore be concluded that for olive stones, both raw and torrified, particle fragmentation does not occur. It is interesting to note that beyond x = 700 mm the PM size distribution and concentration remain constant, which suggest the combustion of particles of olive stones take place at a constant diameter.

Figure 3e and 3f show that for raw wheat straw PM under 10 μm at x = 900 mm represent 8.4% of the total PM and at x = 1100 mm account for 26.4%, while for torrified wheat straw PM under 10 μm at x = 900 mm represent 14% and at x = 1100 mm correspond to 34.5%. Burnout data show that between x =

900 mm and x = 1100 mm particle burnout increases from 84.3% to 87.3% for raw wheat straw and from 76.4% to 80.8% for torrified wheat straw This indicates that, near the exit of the DTF, particles strongly reduce size despite particle burnout increasing only slightly. In this case, it is clear that particle fragmentation occurred, leading to a reduction in particle size and higher concentration of smaller particles. For wheat straw particle fragmentation occurred more significantly than for pine shells. Furthermore, in the case of the torrified wheat straw, particle fragmentation is more severe as it generates more particles of smaller size than in the case of the raw wheat straw.

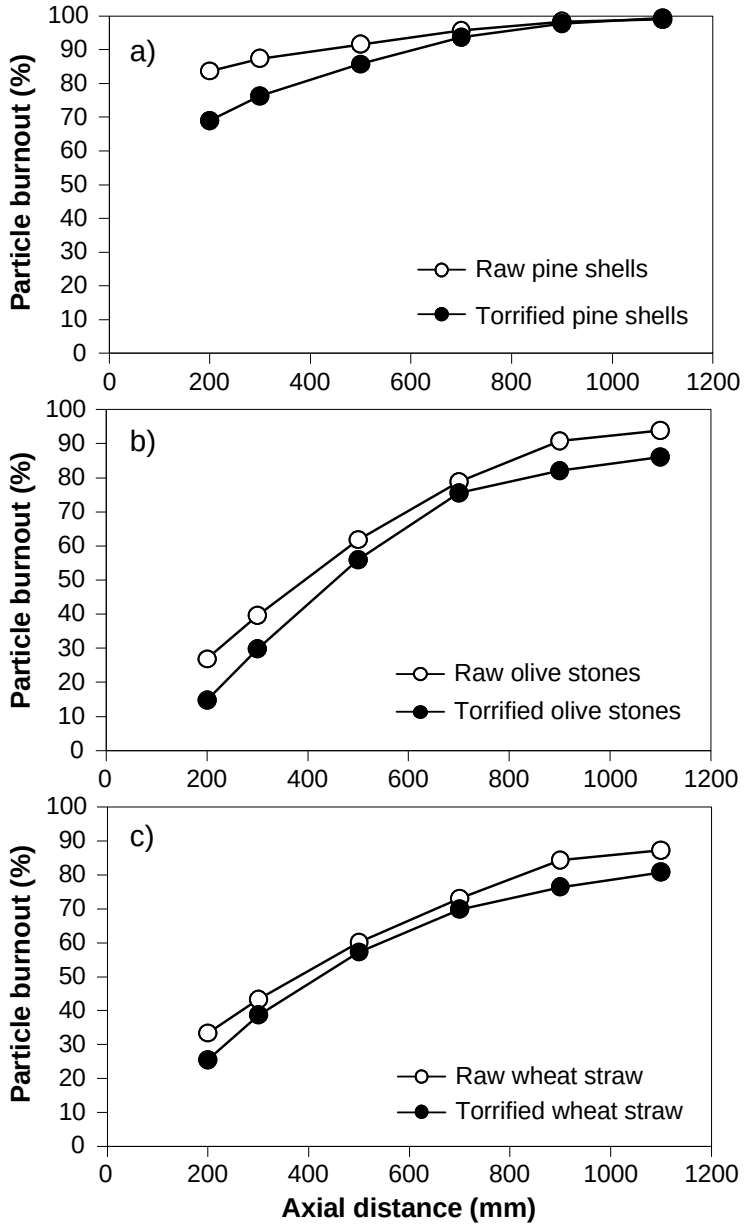

Figure 2: Particle burnout profiles along the axis of the DTF. a) Pine shells, b) olive stones, d) wheat straw.

4 CONCLUSIONS

The main conclusions from this work can be summarized as follows: (i) Pine shells present the lowest PM concentrations due to its lower ash content and highest burnout values; (ii) particle fragmentation does not occur during the combustion of raw and torrified olive stones; (iii) particle fragmentation occurs during the combustion of raw and torrified pine shells and wheat straw, but torrefaction promotes particle fragmentation only in the case of the straw.

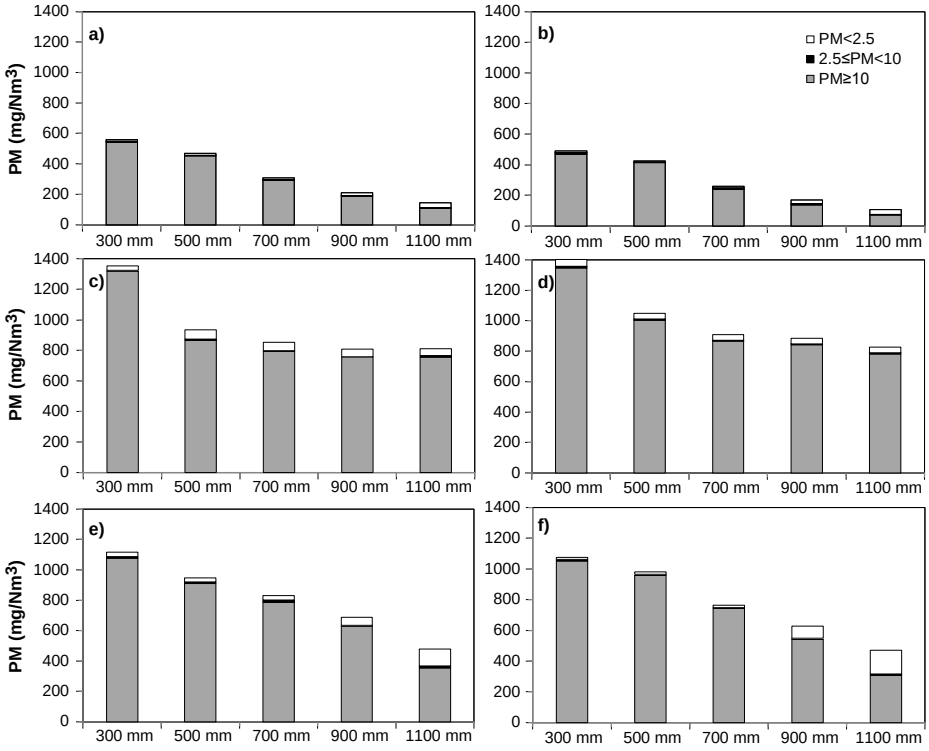

Figure 3: Size-classified PM concentrations along the DTF. a) Pine shells, b) torrified pine shells, c) olive stones, d) torrified olive stones, e) wheat straw, f) torrified wheat straw.

ACKNOWLEDGMENTS

This work was supported by Fundação para a Ciência e a Tecnologia (FCT), through IDMEC, under LAETA Pest-OE/EME/LA0022 and under PTDC/EME-MFE/116832/2010.

REFERENCES

[1] M Xu, D Yu, H Yao, X Liu, Y Qiao (2011). Coal combustion-generated aerosols: Formation and properties. *Proceedings of the Combustion Institute* **33**:1681–1697.

[2] WS Seames (2003). An initial study of the fine fragmentation fly ash particle mode generated during pulverized coal combustion. *Fuel Processing Technology* **81**:109–125.

[3] A Williams, JM Jones, L Ma, M Pourkashanian (2012). Pollutants from the combustion of solid biomass fuels. *Progress in Energy and Combustion Science* **38**:113–137.

[4] JJ Chew, V Doshi (2011). Recent advances in biomass pretreatment – Torrefaction fundamentals and technology. *Renewable and Sustainable Energy Reviews* **15**:4212–4222.

[5] K Svoboda, M Porohely, M Hartman, J Martinec (2009). Pretreatment and feeding of biomass for pressurized entrained flow gasification. *Fuel Processing Technology* **90**:629–635.

[6] WH Chen, WY Cheng, KM Lu, YP Huang (2011). An evaluation on improvement of pulverized biomass property for solid fuel through torrefaction. *Applied Energy* **88**:3636–3644.

[7] V Repellin, A Govin, M Rolland, R Guyonnet (2010). Energy requirement for fine grinding of torrefied wood. *Biomass and Bioenergy* **34**:923–930.

[8] M Phanphanich, S Mani (2010). Impact of torrefaction on the grindability and fuel characteristics of forest biomass. *Bioresource Technology* **102**:1246–1253.

[9] MJ Prins, KJ Ptasinski, F Janssen (2006). Torrefaction of wood. Part 2. Analysis of products. *Journal of Analytical and Applied Pyrolysis* **77**:35–40.

[10] B Moghtaderi, C Meesri, TF Wall (2004). Pyrolytic characteristics of blended coal and woody biomass. *Fuel* **83**:745–750.

[11] G Wang, R Zander, M Costa (2014). Oxy-fuel combustion characteristics of pulverized-coal in a drop tube furnace. *Fuel* **115**:452–460.

[12] G Wang, RB Silva, JLT Azevedo, S Martins-Dias, M Costa (2014), Evaluation of the combustion behaviour and ash characteristics of biomass waste derived fuels, pine and coal in a drop tube furnace, *Fuel* **117**, 809–824.

[13] FF Costa, G Wang, M Costa (2015). Combustion kinetics and particle fragmentation of raw and torrified pine shells and olive stones in a drop tube furnace. *Proceedings of the Combustion Institute, in press.*

V Conferência Nacional de Mecânica dos Fluidos, Termodinâmica e Energia
MEFTE 2014, 11–12 Setembro 2014, Porto, Portugal
APMTAC, 2014

Particle history from massively parallel large eddy simulations of coal combustion in a large-scale laboratory furnace

M Rabaçal[1], M Costa[1], AM Kempf[2]

[1]IDMEC, Departamento de Engenharia Mecânica, Instituto Superior Técnico, Universidade de Lisboa, Portugal
[2]Chair in Fluid Dynamics, Faculty of Engineering, Universität Duisburg-Essen, Duisburg, Germany
email: miriamrabacal@tecnico.ulisboa.pt, mcosta@tecnico.ulisboa.pt, andreas.kempf@uni-due.de

ABSTRACT: A large eddy simulation (LES) of coal combustion in a large-scale laboratory furnace is presented. The massively parallel execution produces a high-resolution representation of the fluid mixing and particle dispersion throughout the whole computational domain. The coal combustion is modelled using the single first order rate model (SFOM) for devolatilization and the Smith model for char combustion. Optimized kinetic constants for the furnace operating condition were obtained through an iterative procedure between particle heating rates from full LES runs and the advanced model Chemical Percolation Devolatilization (CPD). Gas phase combustion was modelled using the eddy break up model (EBU). Radiation was modelled using the discrete ordinates method (DOM). The particle trajectory is tracked allowing to follow the particle's combustion history and to obtain a better understanding of the conditions that coal particles are subjected to in the investigated test case. Particles experience various heating rates and multiple surrounding environments depending on their trajectory, which has an impact on the progress of combustion. Quasi-thermal equilibrium is observed and the gaseous conditions that maximize char combustion rate were identified from the simulation data for this particular test case.

KEY-WORDS: Large eddy simulation; Massively parallel execution; Large-scale coal combustion; Coal particle history.

1 INTRODUCTION

Europe has seen a significant increase in coal imports from the United States of America as result of a decreasing use of nuclear power in some countries and coal's relatively low price [1]. The increased usage of coal creates a need for more efficient coal technologies [2]. LES of coal combustion has emerged in the last years and much progress has been made, although simulations have typically targeted laboratory coal flames [3]. Recently, simulations of large-scale oxy-coal combustion using LES and Reynolds averaged Navier-Strokes have shown that in possession of superior turbulent flow prediction capabilities, the combustion models will finally become the bottle-neck [4].

In a previous work [5], we showed that the classical coal combustion models when used in a high resolution, massively parallel LES lead to satisfactory predictions of the in-flame gas properties, namely gas temperature and gas species concentrations. Following this previous work, this study presents further insights into the coal combustion processes that are not currently available by other means than LES. Particle combustion history is tracked and the effects of the surrounding environment on burnout progress are discussed.

2 COMBUSTION MODELING

Coal particles are considered to be thermally thin. The energy balance imposed to the particle accounts for heat transfer due to convection, radiation, and char combustion. The flow is assumed to be diluted, so particle interactions can be neglected. The particles are assumed to be spherical and non-deformable and only drag and gravity forces are considered to act on the particles, as coal particles have a considerably higher density than the carrier gas.

Devolatilization is modelled using SFOM [6] with kinetic constants optimized to the heating conditions of the studied furnace and coal properties [5]. The optimization consists of an iterative process between full LES simulations, from which particle heating rates are obtained, and devolatilization predictions using the advanced CPD model available in the Particle Kinetics Pre-processor [5]. Char combustion is modelled using the Smith model, accounting for structural and pore diffusion effects [7]. Heterogeneous combustion is simplified to the oxidation of solid carbon by O_2, producing CO. Gaseous combustion

follows a three-step mechanism where volatiles are an assumed postulate substance. Reaction rates are modelled using the classical EBU model. The general radiative heat transfer equation is solved using the DOM [8], being discretized and solved for 24 directions using the S4 approximation. The participative medium's spectral properties are approximated using a grey gas assumption and particle radiative properties follow a large particle assumption. A more detailed description of the models used can be found elsewhere [5].

3 EXPERIMENTAL CONDITIONS

The studied test case is a 100 kW coal flame co-fired with natural gas in the Instituto Superior Técnico (IST) large-scale laboratory furnace for which detailed in-flame measurements are available [9]. The size of the furnace is sufficient to emulate large-scale combustion conditions – high turbulence and radiative heat transfer – while allowing in-flame diagnostics. Figure 1 shows a schematic of the furnace rooftop and the particle size distribution of the coal used.

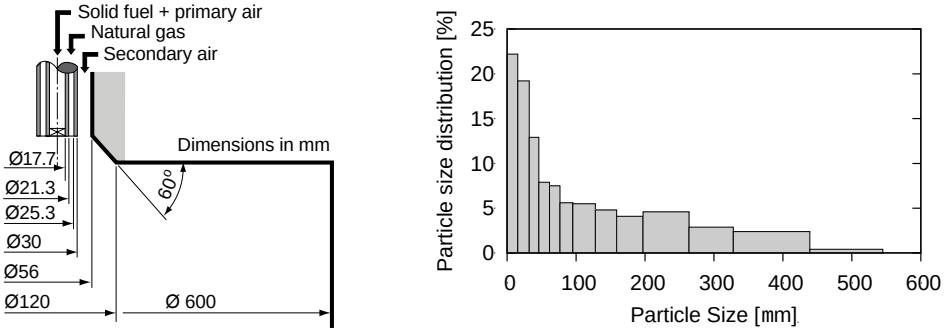

Figure 1: Schematic of the furnace rooftop (left) and particle size distribution of the coal (right).

The furnace has an internal diameter of 0.6 m and a height of 2.4 m. Its top half is lined with refractory cement and the whole furnace is water-cooled. Coal is transported with air and injected through the central jet, natural gas is injected through the intermediate annular jet and secondary swirl air is injected through the outer annular jet. A bituminous coal from the United Kingdom was used. Table 1 lists the operating conditions and the coal properties. In the absence of particle structural parameter measurements, the particle specific surface area and mean pore radius were estimated using appropriate correlations.

Table 1: Operating conditions and coal properties.

Operating conditions			Proximate Analysis [% wt,ar]		Ultimate Analysis [% wt,ar]	
Total thermal input	100	kW	Volatiles	44.6	Carbon	79.3
Excess air	5	%	Fixed carbon	51.4	Hydrogen	5.9
Coal mass flow rate	7.27	kg/h	Moisture	1.7	Nitrogen	1.9
Natural gas mass flow rate	3.16	kg/h	Ash	2.3	Sulphur	0.5
Primary air mass flow rate	7.96	kg/h			Oxygen	8.4
Secondary mass flow rate	130	kg/h	LHV	29.2 MJ/kg	Specific heat	1380 J/kg.K
Secondary air swirl number	1	-	Density	670 kg/m^3	Porosity	0.7 [-]

4 NUMERICAL METHODS

The in-house code PsiPhi [10] was used to solve the implicitly filtered, low-Mach number Navier-Stokes equations for a variable density flow. Continuity is ensured by a projection method. The dispersed phase is treated within a Lagrangian framework with two-way coupling between the dispersed and continuous phase.

Inlet mean velocity profiles were assigned using a 7th-power law profile matching the mass flow of each stream. Turbulence was modelled using the classical Smagorinsky model with a modelling constant of Cs = 0.173 [11]. Pseudo-turbulent inflow conditions were generated using a version of Klein's turbulence generator [12]. The furnace geometry is described by immersed boundaries and no wall modelling was employed since the flame anchors far from the walls. The convective fluxes are approximated with a 2nd-order central differencing scheme for momentum and a total variation

diminishing scheme for scalars. Time integration is performed using an explicit, low storage, 3rd-order Runge-Kutta scheme.

Due to the relatively wide particle size distribution, it was necessary to represent each physical particle by one numerical particle. The particles were injected into the domain using a random distribution fitted to the particle size distribution and randomly positioned within the injection plane.

The furnace geometry was described by an equidistant Cartesian mesh with 1200x600x600 mm in size, representing the refractory lined section of the furnace. Simulations were performed using 3 different cell sizes, coarse with $\Delta = 3.0$ mm, medium with $\Delta = 2.0$ mm, and fine with $\Delta = 1.0$ mm, resulting in a total of 16 million, 54 million, and 432 million cells, respectively. These resolutions resulted in maximum viscosity ratios of μ_t/μ_l of 5.29, 4.23, and 1.29. Within the quarl the ratio was lower than 60, 40, and 20, with exception of single-located wall cells outside of the quarl, where the ratio could reach up to 100, 70 and 40.

The code PsiPhi was optimised for massively parallel execution and ran on SuperMUC (LRZ, Munich, Germany), through a PRACE project. The structured Cartesian grid of equidistant cells provides good numerical accuracy, high parallel efficiency and allows for good vectorization by avoiding slow, non-sequential memory access. The block-structured domain allows for maximum efficiency during communication between CPUs and specific care has been devoted to improving simulation capabilities with MPI parallelization. As a prerequisite, strong scaling tests were performed on a Cray-XT6m up to 3840 cores where a very good parallel scaling was demonstrated. For the afore-mentioned grid sizes, 432, 960 and 7680 CPUs were used, leading to final computational costs of 80 thousand, 200 thousand, and 1 million CPU hours. The iterative kinetic pre-processing was performed using the coarse grid and required a total of 31 thousand CPU hours.

5 RESULTS

Figure 2 shows instantaneous high-resolution views of the near burner region. Figures 2(a)-(c) show the plane containing the centreline and Figure 2(d) shows the volume rendering of the volatile gas reaction rate. These images were taken from the fine grid simulation after a physical run time of 1.0 s. The simulation data indicate that the flame stabilizes very close to the burner exit and that volatile combustion occurs preferentially inside the internal recirculation zone (IRZ) – see below.

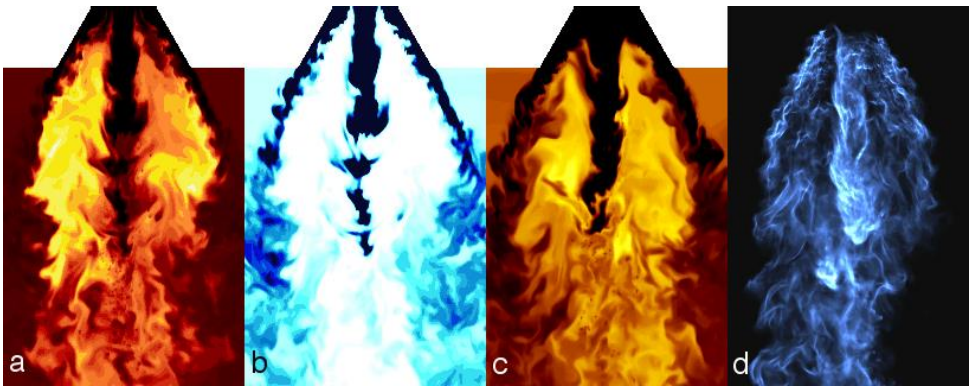

Figure 2: Instantaneous high-resolution views of the near burner region. a) Gas temperature; b) O_2 concentration; c) CO_2 concentration; d) volume rendering of volatile gas reaction rate.

The following results correspond to the coarse grid simulation, where a total run time of 6 s was achieved. Particle data were collected every 0.0003 s during a physical runtime of 1.2 s. A total of 30 particles were selected randomly at 2 injection steps, t = 2 s and t = 3 s, and were tracked during 0.4 s. Finally, scatter data were obtained from a total existing 3.8 million particles at the physical runtime of t = 2.9 s.

Figure 3 shows the instantaneous particle location (in the plane that contains the centreline) coloured by temperature and with size scaled by the particle diameter. It takes approximately 0.9 s for the coal particles to be flushed through the domain; evidence for the need long simulated times. In this figure the internal recirculation zone (IRZ) is denoted by the circle where axial velocity is negative. Smaller particles with lower momentum are entrained in the negative velocity whereas larger particles with higher momentum are capable of penetrating through the IRZ. In this zone particles are heated up to

approximately 2200 K. The figure captures an instantaneous asymmetric feature of the flow, marked by the arrow, where particles are deflected from the IZR preferentially towards the upper radial direction.

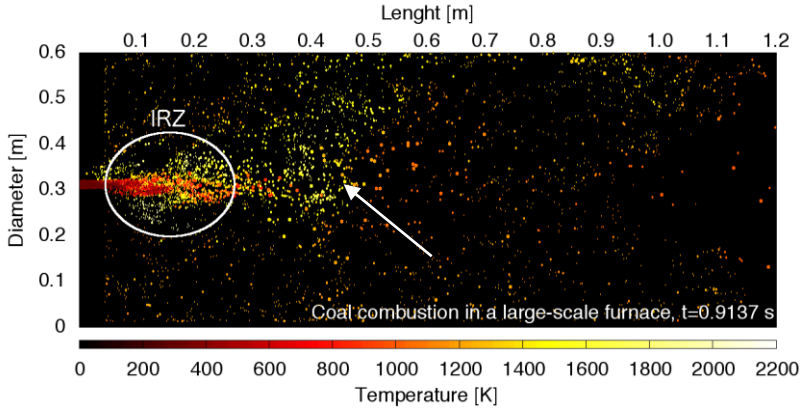

Figure 3: Particle instantaneous location within the furnace at the physical runtime of t = 0.9137 s.

Table 2 lists the properties of the coal particles that were tracked. During devolatilization particles are subjected to different heating rates, varying up to one order of magnitude. Heating rates vary between 10^4 and 10^5 $K.s^{-1}$. The larger the size, the longer it takes to reach a high burnout. For most of the tracked particles 0.4 s is enough to ensure a high burnout.

Table 2: Properties of 6 particles from the sample for history tracking.

Particle ID	a	b	c	d	e	f
Initial size [μm]	15	15	46	7.5	76	197
Heating rate during devolatilization [K/ms]	191	144	324	175	99	42
Burnout at t = 0.24 s [%]	99.8	99.7	99.6	99.7	90.4	62.9

Figure 4 shows the particle history of the particles listed in Table 2. The figure shows particle temperature and burnout as well as the gas temperature, and O_2 and CO_2 mass fractions as seen by the particle. The particles are close to thermal equilibrium with the surrounding gas and are subjected to both heating and cooling due to the particular characteristics of the flow [5]. Particles are initially surrounded by a gas of high temperature and little or no surrounding O_2 and subsequently move to a region of lower temperatures with the presence of O_2.

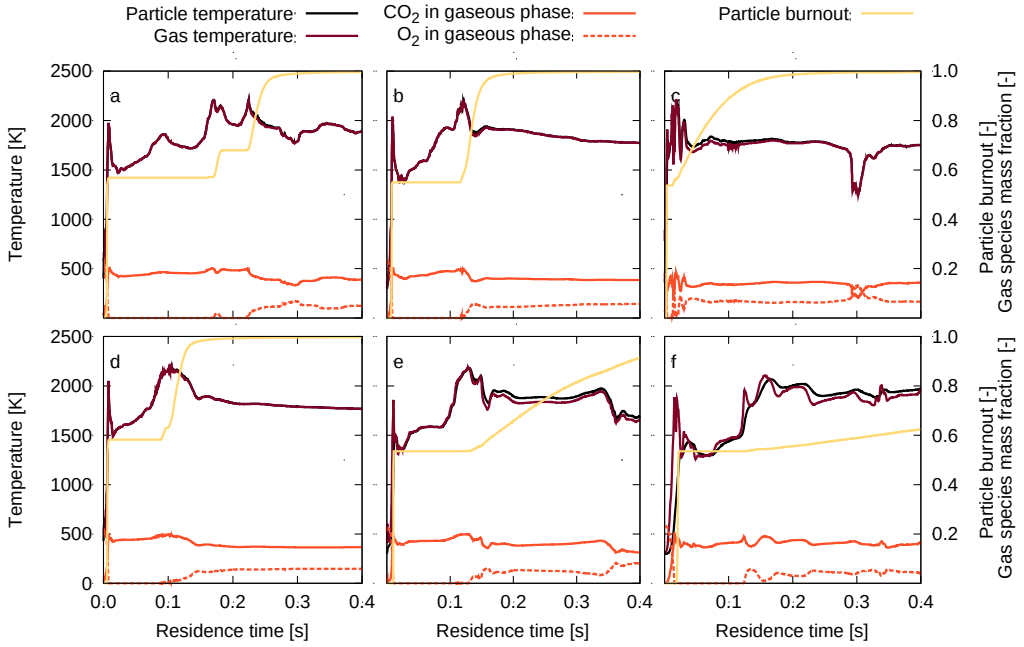

Figure 4 – Particle combustion history of 6 selected coal particles.

The burnout curve shows two slopes, the first corresponding to devolatilization and the second corresponding to char combustion, with a plateau in between. Particle devolatilization occurs immediately after injection lasting a few milliseconds owing to the high heating rates. Char combustion does not necessarily follow devolatilization immediately and the delay can take up to 0.15nd seconds depending on the surrounding conditions. The char combustion model used in this work only considers the reaction between C (solid) and O_2, producing CO. Char combustion rates also vary significantly as typified by the different burnout slopes.

Figure 5 shows the particle temperature as a function of gas temperature and the heating rate during devolatilization as a function of particle temperature, both with points coloured by particle diameter. There is a strong tendency for thermal equilibrium for smaller particles (<100 μm) and to a certain degree also for larger particles (>100 μm). In the region bellow ~1200 K the scattered points cluster mainly in the thermal equilibrium curve ($y = x$). Still in this region, above the thermal equilibrium curve a few points can be found with different sizes corresponding to hot particles that have just been entrained in the cooler zones of the furnace. Above ~1200 K, large particles also tend to cluster close to the thermal equilibrium curve, in the region that resembles a leaf shape, with a maximum deviation of less than 20 %. Below the thermal equilibrium curve, the points corresponding to larger particles cluster preferentially at temperatures lower than the gas temperature, due to their higher thermal inertia. The right plot reinforces the observations of thermal inertia effects by showing that during devolatilization larger particles (>200 μm) are subjected to much lower heating rates than smaller particles – up to 3 orders of magnitude lower.

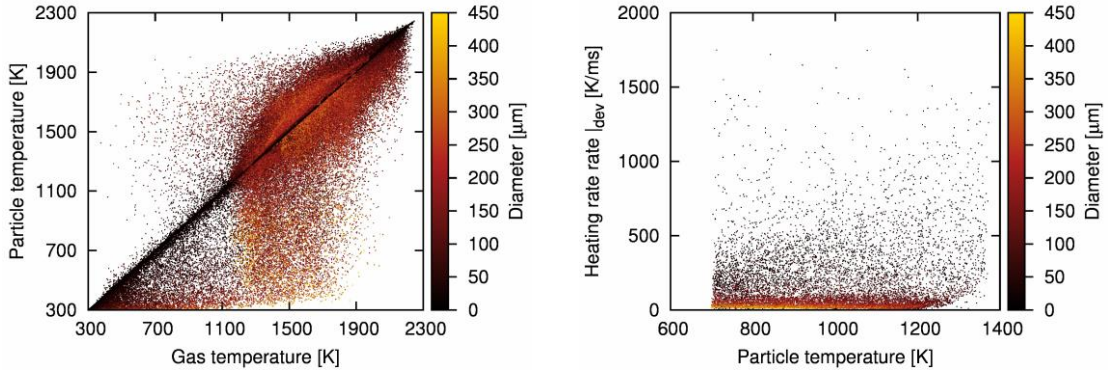

Figure 5 – Particle temperature as a function of gas temperature (left) and heating rate during devolatilization as a function of particle temperature (right).

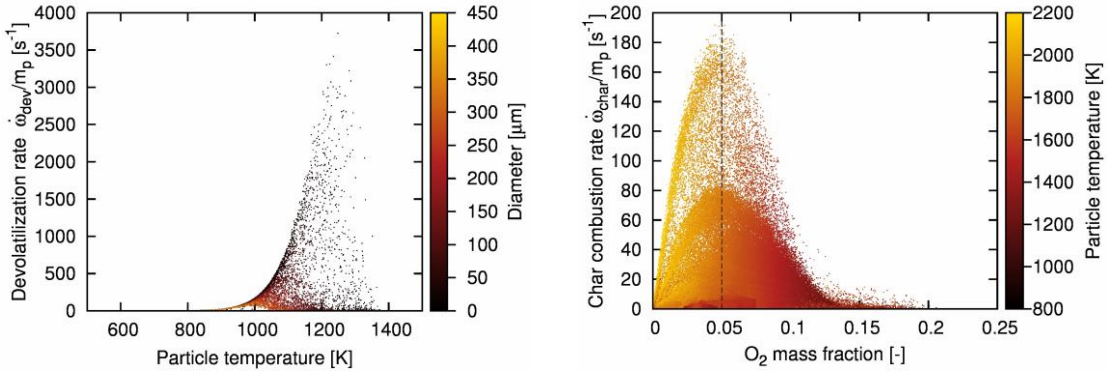

Figure 6 – Devolatilization rate as a function of particle temperature (left) and char combustion rate as a function of oxygen mass fraction (right).

Figure 6 shows the devolatilization rate as a function of particle temperature with points coloured by diameter and the char combustion rate as a function of oxygen mass fraction with points coloured particle temperature, both normalized by the particle mass. Note that a lower number of points is plotted in the left plot, this is due to the accumulative feature of the flow and the slow nature of char combustion. Devolatilization rates are typically higher for smaller particles (<100 μm) as they are subjected to higher

heating rates. Char combustion rates are at their peak at a O_2 mass fraction of 0.05 and a particle temperature of approximately 1900 K. Left of the vertical dashed line, char combustion is limited by the availability of oxygen and on the right side char combustion rate is limited by temperature. The vertical scattering of the points is due to diffusion limitations – diffusion decreases when temperature decreases – and also due to structural properties of the particles (diameter, surface area and pore size).

6 CONCLUSIONS

A massively parallel large eddy simulation of coal combustion in a large-scale laboratory furnace is presented. Coal combustion is modelled using classical models with optimized kinetic constants for devolatilization. Particle history is tracked giving an insight to coal combustion that currently is only available in LES. It was observed that in this flow, particles are subjected to various heating rates, including heating and cooling. Devolatilization occurs immediately after injection and char combustion rate and final stages of burnout are dependent on subsequent particle trajectory. Particles tend to be in a quasi-thermal equilibrium state with the surrounding gas, although deviations were observed particularly for particles larger than 200 μm owing to their higher thermal inertia. Thermal inertia also affects devolatilization, as larger particles present lower devolatilization rates in consequence. In the studied furnace the optimum conditions for char combustion were found to be at an O_2 mass fraction of 0.05 and a particle temperature of 1900 K. Char combustion limitations arise from low temperatures, low oxidizer availability and low oxidizer diffusion.

ACKNOWLEGMENTS

This work was partially supported by Fundação para a Ciência e Tecnologia (FCT), through IDMEC, under LAETA Pest-OE/EME/LA0022. M. Rabaçal acknowledges FCT for the provision of Scholarship SFRH/BD/72583/2010. M. Rabaçal and A.M. Kempf acknowledge PRACE for awarding access to SuperMUC based at the Leibniz-Rechenzentrum, Munich, Germany (project 2013081677). The PRACE grant was made possible by the access given to the Cray of the Centre for Computational Sciences and Simulation (CCSS), University of Duisburg-Essen.

REFERENCES

[1] WEC (2013). *2013 World Energy Issues Monitor*, World Energy Council, London, United Kingdom.

[2] P Edge, M Gharebaghi, R Irons, R Porter, R Porter, M Pourkashanian, D Smith, P Stephenson, A Williams (2011). Combustion modelling opportunities and challenges for oxy-coal carbon capture technology. *Chemical Engineering Research & Design* **89**(9):1470–1493.

[3] R Kurose, H Makino (2003). Large eddy simulation of a solid-fuel jet flame. *Combustion and Flame* **135**:1–16.

[4] P Edge, S Gubba, L Ma, R Porter, M Pourkashanian, A Williams (2010). LES modelling of air and oxy-fuel pulverised coal combustion-Impact on flame properties. *Proceedings of the Combustion Institute* **33**:2709–2716.

[5] M Rabacal, BM Franchetti, F Cavallo Marincola, F Proch, M Costa, C Hasse, AM Kempf (Accepted). Large eddy simulation of coal combustion in a large-scale laboratory furnace. *Proceedings of the Combustion Institute.*

[6] S Badzioch, PGW Hawksley (1970). Kinetics of thermal decomposition of pulverized coal particles. *Industrial & Engineering Chemistry Process Design and Development* **9**(4):521–530.

[7] IW Smith (1992). The combustion rates of coal chars: A review. *Symposium (International) on Combustion* **19**:1045–1065.

[8] JS Truelove (1987). Discrete-ordinate solutions of the radiation transport equation. *Journal of Heat Transfer* **109**(4):1048–1051.

[9] A Ribeirete, M Costa (2009). Detailed measurements in a pulverized-coal-fired large-scale laboratory furnace with air staging. *Fuel* **88**(1):40–45.

[10] B Franchetti, F Cavallo Marincola, S Navarro-Martinez, A Kempf (2013). Large Eddy simulation of a pulverised coal jet flame. *Proceedings of the Combustion Institute* **34**:2419–2426.

[11] DK Lilly (1967). The representation of small-scale turbulence in numerical simulation experiments. In *Proceedings of the IBM Scientific Computing Symposium on Environmental Sciences*, IBM Data Processing Division, White Plains, New York.

[12] A Kempf, S Wysocki, M Pettit (2012). An efficient, parallel low-storage implementation of Klein's turbulence generator for LES and DNS. *Computers and Fluids* **60**:58–60.

Session 4

Chairman

Maria Manuela Carvalho Lemos Lima | U.Minho

This page was intentionally left blank

Effects of viscous heating on the heat transfer between a rotating cylinder and the surrounding fluid medium

AA Soares[1,3,4], L Caramelo[1,4], Abel Rouboa[2,3]

[1]Department of Physics/ECT, University of Trás-os-Montes e Alto Douro, Quinta de Prados, 5000-801 Vila Real, Portugal
[2]Department of Engineering/ECT, University of Trás-os-Montes e Alto Douro, Quinta de Prados, 5000-801 Vila Real, Portugal
[3]INEGI, Faculty of Engineering, University of Porto, 4200-465 Porto, Portugal
[4]CITAB, University of Trás-os-Montes e Alto Douro, Quinta de Prados, 5000-801 Vila Real, Portugal
email: asoares@utad.pt, lcaramel@utad.pt, rouboa@utad.pt elsac@fe.up.pt

ABSTRACT: This paper examines numerically the effects of viscous heating on the forced convection heat transfer between an unconfined rotating cylinder and the surrounding fluid medium. The forced convection heat transfer across an isothermal rotating cylinder is investigated for Reynolds numbers $1 \le Re \le 40$, dimensionless rotational velocities $0 \le \alpha \le 3$, Prandtl numbers Pr = 1 and 100, and Brinkman numbers $0 \le Br \le 1$. The isotherm patterns are presented for the varying values of the Brinkman number, Prandtl number and rotational velocity rate in the steady regime. The variation of the local and average Nusselt numbers with Reynolds number, Brinkman number, Prandtl number and rotational velocity rate are also presented for the range of conditions studied.

KEY-WORDS: Viscous heating; Rotating cylinder; Prandtl number; Nusselt number; Brinkman number.

1 INTRODUCTION

In most practical situations, viscous heating (dissipation) always contribute, how so ever small, to the overall rate of heat transfer between rotating cylinders and the surrounding fluid medium. This contribution progressively increases with the increasing velocity of the imposed flow, *i. e.*, with the increasing of the Reynolds number and/or the cylinder rotation rate. Hence, the temperature gradients induced by the strain rates are influenced by the Reynolds number and the cylinder rotation rate, which, in turn, influence the rate of heat transfer (or the Nusselt number). The viscous dissipation effects tend to be significant when either the viscosity is large or rate of shearing is large and/or when the fluid has a low thermal conductivity, which increases the temperature gradients. This phenomenon can also give rise to local hot (cold) spots which may be detrimental to the processing of temperature-sensitive materials.

It has clearly been shown that in channel (pipe/duct) Brinkman numbers are of the order of 1 whereas in porous media flows they can be as large as 1000, *e.g.* [1-5]. Because the rotational velocity is not very high, the problem of the flow past a rotating cylinder is closer to the channel flow situation, and choice of range $0 \le Br \le 1$ is reasonable from a practical standpoint.

The aims of the present study is to investigate numerically the heat transfer characteristics between the 2D laminar incompressible flow and a rotating circular cylinder taking into account the viscous heating, and then to further understand the corresponding underlying mechanism. For this study, we will concentrate on discussing the combined effects of viscous heating, rotational speed and Prandtl number on the heat transfer for a constant temperature imposed on the surface of the cylinder. Results elucidating the effect of Brinkman, Reynolds and Prandtl numbers on the local and surface-averaged Nusselt numbers are presented and discussed herein. The results are found to be in a good agreement with numerical data for a rotating circular cylinder without viscous dissipation [6, 7].

2 GOVERNING EQUATIONS AND BOUNDARY CONDITIONS

Consider a uniform and incompressible flow of a Newtonian fluid past an unconfined rotating circular cylinder of diameter *d*. Cylinder is rotating in a counterclockwise direction with constant angular velocity Ω. The approaching velocity of the fluid is U_∞ and the ambient temperature is assumed to be T_∞. The thermal boundary condition at surface of the cylinder is assumed to be isothermal with temperature T_w. The effect of temperature variation on thermophysical fluid properties (density ρ, specific heat at constant pressure c_p, thermal conductivity k, and viscosity μ) is considered negligible. The flow is assumed to be steady, laminar and two dimensional.

The two dimensional steady governing partial differential equations in their dimensionless form are written as follows:

– Continuity equation

$$\frac{\partial u}{\partial x}+\frac{\partial v}{\partial y}=0 \tag{1}$$

– *x*-component of momentum equation

$$\frac{\partial (uu)}{\partial x}+\frac{\partial (uv)}{\partial y}=-\frac{\partial p}{\partial x}+\frac{1}{Re}\left(\frac{\partial^2 u}{\partial x^2}+\frac{\partial^2 u}{\partial y^2}\right) \tag{2}$$

– *y*-component of momentum equation

$$\frac{\partial (uv)}{\partial x}+\frac{\partial (vv)}{\partial y}=-\frac{\partial p}{\partial y}+\frac{1}{Re}\left(\frac{\partial^2 v}{\partial x^2}+\frac{\partial^2 v}{\partial y^2}\right) \tag{3}$$

– energy equation

$$u\frac{\partial T}{\partial x}+v\frac{\partial T}{\partial y}=\frac{1}{RePr}\left(\frac{\partial^2 T}{\partial x^2}+\frac{\partial^2 T}{\partial y^2}\right)+\frac{Br}{RePr}\Phi \tag{4a}$$

where

$$\Phi=2\left(\frac{\partial u}{\partial x}\right)^2+2\left(\frac{\partial v}{\partial y}\right)^2+\left(\frac{\partial v}{\partial x}+\frac{\partial u}{\partial y}\right)^2 \tag{4b}$$

is the viscous dissipation function for a incompressible flow. In physical terms, the relative measure of the heat produced due to viscous dissipation and that transferred by conduction is quantified by the Brinkman number (*Br*).

The dimensionless groups appearing in equations (2) to (4) are defined as:

– Reynolds number (*Re*)

$$Re=\frac{\rho U_\infty d}{\mu} \tag{5}$$

– Prandtl number (*Pr*)

$$Pr=\frac{c_p \mu}{k} \tag{6}$$

– Brinkman number (*Br*) for the constant temperature boundary condition

$$Br=\frac{\mu U_\infty^2}{k(T_w-T_\infty)}. \tag{7}$$

Furthermore, the governing equations (1)–(4) have been rendered dimensionless using the following scaling variables: U_∞ for the velocities, ρU_∞^2 for the pressures and *d* for the lengths. The temperature is made dimensionless by using T_w-T_∞.

The physically realistic boundary conditions in dimensionless form for the flow across a rotating circular cylinder are written as follows:

– at the inlet boundary

$$u=1,\ v=0 \text{ and } T=0 \tag{8a}$$

– on the surface of the cylinder

$$u=-\alpha\sin(\theta),\ \ v=-\alpha\cos(\theta) \tag{8b}$$

where the dimensionless rotational velocity α, for the angular velocity Ω of the cylinder with diameter *d*, is

$$\alpha = \frac{d\,\Omega}{2U_{\infty}}. \tag{8c}$$

Thermal condition on the cylinder surface is given by

$$T = 1 \tag{8d}$$

at the exit boundary.

The standard default option in *Fluent* known as "outflow" has been used at the exit boundary. Qualitatively, this option is similar to the homogeneous Neumann conditions, that is,

$$\frac{\partial u}{\partial x} = 0,\ \frac{\partial v}{\partial x} = 0 \text{ and } \frac{\partial T}{\partial x} = 0\ . \tag{8e}$$

The numerical solutions of equations (1)–(4) together with the above-noted boundary conditions yields the pressure, velocity and temperature fields which in turn can be processed further to obtain the values of the drag coefficients, local and averaged Nusselt numbers for the thermal boundary condition investigated.

In this present work, the Navier-Stokes equations have been solved using Fluent. The O-type mesh, with structured quadrilateral cells of non-uniform mesh spacing, has been used. The two-dimensional, steady, laminar, segregated solver module of Fluent was used to solve the incompressible viscous flow on the full computational domain for varying conditions of Re, Br, and Pr. The semi-implicit method for the pressure linked equations (SIMPLE) scheme was used for solving the pressure-velocity coupling. The second order upwind scheme has been used to discretize the convective terms in the governing equations. The Gauss-Siedel point-by-point iterative method in conjunction with the algebraic multi-grid (AMG) method solver was been used to solve the system of algebraic equations. Relative convergence criteria of 10–9 for the continuity, and x – and y -components of the velocity were prescribed. In addition, the values of the drag coefficients were also monitored and only when these values had stabilized to four significant digits were these values finally accepted.

3 RESULTS

3.1 Isothermal patterns

Representative plots showing the dependence of the isothermal contours, in the vicinity of the rotating cylinder (α = 3), on the Reynolds number (*Re*), Brinkman number (*Br*), and Prandtl number (*Pr*) are presented in Figures 1-4. For fixed values of the *Re* and *Pr* numbers, an increasing of *Br* results in a separation between the isothermal contours as a consequence of the increases of the temperature around rotating cylinder. For fixed values of *Re* and *Br* numbers an opposite behaviour is observed with increasing Prandtl number.

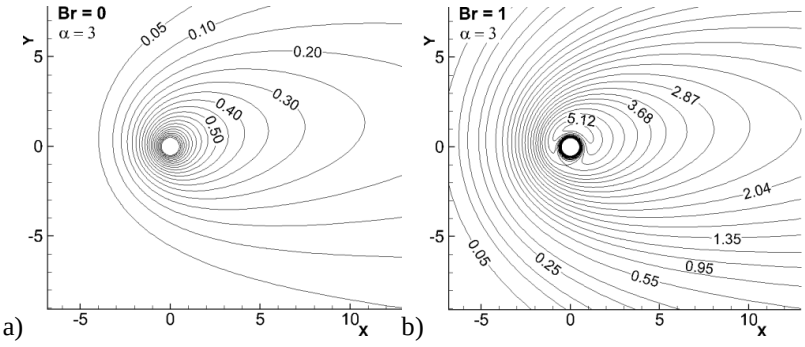

Figure 1: Isothermal contours for α = 3, *Re* =1, *Pr* = 1.a) *Br* = 0, b) *Br* = 1.

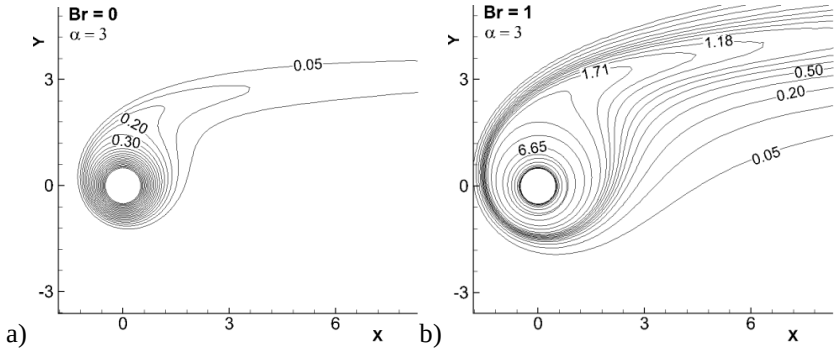

Figure 2: Isothermal contours for α = 3, *Re* = 1, *Pr* = 100. a) *Br* = 0, b) *Br* = 1.

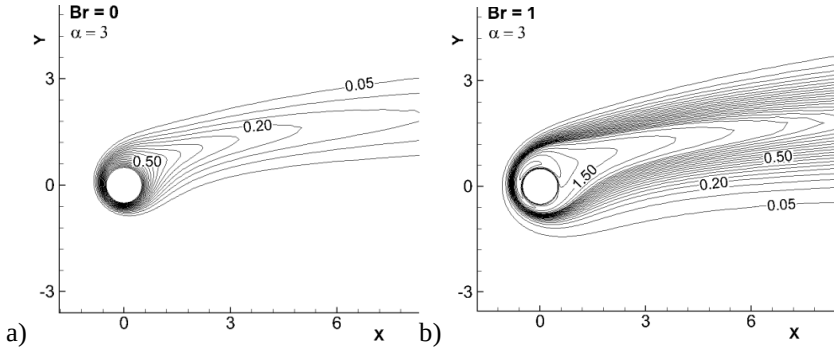

Figure 3: Isothermal contours for α = 3, *Re* = 40, *Pr* = 1. a) *Br* = 0, b) *Br* = 1.

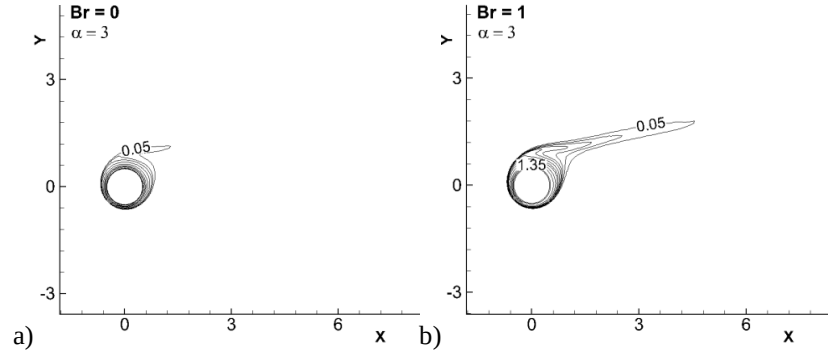

Figure 4: Isothermal contours for α = 3, *Re* = 40, *Pr* = 100. a) *Br* = 0, b) *Br* = 1.

3.2 Local Nusselt number

Figure 5 shows the effect of Brinkman number *Br* on the local Nusselt number profiles, over the cylinder surface, for dimensionless rotational velocity α = 3. It was shown that the higher values of *Br* decreases the local Nusselt number for both conditions *Re*=1 and *Pr* = 1, and *Re* = 40 and *Pr* = 100. Despite the higher Prandtl number (*Pr* =100) the aforementioned behaviour is more pronounced for *Re*=1 and *Pr* = 1 than for *Re* = 40 and *Pr* = 100.

The negative values of Nu can be attributed to the role of viscous dissipation, which is equivalent to that of an energy source, due to the internal heating effect of viscous dissipation on fluid temperature. Consequently, an increase in viscous dissipation changes the overall heat balance. As a result, for fixed values of α, Re and Pr, when Br exceeds a critical value, the heat generated internally by the viscous dissipation process will overcome the effect of the cylinder surface heating under favourable conditions, resulting in negative Nu.

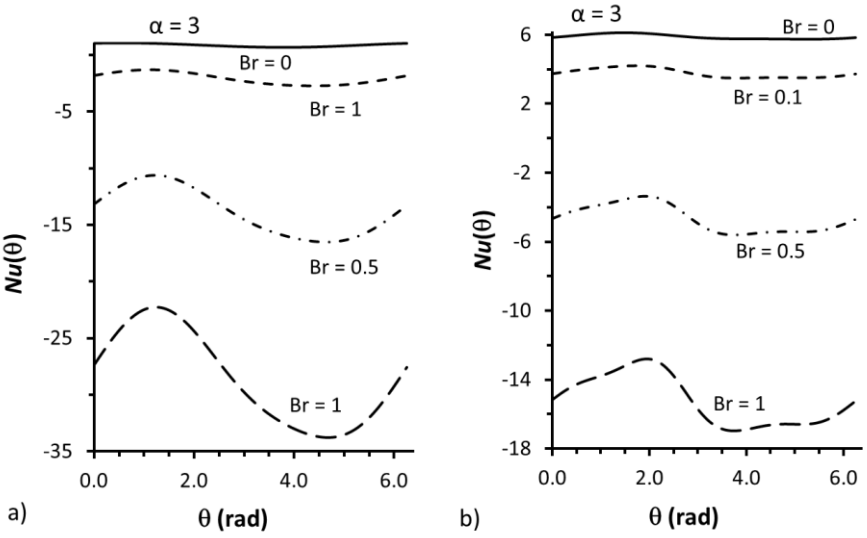

Figure 5: Local Nusselt number *Nu* for α = 3. a) *Re* = 1 and *Pr* =1, b) *Re* = 40 and *Pr* =100.

3.3 Average Nusselt number

For a fixed value of *B*r and α = 0, the magnitude of the average *Nu* number increases with increasing *Re* number for both *Pr* =1 and 100. This can be explained as when *Re* number increases the inertia of flow increases thereby increasing the heat transfer. The decrease in the average *Nu* number with *Br* is more pronounced for higher values of *Re* and lower values of *Pr*.

An increase in the value of the *Br* number, the average *Nu* number decreases for the fixed values of the *Re*, α and *Pr* numbers. The negative values of *Nu* indicate that heat transfer occurs from fluid to the cylinder, see Figure 5 and 6. The local and average Nusselt numbers increase with increasing values of Reynolds, Prandtl, and with the decreasing values of the Brinkman number and rotational velocity.

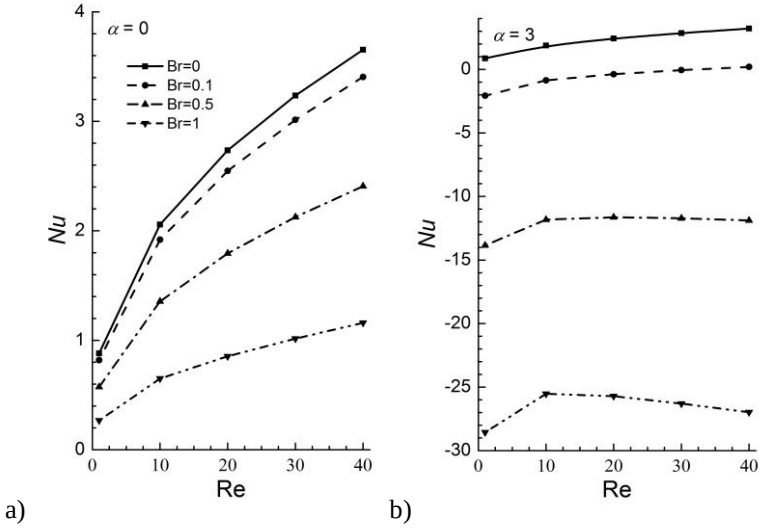

Figure 6: Average Nusselt number *Nu* for *Pr* =1. a) α = 0 and b) α = 3.

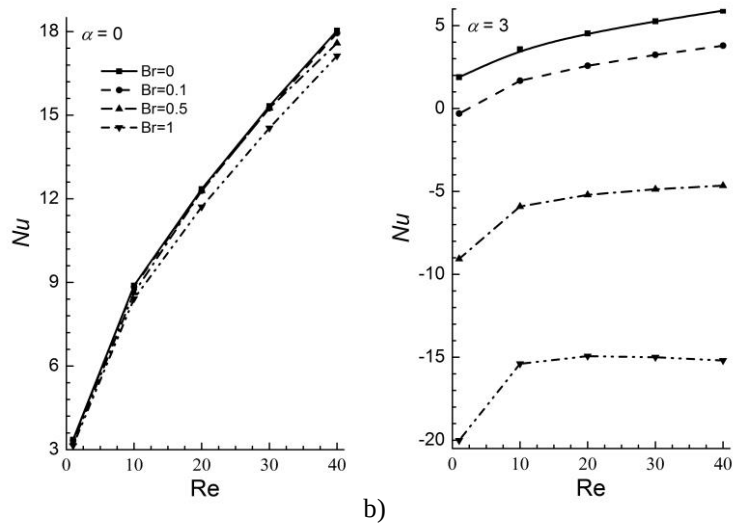

a) b)

Figure 7: Average Nusselt number *Nu* for *Pr* = 100. a) α = 0 and b) α = 3.

4 CONCLUSIONS

This paper presents the effect of viscous dissipation *Br* on heating on the forced convection heat transfer between an unconfined rotating cylinder and the surrounding fluid medium.

Increasing value of the Brinkman number lowers the values of local and average Nusselt numbers. Brinkman and Prandtl numbers have opposite effects on the distribution of the isothermal around rotating cylinder and consequently on the local and average Nusselt numbers.

Broadly, the rate of heat transfer increases with the increasing Reynolds and Prandtl numbers, and with the decreasing values of the Brinkman number and rotational velocity. The dependence is strongest on the Reynolds number; however it is possible to control the rate of heat transfer by imposing to the flow the appropriate combinations of the rotational velocity, Reynolds number, Prandtl number and Brinkman number in a given application.

REFERENCES

[1] PM Coelho, FT Pinho (2009). A generalized Brinkman number for non-Newtonian duct flows. *Journal of Non-Newtonian Fluid Mechanics* **156**:202–206.

[2] RP Chhabra, AA Soares, FM Ferreira, L Caramelo (2007). Effects of viscous dissipation on heat transfer between an array of long circular cylinders and power law fluids. *Canadian Journal of Chemical Engineering* **85**:808–816.

[3] K Hooman, A Pourshaghaghy, A Ejlali (2006). Effects of viscous dissipation on thermally developing forced convection in a porous saturated circular tube with an isoflux wall. *Applied Mathematics and Mechanics* **27**:617–626.

[4] O Aydin (2005). Effects of viscous dissipation on the heat transfer in forced pipe flow. Part 1: Both hydro-dynamically and thermal fully developed flow. *Energy Conversion and Management* **46**:757–769.

[5] O Aydin (2005). Effects of viscous dissipation on the heat transfer in forced pipe flow. Part 2: Thermally developing flow. *Energy Conservation and Management* **46**:3091–3102.

[6] V Sharma, AK Dhiman (2012). Heat transfer from a rotating circular cylinder in the steady regime: effects of Prandtl number. *Thermal Science* **16**:79–91.

[7] RP Bharti, RP Chhabra, V Eswaran (2007). A Numerical Study of the Steady Forced Convection Heat Transfer from an Unconfined Circular Cylinder. *Heat and Mass Transfer* **43**(7) :639–648.

V Conferência Nacional de Mecânica dos Fluidos, Termodinâmica e Energia
MEFTE 2014, 11–12 Setembro 2014, Porto, Portugal
APMTAC, 2014

Comparison of different formulations for transient radiative transfer problems in absorbing and scattering three-dimensional media

P Pereira[1], M Roger[2], PJ Coelho[1]

[1]Mechanical Engineering Department, IDMEC, LAETA, Instituto Superior Técnico, Universidade de Lisboa, Av. Rovisco Pais, 1049-001 Lisboa, Portugal
[2]Université de Lyon, CNRS, CETHIL, UMR5008, F-69621 Villeurbanne, France
email: pmcpereira7@gmail.pt, maxime.roger@insa-lyon.fr, pedro.coelho@tecnico.ulisboa.pt

ABSTRACT: Four different formulations for the solution of transient radiative transfer in a three-dimensional absorbing and scattering medium are compared in this work. Two of these formulations are frequently used and well-known in the radiative transfer community: the radiative transfer equation, and the diffusion equation, based on the P1 approximation. The other two are based on a multiscale approach, where the radiative intensity is decomposed into a macroscopic and a mesoscopic components. One of these multiscale models is called the hybrid transport-diffusion model, while the other is called the micro-macro model. The major difference between the two multiscale models lies in the way the macroscopic component is defined. These multiscale models aim to improve the efficiency of the numerical simulation of radiative transfer in transient problems. This kind of problems appears, for example, in optical tomography applications, where the propagation of a laser inside a biological tissue must be simulated efficiently in order to determine the optical properties of the tissue and to detect the presence of tumours or inhomogeneities. The influence of the spatial and temporal discretization schemes is also investigated. The results show that second-order accurate discretization schemes greatly improve the solution accuracy when the optical thickness of the medium and the scattering albedo are large. The two multiscale models improve the efficiency of the calculations when the scattering optical thickness is large.

KEY-WORDS: Radiative transfer; Discrete ordinates method; P1 approximation; Diffusion approximation; Hybrid transport-diffusion model; Micro-macro model.

1 INTRODUCTION

As widely known, the interest in the study of transient radiative transfer has been increasing for the last few decades. Many research fields, such as optical tomography, laser micromachining, remote sensing and others make use of short pulse lasers that require to take into account transient effects [1].

Various models have been developed and tested over the years to solve the transient radiative transfer equation (RTE) [2] with different results and trade-offs, such as the Monte Carlo (MC), the finite volume method (FVM) and the discrete ordinates method (DOM). Although the RTE is extensively used, the approximate diffusion equation (DE) is sometimes preferred, particularly in optically thick media, due to the lower computational requirements.

In the present work, four three-dimensional radiative transfer formulations are compared: the RTE, the DE, the hybrid transport-diffusion model (HTD) [3] and the micro-macro model (MM) [4]. The last two formulations are multiscale models developed in our previous works. In the RTE, the radiation intensity is decomposed into a collimated component, associated to the laser beam incident on the domain under consideration, and a diffuse component. Hence, the RTE yields two transport equations, each one for a component of the radiation intensity. This is the first formulation considered in the present work. The second one is a simplified formulation obtained when the P1 and the diffusion approximations for the diffusive component are used, yielding the so-called diffusion equation. The two multiscale models tested in this study are based on the decomposition of the diffuse component of the radiation intensity into a macroscopic component and a mesoscopic one. The major difference between the two multiscale models lies in the way the macroscopic component is defined. In the HTD model, the macroscopic component is chosen equal to the solution of the diffusion equation, while in the MM model the macroscopic component is defined as the fluence rate (the integral of the radiative intensity over the solid-angle space).

In the present work, the efficiency of the various models, regarding accuracy and computational requirements, are compared for a three-dimensional test case related to optical tomography applications, following previous one-dimensional applications reported in [3-4].

2 THEORY

2.1 Radiative transfer models

2.1.1 Radiative transfer equation

The transient radiative transfer equation (RTE) for absorbing and scattering media can be written as [2]:

$$\frac{1}{c}\frac{\partial I}{\partial t}+\mathbf{u}\cdot\nabla I=-(k_a+k_s)I+k_s\int_{4\pi}p(\mathbf{u}\cdot\mathbf{u}')I'\,d\,\mathbf{u}' \tag{1}$$

where $I = I(\mathbf{x},\mathbf{u},t)$ represents the radiation intensity at location $\mathbf{x}$, propagation direction $\mathbf{u}$ and time t. The speed of light is represented by c, k_a is the absorption coefficient, k_s is the scattering coefficient, p is the normalized scattering phase function, $\mathbf{u}'$ is the incident direction and I' stands for $I=I(\mathbf{x},\mathbf{u}',t)$. When the medium is subjected to laser irradiance it is convenient to decompose the radiation intensity into its collimated component, I_c, and its diffuse component, I_d, according to $I(\mathbf{x},\mathbf{u},t) = I_c(\mathbf{x},t) + I_d(\mathbf{x},\mathbf{u},t)$. Thus, two equations are obtained:

$$\frac{1}{c}\frac{\partial I_c}{\partial t}+\mathbf{u}\cdot\nabla I_c=-(k_a+k_s)I_c \tag{2}$$

$$\frac{1}{c}\frac{\partial I_d}{\partial t}+\mathbf{u}\cdot\nabla I_d=-(k_a+k_s)I_d+k_s\int_{4\pi}p(\mathbf{u}\cdot\mathbf{u}')I_d'\,d\mathbf{u}'+k_s\,p(\mathbf{u}\cdot\mathbf{u}_c)I_c \tag{3}$$

Subscripts c and d stand for the collimated and diffusive components, respectively.

2.1.2 Diffusion equation

The diffusion equation (DE) can be deduced by integrating the RTE over a solid angle and applying the P1 approximation expressed by $I_d(\mathbf{x},\mathbf{u},t)\approx I_d^{\lim}(\mathbf{x},\mathbf{u},t)=\left(G_d^{\lim}(\mathbf{x},t)+3\mathbf{q}_d^{\lim}\cdot\mathbf{u}\right)/4\pi$, where G is the incident radiation, $\mathbf{q}$ the radiative heat flux vector, and superscript lim denotes the diffusion limit. The following DE is obtained for the diffuse component:

$$\frac{1}{c}\frac{\partial G_d^{\lim}}{\partial t}-\nabla\cdot\left(D\nabla G_d^{\lim}\right)=-k_aG_d^{\lim}+k_s\,I_c-\nabla\cdot\left(3Dk_s\,g\,I_c\,\mathbf{u}_c\right) \tag{4}$$

where D is the diffusion coefficient, given by $D=\left[k_a+k_s(1-g)\right]/3$, and g is the asymmetry factor of the phase function [2].

2.1.3 Micro-macro model

In the MM model the diffuse component is decomposed as $I_d(\mathbf{x},\mathbf{u},t)=G_d(\mathbf{x},t)/4\pi+\varepsilon_d(\mathbf{x},\mathbf{u},t)$. The incident radiation, G_d, is the macroscopic component, and it can be shown that it satisfies the following equation:

$$\frac{1}{c}\frac{\partial G_d}{\partial t}+\langle\mathbf{u}\cdot\nabla\varepsilon_d\rangle=-k_aG_d+k_s\,I_c \tag{5}$$

where symbol $\langle-\rangle$ represents the integral over the solid-angle space of 4π. The transport equation for the mesoscopic component, which results from the RTE, is the following [4]:

$$\frac{1}{c}\frac{\partial\varepsilon_d}{\partial t}+\mathbf{u}\cdot\nabla\varepsilon_d=-(k_a+k_s)\varepsilon_d+k_s\int_{4\pi}p(\mathbf{u}\cdot\mathbf{u}')\varepsilon_d'\,d\mathbf{u}'+k_s\,I_c\left(p(\mathbf{u}\cdot\mathbf{u}_c)-\frac{1}{4\pi}\right)+\frac{1}{4\pi}\left(\langle\mathbf{u}\cdot\nabla\varepsilon\rangle-\mathbf{u}\cdot\nabla G\right) \tag{6}$$

The system of equations (2), (5) and (6) is equivalent to the transient RTE. However, the exact boundary conditions are not preserved. In this case, artificial boundary conditions of Neumann type are used (see [4] for details).

2.1.4 Hybrid Transport-Diffusion model

The HTD model relies on a diffuse component decomposition similar to that used in the MM model, according to $I_d(\mathbf{x},\mathbf{u},t)=G_d^{\lim}(\mathbf{x},t)/4\pi+\varepsilon_d(\mathbf{x},\mathbf{u},t)$. The difference is that the macroscopic unknown in the HTD model is the incident radiation at the diffusive limit, $G_d^{\lim}$, which satisfies the diffusion equation (DE). The transport equation for the mesoscopic component, ε_d, is deduced from Eqs. (3) and (4) yielding:

$$\frac{1}{c}\frac{\partial \varepsilon_d}{\partial t}+\mathbf{u}\cdot\nabla\varepsilon_d=-(k_a+k_s)\varepsilon_d+k_s\int_{4\pi}p(\mathbf{u}\cdot\mathbf{u}')\varepsilon_d'\,d\mathbf{u}'+k_s\,I_c\left(p(\mathbf{u}\cdot\mathbf{u}_c)-\frac{1}{4\pi}\right)+ \\ +\frac{1}{4\pi}\left[\nabla\cdot\left(3Dk_s\,g\,I_c\,\mathbf{u}_c-D\nabla G_d^{\lim}\right)-\mathbf{u}\cdot\nabla G_d^{\lim}\right] \tag{7}$$

Unlike the MM model, the three governing equations (2, 4 and 7) are decoupled, which means that the equations for the HTD model are easier to solve than those for the MM model.

The exact boundary conditions for the radiation intensity are conserved in the HTD model. The boundary conditions for ε_d are defined according to that chosen for $G_d^{\lim}$, in order to match the exact radiation intensity on the walls. The Marshak boundary conditions were used for $G_d^{\lim}(\mathbf{x}_\mathbf{w},t)$ [2].

2.2 Numerical Schemes

The RTE for the diffuse component, Eq. (3), and Eqs. (6) and (7) of the multiscale models were solved using the discrete ordinates method (DOM). In the DOM, the governing integro-differential equation is replaced by a discrete set of *N* coupled equations that describe the radiation intensity (or mesoscopic component) field along *N* directions. A quadrature replaces the integrals over solid angles. In this study, an S_{12} quadrature was employed. The spatial discretization was carried out using the finite volume method. The convective-like term was discretized using either the step scheme (first-order accurate) or the CLAM scheme (second-order accurate). The transient term was also discretized using either a first order (explicit Euler) or a second-order (Runge-Kutta) scheme. The discretization schemes may be critical in order to achieve accurate results, depending on the radiative properties of the problem under consideration, as shown by the results presented below.

3 TEST CASE

A simple three-dimensional test case was considered to compare the accuracy and efficiency of the different models and discretization schemes. It consists of a three-dimensional cubic enclosure of side $L=1\text{m}$, schematically shown in Figure 1, containing a scattering and absorbing homogeneous medium and subjected to an incident laser source in one boundary, while the remaining boundaries are black (absorb all incident radiation) and cold (non-emitting). The medium is cold, as often considered in problems of light propagation in biological tissues, and the scattering is described by the Henyey-Greenstein phase function [2]. A pulse laser Gaussian in time and uniform in space is simulated according to:

$$I_c(\mathbf{x}_o,\mathbf{u},t)=I_o\,\delta(\mathbf{u}-\mathbf{u}_c)\exp\left[-4(\ln 2)\left((t-t_c)/t_p\right)^2\right],\quad 0<t<2t_c \tag{8}$$

where $\mathbf{x}_o$ is the emitting wall location, δ is the Dirac delta function and I_o is the maximum radiative intensity of the pulse, which occurs at $t = t_c = 3t_p$. A dimensionless time parameter defined as $t_p^*=c(k_a+k_s)t_p$ is fixed equal to 0.5. The laser is normal to the boundary (see Figure 1). After $2t_c$ the medium is free from irradiation. In this work we are concerned with the temporal signature of the incident radiation at the wall opposite to the laser. This is quantified by the dimensionless transmittance given by:

$$T(t)=T_c(t)+T_d(t)=\frac{I_c(\mathbf{x}_L,\mathbf{u},t)}{I_o}\mathbf{u}_c\cdot\mathbf{n}+\int_{2\pi}\frac{I_d(\mathbf{x}_L,\mathbf{u},t)}{I_o}(\mathbf{u}_c\cdot\mathbf{n})d\mathbf{u} \tag{9}$$

where $\mathbf{x}_L$ is the wall located at (x=L, y, z) and $\mathbf{n}$ is the unit vector normal to the wall in positive x direction.

A simulation is defined by three main optical parameters: optical thickness, $\tau=(k_a+k_s)\times L$, albedo, ω, and asymmetry factor, g. The influence of each individual parameter on the transmittance is investigated. A previously validated Monte Carlo algorithm [3] is used to provide benchmark results.

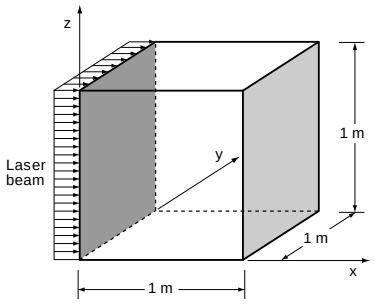

Figure 1: Schematic of the test case.

4 RESULTS

The enclosure is divided into 50 divisions in each direction ($N_x = N_y = N_z = 50$), resulting in $\Delta x = \Delta x = \Delta x = 0.02$ m, and the time step is defined as $\Delta t = \alpha \cdot \Delta x / c$, for the RTE, HTD and MM formulations, and as $\Delta t = \alpha \cdot (\Delta x)^2 / (10D \cdot c)$ for the DE, where the stability parameter α was set to 0.5.

We first investigate the influence of the numerical schemes. A relatively demanding scenario ($\tau = 20$, $\omega = 0.5$, $g = 0.3$) was chosen to magnify the differences between the various discretization schemes. Figure 1(a) shows the results obtained using the first-order step and Euler explicit schemes. The numerical errors are very large for all the formulations, taking the Monte Carlo solution as reference. It is important to point out that the errors would be much smaller for lower values of τ, ω or g, but we have chosen the present values to highlight the differences between the discretization schemes, as mentioned above. The error in the prediction of the maximum transmittance is of the order of magnitude of the collimated peak itself, resulting in a transmittance curve that has two peaks. This phenomenon, also known as false scattering, generates a non-physical solution, since the transmittance becomes different from zero well before the first collimated photons reach the boundary $x = L$ at $t = L/c = 3.33\times10^{-9}$ s. Decreasing the mesh size and/or the time step improves the solution, as shown in [5]. Another solution is to increase the order of the spatial and/or temporal scheme, as was done in Figure 2(b) using the CLAM/Euler schemes. The CLAM scheme largely reduces numerical diffusion, but the errors remain large. It is further shown in Figure 2(c) that a second-order scheme in time associated with a first-order one in space has no significant impact on the numerical diffusion, and the magnitude of the peak of the transmittance almost does not change. In Figure 2(d) second-order spatial and temporal discretization schemes were employed. In this case, the CLAM/Runge-Kutta schemes provide a sharper increase in transmittance, with less numerical diffusion, and a peak nearest to that observed with the MC reference solution.

Considering the above results, only second-order schemes were used in the following analysis. As in the previous simulations, a 50×50×50 grid is used and the time step remains the same. The radiative properties of the medium are $\tau = 20$, $\omega = 0.5$, $g = 0$ in the basis case, and then the effect of each property is individually investigated.

The results presented in Figure 3(a) show relatively good agreement of all the models with the MC reference solution. The DE predicts the earliest transmittance signal among all the models, but it simulates slightly better the sharp increase in transmittance. However, the residual diffuse transmittance for $t > 3.7\times10^{-9}$ s is largely underestimated. The RTE, MM and HTD originate almost similar solutions with some minor differences of the maximum transmittance and an overestimation of after-peak transmittance by the MM model. In Figure 3(b) the extinction coefficient was reduced to 10. As expected, the transmittance increases and the curve widens. The behaviour of the various models mentioned above for $\tau = 20$ is also observed for $\tau = 10$, but strongly attenuated.

The impact of increasing the albedo from 0.5 to 0.9 is shown in Figure 3(c). In the case of a large albedo, the collimated component of transmittance becomes negligible compared to the diffuse one. The curves now exhibit two peaks: the first one at $t \approx 3.6\times10^{-9}$ s, which is barely visible, is due to the collimated component, while the second peak, at $t \approx 7\times10^{-9}$ s, is due to the diffuse component. The transmittance curve is much smoother and the peak transmittance is achieved later than for $\omega = 0.5$, because the average residence time of the photons in the medium is higher due to the increased scattering coefficient. When scattering dominates over absorption, the P1 approximation, which assumes that the radiative intensity is almost isotropic, yields better accuracy inside the domain, and the performance of the HTD model is

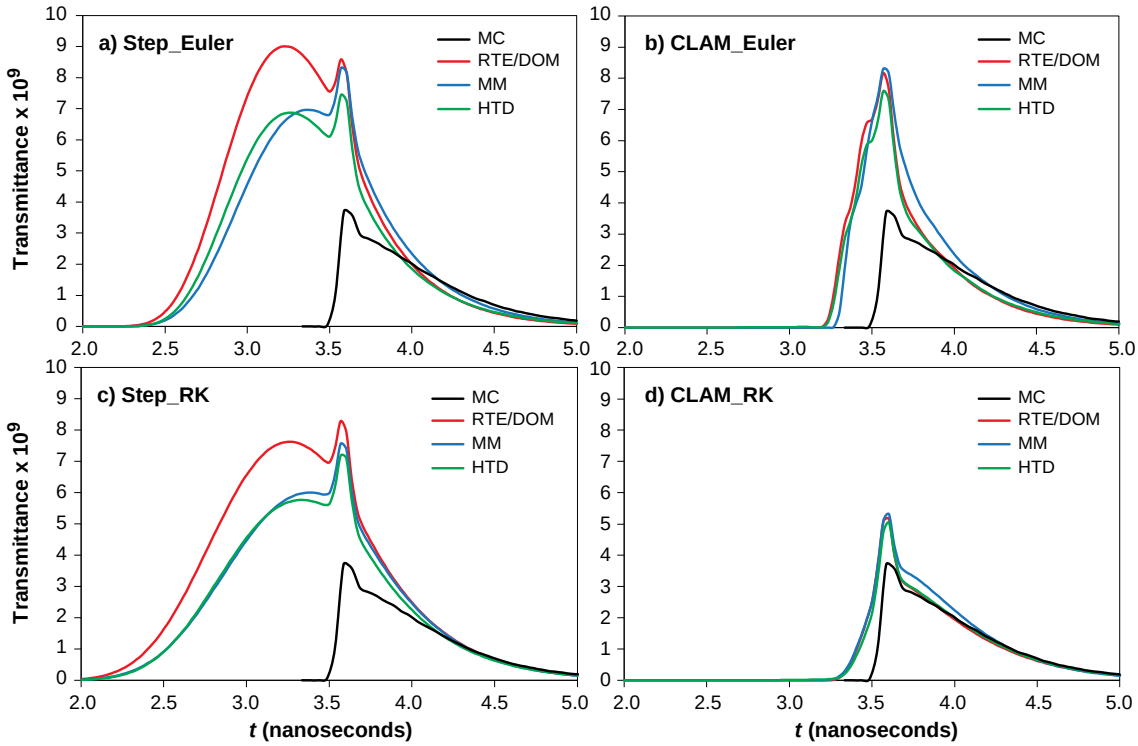

Figure 2: Influence of the spatial and angular discretization schemes on the transmittance through the boundary opposite to the incident laser pulse for $\tau = 20$, $\omega = 0.5$, $g = 0.3$.

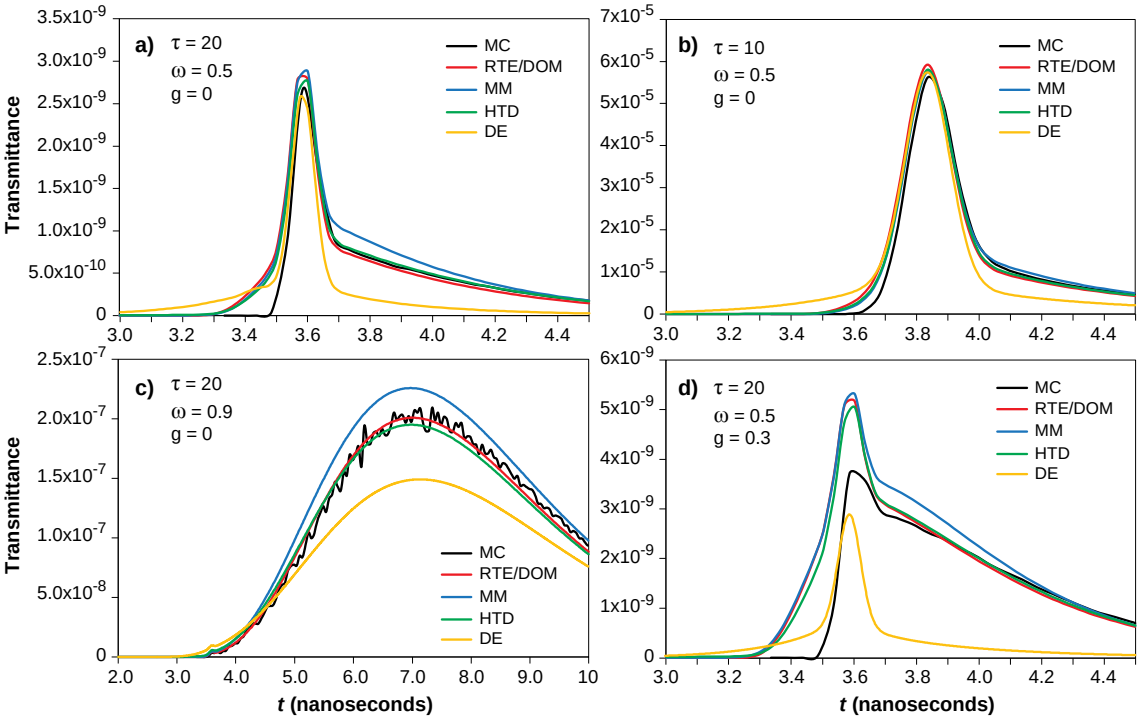

Figure 3: Influence of the radiative properties of the medium on the transmittance through the boundary opposite to the incident laser pulse.

improved. Still, the DE approximation yields a high error (up to 25%), mainly because its accuracy is poor near the boundaries of the domain, where transmittance is computed. The MM model overestimates the diffuse transmittance for this case (up to 12%). The MC oscillations could be overcome by increasing the number of photon bundles.

In Figure 3(d) the influence of the asymmetry factor g was studied. In the case of $g = 0.3$, the models are unable to correctly simulate the forward scattering, as formerly observed in Figure 2. This may be explained by the classical DOM error in forward peaked scattering media [3]. The DE yields again rather poor results, particularly in the prediction of the after-peak transmittance, with errors up to 85%. The other models perform better, despite the large errors in the prediction of the peak transmittance (35% for MM, 33% for RTE and 30% for HTD). These are caused by the lack of conservation of the scattered energy, as discussed in detail by Hunter and Guo [6], and may be successfully overcome by normalizing the phase function. Work is presently in progress to implement this normalization. The HTD multiscale model performs slightly better than RTE and MM, being closer to the MC reference results.

When the CLAM/Runge-Kutta schemes are used, the computational time required by the HTD is almost identical to that of the RTE ($t_{HTD} \approx 0.99\ t_{RTE}$) and twice as much the MM computational time ($t_{HTD} \approx 2.05\ t_{MM}$). The computational time is much lower for the DE.

5 CONCLUSION

Four different formulations for transient radiative transfer are compared, in three-dimensional absorbing and scattering media. The performance of these formulations is investigated using either first or second-order spatial and temporal discretization schemes and by changing the radiative properties of the medium. The effect of the numerical schemes on the accuracy of the models is very important if the optical thickness of the medium and the albedo are large, and the scattering is anisotropic. In such a case, increasing the order of accuracy of the spatial discretization scheme has a greater impact on the accuracy than increasing the order of accuracy of the temporal discretization, but using second order schemes for both spatial and temporal discretization yields the most accurate results. Still, in more demanding scenarios, numerical diffusion, as well as the lack of conservation of scattered energy, may generate significant errors. The parametric study shows that the HTD multiscale model performs either similarly or better than the other models, depending on the radiative properties of the medium, and is more efficient than the RTE model. The DE model confirmed its limitations near the boundaries, where transmittance is defined, that are more obvious in more demanding scenarios. The MM multiscale model presents a very good relation between accuracy and computational time, but overestimates the diffuse transmittance.

ACKNOWLEDGMENTS

This work is financially supported by national funds through FCT – Fundação para a Ciência e Tecnologia under the project PTDC/EMS-ENE/1028/2012.

REFERENCES

[1] AJ Welch, MJC Van Gemert (2011). *Optical-Thermal Response of Laser-Irradiated Tissue*, 2nd edition, Springer, The Netherlands.

[2] MF Modest (2013). *Radiative Heat Transfer*, 3rd edition, Academic Press, New York, USA.

[3] M Roger, C Caliot, N Crouseilles, PJ Coelho (Submitted). A hybrid transport-diffusion model for radiative transfer in absorbing and scattering media. *Journal of Computational Physics*.

[4] M Roger, N Crouseilles, PJ Coelho (2014). The micro-macro model for transient radiative transfer simulations. In *Proceedings of the 15th International Heat Transfer Conference*, 10–15 Aug 2014, Kyoto, Japan.

[5] Z Guo, S Kumar (2002). Three-dimensional discrete ordinate method in transient radiative transfer. *Journal of Thermophysics and Heat Transfer* **16**(3):289–296.

[6] B Hunter, Z Guo (2012). Phase-function normalization in the 3-D discrete-ordinates solution of radiative transfer — Part I: Conservation of scattered energy and asymmetry factor. *Numerical Heat Transfer, Part B: Fundamentals* **62**:203–222.

V Conferência Nacional de Mecânica dos Fluidos, Termodinâmica e Energia
MEFTE 2014, 11–12 Setembro 2014, Porto, Portugal
APMTAC, 2014

Robust and accurate algorithm for wall-confined flows using incompressible SPH

Sh Khorasanizade, JMM Sousa

LAETA, IDMEC, Instituto Superior Técnico, Universidade de Lisboa, Av. Rovisco Pais, 1049-001 Lisboa, Portugal
email: shahab.khorasanizade@ist.utl.pt, msousa@ist.utl.pt

ABSTRACT: An accurate and robust implementation of ISPH has been used to test the performance of three new boundary condition treatments for wall-confined, incompressible flows. Our aim is to improve the capabilities of ISPH in the presence of solid walls, complex geometries and inflow/outflow regions. The new proposals have proved to allow significant improvements with respect to results available in the literature.

KEY-WORDS: Meshless; SPH; Incompressible flow; Wall boundary condition; Inflow/outflow BC.

1 INTRODUCTION

Smoothed Particle Hydrodynamics (SPH) is a Lagrangian technique where the medium under observation is modeled employing a number of discrete particles, whose movement describes the motion in the medium [1]. In order to calculate the particle variables, its interaction with the neighboring ones is accounted for through the use of a filtering procedure involving the use of a kernel function and, subsequently, by making a summation over all particle interactions. The underlying meshless character is a major advantage of SPH over traditional grid-based methods.

Two main methodologies are considered in the framework of SPH to simulate incompressible flows [2]. The first, called Weakly Compressible SPH (WCSPH) consists in the approximation of simulating an incompressible flow allowing for a small compressibility level. The second methodology, known as Incompressible SPH (ISPH), simulates the flow enforcing the incompressibility condition by means of a divergence-free velocity field, which generally brings up the need to solve a system of linear equations. The application of SPH in incompressible flow world started by the work of Morris *et al.* [3] and continued to this day. Although most of SPH studies are limited to free surface flows, thanks to its natural capabilities for the simulation of such flows, some other studies have been undertaken to improve the method for confined flows as well [2], [4]–[8].

In the framework of ISPH, a new method has been introduced by Hosseini and Feng [6], which is called rotational ISPH. With respect to the original ISPH [9], it showed considerably lower errors in the results of flow calculations. For example, at Reynolds number $Re = 1$, employing 10 particles along the edge of a square obstacle, the error obtained in original ISPH and rotational one are 20% and 5%, respectively. Due to the larger errors in original ISPH and the fact that there is no robust and accurate version of original ISPH yet, there is a strong need to find the best and the most robust algorithm and associated tools, despite that the rotational scheme has proven to generate good results, and faster convergence for flows at low *Re*.

The treatment of solid walls in SPH simulations, however, needs especial care. A variety of methods has been proposed, such as the use of image particles [9], dummy particles [2] and the Multiple Boundary Tangent method (MBT) [10], to name a few. Any of these methods may be used to place the particles inside the solid wall, whereas the choice of the velocity Boundary Condition (BC) is less straightforward and it has a large effect on the results as investigated by Basa *et al*. [11]. Some of these features have also been studied by González *et al*. [12] for various implementations. It was demonstrated that an inconsistent shear force calculation at initial steps can later be balanced by another boundary force appearing when slip velocities are present at the boundary. As an example, the foregoing issues become of great concern when dealing with confined flow problems such as the lid-driven cavity and a powerful remedy is proposed in the present work.

Problems with inflow and outflow sections are often treated within SPH by the specification of periodic BC. This generally requires the use of longer computational domains and some previous knowledge on

the value of the driving force to be prescribed. The latter disadvantage has been circumvented before via implementation of a time-dependent, self-adjusting driving force based on a ratio of flow rates [7]. This idea has also been used here in the deployment of a truly open BC treatment, for which very few examples can be found in the context of ISPH [6]. The novel method proposed for open BC enabled us to perform accurate simulations of unsteady flow problems in the presence of vortex shedding through the outflow boundary.

As mentioned earlier, its meshless character is a major advantage of SPH over traditional grid-based methods, especially when it comes to complex geometries. Anyhow, once the SPH particles reach a solid wall, no matter the complexity, they should feel the existence of it. A robust, general, fast and easy to implement algorithm is always required. In the context of SPH, complex walls can be simulated using either MBT [10] or semi-analytical approaches [13]. The former is computationally expensive as it over-generates particles inside the wall from single parent particle. In contrast, the later seems to effectively predict the flow with reasonable computational cost [14] for the lid-driven cavity and some open surface flows with complex geometries.

In the present work we introduce a new solid wall BC treatment via changing the velocity profile for the particles placed inside the wall, with the aim of calculating wall viscous forces more accurately. Later this method is used along with our new complex wall treatment, which assumes the solid wall to be formed by a number of connected segments, hereinafter called Segment Boundary Implementation (SBI). The newly developed Open BC is later tested in the flow over a circular obstacle at different values of *Re*. All of the above mentioned tools are applied to the standard ISPH algorithm proposed by Xu *et al.* [4], thus allowing us to skip the details of the method here. The reader is encouraged to thoroughly read the mentioned contribution.

2 METHODOLOGY

2.1 Solid wall BC treatment

The widely used technique of image particles [9] is employed to model the presence of solid walls. Throughout the present study, no-slip BC for velocity and a homogenous Neumann condition for pressure are used. The implementation of no-slip BC may be carried out in different ways (see, e.g., [3], [9]). As noted by Basa *et al*. [11], the no-slip condition obtained by the simple use of image particles [9] generally results in the underestimation of wall viscous forces. A correct evaluation of these forces is of great interest, so the foregoing authors have suggested the use of a linear extrapolation applied to the tangential velocity component. However, a new proposal still allowing major improvements in the calculation of the wall viscous forces is made here. It is built on the same idea as the concept of Morris *et al*. [3], but with a slightly different formulation. Namely, the present methodology is applied to both velocity components.

Similarly to [3], a parameter β is defined, but the following relation is used instead

$$\beta = max\left(\beta_{max}, 1+\frac{d_{BC}}{d_f} \right). \tag{1}$$

where β_{max} is an empirical parameter to be defined for the case of interest. The second term inside the parenthesis corresponds to a linear extrapolation of velocity inside the wall, where d_{BC} and d_f denote normal distances to the boundary of the image particle and the fluid particle, respectively. The velocity distribution of image particles is later shaped according to

$$\boldsymbol{u}_f - \boldsymbol{u}_{BC} = \beta\left(\boldsymbol{u}_f - \boldsymbol{u}_{wall}\right). \tag{2}$$

where the subscripts *f*, *BC* and *wall* represent fluid, image particle and wall values, in that order.

2.2 Algorithm for complex solid walls

In computer graphics there is not any “real” curve, but each object is represented by series of connected straight lines instead. Hence, one can always use the same technique to represent any wall in the context of SPH by simply placing a number of nodes (which do not necessarily participate in the flow computation) over the edge and connect each pair of nodes by a straight line. Doing so, the traditional image particle method [9] can be used to produce the particles with the corner correction [7]. This method allows the SPH codes to avoid the need of any knowledge of the curve function as only a series of lines is

used. Moreover, no over-creation of particles occurs, as each fluid particle in vicinity of the wall is just mirrored once with respect to the closest line or corner.

2.3 Open BC treatment

Earlier it was mentioned that no proper inflow/outflow BC exists in ISPH than can be used at high *Re* in complex flows. Here we use a time-dependent driving force [7], applying it to all the particles. In this way, we make sure the flow rate in remains constant in the computational domain and reduce the workload on the solver as the pressure in the field is divided into two quantities: solver pressure and driving-force-induced pressure. Two buffer regions are used at the inlet and outlet, with a prescribed velocity profile at the inlet; for the outlet region, as the fluid particles cross the exit plane and enter the buffer, their velocities are frozen (do not change anymore) and only their pressure is equalized to the fluid particle closest to them.

3 TEST CASES

3.1 Lid-driven cavity flow

In the present study, this fully wall-bounded flow is studied at a moderate, *Re* = 1000, using the modified solid wall BC treatment, and results are compared with those available in the literature. The value of β_{max} = 5 is used here. This was found as the largest usable value above which the simulation becomes computationally unstable. Unfortunately, the mechanism responsible for such a behavior is not completely understood yet. Figure 1 shows a comparison of vertical and horizontal velocity profiles obtained by the present method with respect to those of Ghia *et al.* [15], with a similar spatial resolution (*L*/130, *L* being the side length of cavity), and Xu *et al.* [4] employing a higher spatial resolution (*L*/160). Close agreement with the results from the benchmark and drastic improvement with respect to previous ISPH calculations are evident.

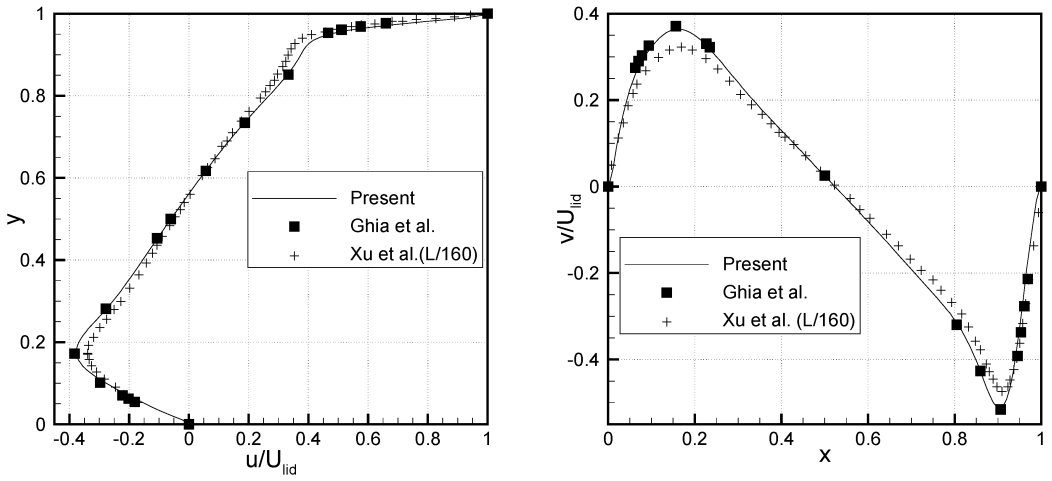

Figure 1: Velocity profiles along vertical (left) and horizontal (right) centerlines for *Re* = 1000 compared with the results of Xu *et al.* [4] and Ghia *et al.* [15].

3.2 Flow over a square obstacle

Our new proposal for inflow/outflow BC is tested in the flow over a square obstacle with a computational domain exhibiting the same characteristics as in [6]. The present results are compared with those of Breuer *et al.* [16]. Contrary to what Hosseini and Feng [6] showed based on their inflow/outflow BC, we have also considered unsteady flow regimes, but their treatment did not allow them to investigate such flows. The lowest spatial resolution (*B*/10, *B* being side length of the obstacle) used by Breuer *et al.* [16] was implemented, as our code is currently only capable of dealing with uniform resolutions. A comparison of total drag coefficient and Strouhal number values is shown in Table 1. It can be seen that the results are in good agreement.

Table 1: Comparison of total drag coefficient (C_d) and Strouhal (St) number in the flow over a square obstacle at two different Re.

		Present method	Breuer *et al.* [16]	Error %
Re = 60	C_d	3.17	3.26	2.72
	St	0.18	0.18	0.28
Re = 100	C_d	3.12	3.11	0.56
	St	0.20	0.21	2.38

3.3 Flow over a circular obstacle

The flow over a circular obstacle at moderate Re also exhibits complex features such as vortex shedding, thus making this case suitable to test our SBI method in an inflow/outflow arrangement. Here the flow is simulated at Re = 100, with a blockage ratio (ratio of obstacle diameter to channel width) of 20%. The present method predicts total drag and Strouhal number to be 2.38 and 0.272, respectively, whereas Prasad *et al.* [17], calculating these values with a high-order scheme and higher resolution, have obtained 2.76 and 0.272, respectively. An instantaneous velocity vector around the obstacle overlaid by the pressure contours is depicted in Figure 2. The separation points in both sides of the obstacle are clear, portraying the capabilities of this method, despite the lower spatial resolution used when compared to reference [17].

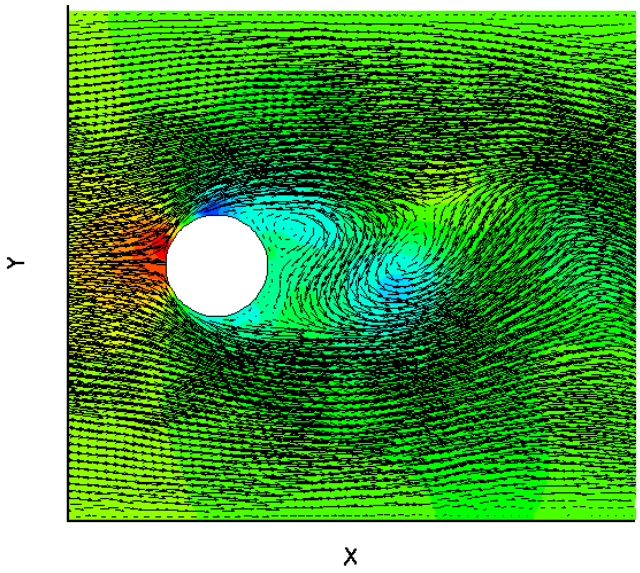

Figure 2: Instantaneous velocity vector field overlaid by the pressure contour for flow over a circular obstacle at Re = 100.

4 CONCLUSION

A fully incompressible SPH algorithm (ISPH) is implemented here to simulate internal incompressible flows. Three new boundary treatments are introduced to improve the capabilities of SPH around solid walls with complex geometries and inflow/outflow regions. Results have been compared with those available in the literature and good agreement has been demonstrated. Further improvements in meshless methods can lead to competitiveness with more traditional CFD methods and, since meshless methods can cope with complex geometries more easily, this may prove to be a decisive advantage with respect to traditional CFD methods.

ACKNOWLEDGMENTS

This work has been partially supported by Fundação para a Ciência e a Tecnologia (FCT) via grant PTDC/EME-MFE/103640/2008. The financial support for the Ph.D. studies of Sh. Khorasanizade via FCT scholarship SFRH/BD/75057/2010 is also acknowledged.

REFERENCES

[1] GR Liu, MB Liu (2003) *Smoothed Particle Hydrodynamics: A Meshfree Particle Method*, World Scientific Publishing Co. Pte. Ltd.

[2] ES Lee, C Moulinec, R Xu, D Violeau, D Laurence, P Stansby (2008) Comparisons of weakly compressible and truly incompressible algorithms for the SPH mesh free particle method. *Journal of Computational Physics* **227**:8417–8436.

[3] JP Morris, PJ Fox, Y Zhu (1997) Modeling low Reynolds number incompressible flows using SPH. *Journal of Computational Physics* **136**:214–226.

[4] R Xu, P Stansby, D Laurence (2009) Accuracy and stability in incompressible SPH (ISPH) based on the projection method and a new approach. *Journal of Computational Physics* **228**:6703–6725.

[5] S Shahriari, IG Hassan, L Kadem (2013) Modeling unsteady flow characteristics using smoothed particle hydrodynamics. *Applied Mathematical Modelling* **37**:1431–1450.

[6] SM Hosseini, JJ Feng (2011) Pressure boundary conditions for computing incompressible flows with SPH. *Journal of Computational Physics* **230**:7473–7487.

[7] S Khorasanizade, JMM Sousa, JF Pinto (2012). On the use of a time-dependent driving force in SPH simulations. In *Proceedings of 7th International SPHERIC Workshop*, Prato, Italy.

[8] MS Shadloo, A Zainali, M Yildiz, A Suleman (2012) A robust weakly compressible SPH method and its comparison with an incompressible SPH. *International Journal for Numerical Methods in Engineering* **89**:939–956.

[9] SJ Cummins, M Rudman (1999). An SPH Projection Method. *Journal of Computational Physics* **152**:584–607.

[10] M Yildiz, RA Rook, A Suleman (2009). SPH with the multiple boundary tangent method. *International Journal for Numerical Methods in Engineering* **77**:1416–1438.

[11] Basa, M., Quinlan, N. & Lastiwka, M. (2009). Robustness and accuracy of SPH formulations for viscous flow. *International Journal for Numerical Methods in Fluids* **60**:1127–1148.

[12] L González, A Souto-Iglesias, F Macià, A Colagrossi, M Antuono (2011). On the non-slip boundary condition enforcement in SPH methods. In *Proceedings of 6th International SPHERIC Workshop*, Hamburg, Germany.

[13] M Ferrand, DR Laurence, BD Rogers, D Violeau, C Kassiotis (2013), Unified semi-analytical wall boundary conditions for inviscid, laminar or turbulent flows in the meshless SPH method. *International Journal for Numerical Methods in Fluids* **71**:446–472.

[14] A Leroy, D Violeau, M Ferrand, C Kassiotis (2014). Unified semi-analytical wall boundary conditions applied to 2-D incompressible SPH. *Journal of Computational Physics* **261**:106–129.

[15] U Ghia, K Ghia, C Shin (1982). High-Re solutions for incompressible flow using the Navier-Stokes equations and a multigrid method. *Journal of Computational Physics* **48**:387–411.

[16] M Breuer, J Bernsdorf, T Zeiser, F Durst (2000). Accurate computations of the laminar flow past a square cylinder based on two different methods: lattice-Boltzmann and finite-volume. *International Journal of Heat and Fluid Flow* **21**:186–196.

[17] K Prasad, SB Paramane, A Agrawal, A Sharma (2011). Effect of channel-confinement and rotation on the two-dimensional laminar flow and heat transfer across a cylinder. *Numerical Heat Transfer, Part A: Applications* **60**:699–726.

This page was intentionally left blank

V Conferência Nacional de Mecânica dos Fluidos, Termodinâmica e Energia
MEFTE 2014, 11–12 Setembro 2014, Porto, Portugal
APMTAC, 2014

Modeling of complex solid-fluid flows with meshless particulate methods

RB Canelas[1], AJC Crespo[2], JM Domínguez[2], RML Ferreira[1]

[1]Centro de Estudos de Hidrossistemas (CEHIDRO), Instituto Superior Técnico, Universidade de Lisboa, Av. Rovisco Pais, 1049-001 Lisboa, Portugal
[2]Environmental Physics Laboratory (EPHYSLAB), Universidade de Vigo, As Lagoas, 32004 Ourense, Spain
email: ricardo.canelas@ist.utl.pt, alexbexe@uvigo.es, jmdominguez@uvigo.es, ruimferreira@ist.utl.pt

ABSTRACT: Solid material advected by a fluid flow may contribute significantly to the momentum balance. Of special interest are highly unsteady free-surface flows like flash floods, dam-break flows or tsunamis propagating inland; these flows possess an enormous potential of incorporating solids, as exemplified by the debris-flow events in Madeira Islands, 2011, or shown in video footages of the Tohoku tsunami disaster.

The motion of the solid mass may be difficult to predict due to the complexity of the modes of momentum transfer by the fluid motion and due to its interactions with other solids. A unified discretization of rigid solids and fluids that allows for detailed and resolved simulations of the fluid-solid phases is presented. The model is based on the fundamental conservation laws of hydrodynamics, namely the continuity and Navier-Stokes equations, and the equation of conservation of momentum of solid bodies. Details of contact mechanics are derived from state-of-the-art formulations considering normal and frictional contacts. The coupled numerical solution, based on the fully meshless Lagrangian method Smoothed Particle Hydrodynamics (SPH) [1] and Discrete Element Method (DEM) [2], resolves solid-solid and solid-fluid interactions in a broad range of scales. This method allows for a detailed description of momentum transfer at solid boundaries and allows for upscaling of the flow description to large scales typical of engineering problems, such as transport of debris or hydrodynamic actions on structures. Such class of simulations, due to the size of the domain and required resolutions, are made practical due to a careful implementation using novel, highly parallel, computational architectures as GPUs.

General overviews of the conceptual models, numerical discretization and implementation are addressed, and results for complex multiphasic flows are shown. Initial validations based on experimental work are drawn and discussed.

KEY-WORDS: SPH; DEM; Meshless; Free-surface.

1 INTRODUCTION

The transport of solid material by a fluid flow is a common phenomenon and, at the engineering scales, it may be associated with catastrophic events such as debris flows on urban terrain. The importance of means to allow for risk analysis and consequent planning cannot be overstated by the very nature of such events. They are usually unpredictable in frequency and magnitude and the destructive potential can be almost boundless, both in terms of property as in terms of human lives.

The main difficulties with modelling such class of events arise from the characteristics of the phenomena and scale. The latter poses a problem even for the simplest models, since modelling even a single event can require remarkably large domains. This relates directly with the former, since the type of interaction and its relevant scales may require very high resolution adding to such large domains. The kind of non-linear and multiscale problem that is being addressed poses severe limitations to the usage of simple models. Adequate closures for continuum models, for example, often require relevant simplifications from the rheological standpoint, greatly reducing their validity for generalized scenarios [3]. Furthermore, experimental validation of such models is remarkably complex and also relies on simplifications, both on the setup and on the analysis of the data ([11], [13]).

A model that can shed light into the mechanisms of these flows must attempt to characterize all relevant interactions. Within the meshless framework, efforts have been made on unifying solid and fluid modelling. [4] modelled a rigid body as a collection of Moving Particle Simulation (MPS) fluid particles, rigidified by default. This has become the standard approach due to its simplicity and good results. [10]

modelled the effects of wave interaction on a caisson breakwater resorting to Smoothed Particle Hydrodynamics (SPH) and some special considerations for the particles that made up the solid body, including a form of frictional behavior. For normal interactions, continuum potential based forces have been used ([9], [10]), but are not based in mechanics of contact of rigid bodies. Contact laws like the non-linear Hertzian models have been used extensively in the Discrete Element Method (DEM) literature, being regarded as one of the most physically based available class of contact laws, allowing for the inclusion and consideration of distinct materials in such interactions [5].

This work builds upon the DualSPHyics code (www.dual.sphysics.org), by introducing a model where inter particle forces of rigid body particles are taken from the contact law theories. The implementation allows for a generalization of the shape possible for a typical DEM particle. The very same particles are regarded by the fluid particles as SPH particles, possibly with a different density, allowing for a natural coupling between SPH and DEM. Buoyancy and drag are naturally present when considering the floating rigid body as a cluster of SPH nodes, and so no other forces needed to be included in the discretization of the equations. The DualSPHysics code enables simulation of very well resolved cases with a reasonable computation time by using GPU cards (Graphics Processing Units) as the execution devices. This allows to somewhat alleviate the previously expressed concerns about requirements of scale and resolution, since the computations are made up to two orders of magnitude faster than on normal CPU systems.

An experimental campaign portraying sets of rigid bodies subjected to a dam-break wave is used to validate model. Initial comparisons are made by direct visual comparison of the behavior of the system.

2 FORMULATION

In SPH, the fluid domain is represented by a set of nodal points where physical properties such as mass, velocity, pressure and vorticity are known. These points move with the fluid in a Lagrangian manner and their properties change with time due to the interactions with neighboring particles. The term Smoothed Particle Hydrodynamics arises from the fact that the nodes, for all intended means, carry the mass of a portion of the medium, hence being easily labelled as Particles, and their individual angular velocity is disregarded, hence the Smooth. The method relies heavily on integral interpolant theory [7], that can be resumed to the exactness of

$$A(\mathbf{r}) = \int_{\Omega} A(\mathbf{r}') W(\mathbf{r} - \mathbf{r}') d\mathbf{r}', \tag{1}$$

for any continuous function $A(\mathbf{r})$ defined in $\mathbf{r}'$, r is a distance and W a suitable weight function, called a kernel function. W should be an even function, defined on a compact support, *i.e.* if the radius is ϵh then $W(\mathbf{r} - \mathbf{r}', h) = 0$ if $|\mathbf{r} - \mathbf{r}'| \geq \epsilon h$, with $\lim_{h \to 0} W = \delta$ and

$$\int_{\Omega} W(\mathbf{r}', h) d\mathbf{r}' = 1 \tag{2}$$

where δ is the Dirac delta function and h is the smoothing length and defines the size of the kernel support. An approximation to discrete Lagrangian points can be made, by a proper discretization of the kernel function

$$A_i \approx \sum_j A_j V_j W(\mathbf{r}_{ij}, h), \tag{3}$$

called the summation interpolant, extended to all particles j, $|\mathbf{r}_{ij}| = |\mathbf{r}_i - \mathbf{r}_j| \leq \epsilon h$, where V_j is the volume of particle j and A_i is the approximated variable at particle i. The cost of such approximation is that particle first order consistency, *i.e.*, the ability of the kernel approximation to reproduce exactly a first order polynomial function, may not be assured by the summation interpolant, since

$$\sum_j V_j W(\mathbf{r}_{ij}, h) \approx 1, \tag{4}$$

which is especially understandable in situations where the kernel function does not verify compact support, for example near the free surface or other open boundaries. Corrections are used in order to ensure consistency [7].

A spatial first order derivative can be written as the gradient of the kernel function.

3 DISCRETIZATION OF GOVERNING EQUATIONS

3.1 Fluid equations of motion in SPH

The nature of the classical SPH formulation renders an incompressible system undesirable to model [2], and as a result most studies rely on the discretization of the compressible Navier-Stokes system

$$\frac{d\mathbf{v}}{dt} = -\frac{\nabla p}{\rho} + \nabla\boldsymbol{\tau} + \mathbf{g}; \qquad \frac{d\rho}{dt} = -\rho\,\nabla\mathbf{v}, \tag{5}$$

where $\mathbf{v}$ is the velocity field, p is the pressure, ρ is the density and $\boldsymbol{\tau}$ and $\mathbf{g}$ are the stress tensor and body forces, respectively. The continuity equation is traditionally discretized by employing the notion that $\rho\nabla\mathbf{v} = \nabla(\rho\mathbf{v}) - \mathbf{v}\nabla\rho$, rendering

$$\frac{d\rho_i}{dt} = -\rho_i \sum_j m_j(\mathbf{v}_i - \mathbf{v}_j)\nabla W(\mathbf{r}_{ij}, h) \tag{6}$$

This produces a zero divergence field for a $\mathbf{v} = k$ field. The momentum equation can be written as

$$\begin{aligned}\frac{d\mathbf{v}_i}{dt} = &-\sum_j m_j\left(\frac{p_i}{\rho_i^2} + \frac{p_j}{\rho_j^2}\right)\nabla W(\mathbf{r}_{ij}, h) + \sum_j m_j\left(\frac{4\mu\mathbf{r}_{ij}\nabla W(\mathbf{r}_{ij}, h)}{(\rho_i + \rho_j)(|\,r_{ij}\,|^2 + \eta^2)}\right)\mathbf{v}_{ij} + \\ &\sum_j m_j\left(\frac{\tau_i}{\rho_i^2} + \frac{\tau_j}{\rho_j^2}\right)\nabla W(\mathbf{r}_{ij}, h) + \mathbf{g}\end{aligned} \tag{7}$$

The first term of the right side is a symmetrical, balanced form of the pressure term [7]. The second and third terms represent a laminar viscosity term [8] and a sub-particle stress (SPS) [1], respectively. The SPS term introduces the effects of turbulent motion at smaller scales than the spatial discretization. Following the eddy viscosity assumption and using Favre-averaging, the SPS stress tensor for a compressible fluid can be written as

$$\frac{\boldsymbol{\tau}_{\alpha\beta}}{\rho} = 2\nu_t\mathbf{S}_{\alpha\beta} - \frac{2}{3}k\boldsymbol{\delta}_{\alpha\beta} - \frac{2}{3}C_I\Delta^2\boldsymbol{\delta}_{\alpha\beta}\,|\,\mathbf{S}_{\alpha\beta}\,|^2, \tag{8}$$

where $\boldsymbol{\tau}_{\alpha\beta}$ is the sub-particle stress tensor, $\nu_t = (C_S\,|\,\mathbf{r}_{ij}\,|)^2\,|\,\mathbf{S}_{\alpha\beta}\,|$ is the eddy viscosity, C_S is the Smagorinsky constant, k is the SPS turbulence kinetic energy, $C_I = 6.6\times10^{-3}$ and $\mathbf{S}_{\alpha\beta}$ is the local strain rate tensor, with $|\,\mathbf{S}_{\alpha\beta}\,| = (2\mathbf{S}_{\alpha\beta}\mathbf{S}_{\alpha\beta})^{1/2}$.

3.2 Rigid bodies and contact laws

Newton's equations for rigid body dynamics are discretized as

$$M_I\frac{d\mathbf{V}_I}{dt} = \sum_{k\in I} m_k\mathbf{f}_k; \qquad I_I\frac{d\boldsymbol{\Omega}_I}{dt} = \sum_{k\in I} m_k(\mathbf{r}_k - \mathbf{R}_I)\times\mathbf{f}_k, \tag{9}$$

where body I possesses a mass M_I, velocity $\mathbf{V}_I$, inertial tensor $\mathbf{I}_I$, angular velocity $\boldsymbol{\Omega}_I$ and center of gravity $\mathbf{R}_I$. $\mathbf{f}_k$ is the force by unit mass applied to particle k, belonging to body I. This force encompasses body forces, fluid resultants as well as the result of any rigid contact that might occur.

The contact force $\mathbf{F}_i^T$ acting on particle i resulting from collision with particle j is decomposed into $\mathbf{F}_n$ and $\mathbf{F}_t$, normal and tangential components respectively. Both of these forces are further decomposed into a repulsion force, $\mathbf{F}^r$, that takes into account the deformation of the particle, and a damping force, $\mathbf{F}^d$, for the dissipation of energy during the deformation.

In the current work, the normal forces are given by a modified, non-linear, Hertzian model [5]

$$\mathbf{F}_{n,ij} = \mathbf{F}_n^r + \mathbf{F}_n^d = k_{n,ij}\delta_{ij}^{3/4}\mathbf{e}_{ij} - \gamma_{n,ij}\delta_{ij}^{1/4}\dot{\delta}_{ij}\mathbf{e}_{ij}, \tag{10}$$

where $k_{n,ij}$ is the stiffness constant of pair ij, $\delta_{ij} = \max(0, (d_i + d_j)/2 - |\,\mathbf{r}_{ij}\,|)$ is the particle overlap, $\mathbf{e}_{ij}$ is the unit vector between the two mass centers and $\gamma_{n,ij}$ is the damping constant. The stiffness and damping constants are given by [5]

$$k_{n,ij} = \frac{4}{3} E^* \sqrt{R^*}; \quad \gamma_{n,ij} = C_n \sqrt{6 M^* E^* \sqrt{R^*}}, \tag{11}$$

with C_n of the order of 10^{-5}. The other parameters are given by

$$\frac{1}{E^*} = \frac{1-\nu_I^2}{E_I} + \frac{1-\nu_J^2}{E_J}; R^* = \frac{r_i r_j}{r_i + r_j}; M^* = \frac{m_I m_J}{m_I + m_J}, \tag{12}$$

where E is the Young modulus, ν is the Poisson ratio and m is the mass of the body.

Regarding tangential contacts, the complex mechanism of friction is modelled by a linear dash-pot bounded above by the Coulomb friction law. The Coulomb law is modified with a sigmoidal function in order to make it continuous around the origin regarding the tangential velocity [12]. One can write

$$\mathbf{F}_{t,ij} = \min(\mu_{IJ} \mathbf{F}_{n,ij} \tanh(8\dot{\delta}_{ij}^t) \mathbf{e}_{ij}^t; \quad \mathbf{f}_t^r + \mathbf{f}_t^d), \qquad \mathbf{F}_t^r + \mathbf{F}_t^d = k_{t,ij} \delta_{ij}^t \mathbf{e}_{ij}^t - \gamma_{t,ij} \dot{\delta}_{ij}^t \mathbf{e}_{ij}^t \tag{13}$$

μ_{IJ}, the friction coefficient at the contact of I and J, should be expressed as a function of the two friction coefficients of the distinct materials. The stiffness and damping constants are derived to be $k_{t,ij} = 2/7 k_{n,ij}$ and $\gamma_{t,ij} = 2/7 \gamma_{n,ij}$, as to insure internal consistency of the time scales required for stability. This mechanism models the static and dynamic friction mechanisms by a penalty method. The body does not statically stick at the point of contact, but is constrained by the spring-damper system.

3.3 Pressure field and stability region

The presented compressible formulation of SPH for the Navier-Stokes employs an equation of state to determine the pressure field, in order not to solve an additional partial differential equation, that relies on the correct tracking of a free surface, such as the Poisson equation. Following [7], the commonly used estimate relationship between pressure and density is Tait's equation.

The stability region must be modified to accommodate another restriction, the DEM compatible time-step. The *CFL* condition can be written as

$$\Delta t = C \min\left[\min_i \left(\sqrt{\frac{h}{|\mathbf{f}_i|}} \right); \min_i \left(\frac{h}{c_0 + \max_j \left| \frac{h \mathbf{v}_{ij} \mathbf{r}_{ij}}{\mathbf{r}_{ij}^2} \right|} \right); \min_i \left(\pi / C50 \sqrt{\frac{k_{n,ij}}{m_{IJ}}} \right) \right], \tag{14}$$

where C is the *CFL* constant of the order of 10^{-1} determined in accordance with the case. The first term results from the consideration of force magnitudes, the second is a combination of the *CFL* condition for numerical information celerities and a restriction arising from the viscous terms [2] and the third term takes into account a theoretical solution for the DEM stability constraints that disregards the *CFL*. If the sound celerity in the simulation is too high, it will render Δt very small and the computation more expensive. Following [7], c_0 is kept to an artificial value of around 10 times the maximum flow speed, restricting the relative density fluctuations at less than 1%. As a consequence, the estimated pressure field by equation (14) usually shows some instabilities and may be subject to scattered distributions. The diffusive terms introduced in [6], designed to smooth the oscillations in the pressure field are used in equation (6). These terms do not allow for an exact hydrostatic solution since a net force is developed near the free surface, but the test cases in this work represent a very unsteady flow, for which such terms are acceptable.

4 RESULTS

The experimental campaign took place in the Wave Channel of the Hydraulics Laboratory (LHIST) of the Civil Engineering Department at Instituto Superior Técnico, Lisbon, Portugal. The flume was sectioned at 8.0 m long and is 0.70 m wide, with glass side walls in order to grant optical access to the flow. The material can be considered very smooth both in the walls and the bed. The installed gate provides an 'instantaneous' removal for the dam-break, with an opening time of 0.21 s, lesser than the required theoretical limit for a dam-break $t_o(h_0 = 0.40) = \sqrt{2h_0/g} \approx 0.29\,\text{s}$. The objects were 0.15 m side PVC cubes, filled with a material that resulted in a final relative density 0.8. The instrumentation consisted of

three synchronized video cameras pointing from the upstream, top and downstream directions, as well as a high-speed camera on the side, normal to the flume wall.

The simulations were ran with a *CFL*=0.2, $\alpha = 0.05$, $\epsilon = 0.5$, initial $dx = 0.01$ m and a Wendland kernel with $h = 0.87\sqrt{3dx^2}$. This resolution results in approximately 10^6 particles. The used integration scheme was a predictor–corrector Sympletic. For the rigid contact formulation, $E = 3\times10^3$ kN/m^2, $\nu = 0.23$ and $\mu = 0.45$. These values are typically dependent on the used integrator scheme and are, therefore, subject of fine tuning in order to reproduce correctly the desired behavior [5].

Visualization is performed using an interpolation using the same kernel as for the simulation in order to generate a free surface as a mass isosurface. The objects are represented as polygons that track the underlying particles used for the computation.

The test consists of a cube wall made of 6 cubes, with 3 vertical levels. Such configuration provides added complexity to the system, since several contacts are resolved. Figures 1 to 3 show a top-view, with experimental results in the top and numerical solution in the bottom.

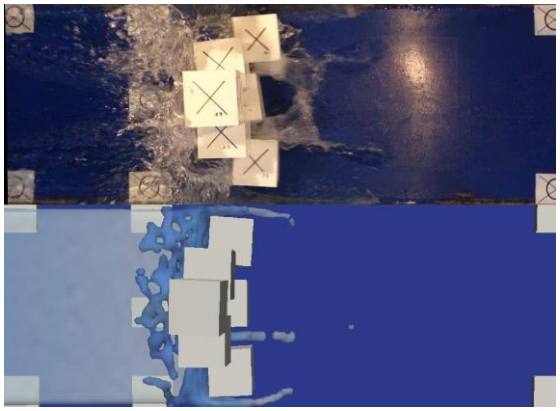

Figure 1: $t = 0.82$ s.

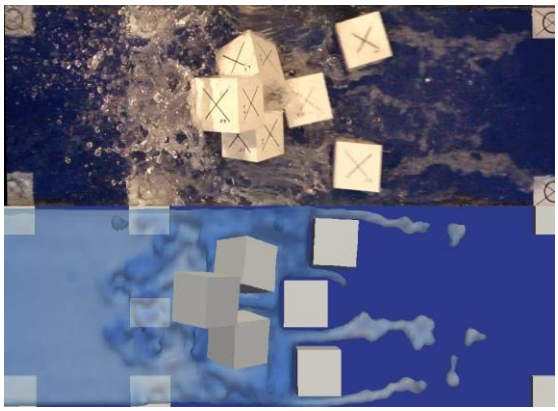

Figure 2: $t = 1.08$ s.

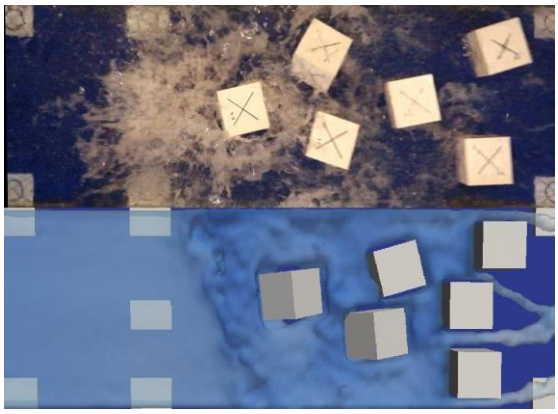

Figure 3: $t = 1.46$ s.

The results reveal some of the mechanisms of collapse of the structure. The bottom cubes are quickly mobilized by the fluid force, from the pressure rise upstream and slide between the bed and the upper cubes. A small amount of moment is transferred by friction to the top cubes, and these eventually rotate around the edge of the bottom cubes, finally interacting with the fluid and the flume bed. Discrepancies in the fluid motion are noticeable, beyond the artefacts introduced by the surface reconstruction algorithm. These seem to arise from the resolution requirements to effectively model every relevant scale of the experiment. The Reynolds number for the objects is of the order of 4×10^5, many orders of magnitude higher than the initial 0.010 m discretization allows to resolve gracefully. This should be responsible for most of these discrepancies, such as the dry bed downstream of the objects, angle of the flow separation upon impact and structure of the wave front. It is hypothesized that it is also responsible for most of the mismatch in the motion of the objects: important scales of the moment transferring mechanisms are not being fully resolved.

5 CONCLUSIONS AND FUTURE WORK

The purpose of the work is to present a generalized DEM model implemented within a Smoothed-Particle-Hydrodynamics model. The simple validation presented serves as a benchmark for the model, demonstrating it copes well with the difficulties of modelling complex scenarios even if under-resolved. The model is expected to give more accurate results with increased resolution and more robust boundary conditions, leading to lesser dissipation and a more consistent description of the near bed flow structures and the ones forming at the impact locus. Considerations regarding the viscous formulations are being studied and solutions for drag-dominated flows compare well with other data. The largest difficulty in increasing resolution is machine memory, since there are a large number of particles in the flume reservoir upstream that need to be modelled. Works with multi-GPU parallelization are being carried, with promising results in bypassing such limitations, allowing for more complete validations and eventually the production of highly resolved data of real scale flows with incorporated solid material.

ACKNOWLEDGMENTS

This research was partially supported by project PTDC/ECM/117660/2010, funded by the Portuguese Foundation for Science and Technology (FCT) and by Xunta de Galicia under project Programa de Consolidación e Estructuración de Unidades de Investigación Competitivas (Grupos de Referencia Competitiva) co-funded by European Regional Development Fund (FEDER), and by Ministerio de Economía y Competitividad under Project BIA2012-38676-C03-03. First author acknowledges FCT for his PhD grant, SFRH/BD/75478/2010.

REFERENCES

[1] RA Dalrymple, BD Rogers (2006). Numerical modeling of water waves with the SPH method. *Coastal Engineering* **53**(2–3):141–147.

[2] M Gomez-Gesteira, BD Rogers, RA Dalrymple, AJC Crespo (2010). State-of-the-art of classical SPH for free-surface flows. *Journal of Hydraulic Research* **48**(Supp1):6–27.

[3] RM Iverson (2003). The debris-flow rheology myth. In D Rickenmannm, CL Chen, Eds., *Debris-Flow Hazards Mitigation: Mechanics, Prediction, and Assessment*, 303–314, Millpress, Rotterdam.

[4] S Koshizuka, A Nobe, Y Oka (1998). Numerical analysis of breaking waves using the moving particle semi-implicit method. *International Journal for Numerical Methods in Fluids* **26**:751–769.

[5] M Lemieux, G Léonard, J Doucet, L-A Leclaire, F Viens, J Chaouki, F Bertrand (2008). Large-scale numerical investigation of solids mixing in a V-blender using the discrete element method. *Powder Technology* **181**(2):205–216.

[6] D Molteni, A Colagrossi (2009). A simple procedure to improve the pressure evaluation in hydrodynamic context using SPH. *Computer Physics Communications* **180**:861–872.

[7] JJ Monaghan (2005). Smoothed particle hydrodynamics. *Reports on Progress in Physics* **68**(8):1703–1759.

[8] JP Morris, PJ Fox, Y Zhu (1997). Modelling low Reynolds number incompressible flows using SPH. *Journal of Computational Physics* **136**:214–226.

[9] BD Rogers, RA Dalrymple (2008). SPH modeling of tsunami waves. In PL-F Liu, H Yeh, C Synolakis, Eds., *Advanced Numerical Models for Simulating Tsunami Waves and Runup*, 75–100, World Scientific.

[10] BD Rogers, RA Dalrymple, PK Stansby (2010). Simulation of caisson breakwater movement using 2-D SPH. *Journal of Hydraulic Research* **48**(Supp1):135–141.

[11] C Shu, J Xia, RA Falconer, B Lin (2011). Incipient velocity for partially submerged vehicles in floodwaters. *Journal of Hydraulic Research* **49**:709 –717.

[12] D Vetsch (2012). *Numerical Simulation of Sediment Transport with Meshfree Methods*, Mitteilungen 219, Versuchsanstalt für Wasserbau, Hydrologie und Glaziologie (VAW), R Boes, Hrsg., ETH Zürich..

[13] J Xia, FY Teo, B Lin, RA Falconer (2011). Formula of incipient velocity for flooded vehicles. *Natural Hazards* **58**:1–14.

V Conferência Nacional de Mecânica dos Fluidos, Termodinâmica e Energia
MEFTE 2014, 11–12 Setembro 2014, Porto, Portugal
APMTAC, 2014

A constrained dynamic subgrid-scale model for the large-eddy simulation of the atmospheric boundary layer

A Silva Lopes, JMLM Palma

CEsA – Centre for Wind Energy and Atmospheric Flows, Faculdade de Engenharia, Universidade do Porto,
Rua Dr. Roberto Frias, 4200-465 Porto, Portugal
email: asl@fe.up.pt, jpalma@fe.up.pt

ABSTRACT: Wall-modelled large-eddy simulation may be the best available tool for most flows of practical interest that occur at high-Reynolds number near a surface. With such approach, the surface-shear is obtained from the velocity at a grid node close to the surface, the large, geometry dependent, scales are resolved and only the small, subgrid-scale, structures must be modelled. The dynamic model has been successfully used in a broad range of flows for such purpose, but its utilisation with a wall-model is questionable because, near the surface, the smallest resolvable scales approach the integral scale. In this work, a recently proposed constrained dynamic subgrid model was adapted for the large-eddy simulation of the atmospheric boundary layer. This model avoided the underdissipative character of the base dynamic model and, compared with a reference solution, allowed to increase the resolved turbulence and provided better predictions of the velocity gradient near the surface.

KEY-WORDS: Large-eddy simulation; Subgrid model; Atmospheric boundary layer.

1 INTRODUCTION

Large-eddy simulation (LES) has been a valuable tool for the study of flows of practical interest [1], since the range of time and length scales that they exhibit makes direct numerical simulation (DNS) unfeasible now and in the foreseeable future. The main advantage of LES is that the large, geometry dependent, scales are resolved and these determine important flow dynamics and statistics. However, in flows that occur at high-Reynolds number near a surface, even LES can be prohibitively expensive, because the small structures in the near-wall region must be resolved and the resolution required is similar to a DNS [2]. Also, meteorological and oceanography flows, for instance, occur over rough surfaces, with details that cannot be properly discretised [3]. In these cases, the solution that allows to resolve only the large scales is a wall-modelled LES (WMLES), where the surface-shear is obtained from the velocity at a grid node close to the surface, assuming some kind of equilibrium.

Since large-scales are resolved with LES, subgrid-scale (SGS) stresses constitute only a fraction of the turbulent stresses; their models are expected to be simpler and more accurate than turbulence models for the Reynolds-averaged Navier-Stokes (RaNS) method, because the small scales are more universal and isotropic than the large ones. The most widely used SGS model is probably the dynamic model [4],[5]. It is based on the Smagorinsky model [6] but uses a secondary filter, with a filter-length larger than the primary, to determine the Smagorinsky coefficient. It overcomes most of the deficiencies of the base model in the near-surface regions and in flows with shear, rotation or transition to turbulence, gets all the information from the resolved fields and does not require any tuneable parameter.

Although, the utilisation of the dynamic model along a wall-model raises some questions: with a wall-model, the smallest resolved scales near the surface approach the integral scale. However, the dynamic model is expected to perform well only if the smallest resolved scales are in the inertial range [7]. To overcome this problem, a correction to the dynamic model was proposed [8], which uses an additional test-filter to account for the variation of the model coefficient with grid resolution. However, this scale-dependent model suffers from an underdissipative character when used with finite differences, instead of spectral methods [9]. Recently, Verma *et al.* [10] proposed to alleviate the near-wall resolution requirements of an LES, decreasing the range of resolvable scales, and constraining the dynamic model, with externally prescribed average Reynolds stresses near the surface. Although initially it was not directed to be used with a wall-model, the success of its application rendered important to verify whether it could be used with a range of resolved scales even smaller, as is the case of the LES of the atmospheric boundary layer.

The objective of this work is to test the utilisation of a dynamic constrained subgrid model for the large-eddy simulation of the atmospheric boundary layer. A model close to the formulation of Verma et al. [10], constrained considering the Germano identity error, will be used. Results will be compared with a model that changes from the dynamic approach to a damped Smagorinsky model near the surface, which was already used with success in the simulation of atmospheric flows [11].

2 MATHEMATICAL MODEL AND NUMERICAL TECHNIQUES

The governing equations are the filtered continuity and Navier-Stokes equations, for the conservation of mass and momentum,

$$\frac{\partial \overline{u}_i}{\partial x_i} = 0\,, \tag{1}$$

$$\frac{\partial \overline{u}_i}{\partial t} + \frac{\partial\left(\overline{u}_j \overline{u}_i\right)}{\partial x_j} = \nu \frac{\partial^2 \overline{u}_i}{\partial x_j \partial x_j} - \frac{\partial \tau_{ij}}{\partial x_j} - \frac{1}{\rho}\frac{\partial \overline{p}}{\partial x_i}\,, \tag{2}$$

where u_i is the Cartesian component of the velocity in the x_i direction, p is the pressure, ρ and ν are the standard air density and kinematic viscosity and the overline denotes a filtered quantity. $\tau_{ij} = \overline{u_i u_j} - \overline{u}_i \overline{u}_j$ are the subgrid stresses, modelled using one of the variants of the dynamic model described next.

2.1 Base Dynamic Model

The dynamic model [4] uses an eddy-viscosity assumption to determine the subgrid stresses,

$$\tau_{ij} - \frac{1}{3}\delta_{ij}\tau_{kk} = -2\nu_t \overline{S}_{ij} = -2\left(C\overline{\Delta}\right)^2 \left|\overline{S}\right| \overline{S}_{ij}\,, \tag{3}$$

where $\overline{\Delta} = \left(\Delta x \Delta y \Delta z\right)^{1/3}$ is the filter size, $\overline{S}_{ij} = \left(\partial \overline{u}_i / \partial x_j + \partial \overline{u}_j / \partial x_i\right)/2$ is the resolved strain-rate tensor and $\left|\overline{S}\right| = \left(2\overline{S}_{ij}\overline{S}_{ij}\right)^{1/2}$ is its magnitude; C is the coefficient of the model, equivalent to the Smagorinsky coefficient (C_S) in the standard Smagorinsky model. The dynamic procedure consists in determining the coefficient C that minimizes the Germano-identity error,

$$\varepsilon_{ij}^L = \left(C\overline{\Delta}\right)^2 M_{ij} - L_{ij}\,, \tag{4}$$

with $M_{ij} = 2\left[\left|\overline{S}\right|\overline{S}_{ij} - \alpha^2 \left|\overline{S}\right| \overline{S}_{ij}\right]$ and $L_{ij} = \overline{u}_i \overline{u}_j - \hat{\overline{u}}_i \hat{\overline{u}}_j$. ($\hat{}$) represents a test-filter operation and $\alpha = \hat{\overline{\Delta}} / \overline{\Delta}$ is the ratio between the test and primary filter widths ($\alpha = 2$ here).

The coefficient that minimizes the error of the Germano identity is obtained from

$$\left(C\overline{\Delta}\right)^2 = \frac{\left\langle L_{ij} M_{ij} \right\rangle}{\left\langle M_{ij} M_{ij} \right\rangle}\,, \tag{5}$$

where $\langle\ \rangle$ denotes some kind of averaging, here along pathlines, required to avoid negative eddy-viscosity.

2.2 Constrained Dynamic Model

Verma *et al.* [10] proposed adding a constrain to the dynamic model such that, near the surface, the model approaches, in a time-average (RaNS) sense, a prescribed distribution R_{ij} of Reynolds stresses. According with their proposal, the model coefficient is determined from

$$\left(C\overline{\Delta}\right)^2 = \frac{\left\langle L_{ij} M_{ij} \right\rangle + \omega^R A_{ij} B_{ij}}{\left\langle M_{ij} M_{ij} \right\rangle + \omega^R B_{ij} B_{ij}}\,, \tag{6}$$

where ω^R is a weigh function, $A_{ij} = \left\langle \overline{u}_i \overline{u}_j \right\rangle_t - \left\langle \overline{u}_i \right\rangle_t \left\langle \overline{u}_j \right\rangle_t - R_{ij}$ and $B_{ij} = 2\left\langle \left|\overline{S}\right| \overline{S}_{ij} \right\rangle_t$, with $\langle\ \rangle_t$ representing a time average. The idea is constraining the model coefficient such that the sum of the resolved with the

subgrid stresses approaches the desired total R_{ij}, assumed to be known, for instance, from a RaNS simulation.

Verma *et al.* proposed to determine ω^R from

$$\omega^R = C_\omega \max\left(\varepsilon - \varepsilon_t\right)^n, \tag{7}$$

where

$$\varepsilon = \varepsilon_{ij}^L \varepsilon_{ij}^L / \tau_{ij}^M \tau_{ij}^M, \tag{8}$$

is the Germano-identity error normalized by the base dynamic model SGS stresses and the constrain is active ($\omega^R > 0$) only when ε exceeds the threshold value ε_t.Here, only the Reynolds shear stress $R_{13} = \langle u'w' \rangle$ was constrained, using an equilibrium profile given by the reference simulation. After several tests, $C_\omega = 0.5$, $n = 1.2$, and $\varepsilon_t = 50$ where chosen, since the values originally proposed were not able to approach the prescribed total Reynolds shear stress

2.3 Blended Dynamic and Smagorinsky Damped Models

To avoid the underdissipative character of the base dynamic model with a wall-model, Siva Lopes *et al.* [11] merge the Lagrangian dynamic and the damped Smagorinsky models near the surface. The blending is achieved using the expression

$$C^2 = \omega^S C_{Smag.}^2 + \left(1 - \omega^S\right) C_{Dyn.}^2, \tag{9}$$

where $C_{Dyn.}$ is the base dynamic model coefficient, determined according with equation (5), and $C_{Smag.}$ is the coefficient of the damped Smagorinsky model. The function ω^S assures the blending of the models, with $\omega^S = \cos^2\left(\pi/2 \cdot z/z_{\max}\right)$ if $z < z_{\max}$ and $\omega^S = 0$ otherwise. $z_{\max}$ is the maximum distance to the surface where the models are merged. Here, $z_{\max} = 125$ m guaranteed a smooth transition, without any spikes both in the model coefficient C and in eddy-viscosity.

The Smagorinsky model uses a constant value for the coefficient; however, the constant needs to be decreased (damped) near a solid boundary. Mason and Thomson [12] proposed the following expression for boundaries with roughness length z_0:

$$C_{Smag.} = \left[C_S^{-m} + \left(\kappa \frac{z + z_0}{\bar{\Delta}} \right)^{-m} \right]^{-m}, \tag{10}$$

where κ is the von~Kármán constant and z is the distance to the surface. Here, the values $C_S = 0.16$ and $m = 2$ were used. Essentially, the eddy-viscosity must be decreased near the surface, to approach a RaNS mixing-length eddy-viscosity ($\nu_t = u_\tau \kappa\left(z + z_0\right)$, where u_τ is the friction velocity) and account for the total stress.

3 PHYSICAL DOMAIN AND BOUNDARY CONDITIONS

The computational domain considered was a box with dimensions 6000 m × 3000 m × 1000 m in the streamwise, spanwise and vertical directions. Periodic conditions were used in the streamwise and spanwise directions. The wall-model of Marusic *et al.* [13] was used at the bottom rough surface, with $z_0 = 3$ cm, and a free-slip condition was used at the top. The streamwise pressure gradient was calculated at each time-strep to maintain a constant average wind-speed of $U_b = 16.6$ m/s. The constrained Reynolds shear stress was $\langle u'w' \rangle = -u_\tau^2\left(1 - z/H\right)$, with $u_\tau = 0.654$ m/s, which was the value obtained in the simulation with the blended dynamic and Smagorinsky damped models.

Most of the results were obtained using a grid with $120 \times 120 \times 50$ nodes and resolution $\Delta x = 50$ m, $\Delta y = 25$ m, $\Delta z_{\min} = 7$ m and $\Delta z_{\max} = 35$ m. It was refined in the vertical direction near the surface and expanded from there to the domain top, with an expansion factor always lower than 1.05.

4 RESULTS

Validation of numerical simulations of the neutrally stable atmospheric boundary layer (ABL) is usually done by comparison with the log-law, since it is expected that the mean velocity displays a logarithmic profile in the lower part (around 10–20%). Here, it was observed that the velocity was usually larger than the log-law (Figure 1a), which was related with an overshot in the non-dimensional mean velocity

gradient, $\phi = \kappa z / u_\tau \cdot \partial U / \partial z$, near the surface ($z/H \approx 0.02$, Figure 1b). This is a well-known problem of large-eddy simulations of the ABL [12], especially with the Smagorinsky model, connected with the relative magnitude of the resolved and subgrid stresses near the surface and with the wall-normal resolution. Indeed, the reference simulation had a wider peak of ϕ than the simulation with the constrained model because it had the highest model coefficient near the surface (Figure 1e). While with spectral methods the overshot can be mostly eliminated using the appropriate grid resolution [14], the same approach was not effective with finite differences, probably due to the damping of the high wave-numbers. Nevertheless, the values shown here by the non-dimensional velocity gradient ϕ are similar to those reported in the literature with the Smagorinsky model [9]. Peak values for the root mean square of the velocity fluctuations (Figure 1c) were also similar to those found in the literature [9], with the high anisotropy in the streamwise direction being also related to the overshot in the velocity gradient [14].

Compared to the base dynamic model, the enforcement of the constrain resulted in an increase of the model coefficient near the surface, until $z/H \approx 0.05$, with a peak of $C \approx 0.11$ by $z/H \approx 0.02$ (Figure 1e). This increased the subgrid stresses and avoided the underdissipative character of the base model. The resolved shear stress became larger than the modeled by $z/H \approx 0.02$ (Figure 1d), which means that the RaNS character was restricted to the first two grid nodes from the surface. Although the coefficient increased relatively to the base dynamic model was, it remained lower than in the reference simulation, which resulted in more resolved turbulence (Figures 1c–d) and smaller structures near the surface. The long, nonphysical, structures are one problem of the Smagorinsky model and Mason and Thomson [12] suggest that they are responsible for the high velocity gradient near the surface, so decreasing their length was seen as an improvement.

Finally, the normalized Germano-identity error was smaller with the constrained models than in the reference simulation (Figure 1f). Verma *et al.* [10], in their simulations without a wall-model, observe also a reduction of the Germano-identity error between the base dynamic and the constrained models, but consider that it is caused by a reduction of resolved turbulence near the surface, which decreases the tensors L_{ij} and M_{ij}. However, since here the constrained model provided higher resolved Reynolds stress near the surface than the reference simulation (Figure 1d), the lower Germano-identity error may signal that the constrained models are providing a better coefficient, even if one must remember that the considerations of the base dynamic model (scale-invariance and test filter in the inertial range) are not valid for the under-resolved, near-surface, turbulence.

5 CONCLUSIONS

The constrained dynamic subgrid-scale model proposed by Verma *et al.* [10] was adapted to the large-eddy simulation of the atmospheric boundary-layer. While the original formulation intended only to relax the near-wall resolution requirements of a wall-resolved large-eddy simulation, here it was used with a wall-model. The resultant model has effectively a hybrid character: it keeps the subgrid-scale character of the base model far from the surface and gains a RaNS character near the surface, where the modelled stresses become larger than the resolved.

With the appropriate choice of parameters, the constrained model provided solutions with the intended total Reynolds shear stress and avoided the underdissipative character of the base dynamic model. The constrained zone occupied around 5% of the bottom boundary layer height, and the modelled shear stress was larger than the resolved in approximately half of that region. Comparing with a reference solution, obtained with a subgrid-scale model that combined a damped Smagorinsky model near the surface and the dynamic model far away, the constrained model determined a lower coefficient near the surface; smaller structures were resolved, with higher turbulent fluctuations and Reynolds shear stress, which resulted in a better prediction of the velocity gradient.

Despite the promising results, further work is required to measure the sensitivity of the model to the weight function, changes in grid resolution and even to details of implementation of the base dynamic model as, for instance, the type of averages used to stabilise the model coefficient. Furthermore, the model depends on an external specification of a target total Reynolds shear stress, which makes its application to complex flows dependent of the existence of such result. However, the constrained model can be used as a reference for other hybrid subgrid-scale models that do not require the specification of the Reynolds stresses.

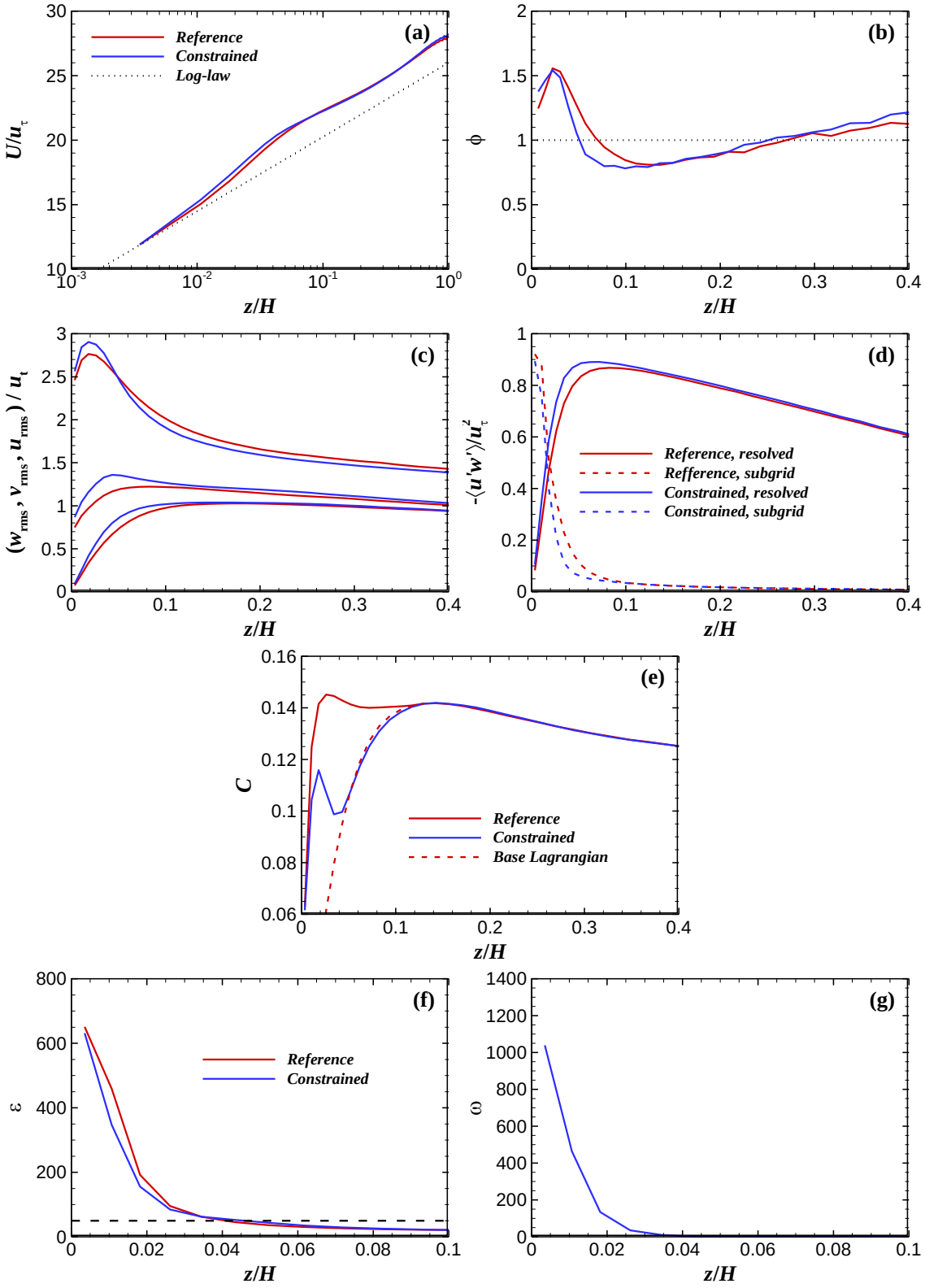

Figure 1: (a) Mean velocity profiles, (b) non-dimensional velocity gradient, (c) root mean square of velocity fluctuations, (d) resolved and modelled Reynolds shear stress, (e) model coefficient, (f) normalised Germano-identity error and (f) weight function.

ACKNOWLEDGMENTS

A Silva Lopes is a research fellow under *Programa Ciência* of the Portuguese Foundation for Science and Technology (FCT). These research activities were developed as part of the work program of the Centre for Wind Energy and Atmospheric Studies, a unit sponsored by the Portuguese Foundation for Science and Technology (FCT).

REFERENCES

[1] K Mahesh, GS Constantinescu, S Apte, G Iaccarino, F Ham, P Moin (2006). Large-eddy simulation of reacting turbulent flows in complex geometries. *Journal of Applied Mechanics* **73**:374–381.

[2] U Piomelli, E Balaras (2002). Wall-layer models for large-eddy simulations, *Annual Review of Fluid Mechanics* **34**:349–374.

[3] PJ Mason, NS Callen (1986). On the magnitude of the subgrid-scale eddy coefficient in large-eddy simulations of turbulent channel flow. *Journal of Fluid Mechanics* **162**:439–462.

[4] M Germano, U Piomelli, P Moin, WH Cabot (1991). A dynamic subgrid-scale eddy viscosity model. *Physics of Fluids A* **3**:1760–1765.

[5] DK Lilly (1992). A proposed modification of the Germano subgrid-scale closure method. *Physics of Fluids A* **4**:633–635.

[6] J Smagorinsky (1963). General circulation experiments with the primitive equations. I: The basic experiment. *Monthly Weather Review* **91**:99–164.

[7] SB Pope (2004). Ten questions concerning the large-eddy simulation of turbulent flows. *New Journal of Physics* **6**:35.

[8] F Porté-Agel, C Meneveau, MB Parlange (2000). A scale-dependent dynamic model for large-eddy simulation: application to a neutral atmospheric boundary layer. *Journal of Fluid Mechanics* **415**:261–284.

[9] G Kirkil, J Mirocha, E Bou-Zeid, FK Chow, B Kosović (2012). Implementation and evaluation of dynamic subfilter-scale stress models for large-eddy simulation using WRF. *Monthly Weather Review* **140**:266–284.

[10] A Verma, N Park, K Mahesh (2013). A hybrid subgrid-scale model constrained by Reynolds stress. *Physics of Fluids* **25**:110805.

[11] A Silva Lopes, JMLM Palma, FA Castro (2007). Simulation of the Askervein flow. Part 2: Large-eddy simulations. *Boundary-Layer Meteorology* **125**:85–108.

[12] P Mason, DJ Thomson (1992). Stochastic backscatter in large-eddy simulations of boundary layers. *Journal of Fluid Mechanics* **242**:51–78.

[13] I Marusic, GJ Kunkel, F Porté-Agel (2001). Experimental study of wall boundary conditions for large-eddy simulation. *Journal of Fluid Mechanics* **446**:309–320.

[14] JG Brasseur, T Wei (2010). Designing large-eddy simulation of the turbulent boundary layer to capture law-of-the-wall scaling. *Physics of Fluids* **22**:021303.

Numerical simulation of the thermal effects of localized fires

C Balsa[1,2], B Béjannin[3], S Mouysset[4], P Piloto[1,5]

[1]Instituto Politécnico de Bragança, Campus de Santa Apolónia, 5300-253 Bragança, Portugal.
[2]Centro de Estudos de Energia Eólica e Escoamentos Atmosféricos (CEsA), FEUP, Rua Dr. Roberto Frias, 4200-465 Porto, Portugal
[3]Universitée de Toulouse, INP(ENSEEIHT)-IRIT, 2, rue Charles Camichel, B.P. 7122, 31071 Toulouse Cedex 7, France
[4]University of Toulouse, IRIT-UPS, 2, rue Charles Camichel, B.P. 7122, 31071 Toulouse Cedex 7, France
[5]Instituto de Engenharia Mecânica (IDMEC), FEUP, Rua Dr. Roberto Frias, 4200-465 Porto, Portugal
email: balsa@ipb.pt, baptiste.bejannin@etu.enseeiht.fr, Sandrine.Mouysset@irit.fr, ppiloto@ipb.pt

ABSTRACT: The thermal effects of a localized fire bellow a concrete slab with the length of 10 m and the thickness of 30 cm is simulated. The nonlinear equation of heat transfer was solved by finite differences using an implicit scheme. The appropriate mesh size in the direction corresponding to the heat flux resulting from the fire was defined. The temperature results of the two dimensional simulation does not depend on the dimension of the mesh size in the horizontal direction (perpendicular to the heat flux).

KEY-WORDS: Fire; Heat transfer; Concrete slab; Eurocode; Finite differences; Mesh size.

1 STATEMENT OF THE PROBLEM

The main objective of this work is the development of a scientific programming tool that allows modelling the temperature distribution inside a concrete slab subjected to a localized fire. This paper intends to analyse the effect of a car fire accident inside a compartment, made of concrete. When flash-over is unlikely to occur, thermal effects of a localised fire should be taken into account [1].

To obtain the thermal effect of the localized fire, the heat released rate of a utilitarian car was used. The net heat flux incident on the exposed surface of concrete slab was also calculated according to the simplified formulas of Eurocode [1].

The slab has a length of 10 m and a thickness of 30 cm, but the problem is reduced to the vertical section of the slab that is positioned above the axis of the flame. In this way we obtain a two dimensional domain, corresponding to a very flat rectangular area. Figure 1 represents the section of the compartment where the analysed area is at the top, where r corresponds to the horizontal distance to the vertical axe of the flame.

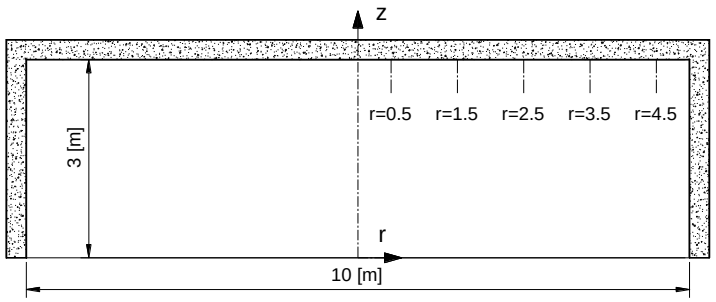

Figure 1: Geometry of the compartment.

The temperature inside the plate is governed by the equation of heat transfer:

$$\frac{\partial}{\partial x}\left(k\frac{\partial T}{\partial x}\right)+\frac{\partial}{\partial y}\left(k\frac{\partial T}{\partial y}\right)=\rho c\frac{\partial T}{\partial t} \tag{1}$$

where k, ρ and c are, respectively, the thermal conductivity, the specific mass and the specific heat of the concrete. The solution is nonlinear, because the material properties varies with temperature. Inside the slab we consider that x is the vertical direction, coincident with the main axis of the flame (z-axis in Figure 1), y is the horizontal direction, perpendicular to the axis of the flame.

The numerical solution of equation (1) is obtained by finite difference using implicit discretization schemes. The code is implemented in Matlab. This work follows a previous publication [2] which was addressed to solve the same problem using an explicit scheme.

Section 2 is devoted to the description of the boundary conditions of the slab. Its definition is extremely important because it is through the boundary conditions that the effects of fire are transmitted to the slab. Thereafter, in section 3, we analyse the effect of mesh size in the parallel direction to the axis of the flame, where there is a large temperature gradient on the exposed surface. Section 4 shows the results of simulation in two dimensions covering the vertical section of the slab immediately above the axis of the flame. Section 6 finishes with some observations about the results obtained.

2 BOUNDARY CONDITIONS

The boundary conditions allow transfer to the slab the heat released by the localised fire. The Gasemi method was considered to setup the boundary conditions [1]. This method is applied when the flame is impacting the ceiling. The resulting heat flux ($\dot{h}$) depends on the parameters illustrated in Figure 2 [1]. *H* (m) is the height of the compartment. *D* (m) is the is the diameter of the fire, *r* (m) is the horizontal distance between the vertical axis of the fire and the ceiling point where the heat flux is calculated, L_h (m) is the horizontal flame length that depends on *H* and on *Q*, the rate of heat release of the fire.

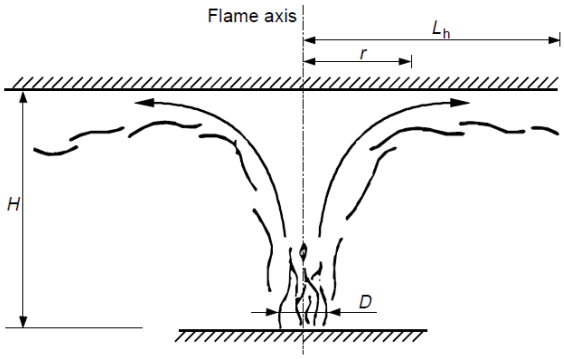

Figure 2: Geometry of the compartment [1].

The heat flux $\dot{h}$ [W/m^2] received by the exposed surface area at the level of the ceiling is given by:

$$\begin{aligned} \dot{h} &= 100000 && \text{if} \quad y \le 0.3 \\ \dot{h} &= 136300 - 121000\,y && \text{if} \quad 0.3 < y \le 1 \\ \dot{h} &= 15000\,y^{-3.7} && \text{if} \quad 1 < y \end{aligned} \tag{2}$$

The parameter *y* depends on the diameter *D* and on the heat release rate *Q*. For the heat release of the fire we have choose the typical curve that corresponds to a utility car. This curve as trapezoidal form with a maximum value equal to 18 MW that corresponds to a conservative value for the dimensioning [3].

The net heat flux $\dot{h}$ that affects the exposed surface of the slab along its entire length (from $r = 0$ to $r = 5$), from the beginning ($t = 0$) to the end of the fire duration ($t = 1500$ s). The values of the net heat flux are represented in Figure 3 for different values of *r*. We consider also that he values of the heat flux are symmetric relatively to the axe o of the flame (see Figure 2).

Additionally, the heat of the slab loosed by radiation and convection was also considered. In the exposed surface area the heat flux by radiation is calculated using equation (3),

$$h_r = \phi \varepsilon_m \varepsilon_f \sigma \left[(\theta_m + 273)^4 - 293^4 \right] \tag{3}$$

where ϕ represents the configuration factor, ε_m is the surface emissivity of the member, ε_f is the emissivity of the fire, σ is the Stephan Boltzmann constant and θ_m is the surface temperature of the member [°C]. In the unexposed and exposed surfaces of the slab, the convective heat flux is also calculated according to equation (4),

$$h_c = \alpha_c (\theta_m - 20) \tag{4}$$

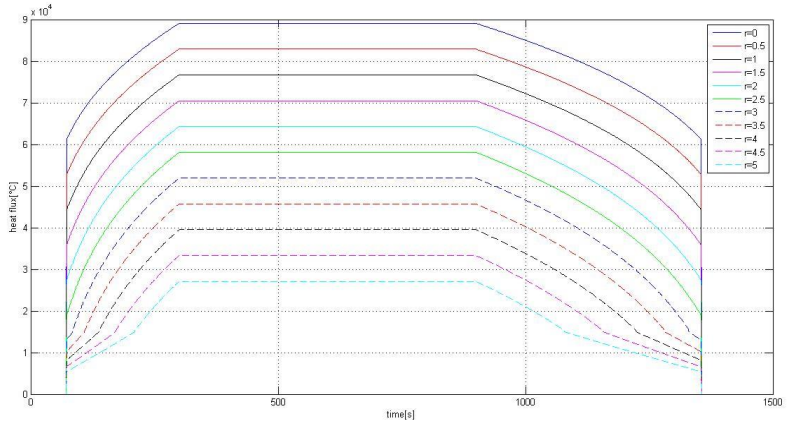

Figure 3: Net heat flux $\dot{h}$ for different values of *r*.

where α_c is the coefficient of heat transfer by convection [W/m^{2}K]. The insulation boundary condition was imposed on the left and right side of the slab.

3 SETUP OF THE GRID SIZE IN ONE DIMENSION

The numerical solution of equation (1) in one dimension was solved along the vertical direction that corresponds to the axis of the flame ($r = 0$ in Figure 1). The grid size by finite differences was defined using an implicit scheme as described by Patankar [4].

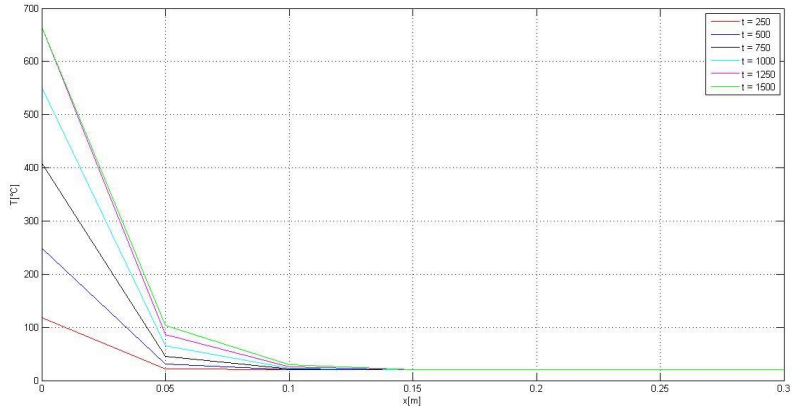

Figure 4: Temperatures across the slab on the axe of the flame obtained with $\Delta x = 0.5\times10^{-2}$ m.

The grid size was set up with a uniform value and then the variation effect was analysed. Figure 4 shows the variation of the temperature across the slab on the axis of the flame at different times, obtained with $\Delta x = 0.5\times10^{-2}$ m. The maximum temperature is near to 700 ºC and occurs in the exposed side of the slab. During fire development, temperature inside the slab increases as well as the maximum temperature at the exposed side. When fire approaches the end and the incident heat flux is almost zero, the temperature of the exposed surface is lower than the temperature inside the slab. Figure 5 represents the temperature solution with a grid size five times smaller.

Results of Figures 4 and 5 show that the problem is sensitive to the dimension of the spatial grid. If grid size Δx is reduced to 10^{-3} m the temperature curves are shifted to higher values (see Figure 5). This sensitivity is probably due to the high temperature gradient near the exposed side of the slab. Due to the thermal conductivity of the concrete there is a large temperature difference between the exposed side and the neighbouring points. Smaller values of the grid size Δx allows to better capture the temperature variation near the exposed side. As can be seen in Figure 5, this seems to be linear in the beginning of the fire.

Figure 6 shows the temperature evolution of the exposed surface of the slab for different grid size. As we can observe, smaller values of Δx lead to temperature curves with higher values. But values of Δx smaller than 10^{-3} m are responsible just for slight increases in temperature.
The results obtained with $\Delta x = 10^{-3}$ m are satisfactory. However, in order to reduce the computational effort, a grid with variable step was implemented. This grid size was modified by a factor φ higher than 1.0 to increase the grid where there is no significant temperature gradient

$$\Delta x_{i+1} = \varphi \, \Delta x_i . \tag{5}$$

Figure 7 contains the evolution of the temperature at the bottom of the slab resulting from different grid with different values of the step factor φ. As comparison it is also included the curve resulting from the discretization with a constant step $\Delta x = 10^{-3}$ m. The values obtained with $\varphi = 1.4$ are very close to the values obtained with a constant step $\Delta x = 10^{-3}$ m and enables a considerable reduction in terms of computational work because it reduces the total number of operation and the requirements of memory storage. From now on, the grid size will be described by equation (5) using $\varphi = 1.4$.

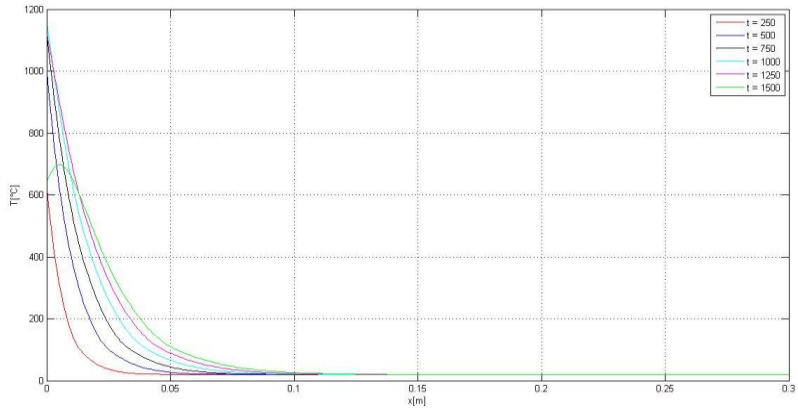

Figure 5: Temperatures across the slab on the axis of the flame obtained with $\Delta x = 10^{-3}$ m.

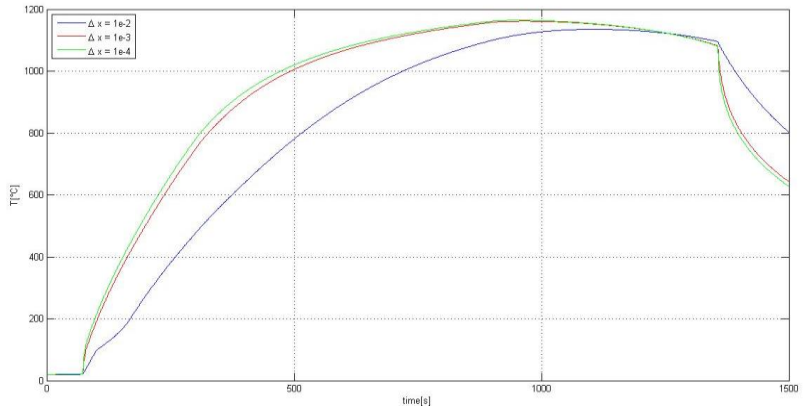

Figure 6: Temperatures at the bottom of the slab on the axis of the flame, for different values of Δx.

4 TWO DIMENSIONAL SIMULATION

To determine the temperature field in the cross section of the slab located on the axis of the flame, an implicit scheme described by Patankar [4] was used. The Cartesian coordinates are *y* as the horizontal direction and *x* as the vertical direction (similarly to the resolution in one dimension).

We verify that the step size in the horizontal direction (Δy) does not affect the results. Figure 8 presents the temperature field inside the slab at t=1300 s, obtained with $\Delta y = 0.1$ m and $\Delta y = 0.5$ m. We can observe that the temperature distribution obtained with the two different mesh sizes are very close to each other.

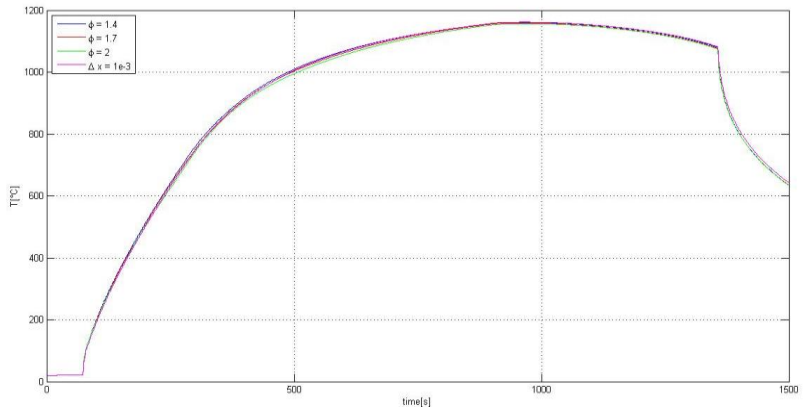

Figure 7: Temperatures at the bottom of the slab on the axis of the flame, for different step factor φ .

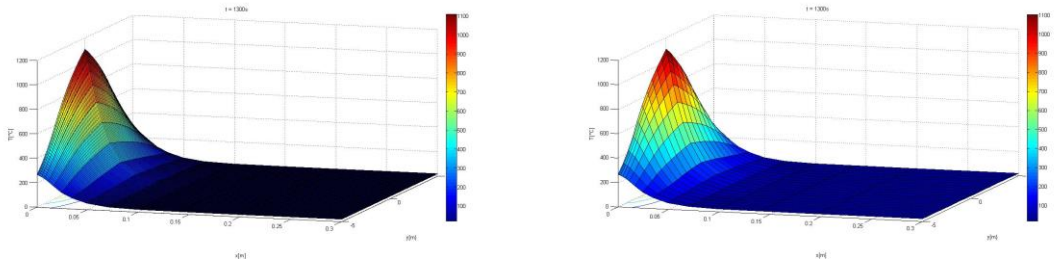

$\Delta y = 0.1\,\text{m}$ and $t = 1300\,\text{s}$ $\Delta y = 0.5\,\text{m}$ and $t = 1300\,\text{s}$

Figure 8: Temperatures inside the slab at t = 1300 s, for different values of Δy .

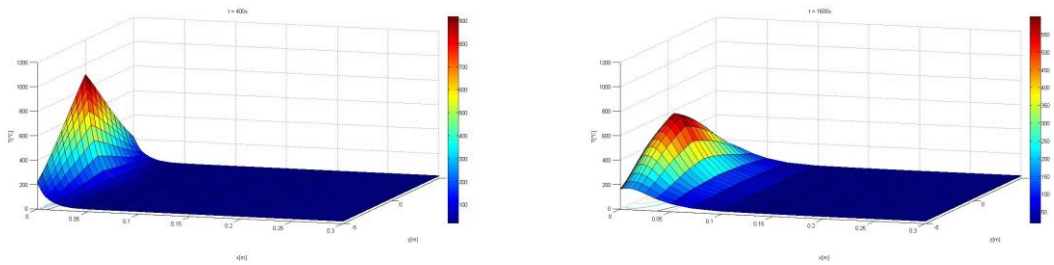

Figure 9: Evolution of the temperature inside the slab.

In Figure 9 we show the temperature distribution within the slab in two different time instants ($t = 400\,\text{s}$ and $t = 1600\,\text{s}$) of the fire. The highest temperatures occur always near the edge in contact with the flames. Most of the slab remains at low temperatures and little affected by heat.

5 CONCLUSIONS

The solution of heat transfer equation in a concrete slab subject to a localized fire is a very sensitive problem due to the high temperature gradients existing in the exposed surface. Because of the low conductivity of the concrete there is a large temperature gradient between the exposed surface boundary of slab and the neighbouring points. Large values of the grid size in this direction can lead to erroneous results.

Due to the geometry of the slab section, with a length much larger than its height, the temperature inside propagates mainly in the vertical direction. The variation of the horizontal discretization step affects very little the results. The problem can be reduced to a set of one-dimensional problems.

REFERENCES

[1] CEN – Comité Europeu de Normalização (2004). *EN1992-1-2 - Eurocódigo 2: Projecto de Estruturas de Betão – Parte 1–2: Regras Gerais – Verificação da Resistência ao Fogo*, Bruxelas.

[2] NGR Caiado (2012). *Simulação Numérica do Comportamento Térmico de Compartimentos Sujeitos a Incêndios Localizados*, Tese de Mestrado, Escola Superior de Tecnologia e Gestão, Instituto Politécnico de Bragança.

[3] C Harmemza, AMC Santiago, LAP Simões da Silva (2011). Metodologias de dimensionamento de parques de estacionamento abertos mistos aço-betão em situação de incêndio. In *VIII Congresso de Construção Metálica e Mista*, Guimarães, Portugal.

[4] SV Patankar (1980). *Numerical Heat Transfer and Fluid Flow*, Taylor & Francis, USA.

[5] L Piegl, W Tiller (1995). *The NURBS Book*, Springer.

V Conferência Nacional de Mecânica dos Fluidos, Termodinâmica e Energia
MEFTE 2014, 11–12 Setembro 2014, Porto, Portugal
APMTAC, 2014

Saltwater experiments of air curtains to smoke control in fires

JC Viegas, H Cruz

Laboratório Nacional de Engenharia Civil, Av. do Brasil 101, 1700-066 Lisboa, Portugal
email: jviegas@lnec.pt, htcruz@lnec.pt

ABSTRACT: The smoke flow inside buildings is a major cause of death in the event of fires. Fire or smoke doors are currently used, together with smoke control systems, to avoid the smoke flow beyond the boundaries of fire compartment. In this research it is proposed to use downward air curtains to stop smoke flow, which do not impair the visibility in escape routes. The methodology followed in this research includes: (i) the development of an analytical model that relates the relevant characteristic quantities of a plane jet with the characteristics of the environment in which the fire develops, (ii) small scale experiments with salt water modelling to assess the parameters that control the smoke tightness of the air curtain, (iii) CFD simulations to assess the performance of a full scale air curtain near a fire source and (iv) fire experiments with a full-scale test specimen. In this paper the analytical model and saltwater experiments are presented. Test results confirm that vertical downward air curtains are able to avoid the smoke flow through openings and show good agreement with the theoretical model for the prediction of the minimum exhaust rate from fire compartment. It was shown that the exhaust flow rate depend on air curtain flow rate and fluid heat expansion due to fire. Test results also allow the assessment of the minimum nozzle air velocity to avoid smoke leakage.

KEY-WORDS: Fire safety; Smoke control; Plane jets; Experiments; Saltwater modelling.

1 INTRODUCTION

The smoke flow inside buildings is a major cause of death in the event of fires. The technology currently used to prevent this event relies on the enclosure of building spaces by fire resistant walls, on the use of fire resistant doors and the use of smoke control. In many cases closing passageways with fire doors makes difficult to identify the escape route and can delay people egress; in other cases the use of fire gates makes difficult to use them as escape routes When the spread of fire through the void is unlikely, it is acceptable the use of an air curtain if it is effective in stopping the smoke flow. Air curtains do not impair the visibility of building occupants in evacuation and do not cause difficulties for people using escape routes.

There are several applications of this concept in tunnels [1] and in building corridors [2], but these are based on the pull-push principle applied to horizontal air curtains. Several other authors studied the application of single vertical air curtains (upwards or downwards) [3, 4, 5, 6, 7, 8] and there is also research on double vertical air curtains [9]. Some studies used CFD simulations to assess the performance of air curtains relating to curtain tightness on corridors [8], to fire/explosion accident in a clean room [10] and to contaminants dispersion from clean rooms [11]. In Portugal a study was carried out to evaluate the performance of air curtains to separation of different environmental conditions [12], however it reports temperature differences much lower than the expected in case of fire.

The mentioned research is not presenting clearly the need of smoke exhaust in the fire compartment, which the authors of this paper consider to be a key issue for the success for the smoke tightness by air curtains for high temperature smoke. Therefore, it is clear the need of research under this topic in order to apply air curtains in a more general way to the open boundaries of fire compartments.

This project has the objective of developing and applying the technology of air curtains to limit the smoke flow through the building openings. The methodology followed in this research includes: (i) the development of an analytical model that relates the relevant characteristic quantities of a plane jet with the characteristics of the environment in which the fire develops, (ii) small scale experiments with salt water modelling to assess the parameters that control the smoke tightness of the air curtain, (iii) CFD simulations to assess the performance of a full scale air curtain near a fire source and (iv) fire experiments with a full-scale test specimen. In this paper the analytical model and saltwater experiments are presented.

The analytical model assumes that the pressure due to the jet momentum balances the pressure due to buoyancy at the opening. This model also includes a simplified analytical methodology for estimating the temperature inside the fire compartment.

Several vertical downward plane jets and horizontal plane jets were tested in a small-scale model (1/20). The buoyancy due to fire was reproduced by density difference between saltwater and freshwater. The model, made by Plexiglas, includes one compartment connected to outside by a single opening which is protected by the plane jet. The similarity laws between flows allow extrapolate these results to real fire cases.

The results showed that it is feasible to avoid the leakage of the denser fluid (simulating smoke) to outside of the compartment using a plane jet (curtain) flowing a less dense fluid. The tests clearly showed that the plane jet is critical to the tightness because when it is stopped (with no change of other relevant parameters, including exhaust flow rate and the intensity of the saltwater source) the loss of tightness occurs immediately. Thus, the test results demonstrate the feasibility of the use of air curtains to control smoke and allow the experimental assessment of the parameters that control tightness.

2 METHODS

2.1 Analytical model

The smoke tightness due to an air curtain (plane jet) is based on the balance of the air curtain momentum and the momentum of the smoke flow. The nozzle of the plane jet is put at the door soffit level and is flowing downward, being $\propto_0$ the angle between the curtain axis and the vertical plane. The initial momentum J_0 jet per unit of width (of the opening) is given by equation (1).

$$J_0 = \rho b_0 u_0^2 \tag{1}$$

where ρ is the fluid density, b_0 is the thickness of the jet nozzle and u_0 is the initial jet velocity. This work considers that the jet momentum is conserved. Since the smoke flow (this case is horizontal) is normal to the plane of the opening (vertical), only the momentum due to the horizontal component of jet velocity is concerned, according to the equation (2).

$$J_{0h} = \rho b_0 u_0^2 \text{sen} \propto_0 \tag{2}$$

The effect of this momentum (per unit width of the jet) in pressure is assessed by the equation (3), where h is the vertical height over which the horizontal component of the velocity of the jet comes to zero (i.e. wherein the jet beds to the vertical).

$$\Delta P_a = \frac{\rho_0 b_0 u_0^2 \text{sen} \propto_0}{h} \tag{3}$$

When there is a difference in fluid density between indoor and outdoor, assuming uniform density at each environment, the value of the pressure difference is given by the equation (4).

$$\Delta P_s = gH(\rho_0 - \rho_1) \tag{4}$$

being H the height above the neutral plane (when the difference in densities is uniform, the pressure difference varies linearly with the height). Since the effect of the jet is relevant above the neutral plane only, when inside pressure is higher than outside pressure, then h in the equation (3) is the height of the opening soffit above neutral plane. Maximum pressure difference occurs near the soffit of the opening. Dividing equation (3) by equation (4) is obtained a pressure ratio that is a measure of the performance of the curtain, as shown in equation (5):

$$\frac{\Delta P_a}{\Delta P_s} = \frac{\rho_0 b_0 u_0^2 \text{sen} \propto_0}{gh^2(\rho_0 - \rho_1)} \tag{5}$$

Equation (6) defines the deflection modulus D_m [12], which is proportional to the equation (5).

$$D_m = \frac{\rho_0 b_0 u_0^2}{gh^2(\rho_0 - \rho_1)} \tag{6}$$

The smoke tightness is obtained combining the jet momentum with the inlet velocity through the opening due to the smoke exhaust at the compartment. The inflow velocity u_a through the opening contributes also to retain the smoke; therefore, its momentum must be considered and the equation (3) is modified as presented in equation (7).

$$\Delta P_a = \frac{\rho_0 b_0 u_0^2 \text{sen}\alpha_0 + \rho_0 h u_a^2}{h} \quad (7)$$

Then equation (5) takes the form of the equation (8).

$$\frac{\Delta P_a}{\Delta P_s} = \frac{\rho_0 b_0 u_0^2 \text{sen}\alpha_0 + \rho_0 h u_a^2}{g h^2 (\rho_0 - \rho_1)} \quad (8)$$

The minimum ratio $\Delta P_a / \Delta P_s = B$ was assessed by saltwater experiments. Knowing this value, the minimum jet velocity that complies with the smoke tightness requirement is given by the equation (9).

$$u_0 = \sqrt{\frac{B g h^2 (\rho_0 - \rho_1) - \rho_0 h u_a^2}{\rho_0 b_0 \text{sen}\alpha_0}} \quad (9)$$

The difference of densities can be obtained from the ideal gas equation and may be expressed in terms of indoor and outdoor temperatures, considering the equation (10)

$$\rho_0 T_0 = \rho_1 T_1 \Leftrightarrow \rho_0 \frac{T_0}{T_1} = \rho_1 \quad (10)$$

Combining equations (9) and (10), the equation (11) is obtained.

$$u_0 = \sqrt{\frac{B g h^2 \left(1 - \frac{T_0}{T_1}\right) - \rho_0 h u_a^2}{\rho_0 b_0 \text{sen}\alpha_0}} \quad (11)$$

Another part of the problem is to estimate the exhaust flow rate of the smoke control system of the compartment to keep the smoke tightness at the door. As it will be shown, it is impossible to get the smoke tightness at the door without smoke exhaust from the compartment. It is well known that it is possible to get smoke tightness at the door if the exhaust is high enough; the advantage of the use of the air curtain is to reduce significantly the exhaust flow rate needed to avoid smoke leakage through the door. Having this view, the problem of the use of air curtains to keep the opening tight is solved if the jet velocity u_0 and the exhaust flow rate are determined in function of the fire scenario. From equation (11) the assessment of u_0 is solved, if B is known. In this step is necessary to assess the exhaust flow rate.

For a compartment with a fire source and an outside opening it is clear that to prevent the smoke flow through this opening to the outside shall be considered (i) the thermal expansion of the smoke into the compartment and (ii) the outer flow entrained by the plane jet at the door. It is also clear that eddies due to jet turbulence near the door may transport to outside smoke mixed into the jet flow. At this step of the work it will be considered that eddy smoke transport will be prevented by increasing the estimation of the outer flow entrained by plane jet at the door.

The thermal expansion of fluid $\Delta \dot{V} = \dot{V}_1 - \dot{V}_0$ (the indices 0 and 1 represent the initial and final states) due to the convective part of the heat release rate $\dot{Q}_c$ can be estimated taking into account that the thermal energy conservation can be simplified to the equation (12).

$$\dot{Q}_c = \dot{M} \overline{C_p} (T_1 - T_0) \quad (12)$$

where $\dot{M}$ is the mass flow rate of the fluid, $\overline{C_p}$ is the average specific heat at constant pressure (considering here the average is an approach, which does not have significant consequences since the final equations will be adjusted by empirical coefficients), T_1 the absolute temperature of the hot fluid and T_0 is the initial temperature. Using the equation (10), the equation (12) can be rewritten as follows:

$$\dot{Q}_c = \dot{V}_0 \rho_0 \overline{C_p} \left(\frac{\rho_0}{\rho_1} - 1\right) T_0 \quad (13)$$

$$\frac{\dot{Q}_c}{\rho_0 \overline{C_p} T_0} = \dot{V}_0 \left(\frac{\rho_0}{\rho_1} - 1\right) = \dot{V}_1 - \dot{V}_0 = \Delta \dot{V} \quad (14)$$

The flow rate $\dot{V}$ of the plane jet is given by equation (15) [13]:

$$\dot{V} = 0{,}44 \left(\frac{x}{b_0}\right)^{0{,}5} \dot{V}_0 = 0{,}44 \left(\frac{x}{b_0}\right)^{0{,}5} u_0 \, b_0 w = 0{,}44 (b_0 x)^{0{,}5} u_0 \, w \quad (15)$$

where x is the distance from the nozzle, b_0 is the thickness of the nozzle, w is the width of the nozzle (and door) and $\dot{V}_0$ is the jet flow rate at the nozzle. The minimum exhaust flow rate of smoke from the compartment will be the sum of the corresponding thermal expansion with at least the entrained flow of the

jet from outside. The jet is entraining fluid from both sides, but just the flow rate coming from outside and the flow rate at the nozzle corresponds to mass intake into the compartment. We shall keep in mind that turbulent transport in the jet may require higher flow rate to keep the smoke tightness. Thus, the minimum exhaust flow rate $\dot{V}_{exaust}$ includes the thermal expansion and a portion proportional to the jet flow rate, according to the equation (16):

$$\dot{V}_{exaust} = \frac{\dot{Q}_c}{\rho_0 \overline{C_p} T_0} + A {b_0}^{0,5} u_0 \tag{16}$$

being A a constant of proportionality, that includes geometry of the opening, to be assessed by experiments.

In order to fully solve the equation (11) is necessary to estimate the smoke temperature T_1 and h. This temperature depends on the convective part of the heat release rate $\dot{Q}_c$ (it is assumed here that at the initial stage of the fire all the radiated energy is being absorbed by the surrounding, not contributing to the heating of the smoke) and the exhaust flow rate. The equation (12) is used to estimate the average temperature of the smoke, but now the values of the specific heat at constant pressure corresponding to the initial and final temperatures are considered (C_{p0} and C_{p1}), as shown in equation (17):

$$\dot{Q}_c = \dot{M}\left(C_{p1} T_1 - C_{p0} T_0\right) \tag{17}$$

Since the exhaust fans keep approximately constant the volume flow rate, it is convenient to express the equation (17) in function of fan volume flow rate, as shown in the equation (18).

$$\dot{Q}_c = \rho_1 \dot{V}_{exaust}\left(C_{p1} T_1 - C_{p0} T_0\right) = \rho_0 \frac{T_0}{T_1} \dot{V}_{exaust}\left(C_{p1} T_1 - C_{p0} T_0\right) = \rho_0 T_0 \dot{V}_{exaust}\left(C_{p1} - C_{p0} \frac{T_0}{T_1}\right) \tag{18}$$

$$C_{p0} \frac{T_0}{T_1} = C_{p1} - \frac{\dot{Q}_c}{\rho_0 T_0 \dot{V}_{exaust}} \tag{19}$$

The final temperature is then calculated according to the equation (20). The final temperature dependence on C_{p1} requires an iterative solution.

$$T_1 = \frac{C_{p0} T_0}{C_{p1} - \frac{\dot{Q}_c}{\rho_0 T_0 \dot{V}_{exaust}}} \tag{20}$$

There are a number of methods that allow estimating the position of the neutral plane (eg, see [14]). The results of the experiments show that the flow near the jet is quite complex and that the neutral plane may be strongly disturbed. Therefore, further results will be referenced to the height of the opening.

2.2 Saltwater modelling

In fire scenarios the flow is buoyancy driven. Using saltwater and freshwater is a good way to scale the density difference that occurs between smoke and fresh air. In this approach just convection is retained; it do not allow reproducing radiation heat transfer or chemical reactions. Therefore, just the phenomena related with the flow driven by the air curtain near the opening are studied. This allows some simplification on the experiments, namely: (i) the saltwater (simulating smoke) feeds directly the smoke layer (this avoids the plume flow, which is irrelevant for the jet flow, and as the advantage that the saltwater layer density is easier to control) and (ii) the velocity through the opening is created by an exhaust in the fresh water layer (in this way the total mass of saltwater needed for experiments is much lower). To reduce the problem of smoke control only to their convective part is an approximation that is reasonable in an initial stage of fire, while fresh air flow rate is high and the heat release rate of the heat source is still relatively low, thus corresponding with many scenarios of smoke control.

Saltwater similarity is a good way to generate buoyancy and this is made generally using a source of saltwater (coloured for visualization) to simulate the convective plume in a freshwater environment. Having the saltwater a greater density than freshwater, the plume is generated downward, forcing the similarity to be interpreted upside down. However, except this minor inconvenience, this concept of similarity allows to minimize the salt consumption.

The equations of continuity (21), momentum transport (22) and energy conservation (in the form of transport equation) (23) are shown below [15]. Table 1 presents the similarity between the dimensionless variables in the prototype and in the model.

$$\frac{D\,\bar{u}^*}{D\,t^*} = 0 \tag{21}$$

$$\frac{D\bar{u}^*}{Dt^*} + \nabla^*\bar{p}^* - \theta^*\bar{k} = \left(\frac{1}{Re}\right)\nabla^{*2}\bar{u}^* \quad (22)$$

$$\frac{D\theta^*}{Dt^*} = GQ^* + \left(\frac{1}{Re\ Pr\ *}\right)\nabla^{*2}\theta^* \quad (23)$$

In these equations H and L represent the enclosure height of the prototype and the diameter of the fire in the prototype, respectively. U is the velocity scale of the fluid, ζ is the density (or temperature) perturbation scale, Q_0, u , ρ_0, T_0, g, μ, k and c_p respectively represent the convective heat release rate, the velocity, the cold fluid density, the initial temperature, the acceleration of gravity, the viscosity, the thermal conductivity and the specific heat at constant pressure of the air at $\bar{x}_g$ point and t_g time, at the prototype, or the t_s time and the $\bar{x}_s$ point at the model. The variables applied to the saltwater model are h and l, representing respectively the height and the diameter of the saltwater source. Y is the mass fraction of salt, $\mathfrak{D}$ is the mass diffusivity, $\dot{m}_0$ is the mass flow of salt at source and Re, Pr and Sc, respectively represent the Numbers of Reynolds, Prandtl and Schmidt.

Table 1: Dimensionless variables for fire similarity with saltwater [15].

Dimensionless variable	Definition		Dimensionless variable	Definition	
	Prototype	Model		Prototype	Model
θ^*	$\frac{(T-T_0)}{T_0\zeta}$	$\frac{Y}{\zeta}$	$P = Pr = Sc$	$\frac{\mu c_p}{k}$	$\frac{\mu}{\rho_0}\mathfrak{D}$
t^*	$\frac{t_g U}{H}$	$\frac{t_s U}{h}$	ζ	U^2/gH	U^2/gh
$\bar{u}^*$	$\frac{\bar{u}}{U}$	$\frac{\bar{u}}{U}$	U	$\left(\frac{\dot{Q}_0 g}{\rho_0 c_p T_0 H}\right)^{1/3}$	$\left(\frac{\dot{m}_0 g}{\rho_0 h}\right)^{1/3}$
$\bar{p}^*$	$\bar{p}/\rho_0 U^2$	$\bar{p}/\rho_0 U^2$	Re	$\rho_0 UH/\mu$	$\rho_0 Uh/\mu$
∇^*	$H\nabla$	$h\nabla$	G	$(H/L)^3$	$(h/l)^3$
$\bar{x}^*$	$\bar{x}_g/H$	$\bar{x}_s/h$	Q*	$\dot{Q}'''/(\dot{Q}_0/L^3)$	$\dot{m}'''/(\dot{m}_0/l^3)$

To ensure a similarity between flows, they must be both fully turbulent at the source and the momentum of the source shall be small when compared to the buoyancy (heat source momentum at the origin is zero); according to [15], to satisfy this condition is required that the ratio F (24) is always less than 1 at the plume, except near the source (u_0 being the velocity at source and z the height). According to [15], it is reasonable that F <1 for z> 0.2 H.

The relationship between buoyancy in the saltwater model and temperature difference in prototype can be estimated according to (25) (Froude Number similarity). The subscripts m and P stands to model and prototype, respectively. To get the full dynamic similarity is required that flows have the same turbulent behaviour.

$$F = \rho u_0 / 2(\rho - \rho_0)gz \quad (24)$$

$$\frac{u_m}{u_P} = \frac{\sqrt{2gl_m(\rho-\rho_0)_m/\rho_m}}{\sqrt{2gl_P(\rho-\rho_0)_P/\rho_P}} \Leftrightarrow (T-T_0)_P = \frac{L}{l}\left[1-\left(\frac{\rho_0}{\rho}\right)_m\right]T_{0P} \quad (25)$$

2.3 Saltwater experiments

The saltwater experiments have been carried out inside a glass tank 0.55 m high, 1.40 m long and 0.45 m wide. A Plexiglas model was placed 100 mm above the tank bottom and it is 0.250 m high, 0.400 m long and 0.250 m wide (Figure 1). It has a vertical opening 0.125 m x 0.125 m, with the sill at the bottom level of the model. The smoke is simulated by a saltwater in a freshwater environment. The model is put inside the tank upside down. The saltwater was coloured to allow observation. This model represents a compartment in the geometrical scale 1/20.

The saltwater is pumped directly into saltwater layer at a flow rate of 0.0427 l/s. The downwards plane jet is located outside the model and is fed with freshwater (taken from the tank). Compartment exhaust is made at the bottom (top, in the upside down model) of the vertical wall opposite to the opening. There is a feeding of freshwater to the tank in order to keep the water level. The testing parameters are shown in Table 2. The flow parameters were measured at steady state before testing or, whenever relevant, they have been

adjusted (one at a time) during the test to get smoke tightness at the opening. The jet angle (with vertical) and the nozzle thickness were varied (at a time) for each of the jet configurations. In each test the parameters jet velocity and exhaust flow rate were adjusted until no saltwater leakage is visible (Fig. 1). The flow rate was determined by calibration of the respective valve position.

The no smoke (coloured saltwater) leakage threshold was assessed visually through the opening and recorded on video. The bigger component of the uncertainty of the experiments is the visual assessment of the saltwater tightness.

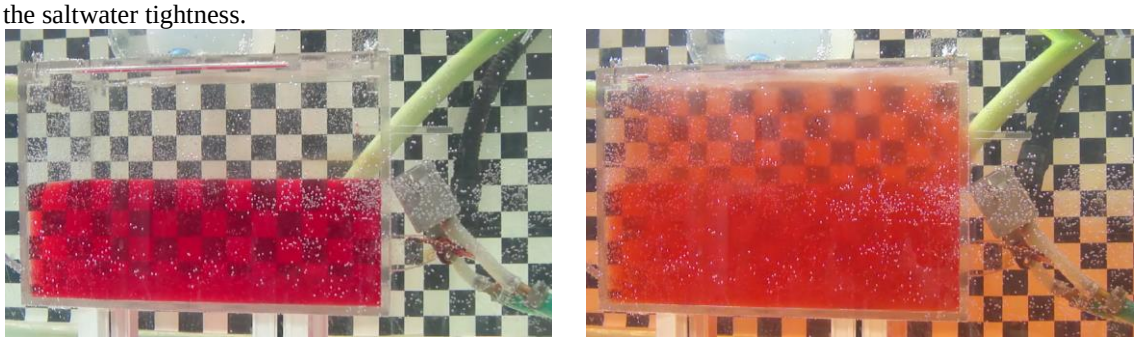

Figure 1: Saltwater model before testing (left) and during test (right), showing saltwater tightness.

Table 2: Saltwater test parameters.

Test number	b_0 [m]	u_0 [m/s]	$\propto_0$ [º]	Initial ρ_0 [kg/m³]	Final ρ_0 [kg/m³]	ρ_1 [kg/m³]	u_a [m/s]
1	0.00250	0.560	25	970.0	970.0	1023.40	0.0394
2	0.00500	0.560	25	968.7	968.7	1026.30	0.0508
3	0.00125	0.560	25	968.6	968.6	1027.80	0.0337
4	0.00750	0.458	25	976.4	976.4	1033.90	0.0436
5	0.00750	0.458	25	964.2	974.7	1020.10	0.0561
6	0.00125	0.700	25	968.1	975.4	1025.90	0.0289
7	0.00125	0.850	25	960.2	977.3	1024.40	0.0371
8	0.00125	1.000	25	963.2	973.3	1028.00	0.0376
9	0.00125	1.000	30	965.5	978.9	1026.90	0.0382
10	0.00125	0.850	30	973.0	975.5	1025.50	0.0384
11	0.00125	0.700	30	969.8	977.9	1026.70	0.0325
12	0.00125	0.560	30	969.8	974.8	1026.70	0.0310
13	0.00125	0.560	35	972.4	972.6	1031.70	0.0467
14	0.00125	0.700	35	975.8	979.6	1026.20	0.0462
15	0.00125	0.850	35	955.3	956.0	1019.00	0.0403
16	0.00125	1.000	35	955.3	956.9	1019.00	0.0559
22	0.00125	0.401	30	965.4	967.9	1032.10	0.0269

3 ANALISYS OF THE EXPERIMENTS

Test results were used to calculate $\Delta P_a/\Delta P_s$, according to equation (8). Dependence of the results was found only on the calculated average opening velocity u_a , on the jet velocity u_0 and on the nozzle thickness b_0 and a new equation was set, being the parameters adjusted by the least square method. Equation (26) was simplified to equation (27) and dependence on buoyancy $gh^2(\rho_0 - \rho_1)$ was searched. It was found that this set of data is not related with buoyancy, being equation (28) the best fit with B=555.78. Graphics of Figure 2 (the function in y-axis is presented in left lower corner and the variable of x-axis is u_a) show that R^2 is better in the case of equation (28).

$$\frac{\Delta P_a}{\Delta P_s} = \frac{\rho_0 b_0 u_0^2 \text{sen}\propto_0 + \rho_0 h u_a^2}{78.83\ gh^2(\rho_0-\rho_1)u_a^{1.051}u_0^{1.183}b_0^{0.506}} \quad (26)$$

$$\frac{\Delta P_a}{\Delta P_s} = \frac{\rho_0 b_0 u_0^2 \text{sen}\propto_0 + \rho_0 h u_a^2}{75.08\ gh^2(\rho_0-\rho_1)u_a\ u_0\ b_0^{0.5}} \quad (27)$$

$$\frac{\Delta P_a}{\Delta P_s} = \frac{\rho_0 b_0 u_0^2 \text{sen}\propto_0 + \rho_0 h u_a^2}{B\ u_a\ u_0\ b_0^{0.5}} \quad (28)$$

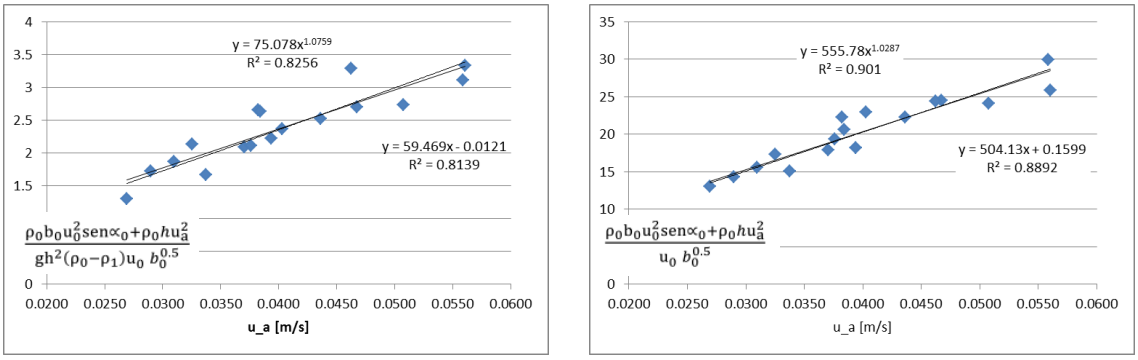

Figure 2: Best fit of experimental results, by power law and linear relation.

Solving equation (28) it is possible to obtain the value of the inlet velocity u_a , as shown in equation (29), being A constant depending on problem initial conditions and geometry. It is now clear that this test result corresponds to the equation (15) that was obtained with theoretical considerations; therefore equation (29) shall replace equation (15) in the mathematical model.

$$u_a = \left(\frac{B}{2\rho_0 h} - \sqrt{\frac{B^2}{4\rho_0^2 h^2} - \frac{\text{sen}\alpha_0}{h}}\right) u_0\, b_0^{0.5} \Leftrightarrow u_a = A u_0\, b_0^{0.5} \tag{29}$$

Only in test 22 the jet velocity was set to a minimum. In all other cases the jet velocity was higher; therefore, the saltwater tightness at the opening was conditioned by jet turbulence and jet entrained flow rate from outside, which shall be balanced by exhaust flow rate. That is why equation (28) does not depend on buoyancy. Only the results of test 22 will be directly related with buoyancy; thus, these results may be used in equation (8) to get the tightness condition related to buoyancy, as shown in equation (30), where equation (29) was included. Thus, equation (31) replaces equation (9) in the analytical model. These equations do not depend on the model scale.

$$\frac{\Delta P_a}{\Delta P_s} = \frac{\rho_0 b_0 u_0^2}{g h^2 (\rho_0 - \rho_1)} (\text{sen}\,\alpha_0 + h A^2) = 0.0184 \tag{30}$$

$$u_0 = \sqrt{\frac{0.0184\, g h^2 (\rho_0 - \rho_1)}{\rho_0 b_0 (\text{sen}\alpha_0 + h A^2)}} \tag{31}$$

Finally, in these experiments the time scale is $t_m/t_P = 1$ and the geometric scale is $l/L = 1/20$ (geometric similarity), thus the velocity scale is $u_m/u_P = 1/20$ (kinematic similarity). According to equation (25), that respects the Froude Number, the buoyancy of the test 22 correspond to the temperature difference of 372 K (being $T_{0P} = 293\ K$). Dynamic similarity is not fully respected in these experiments because Reynolds Number in the model is ranging from 500 to 3400, while in prototype the flow will be fully turbulent.

4 CONCLUSIONS

In this paper was developed a set of equations that describe the fire smoke tightness of a downward air curtain applied to an opening. Saltwater modelling was used to study the performance of this kind of flows and the experiments allow the following conclusions:

1. Downward air curtains may be successfully applied to avoid the smoke due to a fire flow through an opening, but require smoke exhaust in the fire compartments.
2. The test results show that the minimum jet velocity required to obtain the smoke tightness of the opening may be given by equation (31).
3. Minimum saltwater exhaust flow rate from the compartment is given by the equation (29), that agrees with equation (15) of the theoretical model. To obtain the minimum smoke exhaust flow rate the term corresponding to smoke expansion due to heating shall be added.

Further work is required to verify the equation (31) under different buoyancy conditions. Full-size experiments including a prototype of the air curtain and using a fire source will be developed to verify the smoke tightness model and to adjust the model for fully turbulent flow.

ACKNOWLEDGMENTS

This research was undertaken as part of a research project supported by the ADI – Agência de Inovação under Grant QREN n.º 23226 (Smoke Shield).

REFERENCES

[1] S Gupta, M Pavageau, JC Elicer-Cortés (2007). Cellular confinement of tunnel sections between two air curtains. *Building and Environment* **42**:3352–3365.

[2] H Sakurai, T Hayashi, M Shibata, K Kanehara (1980). Researches on air shutter for fire defence. *Fire Safety Journal* **2**:9–16.

[3] F Cumo, S Rossetti, G Guidi (2000). 3D simulation of dynamic barriers against fume and gaseous toxic substances. In *Proceedings of Ventilation 2000, the 6th International Symposium on Ventilation for Contaminant Control*, 4–7 June, Helsinki, Finland.

[4] MD de Virel, C Solliec, L Guyonnaud (1998). Mise en sécurité contre fumées d'incendie. *Face au Risque* **348**:13–18.

[5] MS Altinakar, A Weatherill (2001). Use of an inclined air curtain for preventing smoke propagation in a tunnel during fire emergency. In Proceedings *of the 4th International Conference on Safety in Road and Rail Tunnels*.

[6] F Gugliermetti, L Santarpia, G Zori (2003). Air curtain applied to fire smoke pollution control. In *Air Pollution 2003, the 11th International Conference on Modelling, Monitoring and Management of Air Pollution*, September 17–19, Catania, Italy, 541–549.

[7] M Sawley, A Drotz, B Greiveldinger (2004). Numerical flow simulation of an air curtain for road tunnel fire safety. *EPFL Supercomputing Review* **14**:3–6.

[8] LH Hu, JW Zhou, R Huo, W Peng, HB Wang (2008). Confinement of fire-induced smoke and carbon monoxide transportation by air curtain in channels. *Journal of Hazardous Materials* **156**:327–334.

[9] F Felis, M Pavageau, JC Elicer-Cortés, T Dassonville (2010). Simultaneous measurements of temperature and velocity fluctuations in a double stream-twin jet air curtain for heat confinement in case of tunnel fire. *International Communications in Heat and Mass Transfer* **37**:1191–1196.

[10] YP I, YL Chiu YL, SJ Wu (2009). The simulation of air recirculation and fire/explosion phenomena within a semiconductor factory. *Journal of Hazardous Materials* **163**:1040–1051.

[11] Y-C Shih, A-S Yang, C-W Lu (2011). Using air curtain to control pollutant spreading for emergency management in a cleanroom. *Building and Environment* **46**:1104–1114.

[12] LPC Neto (2006). *Estudo de Sistemas de Vedação Aerodinâmica do Tipo Cortina de Ar*, Tese de Doutoramento, Faculdade de Ciências e Tecnologia da Universidade de Coimbra.

[13] RD Blevins (1984). *Applied Fluid Dynamics Handbook*, Van Nostrand Reinhold Company Inc., New York, USA.

[14] JC Viegas (2008). *Utilização de Ventilação de Impulso em Parques de Estacionamento Cobertos*, Série Teses e Programas de Investigação 55, Laboratório Nacional de Engenharia Civil, Lisboa.

[15] KD Steckler, HR Baum, JG Quintiere (1988). Salt water modelling of fire induced flows in multicompartment enclosures. *Symposium (International) on Combustion* **21**(1):143–149.

Session 5

Chairman

Rui Miguel Lage Ferreira | U.Lisboa

This page was intentionally left blank

V Conferência Nacional de Mecânica dos Fluidos, Termodinâmica e Energia
MEFTE 2014, 11–12 Setembro 2014, Porto, Portugal
APMTAC, 2014

3D numerical simulation of flow at a 70º open-channel confluence

M Brito[1], OB Canelas[2], JL Leal[2,3], AH Cardoso[1]

[1]CEHIDRO, Instituto Superior Técnico, Universidade de Lisboa, Av. Rovisco Pais, 1049-001 Lisboa, Portugal
[2]UNIDEMI, Faculdade de Ciências e Tecnologia, Universidade Nova de Lisboa, Monte da Caparica, 2829-516 Almada, Portugal
[3]Faculty of Engineering and Science, University of Adger, Postboks 509, 4898 Grimstad, Norway
email: moises.brito@ist.utl.pt, olga.birjukova@ist.utl.pt, joao.leal@uia.no, antonio.cardoso@ist.utl.pt

ABSTRACT: The flow patterns in open-channel confluences are very complex due to the flow interaction between the main and the tributary channels. The interaction between flows generates complex turbulent structures and results in the development of the following distinctive zones: stagnation, deflection, separation, shear layers, maximum velocity and recovery zones. These turbulent structures are controlled by several variables such as flow discharge in both channels, confluence angle and channel geometry including longitudinal slope and boundary roughness. This renders the detailed description of the flow patterns a difficult challenge. The numerical simulation constitutes an important tool for describing these flows. Therefore, the main goal of this paper is the 3D numerical simulation of the flow at a 70º open-channel confluence. Simulations using Reynolds-averaged Navier-Stokes (RANS) equations and five turbulence closure models (k-ε, RNG k-ε, k-ω, SST k-ω, EARSM) were performed. The volume of fluid (VoF) model is used to simulate the air-water interaction at the free-surface. The results of the numerical model are compared with detailed measured experimental data. The results of the simulations demonstrate that the use of simple two-equation turbulence models is not enough to get an accurate flow field description of complex flows such as those observed in confluences. The use of EARSM allows a fairly good representation of the geometry of the separation zone, but it underestimates the time-averaged streamwise velocity in the maximum velocity zone due to the large experimental deformation of free surface, which is not well reproduce by the model.

KEY-WORDS: Confluence; CFD; Turbulence; RANS; EARSM.

1 INTRODUCTION

Open-channel confluences are common in natural rivers and hydraulic engineering works such as irrigation channels, wastewater treatment facilities and fish passage conveyance structures. Flow properties in confluences are complex due to the interaction between the main channel (MC) and tributary channel (TC) flows [1]. The interaction between flows generates complex turbulent structures and results in the development of the following distinctive zones [2]: (1) a zone of flow stagnation at the upstream confluence corner, (2) flow deflection where TC joins the MC, (3) a flow separation zone below the downstream confluence corner, (4) an area of maximum velocity, (5) a gradual flow recovery downstream from the flow separation zone and (6) several distinct shear layers associated with vortex generation (Figure 1). The flow stagnation zone is created by a deflection of both streams at the confluence. This zone is associated with an increase of pressure and flow depth along with a decrease of flow velocities and shear stresses. The directional change of the TC flow creates a zone of flow separation with a horizontal recirculation due to the flow detachment from the inner wall in the TC and its reattachment further downstream [3]. The separation zone delimits the effective width of the MC due to the reduced pressure and flow recirculation, which on the other hand, promote sediment accumulation [4]. The maximum velocity zone appears downstream of the confluence, namely at the contracted cross-section beside the separation zone. Shear layers are formed along the contact of the zones of flow separation and of maximum velocity, and are characterized by high turbulence intensities and shear stresses, as well as the presence of well-organized flow structures. As the shear layer expands laterally and dissipates, the flow recovers toward a straight shear flow in the downstream of the confluence. These zones are influenced by several variables such as flow discharges in both channels, angle of confluence, MC and TC geometry including longitudinal slope and boundary roughness [4]. Therefore, the detailed description of the flow patterns becomes very difficult. Hence, in the past, different approaches have been used to investigate the dynamics of confluence flows. Some laboratory (e.g. [1], [2], [5], [6]) and

numerical (e.g. [7], [8], [9]) studies have been carried out in an attempt to establish relationships among the above-mentioned variables. These studies provided useful information on free-surface, flow deflection and separation, secondary recirculation, shear layers and velocity vector fields. However, the characterization of the flow patterns provided in the previous studies is not satisfactory enough. The main aim of this work is to contribute to the understanding of open-channel confluence flows. In order to achieve this objective, 3D numerical simulations of the flow at a 70º open-channel confluence were performed using different turbulence closures and the results were compared to experimental data.

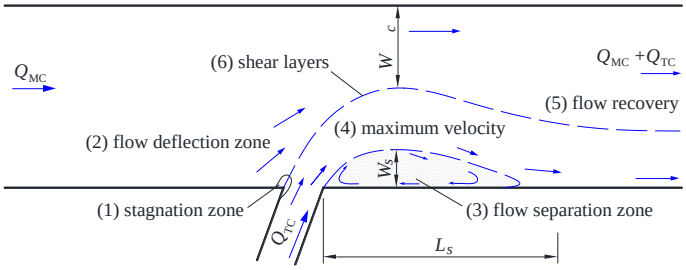

Figure 1: Schematic model of characteristic zones of open-channel confluences (modified from [2]).

2 EXPERIMENTAL SETUP

The experimental campaign was carried out in a horizontal and rectangular channel at the Hydraulics Laboratory of Instituto Superior Técnico [10]. The MC was made of polished concrete and was 1 m wide and 12 m long (Figure 2). The TC was built of PVC and was 0.15 m wide and 4.5 m long. This channel was connected to the MC 5 m downstream from the MC inlet, forming a 70º confluence angle so as to represent common natural conditions [10]. The experimental campaign was carried out for constant flow discharge ratio, $Q_r = Q_{TC} / Q_{MC} = 0.114$, where the flow discharge in the TC is $Q_{TC} = 0.005$ m^3/s and in the MC is $Q_{MC} = 0.044$ m^3/s. The flow depth upstream from the confluence in the MC is $H = 0.11$ m. Instantaneous velocity field was obtained using an Acoustic Doppler Velocimeter at a sampling rate of 100 Hz and over a dense sampling grid consisting of 6,012 points within the MC. The three components of the velocity vector were measured in 19 cross-sections resulting in 334 vertical profiles with 18 points each (Figure 2). The adopted sampling time was 90 s at each point.

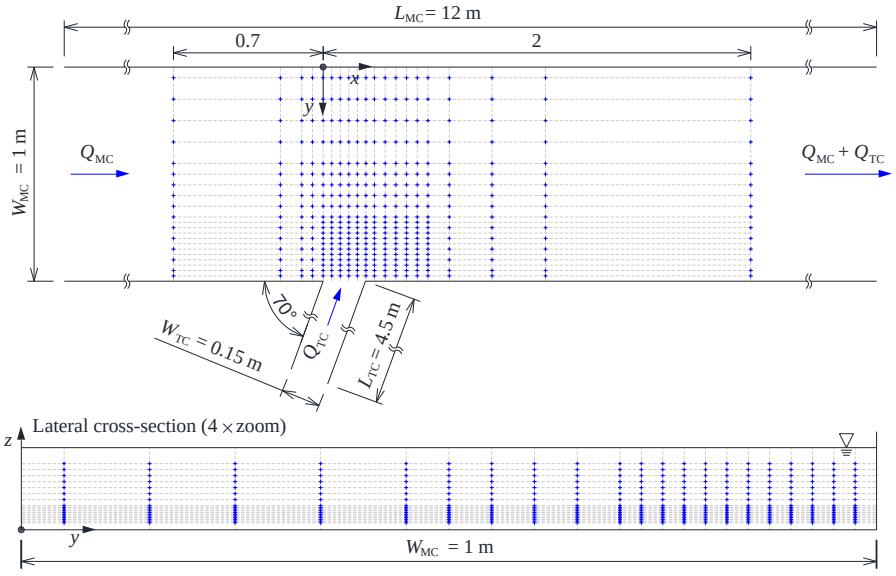

Figure 2: Plan and lateral cross-section of the MC with the measurement grid.

3 NUMERICAL MODEL

The flow dynamics is modelled by numerically solving of the 3D RANS equations [12], [13]:

$$\rho\left[\frac{\partial \overline{u}_i}{\partial t}+\frac{\partial}{\partial x_i}\left(\overline{u}_i\overline{u}_j\right)\right]=-\frac{\partial \overline{p}}{\partial x_i}+\frac{\partial}{\partial x_i}\left[\mu\left(\frac{\partial \overline{u}_i}{\partial x_j}+\frac{\partial \overline{u}_j}{\partial x_i}\right)\right]+\frac{\partial}{\partial x_i}\left(-\rho\overline{u_i'u_j'}\right)+\rho g_i \qquad (1)$$

where x_i are the components of Cartesian coordinate, u_i are the components of instantaneous velocity, g_i is the gravity acceleration in i direction, $-\rho\overline{u_i'u_j'}$ are the time-averaged Reynolds shear stresses, t is time, p is pressure, ρ and μ are the fluid density and dynamic viscosity, respectively. For closing the RANS equations it is necessary to model the time-averaged Reynolds shear stresses [12]. In the present study, steady-state simulations using two-equation models (*k*-ε, Re-Normalization Group (RNG) *k*-ε, *k*-ω, Shear Stress Transport (SST) *k*-ω) and Explicit Algebraic Reynolds Stress Model (EARSM) were performed. Two-equation models determine the turbulence kinetic energy, $k=\overline{u_i'u_i'}$, and dissipation rate, ε, from transport equations [13]. These models allow the turbulence length scale, $\ell = k^{3/2}/\varepsilon$, distribution to be determined even in complex flow situations. Therefore, two-equation models are the simplest models that promise success for flows whose length scale cannot be prescribed empirically in an easy way. In the *k*-ε model the kinematic eddy viscosity, ν_T, is expressed as the product of a velocity scale, $k^{1/2}$, and a length scale, ℓ. The dissipation rate is not the only possible length scale determining variable. The *k*-ω model uses the turbulence frequency $\omega = \varepsilon/k$ as the second variable and the length scale becomes $\ell = k^{1/2}/\omega$ [12]. The RNG *k*-ε model represents the effects of small-scale turbulence by means of a random forcing function in the RANS equations [12]. This model procedure systematically removes the small scales of motion from the governing equations by expressing their effects in terms of larger scale motions and a modified eddy viscosity. The SST *k*-ω model accounts for the transport of the turbulent shear stress and uses a combination of the best features of the *k*-ε model for free turbulence and *k*-ω model for the solution of the wall turbulence [12]. The EARSM model represents an extension of the standard *k*-ε model which solves algebraic equations for Reynolds stresses. The model is derived from the Reynolds stress transport equations and gives a nonlinear relation between the Reynolds stresses and the mean strain-rate and vorticity tensors [14]. The use of these models in this study aims to determine the possible highly accurate predictions of the onset and the amount of flow separation under adverse pressure gradients. The numerical scheme uses finite element-based control volume method, where the governing equations are discretized over each control volume. Advection terms in RANS equations are discretized using second order high resolution scheme, shape functions are used to evaluate spatial derivatives for all the diffusion terms and pressure gradient terms. The resulting system is then solved in a coupled manner, and the results are interpolated to the grid nodes. The VoF method for modelling the free-surface is used [11]. The stopping criterion for iterative calculations was set to be 0.001% for the normalized error in all equations, this led to an error of mass flow imbalance smaller than 0.1%.

3.1 Computational domain and conditions

The computational domain covering all the experimental measuring region, 1 m wide and 3 m long, was discretized using approximately 1,000,000 regular hexahedral elements aligned to the main flow direction and refined for regions close to the walls, free-surface and in the stagnation, deflection, separation zones (Figure 3).

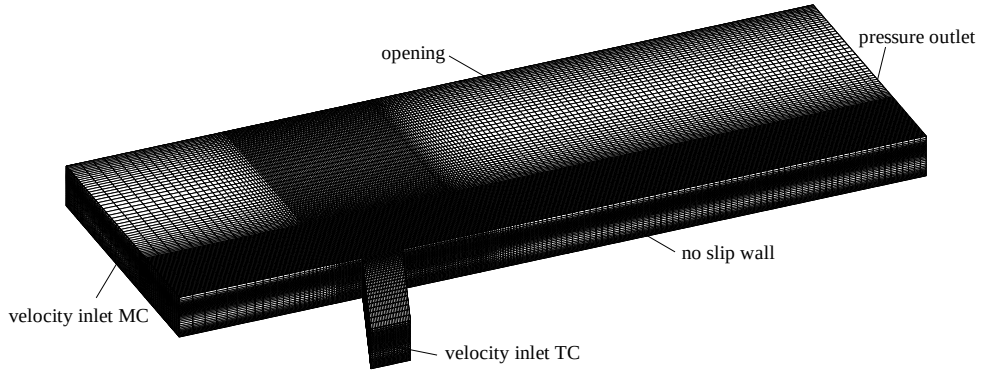

Figure 3: Computational grid and boundary conditions.

For turbulence modelling near the channel bed, wall functions were used and the non-dimensional vertical coordinate, z^+, values of the element closest to the channel bed were kept around 30. The lateral wall was prescribed with a non-slip boundary condition. The experimental cross-section velocity field and the flow depth measured at the first cross-section were prescribed at the MC inlet and a cross-section averaged velocity was prescribed at the TC inlet. A hydrostatic pressure profile with zero velocity

derivatives was set at the outlet. The upper boundary condition was prescribed on the air, at 0.04 m above the expected free-surface, with opening condition to allow constant zero pressure at the free-surface.

4 RESULTS AND DISCUSSION

4.1 Selection of a turbulence model

The experimental and numerical results obtained with *k*-ε, RNG *k*-ε, *k*-ω, SST *k*-ω and EARSM models are compared for selection of a suitable turbulence model for further study. Figure 4 presents the dimensionless width, W_S, and length, L_S, of the separation zone at horizontal plane $z/H = 0.47$. L_S is defined as the distance from the downstream corner of the confluence to the reattachment point of the flow [9]. W_S is defined by the zero derivative of the streamline passing in the reattachment point.

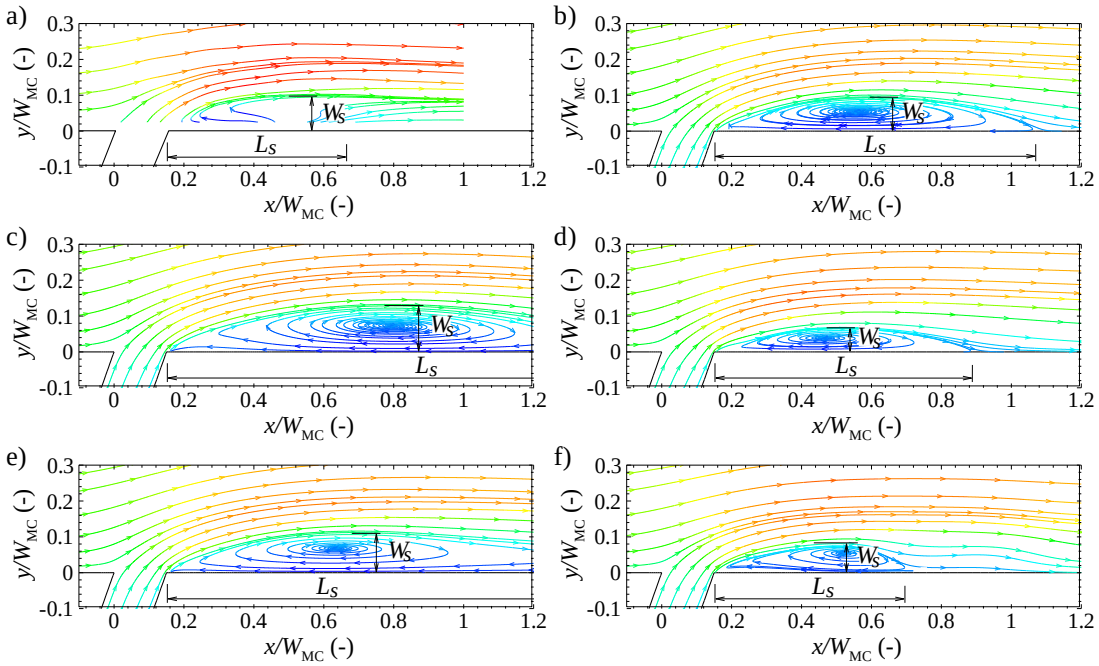

Figure 4: Geometry of separation zone: a) experimental; b) *k*-ε; c) RNG *k*-ε; d) *k*-ω; e) SST *k*-ω; f) EARSM.

Figure 4 shows that the experimental $W_S/W_{MC} \approx 0.097$ and $L_S/W_{MC} \approx 0.52$ and all the turbulence closure models overestimate the length of the separation zone. The two-equation turbulence models (*k*-ε, RNG *k*-ε, *k*-ω, SST *k*-ω) present higher discrepancies between the experimental, especially for the RNG *k*-ε and SST *k*-ω models. The EARSM model shows the small relative error for the geometry of separation zone (Table 1). For this model, the general agreement between numerical predictions and measured length and width of separation zone is very good and this gives sufficient confidence to use the EARSM model to further the 3D flow at a 70º open-channel confluence.

Table 1: Length and width of separation zone.

	experimental	*k*-ε	RNG *k*-ε	*k*-ω	SST *k*-ω	EARSM
W_S/W_{MC}	0.097	0.092	0.123	0.067	0.102	0.087
Width relative error	–	5%	27%	31%	5%	10%
L_S/W_{MC}	0.52	0.89	1.32	0.73	1.39	0.54
Length relative error	–	84%	>100%	40%	>100%	4%

4.2 Velocity field and separation zone

The EARSM model reproduces the experimental time-averaged streamwise velocity, $\bar{u}$, and crosswise, $\bar{v}$, presenting values of the same order of magnitude and shows a good agreement with experimental data at the cross-section $x/W_{MC} = 0.35$ (Figure 5). However, the model underestimates the maximum velocity in the contracted zone ($y/W_{MC} \approx 0.9$), due to the large deformation of free-surface (Figure 7).

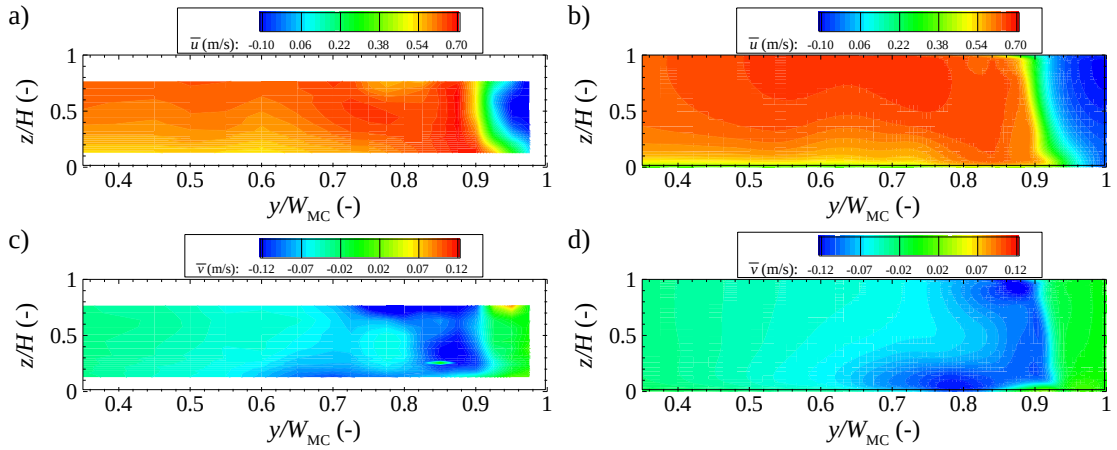

Figure 5: Contour lines of the $\bar{u}$ and $\bar{v}$: a), c) experimental; b), d) numerical.

Figure 5 shows that the entry of the lateral flow into the MC causes an increase of $\bar{v}$ near the channel wall ($y/W_{MC}=1$). The model is capable of simulate the entire flow field, except near the free-surface. For the $\bar{v}$ component the results show that the model is able to simulate this flow, although the location and intensity of maximum velocity are different from the experimental ones. This can be ascribed to the reduction of experimental flow depth in the separation zone (Figure 7). The simulation presents a lower width of the separation zone than the experimental near the free-surface. The experimental and numerical scales of separation zone along the water depth are represented in Figure 6. It is also clear that the numerical length and width of separation zone is smaller than the experimental near the free-surface.

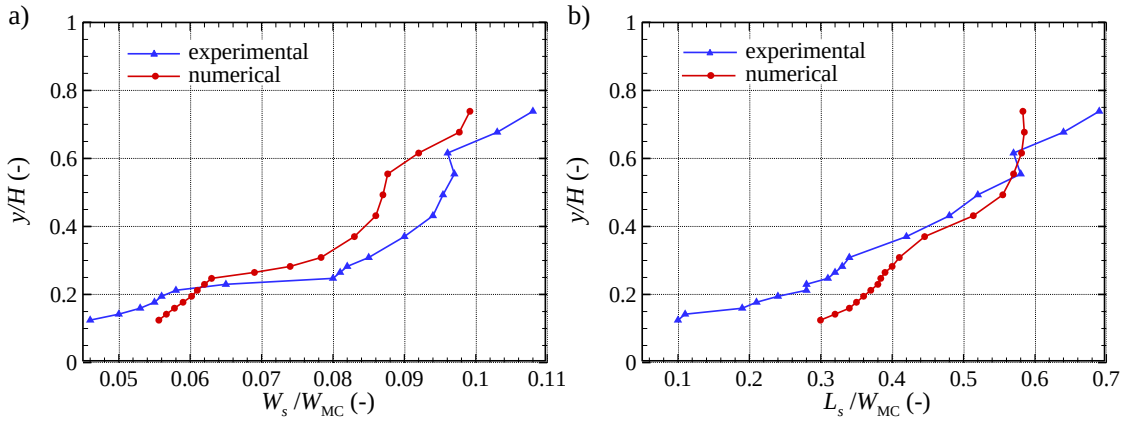

Figure 6: Geometrical changes of separation zone along water depth: a) width; b) length.

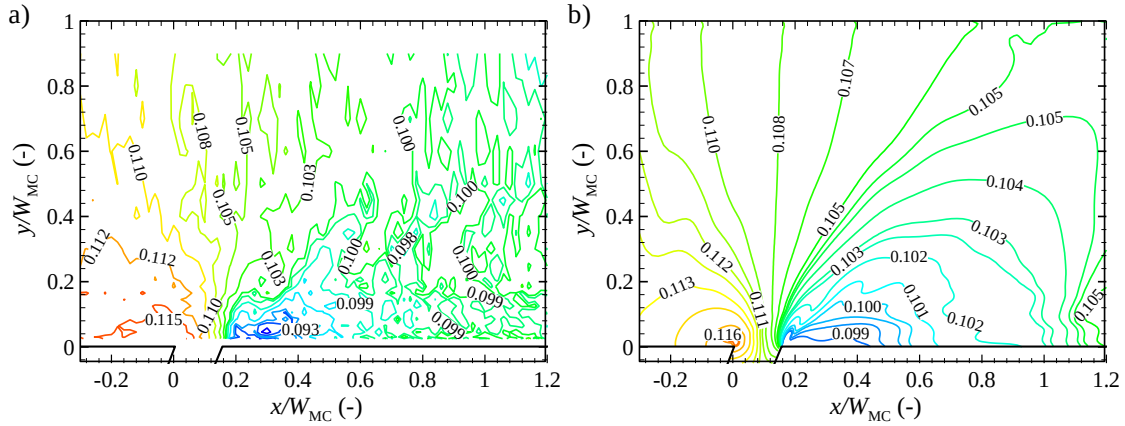

Figure 7: Water free surface: a) experimental; b) numerical.

4.3 Free-surface elevation

The results of the water surface elevation normalized by H, obtained with the numerical model are compared to the experimental ones (Figure 7). The results show a good agreement between the numerical model and experimental results. However, in the separation zone the numerical model gives worst results for the free-surface deformation.

5 CONCLUSION

In this paper, numerical solutions for the geometry of separation zone of the flow at a 70º open-channel confluence were obtained for different turbulence closure models (k-ε, RNG k-ε, k-ω, SST k-ω, and EARSM). The EARSM model presents a good agreement between simulation predictions and measured geometry of the separation zone and this gives sufficient confidence to use the numerical model to further investigate the 3D numerical simulations. However, the EARSM underestimate the streamwise time-averaged streamwise velocity in the maximum velocity zone due to the large experimental deformation of free-surface, which is not well reproduced in the simulations. The numerical results confirm the relevance of modeling anisotropy in the sense that it generates secondary flow responsible for changing the geometry of separation zone and contour lines of velocity, especially along the contact of the zones of flow separation and of maximum velocity, characterized by high turbulence intensities and shear stresses. The use of Zonal RANS-LES [15] models will also be tested in future studies to improve results in the flow separation region. Further analysis of the flow patterns including the characterization of the bed shear stress, turbulent kinetic energy and deformation of free surface is also required.

ACKNOWLEDGMENTS

The authors wish to acknowledge the financial support of the Portuguese Foundation for Science and Technology through the project PTDC/ECM/118775/2010.

REFERENCES

[1] JL Best, I Reid (1984). Separation zone at open channel junctions. *Journal of Hydraulic Engineering* **110**(11):1588–1594.

[2] JL Best (1987). Flow dynamics at river channel confluences: implications for sediment transport and bed morphology. In FG Etheridge, RM Flores, MD Harvey, Eds., *Recent Developments in Fluvial Sedimentology*, SEPM Special Publication 39, 27–35, SEPM, Tulsa, Oklahoma.

[3] JL Best, AG Roy (1991). Mixing-layer distortion at the confluence of channels of different depth. *Nature* **350**:411–413.

[4] LJ Weber, ED Schumate, N Mawer (2001). Experiments on flow at a 90º open-channel junction. *Journal of Hydraulic Engineering* **127**(5):340–350.

[5] JL Best (1988). Separation zone at open-channel junctions. *Journal of Hydraulic Engineering* **113**(4):545–548.

[6] NB Webber, CA Greated (1966). An investigation of flow behaviour at the junction of rectangular channels. *Proceedings of the Institute Civil Engineers* **34**:321–334.

[7] KF Bradbrook, PM Biron, SN Lane, KS Richards, AG Roy (1998). Investigation of controls on secondary circulation in a simple confluence geometry using a three-dimensional numerical model. *Hydrological Processes* **12**(8):1371–1396.

[8] JC Huang, LJ Weber, YG Lai (2002). Three-dimensional numerical study of flows in open-channel junctions. *Journal of Hydraulic Engineering* **128**(3):268–280.

[9] MD Thanh, I Kimura, Y Shimizu, T Hosoda (2010). Numerical simulation of flow at an open-channel confluence using depth-averaged 2D models with effects of secondary currents. *Journal of Applied Mechanics* **15**:769–780.

[10] O Birjukova, S Guillen, F Alegria, AH Cardoso (2014). Three dimensional flow field at confluent fixed-bed open channels. In AJ Schleiss, G de Cesare, MJ Franca, M Pfister, Eds., *River Flow 2014*, CRC Press.

[11] BE Launder, DB Spalding (1974). The numerical computation of turbulent flows. *Computer Methods in Applied Mechanics and Engineering* **3**:269–289.

[12] HK Versteeg, W Malalasekera (2007). *An Introduction to Computational Fluid Dynamics: The Finite Volume Method*, 2nd edition, Prentice Hall, Harlow, UK.

[13] JH Ferziger, M Peric (2013). *Computational Methods for Fluid Dynamics*, 3rd edition, Springer-Verlag, Berlin, Germany.

[14] S Wallin, A Johansson (2000). A complete explicit algebraic Reynolds stress model for incompressible and compressible turbulent flows. *Journal of Fluid Mechanics* **403**:89–132.

[15] FR Menter (2011). *Turbulence Modeling for Engineering Flows*, ANSYS Technical Paper.

V Conferência Nacional de Mecânica dos Fluidos, Termodinâmica e Energia
MEFTE 2014, 11–12 Setembro 2014, Porto, Portugal
APMTAC, 2014

O dispositivo de recuperação de energia das ondas Anaconda: ensaios experimentais em modelo reduzido

AC Mendes, LMA Paredes, FAS Gil, ML Aguiar

Departamento de Engenharia Electromecânica, Laboratório de Mecânica dos Fluidos e Turbomáquinas, Universidade da Beira Interior, 6201-001 Covilhã, Portugal
email: acmendes@ubi.pt

RESUMO: O Anaconda é um dispositivo de conversão de energia das ondas relativamente recente. O sistema consiste essencialmente num longo tubo de borracha, cheio de água, que flutua alinhado com as ondas incidentes. Na extremidade da frente o tubo possui um nariz e a sua extremidade traseira está ligada a um sistema de extracção de potência. Quando é excitado pelas ondas do mar, este tubo flexível desenvolve internamente impulsos de pressão cuja amplitude aumenta em direcção ao sistema de extracção de potência. Neste dispositivo as ondas de pressão dentro do tubo impelem uma massa de água para uma chaminé. As oscilações da coluna de água dentro da chaminé dão por seu lado origem a variações de pressão no ar que está contido numa câmara pneumática superior. Estas variações de pressão podem então ser utilizadas para fazer funcionar uma turbina de ar com alternador. O presente estudo centra-se na análise de desempenho do sistema, quando este interage com ondas regulares de diferentes alturas e comprimentos de onda. Com esta finalidade foram realizados ensaios experimentais em canal de ondas, com um modelo reduzido à escala 1:100 do dispositivo. No nosso modelo físico a câmara pneumática comunica com o meio ambiente exterior através de um orifício. Foram testados orifícios calibrados com diferente diâmetro. Procedeu-se à medição das ondas incidentes, reflectidas e transmitidas, assim como das oscilações do nível de água na chaminé, o que permitiu fazer uma estimativa da energia recuperada pelo dispositivo nas diferentes condições de funcionamento consideradas. São apresentados valores da potência extraída pelo sistema e do rendimento de absorção. Estes valores são finalmente utilizados para previsão do desempenho do dispositivo em condições reais.

PALAVRAS-CHAVE: Anaconda; Energia das ondas; Tubo flexível; Ensaios em canal de ondas.

1 INTRODUÇÃO

O recurso mundial de energia das ondas em águas oceânicas é importante. A potência disponível foi estimada em 2000 a 4000 GW [1]. A questão é saber quanto deste potencial pode ser efectivamente recuperado a custos competitivos. Em [2] são apresentados, de forma clara, os conhecimentos necessários para compreender e resolver a hidrodinâmica dos sistemas de aproveitamento da energia das ondas, à luz da Teoria Linear. Por outro lado, em Falcão [3] é apresentada uma revisão actualizada das principais tecnologias desenvolvidas neste contexto. Embora alguns dispositivos já tenham alcançado um grau de aperfeiçoamento considerável, ainda não se atingiu a fase de exploração comercial. O presente estudo centra-se no dispositivo de energia das ondas Anaconda, que foi proposto e patenteado por Farley e Rainey no Reino Unido [4]. O Anaconda é um sistema inovador que utiliza um longo tubo de borracha, flutuante, para interagir com as ondas incidentes. A proa do tubo está fechada e a sua parte traseira é conectada com o sistema de extracção de potência. O tubo está cheio de água e actua como um dispositivo atenuador das ondas. Trata-se de um sistema muito simples, que pode utilizar tecnologia barata e bem testada: por exemplo um grupo turbina-gerador. Já foram estudados anteriormente dispositivos semelhantes, por via teórica e também experimental, tendo sido demonstrado possuírem boas capacidades para conversão da potência das ondas do mar.

Os primeiros ensaios laboratoriais do dispositivo Anaconda foram realizados por John Chaplin e estão reportados em [5]. Este estudo preliminar, com um pequeno modelo reduzido, revelou ser possível obter frentes de captura de energia equivalentes a 3 ou 4 vezes o diâmetro do tubo do dispositivo, numa gama alargada de frequências de onda incidente. Uma segunda série de ensaios, desta vez com um modelo à escala1: 20, tiveram lugar na Offshore Wave Basin do Denish Hydraulic Institute, em 2010 [6]. Estes ensaios consistiram essencialmente em testes de radiação, conduzidos por imposição de pulsos de pressão no tubo de borracha. Em todos estes ensaios o tubo foi subjugado em ambas as extremidades. O princípio

de funcionamento e a teoria relevante para a análise deste sistema de energia das ondas estão compilados em [7]. Este trabalho extrai importantes conclusões acerca do desempenho e potencialidades do dispositivo.

A presente investigação orienta-se para a análise de desempenho do dispositivo Anaconda, quando equipado com um tubo que flutua livremente frente às ondas incidentes e cuja pulsação activa um sistema pneumático de extracção de potência, que está acoplado à sua parte traseira. O estudo apoia-se na realização de ensaios experimentais em canal de ondas, com um modelo reduzido do dispositivo à escala 1:100. No protótipo do dispositivo o sistema de extracção incorpora uma turbina de ar que acciona um alternador. No nosso modelo físico a câmara pneumática comunica com a atmosfera através de um orifício calibrado, cuja característica simula a impedância da turbina. Foram testados orifícios de diferente diâmetro e, em cada situação, foram efectuadas medições das oscilações da massa de água dentro da coluna do sistema de condicionamento. Foi igualmente conduzida uma análise dos registos do campo de ondas reflectidas e transmitidas no canal hidráulico. Os resultados obtidos permitem estimar a potência extraída pelo sistema e o seu rendimento, variáveis que serão quantificadas e extrapoladas para um sistema operando no mar.

2 MODELO FÍSICO

Foi projectado e construído um modelo reduzido do dispositivo Anaconda, à escala 1:100. Este modelo físico, que se representa na Figura 1, foi ensaiado no canal hidráulico do fluidslab, na Universidade da Beira Interior.

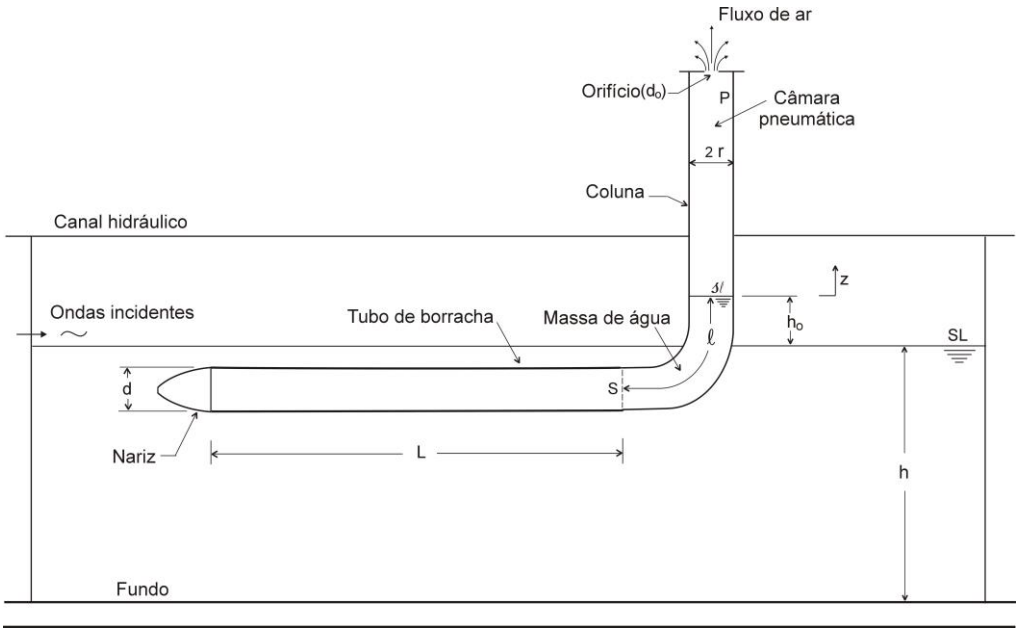

Figura 1: Modelo físico ensaiado no canal hidráulico do *fluidslab*.

As principais dimensões do modelo são dadas na Tabela 1. A instalação experimental consiste num longo tubo de borracha, com 0,904 m de comprimento e um diâmetro de aproximadamente 95,8 mm. A amostra de latex utilizada tem uma espessura de 0,16 mm. A proa do tubo está fechada, terminando por um nariz, e a parte traseira é conectada ao sistema de conversão e extracção de energia. Este compõe-se de uma chaminé transparente com 72,2 mm de diâmetro, que comunica com a atmosfera através de um orifício situado na parte superior. O tubo de borracha está ligado a esta chaminé por intermédio de um cotovelo em PVC, com secção S. O tubo da Anaconda é pressurizado até uma altura de coluna de água h0=0,1 m, por meio de uma pequena bomba instalada no nariz do dispositivo. Acima do nível de água na chaminé existe uma câmara pneumática com 0,572 m de altura. Esta câmara é fechada com uma tampa que possui um orifício de diâmetro d0. Nesta experiência a impedância da turbina é simulada com o auxílio deste orifício calibrado. As ondas incidentes induzem pulsações no tubo de borracha, que vão posteriormente excitar a coluna de água na chaminé. No caso real as oscilações deste pistão de água condicionam a pressão do ar na câmara pneumática, activando deste modo o movimento da turbina de ar.

Tabela 1: Dimensões do modelo (em mm).

L	d	w	h_o	$2r$	h_1	ℓ	h
904	95,8	0,16	100	72,2	572	152	334

O canal hidráulico onde o dispositivo foi testado tem cerca de 8 m de comprimento e 0,3 m de largura. O gerador de ondas é do tipo comporta articulada no fundo do canal. Na extremidade oposta à do gerador situa-se uma praia de dissipação com 1,28 m de comprimento. A profundidade da água no canal é $h = 0,334$ m. O coeficiente de reflexão situa-se abaixo dos 10% na maioria dos casos. As oscilações da coluna de água na chaminé são monitorizadas através de uma sonda de nível do tipo tensão-resistência especialmente construída para o efeito. No canal foram igualmente instaladas outras três sondas do mesmo tipo e respectivos monitores, duas delas entre o gerador e o modelo físico e a outra atrás do modelo, em direcção à praia.

3 EQUIPAMENTO DE MEDIDA

A metodologia adoptada para realizar as medições é relativamente simples e apoia-se no seguinte equipamento de medida. As oscilações da coluna de água no interior da chaminé são monitorizadas por intermédio de uma sonda de nível construída no Laboratório. Este sensor é controlado por um módulo de aquisição KUSB-3100 S, da Keithley. A medição das ondas no canal é efectuada por meio de três sondas resistivas, controladas por um monitor da HR Wallingford com quatro canais. A incerteza das medições destes aparelhos é inferior a 1 mm. O campo de ondas a montante do modelo é igualmente registado por um osciloscópio RT digital TDS220, da Tektronix. A aquisição e processamento dos dados são realizados com um PC ASUS de 64-bit Pentium Dual-Core, CPU E5700 a 3 GHz, com 4 GB RAM. O software de aquisição, controlo da instrumentação e análise dos dados é o TestPoint V7. Os dados de todos os canais foram registados a 200 Hz, durante 15 segundos.

4 CONDIÇÕES DOS ENSAIOS

O modelo foi em primeiro lugar testado com a chaminé completamente desobstruída, de modo a obter a frequência natural do sistema. A frequência própria da coluna de água oscilante ronda os 1,4 Hz. Em seguida o modelo foi ensaiado em ondas regulares com o topo da chaminé obturado com orifícios de diferentes diâmetros. A velocidade de propagação da onda de pressão no tubo é de aproximadamente 1,25 m/s, valor que está na gama de celeridades das ondas geradas em águas restritas no canal. Logo, a frequência de sintonização do tubo de borracha pressurizado é de 1,2 Hz.

Os ensaios realizados cobrem uma gama de alturas de onda $H = 0,12$ a 4,16 cm e frequências $f = 0,57$ a 1,8 Hz. Os períodos das ondas no canal variam entre $T = 0,56$ e 1,76 s, a que correspondem comprimentos de onda $\lambda = 0,50$ a 2,93 m numa profundidade de 33,4 cm. À escala real estas condições correspondem a ondas até 4,16 m e 6 a 18 s de período ($\lambda = 50$ a 293 m). No total foram geradas 252 ondas por cada orifício do sistema de extracção testado, 30 a 40% delas lineares.

5 RESULTADOS EXPERIMENTAIS

A potência média, *P*, extraída das ondas ao longo de um período e o rendimento da máquina, expresso em termos de comprimento de captura *W* referido ao diâmetro do tubo da Anaconda, estão representados nas Figuras 2 e 3 em função da frequência *f* das ondas incidentes. Os resultados apresentados dizem respeito a um dos melhores orifícios do sistema de extracção de energia, com diâmetro igual a 9 mm. Para os restantes diâmetros d_0 ensaiados o comportamento é semelhante. Os resultados foram agrupados por classes de altura de onda *H*.

A potência máxima extraída pelo dispositivo (Figura 2) é de 0,78 W, para ondas de 0,9 s de período e 3,18 cm de altura. Surge um primeiro pico, pronunciado, para uma frequência entre 1,1 e 1,2 Hz, que ocorre sempre nesta frequência independentemente da altura das ondas. Esta é a frequência de sintonização do tubo da Anaconda. Em condições reais isto acontece em águas intermédias com 33,4 m de profundidade, para ondas de 119 m de comprimento e 3,2 m de altura. A potência recolhida pelo dispositivo diminui drasticamente para ondas mais baixas, como seria de esperar. Um segundo pico de potência extraída ocorre para 1,4 Hz, isto é, para períodos de onda de 0,7 s, que atinge mais ou menos 50-70% do primeiro pico. Estas condições correspondem aproximadamente a ondas de 7 s no mar, ou seja

comprimentos de onda à volta dos 80 m. Esta zona coincide com a ressonância da coluna de água oscilante do dispositivo.

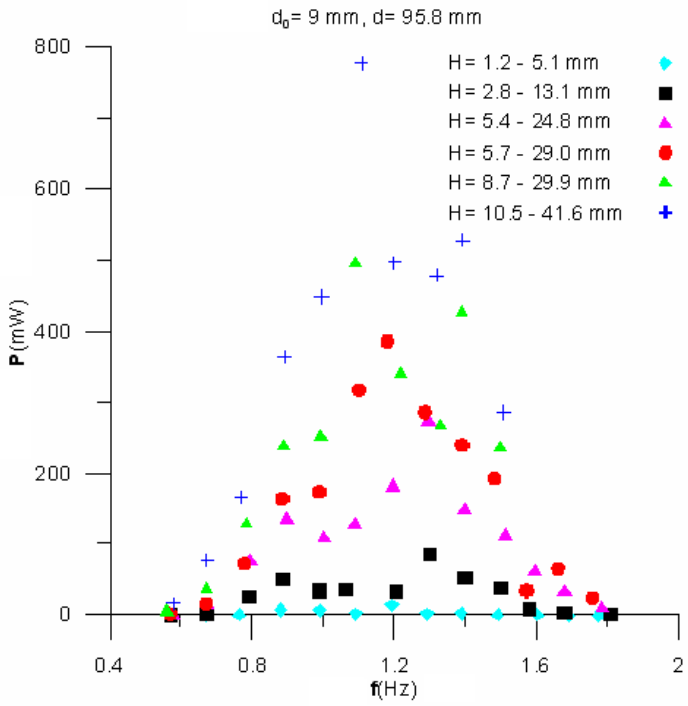

Figura 2: Potência extraída *P* versus frequência *f*, para diferentes alturas de onda *H*.

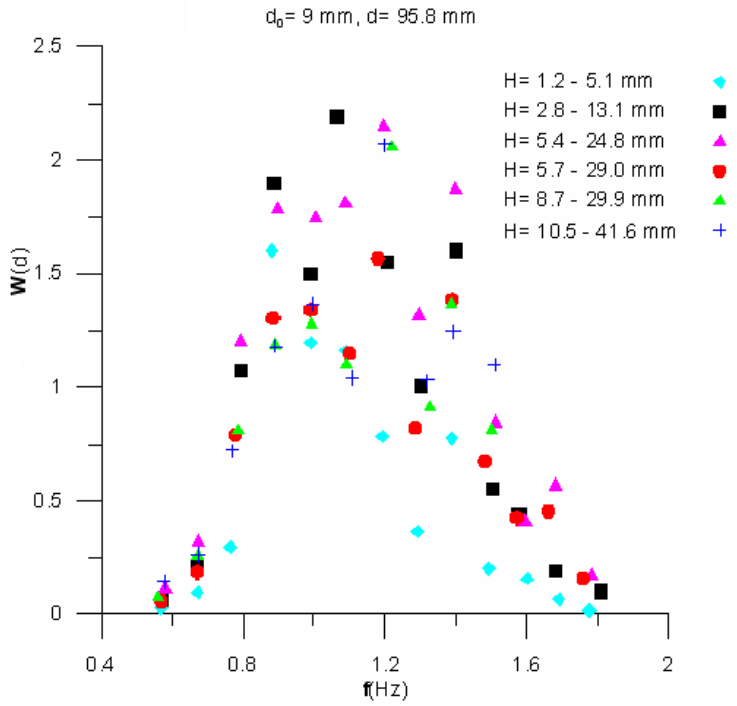

Figura 3: Comprimento de captura W versus frequência f, para diferentes alturas de onda H.

Na Figura 3 podemos observar que o comprimento de captura máximo varia entre 2,0 e 2,25 diâmetros, para ondas de 1,1 a 1,2 Hz e uma altura até 2,79 cm. Em termos do protótipo, cujo tubo tem 7 m de diâmetro, este pode atingir 15,8 m de frente de captura em ondas de 8 a 9 s e 104 a 122 m de comprimento, com alturas até 2,8 m. Nas frequências mais baixas o rendimento não é grandemente afectado pela altura das ondas, ao contrário do que acontece nas frequências acima dos 0,8 Hz. O comprimento de captura tem dois picos relativamente próximos, cujo valor varia entre 1,5 e 2,25 diâmetros, localizados entre 0,9 e 1,2 Hz. Existe igualmente um patamar de rendimento que oscila entre 0,75 e 2,0, em termos de comprimento de captura, para frequências entre 1,3 e 1,5 Hz. Estes valores são estreitamente dependentes da altura das ondas.

6 CONCLUSÕES

O dispositivo de energia das ondas Anaconda é um sistema muito simples e de baixo custo que utiliza uma tecnologia de conversão bem testada, do tipo turbina de ar. O elemento principal do dispositivo, que estabelece a interface com as ondas incidentes, é um longo tubo de borracha. A pulsação interna que as ondas do mar induzem no tubo permite activar todo o sistema de conversão e extracção de potência.

O presente estudo experimental, em modelo reduzido, faz uma análise do desempenho do dispositivo quando este opera com ondas regulares e o tubo flutua livremente face às ondas incidentes. À escala do modelo o sistema de extracção é simulado por meio de um orifício calibrado, através do qual a câmara pneumática do sistema comunica com a atmosfera. Este modelo representa bem a característica da turbina do sistema real, que é verdadeiramente não-linear. É no entanto assumido que a impedância do sistema é constante e independente da pressão na câmara pneumática. Desprezam-se também os efeitos de compressibilidade do ar na câmara.

O comprimento da frente de captura de energia estimado está entre 1,0 e 2,25 diâmetros do tubo, numa larga gama de frequências entre 0,8 e 1,5 Hz. Em termos médios o protótipo deverá conseguir extrair pelo menos 1,5 MW por frente de onda, em condições normais, desde que correctamente sintonizado para ondas de 8 a 11 s. É apropriado referir que a impedância do sistema de extracção ainda pode ser optimizada. Para períodos abaixo dos 8 s, os efeitos de difracção parecem afectar significativamente o desempenho do dispositivo. O efeito de blocagem, que é introduzido pela secção do canal, parece conduzir a uma estimativa por excesso do rendimento do dispositivo. Por outro lado, na gama de frequências entre 0,5 e 0,8 Hz a Anaconda exibe um movimento de cavalgamento das ondas, o que parece no entanto favorecer a captura de energia.

No decurso do presente estudo foi igualmente possível avaliar qual a proporção de energia que é dissipada por histeresis no tubo de borracha. A percentagem de energia perdida por este efeito é na realidade desprezável. No entanto o aparecimento de aneurismas no tubo da Anaconda é uma importante limitação do sistema, o que motiva a procura de novos materiais distensíveis para substituir ou reforçar o latex.

ACKNOWLEDGEMENTS

Este trabalho foi desenvolvido na Universidade da Beira Interior, Covilhã, no quadro do Projecto PTDC/EME-MFE/111763/2009, com o apoio do Programa Factores de Competitividade (COMPETE) e co-financiado pela FCT e União Europeia. Os autores agradecem a boa vontade do Sr. Morgado, que fabricou o modelo físico com a competência de sempre.

REFERÊNCIAS

[1] G Boyle (2004). *Renewable Energy*, Oxford University Press, Oxford, UK.

[2] J Falnes (2005). *Ocean Waves and Oscillating Systems*, Cambridge University Press, Cambridge, UK.

[3] AFO Falcão (2010). Wave energy utilization: A review of the technologies. *Renewable and Sustainable Energy Reviews* **14**:899–918.

[4] FJM Farley, RCT Rainey (2006). Radical design options for wave-profiling wave energy converters. In *Proceedings of the 21st International Workshop on Water Waves and Floating Bodies*.

[5] JR Chaplin, FJM Farley, ME Prentice, RCT Rainey, SJ Rimmer, AT Roach (2007). Development of the Anaconda all-rubber WEC. In *Proceedings of the 7th European Wave and Tidal Energy Conference*.

[6] JR Chaplin, FJM Farley, GE Hearn, V Heller, A Mendes (2010). Hydrodynamic performance of the ANACONDA wavepower device, *Hydralab III Closing Event* (Stakeholder Dissemination Meeting), Hannover.

[7] FJM Farley, RCT Rainey, JR Chaplin (2012). Rubber tubes in the sea, *Philosophical Transactions of the Royal Society A* **370**, 381–402.

This page was intentionally left blank

Quadrant method application to the study of the beginning of sediment motion of sedimentary particles

E Carvalho[1], R Aleixo[2]

[1]Departmento de Engenharia Civil, Faculdade de Engenharia, Universidade do Porto, Rua Dr. Roberto Frias, 4200-465 Porto, Portugal
[2]National Center for Computational Hydroscience Engineering, The University of Mississippi, Mississipi, USA
email: elsac@fe.up.pt, rui.aleixo@ncche.olemiss.edu

ABSTRACT: In the present paper the quadrant analysis method is used to analyse the turbulence over a spherical particle of a uniform spheres bed. Two components velocity fluctuations, (u', v'), were measured with a Laser Doppler Anemometer and divided by four quadrants according to their signal. For each quadrant an event is associated and it is possible to study the contribution of each quadrant to the total Reynolds stress. Each event is associated with a different physical phenomenon, namely ejections and sweeps that can be related with the beginning of the sediment motion. In order to analyse the influence of different variables such as the particle's diameter, D, the flow rate, Q, the channel slope, i, and the distance to the top of the particle's top, y, different experimental conditions on supercritical flows over rough bed were measured.

KEY-WORDS: Quadrant analysis; Supercritical flows; Ejection; Sweep.

1 INTRODUCTION

The study and project of stable channels is an important topic on fluvial hydraulics. It is necessary that the conditions for the initiation of sediment motion be known and understood. To study the stability of fluvial beds it is necessary to characterize the fluid-bed interaction where the flow turbulence and it characteristics play an important role. The quadrant analysis is one method for turbulence study. This method consists in plotting the velocity fluctuations in a four quadrant Cartesian plot, according to the signal of the two components [1]. It allowing also the evaluation of the contribution of each event to the mean value of the Reynolds stress, $|u'v'|$ [2]. Each quadrant is then associated to a turbulent event (Figure 1):

- 1st Quadrant: for u'>0 and v'>0; it is associated to outward interactions;
- 2nd Quadrant: for u'<0 and v'>0; it describes the ejection events;
- 3rd Quadrant: for u'<0 and v'<0; it is related to inward interactions;
- 4th Quadrant: for u'>0 and v'<0; it refers to sweep events.

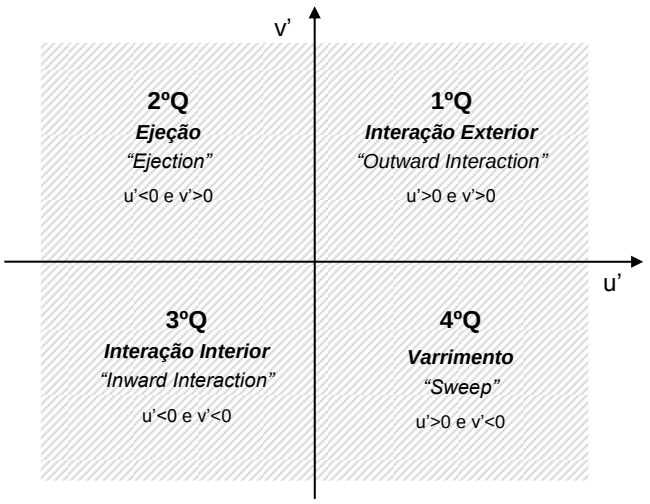

Figure 1: Velocity fluctuations Cartesian plot for quadrants analysis and events.

With the quadrant method it is also possible to make a conditional analysis by defining a hyperbolic region, referred as the hole, delimited by a curve |*u*'*v*'| = constant (as depicted in Figure 3). The dimension of the hole, *H*, represents the threshold [2] and it is defined by:

$$\left|u'v'\right| = H\left(\overline{u'u'}\right)^{0.5}\left(\overline{v'v'}\right)^{0.5} \tag{1}$$

where $\left(\overline{u'u'}\right)^{0.5}$ and $\left(\overline{v'v'}\right)^{0.5}$ are the rms of the velocity components *u* and *v*, respectively.

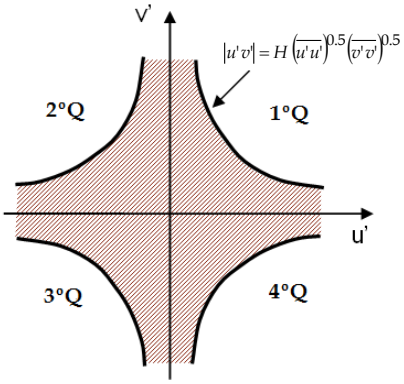

Figure 2: Definition of the hyperbolic region.

With this method it is possible to eliminate the smaller contributions inside the hyperbolic region, considering just the larger contributions of the events associated to each quadrant. The contributions for the total Reynolds stress, |*u*'*v*'|, of the quadrant *i*, out of the hyperbolic region with dimension *H*, is given by [2, 3]:

$$\left\langle u'v'\right\rangle_{i,H} = \lim_{T\to\infty}\frac{1}{T}\int_0^T u'(t)\,v'(t)\,I_{i,H,t}(u',v')dt \tag{2}$$

where $I_{i,H,t}$ is the detection function, defined by:

$$I_{i,H,t}(u',v') = \begin{cases} 1 & \text{if } (u',v') \in Q_i \text{ and } \left|\sqrt{\overline{u'^2}}\sqrt{\overline{v'^2}}\right| \geq H\left|u'v'\right| \\ 0 & \text{otherwise} \end{cases} \tag{3}$$

The fraction contribution of each event to $\overline{u'v'}$, $S_{i,H}$, is defined by:

$$S_{i,H} = \frac{\left\langle u'v'\right\rangle_{i,H}}{\overline{u'v'}} \tag{4}$$

The sum of the fraction contributions of all events in a measuring point, for $H = 0$, is equal to one.

$$\sum_{i=0}^{4}\left[S_{i,H}\right]_{H=0} = 1 \tag{5}$$

As an example, Figure 3 shows: (a) the representation of the two velocity components fluctuations, allowing for the identification of the pairs of values associated to events of each quadrant and (b) the correspondent conditional analysis ($H = 1$) for which the values with that respect the condition:

$$u'v' \geq \left(\overline{u'u'}\right)^{0.5}\left(\overline{v'v'}\right)^{0.5} \tag{6}$$

are represented.

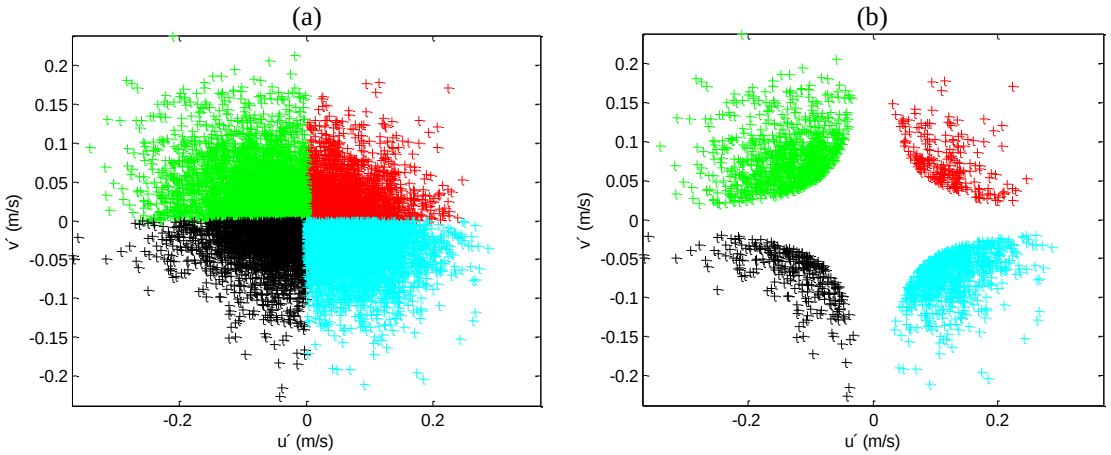

Figure 3: (a) Fluctuations contributions for $H = 0$; (b) Condition analysis for $H = 1$.

2 EXPERIMENTAL SETUP

The experiments were carried out in the channel of FEUP's Hydraulics Laboratory (Figure 4). This channel is 17 m long, has a section of 0.4×0.6 m^2 and its slope is adjustable. Both sides of the channel have glass windows to allow the optical access to the interior. The flow rate is controlled by means of a valve and it is measured by an electromagnetic flowmeter, both located upstream of the channel. At the channel outlet a sluice gate allows controlling the water level.

Figure 4: Experimental setup (FEUP's Hydraulic Laboratory channel).

A double bottom with 8 m length was placed inside the channel in order to allow the use of different roughness beds. For this study, a uniform spheres bed with triangular arrangement was considered. Two beds made of particles with diameters of 4 mm and 5 mm respectively (Figure 5) were tested. The spheres were glued in an area of 0.4 × 10 m^2 and test section was located at 6.5 m from the beginning of the double bed, to ensure the development of the turbulent boundary layer, which was confirmed by the measured velocity profiles.

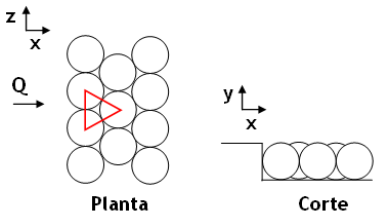

Figure 5: Bed spheres triangular arrangement.

Velocity profiles measurements were made by means of a two components Laser Doppler Anemometer system and the signal was processed by a DANTEC burst spectrum analyzer. The LDA is an established and well known technique and a complete description can be found in [4, 5], for example. Table 1 presents the main characteristics of the LDA system used in this study.

Table 1: LDA main characteristics.

	LDA1	LDA2
Wavelength	514.5 nm	488 nm
Control Volume Dimensions		
Major axis	2.825 mm	2.679 mm
Minor axis	0.08189 mm	0.07767 mm

Different flow conditions were considered for the measurement of the two velocity components over a loose particle of the bed. This allowed the analysis of the different parameters influence on the contributions for the Reynolds stress mean value. A total of 72 test conditions were measured for 6 flow rates, Q, two channel slopes, i, two diameters, D, and 3 distances from the top of the sphere, y (see Table 2). For each condition 100000 velocity samples were considered.

Table 2: Tested conditions.

i	1.30 %			0.80 %			
y	2.5 mm	4.25 mm	10 mm	2.5 mm	4.25 mm	10 mm	
D = 4 mm	5	5	5	5	5	5	Q (L/s)
	10	10	10	10	10	10	
	12.5	12.5	12.5	12.5	12.5	12.5	
	15	15	15	15	15	15	
	17.5	17.5	17.5	17.5	17.5	17.5	
	20	20	20	20	20	20	
D = 5 mm	5	5	5	5	5	5	
	10	10	10	10	10	10	
	12.5	12.5	12.5	12.5	12.5	12.5	
	15	15	15	15	15	15	
	17.5	17.5	17.5	17.5	17.5	17.5	
	20	20	20	20	20	20	

3 EXPERIMENTAL RESULTS AND CONCLUSIONS

The quadrant analysis was applied to supercritical flows for the aforementioned flow conditions. The two velocity components were measured for each condition allowing the application of the quadrant method. Figures 3 presents (a) the fraction contributions of each quadrant to the Reynolds stress, for different flow rates, and (b) the difference between the contributions of the ejections and sweep events.

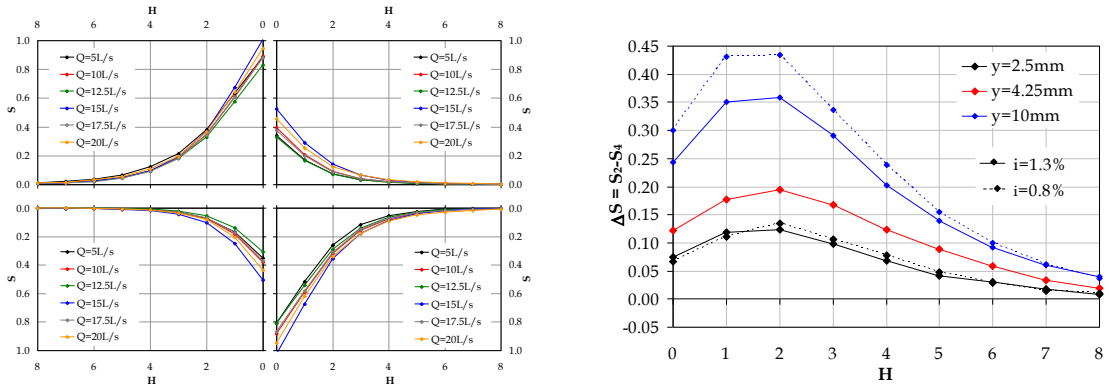

Figure 6: (a) contributions of each quadrant to Reynolds stress; (b) difference between the ejections and sweeps contributions.

The analysis of the results allowed to conclude that ejection and sweep events have higher contributions to Reynolds stresses. Ejections and sweeps have similar contributions values. The sum of the contributions of the second and fourth quadrants, positive contribution to Reynolds stress, is around 160% for H = 0. The interaction events (corresponding to the first and third quadrants) have a total contribution

of 60%. From the study of the contributions for different distances from the top of the spheres it was possible to verify that the sweep events have higher contributions near the wall. With the increase of the distance it is possible to observe that the contributions of the ejections increase.

These experiments have shown that the beginning of sediment motion is either triggered by an ejection or sweep event. More experiments have to be made with imaging techniques to capture the turbulent event capable of triggering the sediment motion.

ACKOWLEDGEMENTS

This work was funded by a PhD scholarship ref. SFRH/BD/19575/2004 from Fundação para a Ciência e a Tecnologia, Portugal.

REFERENCES

[1] W Willmarth, S Lu (1972). Structure of the Reynolds stress near the wall. *Journal of Fluid Mechanics* **55**(1):65–92.

[2] I Nezu, H Nakagawa (1993). *Turbulence in Open Channel Flows*, AA Balkema, Rotterdam.

[3] S Dey, A Papanicolaou (2008). Sediment threshold under stream flow: A state-of-the-art review. *KSCE Journal of Civil Engineering* **12**(1):45–60.

[4] F Durst, A Melling, JH Whitelaw (1976). *Principles and Practice of Laser Doppler Anemometry*, Academic Press, London.

[5] C Tropea, A Yarin, J Foss, Eds. (2006). *Springer Handbook of Experimental Fluid Mechanics*, Springer-Verlag Berlin Heidelberg.

This page was intentionally left blank

V Conferência Nacional de Mecânica dos Fluidos, Termodinâmica e Energia
MEFTE 2014, 11–12 Setembro 2014, Porto, Portugal
APMTAC, 2014

Experimental study of scour around circular and elongated bridge piers with and without pier slot

ML Azevedo, FC Leite, MMCL Lima

Departamento de Engenharia Civil, Escola de Engenharia da Universidade do Minho, Campus de Azurém, 4800-058 Guimarães, Portugal
email: a58581@alunos.uminho.pt, franciscacostaleitee@gmail.com, mmlima@civil.uminho.pt

ABSTRACT: This work describes an experimental study of clear water scour around bridge piers, placed in a cohesionless bed of sediments. The use of pier slot as a flow-altering countermeasure against bridge scour is evaluated, in the case of circular and elongated piers. Four piers with 20 mm of transversal dimension were used, with one circular pier and one elongated pier that featured a slot, corresponding to a flow-altering countermeasure. Sand with a mean diameter of 0.33 mm was used, in a free surface flow with a water depth equal to 5 cm and a flow rate equal to 12.96 m^3h^{-1}. The temporal evolution of the maximum scour depth was studied and the topography of the scour cavity was analyzed. The scour hole maximum depth was higher in case of the simple piers, when compared with piers with slot. It was observed that the scour hole maximum depth was smaller in case of elongated piers, when compared with circular piers. The bed slope upstream from the pier was higher than the one observed downstream from the pier. In case of pier slot measurements, both upstream and downstream slopes were reduced, when compared with the simple pier measurements. When comparing the initial and the equilibrium phases of scour, it was observed that bed slopes decrease as the duration of the experiments increases.

KEY-WORDS: Scour; Bridge piers; Scour cavity topography; Flow-altering countermeasures; Pier slot.

1 INTRODUCTION

One of the causes associated with the collapse of bridges is the phenomenon of scour around bridges piers. It is important to predict the maximum scour depth around the piers, because the structure may collapse, originating accidents that may put human lives at risk.

The majority of studies focus on circular piers [1, 2], predicting the maximum scour depth [3] and its temporal evolution [4]. A different approach studies experimentally solutions that avoid scour or minimize its effects, such as flow-altering or bed altering countermeasures [5]. Furthermore, the knowledge related with the topography of the scour cavity [6, 7, 8] may be relevant for the validation of numerical methods [9].

The present study main objectives are to study the temporal evolution of the maximum scour depth for circular and round nose rectangular piers, i.e. elongated piers, as bridge piers are not usually circular [10, 11], and to evaluate the use of a slot as a flow-altering countermeasure. This study focus on the characterization of the scour cavity topography, by means of paraffin and Vaseline casts.

A brief presentation of theoretical concepts, involved in scour around a bridge pier, is presented in the following section. The experimental set-up and measuring equipment are described in section 3. The results and their discussion are presented in Section 4. Section 5 is the final section, with the main conclusions.

2 BRIDGE PIER SCOUR

Water flow above sediment beds, either in rivers or in the sea, may cause erosion. Sediment transport occurs due to the existence of an interface between the flow and the moving boundary.

The erosion may be classified as local erosion, or scour, if it occurs due to the existence of an obstacle to the flow, such as a bridge pier or abutment. Otherwise the erosion is classified as global erosion if it occurs naturally, without the existence of an obstacle. Scour may occur under two different flow conditions: clean-water scour and live-bed scour. Clear-water scour occurs when there is no transport of bed material upstream from the structure. Live-bed scour occurs when there is bed material transport upstream from the structure, and is cyclic in nature.

The main variables that affect the magnitude of maximum bridges piers scour depth are [12]: the flow approach velocity, the water depth, the pier transversal dimension, the pier length if it is not aligned with the main stream direction, the size and gradation of bed material, the angle of attack of the approach flow to the pier and the pier's shape.

In case of cylindrical piers [13] a down flow is observed at the upstream nose of the pier, and a horseshoe vortex develops due to the pileup of water on the upstream surface of the obstruction and subsequent acceleration of the flow around the nose of the pier. The simultaneous action of the downward flow and the separated flow, which occurs as a result of the change of pressure field, generates a horseshoe vortex, considered primarily responsible for the formation of local scour process [12]. The scour hole increases in both depth and extending upstream, while the horseshoe vortex continues to dig the bed. Sediments are transported downstream, and eventually sediment in regions of lower turbulence. As the depth of scour increases the transport rate from the base of the pier diminishes. For clear-water scour, the scour process ceases when the shear stress caused by the horseshoe vortex equals the critical shear stress of the sediment particles at the bottom of the scour hole.

The piers protection against local scour is a point of great importance in the safety of bridges, since excessive scour may compromise its structural function, or even lead to its collapse. Countermeasures against pier scour can be classified into two categories [5]: flow-altering countermeasures and bed-armoring countermeasures. The operating principle of the flow altering countermeasures is the decrease of the intensity of the down flow and horseshoe vortex, which are the main causes of local scour. Moreover, the bed-armoring countermeasures consist in the creation of a physical barrier (as in the case of riprap, gabions or cable-tied blocks) against possible local scour.

3 EXPERIMENTAL METHOD

In this section, the experimental setup (subsection 3.1), the test section (subsection 3.2), the procedure followed during the tests (section 3.3) and the experimental conditions (subsection 3.4) are described.

3.1 Experimental Setup

Experiments were conducted in the Hydraulics Laboratory of the Civil Engineering Department of the University of Minho, in a 0.3 m wide and 14 m long flume, with a bottom slope of 1/500. The flow rate was measured by an electromagnetic flow meter (Endress+Hauser, model Promag 30F) and the water depth was controlled by a sluice gate at the downstream extremity of the flume.

3.2 Test Section

The test section consisted of a box, 10 cm deep and 2.0 m long, filled in with sand with a mean diameter of 0.33 mm, were the vertical piers were mounted. The sand box was preceded by a ramp with a slope of 0.1 and a length of 1.0 m, and a horizontal platform 2.0 m long and 10 cm high.

Table 1: Geometry of the piers adopted for the experimental study.

Pier	D (mm)	L (mm)	L_S (mm)	W_S (mm)
circular	20	20	–	–
elongated	20	40	–	–
circular with slot	20	20	50	5
elongated with slot	20	40	50	5

Experiments were conducted for four different vertical piers (Table 1). Two of the piers were circular with 20 mm diameter (D), and the other two piers were elongated. The elongated piers, rectangular piers with round nose shapes, had a transverse dimension of 20 mm, and a length (L) in the direction of the flow equal to 2 pier diameters. One of the elongated piers and one of the circular piers featured a slot, oriented in the flow direction, 5 mm wide and 50 mm high. The slot was half buried at the beginning of the experiments, as evidence exists that this relative position between the slot and the initial bed of sediments level causes the maximum scour depth reduction when comparing simple piers and piers with slot [5]. Two simple piers, without slot, were also tested for comparison purposes. Figure 1 presents the geometry of the elongated pier with slot. All piers featured a built in scale, with 1 mm resolution, that allowed the measurement of scour depth at their upstream extremity.

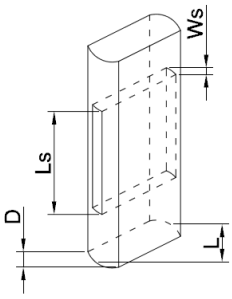

Figure 1: Geometrical parameters of an elongated pier with slot.

3.3 Procedure

This subsection describes the experimental procedure adopted for the tests and the analysis of the configuration of local scour cavities. After leveling the sand and carefully placing the pier vertical and centered in the test section, the filling of the flume is initiated. For this purpose two centrifugal pumps were used simultaneously, the one of the flume system that discharged upstream from the test section and one additional pump discharging downstream. The simultaneous use of both pumps allows the gradual water level rise, avoiding sediment transport in the vicinity of the pier. After the flume is filled up to the pre-established water level, the downstream pump was removed, and the pump of the flume was set to the desired water flow rate. The water level in the channel was controlled by a weir gate downstream of the flume. Once the desired water level and flow rate were attained, the experiments were carried out.

After the established time duration of each experiment, the pump of the system is turned off and the water is allowed to slowly drain, in order to empty the test section without altering the scour cavity configuration. After the channel was emptied and the sand dried, the molding process of the scour cavity was initiated. This process consists in heating a mixture of paraffin and Vaseline, which is poured into the test section, where a formwork was previously placed. The casts were taken with the maximum dimensions of 406 mm x 254 mm. After cooling the cast, the pier was removed and the cast was gently cleaned using a brush, in order to remove the sand grains that were attached to it.

The casts were then subject to a three dimensional laser scan, using Roland's 3D Laser Scanner LPX-600, with a resolution of 0.8 mm. The digital image of the cast was analyzed using AutoCad, in order to determine the dimensions and topography of the scour cavity.

3.4 Experimental Conditions

Water depth (h) was 50 mm, value selected in order to avoid shallow flows ($h/D \geq 2.5$) and secondary flows ($B/h \geq 5$). Water flow rate was equal to 12.96 m^3h^{-1}, corresponding to a ratio U/U_c equal to 0.9 between the mean horizontal velocity (U) and the critical velocity (U_c). The critical velocity was equal to 0.27 ms^{-1} [12]. This value was verified experimentally, using the sand box without the pier, establishing the desired water depth and increasing stepwise the flow rate until the motion of sediments was observed.

Two sets of experiments were carried out. In the first set, experiments were run until the equilibrium phase of the scour process was attained. After analyzing the first set results, a second set of experiments with durations corresponding to the end of the initial phase of the scour process was carried out.

4 RESULTS

In this section we present the results of the temporal evolution of the maximum scour depth (section 4.1), and of the configuration of the scour cavity (subsection 4.2).

4.1 Maximum scour depth

Figure 2 shows the results of the temporal evolution of the maximum scour depth (Y_s), measured at the upstream extremity of the piers. In the initial phase of the scour process, simple piers present identical maximum scour depths, showing that the scour evolution is not affected by the length of the pier in the flow direction. However, the main phase of the scour process is shorter in case of the elongated pier, and for this pier the equilibrium phase is attained earlier. The maximum equilibrium scour depth is smaller in case of the simple elongated pier, when compared with the simple circular pier. This may be due to the

existence of a flow contraction that secludes the horseshoe vortex inside the scour cavity, making it more difficult for the sediments that are being eroded by the horseshoe vortex to escape this region. Comparing the results obtained for the piers with slot, the elongated pier presents higher maximum scour depth values, indicating that in this case the flow-altering measure is less effective.

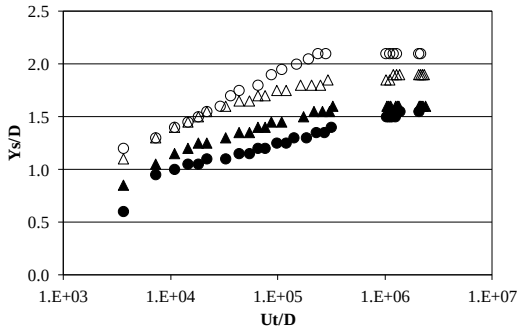

Figure 2: Maximum scour depth temporal evolution (○: circular simple pier; △: elongated simple pier; ●: circular pier with slot; ▲: elongated pier with slot).

It was considered that the equilibrium maximum scour depth (Y_s^e) was attained when the maximum scour depth did not change more than 0.05 *D* for a period of 24 hours [4]. When comparing piers with slot with simple piers, results show that the piers with slot present smaller values of the equilibrium maximum scour depth (Table 2). The maximum scour depth reduction, calculated by

$$r[\%] = \frac{Y_{s\ \text{simple pier}}^e - Y_{s\ \text{pier with slot}}^e}{Y_{s\ \text{simple pier}}^e} \times 100 \quad (1)$$

is equal to 26 % and 16%, for the circular and elongated piers, respectively. These values are slightly smaller than those of [5], who obtained 30 % of reduction in case of circular piers.

Table 2. Equilibrium maximum scour depth.

Pier	Y_s^e (mm)
circular	42
circular with slot	31
elongated	38
elongated with slot	32

4.2 Analysis of the configurations of scour cavities

Figures 3 and 4 show the topography of the scour cavities, after the equilibrium maximum scour depth has been attained. All cavities are approximately symmetrical in relation with the direction of the flow. These results confirm that the maximum scour depth occurs immediately upstream from the pier. They present higher slopes upstream from the pier, and downstream from the pier the slopes are smoother and the scour cavity extends to larger distances downstream.

The scour cavities topography allows the determination of their longitudinal profiles and the measurement of the angle between the bottom of the bed of the scour cavity and the initial sand level, both upstream and downstream (Table 3). These angles were determined for casts corresponding to the end of the initial phase and to the equilibrium phase of the scour process.

Table 3. Angle between the bed of the scour cavity and the initial sand level, upstream (α) and downstream (β).

Pier	End of the initial phase		Equilibrium phase	
	α (º)	β (º)	α (º)	β (º)
circular	60.5	52.1	38.9	10.3
circular with slot	46.3	35.6	38.4	7.2
elongated	45.5	27.9	42.6	10.5
elongated with slot	53.2	33.1	35.2	7.1

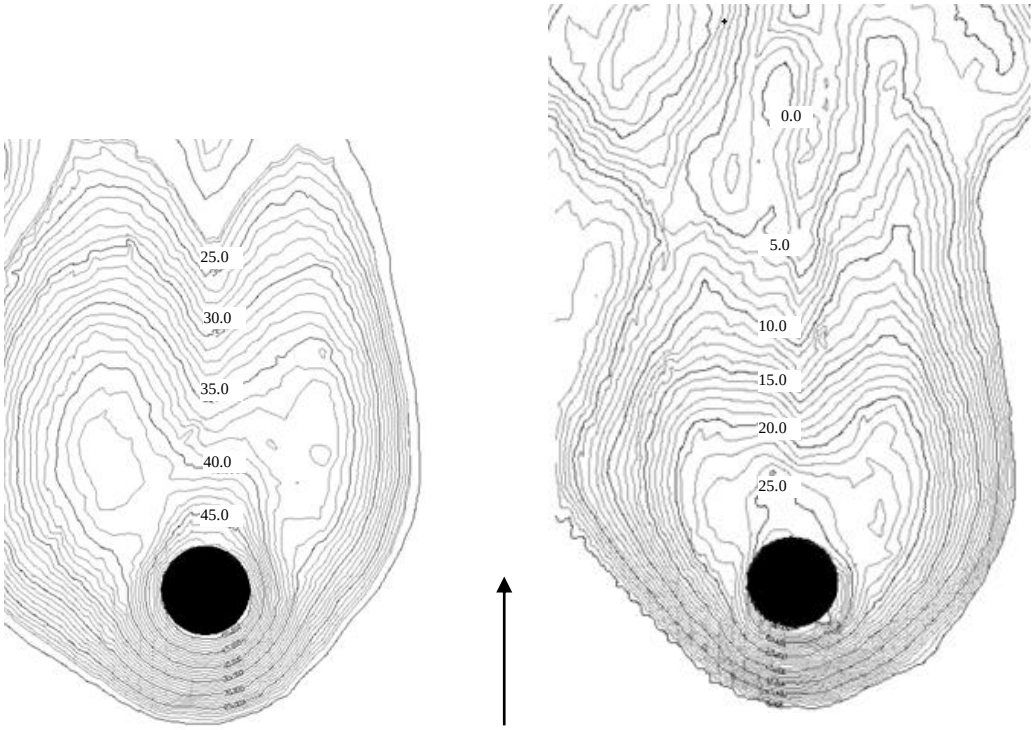

(a) (b)

Figure 3: Configuration of the scour cavities in case of circular piers – (a) simple pier, (b) pier with slot. Arrow indicates the flow direction. 1 mm spacing between contour lines, contour lines levels in mm.

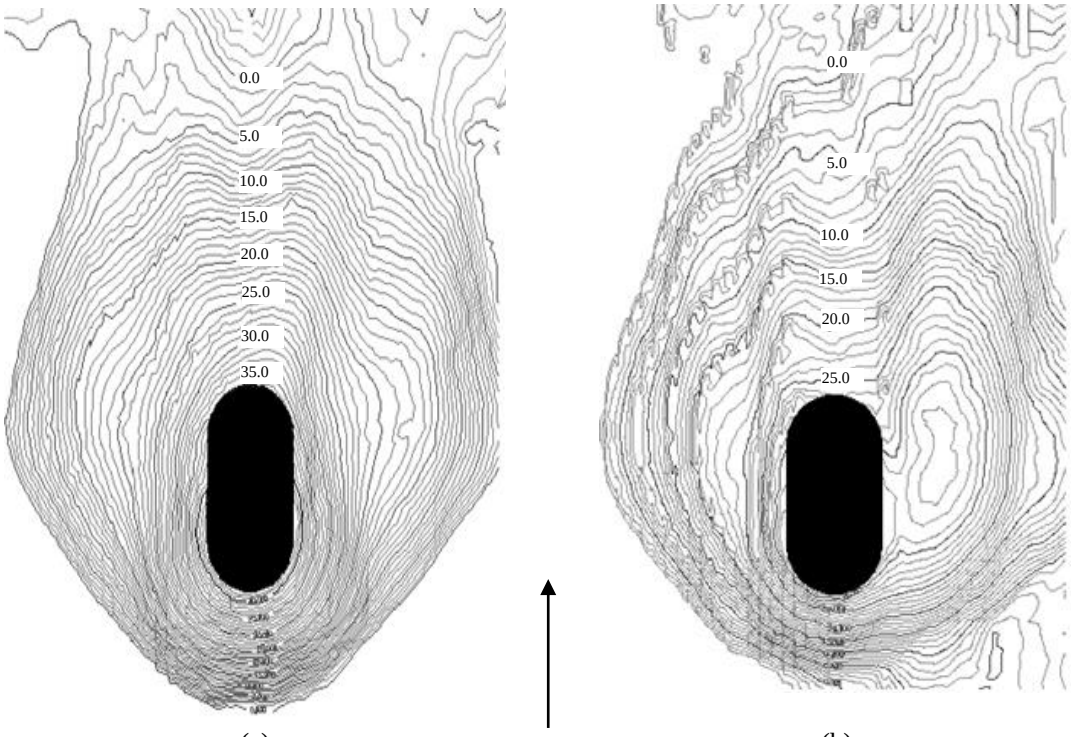

(a) (b)

Figure 4: Configuration of the scour cavities in case of elongated piers – (a) simple pier, (b) pier with slot. Arrow indicates the flow direction. 1 mm spacing between contour lines, contour lines levels in mm.

Results show that the angle upstream from the pier is higher than the one observed downstream from the pier. All angles decrease as the duration of the experiments increases, when the initial and equilibrium phases of scour are compared. In the equilibrium phase the angle upstream from the pier is identical to the natural repose angle of sand [14]. The angles downstream are significantly reduced, but similar when comparing the circular and elongated piers. In case of piers with slot, both upstream and downstream angles are reduced, when compared with the simple pier measurements.

5 CONCLUSIONS

The influence of the piers geometry and the use of a slot as flow-altering countermeasure in the scour process were analyzed. Maximum scour depth evolves at a faster rate during the initial phase and occurs at the point immediately upstream of the pier, regardless of its configuration. Scour depth is smaller in elongated piers than in circular piers, regardless of the presence of the countermeasure. Comparing piers with slot with simple piers, a reduction of the maximum scour depth between 26% and 16% is observed, for the circular and elongated pier, respectively. The use of paraffin and Vaseline casts allows the analysis of the topography of the scour cavity. The angle between the bed of the scour cavity and the initial sand level is higher upstream from the pier, when compared with the angle of the downstream scour cavity slope. The angles between the bottom of the bed of the scour cavity and the initial sand level decrease with the implementation of the flow-altering countermeasure, both in circular and elongated piers. When comparing the initial and the equilibrium phases of scour, it was observed that the angles decrease as the duration of the experiments increases.

ACKNOWLEDGMENTS

The authors thank Mr. João Rui Oliveira, technician of the Hydraulics Laboratory of the University of Minho for his help with the experiments, and Prof. Fernando Duarte for the availability to use the Roland 3D Laser Scanner of the Polymers Department of the University of Minho.

REFERENCES

[1] HNC Breusers, G Nicollet, HW Shen (1977). Local scour around cylindrical piers. *Journal of Hydraulic Research* **15**(3):211–252.

[2] S Dey, RV Raikar (2007). Characteristics of horseshoe vortex in developing scour holes at piers. *Journal of Hydraulic Engineering* **133**(4):399–413.

[3] DF Hill, BD Younkin (2006). PIV measurements of flow in and around scour holes. *Experiments in Fluids* **41**(2):295–307.

[4] BW Melville, Y-M Chiew (1999). Time scale for local scour at bridge piers. *Journal of Hydraulic Engineering* **125**(1):59–65.

[5] A Tafarojnoruz, R Gaudio, F Calomino (2012). Evaluation of flow-altering countermeasures against bridge pier scour. *Journal of Hydraulic Engineering* **138**(3):297–305.

[6] R Gaudio, A Tafarojnoruz, F Calomino (2012). Combined flow-altering countermeasures against bridge pier scour. *Journal of Hydraulic Research* **50**(1):35–43.

[7] C Grimaldi, R Gaudio, F Calomino, AH Cardoso (2009). Control of scour at bridge piers by a downstream bed sill. *Journal of Hydraulic Engineering* **135**(1):13–21.

[8] C Grimaldi, R Gaudio, F Calomino, AH Cardoso (2009). Countermeasures against local scouring at bridge piers: slot and combined system of slot and bed sill. *Journal of Hydraulic Engineering* **135**(5):425–431.

[9] A Khosronejad, S Kang, F Sotiropoulos (2012). Experimental and computational investigation of local scour around bridge piers. *Advances in Water Resources* **37**:73–85.

[10] MMCL Lima, EPM Leite (2012). Configuração da cavidade de erosão localizada na proximidade de pilares de diferente secção. In *IV Conferência Nacional em Mecânica dos Fluidos, Termodinâmica e Energia, MEFTE 2012*, Paper 91.

[11] SO Lee, TW Sturm (2009). Effect of sediment size scaling on physical modelling of bridge pier scour. *Journal of Hydraulic Engineering* **135**(1):793–802.

[12] EV Richardson, SR Davies (2001). *Evaluating Scour at Bridges*, 4th edition, HEC 18, FHWA-NHI-01-001, US Department of Transportation.

[13] A Roulund, BM Sumer, J Fredsøe, J Michelsen (2005). Numerical and experimental investigation of flow and scour around a circular pile. *Journal of Fluid Mechanics* **534**:351–401.

[14] AH Cardoso (1998). *Hidráulica Fluvial*, Fundação Calouste Gulbenkian, Lisbon, Portugal.

V Conferência Nacional de Mecânica dos Fluidos, Termodinâmica e Energia
MEFTE 2014, 11–12 Setembro 2014, Porto, Portugal
APMTAC, 2014

Shallow water flow around an elongated bridge pier

MMCL Lima

Departamento de Engenharia Civil, Escola de Engenharia da Universidade do Minho, Campus de Azurém, 4800-058 Guimarães, Portugal
email: mmlima@civil.uminho.pt

ABSTRACT: This work describes the free surface flow around an elongated vertical pier, i.e. rectangular pier with round noses. Measurements were made using two-component Laser Doppler Anemometry, with the main objective of studying the turbulent flow field around the pier. The flow was studied for a water depth equal to 5 cm, corresponding to a shallow water flow, and a ratio of 0.6 between the mean approach velocity (0.17 ms^{-1}) and the estimated critical velocity of sand with a mean diameter of 0.376 mm. It was observed that the flow is completely developed as it reaches the pier. Measurements of horizontal and vertical velocities in the vicinity of the pier show the strong interaction between the structure and the flow. The flow decelerates as it approaches the pier, and is deflected towards the bottom. In free surface flows Reynolds shear stresses are usually negative, but in the present case as the flow approaches the pier Reynolds shear stresses become positive and increase. The wake of the pier is characterized by high turbulence intensities. Reverse horizontal velocities were observed downstream of the pier, until a distance equal to one pier transversal dimension.

KEY-WORDS: Laser Doppler Anemometry; Elongated bridge piers; Turbulent flow; Shallow water flow; Reynolds shear stresses.

1 INTRODUCTION

The flow around a circular pier has been the subject of a large number of studies (e.g. [1, 2, 3]). Bridge piers can be mounted on a sediment bed, in which case the interaction of flow, pier and sediments may originate scour. Scour is a complex phenomenon, and experimental studies of the flow initial conditions, i.e. prior to scour cavities development, are useful for the validation of numerical models that predict scour maximum depth [3]. Usually a circular vertical pier configuration is selected, although some studies describe the flow around rectangular bridge piers [4, 5]. Many experimental studies have been conducted for deep water flows, and mean approach velocities approximately equal to 0.9 of the sediment estimated critical velocity. However, shallow water flows can also originate scour, and scour can begin at velocities as low as half of the estimated critical velocity.

The present study main objective is to characterize the turbulent flow field around an elongated pier, in case of shallow water flow over a fixed rough rigid bed, for a mean horizontal approach velocity equal to 60 % of the corresponding critical velocity in case of a sand bed. A brief presentation of theoretical concepts involved in flow around a bridge pier is presented in the following section. The experimental set-up and measuring equipment are described in section 3. The results and their discussion are presented in section 4. Section 5 is the final section, with the main conclusions.

2 FLOW AROUND BRIDGE PIERS

The free surface water flow around a bridge pier is characterized by the existence of a vertical stagnation line in the pier's nose and an elevation of the free surface immediately upstream of the pier with a surface roller [6], along with a depression around the side edge and also downstream of the pier [3]. The difference between the free surface levels at the front and side of the pier causes a pressure gradient that originates a down flow, with also a velocity component in the radial direction. In case the flow Froude number, based on the mean longitudinal approach velocity and the water depth, is relatively low (≈ 0.2), the flow in the radial direction is insignificant [3]. Upstream of the pier a boundary layer separation occurs due to the adverse pressure gradient, and originates a horseshoe vortex system [7, 8]. The size of the horseshoe vortex grows with the ratio between the boundary layer thickness and the pier diameter. For a small value of this ratio, the boundary layer may not separate and no horseshoe vortex is generated [3].

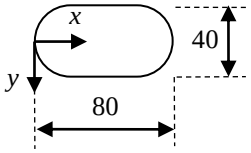

Figure 1: Elongated pier geometry and coordinate axes used (dimensions in mm).

Downstream of the pier, lee-wake vortices are observed and caused by the rotation of the boundary layer over the piers' surface [3]. In this region turbulence intensities increase significantly [2].

Water flow around a bridge pier is considered to be shallow when the water flow depth is smaller than the pier diameter [9]. In studies concerning scour around a bridge pier, this shallowness manifests itself for ratios between the water flow depth and the pier diameter smaller than 2.5 [10] or 6 [11]. In these cases, the surface roller weakens the down flow, interfering with the development of the horseshoe vortex [6]. Shallow water flows present different characteristics in the near wake of a pier [12] that may be relevant for the development of scour cavities in these cases [11].

3 EXPERIMENTAL SET-UP

3.1 Experimental rig

Experiments were conducted in a 0.4 m wide and 16.7 m long water channel at the Hydraulics Laboratory of the Civil Engineering Department of the Faculty of Engineering of the University of Porto. The channel had a horizontal bottom and glass walls. The test section consisted of a rectangular vertical pier with round noses, installed approximately 9.7 m downstream the beginning of the flume. The pier was 40 mm wide (D) and 80 mm long (Figure 1), oriented in the longitudinal channel direction. The origin of the coordinate axes was located at the symmetry axis in the pier upstream nose. The flow characteristics were studied along the longitudinal streamwise direction (x) and the vertical direction (z), at the symmetry axis of the flow ($y = 0$). The pier was mounted in the middle of an acrylic plate 1.8 m long, were a layer of uniform sand with 0.376 mm mean diameter was glued, in order to reproduce the natural roughness of a river stream. Although there is a difference between flows over impermeable and permeable beds [13], in case of flow characterization previous to scour development, a rigid fixed bed is an adequate solution [3]. The flow was controlled by a gate valve and measured by an electromagnetic flow meter (ABB, model IDE41F). Water depth was controlled by a sluice gate at the downstream extremity of the flume.

3.2 Optical system and measuring equipment

The light source was an Argon-ion Laser (Spectra-Physics, Model 177-G0232) operating in multi-mode, and the optical system was a Dantec 60X41 FiberFlow, including a 40 MHz frequency shifter and colour separation, combined with an 85 mm probe together with a beam expander and a 500 mm front lens (Table 1). A colour separator (55X35) split the collected light into two wavelengths before reaching the corresponding photomultipliers (Dantec 57X18). LDA data processing and acquisition was performed using BSA F60 Flow analyser (Dantec). Simultaneous measurements of streamwise longitudinal (horizontal) and vertical velocities were made using the overlapped coincidence method. Positive horizontal velocity corresponded to the direction of flow, and positive vertical velocity corresponded to the upwards direction. Due to the blockage effect of the flat bottom and the free water surface boundaries, no measurements of vertical velocities were possible at distances from the boundaries smaller than 5 mm. For the same reason, no measurements of horizontal velocities were possible at distances from the pier smaller than 2.5 mm.

3.3 Experimental condition

Steady and uniform approach flow was studied for a water depth (h) of 50 mm, corresponding to a ratio $h/D = 1.25$, representative of a shallow water flow. In order to avoid secondary flows [2], the ratio B/h, between the channel width (B) and the water flow depth, was higher than 5. The ratio D/B, between the transversal dimension of the pier and the channel width, was smaller than 0.1 [3, 10] minimizing the blockage effect of the pier.

A mean horizontal approach velocity (U_∞) equal to 0.17 ms^{-1} was selected. This mean velocity corresponded to 60 % of the critical velocity that sets the threshold of incipient sediments' motion with a mean diameter equal to 0.376 mm [14]. The Reynolds number based on U_∞ and transversal dimension of

the pier was equal to 5822 and the Reynolds number based on U_∞ and water depth was equal to 7277. Froude number based on U_∞ and water depth was equal to 0.24, representative of a subcritical flow.

Table 1: Main LDA characteristics.

	Velocity	
	horizontal	vertical
Laser Wavelength (nm)	514.5	488
Half angle of beams in air (º)	1.661	1.661
Control volume size in air (major and minor axis, calculated) (mm×mm)	2.825×0.082	2.679×0.078
Fringe separation (mm)	8.874	8.417
Number of fringes	9	6
Velocimetry conversion factor (MHz s m^{-1})	8.874	8.417

4 RESULTS

Figure 2 shows vertical profiles of mean horizontal (*U*) and vertical (*V*) velocities in the symmetry line ($y = 0$) at eight axial locations upstream ($x < 0$) of the pier's nose. Fluctuating horizontal (uu_{rms}) and vertical (vv_{rms}) velocities are presented at the same locations in Figure 3. Figure 4 shows the corresponding Reynolds shear stresses.

The shallow water flow was completely developed as it reached the pier, as expected because the pier was located more than 120 water depths downstream of the channel inlet [9]. Measurements of horizontal and vertical velocities show the strong interaction between the flow and the structure. The mean horizontal velocity diminishes as the flow approaches the pier. For distances from the pier's nose smaller than 1 *D*, the flow decelerates (Figure 2 (a)), and is deflected towards the bottom (Figure 2 (b)). No mean horizontal negative velocities are observed, although in this region mean (Figure 2 (a)) and fluctuating (Figure 3 (a)) velocities are of the same order. Downwards vertical velocity is highest closest to the pier ($x/D = -0.0625$) at a distance from the bottom approximately equal to $h/4$. These results show a similar pattern to the ones by Graff and Yulistiyanto [2].

Fluctuating horizontal and vertical velocities increase for distances from the piers' nose smaller than 0.25 *D* (Figure 3). Fluctuating horizontal velocity increases both close to the bed and to the free surface (Figure 3(a)), contrary to the work of Graf and Yulistiyanto [2] where the fluctuating velocity only increases near the bed. However, fluctuating vertical velocities are always maxima close to the bed (Figure 3(b)), in agreement with the results of Graf and Yulistiyanto [2]. In free surface flows usually *u* and *v* are correlated negatively, as occurs for distances from the piers' nose greater than 0.25 *D* (Figure 4). If quadrant analysis is performed, events of Q_2 (also known as ejection) and Q_4 (also known as sweep) are more likely to occur in two dimensional surface flows [15], corresponding to regions of turbulence production [16]. If *u* and *v* correlate positively, events of Q_1 (also known as outward interaction) and Q_3 (also known as inward interaction) will occur, and Reynolds shear stresses will be positive. As the flow approaches the pier, Reynolds shear stresses become positive and increase. Positive Reynolds shear stresses correspond to negative bed shear stress, which are an indication of the existence of the horseshoe vortex in front of the pier [3]. Although Reynolds shear stresses values are small, the vertical profiles show a clear trend. For distances from the pier smaller than 0.25 *D*, Reynolds shear stresses near the surface remain close to zero and are highest approximately at half depth ($h/2$).

Figure 5 shows vertical profiles of mean horizontal and vertical velocities at seven axial locations downstream ($x > 0$, $y = 0$) of the pier's nose. Fluctuating horizontal and vertical velocities are presented at the same locations in Figure 6. Figure 7 shows the corresponding Reynolds shear stresses vertical profiles. In the wake of the pier there is a reverse flow until one pier diameter downstream ($x/D = 3$), and then the flow starts to accelerate. This result is in agreement with the length of the turbulent wake equal to 1.3 *D* determined by Yulistiyanto et al. [17] in their simulation of the flow around a circular cylinder for a similar flow Reynolds number, indicating that the wake's length is not influenced by the length of the pier in the flow direction. The flow vertical direction immediately downstream from the pier ($x/D = 2.0625$) is positive, i.e. the fluid is moving upwards. Maximum reverse horizontal flow occurs at $x/D = 2.5$, simultaneously with the maximum negative vertical velocity. At $x/D = 6$ the mean flow hasn't recovered its initial characteristics prior to the pier, indicating that this region is still affected by the wake of the pier.

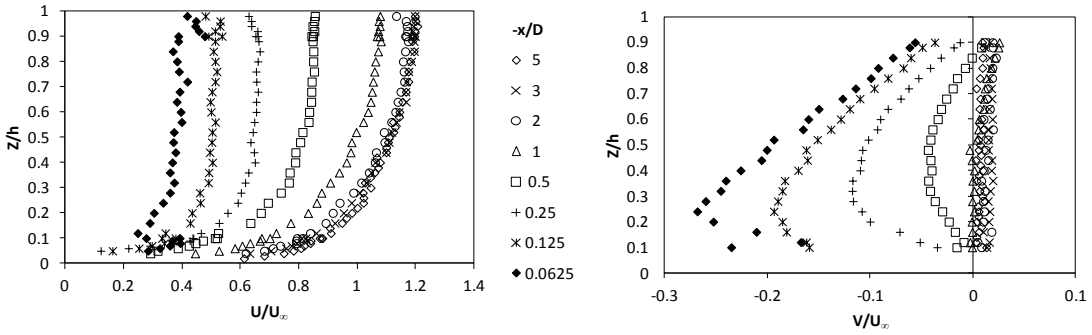

(a) (b)

Figure 2: Vertical profiles of mean horizontal (a) and vertical (b) velocities, normalized by the mean horizontal approach velocity, upstream of the pier.

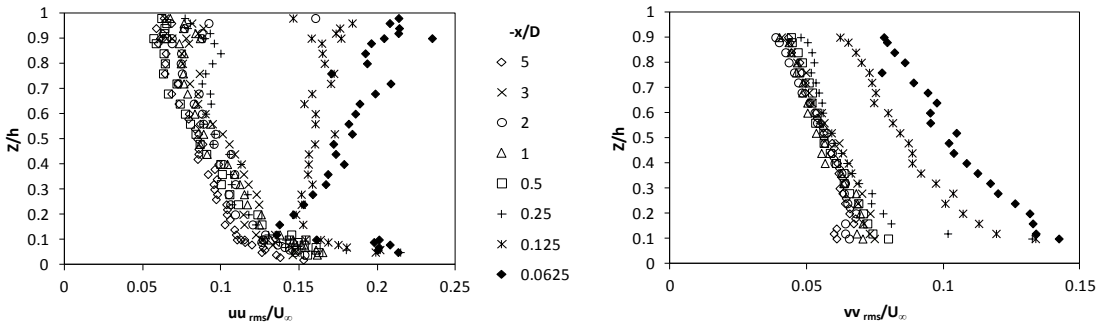

(a) (b)

Figure 3: Vertical profiles of root-mean-square fluctuating horizontal (a) and vertical (b) velocities, normalized by the mean horizontal approach velocity, upstream of the pier.

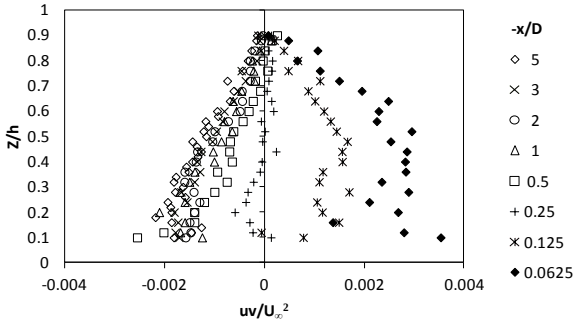

Figure 4: Vertical profiles of Reynolds shear stresses, normalized by the mean horizontal approach velocity, upstream of the pier.

Figure 6 shows horizontal turbulence intensities with maxima between 2.25 and 2.5 *D*. Maxima vertical turbulence intensities are observed for $x/D = 3$. Turbulence intensities are much higher downstream of the pier when compared with the flow upstream of the pier, both for the horizontal and vertical components.

Immediately downstream of the pier, for $x/D = 2.0625$, Reynolds shear stresses (Figure 7) are positive near the bottom. Further downstream Reynolds shear stresses become positive for $h/z > 0.25$. Similar results were observed by Rostamy et al. [18] on the wake of a finite cylinder near the bottom. At $x/D = 6$, Reynolds shear stresses are negative for $z/h > 0.1$, although the shape of the profiles is not the usual in two dimensional free surface flow (see Figure 4, $|x/D| < 0.25$ | for comparison).

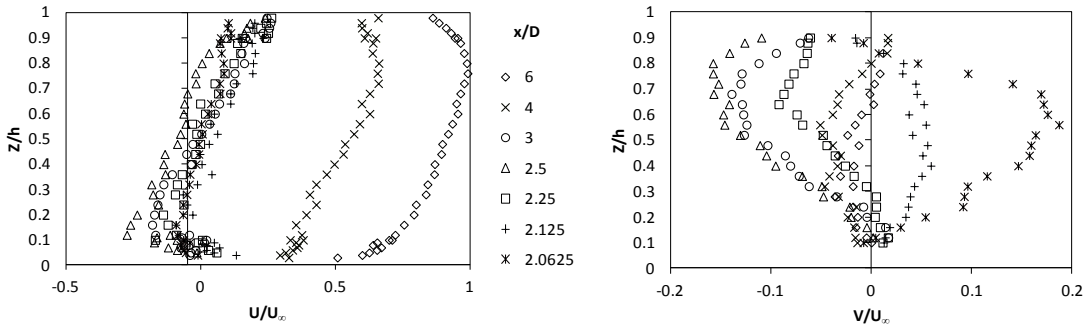

(a) (b)

Figure 5: Vertical profiles of mean horizontal (a) and vertical (b) velocities, normalized by the mean horizontal approach velocity, downstream of the pier.

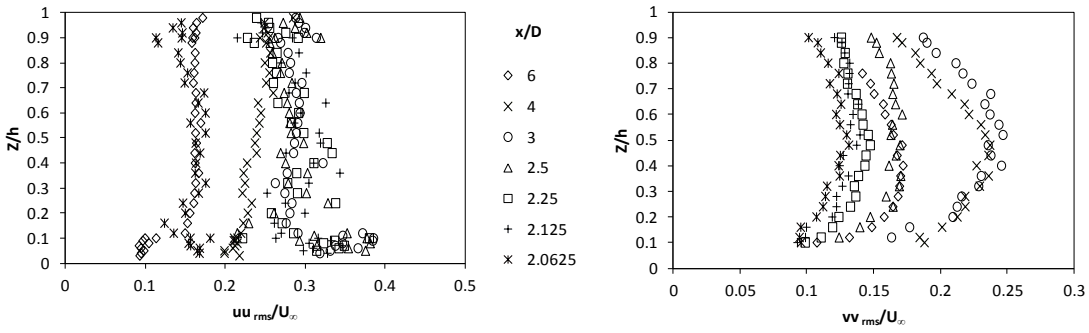

(a) (b)

Figure 6: Vertical profiles of root-mean-square fluctuating horizontal (a) and vertical (b) velocities, normalized by the mean horizontal approach velocity, downstream of the pier.

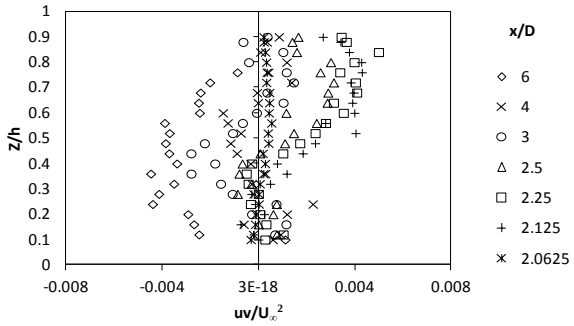

Figure 7: Vertical profiles of Reynolds shear stresses, normalized by the mean horizontal approach velocity, downstream of the pier.

5 CONCLUSIONS

The turbulent shallow water flow field around an elongated pier, mounted on a fixed rough rigid bed, was analysed by two-component Laser Doppler Anemometry. The flow was completely developed as it reached the pier. The flow decelerated when approaching the pier, and was deflected towards the bottom. In the vicinity of the pier Reynolds shear stresses became positive and increased. The wake of the pier was characterized by high turbulence intensities. Reverse horizontal velocities were observed downstream from the pier, until a distance equal to one pier transversal dimension.

ACKNOWLEDGMENTS

This experimental work was performed in the Hydraulics Laboratory of the Civil Engineering Department of the Faculty of Engineering of the University of Porto, during my sabbatical leave, where I was kindly hosted by the late Prof. Maria Fernanda Proença. I thank the Hydraulics Division of the Civil Engineering Department of the Faculty of Engineering of the University of Porto, especially Prof. Francisco Taveira Pinto, for the access to the facilities and equipment during this period. The help of Prof. Elsa Carvalho with the measuring equipment and of Mr. Nelson Silva with the technical support are gratefully acknowledged.

REFERENCES

[1] B Dargahi (1989). The turbulent flow field around a circular cylinder. *Experiments in Fluids* **8**:1–12.
[2] WH Graf, B Yulistiyanto (1998). Experiments on flow around a cylinder; the velocity and vorticity fields. *Journal of Hydraulic Research* **36**(4):637–654.
[3] A Roulund, BM Sumer, J Fredsøe, J Michelsen (2005). Numerical and experimental investigation of flow and scour around a circular pile. *Journal of Fluid Mechanics* **534**:351–401.
[4] WY Chang, G Constantinescu, S Miyawaki, WF Tsai, HC Lien (2010). The flow and turbulence structure at a rectangular bridge pier with a low angle of attack. In A Dittrich, K Koll, J Aberle, P Geisenhainer, Eds., *Proceedings of the River Flow 2010 Conference*, Braunschweig, Germany, Paper A5_06, 681–689.
[5] S Dey, RV Raikar (2007). Clear-water scour at piers in sand beds with an armor layer of gravels. *Journal of Hydraulic Engineering* **133**(6):703–711.
[6] R Ettema, BW Melville, B Barkdoll (1998). Scale effect in pier-scour experiments. *Journal of Hydraulic Engineering* **124**(6):639–642.
[7] WH Graf, I Istiarto (2002). Flow pattern in the scour hole around a cylinder. *Journal of Hydraulic Research* **40**(1):13–20.
[8] GK Kirkil, SG Constantinescu, R Ettema (2008). Coherent structures in the flow field around a circular cylinder with scour hole. *Journal of Hydraulic Engineering* **134**(5):572–587.
[9] H Fu, D Rockwell (2005). Shallow flow past a cylinder: control of the near wake. *Journal of Fluid Mechanics* **539**:1–24.
[10] A Tafarojnoruz, R Gaudio, F Calomino (2012). Evaluation of flow-altering countermeasures against bridge pier scour. *Journal of Hydraulic Engineering* **138**(3):297–305.
[11] BW Melville, Y-M Chiew (1999). Time scale for local scour at bridge piers. *Journal of Hydraulic Engineering* **125**(1):59–65.
[12] H Fu, D Rockwell (2005). Shallow flow past a cylinder: transition phenomena at low Reynolds number. *Journal of Fluid Mechanics* **540**:75–97.
[13] C Manes, D Pokrajac, I McEwan, V Nikora (2009). Turbulence structure of open channel flows over permeable and impermeable beds: A comparative study. *Physics of Fluids* **21**(12):125109.
[14] EV Richardson, SR Davies (2001). *Evaluating Scour at Bridges*, 4th edition, HEC 18, FHWA-NHI-01-001, US Department of Transportation.
[15] J Kim, P Moin, R Moser (1987). Turbulence statistics in fully developed channel flow at low Reynolds number. *Journal of Fluid Mechanics* **177**:133–166.
[16] SB Pope (2000). *Turbulent Flows*, Cambridge University Press, Cambridge, United Kingdom.
[17] B Yulistiyanto, Y Zech, WH Graf (1998). Flow around a cylinder: shallow-water modelling with diffusion-dispersion. *Journal of Hydraulic Engineering* **124**(4):419–429.
[18] N Rostamy, D Sumner, DJ Bergstrom, JD Bugg (2012). Local flow field of a surface-mounted finite circular cylinder. *Journal of Fluids and Structures* **34**:105–122.

Dynamic behaviour of a pipe system under unsteady flow and structure vibration

M Simão[1], J Mora[2], H M Ramos[1]

[1]Departmento de Engenharia Civil, Instituto Superior Técnico, Avenida Rovisco Pais 1, 1049-001 Lisboa, Portugal
[2] Departamento de Ingeniería Hidráulica, Universidad de Guanajuato, Sede Belén: Av. Juárez 77, Zona centro Guanajuato, Gto. C.P. 36000, Guanajuato, México
email: m.c.madeira.simao@ist.utl.pt, jesusmora@ugto.mx, hr@civil.ist.utl.pt

ABSTRACT: In this article the subject fluid structure interaction is approached using a real and a computational model. Different scenarios are tested in a laboratory facility, where analysis of transient phenomena are created. Since it's a fluid-structure elastic phenomenon, it's important to study the phenomenon unsteady flow induced that reflects a structural vibration, developed when the steady-state velocity of a fluid is suddenly altered. Thus, the most adequate approach to model water-hammer phenomena is the one based on CFD (Computational Fluid Dynamics), and the FEM (Finite Element Method) to study the structural characteristics involved in the analysis of under pressure hydraulic structures pipe system. Through these models, it's possible to study the behaviour of the fluid and the structure, as a whole, i.e. enabling the response of the structure change by the flow modification and, consequently, the response of the fluid by structure vibration. In general, simulations based on CFD analyses are used to better understand the dynamic phenomena. As dealing with a joined problem, two domains are created, the fluid-flow and the structure. The analysis are developed in order to show the possible consequences in terms of displacements, when the system is submitted to different loads and type of supports. It is equally emphasized the importance of integrated analysis (fluid-structure interaction) and the purpose of supports in water pipe systems in the infrastructures design.

KEY-WORDS: fluid-structure interaction; FEM; Water hammer; CFD.

1 INTRODUCTION

Water hammer and surge are commonly occurring phenomena in pipe systems, inducing extreme pressure events, leaks ruptures or even dangerous accidents that are rarely well understood due to the numerous variables associated. The flow through a pipe does not seem likely to be able to generate high pressures, or create a risk to joints and mountings, yet the effects of water hammer can be to burst joints and break mountings with relative ease. Water flowing through a length of pipe gains a momentum, induced by the water column inertia, and the rapid closing of a valve requires the dissipation of the excess energy. The energy exerts itself in the form of a momentary increase in pressure above the normal initial pressure. If the valve closes very rapidly the pressure rise can lead to the effect of water hammer, where a wave of flow energy travels within the pipe at the celerity speed, creating potential damage [1].

This research is an ongoing study about hydraulic transients using different numerical methods, comparing them with the experimental tests in a laboratory network. The range of results from the test study of hydraulic transients presented in this research highlights the importance of accurate prediction of the pressure variations in order to ensure that a pipeline's integrity is not compromised.

2 FUNDAMENTALS

Hydraulic transients in closed pipelines have been a subject of theoretical and practical research. A common and simple example is the knocking sound or hammering noise which is often heard when a valve is rapidly closed. The transient state of the flow from time of closure until a new steady state condition is established, is complex due to pressure surges that propagate away from the valve. By closing the valve rapidly, the valve converts the kinetic energy carried by the fluid particles into strain energy in the pipe walls [2]. This results in a "pulse wave" of abnormal pressure to travel from the disturbance into the pipe system. The hammering sound that is sometimes heard results from the fact that a great portion of the fluid's kinetic energy is converted into pressure waves, causing noise and vibrations in the pipe. Energy losses due to mainly friction cause the transient pressure waves to decay until a new steady state is established [3].

During transient events, the maximum pressures can cause damage in pipelines, valves, or other equipment. Sometimes, high pressures may not necessarily destroy pipelines or other devices, but can cause cracks in internal linings, damage connections between pipes or cause deformations in equipment. This equipment could be valves, air valves, or even hydraulic transient protection devices. Moreover, high pressures may result in leakages in hydraulic systems even though no visible damage can be noticed.

Strong hydraulic vibrations may damage pipeline, internal lining, or system equipment. Such long-term moderate surges may gradually lead to fatigue failure. Oscillations of water masses through a pipeline may also cause vibrations and suction of air into the pipeline. Therefore, neglecting such influences during the design phase may lead to system damage. Also, interaction between fluid-structure manifests itself as vibration behaviour and in disturbances in the velocity and pressure variations of the fluid. The additional pressure loads are transmitted to the mechanical supports which may damage them inducing dangerous dynamic instabilities [4].

The elasticity of the pipe boundaries and the compressibility of the fluid prevent these sudden changes in pressure from taking place instantaneously throughout the fluid. The associated pressure changes during a transient period are often very large and occur very rapidly (within a few seconds). If the maximum pressures exceed the bar ratings (mechanical strength) of the piping material, different types of failure such as pipe bursts can occur. Similarly, if the minimum pressure drops below the vapour pressure of the fluid, cavitation can occur and can be detrimental to the pipeline system [5].

3 DESCRIPTION OF THE LABORATORY FACILITY

In order to study the effects of the fluid structure interaction (FSI), several tests were carried out in the laboratory of Guanajuato's University. The following figure shows the installation and all components involved. This system comprises a pump whose characteristic curve was determined by assigning different values of flow and pressure. This pumping system supplies the entire piping network. The distance between the surface of the liquid in the supply tank and the centreline of the pump is negative, so there is a suction lift, and then the water accumulated in the deposit tank is raising up to a maximum head of 30 mwc. The maximum discharge of this installation is about 25 L/s. From upstream to downstream, 4 pressure transducers were installed throughout the facility, 1 relief valve installed immediately downstream of the pump and also 2 flow meters set as Figure 1. The first flow meter (Figure 1) corresponds to an ultrasonic. This needs to be installed about 1/8 of the pipe, so that the reading can be more accurate. However, this type of accessory only works accurately for high flow rates, due to the location of their sensors to the flow volume. Thus two flow meters were used, an ultrasonic and a conventional flow meter, also located in the GI pipe.

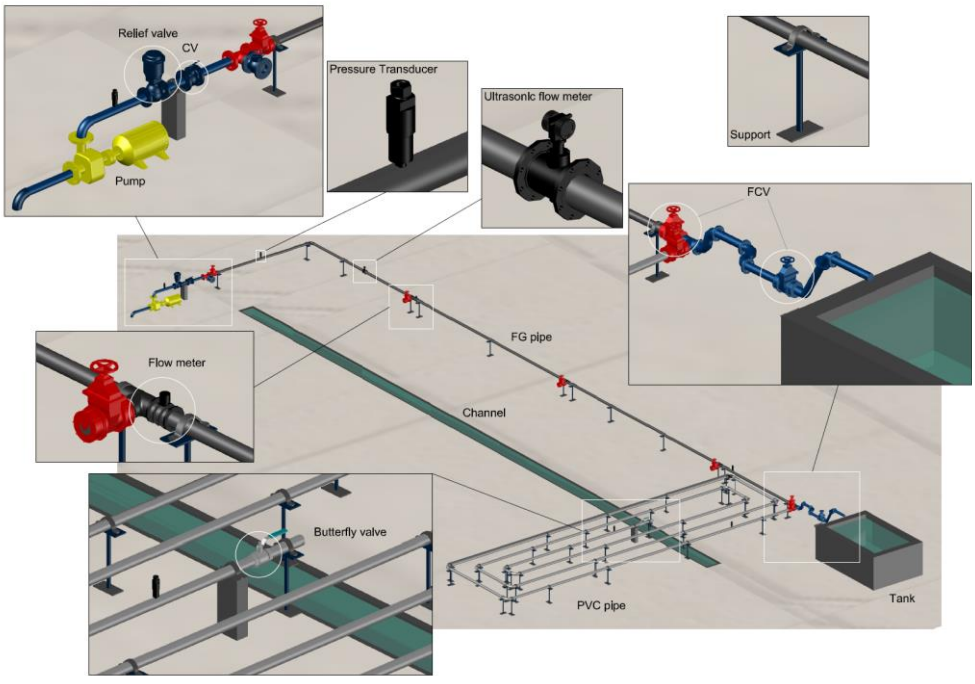

Figure 1: Laboratory of Guanajuato's University (scheme).

The system equipment comprises two types of pipes, galvanized iron (GI) and PVC, with lengths of 30 and 85 m, respectively. Regarding the number and type of fittings, GI pipes accounts: 3 Flow control valves (FCV), 1 check valve (CV) of no-flow control, 1 pump, and a discharge tank. As for PVC pipe, this includes 1 butterfly valve, 1 FCV, and a discharge channel.

The pipes are supported on iron supports approximately 0.5 m height, being attached to them through iron or metal clamps, depending on the type of the piping material (iron - GI, metal – PVC).

Regarding the type of joints, these are elastic, but in case of GI pipe the joints are made through flange couplings, and in case of PVC pipe, by Gibault joints.

3.1 Experimental tests

In the configuration for water hammer tests, the pipes are connected to a constant head of 30 m, varying the discharge. The pump provides the water supply to the constant head inlet. The constant head means that water enters the 30 m before passing through the operated gate valve. From the gate valve, the pressure drops almost 10 m, and the water discharges into the channel tank located downstream of the PVC pipe.

In the experimental tests, the 4 pressure transducers were installed along the entire pipeline, especially where transitory events are caused, i.e. in the PVC pipe. So two of them were installed in PVC pipe being one located immediately upstream of the closing valve, and the other transducer located 2 meters before the GI connection. The remaining two were located in the GI pipe, one near the connection of GI and PVC pipes, and the last one installed upstream of the system, next to the pump (Figure 2).

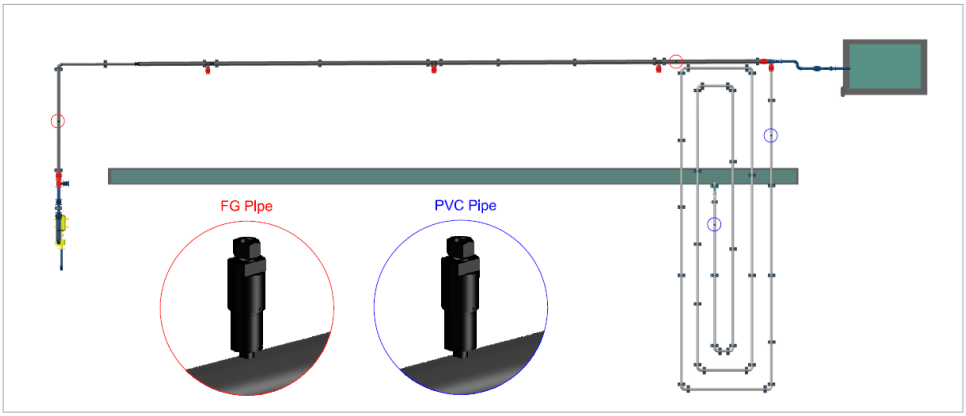

Figure 2: Laboratory of Guanajuato's University (scheme).

These transducers were connected to an oscilloscope in order to measure the pressure as a function of time. The oscilloscope shows the passage of the acoustic wave past each pair of pressure transducers.

To perform surge experiments, a steady flow was created from the upstream tank through the GI pipe, using the pump, the inlet valve and the following manual control valves, up to the discharge tank. With the system in continuous operation, the manual valve installed in the PVC pipe was open and the manual valve closing to the discharge tank was closed, being the system constituted by the two mentioned pipes. Then a known discharge value from the inlet valve to the discharge channel was set, maintaining a steady flow condition. After creating the conditions for steady regime, a surge was created by quickly closing the butterfly valve. Instantly, the closing time of the valve was measured, using a stopwatch, and the oscilloscope started to record the pressure surge. Repeated tests were performed for each discharge values (see Table 1).

According to the type of support and material of the pipes, the celerity was also calculated through:

$$c = \sqrt{\frac{K/\rho}{1+\frac{K}{E_0}\frac{D}{e}\alpha}} \tag{1}$$

where α is a constant that depends on the load conditions and type of wall, K the volume compressibility modulus, E_0 is the elasticity modulus of the pipe material, D the internal diameter and e the thickness. The celerity values of each pipe are presented in Table 2.

Table 1: Discharge values tested in the facility.

Flow meter	Q (L/s)		
	Scenario 1	Scenario 2	Scenario 3
Ultrasonic	9.13	1.034	8.28
Conventional	9.35	1.085	8.50
Average	*v* (m/s)		
	Scenario 1	Scenario 2	Scenario 3
	1.034	1.160	0.940

Table 2: Celerity values for each type of pipe and velocity values in each scenario.

Material	D_i (m)	*c* (m/s)
PVC	0.1073	341.65
GI	0.10474	1310.12

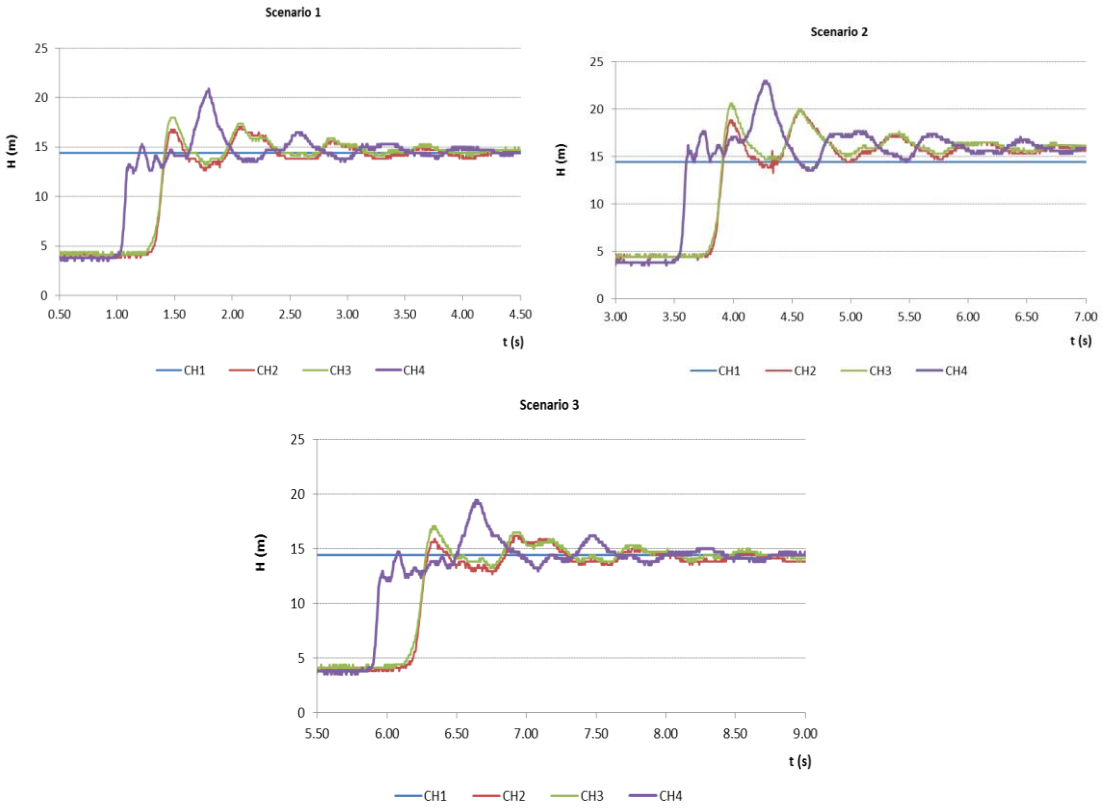

Figure 3: Pressure diagrams obtained from the pressure transducers for each scenario.

For each scenario, pressure diagrams associated to the quickly closure of the butterfly valve, were obtained. Figure 3 shows the diagrams obtained from the 4 pressure transducers. Channel 1 (CH1) represent the upstream transducer, located in GI pipe, CH2 the next transducer, and so on, being CH4 the last transducer located near the butterfly valve. In each scenario, as soon as the butterfly valve is closed, CH4 immediately records the pressure variation, subsequently CH3 starts to record after 0.24 s (time the waves take to cross the pipe length until it reaches the next transducer), followed by CH2 and CH1. A relief wave travels downstream towards the butterfly valve and reaches it at a time $t = T = 2L/c$. A sudden change in pressure occur in CH4, leading to an overpressure after 0.56 s ($T = 2L_T/c$). This over

pressure coincides with the instant that the structure starts to move, immediately after the relief wave reaches the closing valve.

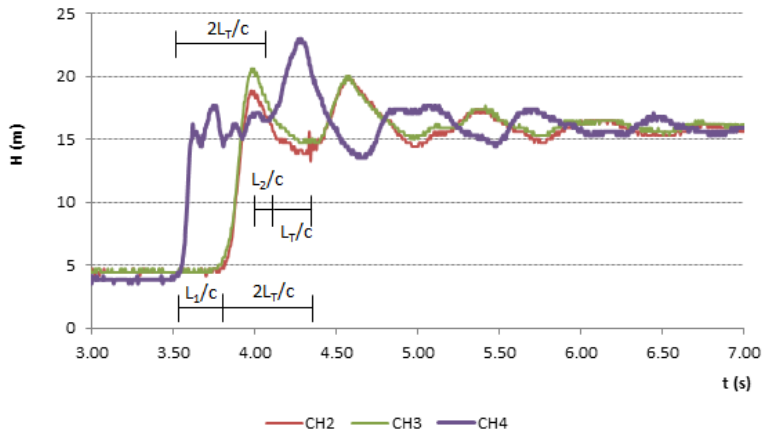

Figure 4: Example of an overpressure obtained in each scenario.

4 COMPUTATIONAL MODELS

After calibrating and studying the flow behaviour, the displacements of the pipes were studied with the use of a CFD model. First the 3D geometry model was introduced, where two types of domains were created, Fluid and Structure. For the fluid flow, the boundary conditions correspond to the tests made "in situ", where upstream the constant pressure inlet obtained in CH1 was introduced and downstream a pressure outlet was set. The pressure outlet corresponds to maximum overpressure achieved in each scenario due to the rapid closing of the butterfly valve. Figure 5 represents the 3D model with the boundary conditions identified in the fluid domain.

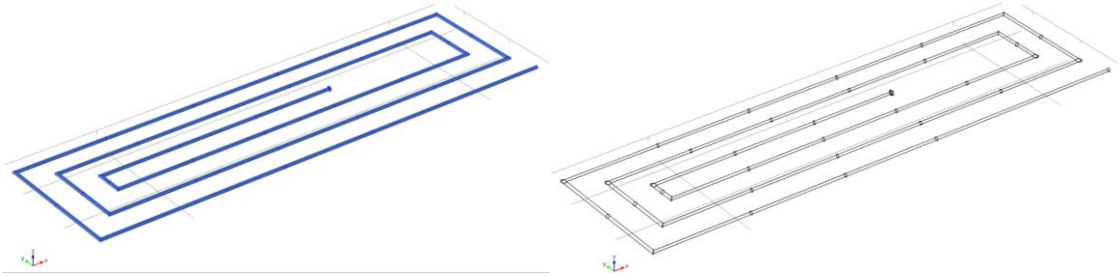

(a) (b)

Figure 5: 3D CFD model: (a) fluid domain; (b) structure domain.

In the structure domain, PVC material was set (Figure 5 b) and the supports of the laboratory facility were introduced, restricting its movements, according to its position.

Regarding the boundary conditions, the solution of fluid-structure interaction means that neither a fluid nor a structural system can be solved independently due to the unknown forces in the interface region [6]. Thus, the solution is based on relations of continuum mean mechanics, solved based on finite element methods. Hence, the results behind the transference of forces and momentums between the fluid and the pipe wall during the occurrence of the unsteady condition crated by the rapidly close of the butterfly valve, in each scenario, are presented in Figure 6.

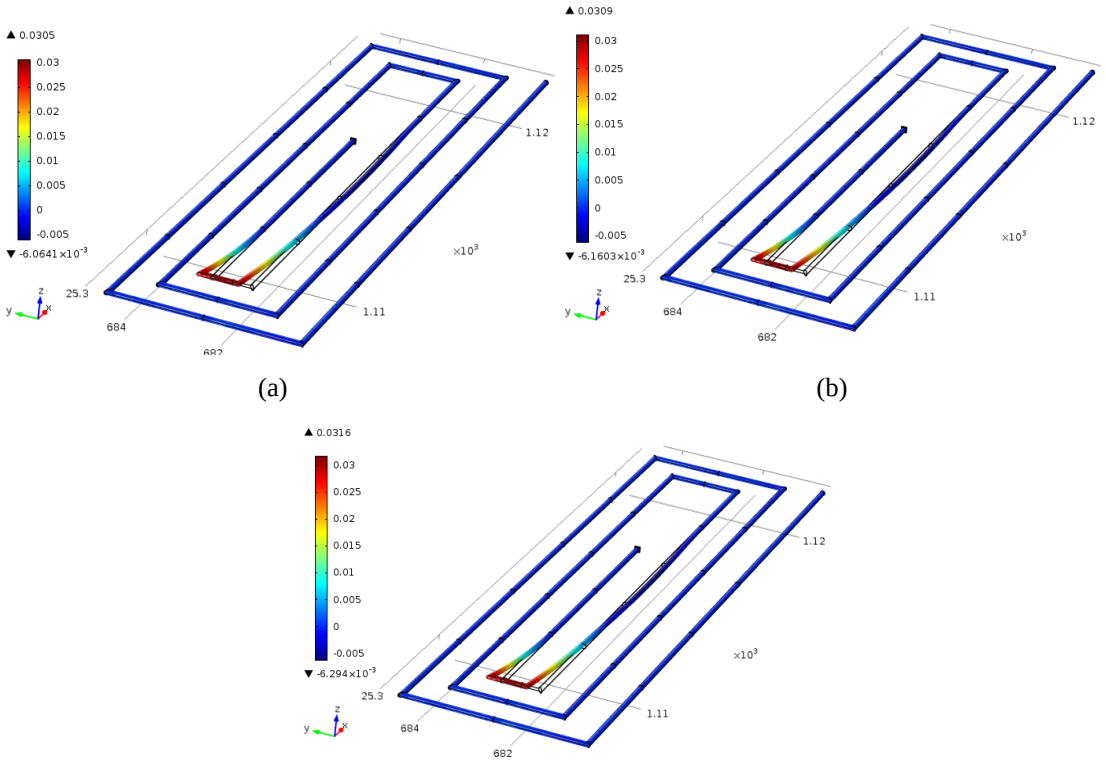

Figure 6: Displacement field in axis-y: (a) scenario 1; (b) scenario 2; (c) scenario 3.

The maximum displacements obtained for each scenario, after the fluid simulation, are associated to the fluid stresses obtained for the last instant. Due to unbalanced interior pressure value in the butterfly valve, the inducing forces responsible for the system's displacement is about 4024 kN, 4615 kN and 3597 kN, in scenario 1, 2, and 3, respectively.

5 CONCLUSIONS

The coupling fluid-structure phenomenon is seen in this ongoing research, as a great approach to describe a fluid-structure interaction case. The hydrodynamic pressure tends to be amplified due to the fluid motion induced by perturbations, which in turn induces some additional structure deformations. Consequently these deformations will also modify the hydrodynamic pressure. Through this work it will be possible to compare the results obtained in the 3D model to those obtained in "situ".

REFERENCES

[1] A Almeida, H Ramos (2010). Water supply operation: diagnosis and reliability analysis in a Lisbon pumping system. *Journal of Water Supply: Research and Technology—AQUA* **59**(1):66–78.

[2] A El-Turki (2013). *Modeling of Hydraulic Transients in Closed Conduits*. MSc thesis, Colorado State University.

[3] PF Boulos, BW Karney, DJ Wood, S Lingireddy (2005). Hydraulic transient guidelines for protecting water distribution systems. *Journal—American Water Works Association* **97**(5):111–124.

[4] ZG Liu, Y Liu, J Lu (2012). Fluid-structure interaction of single flexible cylinder in axial flow. *Computers & Fluid* **56**:143–151.

[5] J Kratz, W Munch, K Ungar (2003). the influence of fluid-structure interaction on pipe system loads. In *Transactions of the 17th International Conference on Structural Mechanics in Reactor Technology* (SMiRT 17). Prague, Czech Republic, August 17–22.

[6] P Moussou, Ph Lafon, S Potapov, L Paulhiac, AS Tijsseling (2004). Industrial cases of FSI due to internal flows. In SJ Murray, Ed., *The Practical Application of Surge Analysis for Design and Operation* (Proceedings of the 9th International Conference on Pressure Surges, Chester, UK, March 24–26, 2004), pp. 167–181, Cranfield, Bedfordshire, BHR Group.

V Conferência Nacional de Mecânica dos Fluidos, Termodinâmica e Energia
MEFTE 2014, 11–12 Setembro 2014, Porto, Portugal
APMTAC, 2014

Sobre a determinação de coeficientes de arrasto de perfis de secções angulosas, isolados ou em grupo, através da Dinâmica de Fluidos Computacional

A Costa, F Paiva, RC Barros

Departmento de Engenharia Civil, Faculdade de Engenharia, Universidade do Porto, Rua Dr. Roberto Frias, 4200-465 Porto, Portugal
email: costa.andreivan@gmail.com, fmp@fe.up.pt, rcb@fe.up.pt

RESUMO: Os perfis de secção angulosa são cada vez mais utilizados em estruturas de grande altura, como torres de telecomunicação, linhas de transporte de energia e eólicas. Assim, o presente trabalho, realizado, teve por base o estudo aerodinâmico deste tipo de perfis onde se estudaram três tipos de disposição dos mesmos. Realizaram-se análises CFD (Computational Fluid Dynamics) para o estudo aerodinâmico, onde se obteve os coeficientes de arrasto gerados para as várias disposições dos perfis em função dos modelos de turbulência RANS K-ε (Reynolds Averaged Navier-Stokes), comparando-os posteriormente com o Eurocódigo EN1991-1-4, norma Britânica e ensaios experimentais de outros trabalhos. Os ensaios foram realizados através do software ANSYS FLUENT e teve como base uma simulação 2D.

PALAVRAS-CHAVE: Coeficientes de arrasto; CFD; Aerodinâmica; Cantoneiras; Eurocódigo.

1 INTRODUÇÃO

A dinâmica de fluidos computacional, geralmente denominada como CFD, é a análise de sistemas envolvendo fluxo de fluidos, transferência de calor e fenómenos associados, tais como reações químicas por meio de simulação por computador [1].

Os aspetos físicos de qualquer fluxo de fluido são regidos por três princípios fundamentais e uma Equação Matemática:

- Princípio da Conservação da Massa;
- Princípio da Conservação da Quantidade de Movimento;
- Equação de estado do fluido;
- Princípio da conservação da energia.

Num grande número de aplicações é possível simplificar os problemas de dinâmica dos fluidos. Nos casos em a velocidade do escoamento sejam muito inferiores a Mach 1, razão entre a velocidade de escoamento e a velocidade do som, mais precisamente inferiores a 0.3, segundo [2], e visto ser o caso em estudo, então podemos considerar que o fluido é incompressível, logo não tem interesse a consideração da temperatura. Assim sendo, passam a ser três os princípios que regem o fluxo do fluido:

- Princípio da Conservação da Massa;
- Princípio da Conservação da Quantidade de Movimento;
- Princípio da conservação da energia.

As equações correspondentes aos princípios apresentados foram discretizadas aplicando o método de volumes finitos.

1.1 Equações de Navier-Stokes

Estes princípios fundamentais podem ser expressos em termos de equações matemáticas, que geralmente tem a forma de equações diferencias parciais [3]. No caso das equações de equilíbrio dinâmico, as equações que vamos estudar são as equações de Navier-Stokes:

$$\frac{\partial u}{\partial t}+u\frac{\partial u}{\partial x}+v\frac{\partial u}{\partial y}+w\frac{\partial u}{\partial z}=-\frac{1}{\rho}\frac{\partial p}{\partial x}+\frac{\mu}{\rho}\left(\frac{\partial^2 u}{\partial x^2}+\frac{\partial^2 u}{\partial y^2}+\frac{\partial^2 u}{\partial z^2}\right) \quad (1)$$

$$\frac{\partial v}{\partial t}+u\frac{\partial v}{\partial x}+v\frac{\partial v}{\partial y}+w\frac{\partial v}{\partial z}=-\frac{1}{\rho}\frac{\partial p}{\partial y}+\frac{\mu}{\rho}\left(\frac{\partial^2 v}{\partial x^2}+\frac{\partial^2 v}{\partial y^2}+\frac{\partial^2 v}{\partial z^2}\right) \quad (2)$$

$$\frac{\partial w}{\partial t}+u\frac{\partial w}{\partial x}+v\frac{\partial w}{\partial y}+w\frac{\partial w}{\partial z}=-\frac{1}{\rho}\frac{\partial p}{\partial z}+\frac{\mu}{\rho}\left(\frac{\partial^2 w}{\partial x^2}+\frac{\partial^2 w}{\partial y^2}+\frac{\partial^2 w}{\partial z^2}\right) \tag{3}$$

Aqui assumimos: que é um fluido newtoniano, ou seja, é um fluido em que cada componente a tensão de corte é proporcional ao gradiente de velocidade na direção normal a essa componente, como é o caso da água e do ar; a viscosidade, μ, é constante; e a componente da força gravítica, peso próprio, foi incorporada dentro da pressão, p, na direção correspondente [4].

1.2 Modelos de turbulência RANS

O modelo que vamos abordar é um modelo baseado na metodologia $k-\varepsilon$, modelo que será usado nas modelações do próximo capítulo, que pertence à classe de modelos com duas equações, designado por RANS (Reynolds Averaged Navier-Stokes). É uma modelo que resolve as equações de Navier-Stokes de uma forma estatística e é baseado nas equações de transporte para a energia cinética, k, e taxa de dissipação, ε, da turbulência e é usado para praticamente todos os casos de escoamentos, por ser robusto, de relativa rapidez de resolução e precisão em casos com uma grande variação do número de Reynolds. Foram testados os modelos de turbulência $k-\varepsilon$ Standard, $k-\varepsilon$ RNG e $k-\varepsilon$ Realizable.

2 ESTUDO DO ESCOAMENTO EM TORNO DE PERFIS DE SECÇÃO ANGULOSA

De forma a simular o escoamento do fluido em torno das secções, deverá ser criado um género de túnel de vento em redor da secção, designado por domínio de integração. As dimensões usadas são em função do comprimento das abas da secção e foram determinadas com base em vários ensaios realizados onde se observou a influência da interação dos limites de integração nos resultados finais. As mesmas dimensões também se verificaram ser suficientes para que se pudesse observar todos os fenómenos do escoamento em torno da secção. Com isto as dimensões usadas relativas ao afastamento superior e inferior da secção são de três vezes o comprimento da aba e relativas ao afastamento lateral esquerdo e direito são de cinco vezes o comprimento da aba. A secção encontra-se centrada com o domínio de integração. Na Figura 1 é apresentada a secção usada e com as dimensões de $b=h=100$ mm, $r_1=12$ mm, $r_2=6$ mm e $t=10$ mm.

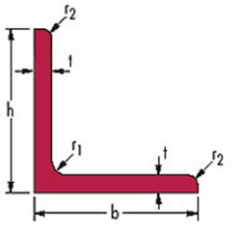

Figura 1: Cantoneira em estudo.

A malha foi gerada automaticamente no ANSYS Meshing com base no modelo de geração de malha para CFD e adaptada para ser analisada no ANSYS Fluent. Posteriormente à sua geração observou-se a geometria dos elementos da malha na proximidade da secção e nos limites do domínio e procedeu-se à alteração e aplicação de metodologias na geração da malha de forma a obter-se uma malha com melhor qualidade e assim fornecer resultados mais próximos da realidade.

2.1 Escoamento em torno de uma secção angulosa isolada

A primeira disposição estudada, foi a secção isolada onde se realizaram ensaios para três ângulos de incidência, 0º, 45º e −180º (ver Figura 2).

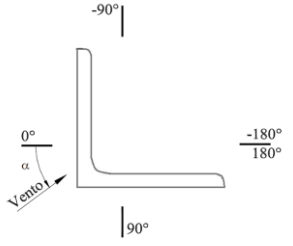

Figura 2: Convenção do sistema de eixos e ângulos de incidência do vento.

Realizados os ensaios, como podem ser vistos os resultados na Tabela 1, verificou-se que para os vários modelos de turbulência o valor do coeficiente de arrasto não se altera, com isto, verificamos que para este caso em estudo os modelos de turbulência não influenciam a precisão dos resultados. Ainda assim é de salientar que na análise no Ansys Fluent, este desaconselha a utilização do modelo Standard para o estudo do escoamento, apresentando uma mensagem de erro, solicitando a substituição do modelo de turbulência Standard para Realizable.

Tabela 1: Coeficientes de arrasto.

	C_D (para diferentes ângulos de incidência)		
Modelo de Turbulência	0º	45º	180º
Standard	2.04	1.55	2.04
RNG	2.04	1.55	2.04
Realizable	2.04	1.55	2.04

A análise comparativa dos resultados teve por base a EN 1991-1-4 [5], a norma Britânica (BS) [6] e resultados experimentais [7]. Analisando a Tabela 2, verificamos que a simulação CFD pelo Ansys Fluent apresenta resultados muito próximos das normas EN 1991-1-4 e Britânica (BS), sendo a EN 1991-1-4, mais conservativa que a norma Britânica (BS), para as direções de 0º e 180º. Relativamente aos resultados obtidos pelos ensaios experimentais, verifica-se que a simulação CFD apresenta valores ligeiramente superiores, esta diferença poderá ser justificada pelas condições de fronteiras adotadas na análise CFD.

Tabela 2: Comparação dos coeficientes de arrasto.

	C_D (para diferentes ângulos de incidência)		
	0º	45º	180º
EN 1991-1-4	2.10	-	2.10
Norma Britânica (BS)	2.00	1.40	1.80
Ensaios Experimentais	1.80	1.47	1.39
Simulação CFD	2.04	1.55	2.04

De forma a perceber como se realiza o escoamento em torno na secção, observando os locais onde se criam as pressões negativas e os locais onde as pressões são máximas, na Figura 3 apresenta-se as linhas de correntes obtidas da análise CFD, pelo Ansys Fluent, para os vários ângulos de incidência estudados e em função da velocidade do escoamento em m/s.

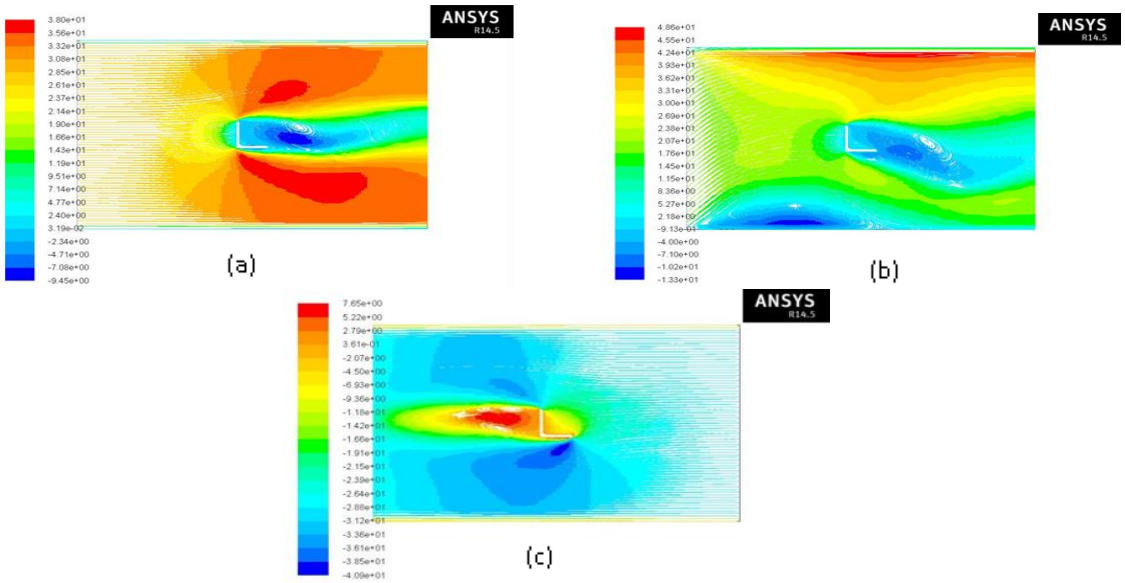

Figura 3: Escoamento ao redor da secção para os ângulos de incidências 0º, 45º e −180º correspondendo a (a), (b) e (c) respectivamente.

2.2 Estudo da interação entre duas secções angulosas

Neste estudo analisou-se o efeito de sombreamento que uma secção provoca sobre uma outra que se encontra no mesmo plano e será determinada a distância em que esse efeito deixa de existir, tal como representado na Figura 4. Para cada distância estudada será ainda determinado o coeficiente de arrasto que se gera.

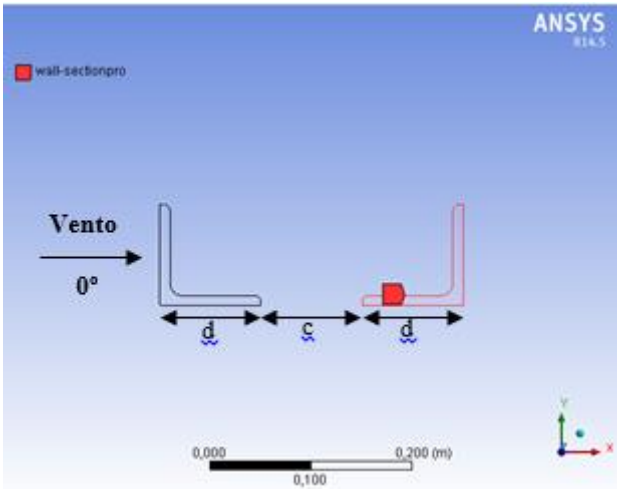

Figura 4: Indicação da secção protegida e do angulo incidência do vento.

O estudo foi iniciado para uma distância entre secções, c, igual ao comprimento da aba da secção, d. À medida que o valor do afastamento (c/d) entre as secções aumenta, é esperado que o efeito de sombreamento diminua, tendendo para um valor do coeficiente de arrasto como se o perfil estivesse isolado. Existe um determinado afastamento para o qual o coeficiente de arrasto do perfil protegido será igual ao de um perfil isolado. Assim, sendo este estudo iterativo finaliza a quando da igualdade de coeficientes de arrasto. O escoamento foi realizado para os vários modelos de turbulência $k-\varepsilon$. Na Tabela 3 apresentam-se os coeficientes de arrasto gerados em função da distância entre secções e para cada modelo de turbulência.

Tabela 3: Coeficientes de arrasto em função do factor (c/d).

	C_D (para diferentes modelos de turbulência)		
c/d	Standard	RNG	Realizable
1	1.73	1.73	1.73
2	1.86	1.86	1.86
4	1.87	1.87	1.87
6	1.87	1.87	1.87
8	1.79	1.79	1.79
10	1.84	1.84	1.84
12	1.97	1.97	1.97

Como já tinha sido concluído no escoamento em torno da secção isolada, a não influencia dos modelos de turbulência nos resultados obtidos, voltou-se a ser verificada neste estudo de interação.

Analisando a Tabela 3, verifica-se que, para uma distância doze vezes superior à distância da aba da secção, existe uma redução do coeficiente de arrasto de aproximadamente 4% em relação ao modelo isolado, valor para a qual assume-se que o efeito de sombra deixa de existir. Salienta-se ainda, que o valor máximo de redução do coeficiente de arrasto atingiu aproximadamente os 18%.

Estudos realizados, sobre a interação de secções no mesmo plano [7], com a mesma orientação das secções apresentada neste estudo, verificaram-se haver reduções máximas no coeficiente de arrasto na ordem dos 25%, diminuindo com o aumento do afastamento. Verificou-se ainda que, para distâncias entre $c/d=10$ e $c/d=15$, o perfil protegido atingia o valor para o coeficiente de arrasto como se a secção se encontra-se isolada, valor, este, que foi verificado na análise CFD pelo Ansys Fluent. Na Figura 5, apresenta-se a evolução das linhas de corrente para $c/d=1$, $c/d=4$, $c/d=8$ e $c/d=12$, os valores estão em m/s.

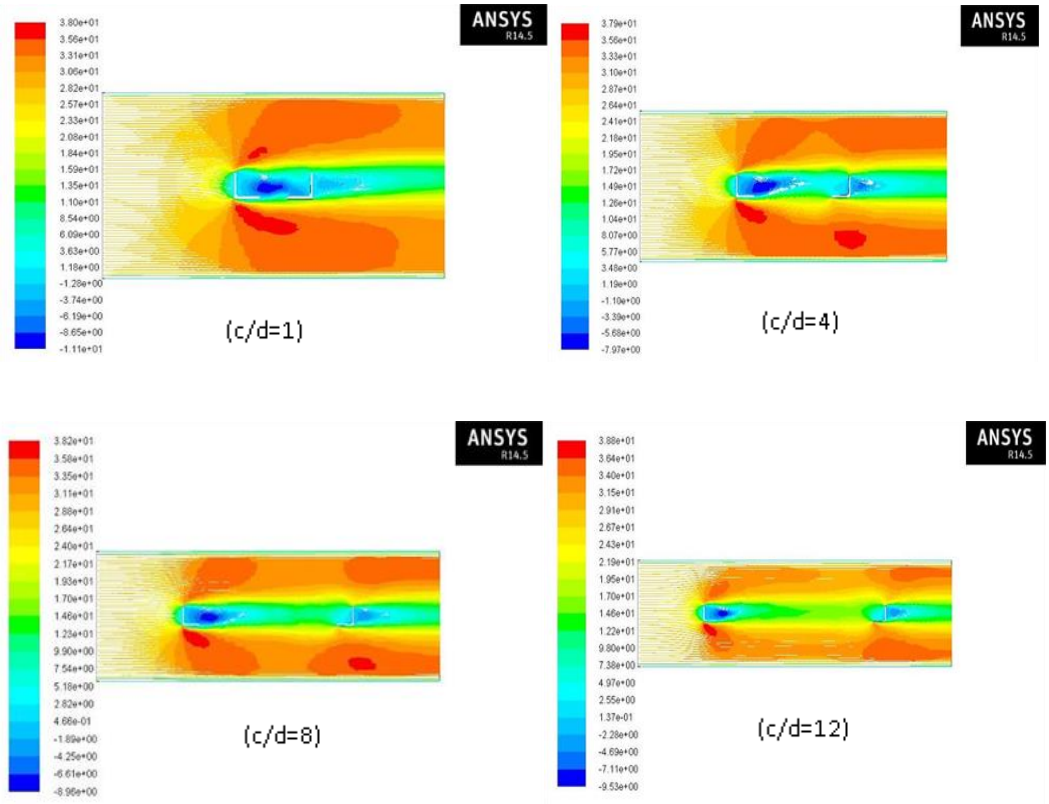

Figura 5: Escoamento ao redor das cantoneiras na direcção 0° em função de c/d .

3 ESCOAMENTO EM TORNO DE UMA ESTRUTURA TRELIÇADA ESPACIAL

Nesta secção será estudado o escoamento em torno de uma estrutura treliçada espacial, onde simula-se a base de uma torre treliçada quadrada através de quadro secções angulosas. De modo a simplificar o caso em estudo, serão apenas modeladas as secções principais da estrutura, sem os elementos de contraventamento como podemos ver na Figura 6. O afastamento entre as secções será fixo, não analisando o efeito de interação. Este estudo resultará na determinação do coeficiente de arrasto, gerado para o angulo de incidência de 0º, que posteriormente será comparado com o determinado pela norma EN 1991-1-4 [5].

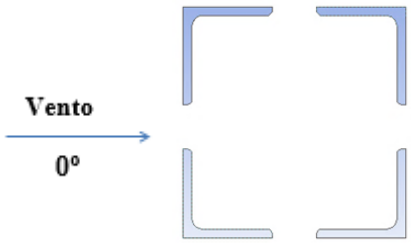

Figura 6: Disposição das cantoneiras.

Realizada a simulação, apresenta-se na Tabela 4 os coeficientes de arrasto obtidos em função dos modelos de turbulência.

Tabela 4: Coeficientes de arrasto em função dos modelos de turbulência.

Modelo de Turbulência	C_D (0º)
Standard	3.94
RNG	3.94
Realizable	3.94

Mais uma vez, analisando os resultados obtidos, verifica-se que os modelos de turbulência, não influenciam os resultados finais.

O objeto de comparação neste estudo foi a EN 1991-1-4 [5] onde se obteve um coeficiente de arrasto de 2.7, cerca de 45% superior ao obtido pela análise CFD. Para este caso em estudo, verificou-se que analise CFD gerou resultados acima do esperado, esta diferença pode ser justificada pela sensibilidade da análise com os efeitos causados de interação entre as secções e pelas recirculações internas a elas inerentes, como ilustrado na Figura 7. Este tipo de fenómenos provocam um efeito de válvula aumentando assim a força gerada pela ação do vento e consequentemente o coeficiente de arrasto.

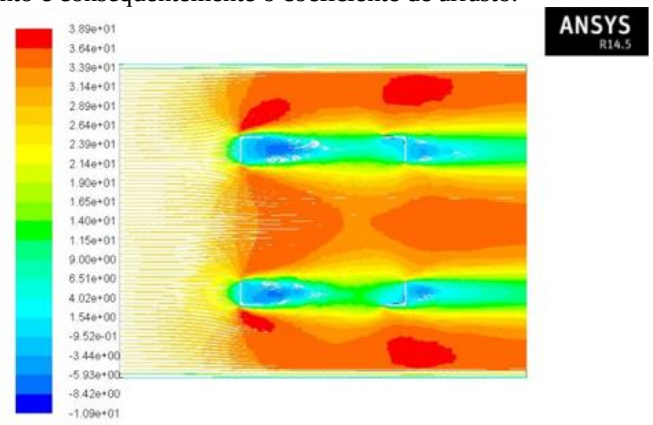

Figura 7: Linhas de corrente ao redor das secções.

4 CONCLUSÕES

Como conclusão deste trabalho pode-se afirmar que a análise CFD pelo Ansys Fluent se mostrou importante na análise dos escoamento, apresentando linhas de corrente de elevada precisão, podendo se observar os vários fenómenos que ocorrem nas zonas contiguas das secções e assim localizar os "HotSpots", locais onde se geram elevadas pressões. Este estudo relevou-se ainda eficaz na determinação dos coeficientes de arrasto gerados, à exceção no caso do estudo de uma estrutura treliçada espacial.

AGRADECIMENTOS

Este trabalho foi apoiado por fundos do projecto VHSSPOLES-Very High Strength Steel Poles (Faculdade de Engenharia da Universidade do Porto, referência 21518) patrocinado pelo Fundo Europeu de Desenvolvimento Regional (FEDER) através do COMPETE (Programa Operacional Factores de Competitividade). Os autores agradecem o apoio financeiro e a oportunidade de contribuir para o desenvolvimento do banco de ensaios da Metalogalva (Trofa, Portugal).

REFERÊNCIAS

[1] HK Versteeg, W Malalasekera (2007). *An Introduction to Computational Fluid Dynamics: The Finite Volume Method*, 2nd edition, Pearson Education, England.

[2] JH Ferziger, M Peric (2002). *Computational Methods for Fluid Dynamics*, 3rd Edition, Springer, Berlim, Germany.

[3] J Novais-Barbosa (1986). *Mecânica de Fluidos e Hidráulica Geral*, Vol. 1, Porto Editora, Porto, Portugal.

[4] MB Abbott, DR Basco (1989). *Computational Fluid Dynamics: An Introduction for Engineers*, Longman Scientific and Technical.

[5] NP EN 1991-1-4:2010/A1 (2010). *Eurocódigo 1 – Acções em Estruturas Parte 1-4 Acções Gerais. Acção do Vento*, 3ª edição, IPQ, Caparica, Portugal.

[6] British Standard CP3:Chapter V-2 (1972). *Code of Basic Data for the Design of Buildings, Loading, Wind Loads*, BSI, England.

[7] T Klein (2004). *Estudo em Túnel de Vento das Características Aerodinâmicas de Torres Metálicas Treliçadas*, Tese de Mestrado, Universidade Federal do Rio Grande do Sul, Brasil.

Session 6

Chairman

António Manuel Gameiro Lopes | U.Coimbra

This page was intentionally left blank

V Conferência Nacional de Mecânica dos Fluidos, Termodinâmica e Energia
MEFTE 2014, 11–12 Setembro 2014, Porto, Portugal
APMTAC, 2014

Improvement of the energy distribution in isotropic turbulent viscoelastic fluid models

PR Resende[1], FT Pinho[2], PJ Oliveira[3]

[1]Grupo de Automação e Sistemas Integráveis, UNESP - Univ. Estadual Paulista, 18087-180, Sorocaba - SP, Brazil
[2]Centro de Estudos de Fenómenos de Transporte, Departamento de Engenharia Mecânica, Faculdade de Engenharia Universidade do Porto, Rua Dr. Roberto Frias s/n, 4200-465 Porto, Portugal
[3]Departamento de Engenharia Electromecânica, Universidade da Beira Interior, Rua Marques D'Avila e Bolama, 6201-001 Covilhã, Portugal
email: resende@sorocaba.unesp.br, fpinho@fe.up.pt, pjpo@ubi.pt

ABSTRACT: Strong anisotropy effects in turbulent viscoelastic fluids flows limits the use of isotropic turbulent closures, for example the *k*-ε and *k*-ω turbulent model types. Existing viscoelastic models based on the Boussinesq hypothesis fail to predict correctly the turbulent kinetic energy behaviour for the various drag reduction (DR) regimes, and in particular at high drag reduction. To address this limitation and in particular to improve the near-wall distribution of the turbulent kinetic energy (TKE) a different closure, based on the fluid relaxation time, has been developed for the Reynolds stress tensor. With the new model the TKE is better predicted close to the wall, where the viscoelastic fluids have more impact, and this improves also the TKE distribution away from the wall. The different contributions to the transport equation of TKE are analyzed, showing the impact of the new model, and the effect of drag reduction increase on the distribution is investigated in detail.

KEY-WORDS: Viscoelastic fluids; Turbulence; Isotropic models; Energy distribution.

1 INTRODUCTION

The increased availability of powerful computational resources has fostered research on Direct Numeric Simulation (DNS) of viscoelastic pipe and channel flows, [1-4]. This has allowed an increased understanding of turbulence of viscoelastic solutions as well as the analysis of time-averaged quantities of the governing equations that have helped the development of adequate turbulence closures for the various drag reduction regimes.

The first viscoelastic turbulence models developed for viscoelastic fluids following this type of approach were by Pinho et al. [5] and Resende et al. [6]. They relied on several viscoelastic closures in the context of isotropic turbulent models leading originally to a *k*-ε type turbulence model. Those models were able to capture with good accuracy the flow characteristics in the low and intermediate regimes of DR, but the Boussinesq hypothesis becomes increasingly difficult to justify as DR increases because of the increasingly strong turbulence anisotropy. Hence, the previous models were not able to predict correctly the turbulent kinetic energy at high drag reductions and for this reason a new model for the Reynolds stress tensor is here developed that attempts to address those limitations. In section 2 the governing equations and model are presented, its performance is discussed in section 3 and the conclusions summarize the main findings.

2 GOVERNING EQUATIONS

The governing equations for turbulent flows of viscoelastic fluids using the Finitely Extensive Nonlinear Elastic constitutive equation with the Peterlin approximation (FENE-P) in the context of Reynolds-averaged quantities are the Reynolds-averaged continuity equation, momentum equation and a Reynolds-averaged evolution equation for the conformation tensor together with an expression relating the conformation tensor with the polymer stress tensor. The momentum equation is giving by

$$\rho\frac{\partial U_i}{\partial t}+\rho U_k\frac{\partial U_i}{\partial x_k}=-\frac{\partial \overline{p}}{\partial x_i}+\eta_s\frac{\partial^2 U_i}{\partial x_k\partial x_k}-\frac{\partial}{\partial x_k}\left(\rho\overline{u_i u_k}\right)+\frac{\partial \overline{\tau}_{ik,p}}{\partial x_k} \tag{1}$$

where U is the mean velocity, $\overline{p}$ is the mean pressure, ρ is the fluid density, η_s is the solvent viscosity, $\overline{\tau}_{ik,p}$ is the Reynolds-averaged polymer stress and $-\rho\overline{u_i u_k}$ is the Reynolds stress tensor. Uppercase letters and overbars denote Reynolds-averaged quantities, whereas lowercase letters and primes denote fluctuations.

The Reynolds-averaged polymer stress $\overline{\tau}_{ij,p}$ is based on the FENE-P model and is defined by the following equation

$$\overline{\tau}_{ij,p} = \frac{\eta_p}{\lambda}\left[f\left(C_{kk}\right)C_{ij} - f\left(L\right)\delta_{ij} \right] + \frac{\eta_p}{\lambda}\overline{f\left(C_{kk}+c_{kk}\right)c_{ij}} \tag{2}$$

where η_p and λ are the polymer viscosity coefficient and the relaxation time of the fluid, respectively. The two functions are based on L^2, the maximum dimensionless extensibility of the model dumbbell, and are given by

$$f\left(C_{kk}\right) = \frac{L^2-3}{L^2-C_{kk}} \text{ and } f\left(L\right)=1 \tag{3}$$

The Reynolds-averaged equation describing the evolution of conformation tensor (C_{ij}) is subsequently combined with Eq. (2) to give Eq. (4), where the first-term inside the brackets on the left-hand-side is Oldroyd's upper convective derivative of C_{ij}. The various terms of Eq. (4) have specific designations given below the horizontal brackets.

$$\left[\underbrace{\frac{\partial C_{ij}}{\partial t} + U_k\frac{\partial C_{ij}}{\partial x_k}}_{DC_{ij}/Dt} - \underbrace{\left(C_{jk}\frac{\partial U_i}{\partial x_k} + C_{ik}\frac{\partial U_j}{\partial x_k} \right)}_{M_{ij}} \right] + \underbrace{\overline{u_k\frac{\partial c_{ij}}{\partial x_k}}}_{CT_{ij}} - \underbrace{\left(\overline{c_{kj}\frac{\partial u_i}{\partial x_k}} + \overline{c_{ik}\frac{\partial u_j}{\partial x_k}} \right)}_{NLT_{ij}} = -\frac{\overline{\tau}_{ij,p}}{\eta_p} \tag{4}$$

The NLT_{ij} term is calculated using the closure developed by Resende et al. [6], given by Eq. (5), and the contribution of CT_{ij} is neglected as previously suggested by DNS data analysis, cf. Li et al. [3].

$$\begin{aligned} NLT_{ij} \equiv{}& \overline{c_{kj}\frac{\partial u_i}{\partial x_k}} + \overline{c_{ik}\frac{\partial u_j}{\partial x_k}} \approx C_{F1}\left[0.055\left(\frac{We_{\tau 0}}{25}\right)^{1.07} + 0.116 \right]\times\frac{C_{ij}\times f(C_{mm})}{\lambda} + \\ &+\frac{\lambda}{f(C_{mm})}\left[C_{F3}\times\left(\frac{25}{We_{\tau 0}}\right)^{0.55}\times\left(\begin{array}{l} \dfrac{\partial U_j}{\partial x_n}\dfrac{\partial U_m}{\partial x_k}C_{kn}\dfrac{\overline{u_i u_m}}{\nu_0\sqrt{2S_{pq}S_{pq}}} + \dfrac{\partial U_i}{\partial x_n}\dfrac{\partial U_m}{\partial x_k}C_{kn}\dfrac{\overline{u_j u_m}}{\nu_0\sqrt{2S_{pq}S_{pq}}} + \\ \dfrac{\partial U_k}{\partial x_n}\dfrac{\partial U_m}{\partial x_k}\left(C_{jn}\dfrac{\overline{u_i u_m}}{\nu_0\sqrt{2S_{pq}S_{pq}}} + C_{in}\dfrac{\overline{u_j u_m}}{\nu_0\sqrt{2S_{pq}S_{pq}}} \right) \end{array} \right) \right] - \\ &-\frac{\lambda}{f(C_{mm})}\times f_{F1}\times C_{F4}\times\left(\frac{25}{We_{\tau 0}}\right)^{0.55}\times\left[C_{jn}\frac{\partial U_k}{\partial x_n}\frac{\partial U_i}{\partial x_k} + C_{in}\frac{\partial U_k}{\partial x_n}\frac{\partial U_j}{\partial x_k} + C_{kn}\frac{\partial U_j}{\partial x_n}\frac{\partial U_i}{\partial x_k} + C_{kn}\frac{\partial U_i}{\partial x_n}\frac{\partial U_j}{\partial x_k} \right] + \\ &+\frac{\lambda}{f(C_{mm})}\left[\frac{C_{\varepsilon_F}}{We_{\tau 0}}\frac{4}{15}\times\frac{\varepsilon^N}{\left(\nu_s+\nu_{\tau_P}\right)}C_{mm}\times f_{F2}\times\delta_{ij} \right] - C_{F2}We_{\tau 0}^{\,0.74}\left[C_{kj}\frac{\partial U_i}{\partial x_k} + C_{ik}\frac{\partial U_j}{\partial x_k} \right] \end{aligned} \tag{5}$$

In Eq. (5) $We_{\tau 0}$ is the Weissenberg number, defined as $We_{\tau 0} = \lambda u_\tau^{\,2}/\nu_0$ based on the friction velocity, u_τ, and on the total zero shear-rate kinematic viscosity, i.e., the sum of the kinematic viscosities of the solvent and polymer, $\nu_0 = \nu_s + \nu_p$, k and ε^N are the turbulent kinetic energy and the rate of dissipation, respectively, and S_{ij} is the rate of deformation tensor, $S_{ij} = \left(\partial U_i/\partial x_j + \partial U_j/\partial x_i\right)/2$.

The Reynolds stress in Eq. (1) is modeled by the Boussinesq hypothesis through the following equation,

$$-\rho\overline{u_i u_j} = 2\rho\left(\nu_T + \nu_T^{\,p^*}\right)S_{ij} - \frac{2}{3}\rho k\delta_{ij} \tag{6}$$

where ν_T is the turbulent viscosity and $\nu_T^{\,p^*}$ is the extra polymeric turbulent viscosity, respectively. The turbulent viscosity, defined by Eq. (7), was developed by Resende et al. [6] considering both Newtonian and non-Newtonian contributions given in Eqs. (8).

$$\nu_T = \nu_T^{\,N} - \nu_T^{\,P} \tag{7}$$

$$\nu_T{}^N = C_\mu \times f_\mu \times \frac{k^2}{\varepsilon^N} \text{ and } \nu_T{}^P = C_\mu{}^P \times f_{DR}{}^p \times \left(\frac{C_{mm}}{L^2}\right)^{0.25} \times \frac{k^2}{\varepsilon^N} \tag{8}$$

The closures for the turbulent viscosities involve the damping function f_μ defined by $f_\mu = \left[1-\exp\left(-y^+/26.5\right)\right]^2$, and the coefficient C_μ equal to 0.09. To incorporate drag reduction effects upon the turbulent viscosity the damping function $f_{DR}{}^p$ and the coefficient $C_\mu{}^P$ were introduced,

$$\nu_T = C_\mu \times f_\mu \times \frac{k^2}{\tilde{\varepsilon}^N}\left(1 - C_\mu{}^P \times f_{DR}{}^P \times \left(\frac{C_{mm}}{L^2}\right)^{0.25}\right) \tag{9}$$

with $f_{DR}{}^P = \left[1-\exp\left(-We_{\tau 0}/6.25\right)\right]^4$ and $C_\mu{}^P = 0.962$.

The main purpose of the extra polymeric turbulent viscosity, shown in Eq. (6), is to correct the balance of energy especially in the production term, P_k, next to the wall. The closure was developed following the ideas of Iaccarino et al. [7], and is given by

$$\nu_T{}^{p*} = 0.8\left(\frac{25}{We_{\tau 0}}\right)\frac{\lambda k}{C_{mm}} \tag{10}$$

Without the extra polymeric turbulent viscosity the turbulent kinetic energy (k) would vary in inverse proportion to the drag reduction as in previous models [6, 8] and in contrast to the correct behavior [9, 10]. The inclusion of this new quantity makes turbulent kinetic energy to increase with DR, as it should. Figure 1 compares the prediction (solid lines) of the production of k, P_k, with the results of DNS simulations (symbols) at DR=18% and 37%, corresponding to low and intermediate DR, respectively. The new model clearly improves on the predictions of the previous model, also included as dashed lines, especially close to the wall (y^+<20). The peak value of P_k is predicted to within 10% and its location is also well predicted, for both drag reductions.

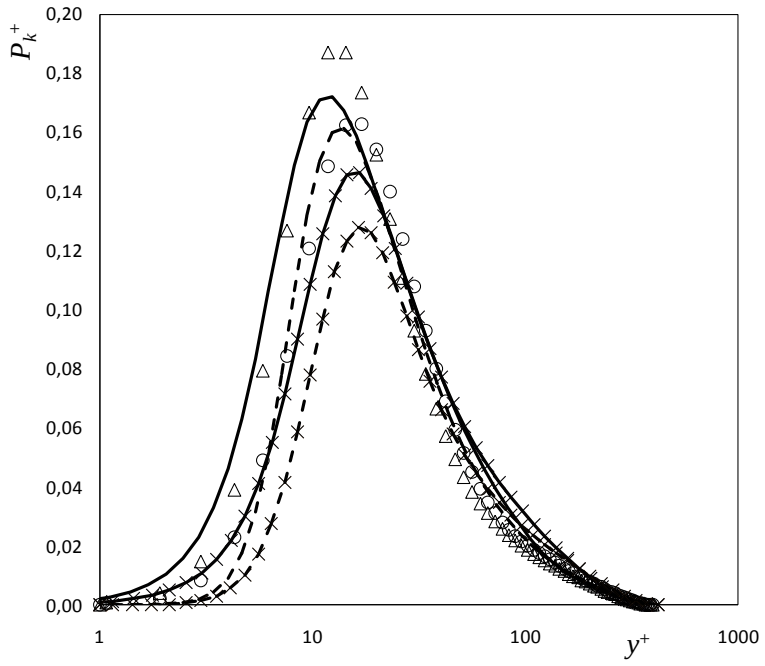

Figure 1: Comparison between DNS data (symbol: Δ DR=18%; ○ DR=37%) and predictions of the production term, P_k, with (continuum lines: — DR=18%; ⋇ DR=37%) and without (dash lines: — — DR=18%; —×— DR=37%) the extra polymeric turbulent viscosity, Eq. (10).

The closure for the Reynolds stress tensor requires the two remaining transport equations, one for the turbulent kinetic energy and the other for its rate of dissipation given by Eqs. (11) and (12), respectively

$$\frac{\partial \rho k}{\partial t}+\frac{\partial \rho U_i k}{\partial x_i}=\frac{\partial}{\partial x_i}\left[\left(\eta_s+\frac{\rho f_T \nu_T}{\sigma_k}\right)\frac{\partial k}{\partial x_i}\right]+P_k-\rho\tilde{\varepsilon}^N-\rho D+Q^V-\rho\varepsilon^V \tag{11}$$

$$\frac{\partial \rho \tilde{\varepsilon}^N}{\partial t}+\frac{\partial \rho U_i \tilde{\varepsilon}^N}{\partial x_i}=\frac{\partial}{\partial x_i}\left[\left(\eta_s+\frac{\rho f_T \nu_T}{\sigma_\varepsilon}\right)\frac{\partial \tilde{\varepsilon}^N}{\partial x_i}\right]+f_1 C_{\varepsilon_1}\frac{\tilde{\varepsilon}^N}{k}P_k-f_2 C_{\varepsilon_2}\rho\frac{\tilde{\varepsilon}^{N^2}}{k}+\rho E+E_{\tau_p} \tag{12}$$

where the turbulence production is $P_k=-\rho\overline{u_i u_j}\partial U_i/\partial x_j$, and Q^V and ε^V are viscoelastic terms in the equation for *k* representing the viscoelastic turbulent transport (Eq. (13)) and the viscoelastic dissipation (Eq. (14)). The second transport equation is actually for the modified rate of dissipation, $\tilde{\varepsilon}^N$, which is related to the true rate of dissipation through $\varepsilon^N=\tilde{\varepsilon}^N+D$, where term *D* is given by Eq. (16), which also contains a viscoelastic contribution by $\nu_{\tau_p}=\tau_{12}{}^P/\left(\partial U/\partial y\right)$. The transport equation for the modified rate of dissipation includes also a viscoelastic destruction term denoted E_{τ_p} and modelled in Eq. (15)).

$$Q^V\equiv\frac{\partial\overline{\tau'_{ik,p}u_i}}{\partial x_k}\approx\frac{\eta_p}{\lambda}\frac{\partial}{\partial x_k}\left[f\left(C_{mm}\right)\left(\frac{C_{ik}FU_i+CU_{iik}}{2}\right)\right] \tag{13}$$

$$\varepsilon^V\equiv\frac{1}{\rho}\overline{\tau'_{ik,p}\frac{\partial u_i}{\partial x_k}}\approx 1.37\times f_{DR}{}^p\frac{\eta_p}{\rho\lambda}f(C_{mm})\frac{NLT_{mm}}{2} \tag{14}$$

$$E_{\tau_p}\approx -f_5\times f_{DR}\times\frac{\tilde{\varepsilon}^{N2}}{k}\left[C_{\varepsilon F1}\times\frac{\varepsilon^V}{\tilde{\varepsilon}^N}+C_{\varepsilon F2}\times\left(\frac{25}{We_{\tau 0}}\right)^{2.1}\times\left(\frac{C_{mm}\times f\left(C_{mm}\right)}{L^2-3}\right)^2\right] \tag{15}$$

$$D=2\left(\nu_s+\nu_{\tau p}\right)\left(\frac{d\sqrt{k}}{dy}\right)^2 \tag{16}$$

$$E=\nu_s\nu_T\left(1-f_\mu\right)\left(\frac{\partial^2 U_i}{\partial y\partial y}\right)^2 \tag{17}$$

$$CU_{ijk}=-C_{\beta 1}\sqrt{\frac{25}{We_{\tau 0}}}\frac{\lambda}{f\left(C_{mm}\right)}\left(\overline{u_i u_m}\frac{\partial C_{kj}}{\partial x_m}+\overline{u_j u_m}\frac{\partial C_{ik}}{\partial x_m}\right)-C_{\beta 2}\left(\frac{We_{\tau 0}}{25}\right)^{1.661}\left[\pm\sqrt{\overline{u_j^2}}C_{ik}\pm\sqrt{\overline{u_i^2}}C_{jk}\right] \tag{18}$$

$$C_{ik}FU_i=C_{FU}\sqrt{\frac{We_{\tau 0}}{25}}C_{kn}\frac{\partial\overline{u_i u_i}}{\partial x_n} \tag{19}$$

The trace of the NLT_{ij} tensor (NLT_{mm}) is calculated by its viscoelastic closure (Eq. (5)). The remaining coefficient values and damping functions used in the viscoelastic turbulent model are listed in Table 1.

Table 1: Parameters values and damping functions.

Parameters values				
$C_{F1}=0.8$	$C_{F2}=0.0091$	$C_{F3}=0.042$	$C_{F4}=1.1$	$C_{\varepsilon_F}=2$
$C_\mu=0.09$	$C_{\varepsilon_1}=1.45$	$C_{\varepsilon_2}=1.9$	$\sigma_k=1.1$	$\sigma_\varepsilon=1.3$
$C_{\beta 1}=0.6$	$C_{\beta 2}=0.05$	$C_{FU}=0.031$	$C_{\varepsilon F1}=1.6$	$C_{\varepsilon F2}=1.74$
Damping functions				
$f_T=1+3.5\exp\left(-\left(\mathrm{Re}_T/150\right)^2\right)$		$f_5=\left[1-\exp\left(-y^+/50\right)\right]$		
$f_1=1$		$f_2=1-0.3\exp\left(-\left(\mathrm{Re}_T\right)^2\right)$		
$f_{F1}=\left(1-0.8\exp\left(-y^+/30\right)\right)^2$		$f_{F2}=\left(1-\exp\left(-y^+/25\right)\right)^4$		

Note: The f_T damping function depends on the turbulent Reynolds number, $\mathrm{Re}_T=k^2/\left(\varepsilon\cdot\nu_s\right)$

3 RESULTS

The performance of the new viscoelastic turbulence model is analyzed here through comparisons with Reynolds-averaged DNS data for turbulent channel flow at the same Reynolds number, $Re_{\tau 0} = 395$, which is defined by $Re_{\tau 0} = h \cdot u_\tau / \nu_0$, based on channel half-height, *h*. Other relevant flow conditions are $\beta = 0.9$, the ratio between the solvent kinematic viscosity and the zero shear-rate kinematic viscosity of the fluid, $\beta = \nu_s / \nu_0$, $L^2 = 900$, and Weissenberg numbers of 25 and 100, equivalent to DR=18% and 37%, respectively.

The DNS and predicted velocity profiles are compared in Figure 2 for DR=18% and 37%, including also the predictions by the previous turbulence model. The new model is better than the previous model [6], but the direct impact of the extra polymeric turbulent viscosity of Eq. (10) upon the momentum equation is rather small because the numerical method used here imposes the drag reduction and computes the required mean velocity.

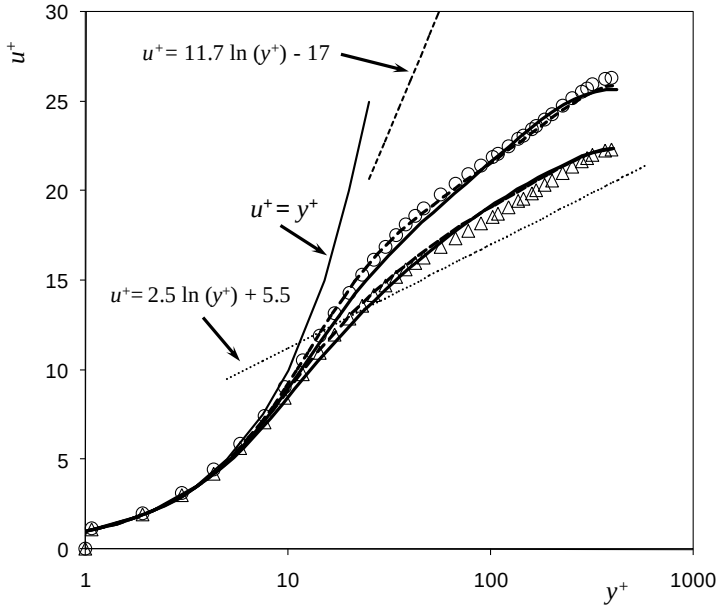

Figure 2: Comparison of the velocity profile between DNS data (symbol: Δ DR=18%; ○ DR=37%) and predictions: with the new model of the extra polymeric turbulent viscosity, Eq. (10), (continuum lines) and without (dash lines), [6].

The main effect of the new model of Eq. (10) is shown in Figure 3, which compares DNS data of the normalized turbulent kinetic energy with the old and new predictions. Whereas the previous closure under-predicted *k* by nearly 30%, the new model predictions are within 10% of the DNS data. The correction is restricted to a small region very close to the wall, but its impact on the profile of *k* is very large and allows the correct prediction of the Reynolds stress without the need to dampen the turbulent kinetic energy. This also allows the use of this full *k*-ε type model to the full range of drag reductions, contrasting with the limited range of the previous model to a value of DR of about 50%.

4 CONCLUSIONS

Previous RANS type turbulence models for FENE-P fluids showed a deficit of *k* very close to the wall and this was traced to a deficit in the production of *k*. In this work a modification is introduced in the closure for the Reynolds stress that corrects that deficiency and consequently the Reynolds shear stress in boundary layer flows becomes well predicted under intense drag reduction conditions without the need for an excessive damping of the turbulent kinetic energy as was the case in some past turbulence models [6]. The modification is the introduction of an extra polymeric contribution to the turbulent viscosity, which is based on the fluid relaxation time. This new contribution is restricted to the near-wall region.

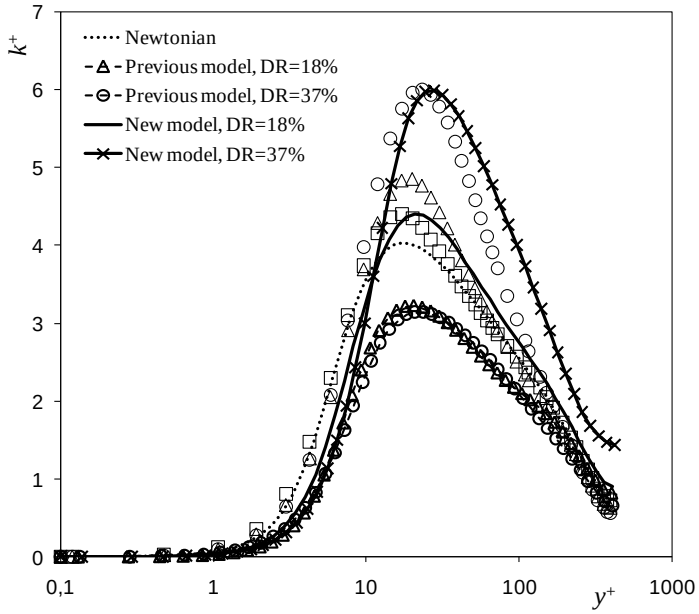

Figure 3: Comparison of turbulent kinetic energy between DNS data (symbols: □ Newtonian; Δ DR=18%; ○ DR=37%) and predictions with the model of the extra polymeric turbulent viscosity, Eq. (10) and without such model [6].

ACKNOWLEDGMENTS

Financial support provided by FAPESP – Fundação de Amparo à Pesquisa do Estado de São Paulo through Project Nº 2013/01521-4 and FUNDUNESP Process / EDITAL Nº: 1854/009/13 - PROPe / CDC is gratefully acknowledged by PR Resende.

REFERENCES

[1] R Sureshkumar, AN Beris, RA Handler (1997). Direct numerical simulation of the turbulent channel flow of a polymer solution. *Physics of Fluids* **9**(3):743–755.

[2] CD Dimitropoulos, R Sureshkumar, AN Beris, RA Handler (2001). Budgets of Reynolds stress, kinetic energy and streamwise entrophy in viscoelastic turbulent channel flow. *Physics of Fluids* **13**(4):1016–1027.

[3] CF Li, VK Gupta, R Sureshkmar, B Khomami (2006). Turbulent channel flow of dilute polymeric solutions: drag reduction scaling and an eddy viscosity model. *Journal of Non-Newtonian Fluid Mechanics* **139**:177–189.

[4] K Kim, CF Li, R Sureshkumar, S Balachandar, R Adrian (2007). Effects of polymer stresses on eddy structures in drag-reduced turbulent channel flow. *Journal of Fluid Mechanics* **584**:281–299.

[5] FT Pinho, CF Li, BA Younis, R Sureshkumar (2008). A low Reynolds number k-ε turbulence model for FENE-P viscoelastic fluids. *Journal of Non-Newtonian Fluid Mechanics* **154**:89–108.

[6] PR Resende, K Kim, BA Younis, R Sureshkumar, FT Pinho (2011). A FENE-P k–ε turbulence model for low and intermediate regimes of polymer-induced drag reduction. *Journal of Non-Newtonian Fluid Mechanics* **166**(12–13):639–660.

[7] G Iaccarino, ESG Shaqfeh, Y Dubief (2010). Reynolds-averaged modeling of polymer drag reduction in turbulent flows. *Journal of Non-Newtonian Fluid Mechanics* **165**(7-8):376–384.

[8] PR Resende, FT Pinho, K Kim, BA Younis, R Sureshkumar (2013). Development of a Low-Reynolds-number k-ω Model for FENE-P Fluids. *Flow, Turbulence and Combustion* **90**(1):69–94.

[9] KD Housiadas, AN Beris (2003). Polymer-induced drag reduction: Effects of the variations in elasticity and inertia in turbulent viscoelastic channel flow. *Physics of Fluids* **15**(8):2369–2384.

[10] CF Li, R Sureshkmar, B Khomami (2006). Influence of rheological parameters on polymer induced turbulent drag reduction. *Journal of Non-Newtonian Fluid Mechanics* **140**:23–40.

A numerical study of the hydrodynamic in feed channels of spiral-wound membrane modules

JC Silva[1], AA Soares[2,3], Abel Rouboa[1,3]

[1]Department of Engineering/ECT, Universidade de Trás-os-Montes e Alto Douro, Quinta de Prados, 5000-801 Vila Real, Portugal
[2]Department of Physics/ECT, Universidade de Trás-os-Montes e Alto Douro, Quinta de Prados, 5000-801 Vila Real, Portugal
[3]INEGI/Faculty of Engineering, University of Porto, Porto, Portugal.
email: joaomcsilva22@gmail.com, asoares@utad.pt, rouboa@utad.pt

ABSTRACT: The flow patterns were examined for a cell of feed channels of spiral wound membrane modules. Having spacer filaments in the feed channel has proved to change dynamically the concentration boundary layer and preventing fouling. This work investigates, for zigzag spacer configurations, the effects of the cell length and filament shape on the recirculation zones and on the wall shear stress for Reynolds numbers ranging from 10 to 200. A laminar flow periodically repeating in successive inter-cell regions was used. The results show the effect of the distance between elliptical filaments in the velocity field, streamlines, pressure drop and in the shear stress developed in the membrane walls.

KEY-WORDS: Desalination; Membrane fouling; Zigzag spacers; Elliptical filament.

1. INTRODUCTION

The performance of a spiral wound membrane is affected by many factors such as leaf geometry (number and dimensions), spacers, fouling propensity, cleaning ability and operating conditions [1]. In a steady-state, the selective rejection of the solute by these membranes increases the solute concentration at the membrane surface. This phenomenon, known as concentration polarization, has adverse effects on the membrane performance, namely the increase of the rate of membrane fouling and the decrease of the productivity and of the quality of the permeated water. Spacers have the main function of separating sheets of membranes in both membrane spiral wound modules as in slits (thin rectangular channels), but they are also a way of increasing the mass transfer, promoting mixing in the flow and minimizing pressure drop [2-4]. Computational fluid dynamics (CFD) has become a widely used tool in studying the hydrodynamic behaviour of nanofiltration and reverse osmosis membrane systems [5]. Many studies using CFD focused on the effect of feed channel spacer on fluid flow and mass transfer with different type of spacers [5, 6]. In more recent work, Saeed *et al*. [7] studied the effect on flow patterns through a spacer filled reverse osmosis membrane when feed spacer filaments are set at various angles with the inlet flow. Results revealed that the alignment of the feed spacers with the flow direction has great influence on the generation of secondary flow patterns through the spacer filled channels. Optimization of the feed spacer orientation can lead to desirable flow patterns generation within the membrane module, leading to enhanced membrane performance. Simplified cylindrical shapes were used for representation of spacer filaments in most of the numerical studies on the effect of feed spacer geometry on mass transfer and fluid flow. Stereomicroscopic observations of the feed spacer revealed that the spacers used in commercially available spiral-wound membrane modules have more complicated geometry, with filaments varying in thickness and thinnings [8]. On the other hand, fouling mitigation may represent the most significant opportunity for operational savings through improved feed spacer design. However, the magnitude of the potential improvement and the means by which spacers can reduce fouling through improved hydrodynamics are not yet well understood [9].

From the numerical simulation of the hydrodynamic in feed channels of a desalination membrane one can infer that the relation between the inter-filaments distance and its shape with the velocity field, streamlines, local and average friction factors, pressure drop and on the shear stress developed in the membrane walls, and the Zigzag configuration of elliptical spacer filaments can promote an active flow recirculation. Further, the combination between the filaments shape with the distance between filaments should take into account to promote active recirculation patterns and consequently mass transfer on the membrane surfaces.

2. GOVERNING EQUATIONS

An incompressible Newtonian fluid was used to simulate the bidimensional steady state laminar flow in a feed channel filled with spacer filaments in a zigzag arrangement, *e.g.* see Figure 2. The governing equations for the fluid flow in feed channel are the continuity and Navier-Stokes equations for incompressible Newtonian fluids. The governing equations can be written as:

continuity equation

$$\frac{\partial v_x}{\partial x}+\frac{\partial v_y}{\partial y}=0, \tag{1}$$

xx-momentum equation

$$\rho\left[\frac{\partial}{\partial x}(v_x{}^2)+\frac{\partial}{\partial y}(v_x v_y)\right]=-\frac{\partial p}{\partial x}+2\mu\frac{\partial}{\partial x}\left(\frac{\partial v_x}{\partial x}\right)+\mu\frac{\partial}{\partial y}\left(\frac{\partial v_x}{\partial y}+\frac{\partial v_y}{\partial x}\right)+\rho g_x \tag{2}$$

and *yy*-momentum equation

$$\rho\left[\frac{\partial}{\partial x}(v_x v_y)+\frac{\partial}{\partial y}(v_y{}^2)\right]=-\frac{\partial p}{\partial y}+2\mu\frac{\partial}{\partial y}\left(\frac{\partial v_x}{\partial y}\right)+\mu\frac{\partial}{\partial x}\left(\frac{\partial v_x}{\partial y}+\frac{\partial v_y}{\partial x}\right)+\rho g_y, \tag{3}$$

where x and y are the spatial coordinates, ρ is the fluid density, μ is the dynamic viscosity, p is the static pressure and g is the gravitational acceleration. The velocity components in x and y directions are v_x $\boldsymbol{v_x}$ and $\boldsymbol{v_y}$, respectively.

For the flow at the inlet and outlet of each cell, the velocity profile is assumed to have a given periodicity. The flow periodicity can be given by the following equations

$$\begin{aligned} v_x(0,y)&=v_x(L,y), \quad \forall y \\ v_y(0,y)&=v_y(L,y), \quad \forall y \end{aligned}, \tag{4}$$

where L is the length of each cell.

To obtain the inlet velocities profiles several simulations were carried out, starting with the flow simulation imposing the boundary condition of constant velocity at the inlet and the outflow *Fluent* condition for outlet boundary condition. When the solution is achieved, the velocity at the inlet is replaced by the solution obtained for the velocity profile in the outlet boundary. This process is repeated until the differences between inlet and outlet velocities profiles were less than 1%. An example of inlet and outlet velocities profiles is shown in Figure 1. No slip conditions were applied to wall boundaries.

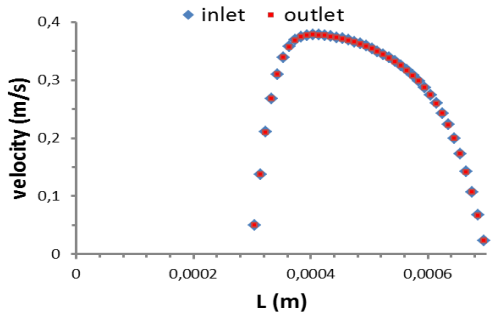

Figure 1: Inlet and outlet velocities profiles for Re = 200 and filament 2.

In this work one defines the Reynolds number as

$$Re = \frac{\rho \bar{v} h}{\mu} \tag{5}$$

where the $\bar{v}$ is the average velocity of inlet. In this work, *Fluent* was used for simulating the hydrodynamic inside spacer-filled channels of a desalination membrane. This code was used to solve the coupled conservation equations of mass and momentum. This code has been used successfully in a large number of studies to simulate the problems in hydrodynamics. In this framework, a second-order central differencing scheme is used for the diffusive terms and a second order upwind scheme for the convective terms. Coupling of the pressure and velocity is achieved using the well-known SIMPLE (Semi-Implicit Method for Pressure-Linked Equations) algorithm. The convergence criteria were set to 10^{-12} for all the relative (scaled) residuals.

3. RESULTS

The results presented here show the velocities distribution, streamlines, pressure drop and shear stress developed in the cell walls with lengths L= 4, 6, 8 and 10 mm and height h= 0,7 mm. Four elliptical filaments with same area (*e.g.* see Figure 4) in zigzag configuration are tested for *Re* =10, 50, 100, 150 and 200, which corresponds to the average velocities of inlet 0.1435, 0.718, 1.435, 2.153 and 2.870 cm/s, respectively.

3.1 Velocity distribution and streamlines

Figure 2 shows the velocity distribution in a cell, filled with filament spacers in zigzag configuration, with typical dimensions of the commercial membrane FilmTec™ Model XLE-4040, length 10 mm and height 0.7 mm. With increasing Reynolds number higher velocities begin to expand by convection for downstream regions of each filament, concentrating mainly in a central strip. For *Re* = 100 and 200, downstream of the filament and close to the channel wall, the flow presents very low velocity magnitude, corresponding to the recirculation zone formed downstream of each filament.

For Reynolds number 10 and filaments 1and 4 (Figure 3), it is clear that higher velocities occur in the filament regions between the filament and the opposite membrane wall. The distribution of velocity field is almost symmetric around every filament, with high velocity values in the central region between the channel wall and the filament. For *Re* = 10, 100 and 200 the aforementioned behaviour for the cell with length L = 10 mm is also observed for L = 4 mm. Comparing the velocity distribution for the channel filled with filament 1 with the channel filled with filament 4 we can see that the average velocity in the channel filled with filament 1 is higher, because for the same *Re* the average inlet velocity is equal for both cases but the entrance is smaller for the case of the filament 4.

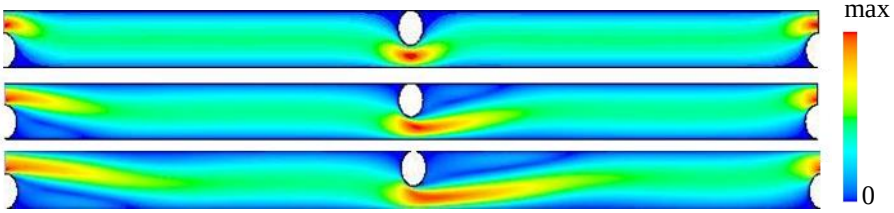

Figure 2: Velocity distribution in a cell with length L = 10 mm for *Re* = 10, 100 and 200 for filament 4.

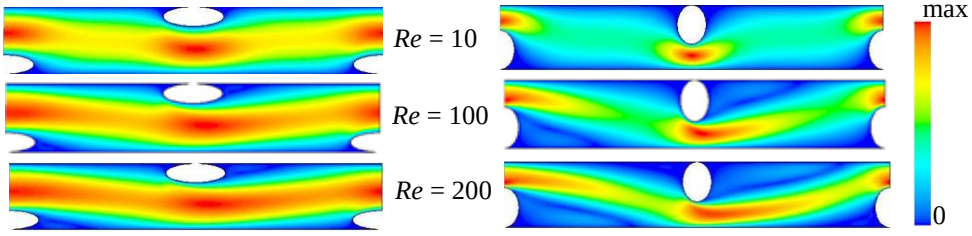

Figure 3: Velocity distribution in a cell with L = 4 mm for *Re* = 10, 100 and 200 for filament 1(left) and filament 4(right).

Figures 4–6 show the effect of the filament configurations in streamlines, for *Re* = 10, 100 and 200. It is possible to identify the recirculation patterns in all cases. The eddy length increases with the increase of *Re* and from filament 1 to filament 4, despite the decreasing of the average velocities in the channels from filament 1 to filament 4. The recirculation patterns are low velocity regions and the cells length (*L*) do not have a visible effect on streamlines behaviour for *L* >4 mm, see Figures 5 and 7. Under the studied conditions, for *L*= 4 mm and higher Reynolds numbers (*Re*> 100) the increasing of eddies is inhibited due to short distance between filaments. The results presented here, for elliptical filaments, are consistent with the observed by Cao *et al.* [6] for cylindrical filaments and suggest that reducing the distance between filaments can lead to more efficient eddies in the promotion of the mass transfer through membrane walls.

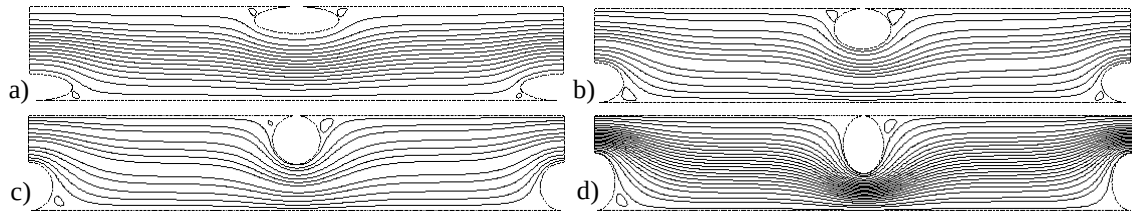

Figure 4: Streamlines for *Re* = 10 and *L* = 4 mm: a) filament 1, b) filament 2, c) filament 3 and d) filament 4.

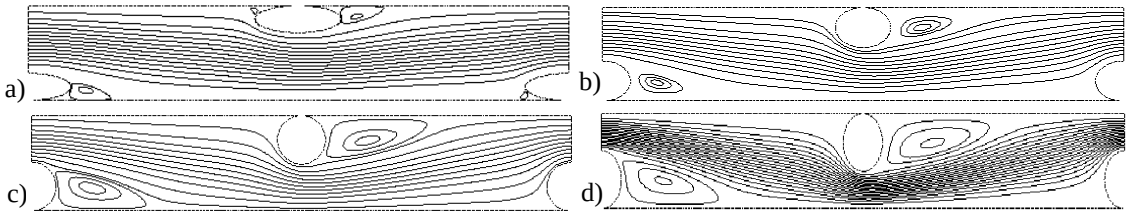

Figure 5: Streamlines for *Re* = 100 and *L* = 4 mm: a) filament 1, b) filament 2, c) filament 3 and d) filament 4.

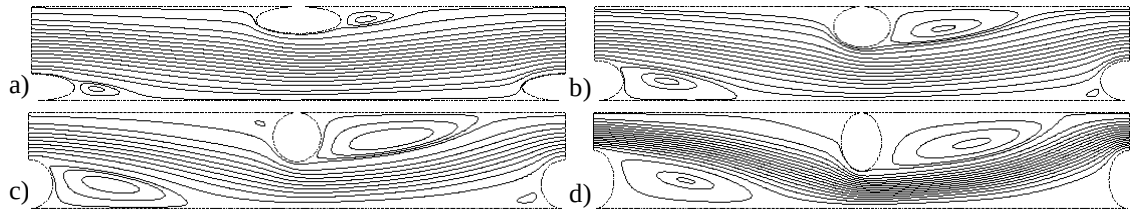

Figure 6: Streamlines for *Re* = 200 and *L* = 4 mm: a) filament 1, b) filament 2, c) filament 3 and d) filament 4.

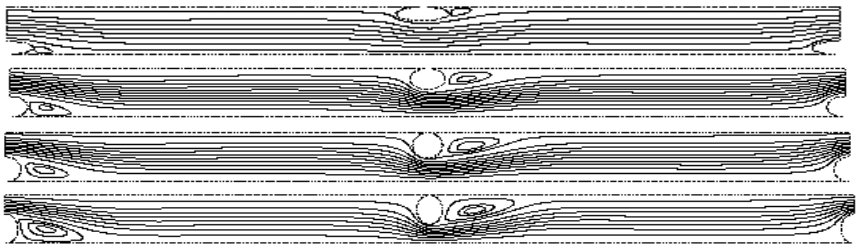

Figure 7: Streamlines for *Re* = 100 and *L* = 10 mm for the filament 1, 2, 3 and 4, top to bottom, respectively.

3.2 Wall shear stress

Figure 8 shows the local wall shear stress over the top wall for *Re* = 100, *L* = 4 and 10 mm, for the four filament shapes studied. As expected, when the distance between filaments increases the local wall shear stresses have qualitatively the same behaviour. The variation of the local shear stress with the shape of

filament is more pronounced for the filament 4, and this variation becomes less pronounced with the increase of the distance between the membrane wall and the filament.

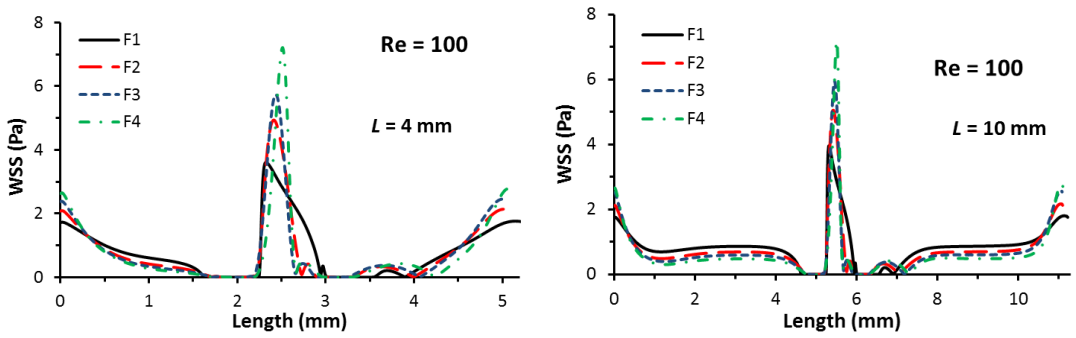

Figure 8: Local wall shear stress for *Re* = 100: a) *L* = 4 mm, b) *L* = 10 mm.

Figure 9 shows the values of the average wall shear stress per unit length (WSS/L), calculated from the shear stress values in both walls of each cell, for all filaments and cell lengths studied, for *Re* =10, 100 and 200, versus usable area percentage. It can be noted that, for a given filament WSS/L values increase with Reynolds number and decrease with *L*. Note that for a fixed *L* the usable area increases from filament 1 to filament 4. For a given *L* and *Re* the variation of average WSS/L with usable area is less than 15%, except for *Re* =10 and *L* > 6 mm. For *L* = 10 mm the variation of WSS/L with usable area increases until 42%, when the filament 1 is replaced by the filament 4.

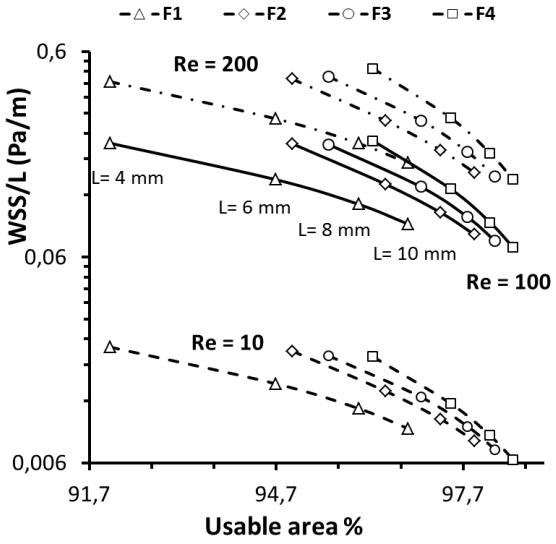

Figure 9: Average wall shear stress per unit length versus usable area percentage.

3.3 Pressure drop

Figure 10 shows the values of the pressure drop per unit length, for all filaments and cell lengths studied, for *Re* =10, 100 and 200 versus usable area percentage. As expected, the pressure drop per unit length decreases as the spacing between filaments increases (usable area increases too). This happens due to the decrease in the number of filaments per unit length. The reduction of the number of filaments per unit length leads to the decrease of average wall shear stress (Figure 9) and consequently decreases the total drag flow.

For a given filament the pressure drop per unit length increases with Reynolds number and decreases with *L*. For a given *L* and *Re* the pressure drop per unit length increases with usable area (area increases from filament 1 up to filament 4).

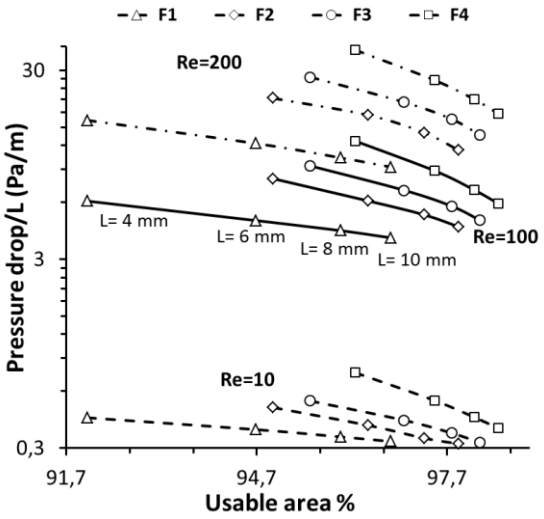

Figure 10: Pressure drop per unit length versus usable area percentage.

4. CONCLUSION

Increasing Reynolds number results in an increase of the velocity and consequently downstream of the filaments are formed recirculation zones of low velocities. The recirculation zones increase with increasing Reynolds number. The eddy length increases from filament 1 to filament 4. The variation of local WSS with the filament shape becomes less pronounced with the increase of the distance between filament and membrane wall. The average WSS/L increases with Reynolds number and decreases with cell length (L). The usable area increases from filament 1 to filament 4, and for a fixed L and Re the variation of average WSS/L with usable area is less than 15%, except for Re =10 and L > 6 mm. For L = 10 mm, the variation of WSS/L with usable area increases until 42% when the filament 1 is replaced by the filament 4. The pressure drop per unit length decreases as the spacing between filaments increases. For a fixed filament the pressure drop per unit length decreases with increases of the usable area. However, to optimize the process of mass transfer is need to take into account the complex interplay between the kinematic (Re) and physical characteristics (length, height and filament shape) of the system to better understand the effect of these characteristics on mass transfer.

REFERENCES

[1] J Schwinge, PR Neal, DE Wiley, DF Fletcher, AG Fane (2004). Spiral wound modules and spacers: Review and analysis. *Journal of Membrane Science* **242**:129–153.

[2] CC Zimmerer, V Kottke (1996). Effects of spacer geometry on pressure drop, mass transfer, mixing behavior, and residence time distribution. *Desalination* **104**:129–134.

[3] V Geraldes, V Semião, MN Pinho (2002). Flow management in nanofiltration spiral wound modules with ladder-type spacers. *Journal of Membrane Science* **203**:87–102.

[4] AL Ahmad, KK Lau (2006). Impact of different spacer filaments geometries on 2D unsteady hydrodynamics and concentration polarization in spiral wound membrane channel. *Journal of Membrane Science* **286**:77–92.

[5] GA Fimbres-Weihs, DE Wiley (2010). Review of 3D CFD modeling of flow and mass transfer in narrow spacer-filled channels in membrane modules. *Chemical Engineering and Processing* **49**:759–781.

[6] CP Koutsou, SG Yiantsios, AJ Karabelas (2007). Direct numerical simulation of flow in spacer-filled channels: effect of spacer geometrical characteristics. *Journal of Membrane Science* **291**:53–69.

[7] A Saeed, R Vuthaluru, Y Yang, HB Vuthaluru (2012). Effect of feed spacer arrangement on flow dynamics through spacer filled membranes. *Desalination* **285**:163–169.

[8] J Johnson, M Busch (2010). Engineering aspects of reverse osmosis module design. *Desalination and Water Treatment* **15**:236–248.

[9] JS Vrouwenvelder, C Hinrichs, AR Sun, F Royer, JAM van Paassen, SM Bakker, WGJ van der Meer, JC Kruithof, MCM van Loosdrecht (2008). Monitoring and control of biofouling in nanofiltration and reverse osmosis membranes. *Water Science and Technology* **8**:449–458.

[10] Z Cao, DE Wiley, AG Fane (2001). CFD simulations of net-type turbulence promoters in a narrow channel. *Journal of Membrane Science* **185**:157–176.

Development length in channel flows of inelastic fluids described by the Sisko viscosity model

LL Ferrás[1], C Fernandes[1], O Pozo[1], AM Afonso[2], MA Alves[2], JM Nóbrega[1], FT Pinho[3]

[1]Instituto de Polímeros e Compósitos/I3N, Universidade do Minho, Campus de Azurém 4800-058 Guimarães, Portugal
[2]Departamento de Engenharia Química, Centro de Estudos de Fenómenos de Transporte, Faculdade de Engenharia da Universidade do Porto, Rua Dr. Roberto Frias s/n, 4200-465, Porto, Portugal
[3]Centro de Estudos de Fenómenos de Transporte, Faculdade de Engenharia da Universidade do Porto, Rua Dr. Roberto Frias s/n, 4200-465, Porto, Portugal
email: luis.ferras@dep.uminho.pt, cbpf@dep.uminho.pt, pozo@dep.uminho.pt, aafonso@fe.up.pt, mmalves@fe.up.pt, mnobrega@dep.uminho.pt, fpinho@fe.up.pt

ABSTRACT: This work presents a numerical study regarding the dimensionless development length, $\mathcal{L}=L/H$ required for fully-developed channel flow of inelastic non-Newtonian fluids described by the generalized Newtonian model with the Sisko viscosity equation. The simulations were carried out for generalized Reynolds numbers in the range $0 < \mathrm{Re}_{gen} \leq 100$, for a flow behaviour index, n, in the range $0.25 < n \leq 2$ and for an infinite dimensionless shear rate viscosity, $\bar{\mu}_\infty$, varying in the range $0 < \bar{\mu}_\infty \leq 5$. A new non-linear relationship between $\mathcal{L}$ and *Re* was derived and for specific values of *n*, new exact solutions are also presented for the velocity profile under fully-developed flow conditions.

KEY-WORDS: Development length; Sisko model; Channel flow.

1 INTRODUCTION

The length required to achieve a fully developed flow in pipes and channels has been for a long time a subject of interest (see [1] and [2] and the references therein). Durst et al. [1] derived a correlation for the development length of Newtonian fluids in pipe and channel flows of Newtonian fluids, and Poole and Ridley [2], extended the work of Durst et al. [1] to the pipe flow of inelastic fluids described by the power-law model. Common to these works is that the development length is determined on the basis of the velocity profile, specifically when the velocity at the centre of the channel reaches 99% of the fully-developed value.

In this work we devise a correlation for the development length of fluids described by the Sisko model [3] in planar channels.

2 GOVERNING EQUATIONS

The governing equations for steady, incompressible, laminar and isothermal flows are the conservation of mass equation

$$\nabla \cdot \mathbf{u} = 0 \tag{1}$$

and the momentum equation,

$$\rho\left(\frac{\partial \mathbf{u}}{\partial t} + \nabla \cdot \mathbf{uu}\right) = -\nabla p + \nabla \cdot \boldsymbol{\tau}, \tag{2}$$

where $\mathbf{u}$ is the velocity vector, ρ is the fluid density, p is the pressure and $\boldsymbol{\tau}$ is the extra stress tensor, that is given by,

$$\boldsymbol{\tau} = \eta(\dot{\gamma})\left(\nabla \mathbf{u} + (\nabla \mathbf{u})^T\right) = 2\eta(\dot{\gamma})\mathbf{D} \tag{3}$$

where $\mathbf{D}$ is the symmetric rate of strain tensor and $\eta(\dot{\gamma})$ is the shear viscosity model that follows the Sisko model,

$$\eta(\dot{\gamma}) = \mu_\infty + K\dot{\gamma}^{n-1} \tag{4}$$

where K is the flow consistency index, μ_∞ is the infinite shear rate viscosity, n is the flow behaviour index and $\dot{\gamma} = \sqrt{2\,\mathrm{tr}(\mathbf{D}^2)}$ ($\mathrm{tr}(\ )$ is the trace of a tensor) is the shear rate.

3 NUMERICAL PROCEDURE

The exact velocity profiles for the fully developed flow, required to identify the fully developed conditions, can only be determined analytically for specific values of the exponent, n = 1/3, 1/2, 1 and 2, but, the exact shear rate profile can be obtained for a wider range of flow index, namely n =1/4, 1/3, 1/2, 2/3, 3/4, 1, 3/2.

When an analytical solution is not possible for fully-developed flow, the shear rate value was used to compute numerically the pressure gradient and the velocity at the centre of the channel, through a numerical method.

For the numerical solution of the system of governing equations ((1)-(4)) we used the Finite Volume Method together with the SIMPLE procedure of Patankar [4] to couple the velocity and pressure fields [5]. The numerical computations were performed with the open source OpenFOAM software [6].

4 RESULTS AND DISCUSSION

The development length $\mathcal{L}$ was defined as the axial distance required for the velocity to reach 99% of the calculated maximum value. The Reynolds number adopted is the generalized version usually employed for power-law fluids, cf. [7],

$$\mathrm{Re}_{gen} = \frac{6\rho U^{2-n} H^n}{K}\left(\frac{4n+2}{n}\right)^{-n}, \tag{4}$$

and the dimensionless infinite shear rate viscosity, $\bar{\mu}_\infty$, is defined as $\bar{\mu}_\infty = \mu_\infty/(\rho UH)$, where U is the flow average velocity and H is the channel width.

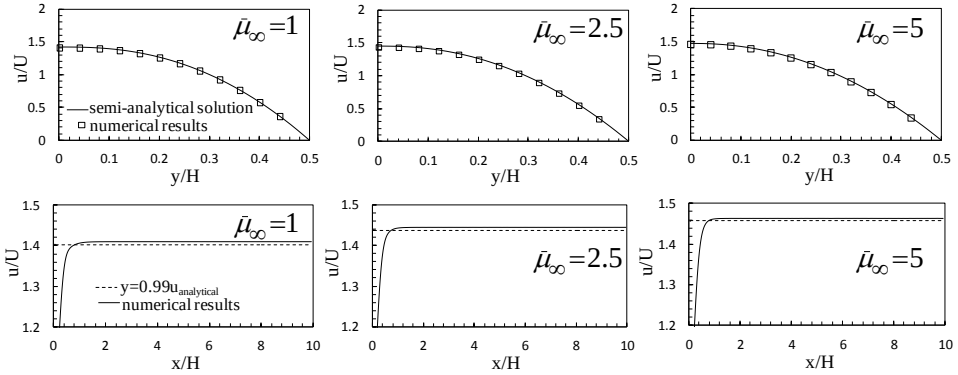

Figure 1: (Top) Comparison between the semi-analytical and the numerical solutions for three different values of $\bar{\mu}_\infty$. (Bottom) Centreline velocity profile along the channel length.

In Figure 1 (Top) we show a good agreement between the numerical and the analytical results, for the fully-developed velocity profile. Figure 1 (Bottom) presents the Centreline velocity profile along the channel length for three different values of $\bar{\mu}_\infty$, with $\mathrm{Re}_{gen} = 1$ and $n = 0.5$. For $\bar{\mu}_\infty = 1$, 2.5 and 5 we obtained a development length, $\mathcal{L}=L/H$, of $0.835, 0.746$ and 0.747, respectively. This shows that the development length decreases with increase of $\bar{\mu}_\infty$, which was expected due to the growth of momentum diffusion along the channel thickness promoted by the increase of $\bar{\mu}_\infty$.

REFERENCES

[1] F Durst, S Ray, B Unsal, OA Bayoumi (2005). The development lengths of laminar pipe and channel flows. *Journal of Fluids Engineering* **127**:1154–1160.

[2] RJ Poole, BS Ridley (2007). Development length requirements for fully-developed laminar pipe flow of inelastic non-Newtonian liquids. *Journal of Fluids Engineering* **129**:1281–1287.

[3] AW Sisko (1958). The flow of lubricating greases. *Industrial & Engineering Chemistry* **50**:1789–1792.

[4] SV Patankar (1980). *Numerical Heat Transfer and Fluid Flow*, Hemisphere, Washington D.C.

[5] PJ Oliveira, FT Pinho, GA Pinto (1998). Numerical simulation of non-linear elastic flows with a general collocated finite-volume method. *Journal of Non-Newtonian Fluid Mechanics* **79**:1–43.

[6] OpenFOAM (2011). The OpenFOAM Foundation [WWW]. Available from: http://www.openfoam.org/.

[7] P. Ternik (2009). Planar sudden symmetric expansion flows and bifurcation phenomena of purely viscous shear thinning fluids. *Journal of Non-Newtonian Fluid Mechanics* **157**:15–25.

Estudo numérico do efeito da esfericidade de aneurismas do tipo sacular na hemodinâmica

SR Marques[1], MP Ferreira[1], AA Soares[2,3], L Morgado[2]

[1]Escola de Ciências e Tecnologia, Universidade de Trás-os-Montes e Alto Douro, Quinta de Prados, 5000-801 Vila Real, Portugal
[2]Departamento de Física, Escola de Ciências e Tecnologia, Universidade de Trás-os-Montes e Alto Douro, Quinta de Prados, 5000-801 Vila Real, Portugal
[3]INEGI, Faculdade de Engenharia, Universidade do Porto, Rua Dr Roberto Frias, 4200-465 Porto, Portugal
email: si_354@hotmail.com, patricia-r-f@hotmail.com, asoares@utad.pt, lmorgado@utad.pt

RESUMO: Este trabalho tem como principal objectivo investigar numericamente a correlação entre a esfericidade de aneurismas do tipo sacular e as tensões de corte desenvolvidas nas paredes dos mesmos. O estudo é realizado em modelos geométricos simplificados de aneurismas da artéria Aorta Abdominal. Considera-se o escoamento do sangue em regime laminar e com comportamento newtoniano. São também apresentados os resultados da distribuição da velocidade e da pressão ao longo da artéria Aorta Abdominal para as condições de esfericidade dos aneurismas e cinemáticas estudadas.

PALAVRAS-CHAVE: Esfericidade; Aneurisma; Hemodinâmica; Tensões de corte; Aorta Abdominal.

1 INTRODUÇÃO

O comportamento dos aneurismas é diferente de caso para caso. O modo como se formam e as principais causas associadas à sua ruptura têm ganho cada vez mais relevo no meio científico. Atualmente sabe-se que a velocidade do sangue, a pressão e as tensões de corte desenvolvidas nas paredes dos aneurismas são fatores relevantes ao seu aparecimento e posterior desenvolvimento, o que torna importante perceber a hemodinâmica no interior dos aneurismas.

A compreensão dos processos subjacentes que levam ao crescimento e enfraquecimento estrutural dos aneurismas da Aorta Abdominal é de fundamental importância tanto para o diagnóstico da progressão da lesão como para o planeamento da intervenção específica em cada paciente. Tem sido sugerido que a degradação da elastina é atribuída à elevada ativação da matriz proteolítica metaloproteinase, que pode ser induzida por vários fatores como a distribuição anormal da tensão de corte nas paredes, respostas inflamatórias e a formação de trombos intraluminais [1,2]. Apesar de ser sugerido que provavelmente o crescimento dos aneurismas ocorre nas regiões onde a parede da artéria está exposta a valores de tensão de corte anormalmente altos, o efeito da tensão de corte na expansão das paredes dos aneurismas ainda não está completamente compreendido. As altas tensões de corte nas paredes são muitas vezes relacionadas com o início de aneurismas cerebrais, enquanto que os baixos valores das tensões de corte nas paredes têm sido associados com a progressão do aneurisma, formação de trombos e sua ruptura [3–6].

Em relação às causas hemodinâmicas da ruptura do aneurisma existem duas teorias correntes. Uma teoria declara que os aneurismas estão sob uma baixa tensão de corte na parede, o que desencadeia processos, como a remodelação da parede arterial, que degradam a qualidade da mesma e originam pontos fracos na parede do aneurisma, resultando em ruptura. A segunda teoria considera que os processos associados com elevadas tensões de corte nas paredes são responsáveis pelos danos causados na parede do vaso, dos quais pode resultar a sua ruptura [1]. Assim, o estudo da dinâmica do escoamento sanguíneo reveste-se de elevada importância para caracterizar em detalhe os campos de tensão de corte de modo a permitir avaliar se os aneurismas estão sujeitos a elevadas ou baixas tensões de corte.

Para melhor compreensão da dinâmica do escoamento poderíamos testar vários parâmetros e verificar se existiria alguma relação entre esses parâmetros e as tensões de corte nas paredes. Neste estudo, testamos a hipótese de que deve existir alguma relação entre a esfericidade dos aneurismas do tipo sacular e a distribuição das tensões de corte nas paredes que por sua vez poderá estar relacionada com a degradação da elastina e consequentemente com o risco de rompimento do aneurisma. Para testarmos a nossa hipótese selecionámos modelos simplificados da bifurcação da artéria Aorta Abdominal com aneurismas do tipo sacular.

Para cada um dos modelos tridimensionais dos aneurismas determinamos numericamente as soluções hemodinâmicas nas mesmas condições com o objetivo de investigar relações entre a esfericidade dos

aneurismas e as alterações do escoamento sanguíneo. É de referir que para os objetivos deste estudo a maior simplificação talvez seja termos considerado o sangue um fluido newtoniano pois espera-se que as taxas de deformação no interior do aneurisma, em geral, sejam inferiores a 100 s^{-1}, valores característicos do comportamento reofluidificante do sangue.

2 EQUAÇÕES DE GOVERNO

As equações governativas que regem o escoamento de fluidos newtonianos e incompressíveis em regime estacionário são as equações de Navier-Stokes, *e.g.* [7]. Estas equações são definidas pela equação de continuidade.

$$\frac{\partial v_x}{\partial x}+\frac{\partial v_y}{\partial y}+\frac{\partial v_z}{\partial z}=0 \tag{1}$$

e as equações da conservação da quantidade de movimento:

$$\rho\left(v_x\frac{\partial v_x}{\partial x}+v_y\frac{\partial v_x}{\partial y}+v_z\frac{\partial v_x}{\partial z}\right)=-\frac{\partial p}{\partial x}+\mu\left(\frac{\partial^2 v_x}{\partial x^2}+\frac{\partial^2 v_x}{\partial y^2}+\frac{\partial^2 v_x}{\partial z^2}\right)+\rho g_x \tag{2a}$$

$$\rho\left(v_x\frac{\partial v_y}{\partial x}+v_y\frac{\partial v_y}{\partial y}+v_z\frac{\partial v_y}{\partial z}\right)=-\frac{\partial p}{\partial y}+\mu\left(\frac{\partial^2 v_y}{\partial x^2}+\frac{\partial^2 v_y}{\partial y^2}+\frac{\partial^2 v_y}{\partial z^2}\right)+\rho g_y \tag{2b}$$

$$\rho\left(v_x\frac{\partial v_z}{\partial x}+v_y\frac{\partial v_z}{\partial y}+v_z\frac{\partial v_z}{\partial z}\right)=-\frac{\partial p}{\partial z}+\mu\left(\frac{\partial^2 v_z}{\partial x^2}+\frac{\partial^2 v_z}{\partial y^2}+\frac{\partial^2 v_z}{\partial z^2}\right)+\rho g_z \tag{2c}$$

onde x, y e z são as coordenadas espaciais, ρ (kg/m^3) a massa volúmica, μ (Pa·s) a viscosidade dinâmica, p (Pa) a pressão estática e g (m/s^2) a aceleração da gravidade. As componentes da velocidade (m/s) nas direções x, y e z são representadas por v_x, v_y v_x e v_z, respetivamente.

As simulações numéricas foram realizadas com recurso ao *software Fluent*. As malhas foram escolhidas de modo a que as soluções encontradas fossem independentes das malhas. De acordo com os testes realizados, os resultados das simulações mostram variações menores do que 2% se utilizaremos malhas mais refinadas. Para discretizar as equações de conservação da quantidade de movimento, foi utilizado o esquema *upwind* de segunda ordem e para a interpolação da pressão recorreu-se ao esquema *standard*. Para o acoplamento entre a pressão e a velocidade (fluido incompressível) nas equações de Navier-Stokes foi utilizado o algoritmo SIMPLE (*Semi-Implicit Method for Pressure Linked Equations*). Na linearização das equações foi usado o método implícito.

A convergência é obtida quando os resíduos para as equações da continuidade e da quantidade de movimento foram, simultaneamente, menores do que 10^{-9}.

2.1 Modelos simplificados dos aneurismas

Para a construção dos modelos simplificados da bifurcação da aorta abdominal com aneurismas foram usadas imagens médicas 2D de Tomografia Computorizada. Dessas imagens foram retirados os parâmetros geométricos utilizados na construção da geometria 3D. Após a construção da geometria 3D da bifurcação da Aorta Abdominal foi adicionado um objecto esférico sobre a bifurcação para construir o modelo do aneurismas, ver Figura 1. Os valores do raio e da posição do centro da esfera sobre o eixo dos zz com origem na entrada da artéria constam na Tabela 1.

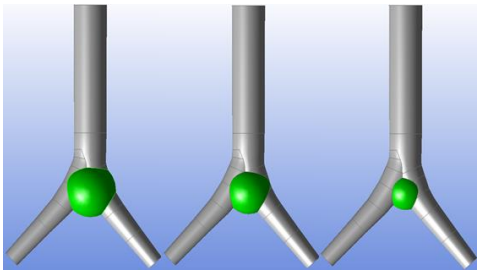

Figura 1: Modelos simplificados da bifurcação da Aorta Abdominal com aneurismas de diferentes raios na mesma posição.

2.2 Condições fronteira

Para a resolução numérica das equações de governo que regem o escoamento sanguíneo nos modelos geométricos da bifurcação da artéria Aorta Abdominal, além do domínio computacional definido pelas geometrias 3D da artérias e das propriedades do sangue (massa volúmica 1050 kg/m^3 e viscosidade dinâmica 0,00319 Pa·s), é necessário definirmos as condições fronteira para cada um dos domínios computacionais usados. O sangue é considerado um fluido incompressível e isotérmico com propriedades constantes. O escoamento ocorre ao longo da artéria Aorta Abdominal desde a entrada na Aorta Abdominal até às saídas nas artérias Ilíacas Esquerda e Direita, ver Figura 1.

Na entrada da artéria Aorta Abdominal considera-se o perfil da velocidade completamente desenvolvido de acordo com a equação

$$v_z(r) = 2\bar{v}\left[1-\left(\frac{r}{R}\right)^2\right] \tag{3}$$

A velocidade média, $\bar{v}$, considerada é 0,1 m/s o que corresponde a um número de Reynolds e caudal de 724 e 3,80 L/min, respetivamente. O raio da artéria, *R*, na entrada é de 11 mm [7]. A velocidade média usada neste estudo corresponde a uma das velocidades adquiridas pelo sangue na artéria Aorta Torácica durante cada um dos ciclos cardíacos [8]. Esta velocidade garante que o escoamento seja sempre laminar.

Para as saídas impôs-se que a soma dos caudais nas ilíacas seja igual ao caudal na entrada, sendo o caudal em cada uma das ramificações 50% do caudal de entrada. Para esta situação é escolhida, no programa *Fluent*, a condição fronteira *outflow*.

Nas paredes considerou-se a condição normal de não deslizamento o que corresponde a impor uma velocidade nula junto das paredes.

2.3 Esfericidade dos aneurismas

Este estudo centra-se na hipótese de que deve existir algum parâmetro geométrico da cavidade dos aneurismas que pode ser relacionado com a hemodinâmica no interior da cavidade. Assim, como primeira abordagem parece-nos lógico testarmos a esfericidade dos aneurismas para procuramos essas relações.

A esfericidade foi definida de acordo com Wadell [9]. A esfericidade é uma medida de quão esférico é um objeto. Tendo em conta esta definição, a esfericidade Ψ do aneurisma é dada pela relação entre a área da superfície da esfera, com o mesmo volume do aneurisma, pela área da superfície que envolve o aneurisma:

$$\Psi = \frac{\pi^{\frac{1}{3}}(6V_e)^{\frac{2}{3}}}{A_a} \tag{4}$$

onde V_e é o volume da esfera (igual ao volume do aneurisma) e A_a é a área da superfície que envolve o aneurisma. Todo o aneurisma que não seja esférico tem uma esfericidade inferior a 1.

Considera-se o aneurisma como sendo o volume acrescentado à artéria sem aneurisma, ver Figura 2.

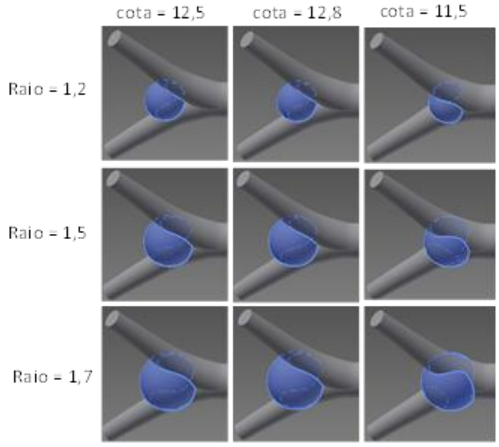

Figura 2: Modelos dos aneurismas em azul. Raio e cota em cm.

Neste trabalho são analisados nove aneurismas com o raio, cota, área, volume e esfericidade indicadas na Tabela 1. A esfericidade aumenta tanto com o aumento do raio como com o aumento da cota, isto é, aumenta com o afastamento relativamente à bifurcação da artéria.

Tabela 1: Características geométricas dos aneurismas

Raio (cm)	Cota (cm)	Área (cm^2)	Volume (cm^3)	Ψ
1,2	11,5	14,272	0,170	0,100
1,2	12,5	17,323	3,017	0,583
1,2	12,8	17,806	3,850	0,667
1,5	11,5	29,153	3,705	0,397
1,5	12,5	28,485	7,557	0,654
1,5	12,8	28,334	8,798	0,727
1,7	11,5	43,366	10,976	0,550
1,7	12,5	37,772	11,971	0,670
1,7	12,8	37,321	13,442	0,730

3 RESULTADOS E DISCUSSÃO

3.1 Campo de velocidades e pressões

A Figura 3 mostra a distribuição das velocidades, no plano medial da artéria e em três planos transversais, para os casos dos aneurismas de raio 1,7 cm e cota 12,8 cm, e de raio 1,2 cm e cota 11,5 cm. O plano P3 corresponde à linha L2. A figura sugere a formação de redemoinhos nos aneurismas e na entrada da ilíaca esquerda identificada pela linha L4. Da comparação entre as Figuras 3a) e 3b) observa-se, como esperado, que o aumento da cota do aneurisma resulta no aparecimento de zonas de recirculação mais extensas, uma vez que o aneurisma também se torna mais extenso.

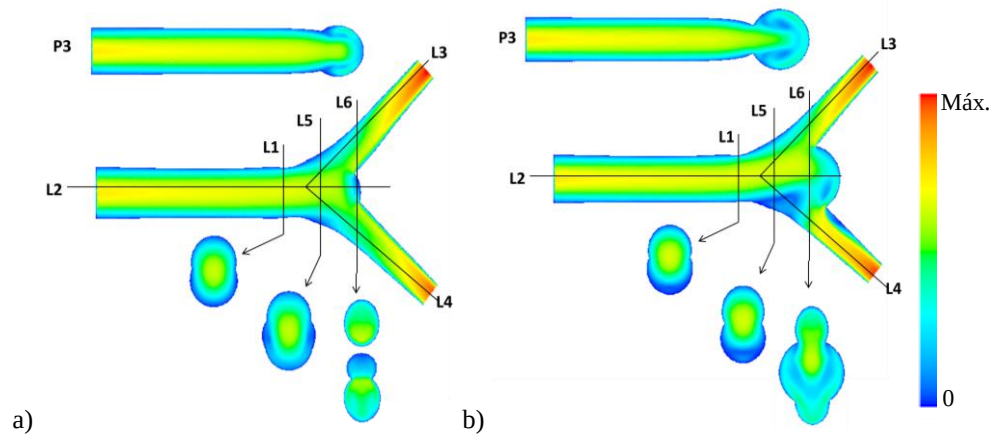

Figura 3: Distribuição das velocidades para os casos da artéria com os aneurismas de a) raio 1,2 cm e cota 11,5 cm, e de b) raio 1,7 cm e cota 12,8 cm.

A Figura 4 mostra a distribuição das pressões, no plano medial da artéria e em três planos transversais, para os casos dos aneurismas com raio 1,7 cm e cota 12,8 cm, e com raio 1,2 cm e cota 11,5 cm. O plano P3 corresponde à linha L2. Na figura observa-se que os aneurismas são propícios ao aparecimento de pressões mais elevadas assim como ao desenvolvimento de gradientes de pressão elevados. Este comportamento é mais acentuado em aneurismas mais desenvolvidos.

A análise dos perfis das velocidades e das pressões ao longo da linha L2, ver Figuras 3 e 4, revelaram que os perfis para os casos da artéria com aneurisma têm qualitativamente o mesmo comportamento que o caso da artéria sem aneurisma. Para as linhas L3 e L4, o comportamento dos perfis das velocidades e das pressões nas artérias com aneurisma diferem do caso em que a artéria não tem aneurisma.

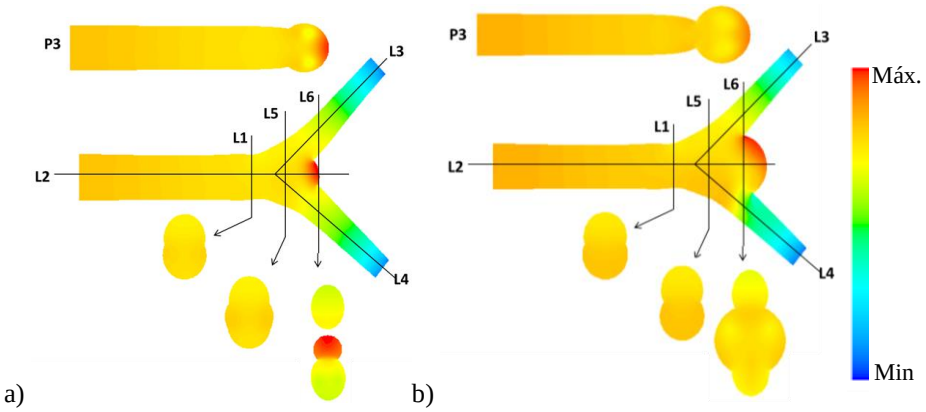

Figura 4: Distribuição das pressões para os casos da artéria com os aneurismas de a) raio 1,2 cm e cota 11,5 cm, e de b) raio 1,7 cm e cota 12,8 cm.

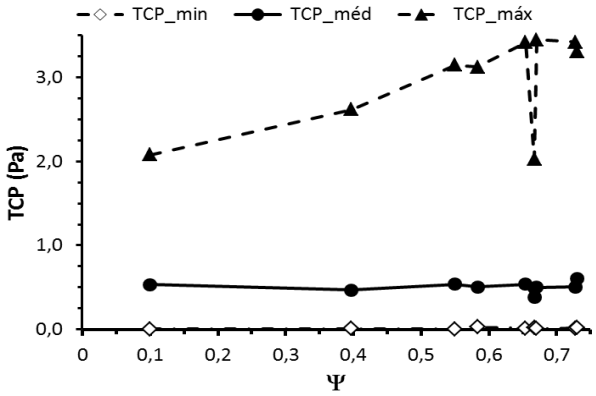

Figura 5: Valores mínimos, médios e máximos das tensões de corte nas paredes do aneurisma em função da esfericidade do aneurisma.

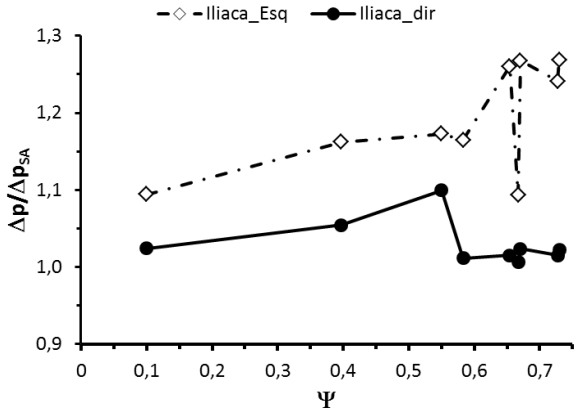

Figura 6: Diferença de pressões entre a entrada da artéria Aorta Abdominal e as saídas das Ilíacas normalizadas ao caso da artéria sem aneurisma (SA) em função da esfericidade do aneurisma.

3.3 Tensões de corte nas paredes dos aneurismas

Da análise das tensões de corte nas paredes dos aneurismas em função da esfericidade, verifica-se que não existe uma variação significativa com a esfericidade. A variação máxima (1,4 Pa) ocorre para as TCP máximas. Os valores máximos das TCP ocorrem na aresta formada entre o aneurisma e a artéria e dependem da forma como foi construída a imagem 3D. Os valores das TCP médias e mínimas são inferiores a 0,7 Pa para todos os aneurismas. Segundo Malek *et al* [10] os valores normais das TCP de uma artéria saudável então compreendidos entre 1 e 7 Pa.

3.4 Diferenças de pressão

Foram também analisados os efeitos da presença do aneurisma, através da sua esfericidade, na diferença de pressão entre a entrada da artéria Aorta Abdominal e a saída das Ilíacas. A Figura 6 mostra a diferença de pressões entre a entrada da artéria Abdominal e as saídas das Ilíacas normalizadas ao caso da artéria sem aneurisma (SA) em função da esfericidade. A presença do aneurisma resulta num aumento da diferença de pressão em ambos os ramos. Em todos os casos, a diferença de pressão é maior para a Ilíaca Esquerda. Não existe uma relação clara entre as diferenças de pressão e a esfericidade dos aneurismas.

4 CONCLUSÕES

Neste estudo, testamos a hipótese da existência de alguma relação entre a hemodinâmica e a esfericidade dos aneurismas do tipo sacular, na bifurcação da artéria Abdominal.

Os valores máximos das tensões de corte ocorrem nas paredes da artéria e os valores mínimos nas paredes do aneurisma. Em média, as tensões de corte são mais baixas na parede do aneurisma do que nas paredes da artéria. Os resultados sugerem que a esfericidade não tem influência significativa nas tensões de corte médias desenvolvidas na parede do aneurisma.

Na presença dos aneurismas, as diferenças de pressão entre a entrada na Aorta Abdominal e cada uma das saídas nas ramificações da bifurcação (artérias Ilíacas) foram sempre superiores quando comparadas com a artéria sem aneurisma. As diferenças entre a pressão à entrada da Aorta Abdominal e a média das pressões à saída das Ilíacas crescem com esfericidade até 15%.

O estudo permite, ainda, inferir que deve ser possível definir um parâmetro geométrico mais adequado que relacione as tensões de corte nas paredes do aneurisma com a área e a forma do aneurisma.

REFERÊNCIAS

[1] V Fontaine, M-P Jacob, X Houard, P Rossignol, D Plissonnier, E Angles-Cano, J-B Michel (2002). Involvement of the mural thrombus as a site of protease release and activation in human aortic aneurysms. *The American Journal of Pathology* **161**:1701–1710.

[2] K Shimizu, RN Mitchell, P Libby (2006). Inflammation and cellular immune responses in abdominal aortic aneurysms. *Arteriosclerosis, Thrombosis, and Vascular Biology* **26**:987–994.

[3] M Shojima, M Oshima, K Takagi, R Torii, M Hayakawa, K Katada, A Morita, T Kirino (2004). Magnitude and role of wall shear stress on cerebral aneurysm: Computational fluid dynamic study of 20 middle cerebral artery aneurysms. *Stroke* **35**:2500–2505.

[4] L Boussel, V Rayz, C McCulloch, A Martin, G Acevedo-Bolton, M Lawton, R Higashida, WS Smith, WL Young, D Saloner (2008). Aneurysm growth occurs at region of low wall shear stress: Patient-specific correlation of hemodynamics and growth in a longitudinal study. *Stroke* **39**:2997–3002.

[5] D Bluestein, L Niu, RT Schoephoerster, MK Dewanjee (1996). Steady flow in an aneurysm model: Correlation between fluid dynamics and blood platelet deposition. *Journal of Biomechanical Engineering* **118**:280–286.

[6] A Valencia, H Morales, R Rivera, E Bravo, M Galvez (2008). Blood flow dynamics in patient-specific cerebral aneurysm models: The relationship between wall shear stress and aneurysm area index. *Medical Engineering & Physics* **30**:329–340.

[7] T Shipkowitz, VGJ Rodgers, LJ Frazin, KB Chandran (1998). Numerical study on the effect of steady axial flow development in the human aorta on local shear stresses in abdominal aortic branches. *Journal of Biomechanics* **31**:995–1007.

[8] E Soudah, EYK Ng, TH Loong, M Bordone, U Pua, S Narayanan (2013). CFD modelling of abdominal aortic aneurysm on hemodynamic loads using a realistic geometry with CT. *Computational and Mathematical Methods in Medicine* **2013**:472564.

[9] H Wadell (1935). Volume, shape and roundness of quartz particles. *The Journal of Geology* **43**(3):250–280.

[10] AM Malek, SL Alper, S Izumo (1999). Hemodynamic shear stress and its role in atherosclerosis. *The Journal of the American Medical Association* **282**(21):2035–2042.

V Conferência Nacional de Mecânica dos Fluidos, Termodinâmica e Energia
MEFTE 2014, 11–12 Setembro 2014, Porto, Portugal
APMTAC, 2014

3D numerical simulation of a Taylor drop rising in a vertical column

FJN Direito, JDP Araújo, JBLM Campos, JM Miranda

Centro de Estudos de Fenómenos de Transporte, Departamento de Engenharia Química, Faculdade de Engenharia, Universidade do Porto, Rua Dr. Roberto Frias, 4200-465 Porto, Portugal
email: deq11009@fe.up.pt, daraujo@fe.up.pt, jmc@fe.up.pt, jmiranda@fe.up.pt

ABSTRACT: Albeit the growing importance of alternative energy resources, petroleum will still have a central role in the next decades. In order to respond to the new challenges, there is an increasing need of economic (and technical) efficiency in enhanced oil recovery procedures, which demands a better understanding of the physical phenomena behind the rise of oil in a vertical pipe. In oil wells, one of the most important patterns is slug flow. Slug flow between a liquid and a gas phase has been the subject of an intensive study. However, there is still a lack of significant knowledge about liquid-liquid slug interactions, which are important as water comprises a huge amount of a well output. In order to obtain a further insight, two-liquid-phase slug flow was studied by computational fluid dynamics. Both 2D (axisymmetric) and 3D calculations were performed, simulating a single Taylor drop rising in a stagnant vertical column of a heavier liquid. Further numerical studies were performed concerning the coalescence of two drops. Drop shape and terminal velocity data was obtained. Furthermore, it was found that some conditions of interest for these studies show a 3D flow pattern, while others can be simplified to a 2D approach.

KEY-WORDS: Two-phase flow; Taylor drop; Vertical slug flow; Computational fluid dynamics.

1 INTRODUCTION

Despite the growing importance of renewable energy sources, petroleum industry still has a major role in global economy and industry [1]. In order to respond to the new challenges, there is an increasing need of economic and technical efficiency in enhanced oil recovery procedures. That need demands a better understanding of the physical phenomena behind the rise of oil in a vertical pipe from reservoirs.

In oil wells, one of the most important patterns is slug flow. Slug flow can also be found in nuclear industry, chemical reactors, or geothermal power facilities [2].

Liquid-gas slug flow has been the subject of intense study and literature publication. On the other hand, there is still a lack if significant knowledge about the slug flow concerning two liquids. In vertical tubes, such flow pattern occurs when most of the dispersed phase appears as large drops bullet-shaped and occupying most of the tube diameter – Taylor drops. By the passage of a (Taylor) drop, the heavier liquid is forced to flow in the narrow space between the drop and the wall, creating a thin annular film [2]. Depending on conditions, the continuous phase might also be disturbed on the rear of the drop. In some conditions a recirculation region can be observed [3].

Five dimensionless numbers can describe the phenomena of a single Taylor drop rising in a stagnant heavier liquid. The Froude number $Fr = V_T \Big/ \sqrt{\left(\Delta\rho g D/\rho_C\right)}$, includes the terminal velocity, V_T, and, therefore, is usually the output of numerical and experimental studies of slug flow – dependent variable. It also includes the densities of each phase, ρ_C (continuous phase) and ρ_D (dispersed phase) – notice that $\rho_C - \rho_D = \Delta\rho$. The D stands for the tube diameter. The remaining dimensionless groups are the Morton number $M = g\mu_C^4\Delta\rho \Big/ \left(\rho_C^2\sigma^3\right)$ the Eötvös number $Eo = \Delta\rho g D^2/\sigma$, the density ratio, ρ_D/ρ_C, and the viscosity ratio, μ_D/μ_C, between the two phases. On those groups, the σ stands for the interfacial tension between the two liquids and μ is the viscosity, with the subscripts standing for dispersed and continuous phases. Other important groups, Reynolds $Re = \rho_C V_T D/\mu$, and Inverse Viscosity Number $Nf = \sqrt{\rho_C \Delta\rho g D^3}\Big/\mu_C$, can be obtained by combining the other five.

Consider a flow where a continuous phase of heavier liquid has the presence of bubbles or drops. If the dispersed phase suffers a significant increase in its flow rate, those drops start to coalesce, eventually forming drops so large that become Taylor drops. Bannwart *et al* [4] observed such behaviour when studying oil-water flow.

Mandal *et al* [5] studied Taylor drops for several pairs of liquids, and several tube diameters in the lab. Their experimental set-up consisted of a stagnant heavier liquid and a rising drop of the lighter liquid. An adaptation of gas-liquid correlation was fit for a limited range of results. Different drop shapes were observed.

Hayashi *et al* [6] studied individual drop rising in stagnant liquid both in lab and by CFD. They observed several drop shapes. They also focused in developing a correlation for predicting terminal velocity (Froude number). They claim that the density ratio does not influence the Froude number. They also observed that when the continuous phase viscosity is much greater than the viscosity of the lighter liquid, the terminal velocity approaches the one predicted for gas-liquid systems. Furthermore, their correlation shows an upper limit of 0.35 for the Froude number, although no simulations or experiments were done close to such conditions. That limit is, however, of relevance because it is observed [7] in liquid-gas systems.

The first approach for a full study of slug flow is analysing the simple case of a single Taylor drop rising in a stagnant liquid (after acquiring stable shape and velocity – terminal velocity) in a vertical tube. The aim of the present work is to make such study by performing CFD simulations. A further step is then taken by simulating the coalescence of two drops. In this work all liquids have a Newtonian behaviour and both 2D and 3D simulations are performed. Simulations using 2D should be accurate provide the flow is axisymmetric. Initial studies suggested that, for certain conditions, the flow is not symmetric, and so 3D simulations must be employed.

2 CFD MODEL

The simulations presented in the current work (that concern two liquids) were performed using the commercial software Ansys Fluent (release 14), choosing its options of multiphase flow. It includes the volume of fluid (VOF) method as the interface capturing mathematical procedure [8]. This kind of technique requires the usage of an algorithm to reconstruct the interface between the two liquids. The geo-reconstruct was the option chosen. In previous works cited in literature [9], it has been used with good results. Furthermore, preliminary simulations were performed in order to confirm such choice. Geo-reconstruct proved, for the conditions chosen, to be the best option taking into consideration two important factors: spurious velocities and numerical dispersion. The pressure-velocity scheme was PISO. Previous work found PISO to yield a faster convergence. For pressure interpolation the choice was "PRESTO!", the momentum equation was solved by QUICK and the gradients of scalars were computed by using the Green-Gauss node-based method. Those choices had been proven before to work in the simulation of liquid-gas Taylor bubbles [9].

It was used the pressure-based solver and the surface tension model applied was the continuum surface force model. The simulations were performed with a variable time-step option and the Courant number maximum was defined as 0.25.

Three different meshes were used, one for 2D simulations (including coalescence) and two for the 3D simulations. For the 2D mesh cases, the flow is considered axisymmetric. This simplification provides a time-efficient way of performing the simulations. In particular, the mesh used consisted in 52 cells in the horizontal direction and 1144 in the vertical, matching a rectangle whose width is coincident with the real cylinder radius.

In opposition to the 2D approach, the 3D geometry does not consist of any symmetry or other simplification. Thus, it is a cylinder shaped object. In 3D, two meshes with different levels of refinement were used: the rough mesh consisted of about four hundred thousand elements while the fine mesh had about 3.8 million elements.

The initialization of single drop 2D simulation was performed by the creation of a drop made by two bodies: a quarter of circle for the drop nose and a rectangle for the remaining body. This procedure was based in previous know-how within the research group. The 3D simulations were initialized in an analogous fashion: a semi-sphere for the nose region and a cylinder for the remaining drop. Coalescence (performed only in 2D) simulations starting condition were made by a two-step procedure. First, a single drop simulation was performed. Then, drop shape and velocity field (in both phases) were copied to a position behind the original drop. This procedure leads to a two-drop initial set-up.

In all simulations a reference frame attached to the drop was used in order to reduce the necessary mesh/geometry size (in the vertical direction). The physical problem concerns a drop rising in a stagnant

continuous phase, while in the simulations, the drop is still while both the continuous phase and the wall move downwards. The speed at which they move matches the drop terminal velocity.

The terminal velocity is found by an iterative procedure where the moving wall and continuous phase speed are defined trying to match drop velocity.

3 RESULTS

An extensive study was performed to describe the flow of a single Taylor drop. Those results are discussed in the following sections. However some simulations will have a special emphasis. Those simulations are presented in Table 1. In all results presented in this work, the groups M and ρ_D/ρ_C, are kept constant. Therefore, Fr output is studied by changing *Eo* and the viscosity ratio.

It is important to state that in all simulations there was no small drop liberation nor drop disruption.

Table 1: List of relevant simulations.

Sim. id.	*Eo*	*M*	μ_D/μ_C	ρ_D/ρ_C
A	15.8	2.32×10^{-6}	4.09×10^{-2}	7.92×10^{-1}
B	22.0	2.32×10^{-6}	0.100	7.92×10^{-1}
C	30.0	2.32×10^{-6}	0.500	7.92×10^{-1}
D	30.0	2.32×10^{-6}	0.300	7.92×10^{-1}
E	30.0	2.32×10^{-6}	3.00	7.92×10^{-1}
F	22.0	2.32×10^{-6}	0.300	7.92×10^{-1}

3.1 Single drop in 2D

Several simulations were performed in the 2D approach. Some results are summarized in Figure 1, where density ratio and Morton number are kept constant, and compared with the correlation proposed by Hayashi *et al* [6]. The conditions are divided in three groups with different *Eo*. For the same viscosity ratio, a higher *Eo* means a higher *Fr*. Drop shapes are no different from those already found in literature [3,6]. However, it is still not possible to establish a pattern relating shapes and dimensionless groups. Simulations for low viscosity (thus not presented here) ratio yielded unexpected *Fr* values, even passing the 0.35 bound. Some of those simulations are the scope of the comparison in section 3.

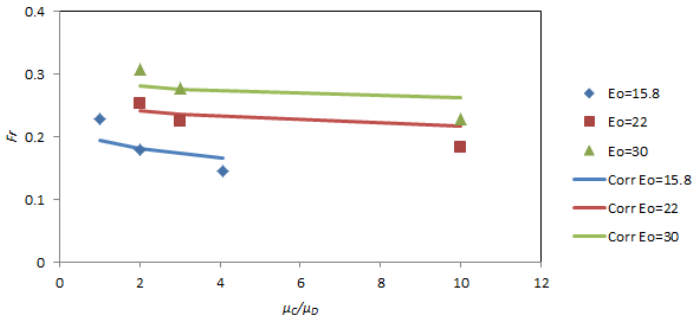

Figure 1: Froude number results (in 2D) for different *Eo*.

3.2 Single drop in 3D

Simulation B performed in 3D is presented in this section. The terminal velocity determined led to *Fr* = 0.267. Concerning the shape, a very important fact must be emphasized: it is not symmetrical, not only in shape but also in the liquid film - Figure 2. Moreover, shape of the bottom base is not stable in time suggesting an oscillation, fact still to be confirmed both by simulation and experiments. It was also suggested the possibility of a movement similar to rotation. No complete answer was found yet due to the difficulty in developing a reliable procedure.

Disturbance on the continuous phase is observed for about twice the tube diameter below the drop.

The radial pattern for the vertical velocity is depicted in Figure 3, where *z* is perpendicular to the axial coordinate. Two important facts are observable in the pattern near the nose. The first concerns the deviation of the minimum velocity. It was expected to find this minimum lying in the axis of the cylinder. The deviation suggests a slight deviation of the nose tip from the axis. In fact, further inspection of the

images acquired from Ansys Fluent confirmed such observation. It was also expected that the right and left regions (in the plane) would be symmetrical, but this is not observed (even though they have analogous shapes), as can be observed by visual inspection of Figure 2. The pattern on the film shows an increase of velocity when we move from the tube wall (where it is equal to V_T) and approach the vicinity of the interface.

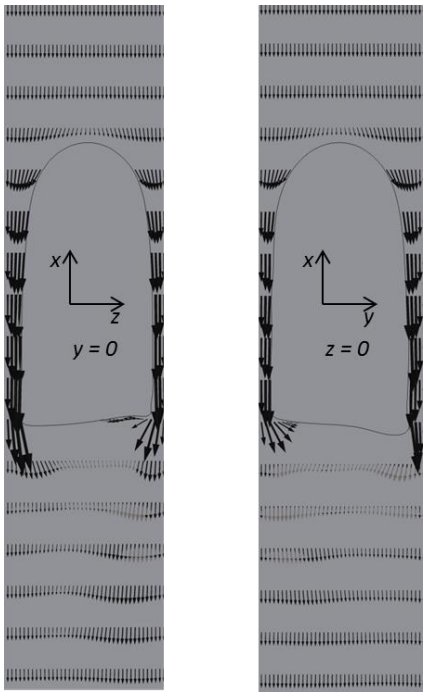

Figure 2: Velocity (drop frame) field for two perpendicular planes – Simulation E.

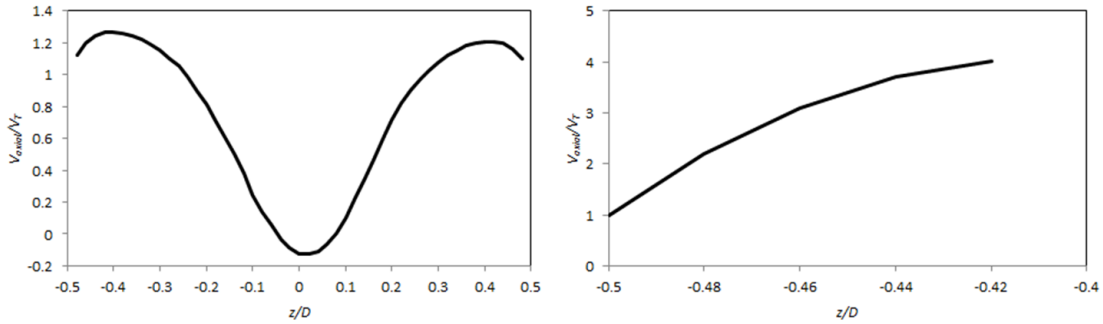

Figure 3: Velocity profile near the nose (left) and in the film (right).

3.3 Single drop: 2D vs 3D

Comparisons between 2D and 3D are made using both the rough and the fine meshes – Table 2. Further simulations were performed in the 3D fine mesh to assess the influence of the drop length. 3D simulations seem to approach an available correlation more than 2D simulations. However, it is also possible to observe that the length of the drop might also have influence. One possible explanation concerns the instability of the bottom of the drops. Further conclusion though, must rely on experimental observation. Furthermore, it is imperative to study the influence of drop length.

Table 2: Froude number comparison between 2D, 3D and correlation.

Sim. id.	Correlation in literature [6]	2D	3D in rough mesh	3D in fine mesh	3D in fine mesh – drop 80 % longer
A	0.216	0.432	0.234	0.220	-
B	0.267	0.479	0.304	0.280	0.269
C	0.294	0.429	-	0.357	0.312
D	0.297	0.454	-	0.322	-
E	0.276	0.277	0.278	-	-
F	0.263	0.411	-	-	-

3.4 Coalescence

Once simulation E was validated by comparison to an available correlation in literature, its data and set-up was the starting stage for a coalescence simulation (2D). From the position, shape and velocity fields of the first drop, a second one was placed below the first. The nose of the second drop was placed in a region where the continuous phase was still disturbed. On that region the downward speed of the continuous fluid is reduced. Thus, the second drop is accelerated towards the first one, as shown in Figure 4 (notice that velocities here, as throughout the entire text are relative to the main drop frame).

During this process, the nose position of the first drop remains unchanged. Further proof of the stability of such drop can be obtaining by observing the almost untouched flow in the liquid film. Both drop shapes are almost constant till moments before the coalescence. The first drop rear also shows little disturbance.

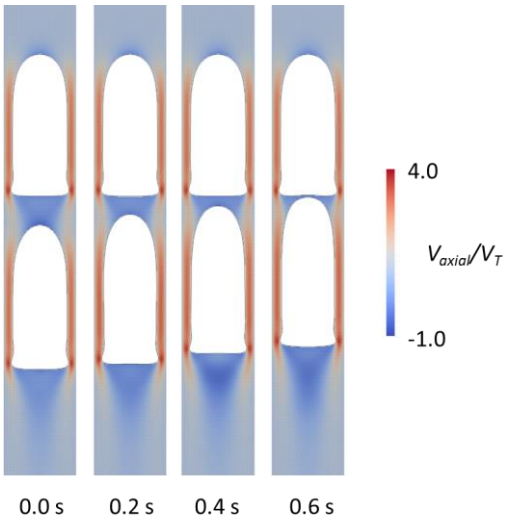

Figure 4: Coalescence of two drops.

4 CONCLUSIONS

A starting insight into the rising of Taylor drops in heavier stagnant liquids is reported, motivated by the importance slug flow has in several fields, but especially in oil wells.

A numerical procedure based on the Ansys Fluent package was implemented, in line with the strong and proven know-how already existing in the research group. Both 2D and 3D simulations were performed.

An intensive study was developed on the influence Eötvös number and viscosity ratio have on Froude number, using 2D axisymmetric geometry/mesh. Even though some trends can be observed, an unexpected behaviour for high values of Froude was detected, motivating the need of performing such studies in 3D. Drop shapes match those already present in literature.

Simulations performed in 3D proved to yield terminal velocities closer to those reported in literature. However, some questions arose. Further numerical and experimental work is required to understand the influence of the instabilities of the drop bottom, and the influence of drop length and its relation to the dimensionless groups. A full description of drop movement (including possible oscillation and rotation) is needed as well. For the conditions simulated, it was found that the flow around the drop is not symmetric.

After validation of a 2D single drop by comparison to literature, those conditions were successfully extended to a case where a second drop is added. The second drop, under the influence of the rear of the first drop accelerates, causing coalescence. During that approach, some interesting facts were observed: the first drop terminal velocity does not change; both drops experience very little shape modifications.

The paths to be taken are clearly very promising and will lead to a better understanding of the phenomena behind liquid-liquid slug flow.

ACKNOWLEDGMENTS

The authors gratefully acknowledge the financial support from the "Fundação para a Ciência e a Tecnologia" (FCT) through Ph.D. Grant SFRH/BD/79264/2011. POCTI (FEDER) also supported this work via CEFT.

REFERENCES

[1] J Sheng (2012). *Modern Chemical Enhanced Oil Recovery*, Elsevier Science & Technology.

[2] TSMM Santos (2007). *Hydrodynamics of Gas-Liquid Flows in Slug Flow Regime*, PhD Thesis, Universidade do Porto, Portugal.

[3] JDP Araújo, JM Miranda, AMFR Pinto, JBLM Campos, Wide-ranging survey on the laminar flow of individual Taylor bubbles rising through stagnant Newtonian liquids. *International Journal of Multiphase Flow* **43**:131–148.

[4] AC Bannwart, OMH Rodriguez, FE Trevisan, FF Vieira, CHM de Carvalho (2009). Experimental investigation on liquid–liquid–gas flow: Flow patterns and pressure-gradient. *Journal of Petroleum Science and Engineering* **65**(1–2):1–13.

[5] TK Mandal, G Das, PK Das (2007). Prediction of rise velocity of a liquid Taylor bubble in a vertical tube. *Physics of Fluids* **19**(12):128109.

[6] K Hayashi, R Kurimoto, A Tomiyama (2011). Terminal velocity of a Taylor drop in a vertical pipe. *International Journal of Multiphase Flow* **37**(3):241–251.

[7] R Clift, JR Grace, ME Weber (2005). *Bubbles, Drops and Particles*, Dover Publications Inc., New York.

[8] CW Hirt, BD Nichols (1981). Volume of fluid (VOF) method for the dynamics of free boundaries. *Journal of Computational Physics* **39**: 201–225.

[9] JDP Araújo, JM Miranda, JBLM Campos (2013). Simulation of slug flow systems under laminar regime: Hydrodynamics with individual and a pair of consecutive Taylor bubbles. *Journal of Petroleum Science and Engineering* **111**:1–14.

V Conferência Nacional de Mecânica dos Fluidos, Termodinâmica e Energia
MEFTE 2014, 11–12 Setembro 2014, Porto, Portugal
APMTAC, 2014

Hemodinâmica em modelos simplificados da bifurcação da artéria Carótida com estenose

DL Martins[1], JC Pires[1], AA Soares[2,3], L Morgado[2]

[1]Escola de Ciências e Tecnologia, Universidade de Trás-os-Montes e Alto Douro, Quinta de Prados, 5000-801 Vila Real, Portugal
[2]Departamento de Física, Escola de Ciências e Tecnologia, Universidade de Trás-os-Montes e Alto Douro, Quinta de Prados, 5000-801 Vila Real, Portugal
[3]INEGI, Faculdade de Engenharia, Universidade do Porto, Rua Dr Roberto Frias, 4200-465 Porto, Portugal
email: daniela_martins93@hotmail.com, joana_p_21@hotmail.com, asoares@utad.pt, lmorgado@utad.pt

RESUMO: Neste estudo são usados modelos geométricos simplificados da bifurcação da artéria Carótida com e sem estenose para investigar a correlação entre as estenoses e a distribuição das tensões de corte desenvolvidas nas paredes da artéria. Os modelos geométricos foram construídos a partir de imagens médicas 2D. Na obtenção das soluções numéricas das equações de Navier-Stokes considerou-se o escoamento do sangue em regime laminar e com comportamento newtoniano. São também apresentados os resultados da distribuição da velocidade e da pressão ao longo da artéria Carótida para as condições físicas e cinemáticas estudadas.

PALAVRAS-CHAVE: Artéria Carótida; Bifurcação; Estenose; Hemodinâmica; Tensões de corte.

1 INTRODUÇÃO

As doenças vasculares são uma das principais causas de morte nos países desenvolvidos. As bifurcações arteriais parecem estar associadas ao aparecimento deste tipo de doenças [1]. A hemodinâmica da artéria Carótida tem interesse especial pois na presença de estenoses pode causar perturbações cerebrais. Muitos dos estudos que têm sido realizados para caraterizar a hemodinâmica local e o seu papel no desenvolvimento precoce da aterosclerose nas artérias indicam que as regiões com risco de desenvolverem aterosclerose estão localizadas preferencialmente nas bifurcações, entroncamentos e regiões com curvaturas acentuadas. Estas regiões apresentam zonas de baixas tensões de corte nas paredes e com interrupção do escoamento *e.g.* [2]. Em contraste, as regiões a jusante das estenoses mais severas experimentam um ambiente biomecânico significativamente diferente quando comparado com vasos saudáveis, devido à presença de escoamentos de transição e turbulento. As tensões de corte nas paredes da estenose são geralmente elevadas, uma vez que a redução da área acelera o escoamento sobre a estenose. Este elevado valor das tensões de corte e a presença de turbulência podem danificar as células endoteliais [3] e provocar ruptura da placa [4]. Além disso, valores altos dos gradientes das tensões de corte nas paredes associados com um escoamento turbulento podem aumentar o transporte de massa para dentro da parede arterial proximal à estenose, o que pode enfraquecer a placa e torná-la vulnerável à ruptura [5]. O escoamento em modelos de estenoses tem vindo a ser estudado para diferentes números de Reynolds e diferentes constrições da área da seção transversal. O escoamento em regime estacionário é um problema mais fácil de resolver numericamente e ainda permite descrever o comportamento do fluxo sanguíneo e da pressão em torno das constrições de vasos sanguíneos em tubos arteriais *e.g.* [6].

O uso de modelos de dinâmica de fluidos computacional tornou-se uma das ferramentas muito eficaz para prever o campo de escoamento dentro bifurcação carotídea, e para a compreensão da relação entre a hemodinâmica local, e o início e progressão de patologias da parede vascular. A aplicação desta técnica a modelos de geometrias tridimensionais realistas de artérias obtidos da imagiologia clínica fornece uma avaliação precisa dos padrões e das tensões de corte em geometrias complexas [7,8].

No presente trabalho estuda-se o escoamento sanguíneo na bifurcação da carótida no sentido de investigar relações entre o desenvolvimento de aterosclerose e as regiões de recirculação. Procura-se também aprofundar o conhecimento da influência do grau de severidade das estenoses na hemodinâmica a partir dos modelos geométricos da artéria Carótida estudados.

2 EQUAÇÕES DE GOVERNO

Assume-se que o escoamento sanguíneo na bifurcação da artéria Carótida é governado pelas equações de Navier-Stokes para um escoamento, newtoniano, estacionário e incompressível em regime laminar. As equações de governo são a equação da continuidade

$$\vec{\nabla}\cdot\vec{v} = 0, \tag{1}$$

e a equação da quantidade de movimento

$$\rho\left(\vec{v}\cdot\vec{\nabla}\right)\vec{v} = -\vec{\nabla}\cdot p + \vec{\nabla}\cdot\tau, \tag{2}$$

onde ρ (kg/m^3) é a massa volúmica, p (Pa) a pressão estática, $\vec{v}$ (m/s) a velocidade e $\boldsymbol{\tau}$ (Pa) o tensor das tensões. Apesar de usarmos um modelo newtoniano para o sangue, em geral, é aceite que o sangue tem um comportamento não newtoniano (reofluidificante) sobretudo para valores baixos da taxa de deformação de corte menores do que 100 s^{-1} [9]. No entanto neste estudo, o sangue é considerado um fluido newtoniano, incompressível e isotérmico com propriedades constantes.

2.1 Geometria

As geometrias 3D da carótida sem e com estenoses foram construídas a partir de dados obtidos de imagens Doppler 2D para um paciente com a carótida estenosada, Figura 1. Das imagens 2D foram retiradas as dimensões usadas na reconstrução 3D da artéria [10].

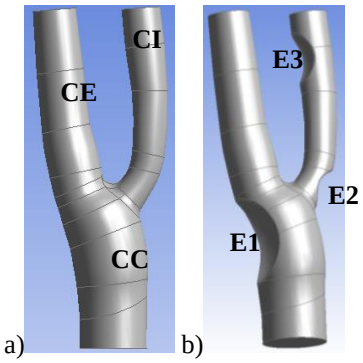

Figura 1: Modelos geométricos simplificados da Carótida estenosada a) sem estenose (SE) b) com estenoses E1, E2 e E3.

Depois de construída a geometria 3D da artéria carótida, foi selecionada uma malha que garante resultados independentes do refinamento desta. Testes realizados para malhas com diferentes refinamentos permitem concluir que se utilizaremos uma malha mais fina não obtemos diferenças maiores do que 3%.

Neste trabalho, o Fluent foi utilizado para simular nas condições do estudo a hemodinâmica na bifurcação da artéria Carótida Comum. Este programa tem sido utilizado com sucesso, num grande número de estudos, para simular problemas deste tipo. No programa, selecionou-se o esquema de diferenciação Upwind de segunda ordem para os temos convectivos e diferenciação central de segunda ordem para os termos difusivos. Para a interpolação da pressão recorreu-se ao esquema Standard. O acoplamento da pressão e da velocidade é feito usando o algoritmo SIMPLE (Semi-Implicit Method for Pressure Linked Equations). Para controlo das soluções usou-se o critério de convergência definido pelos resíduos relativos serem menores do que 10^{-11}.

2.2 Condições fronteira

Consideraram-se oito domínios computacionais. Os domínios computacionais são definidos pelas geometrias 3D estudadas; uma para a Carótida sem estenose e as outras sete para a combinação das três estenoses representadas na Figura 1. O escoamento ocorre ao longo da artéria Carótida Comum (CC) desde a entrada na artéria até às saídas nas ramificações, Carótida Externa (CE) e Carótida Interna (CI), ver Figura 1.

Para as propriedades do sangue considerou-se a massa volúmica 1050 kg/m^3 e a viscosidade dinâmica 0,00319 Pa·s.

Na simulação numérica do escoamento foram impostas as seguintes condições fronteira, para os modelos tridimensionais estudados a fim de obtermos as distribuições das velocidades, das pressões e das tensões de corte nas paredes da artéria.

Na entrada da Carótida Comum considerou-se o perfil da velocidade completamente desenvolvido de acordo com

$$v_z(r) = 2\bar{v}\left[1-\left(\frac{2r}{D}\right)^2\right] \tag{3}$$

Para a velocidade média na entrada $\bar{v}$ considerou-se 0,18 m/s o que correspondente ao número Reynolds e caudal 699 e 0,59 l/min, respectivamente. O diâmetro da artéria, *D*, na entrada é de 5,9 mm. A velocidade média usada neste estudo corresponde a uma das velocidades adquiridas pelo sangue na Carótida Comum durante cada um dos ciclos cardíacos.

Para a velocidade considerada o escoamento é sempre laminar. Na zona mais estreita da artéria sem estenose a velocidade máxima é de 0,44 m/s, o que corresponde a um número de Reynolds de 551.

Nas saídas considerou-se a condição *outflow* do *Fluent* com um caudal de 70% na CE de 30% na CI do caudal de entrada. Nas paredes considerou-se a condição normal de não deslizamento o que corresponde a impor uma velocidade nula junto das paredes.

3 RESULTADOS

Para as condições estudadas, escoamento laminar e estacionário, apresentamos as distribuições das velocidades, das pressões e das tensões de corte nas paredes (TCP) da Carótida. Os resultados no caso da Carótida estenosada são comparados com os resultados obtidos para o caso da Carótida sem estenose com objetivo de avaliarmos o efeito das estenoses na hemodinâmica.

3.1 Distribuição das velocidades

Na Figura 2, são apresentadas as distribuições das velocidades no plano medial da artéria para as geometrias 3D estudadas. O diagrama de cores varia do azul (velocidade nula) para o vermelho (velocidade máxima). Da comparação entre todos os casos verifica-se que a velocidade máxima de 0,59 m/s corre na presença da estenose E2, ver Figura 2c). Em todos os casos na presença de estenoses aparece uma região de baixas velocidades a jusante das estenoses que é propícia à formação de redemoinhos. Velocidades mais elevadas do ciclo cardíaco tenderão a aumentar estas regiões de recirculação tornando redemoinhos mais ativos. Também se observa que a localização da estenose E2 na entrada da CI dá origem a uma região com baixas velocidades mais extensa, no lado oposto à estenose, que se estende até à saída da CI.

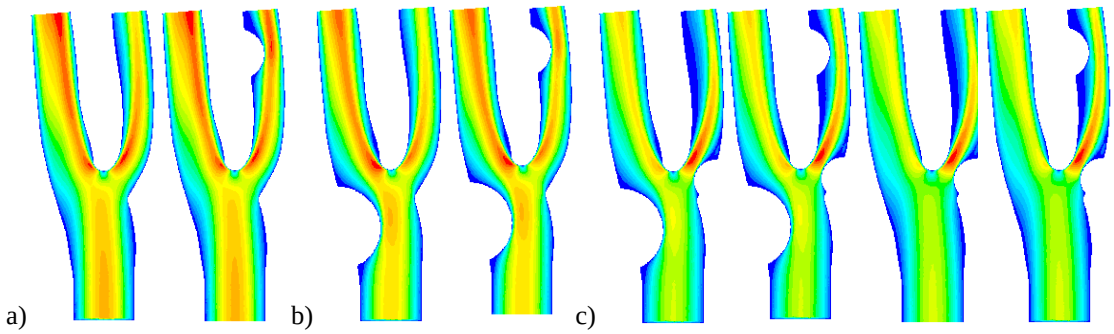

Figura 2: Distribuição das velocidades no plano medial da Carótida. a) sem estenose (SE) e estenose E3, velocidade máxima 0,44 m/s. b) com estenose E1 e E1-3, velocidade máxima 0,48 m/s. c) com estenose E1-2, E1-2-3, E2 e E2-3 velocidade máxima 0,59 m/s.

A Figura 3 mostra a média das velocidades calculada para os pontos internos para cada uma das geometrias 3D. No eixo horizontal é identificada cada uma das geometrias estudadas e estão organizadas da menor área para a maior área da superfície das estenoses. O caso da carótida sem estenose (SE) serve como termo de comparação. A área da superfície das estenoses cresce de 8,62 mm^2 para a estenose E2 até 60,19 mm^2 (E1-2-3) para a soma das áreas das estenoses E1, E2 e E3. Como era esperado a velocidade média cresceu sempre com o aumento da área das estenoses.

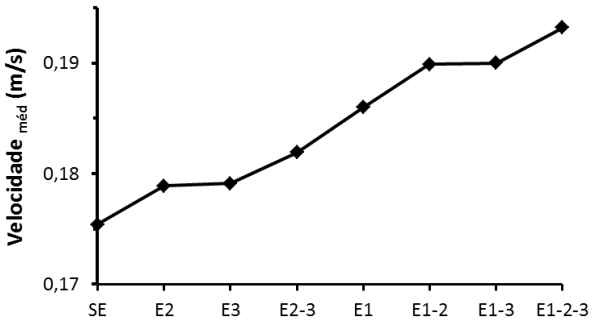

Figura 3: Velocidade média para o escoamento na Carótida sem estenose (SE) e com estenose (de E2 até E1-2-3).

3.2 Tensões de corte nas paredes da Carótida

A Figura 4a) mostra para o caso da artéria com as três estenoses E1, E2 e E3, a distribuição das tensões de corte nas paredes da artéria. A Figura 4b) mostra a distribuição das tensões de corte sobre a superfície das estenoses E1, E2 e E3. Os valores máximos das TCP ocorrem na bifurcação da Carótida e as superfícies das estenoses também são propícias a desenvolverem tensões de corte mais elevadas.

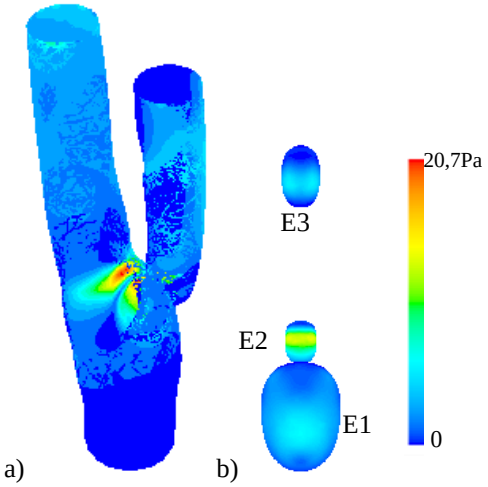

Figura 4: Tensões de corte nas paredes da Carótida com as três estenoses. a) Na parede da carótica e b) na superfície das estenoses E1, E2 e E3.

A Figura 5 mostra os valores máximos, mínimos e médios das TCP da artéria Carótida e das estenoses para os casos estudados. Da Figura 5a) conclui-se que os valores máximos ocorrem sempre fora da superfície das estenoses. Sabemos da Figura 4 que os valores máximos estão localizados na região da bifurcação. Na presença de estenoses, sempre que a estenose E2 está presente é na superfície desta que o valor máximo de tensão de corte ocorre. O menor máximo ocorre na estenose E1. Os casos SE e E3 apresentam valores máximos semelhantes e mais baixos que nos restantes casos. Da Figura 4b) conclui-se que os valores mínimos ocorrem sempre na superfície das estenoses. As estenoses E2 e E3 têm mínimos significativamente mais elevados do que nas restantes combinações de estenoses, E1, E2-3, E1-2, E1-3 e E1-2-3, o que poderá estar relacionado com a sua localização e grau de severidade das estenoses. O grau de severidade foi calculado, para cada estenose, pela relação entre a maior área transversal da estenose e a área correspondente da artéria sem estenose. Assim, obtemos para E1, E2 e E3 os valores 40%, 54% e 47%, respectivamente. Relativamente aos valores médios a Figura 5c) mostra um comportamento semelhante ao observado na Figura 5b).

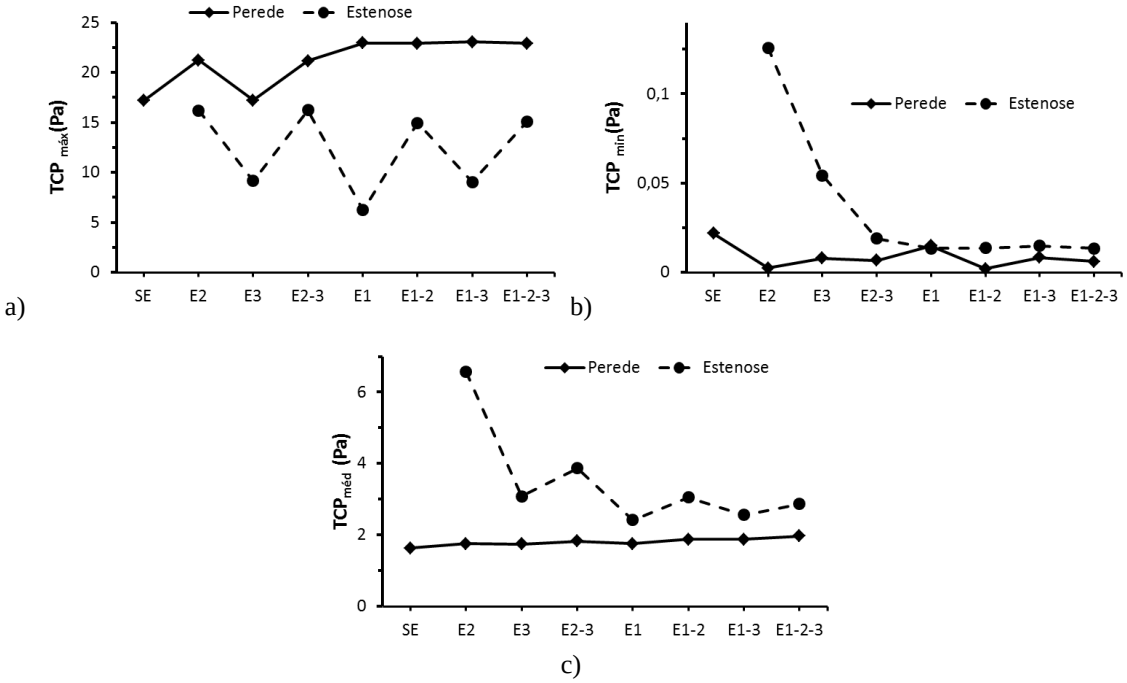

Figura 5: Tensões de corte nas paredes (TCP) da carótida e das estenoses. a) Valores máximos, b) valores mínimos e c) valores médios.

3.3 Distribuição da pressão ao longo da artéria Carótida

Os efeitos da presença de estenoses na diferença de pressão entre a entrada na artéria Carótida Comum (CC) e as saídas nas CE e CI estão representados na Figura 6. A diferença de pressão entre a entrada da CC e as saídas das CE e CI foi normalizada ao caso da Carótida sem estenose (SE) para evidenciar os efeitos da presença das estenoses. Para a diferença de pressão entre a entrada da CC e a saída da CI, a presença das estenoses resulta num aumento da diferença de pressão relativamente ao caso SE. Este comportamento não é observado para a diferença de pressão no ramo da CE, o que pode ser justificado pelo facto das estenoses E2 e E3 estarem localizadas na CI.

Com exceção dos casos E1 e E1-2 para todos os outros casos verifica-se uma ligeira diminuição na diferença de pressão relativamente ao caso SE. A presença da estenose na Carótida Comum tem influência semelhante na diferença de pressão entre a entrada da Carótida Comum e as saídas em ambas a ramificações, CE e CI.

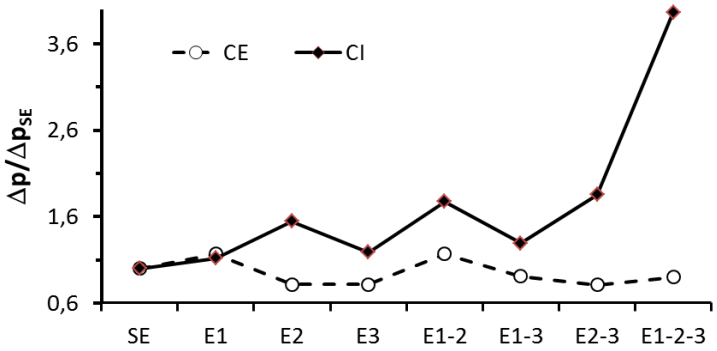

Figura 6: Diferença de pressão entre a entrada da Carótida Comum (CC) e as saídas das Ramificações (CE e CI) normalizada ao caso da Carótida sem estenose (SE).

4 CONCLUSÕES

Neste trabalho estudamos os efeitos da presença de estenoses na hemodinâmica da bifurcação da artéria Carótida Comum. A presença de estenoses revelou alterar significativamente o fluxo sanguino. Inferiu-se que a distribuição da velocidade e pressão ao longo da artéria Carótida sofre alterações significativas dependendo da localização da estenose, do número/área de estenose e grau de severidade.

A presença de estenose, E1, na Carótida Comum tem influência semelhante nas diferenças de pressão entre a entrada da Carótida Comum e a saídas em ambas a ramificações. As maiores diferenças verificadas para às tensões de corte nas paredes ocorrem nos valores mínimos de TCP que são significativamente maiores nos casos das estenoses E2 e E3.

Quanto às diferenças de pressão verifica-se que estas são maiores na Carótida Interna e crescem com o número de estenoses comparativamente com o que ocorre na Carótida Externa, uma vez que as estenoses se localizam na Carótida Interna.

REFERÊNCIAS

[1] DN Ku, DP Giddens, CK Zarins, S Glagov (1985). Pulsatile flow and atherosclerosis in the human carotid bifurcation. Positive correlation between plaque location and low oscillating shear stress. *Arteriosclerosis, Thrombosis, and Vascular Biology* **5**(3):293–302.

[2] S Glagov, C Zarins, DP Giddens, DN Ku (1988). Hemodynamics and atherosclerosis. Insights and perspectives gained from studies of human arteries. *Archives of Pathology & Laboratory Medicine* **112**:1018–1031.

[3] JD Hellums (1977). The resistance to oxygen transport in the capillaries relative to that in the surrounding tissue. *Microvascular Research* **13**:131–136.

[4] SD Gertz, WC Roberts (1990). Hemodynamic shear force in rupture of coronary arterial atherosclerotic plaques. *American Journal of Cardiology* **66**:1368–1372.

[5] N DePaola, MA Gimbrone Jr, PF Davies, CF Dewey Jr (1992). Vascular endothelium responds to fluid shear stress gradients. *Arteriosclerosis, Thrombosis, and Vascular Biology* **12**:1254–1257.

[6] LH Back, YI Cho, DW Crawford, RF Cuffel (1984). Effect of mild atherosclerosis on flow resistance in a coronary artery casting of man. *Journal of Biomechanical Engineering* **106**:48–53.

[7] R Botnar, G Rappitsch, MB Scheidegger, D Liepsch, K Perktold, P Boesiger (2000). Hemodynamics in the carotid artery bifurcation: a comparison between numerical simulations and in vitro MRI measurements. *Journal of Biomechanics* **33**(2):137–144.

[8] Y Hoi, BA Wasserman, EG Lakatta, DA Steinman (2010). Carotid bifurcation hemodynamics in older adults: effect of measured versus assumed flow waveform. *Journal of Biomechanical Engineering* **132**(7):071006.

[9] G Zhang, M Zhang, W Yang, X Zhu, Q Hu (2008). Effects of non-Newtonian fluid on centrifugal blood pump performance. *International Communications in Heat and Mass Transfer* **35**(5):613–617.

[10] LC Sousa, CF Castro, CC António, JMRS Tavares, AMF Santos, RM Santos, P Castro, E Azevedo (2014). Simulated hemodynamics in human carotid bifurcation based on Doppler ultrasound data. *International Journal of Clinical Neurosciences and Mental Health* **1**(Suppl 1):S15.

V Conferência Nacional de Mecânica dos Fluidos, Termodinâmica e Energia
MEFTE 2014, 11–12 Setembro 2014, Porto, Portugal
APMTAC, 2014

Flow topology across the turbulent/non-turbulent interface: the viscous superlayer and turbulent sublayer

R Jaulino, RR Taveira, CB da Silva

LAETA, IDMEC, Instituto Superior Técnico, Universidade de Lisboa, Av. Rovisco Pais 1, 1049-001 Lisboa, Portugal
email: rui_jaulino@hotmail.com, Rodrigo.Taveira@ist.utl.pt, carlos.silva@ist.utl.pt

ABSTRACT: The turbulent/non-turbulent interface (TNTI) is the thin interface layer that separates the flow filed into a turbulent (T) and a non-turbulent (NT) or irrotational flow regions, respectively, and exists in free shear flows such as mixing layers, wakes, jets, and also in boundary layers [1].

An interesting issue in this context consists in the mechanisms of vorticity generation and evolution of the flow topology as the fluid particles from the NT region cross the TNTI into the T region, in a process described as turbulent entrainment [2]. The enstrophy generation across the TNTI was analysed in previous experimental [3] and numerical works [4], while the study of the flow topology in terms of the 2nd and 3rd invariants of the velocity gradient tensor (Q and R) in the TNTI was studied in [5]. DNS of turbulent planar jets showed that the statistics of Q and R already display the classical 'teardrop' shape in a distance of roughly one Taylor scale from the start of the TNTI i.e. it takes the flow only a length scale of $\delta_\omega \sim \lambda$ to be fully formed as the flow particles from the NT enter into the T region. However the details of the formation of the 'teardrop' shape remain largely ignored.

In the present work DNS of shear free turbulence at $\mathrm{Re}_\lambda \approx 115$ are used to study in detail the flow topology inside the TNTI layer, where this layer is separated into its two sub-regions: the viscous superlayer (VSL) with thickness δ_ν where enstrophy diffusion dominates, and the turbulent sub-layer (TSL) with thickness δ_ω dominated by the enstrophy production [1].

Figures 1(a) and 1(b) show conditional mean profiles, as function of the distance from the TNTI (located at $yI = 0$) for the enstrophy, and enstrophy production and diffusion, respectively for the present DNS. Several letters are used to label several stations of locations with the TNTI. The VSL extends from A to C while the TSL can be seen to lay between D to F. In agreement with reference [1] in the present flow $\delta_\omega \sim \delta_\nu \sim \eta$, because at this stage the flow structures are largely formed by 'worms'. The mean trajectory of R, Q (Figure 1(c)) shows the existence of an increasing tendency for the generation of a sheet topology as the flow evolves inside the VSL, followed by an increasing predominance of vortex stretching and formation of tube structures as the flow evolves in the TSL.

Figures 2 and 3 show the evolution of the PDFs of (R , Q) inside the VSL and TSL, respectively. As can be seen the VSL is predominantly responsible for the formation of the 'teardrop' shape in the 4th quadrant (associated with a predominance of sheet structures), while the TSL is responsible for the formation of the 'teardrop' shape in the 2nd quadrant (associated with a predominance of vortex stretching versus vortex compression). In this flow, where the thickness of the TSL is $\delta_\omega \sim \eta$ the 'teardrop' shape' forms in a much shorter distance than in a jet needing only one Kolmogorov micro-scale to form completely.

KEY-WORDS: Turbulent topology; Jets; Entrainment.

RESULTS

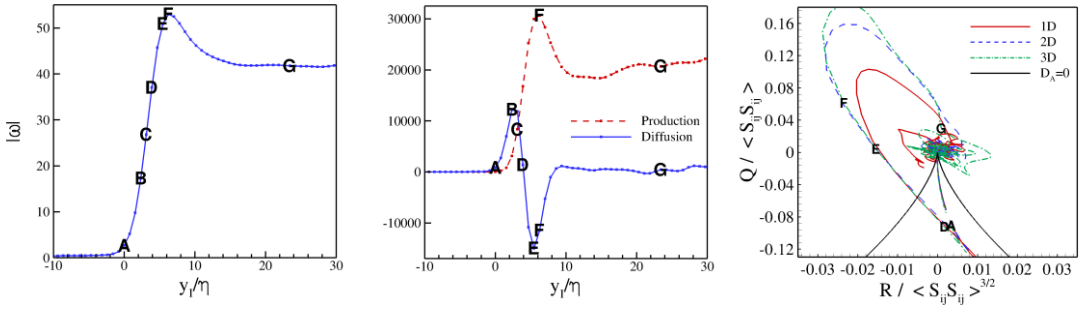

(a) (b) (c)

Figure 1: Mean conditional profiles (as function of the distance from the TNTI – located at $yI = 0$) of (a) enstrophy and (b) enstrophy production and diffusion near the turbulent/non- turbulent interface (TNTI), (c) trajectory of the mean values of R and Q across the TNTI.

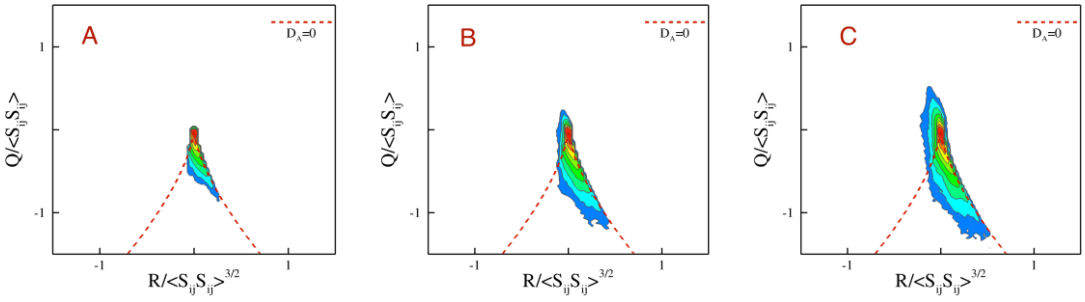

(a) (b) (c)

Figure 2: Joint probability density function of R, Q across the viscous-superlayer region in the flow: (a) start of the viscous superlayer, (b) point of maximum mean enstrophy diffusion, (c) end of the viscous superlayer.

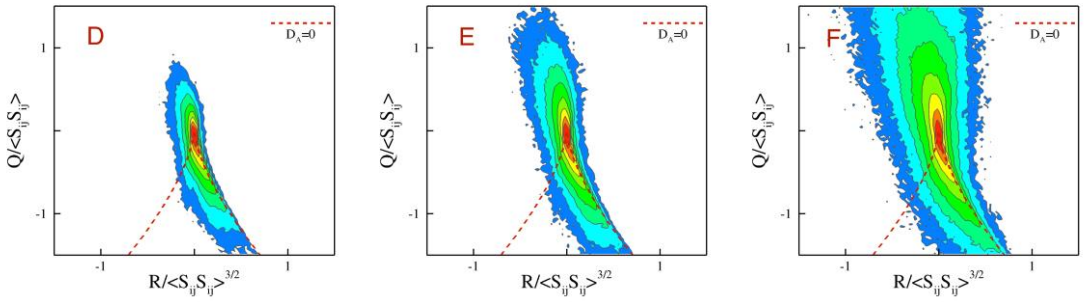

(a) (b) (c)

Figure 3: Joint probability density function of R, Q across the turbulent sublayer region in the flow: (a) point of zero diffusion, (b) point of minimum diffusion, (c) point of maximum enstrophy (peak).

REFERENCES

[1] CB da Silva, JCR Hunt, I Eames, and J Westerweel (2014). Interfacial layers between regions of different turbulent intensity. *Annual Review of Fluid Mechanics* **46**:567–590.

[2] J Westerweel, C Fukushima, JM Pedersen, JCR Hunt (2009). Momentum and scalar transport at the turbulent/non-turbulent interface of a jet. *Journal of Fluid Mechanics* **631**:199–230.

[3] M Holzner, A Liberzon, N Nikitin, W Kinzelbach, A Tsinober (2007). Small-scale aspects of flows in proximity of the turbulent/nonturbulent interface. *Physics of Fluids* **19**:071702.

[4] RR Taveira, J Diogo, D Lopes, CB da Silva (2013). Lagrangian statistics across the turbulent-nonturbulent interface in a turbulent plane jet interface. *Physical Review E* **88**:043001.

[5] CB da Silva, JCF Pereira (2008). Invariants of the velocity-gradient, rate-of-strain, and rate-of-rotation tensors across the turbulent/nonturbulent interface in jets. *Physics of Fluids* **20**: 055101.

Author Index

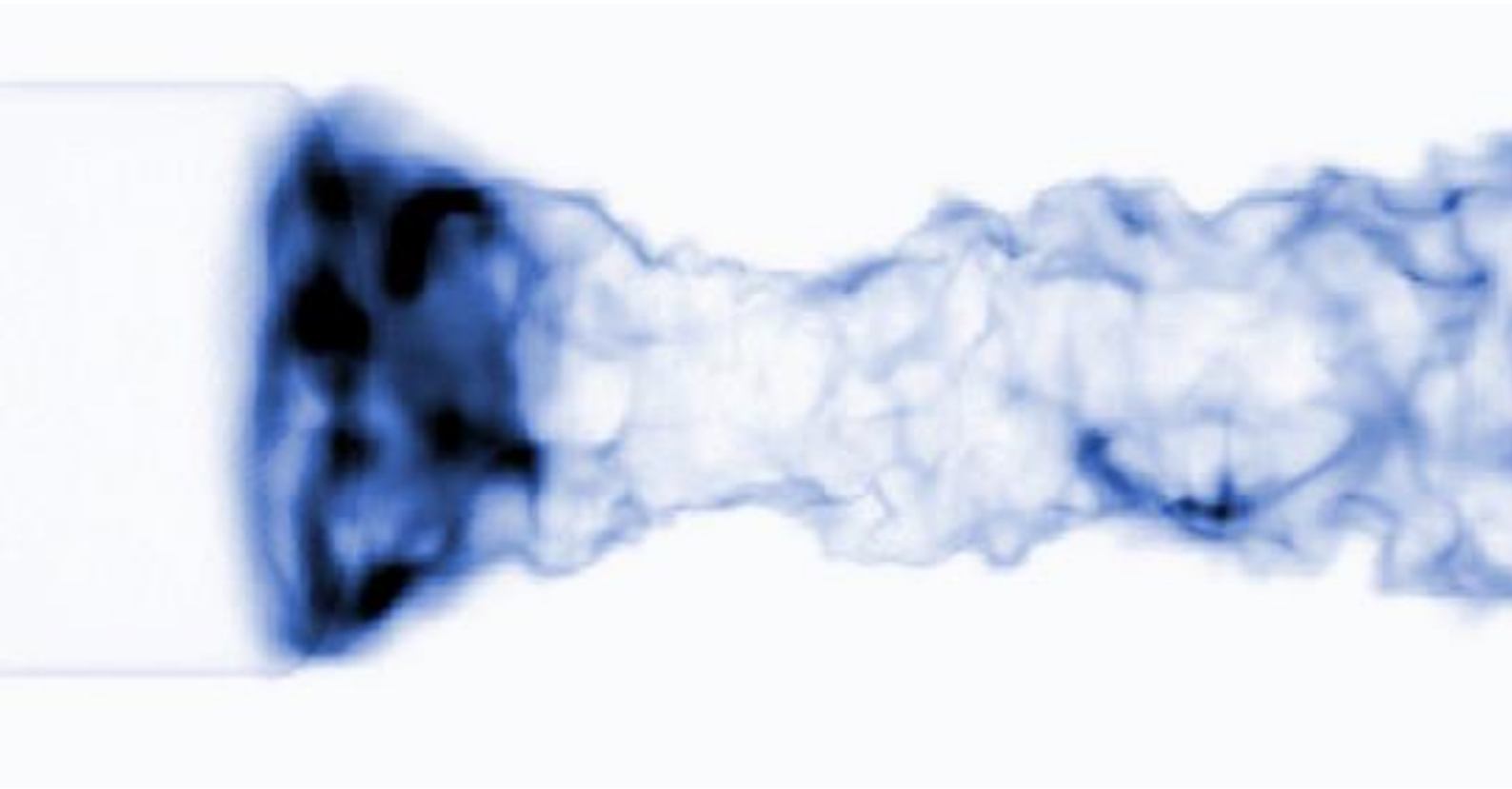

Cover image: Volume rendered image of a large eddy simulation of a non-premixed swirl flame[(*)].
[(*)]O Stein, AM Kempf, J Janicka (2007). LES of the Sydney swirl flame series: An initial investigation of the fluid dynamics. *Combust Sci Tech* **179**:173-189.